W. Richard Webb
William E. Brant
Nancy M. Major

FUNDAMENTALS OF

Body CT

Fourth Edition

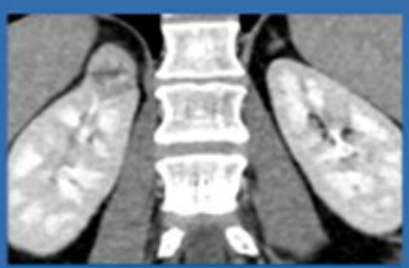

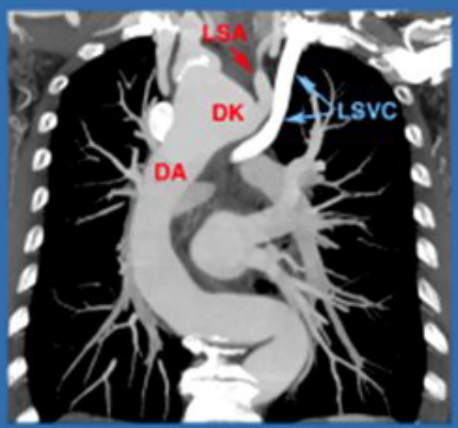

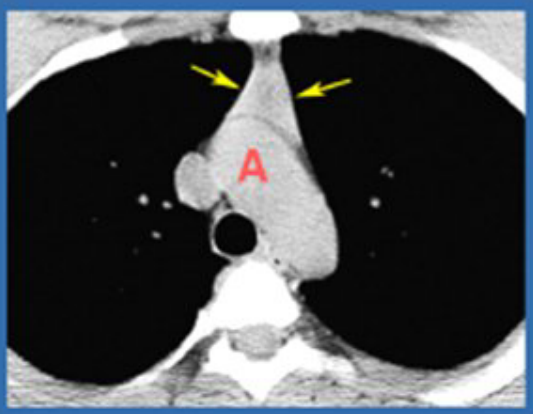

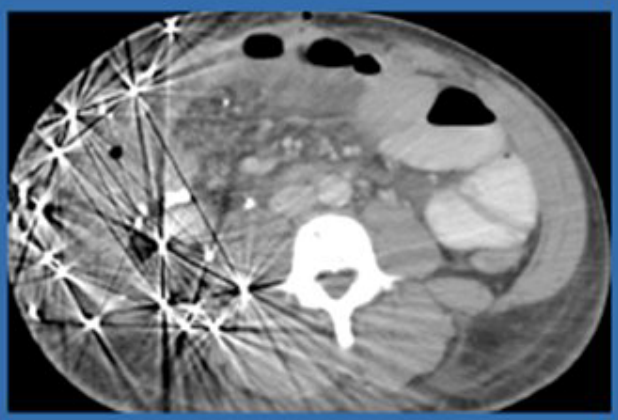

ELSEVIER
SAUNDERS

FUNDAMENTALS OF BODY CT

Fourth Edition

W. Richard Webb, MD
Chief, Thoracic Imaging
Professor Emeritus of Radiology and Biomedical Imaging
Emeritus Member, Haile Debas Academy of Medical Educators
University of California, San Francisco
San Francisco, California

William E. Brant, MD, FACR
Professor Emeritus
Department of Radiology and Medical Imaging
University of Virginia Health System
Charlottesville, Virginia

Nancy M. Major, MD
Musculoskeletal Radiologist
Professor of Radiology
Stony Brook University Hospital
Stony Brook, New York
Mainline Diagnostic Imaging
Bryn Mawr, Pennsylvania

ELSEVIER
SAUNDERS

ELSEVIER
SAUNDERS

1600 John F. Kennedy Blvd.
Ste 1800
Philadelphia, PA 19103-2899

FUNDAMENTALS OF BODY CT, Fourth Edition ISBN: 978-0-323-22146-7

Library of Congress Cataloging-in-Publication Data

Webb, W. Richard (Wayne Richard), 1945- author.
Fundamentals of body CT / W. Richard Webb, William E. Brant, Nancy M. Major. -- Fourth edition.
p. ; cm.
Includes bibliographical references and index.
ISBN 978-0-323-22146-7 (paperback : alk. paper)
I. Brant, William E., author. II. Major, Nancy M., author. III. Title.
[DNLM: 1. Tomography, X-Ray Computed. WN 206]
RC78.7.T6
616.07'572--dc23 2014012926

Content Strategist: Helene Caprari
Content Development Specialist: Kelly McGowan
Publishing Services Manager: Patricia Tannian
Senior Project Manager: Sharon Corell
Manager, Art and Design: Steven Stave

Printed in China

Last digit is the print number: 9 8 7 6 5 4 3 2 1

To Jack and Cole, my grandsons.
They understand the value of fundamentals.
W.R.W.

To my wife and true companion, Barbara.
In memory of my daughter Rachel.
To our children and their spouses and our ten grandchildren: Evan, Finley, Sophia, Katie, Josie, Danielle, Dylan, Grayson, Amelia, and Noah.
W.E.B.

To Kenneth…it was meant to be….
N.M.M.

PREFACE

Despite the fact that we concentrate on the "fundamentals" in this book, the fundamentals keep changing along with advances in CT techniques and our improved understanding of various diseases. This new edition gives us the chance to update important topics and add new material, including a number of new, high-quality images. That is what we have attempted to do, without significantly increasing the size of the book or making it less accessible as a teaching tool.

The half-dozen or so years since the third edition was published have seen continued advances in helical CT techniques. In this edition, we review the various spiral/helical CT protocols currently used in clinical practice for the diagnosis of chest, abdominal, and musculoskeletal abnormalities. We have expanded discussions of high-resolution CT, lung nodule assessment and lung cancer screening, CT pulmonary embolism diagnosis, CT enterography, CT enteroclysis, CT colonography, and optimizing CT techniques in musculoskeletal diagnosis.

New topics, discussions of new diseases (too numerous to mention here), and new images have been added to all chapters, including updated descriptions and illustrations of normal anatomy and incidental findings. Disease classifications, including those for pulmonary adenocarcinoma, diffuse lung diseases, and pancreatic lesions, have been updated where appropriate.

We hope you enjoy and profit from our efforts.

W. Richard Webb
William E. Brant
Nancy M. Major

Preface to the First Edition

Instead of writing a text intended to record everything that is known about body CT or even everything that we know about body CT, we have attempted to write one that teaches how to perform and read body CT scans. In doing this, we have tried to limit ourselves to discussing what is key to understanding body CT from a practical clinical standpoint—the key anatomy, the key concepts, the key diseases, and the key controversies. We have done this at the risk of leaving a few things out, but it isn't necessary to read about everything when you are first learning a subject. In other words, *Fundamentals of Body CT* is not intended to provide more than the best CT texts on the market do, but rather less, with a different emphasis, and in a more manageable package.

Each of us has written a different part of this book, obviously depending on our areas of expertise. Since each of us teaches in a slightly different way, each of the three sections of the book—the thorax, the abdomen, and the musculoskeletal system—is somewhat different in approach. We hope that by preserving our individual styles we have made the book more interesting to read, and for us, it certainly made this book easier to write.

FUNDAMENTALS OF BODY CT

Fourth Edition

ELSEVIER
SAUNDERS

CHAPTER 1

INTRODUCTION TO CT OF THE THORAX: CHEST CT TECHNIQUES

W. Richard Webb

Spiral or helical computed tomography (CT) allows the entire chest to be easily imaged during a single breath hold, with volumetric acquisition and exact registration or overlapping of slices. Two- and three-dimensional reformations may be performed if desired. Because scanning is rapid, contrast agents can be injected quickly, excellent vascular opacification can be achieved, and reduced volumes of contrast agent can be used.

SPIRAL CT IN CHEST DIAGNOSIS

Multiple-detector CT (MDCT) scanners have multiple parallel rows (e.g., 64, 16, or 4) of x-ray detectors, although the number varies with the machine. Generally speaking, MDCT scanners with fewer rows (e.g., 16 or 4) are being replaced with scanners having more rows (e.g., 64), but this is an expensive and, therefore, gradual process.

With MDCT, each of the detector rows records data independently as the gantry rotates; consequently, a volume of the patient is imaged with each gantry rotation. For example, the detector rows in one 64-detector scanner are 0.625 mm in width, and the multiple scanner rows add up to 40 mm (0.625 mm × 64). The term *pitch* refers to the table excursion during a complete gantry rotation divided by the width of all the detectors used (e.g., detector width × number of detector rows). With MDCT, pitch usually ranges from 1 to 2. The higher the pitch, the faster the scan is, but images are generally noisier, spatial resolution is reduced somewhat, and the effective slice thickness (the thickness of the patient that is actually imaged) is increased. Gantry rotation time is usually about 0.5 seconds.

The formula relating scan parameters for MDCT is shown in Fig. 1-1. Assuming a scan volume (patient length from the lung apices to bases) of 30 cm (300 mm), which is generally sufficient to image the chest, a 64-detector scanner with a detector width of 0.625 mm, pitch of 1.5, and gantry rotation time of 0.5 seconds, the total scan duration would be 2.5 seconds. This easily allows imaging of the entire chest during a single breath hold. For MDCT scanners with fewer detector rows (e.g., 16 or 4), the scan duration is longer, but scanning during a single breath hold is still achievable in cooperative patients. For example, with a four-detector-row scanner and a detector width of 1.25, the scan time for a thoracic CT would be 20 seconds. If the patient is dyspneic or uncooperative, respiratory motion may occur during the scan, with resulting degradation of image quality.

SPIRAL CHEST CT: GENERAL PRINCIPLES

The specific protocols used for chest CT depend on the scanner used, the scanner manufacturer, and the reason for the study. However, several general principles apply to all chest scans (Table 1-1).

Scan Levels

Chest CT is usually obtained from a level just above the lung apices (near the suprasternal notch) to the level of the posterior costophrenic angles; these scans also encompass the diaphragm and the upper abdomen. The distance (or volume) needed to cover the thorax is determined by a preliminary projection scan (e.g., "scout view") and is usually about 25 to 30 cm.

Patient Position

Routinely, patients are scanned supine. Prone scans may be obtained for high-resolution CT

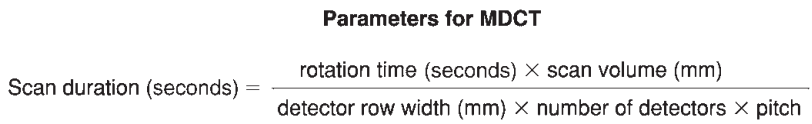

FIGURE 1-1 ■ Parameters for multidetector computed tomography (MDCT).

TABLE 1-1 Chest CT: General Principles

Scan levels	Lung apices to the posterior costophrenic angles
Patient position	Supine; prone scans sometimes used for diagnosis of lung disease or pleural effusions
Lung volume	Full inspiration, single breath hold; expiratory scans sometimes used to diagnose air trapping
Gantry rotation time	Approximately 0.5 s in most instances
Scan duration	Approximately 2.5 s for the thorax using MDCT and fast scanning
Detector width	The thinnest detectors (e.g., 0.625 mm) are typically used for image acquisition
Pitch (table excursion)	Depends on tolerable image noise; increased if noise is OK, decreased if there is a desire for high resolution
Reconstruction algorithm	High-resolution algorithm used for most studies; standard or soft-tissue algorithm usually used for vascular studies
Two- or three-dimensional reconstructions	Not routine; occasionally useful for lung, airway, or vascular studies
Contrast agents	Intravenous contrast injection in some cases; oral contrast agents only for gastrointestinal abnormalities

(HRCT) or to assess movement of pleural fluid collections. The patient may also be positioned prone for biopsy of posterior lung lesions or drainage of pleural fluid collections.

Lung Volume

Scans are routinely obtained after a full inspiration (i.e., at total lung capacity) and during suspended respiration. Post-expiratory scans may be performed in some cases (particularly on HRCT) to assess air trapping.

Gantry Rotation Time

A rapid gantry rotation time is used to reduce the scan time. Times are usually about 0.5 seconds.

Slice Thickness and Pitch (Table Excursion)

Usually, scan data are acquired using the thinnest detector width, and the slice thickness used for scan interpretation is determined by the indication for the scan. For example, if data are recorded using 0.625-mm detectors, slices can be reconstructed at any thickness from 0.625 to 5 mm for viewing. Thinner slices are required for some specific indications, whereas thicker slices may be appropriate for other studies, are quicker to interpret, and do not occupy as much memory when they are stored.

Most chest scans are reconstructed with a thickness of 1 to 1.25 mm. When viewing a study reconstructed with 2.5- or 5-mm-thick slices, if the scan data were collected using thinner detectors and if the scan data are still available (data are usually preserved on the scanner disk for a day or two), thinner slices can be reconstructed at a later time.

Keep in mind that with the spiral technique, the actual thickness of the slice viewed (i.e., "effective slice thickness") may be greater than the slice thickness selected (e.g., 1.25 mm), depending on the pitch or table excursion during gantry rotation; the greater the pitch, the greater the effective slice thickness. Thus, there is a trade-off; with a higher pitch, the study is quicker, but the scans are not quite as good.

Usually, slices are reconstructed at an interval equal to the slice thickness (e.g., 1.25 mm) to provide a volumetric data set. On occasion, scans are reconstructed at overlapping levels (e.g., 1.25-mm slices reconstructed at 0.625-mm intervals), although this is not generally necessary.

Scan Duration

MDCT of the chest can be easily obtained during a single breath hold, generally avoiding respiratory motion artifacts, except in very dyspneic or uncooperative patients. However, if thin slices, high resolution, or limited table excursion is desired, the scan will take longer to obtain and artifacts resulting from respiratory motion or cardiac pulsation are more likely to occur.

Reconstruction Algorithm

Once the scans have been performed, the scan data are reconstructed using an algorithm that determines some characteristics of the resulting

image. For routine chest imaging, a high-resolution algorithm is often used to optimize detail, but this makes the image somewhat grainy in appearance.

A standard or soft-tissue algorithm, which produces a smoother image, is better for assessing thoracic vascular structures (e.g., studies performed for diagnosis of pulmonary embolism, aneurysm, or aortic dissection) but is not optimal for other chest imaging. This algorithm is often used for abdominal imaging.

Two- and Three-Dimensional Reconstruction

Because scan data are acquired continuously and volumetrically using spiral CT, scans may be reconstructed in any plane desired, if appropriate workstations are available. A variety of display techniques have been used for imaging the thorax. These include multiplanar reconstructions, three-dimensional shaded surface display or volume rendering from an external perspective, or shaded surface or volume rendering from an internal (i.e., endoluminal) perspective, also known as virtual bronchoscopy.

Multiplanar, two-dimensional reconstructions offer the advantage of being quickly performed and are sufficient for diagnosis in most cases in which a reformation is considered desirable. Subsequent chapters provide a number of examples of two-dimensional reconstructions. Three-dimensional techniques, such as shaded surface display and volume rendering, can be valuable in selected cases, but they are time-consuming and require considerable operator experience. These techniques are not commonly used in clinical chest imaging, with the exception of virtual bronchoscopy or airway imaging and specialized vascular imaging.

Maximum- or minimum-intensity projection images representing a slab of three-dimensional data reconstructed from a volumetric data set may sometimes be useful in imaging pulmonary, airway, or vascular abnormalities.

Window Settings

For chest CT, scans must be viewed using at least three different window settings. Scans are usually viewed using a workstation having preset windows available. Presets used when reading chest CT are generally termed "lung," "soft-tissue" (or "mediastinal"), and "bone" windows, names that also describe their primary use. Often, these preset windows are adjusted by the viewer during scan interpretation to optimize the visibility of certain structures or abnormalities of interest.

Lung windows typically have a window mean of approximately –600 to –700 HU (Hounsfield units) and a window width of 1000 to 1500 HU. Lung windows best demonstrate lung anatomy and pathology, contrasting soft-tissue structures with surrounding air-filled lung parenchyma.

Mediastinal or *soft-tissue windows* (window mean, 20 to 40 HU; width, 450 to 500 HU) demonstrate soft-tissue anatomy in the mediastinum and in other areas of the thorax, allowing the differentiation of fat, fluid, tissue, calcium, and contrast-opacified vessels. These windows is also of value in providing information about consolidated lung, the hila, pleural disease, and structures of the chest wall. Subsequent chapters discuss more specific uses of these two windows. In the assessment of vascular structures (e.g., for pulmonary embolism or dissection diagnosis), a wider window or higher window mean than that used for a routine mediastinal window is often selected by the radiologist to see better within the dense contrast column.

Bone windows typically have a window mean of approximately 300 to 500 HU and a window width of 2000 HU. They best demonstrate skeletal structures or very dense objects. This window is sometimes valuable in looking at densely opacified vascular structures.

SPIRAL CHEST CT: PROTOCOLS

In most patients, chest CT is performed using a routine protocol. This technique is designed to provide useful information about the lung, mediastinum, hila, pleura, and chest wall. It is valuable in the diagnosis of a variety of diseases and types of abnormalities. Modified CT techniques are used in specific clinical settings or to look for specific abnormalities (e.g., pulmonary embolism, aortic dissection, and diffuse lung disease). Subsequent chapters provide detailed reviews of some specific protocols.

For current scanners with a large number of detector rows (e.g., 64), protocols for evaluation of different sorts of thoracic abnormalities have become more alike, since scanning of thin slices and with excellent contrast opacification can easily be performed during a single breath hold, regardless of why the scan is being done. A general understanding of the principles involved in obtaining CT for specific indications is much more important than knowing detailed specific protocols, because these vary with different scanners and manufacturers, and among different institutions.

Use of Contrast Agents

Chest CT can be performed with or without the administration of an intravenous contrast agent,

depending on the indication for the study. Scans obtained to rule out pulmonary metastases or to assess lung disease generally do not require contrast. Contrast should be used in patients with suspected hilar, mediastinal, or pleural abnormalities and in patients with possible vascular abnormalities. If the indication for a scan is uncertain, use of contrast is generally appropriate.

With MDCT, injection of contrast at 3 to 5 mL/second 10 to 30 seconds before scanning begins and for the duration of the scan series provides excellent opacification of vascular structures. For routine indications, injection of contrast at 3 mL/second is generally sufficient. When a vascular abnormality is suspected, injection at 5 mL/second is typically used. The rate of contrast injection and the scan delay (the time between the start of contrast injection and the start of scanning) vary, depending on the reason for the study.

Scanning is begun when the vessels of interest are opacified. For pulmonary embolism diagnosis, the pulmonary arteries need to be opacified; this usually requires a 10- to 15-second delay, although timing the scan to the aorta or left atrium may be beneficial. For diagnosis of aortic abnormalities, a delay of 20 to 30 seconds is usually needed. The delay varies in individual patients according to a number of factors. Timing the scan delay is usually done using a timing bolus or software available on the scanner, which shows vascular opacification during the injection and begins scanning when contrast appears in the target vessel. The use of an oral contrast agent for opacification of the esophagus and gastrointestinal tract is not necessary unless a specific gastrointestinal (i.e., esophageal) abnormality is suspected.

Routine Chest CT

With a MDCT scanner, I obtain routine chest CT using 0.625-mm detectors, with reconstruction of 1.25-mm slices at 1.25-mm intervals. This allows the entire thorax to be scanned in about 2.5 seconds. Depending on the indication for the study, a high-resolution algorithm or smooth algorithm may be chosen for image reconstruction, and intravenous or oral contrast agents may be used (see previous discussion). Generally speaking, with the exception of vascular imaging protocols, a high-resolution reconstruction algorithm will be chosen for reconstruction of most chest CT studies. This routine protocol is used for evaluation in most patients not being assessed for a specific vascular abnormality, such as pulmonary embolism or possible aortic disease, or in patients being evaluated for a diffuse lung disease, which would require an HRCT protocol.

Vascular Imaging Protocols

In some patients, chest CT is performed primarily for the diagnosis of a vascular abnormality suspected on the basis of clinical symptoms or radiographic findings. Common thoracic vascular abnormalities assessed using CT include pulmonary embolism, aortic dissection or aneurysm, and traumatic aortic rupture. Although protocols for each indication vary among institutions and with different scanners, some general principles apply. Vascular protocols attempt to optimize the degree of contrast enhancement of the vessels of interest and image resolution, while keeping the length of breath hold and the amount of contrast injected at reasonable values. In general, a relatively smooth reconstruction algorithm is preferred for vascular imaging. Reduced image noise with smooth reconstruction makes it easier to see small filling defects (i.e., pulmonary emboli) and subtle differences in contrast enhancement.

Pulmonary Embolism

For the diagnosis of pulmonary embolism using MDCT, slices that are 1.25 mm thick at 1.25-mm intervals are sufficient for diagnosis, although scanning is usually performed using the thinnest detectors available (e.g., 0.625 mm). A smooth reconstruction algorithm is generally used. Intravenous contrast is injected rapidly (e.g., 5 mL/second). Scanning is begun when the scanner shows that the pulmonary arteries or left atrium is opacified. The delay between the start of contrast injection and scanning varies but averages about 10 to 15 seconds if pulmonary artery opacification is desired and is somewhat longer for opacification of the left atrium. In large patients, scan noise may make interpretation difficult. In such patients, reconstruction of slices that are 2.5 mm thick may reduce noise and improve accuracy.

Aortic Disease

Aortic abnormalities assessed using CT include dissection, aneurysm, intramural hematoma, penetrating ulcer, and traumatic aortic rupture. Often, a scan series through the thorax with relatively thick (2.5- or 5-mm) slices precedes contrast injection (to look for a high-attenuation intramural hematoma; see Chapter 3). If only the thoracic aorta is being examined, scans through the thorax may be obtained with a protocol similar to that used for pulmonary embolism

diagnosis (1.25-mm slices reconstructed at 1.25-mm intervals). Intravenous contrast is injected rapidly (e.g., 5 mL/second), and scanning is begun when the scanner shows that the left atrium or aorta is opacified. The scan delay may range from 15 to 30 seconds, depending on the patient. If imaging of the abdominal aorta is also required (e.g., for aortic dissection), scans are continued through the abdomen. Quiet breathing during the abdominal portion of the scan is usually allowed if the patient cannot hold a breath for the duration of the study.

High-Resolution Lung CT

HRCT is used to diagnose diffuse lung diseases, emphysema, bronchiectasis, and focal lung lesions (i.e., a solitary nodule). HRCT requires thin slices (e.g., 0.625 to 1.25 mm) and image reconstruction using a sharp (high-resolution) algorithm, which reduces image smoothing and increases spatial resolution. Although use of a sharp algorithm also increases image noise, this is not usually a problem in the interpretation of lung images. Injection of contrast is not necessary for HRCT but may be used on occasion if pulmonary embolism is also a consideration. Scans performed with the patient supine and prone, and following expiration, are often obtained. *Prone scans* are used to detect subtle posterior lung abnormalities; *expiratory scans* are used to detect air trapping.

Basically, HRCT may be performed in two different ways:

- *Spaced axial imaging.* Thin slices (e.g., 0.625 to 1.25 mm) are performed at spaced intervals (i.e., 1 to 2 cm) without table movement to optimize the spatial resolution. Because of the spaced images, the patient receives a low dose of radiation.
- *Volumetric HRCT using the spiral technique*, thin detectors, and a 1- to 1.25-mm slice thickness for reconstruction. This results in an increased radiation dose and slightly decreased resolution, but the entire thorax is imaged, and two- or three-dimensional reconstruction and assessment of other abnormalities (e.g., pulmonary embolism) are also possible. If desired, the scans can be reconstructed with both a high-resolution algorithm (for diagnosis of lung abnormalities) and a smooth algorithm (for diagnosis of vascular abnormalities).

Dynamic CT Techniques

The term *dynamic CT* means that a number of scans are performed in sequence. Because spiral scanning is continuous, it is a dynamic technique, but dynamic scanning can also be performed without a spiral technique (i.e., without table and patient motion during acquisition of scans). Dynamic scanning may be performed at a single level during expiration to detect air trapping or to assess tracheal or bronchial collapse in patients with tracheomalacia or airway disease. Dynamic scanning may also be performed to assess some vascular abnormalities.

Low-Dose CT

Reducing the radiation dose is desirable whenever possible but generally results in decreased image quality because of increased noise. The term *low-dose CT* usually implies the use of a reduced tube current (milliamperes or mA) during the scan. Low-dose chest CT is typically used in children, for screening of patients (i.e., lung cancer screening), or if multiple follow-up examinations will be necessary.

With current MDCT scanners, the tube current (mA) can be varied or modulated at different levels as the patient is scanned, according to the chest wall thickness or amount of soft tissue within the volume being scanned. Because the lungs are not very dense, not much current is needed when the lungs (rather than the shoulders or liver) are being scanned. This technique can significantly reduce the current and patient dose without much loss of scan quality and is usually employed for routine studies. A fixed, higher current is typically used when high resolution and detail are needed (e.g., for pulmonary embolism diagnosis).

RADIATION DOSE WITH CHEST CT

Although the patient risk from radiation exposure during diagnostic CT is small and difficult to determine, medical radiation does result in a finite risk. In clinical practice, the patient's potential benefits from a CT study need to be balanced against the small risk resulting from CT. In general, if the study has well-defined clinical utility, it is indicated. Nonetheless, it is important for the radiologist to reduce radiation exposure during diagnostic CT, as long as important diagnostic information is not compromised as a result.

The radiation dose and the associated risk to the patient can be calculated using different methods and measurements, none of which is ideal or necessarily predictive of outcome. The calculation most typically used is the effective dose [measured in Sieverts (Sv) or more typically milliSieverts (mSv)], which is determined by

TABLE 1-2 **Radiation Dose for Chest CT Protocols**

Situation	Dose (mSv)
Normal yearly background radiation	2.5–3.2
Chest radiograph (single view)	0.05
Routine chest CT (300 mA)	5–7
Routine chest CT (modulated, approximately 100–150 mA)	1.5–2
HRCT with volumetric imaging (supine, expiratory) (modulated, approximately 100–150 mA)	1.5–2
HRCT with spaced axial images (supine, prone, expiratory)	1
Low-dose volumetric CT (40 mA)	< 0.5–1

mSv, milliSieverts.

summing the doses absorbed by individual organs weighted for their radiation sensitivity. However, since accurate measurement of all organ doses is difficult to obtain during a clinical examination, as are the risk coefficients specific to age, gender, and organ being irradiated, the estimated dose is calculated for an idealized 70-kg, 30-year-old patient. Although limited in accuracy and predictive value, the effective dose expressed in milliSieverts is the method most widely used for quantification of radiation doses and comparison of radiologic procedures. Approximate doses for background radiation and thoracic imaging procedures are listed in Table 1-2.

SUGGESTED READING

Arakawa H, Webb WR: Expiratory high-resolution CT scan. *Radiol Clin N Am* 36:189–209, 1998.

Bankier AA, Tack D: Dose reduction strategies for thoracic multidetector computed tomography: Background, current issues, and recommendations. *J Thorac Imag* 25:278–288, 2010.

Costello P, Dupuy DE, Ecker CP, Tello R: Spiral CT of the thorax with reduced volume of contrast material: A comparative study. *Radiology* 185:663–666, 1992.

Dillon EH, van Leeuwen MS, Fernandez MA, Mali WP: Spiral CT angiography. *AJR Am J Roentgenol* 160:1273–1278, 1993.

Heiken JP, Brink JA, Vannier MW: Spiral (helical) CT. *Radiology* 189:647–656, 1993.

Kalender WA, Seissler W, Klotz E, Vock P: Spiral volumetric CT with single-breath-hold technique, continuous transport, and continuous scanner rotation. *Radiology* 176:181–183, 1990.

Lawler LP, Fishman EK: Multi-detector row CT of thoracic disease with emphasis on 3D volume rendering and CT angiography. *Radiographics* 21:1257–1273, 2001.

Lee CH, Goo JM, Lee HJ, et al.: Radiation dose modulation techniques in the multidetector CT era: From basics to practice. *Radiographics* 28:1451–1459, 2008.

Mahesh M: Search for isotropic resolution in CT from conventional through multiple-row detector. *Radiographics* 22:949–962, 2001.

Mayo JR: The high-resolution computed tomography technique. *Semin Roentgenol* 26:104–109, 1991.

Mayo JR: CT evaluation of diffuse infiltrative lung disease: Dose considerations and optimal technique. *J Thorac Imag* 24:252–259, 2009.

Mayo JR, Webb WR, Gould R, et al.: High-resolution CT of the lungs: An optimal approach. *Radiology* 163:507–510, 1987.

Paranjpe DV, Bergin CJ: Spiral CT of the lungs: Optimal technique and resolution compared with conventional CT. *AJR Am J Roentgenol* 162:561–567, 1994.

Rubin GD, Napel S, Leung AN: Volumetric analysis of volumetric data: Achieving a paradigm shift. *Radiology* 200: 312–317, 1996.

Zwirewich CV, Mayo JR, Müller NL: Low-dose high-resolution CT of lung parenchyma. *Radiology* 180:413–417, 1991.

CHAPTER 2

MEDIASTINUM: INTRODUCTION AND NORMAL ANATOMY

W. Richard Webb

Computed tomography (CT) is commonly used in patients suspected of having a mediastinal mass or mediastinal vascular abnormality (e.g., an aortic aneurysm). In general, CT is obtained in two situations.

First, in patients with an abnormality visible on plain radiographs that suggests or indicates mediastinal pathology, CT is almost always the preferred imaging procedure. In patients with a visible mass, CT can be helpful in confirming the presence of a significant lesion (mediastinal contour abnormalities seen, or imagined, on plain films do not always reflect a real abnormality); defining its location; determining its relationship to vascular or nonvascular structures showing other, unrecognized mediastinal abnormalities and characterizing the mass as solid, cystic, vascular, enhancing, calcified, inhomogeneous, or fatty. Although CT may not be able to diagnose a lesion with certainty, it may help limit the differential diagnosis to a few entities, which in turn may help determine the most appropriate next step, be it percutaneous biopsy, mediastinoscopy, surgery, arteriography, or nothing.

Second, CT is often used to evaluate the mediastinum in patients with normal chest radiographs and a clinical suspicion of mediastinal disease. As an example, patients with lung cancer often have mediastinal lymph node enlargement visible on CT, despite normal chest films. Another example is a patient with myasthenia gravis who has a significant chance of having a thymoma (approximately 15%) that may be detected on CT even if chest films are normal.

NORMAL MEDIASTINAL ANATOMY

The mediastinum is the compartment situated between the lungs, marginated on each side by the mediastinal pleura, anteriorly by the sternum and chest wall, and posteriorly by the spine and chest wall. It contains the heart, great vessels, trachea, esophagus, thymus, considerable fat, and a number of lymph nodes, which are grouped together in specific regions. Many of these structures can be reliably identified on CT by their location, appearance, and attenuation.

In general, for the purpose of CT interpretation, the mediastinum can be thought of as consisting of three almost equal divisions, the first beginning at the thoracic inlet and the third ending at the diaphragm. In adults, each of these divisions is made up of about 15 contiguous 5-mm slices. For lack of official anatomic names, these can be remembered as follows:

1. The *supra-aortic mediastinum*: from the thoracic inlet to the top of the aortic arch.
2. The *subaortic mediastinum*: from the aortic arch to the superior aspect of the heart.
3. The *paracardiac mediastinum*: from the heart to the diaphragm.

In each of these compartments, specific structures are consistently seen and need to be evaluated in every patient. The following description of normal anatomy is not comprehensive but is limited to the most important mediastinal structures. With experience, it is possible to identify everything else. The main goal is to provide an approach to viewing the mediastinum.

Supra-Aortic Mediastinum

In evaluating a CT scan of this part of the mediastinum, it is a good idea to localize the *trachea* before doing anything else (Fig. 2-1*A*). The trachea is easy to recognize because it contains air, is seen in cross-section, and has a reasonably consistent

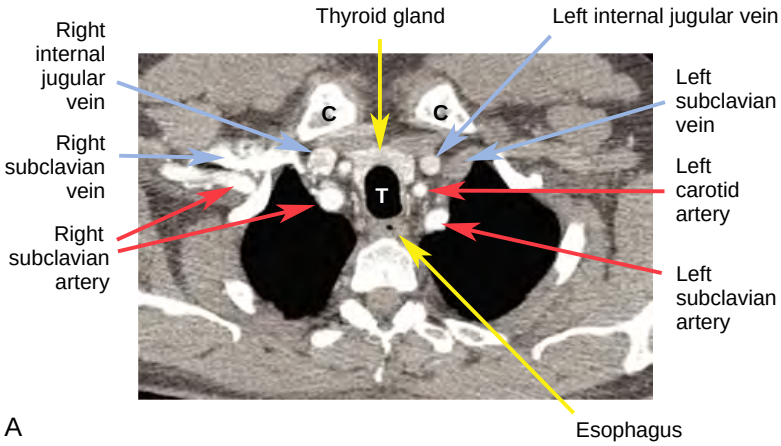

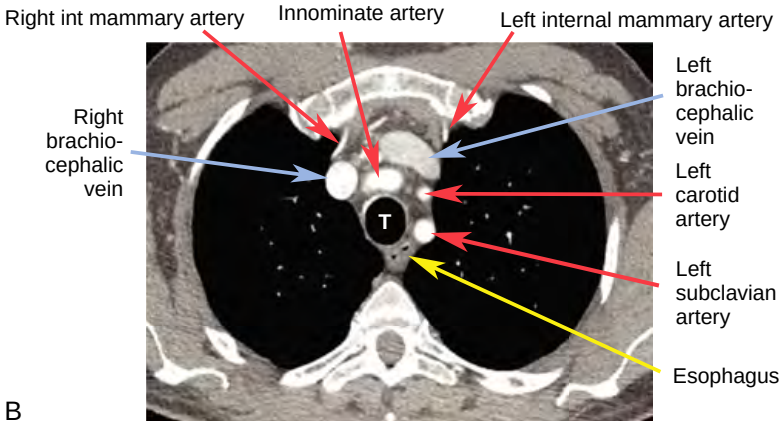

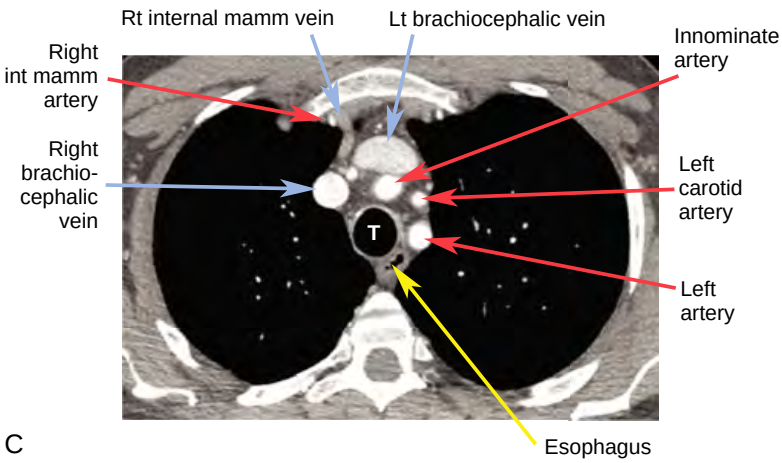

FIGURE 2-1 ■ Supra-aortic mediastinum. Contrast-enhanced computed tomography with 1.25-mm slices. *A*, Near the thoracic inlet, the trachea (T) is clearly seen, with the air-filled esophagus posterior and slightly to the left of it. The right and left subclavian and internal jugular veins are anterior and lateral and can be seen behind the clavicular heads (C) and clavicles. At this level, the axillary veins are also visible (within the axilla). The great arterial branches (right carotid, right subclavian, left carotid, and left subclavian arteries) are visible, lying lateral to the trachea. The thyroid gland is anterior and lateral to the trachea. Because of its iodine content, it appears denser than other soft tissue. *B*, Just below A, the brachiocephalic veins are visible anteriorly. The large arterial branches of the aorta lie posterior to the left brachiocephalic vein. The left subclavian artery is most posterior and is situated lateral to the left tracheal wall, at the 3 or 4 o'clock position relative to the tracheal lumen, and contacting the mediastinal pleura. The left carotid artery is anterior to the left subclavian artery, at about the 2 o'clock position, and is somewhat variable in position. The innominate artery is usually anterior and slightly to the right of the tracheal midline. The internal (int) mammary arteries are visible bilaterally. *C*, At a level below *B*, the left (Lt) brachiocephalic vein is visible crossing the mediastinum from left to right. The subclavian, carotid, and innominate arteries maintain the same relative positions as in *B*. The right (Rt) internal mammary (mamm) vein is visible arising from the right brachiocephalic vein. The densely opacified internal mammary (int mamm) arteries are visible bilaterally, lateral to the internal mammary veins. The esophagus contains a small amount of air in its lumen.

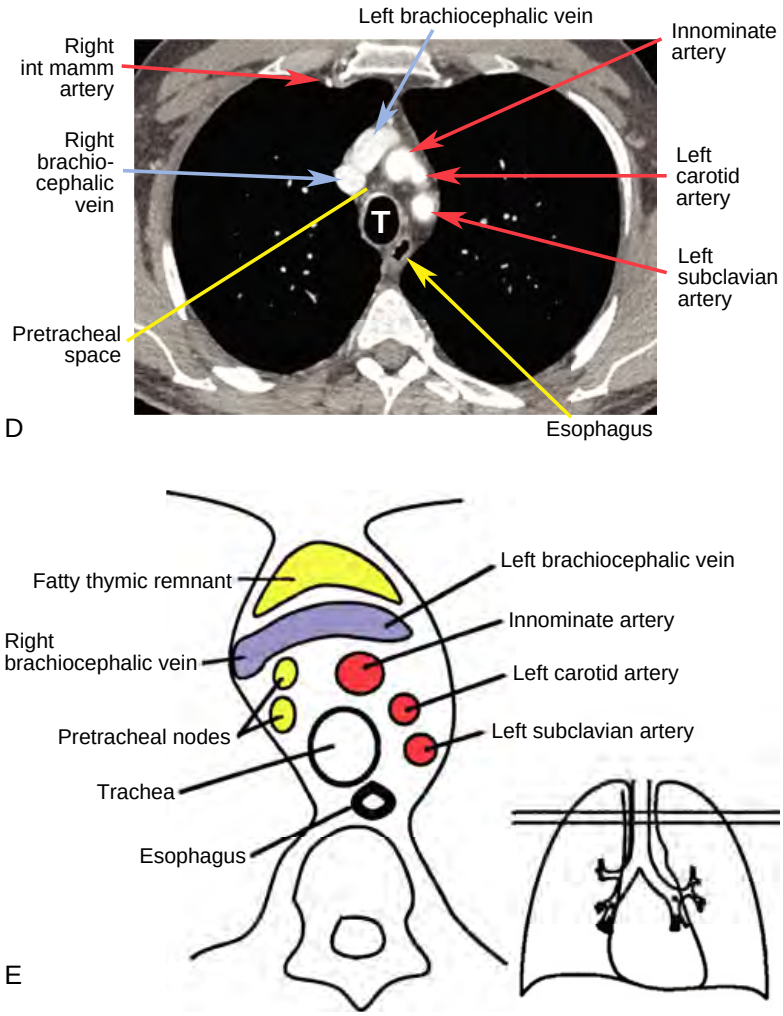

FIGURE 2-1, cont'd ■ *D*, At a level below *C*, the left brachiocephalic vein joins the right brachiocephalic vein, forming the superior vena cava. The major aortic branches are again clearly seen. The fat-filled pretracheal space is anterior to the trachea and posterior and medial to the arteries and veins. int mamm, internal mammary. *E*, Diagram of the supra-aortic anatomy near the level of *D*. The location of the pretracheal lymph nodes is shown, although these are not visible in *D*. The location of the thymic remnant, although not seen well in *D*, is also indicated. The approximate level of the scan in D is indicated by horizontal lines.

round or oval shape. It is relatively central in the mediastinum, from front to back and from right to left, and it serves as an excellent reference point. Many other mediastinal structures maintain a consistent relation to it. If you are unable to find the trachea on a scan of this part of the mediastinum, I would suggest giving up right now.

At or near the thoracic inlet, the mediastinum is relatively narrow from front to back. The *esophagus* lies posterior to the trachea at this level (Fig. 2-1), but depending on the position of the trachea relative to the spine, the esophagus can be displaced to one side or the other, usually to the left. It is usually collapsed and appears as a flattened structure of soft-tissue attenuation, but small amounts of air or air and fluid are often seen in its lumen.

In the supra-aortic mediastinum, the great arterial branches of the aortic arch and the great veins are the most recognizable structures. At or near the thoracic inlet, the *brachiocephalic veins* are the most anterior and lateral vascular branches visible, lying immediately behind the clavicular heads (Fig. 2-1*A* and *B*). Although they vary in size, their positions are relatively constant. The great arterial branches (innominate, left carotid, and left subclavian arteries) are posterior to the veins and lie adjacent to the anterior and lateral walls of the trachea. They can be reliably identified by their relative positions.

Below the thoracic inlet, anterior to the arterial branches of the aorta, the left brachiocephalic vein crosses the mediastinum from left to right

(Fig. 2-1*C*) to join the right brachiocephalic vein, thus forming the *superior vena cava* (Fig. 2-1*C* to *E*). The *left subclavian artery* is most posterior and is situated adjacent to the left side of the trachea, at the 3- or 4-o'clock position relative to the tracheal lumen. The *left carotid artery* is anterior to the left subclavian artery, at 1 or 2 o'clock, and is somewhat variable in position. The *innominate artery* is usually anterior and somewhat to the right of the tracheal midline (11 or 12 o'clock), but it is the most variable of all the great vessels and can have a number of different appearances in various patients or in the same patient at different levels.

Near its origin from the aortic arch, the innominate artery is usually oval and is somewhat larger than the other aortic branches. As it ascends toward the thoracic outlet, it may appear oval or elliptical because of its orientation or because of its bifurcation into the right subclavian and carotid arteries. This vessel can also be quite tortuous and can appear double if both limbs of a U-shaped part of the vessel are imaged in the same slice. Usually, these vessels can be traced from their origin at the aortic arch to the point where they leave the chest, if there is any doubt as to what they represent.

Other than the great vessels, trachea, and esophagus, little is usually seen in the supra-aortic mediastinum. A few lymph nodes are sometimes visible. Small vascular branches, particularly the internal mammary veins, can be seen in this part of the mediastinum. In some patients, the *thyroid gland* may extend into this portion of the mediastinum, and the right and left thyroid lobes may be visible on each side of the trachea. This appearance is not abnormal and does not imply thyroid enlargement or substernal thyroid. On CT, the thyroid can be distinguished from other tissues or masses because its attenuation is greater than that of soft tissue (because of its iodine content).

Subaortic Mediastinum

Like the supra-aortic region, in adults the subaortic mediastinum consists of approximately fifteen 5-mm scans, extending from the aortic arch to the upper heart (Fig. 2-2). Whereas the supra-aortic region largely contains arterial and venous branches of the aorta and vena cava, this compartment contains many of the undivided mediastinal great vessels, such as the aorta, superior vena cava, and pulmonary arteries. This compartment also contains most of the important lymph node groups, which may be abnormal in patients with lung cancer, infectious diseases, sarcoidosis, or lymphoma. In other words, on most CT studies of the mediastinum, this is where the action is. A few key levels in this part of the mediastinum need to be discussed in detail.

Aortic Arch Level

In the upper portion of the subaortic mediastinum compartment, the *aortic arch* is seen easily and has a characteristic but somewhat variable appearance (Fig. 2-2*A*). The anterior aspect of the arch is seen anterior to the trachea, with the arch itself passing to the left of the trachea and the posterior arch usually lying anterior and lateral to the spine. Usually, the aortic arch is about the same diameter in its anterior and middle portions, although the posterior arch is typically somewhat smaller. The position of the anterior and posterior aspects of the arch can vary in the presence of atherosclerosis and aortic tortuosity; in patients with a tortuous aorta, the anterior arch is displaced anteriorly and to the right, whereas the posterior aorta is displaced more laterally and posteriorly, to a position to the left of the spine.

At this level, the *superior vena cava* is visible anterior and to the right of the trachea and is usually oval in shape (Fig. 2-2*A* to *C*). The *esophagus* appears the same as at higher levels and is variable in position. Often, it lies somewhat to the left of the midline of the trachea (and, of course, is behind the trachea).

A somewhat triangular area with the apex of the triangle directed anteriorly and the aortic arch on the left, the superior vena cava and mediastinal pleura on the right, and the trachea viewed posteriorly defines the *pretracheal* or *anterior paratracheal* space (Fig. 2-2*A* and *C*). This fat-filled space is important because it contains middle mediastinal lymph nodes in the paratracheal chain, which are commonly involved in various lymph node diseases. Whenever the mediastinum is being viewed for diagnosis of lymphadenopathy, the radiographer should look here first. Other mediastinal node groups are closely related to this group, both spatially and in regard to lymphatic drainage. It is not uncommon to see a few normal-sized lymph nodes (short axis or least diameter, <1 cm) in the pretracheal space (see the review of mediastinal lymphadenopathy in Chapter 4 for a detailed discussion of this topic).

Anterior to the great vessels (aorta and superior vena cava) is another, somewhat less obvious triangular space called the *prevascular space* (Fig. 2-2*A*, *B*, and *C*). This compartment represents the anterior mediastinum and primarily contains the thymus, lymph nodes, and fat. The apex of this triangular space represents the anterior junction line, which is sometimes visible on chest radiographs.

In young patients, usually teenagers or adults in their early 20s, CT shows the *thymus* to be of soft-tissue attenuation and bilobed or arrowhead-shaped, with each of the two lobes (right and left) contacting the mediastinal pleura. Each lobe usually measures 1 to 2 cm in thickness (measured perpendicular to the pleura), but this varies (Fig. 2-2*B*). In adulthood, the thymus involutes, with soft tissue being replaced by fat. In patients older than 30 years, the prevascular space appears primarily fat-filled, with thin wisps of tissue passing through the fat. Most of this, including the fat, actually represents the thymus. At higher levels, the thymus is sometimes visible anterior to the brachiocephalic arteries and veins, also within the prevascular space.

Azygos Arch and Aortopulmonary Window Level

At a level slightly below the aortic arch, the ascending aorta and descending aorta are visible as separate structures. Characteristically, the ascending aorta (25 to 35 mm in diameter) is slightly larger than the descending aorta (20 to 30 mm).

On the right side, the arch of the *azygos vein* (*azygos* means "unpaired") arises from the posterior wall of the superior vena cava, passes over the right main bronchus (thus it is seen at a higher level than the bronchus itself), and continues posteriorly along the mediastinum, to lie to the right and anterior of the spine (Fig. 2-2*D* and *E*). Below the level of the azygos arch, the azygos vein remains visible in this position. The azygos arch is often visible on one or two adjacent slices and sometimes appears nodular. However, its characteristic location is usually sufficient to correctly identify this structure. When the azygos arch is visible, it marginates the right border of the pretracheal space.

On the left side of the mediastinum, under the aortic arch but above the main pulmonary artery, is the region termed the *aortopulmonary* (or *aorticopulmonary*) *window*. The aortopulmonary window contains fat, lymph nodes (middle mediastinal), the recurrent laryngeal nerve, and the ligamentum arteriosum (the latter two are usually invisible, although a calcified ligamentum is sometimes seen; Fig. 2-2*D* and *E*). *Aortopulmonary window lymph nodes* freely communicate with those in the pretracheal space, and in fact it may be difficult to distinguish nodes in the medial aortopulmonary window from those in the left part of the pretracheal space. In some patients, the aortopulmonary window is not easily apparent, with the main pulmonary artery lying immediately below the aortic arch. In such patients, it is usually difficult to distinguish lymph nodes from volume averaging of the adjacent aorta and pulmonary artery, and caution should be exercised. Scans with thin collimation are helpful in distinguishing nodes from volume averaging.

Main Pulmonary Arteries, Subcarinal Space, and Azygoesophageal Recess Level

At or slightly below the aortopulmonary window, at the level at which the *ascending aorta* is first clearly seen in cross-section (i.e., it is round or nearly round), a portion of the pericardium, usually containing a small amount of pericardial fluid, extends up from below into the pretracheal space and immediately behind the ascending aorta. This part of the pericardium is called the *superior pericardial recess* (Fig. 2-2*F* and *G*). Although it can sometimes be confused with a lymph node, its typical location, immediately behind and hugging the aortic wall, its oval or crescentic shape, and its relatively low (water) attenuation allow it to be distinguished from a significant abnormality. Another part of the pericardial recess can sometimes be seen anterior to the ascending aorta and pulmonary artery (Fig. 2-2*F* and *G*).

At or near this level, the trachea bifurcates into the right and left main bronchi. The *carina* itself is usually visible on CT (Fig. 2-2*F*).

Below the level of the carina and azygos arch (Fig. 2-2*F* to *I*), the medial aspect of the right lung tucks into the posterior portion of the middle mediastinum, in close association with the azygos vein and esophagus. This part of the mediastinum, reasonably called the *azygoesophageal recess*, is important because of the adjacent subcarinal lymph nodes and its close relation to the esophagus and the main bronchi. The contour of the azygoesophageal recess is concave laterally in most normal subjects, and a convexity in this region suggests the possibility of an underlying pathologic process. If a contour abnormality is detected, a close look at the mediastinal windows should be sufficient to delineate the cause of the abnormal contour. If the contour abnormality does not reflect the esophagus or azygos vein, it is abnormal and subcarinal node enlargement is the usual culprit.

In many subjects, the azygoesophageal recess is somewhat posterior to the node-bearing *subcarinal space*, which lies between the main bronchi. Normal nodes are commonly visible in this space, because they are larger than normal nodes in other parts of the mediastinum and up to 1.5 cm in short-axis diameter. The esophagus is usually seen immediately behind the subcarinal space, and distinguishing nodes and esophagus

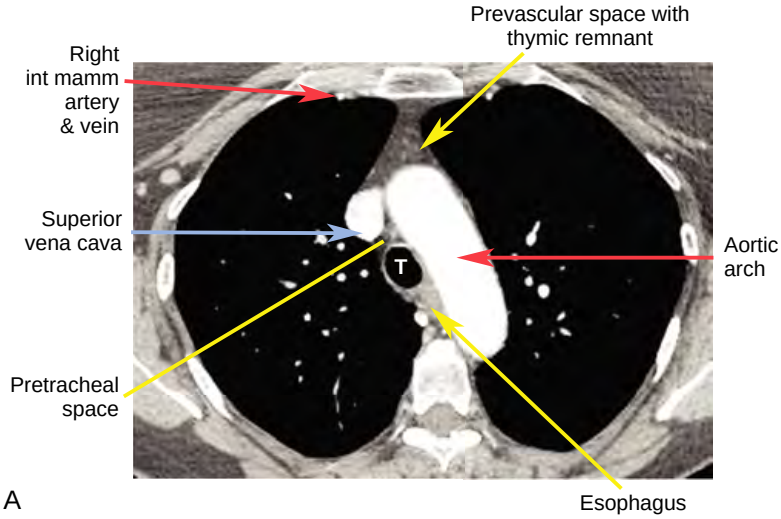

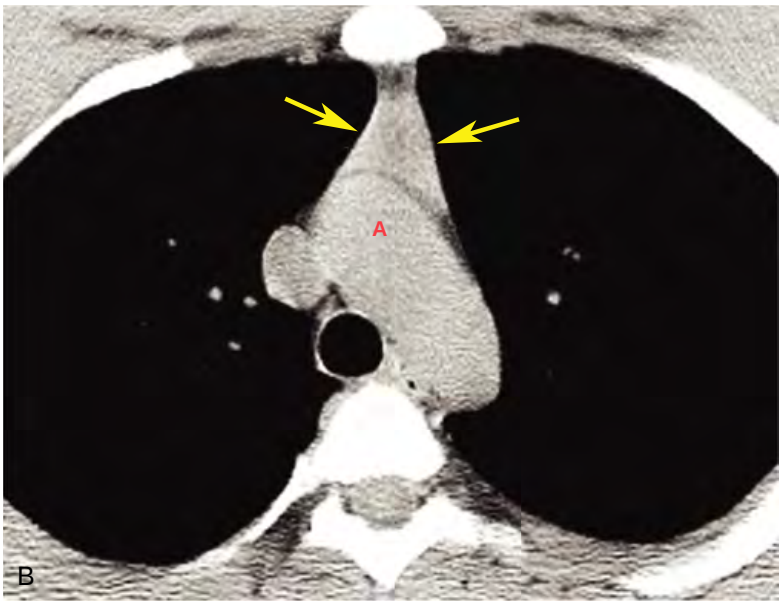

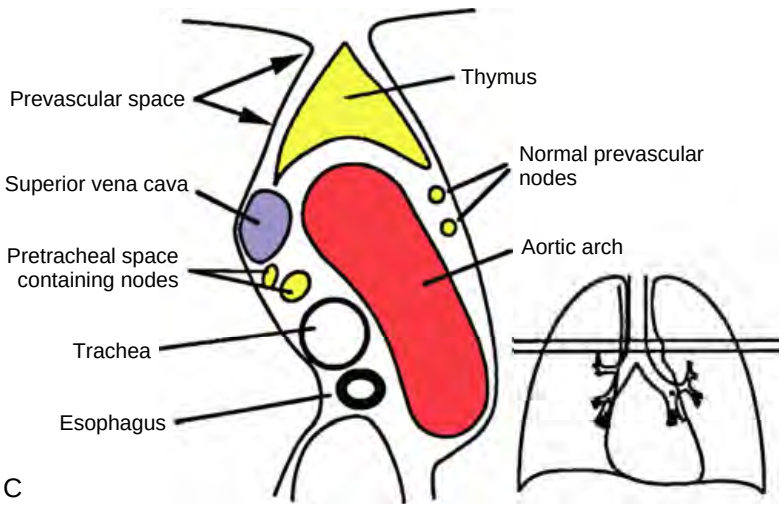

FIGURE 2-2 ■ Subaortic mediastinum. Contrast-enhanced computed tomography with 1.25-mm slices. **Aortic arch level.** *A*, The aortic arch extends from a position anterior to the trachea (T) to the left, with the posterior part of the arch usually lying anterior and lateral to the spine. The superior vena cava contacts the right mediastinal pleura and together with the aortic arch delineates the anterior aspect of the pretracheal space. The prevascular space is anterior to the great vessels and contains the thymus, which is largely replaced by fat in this patient. int mamm, internal mammary. *B*, In a 21-year-old patient, a large normal thymus with soft-tissue attenuation (*arrows*) occupies most of the prevascular space. It is separated from the aortic arch (A) by a fat plane. *C*, Diagram of the mediastinal anatomy at the aortic arch level.

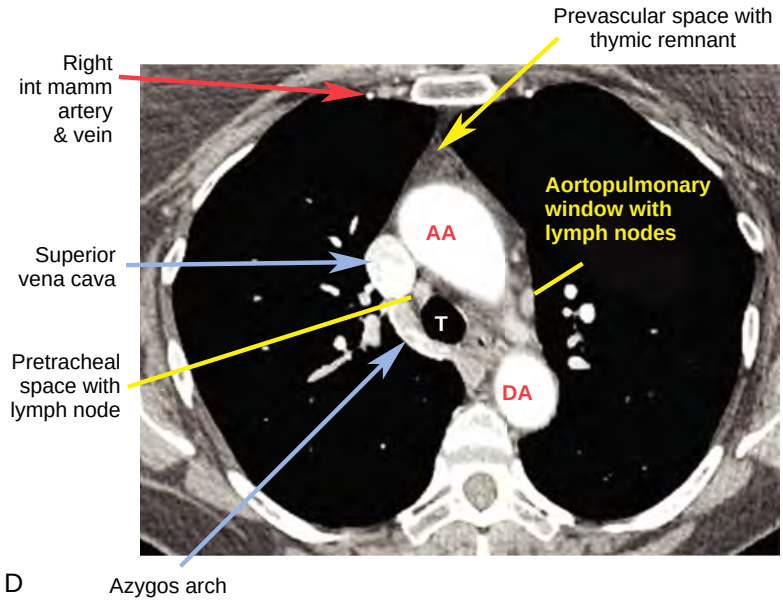

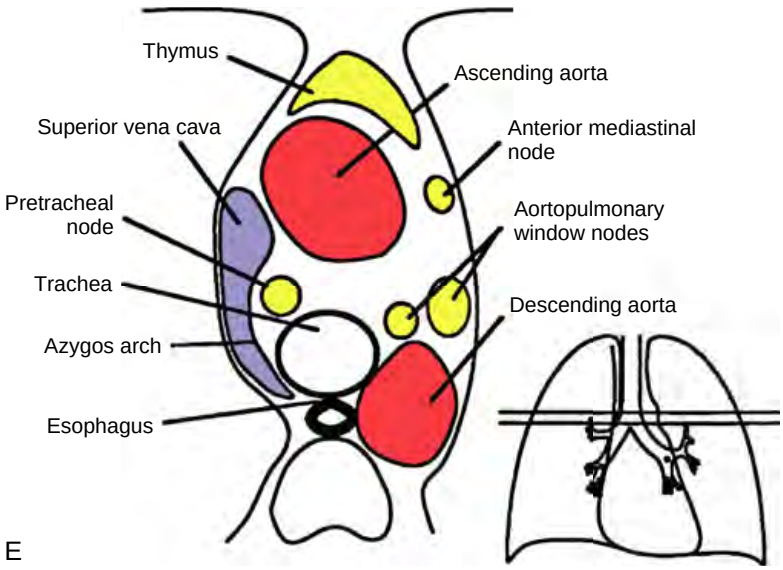

FIGURE 2-2, cont'd ■ Azygos arch and aortopulmonary window level. *D*, At this level, the azygos arch is usually visible arising from the posterior aspect of the superior vena cava, contacting the right mediastinal pleura, and forming the lateral margin of the node bearing pretracheal space. Fat visible under the aortic arch but above the pulmonary artery is in the aortopulmonary window, which also contains lymph nodes. AA, ascending aorta; DA, descending aorta; int mamm, internal mammary; T, trachea. *E*, Diagram of the mediastinal anatomy at the azygos arch and aortopulmonary window level.

may be difficult, unless the esophagus contains air or contrast material. At levels below the subcarinal space, the appearance of the azygoesophageal recess is relatively constant, although it narrows somewhat in the retrocardiac region.

Also at or near this level, the *main pulmonary artery* divides into its right and left branches. The *left pulmonary artery* (Fig. 2-2*F* to *I*) is somewhat higher than the right, usually seen 1 cm above it, and appears to be the continuation of the main pulmonary artery, directed posterolaterally and to the left. The *right pulmonary artery* arises at an angle of nearly 90° to the main and left pulmonary artery and crosses the mediastinum, anterior to the carina or the main bronchi. In this location, the right pulmonary artery effectively fills in the pretracheal space. At the point at which the main bronchi and pulmonary arteries exit the mediastinum, the pulmonary hila are entered (see Chapter 5).

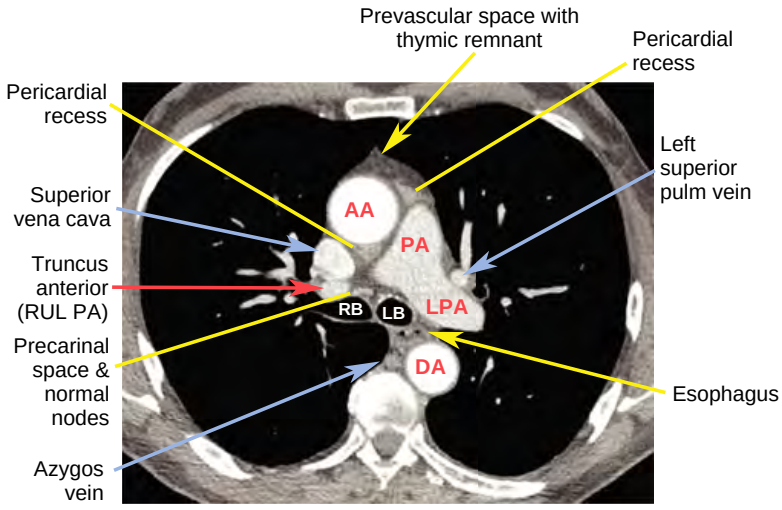

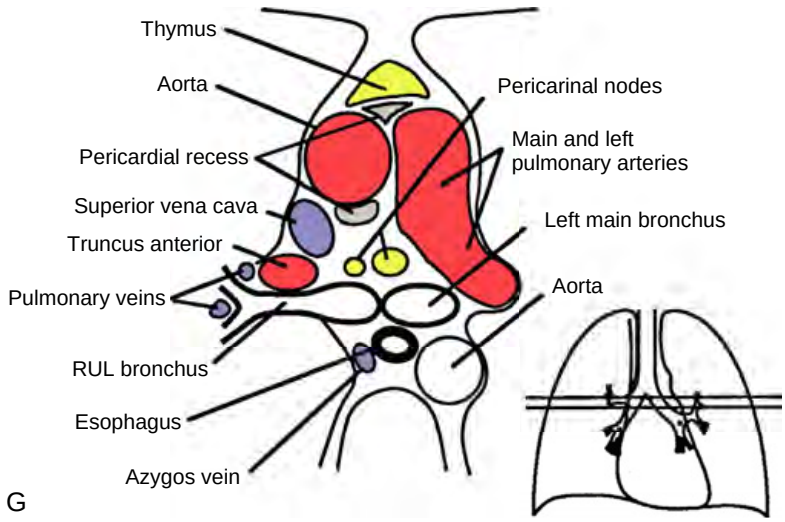

FIGURE 2-2, cont'd ■ Main pulmonary artery, subcarinal space, and azygoesophageal recess level. *F,* At the tracheal carina, the right and left main bronchi (RB and LB, respectively) are visible as separate branches. The main pulmonary artery (PA) is contiguous with the left pulmonary artery (LPA) more posteriorly. The truncus anterior (pulmonary artery supplying most of the right upper lobe) is visible as an oval structure anterior to the right main bronchus. Normal pericardial recesses containing fluid are visible posterior to the ascending aorta (AA) and between the anterior aorta and the main pulmonary artery. These are relatively low in attenuation and should not be confused with abnormal lymph nodes. The precarinal space containing lymph nodes is contiguous with the pretracheal space. DA, descending aorta; pulm, pulmonary; RUL, right upper lobe. *G,* Diagram of the mediastinal anatomy at this level. RUL, right upper lobe.

Paracardiac Mediastinum

On progression caudally through the mediastinum, the origins of the great vessels from the cardiac chambers can be seen to a variable degree. Although CT is not commonly used to diagnose cardiac abnormalities (echocardiography or magnetic resonance imaging is usually preferred), a simple understanding of cardiac anatomy on CT can be helpful in diagnosis, and its use is increasing with gated multidetector techniques.

The *main pulmonary artery* or pulmonary outflow tract is most anterior and is continuous with the right ventricle, which can be seen at lower levels as anterior and to the right of the ascending aorta or left ventricle (Fig. 2-3*A* to *C*). The superior vena cava joins the right atrium, which is elliptical or crescentic. The *right atrial appendage* extends anteriorly from the upper atrium, bordering the right mediastinal pleura.

Between the right atrium and the main pulmonary artery or pulmonary outflow tract, the *aortic root* enters the left ventricle. At this level, it is common in adults to see some coronary artery calcification (Fig. 2-3*A* to *C*), and often, uncalcified

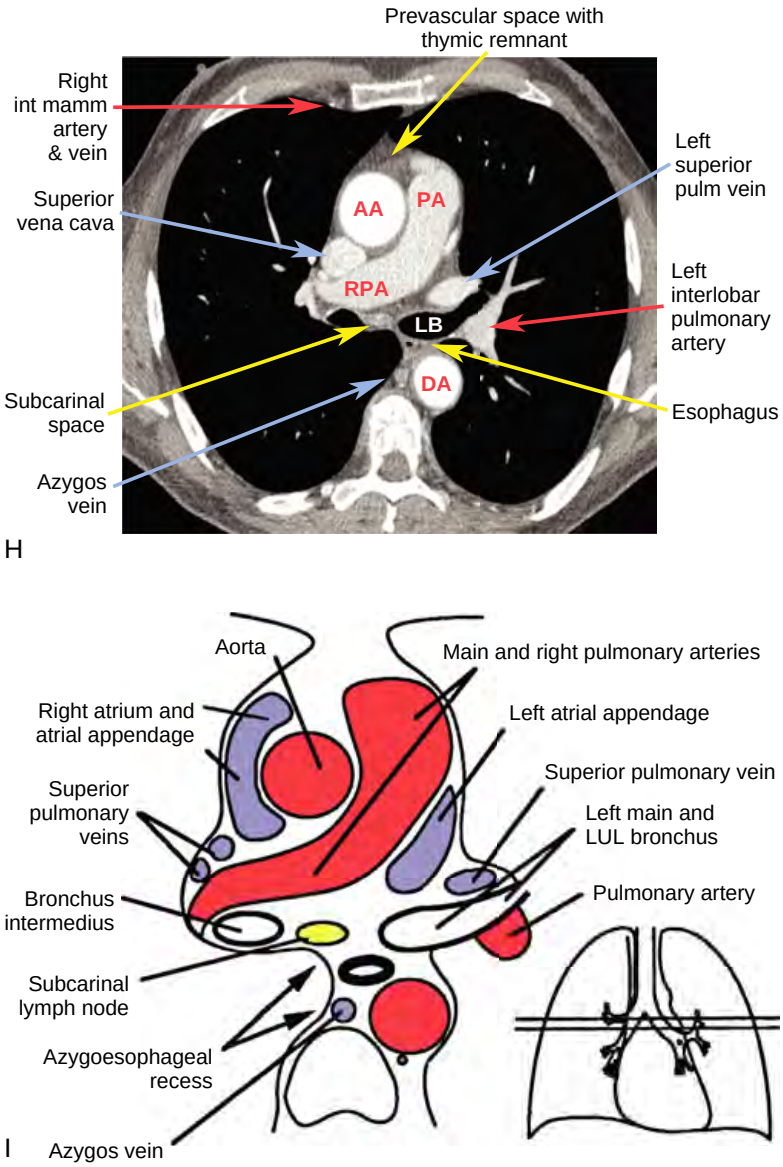

FIGURE 2-2, cont'd ■ *H* and *I*, Scan and diagram below the tracheal carina, at the level of the right pulmonary artery and azygoesophageal recess. The right pulmonary artery (RPA) is visible crossing the mediastinum, filling the pretracheal and precarinal space. A small amount of fat and a normal lymph node are visible in the subcarinal space, slightly anterior to the esophagus, azygos vein, and azygoesophageal recess. The recess appears concave laterally, with the mediastinal pleura closely related to the azygos vein and esophagus. Some structures indicated here are not visible in the scans. AA, ascending aorta; DA, descending aorta; int mamm, internal mammary; LB, left bronchus; LUL, left upper lobe; PA, pulmonary artery; pulm, pulmonary.

coronary arteries (left main coronary artery, left anterior descending coronary artery, circumflex coronary artery, and right coronary artery) are visible surrounded by mediastinal fat. The *left atrium* is posteriorly located, usually appearing larger than the right. The left atrial appendage extends anteriorly and to the left and is visible below the left pulmonary artery, bordering the pleura. On each side, the *superior and inferior pulmonary veins* can be seen entering the left atrium (Fig. 2-3*A* to *E*; see Chapter 5 for further discussion).

Near the level of the *diaphragm*, the *inferior vena cava* is visible as an oval structure extending caudad from the posterior right atrium (Fig. 2-3*H*) and is easily identifiable.

The only other structures of consequence at this level that need to be mentioned are the esophagus, which lies in a retrocardiac location; the azygos vein, which is often still visible in the same relative position as at higher levels; and the hemiazygos vein, which is usually smaller than the azygos and on the opposite side, behind the

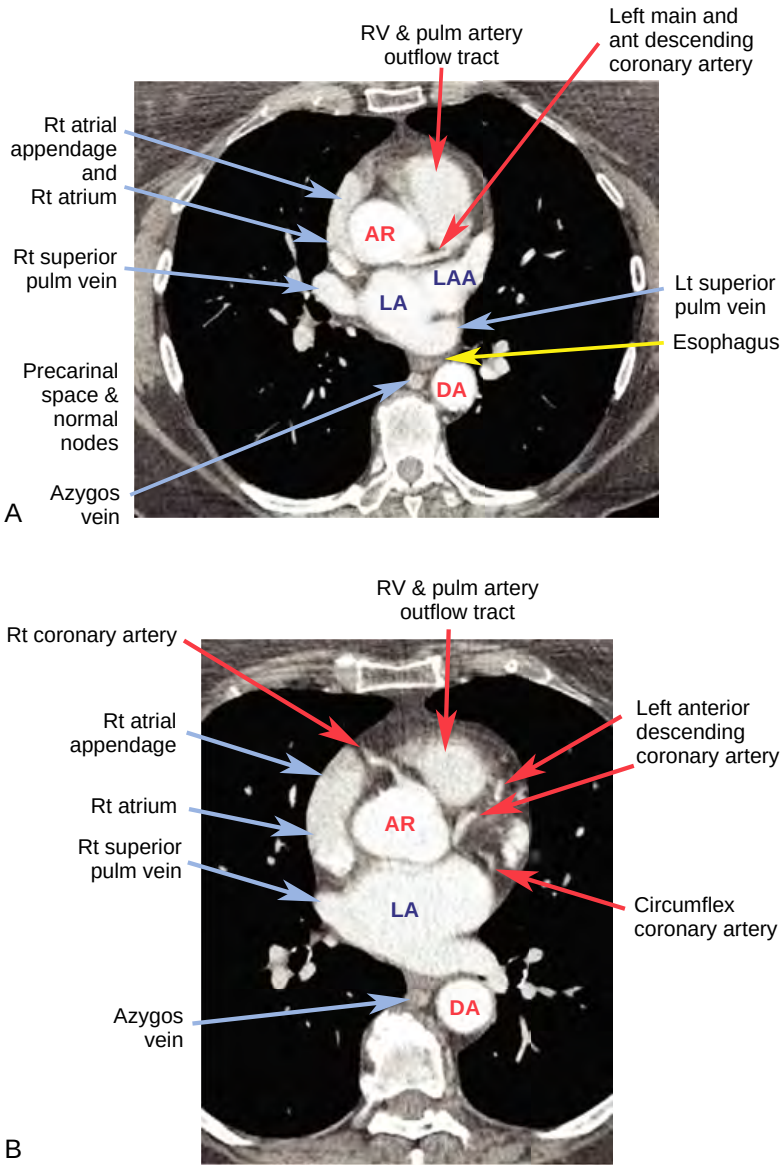

FIGURE 2-3 ■ Paracardiac mediastinum. Contrast-enhanced 1.25-mm-slice spiral computed tomography. *A,* Most cephalad, the origins of the aorta and pulmonary artery are visible, with the aortic root (AR) in a central position. The right ventricular (RV) or pulmonary (pulm) outflow tract or main pulmonary artery is anterior and to the left of the aortic root at this level. The right atrium, with its appendage extending anteriorly, borders the right mediastinal pleura. The superior pulmonary veins usually enter the upper aspect of the left atrium (LA) at this level. The left atrial appendage (LAA) is also seen. The origin of the left main coronary artery (which is short) is visible at this level and is continuous with the anterior (ant) descending coronary artery. DA, descending aorta; Lt, left; Rt, right. *B,* A slice slightly below *A* shows the origin of the right coronary artery and both the left anterior descending and circumflex branches of the left coronary artery.

descending aorta. Paravertebral nodes lie in association with the azygos and hemiazygos veins but are not normally visible.

NORMAL CARDIAC ANATOMY

Without injection of contrast medium, little cardiac anatomy is discernible on CT, but some differentiation of cardiac chambers is possible because of the presence of epicardial fat collections. When contrast medium is used, additional features of cardiac anatomy are visible, depending on the amount and rapidity of contrast medium injection; opacification is less for the myocardium than for intracardiac blood, and the myocardium is often visible as a relatively low-attenuation band after contrast infusion. The interventricular

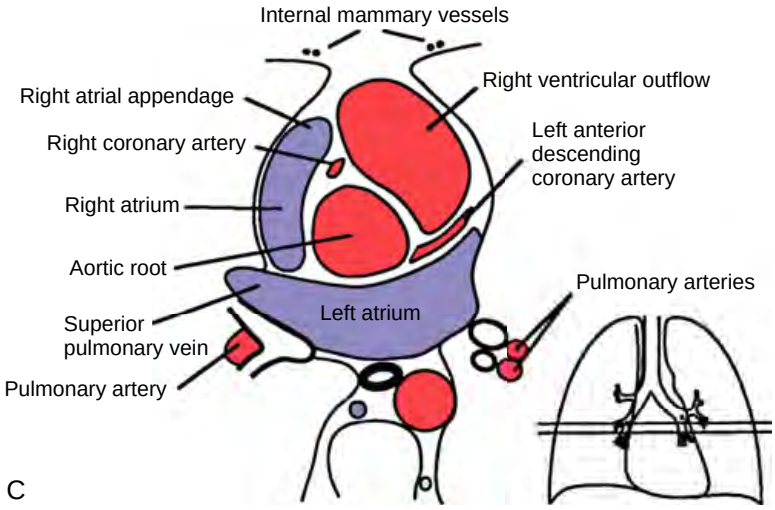

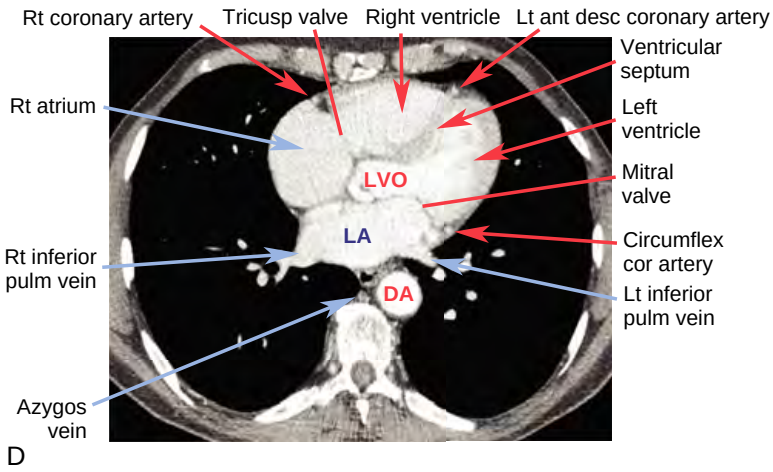

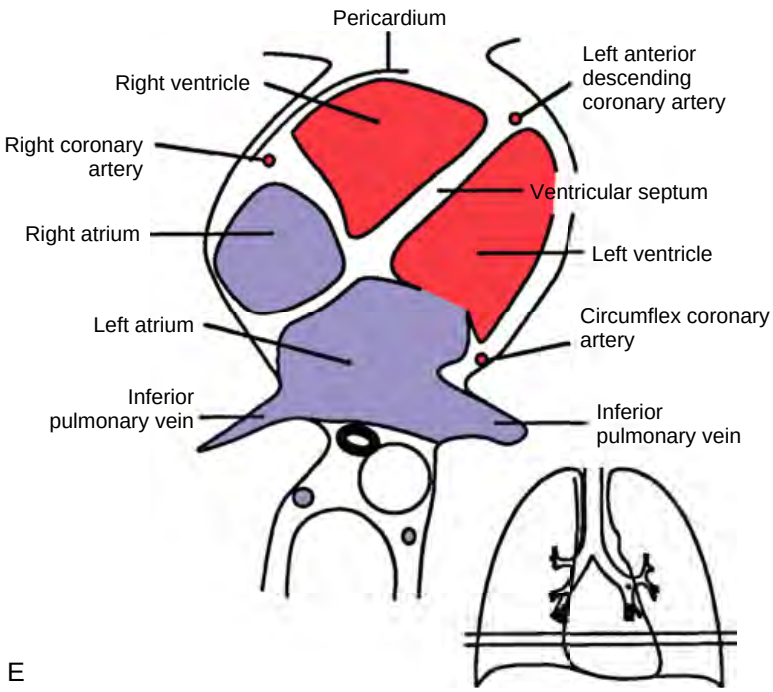

FIGURE 2-3, cont'd ■ *C*, Diagram at the levels of *A* and *B*. *D* and *E*, At a lower level, the right and left atria (LA) and ventricles are visible. The right ventricle (RV) is located anterior and to the right of the left ventricle (LV). The ventricular septum and left ventricular walls are thicker than the right ventricular wall. The locations of the tricuspid (tricusp) and mitral valves can be identified. The left ventricular outflow (LVO) is visible on the scan. ant, anterior; cor, coronary; desc, descending; DA, descending aorta; Lt, left; pulm, pulmonary; Rt, right.

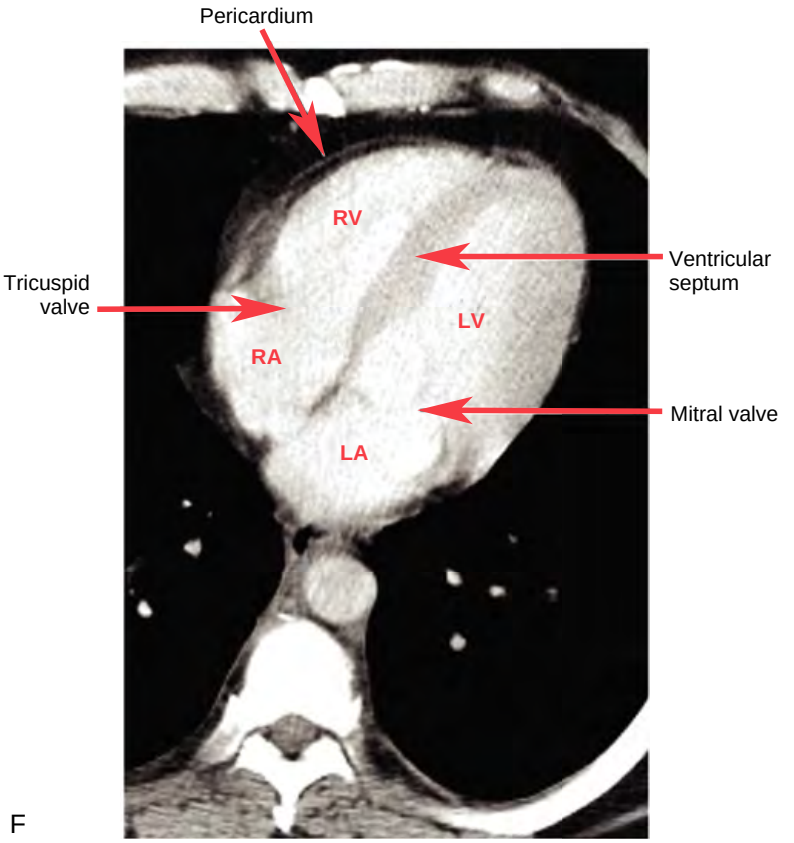

F

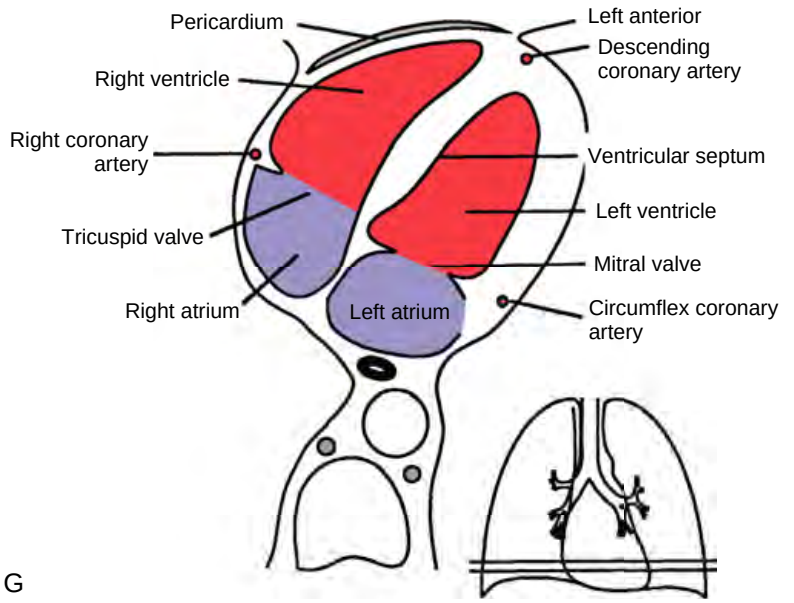

G

FIGURE 2-3, cont'd ■ *F* and *G*, All four chambers are visible at this level, and the locations of the tricuspid and mitral valves can be identified. The interventricular septum and free wall of the left ventricle (LV) are considerably thicker than the wall of the right ventricle (RV). The pericardium is visible as a thin white line surrounded by mediastinal fat. It should appear to be 1 to 2 mm in thickness. LA, left atrium; RA, right atrium.

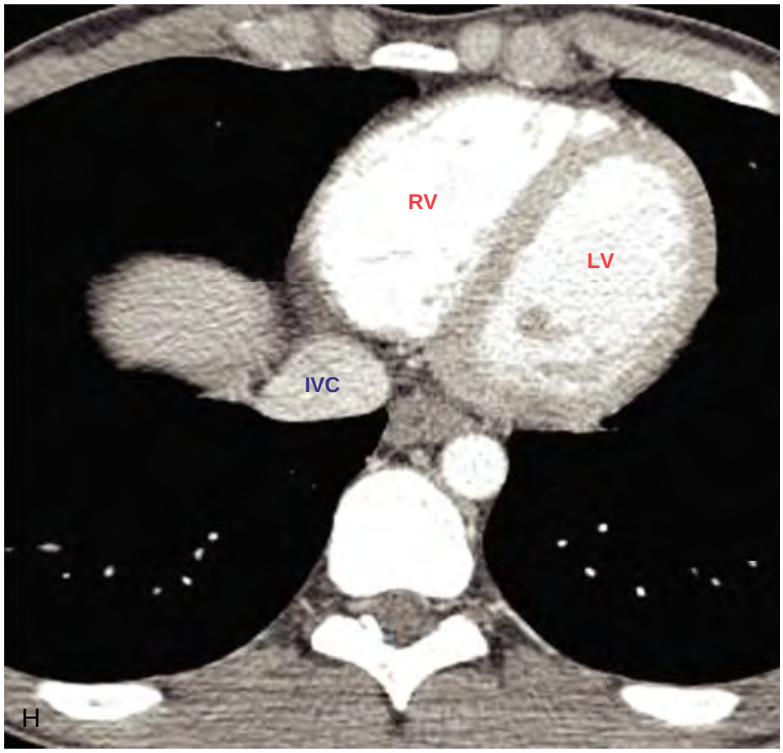

FIGURE 2-3, cont'd ■ *H*, Near the diaphragm, the inferior vena cava (IVC) is visible as a separate structure, below the level of the right atrium. The right and left ventricles (RV and LV, respectively) remain visible.

septum is typically oriented at an angle at about 2 o'clock to the vertical and is convex anteriorly because of the greater left ventricular pressure (Fig. 2-3*F* to *H*). The lateral or "free" left ventricular wall is about three times thicker (approximately 1 to 1.5 cm in thickness) than the right ventricular wall.

Cardiac anatomy is easiest to understand if a scan near the cardiac apex (and diaphragm) is first considered. At this level, the *left ventricle* is elliptical, with its long axis directed laterally and anteriorly (Fig. 2-3*F* to *H*). As the highest-pressure chamber, it dominates cardiac anatomy, and the other cardiac chambers mold themselves to its shape. The *right ventricle*, which is anterior and to the right, is triangular. On scans at this level or slightly above, the plane of the interventricular septum, if continued posteriorly and to the right, separates the lower *right atrium* anteriorly and laterally (and in contiguity with the right ventricle) from the lower *left atrium* posteriorly. The *mitral and tricuspid valves* are located at or near this level and can be seen if there is good contrast opacification of the cardiac chambers.

At higher levels (Fig. 2-3*A* to *D*), the *left ventricular outflow tract* and *aortic valve* are centrally located within the heart. The right ventricular outflow tract is directed toward the left and is visible anterior or to the left of the left ventricular outflow tract. That is, because of twisting of the heart during development, the left ventricular outflow tract is directed rightward and the right ventricular outflow tract is directed leftward. This accounts for the location of the aorta on the right and the pulmonary artery on the left. The aortic and pulmonic valves are located near this level and are sometimes visible in normal subjects.

Pericardium

The normal *pericardium* (the visceral and parietal pericardium and pericardial contents) is visible as a 1- to 2-mm stripe of soft-tissue attenuation parallel to the heart and outlined by mediastinal fat (outside the pericardial sac) and epicardial fat. It is best seen near the diaphragm, along the anterior and lateral aspects of the heart, where the fat layers are thickest (Fig. 2-3*F* to *G*). As stated earlier, extensions of the pericardium into the upper mediastinum can also be seen in healthy persons.

THE RETROSTERNAL SPACE

In a retrosternal location, the *internal mammary arteries and veins* are normally visible 1 or 2 cm lateral to the edge of the sternum on good CT

scans (Fig. 2-2*H*); up to three vessels can be seen on each side (one artery and two veins). These vessels are not of much diagnostic significance, although the veins are commonly enlarged in patients with superior vena cava obstruction, but they are important because they serve to localize the *internal mammary lymph nodes*. Although normal nodes can be seen in several areas of the mediastinum (most notably the pretracheal space, aortopulmonary window, and subcarinal space), normal internal mammary nodes are not large enough to be recognized. A lymph node in this region that is large enough to be visible should be regarded as abnormal. Internal mammary node enlargement is most common in patients with breast cancer or lymphoma.

SUGGESTED READING

Aronberg DJ, Peterson RR, Glazer HS, Sagel SS: The superior sinus of the pericardium: CT appearance. *Radiology* 153:489–492, 1984.

Francis I, Glazer GM, Bookstein FL, Gross BH: The thymus: Reexamination of age-related changes in size and shape. *AJR Am J Roentgenol* 145:249–254, 1985.

Glazer HS, Aronberg DJ, Sagel SS: Pitfalls in CT recognition of mediastinal lymphadenopathy. *AJR Am J Roentgenol* 144:267–274, 1985.

Kiyono K, Sone S, Sakai F, et al.: The number and size of normal mediastinal lymph nodes: A postmortem study. *AJR Am J Roentgenol* 150:771–776, 1988.

Müller NL, Webb WR, Gamsu G: Paratracheal lymphadenopathy: Radiographic findings and correlation with CT. *Radiology* 156:761–765, 1985.

Müller NL, Webb WR, Gamsu G: Subcarinal lymph node enlargement: Radiographic findings and CT correlation. *AJR Am J Roentgenol* 145:15–19, 1985.

Tecce PM, Fishman EK, Kuhlman JE: CT evaluation of the anterior mediastinum: Spectrum of disease. *Radiographics* 14:973–990, 1994.

Zylak CJ, Pallie W, Pirani M, et al.: Anatomy and computed tomography: A correlative module on the cervicothoracic junction. *Radiographics* 3:478–530, 1983.

CHAPTER 3

MEDIASTINUM: VASCULAR ABNORMALITIES AND PULMONARY EMBOLISM

W. Richard Webb

AORTIC ABNORMALITIES

Computed tomography (CT) is commonly used to diagnose abnormalities of the aorta or its branches when suspected clinically or because of plain radiographic abnormalities.

Congenital Anomalies

Congenital abnormalities of the aorta and its branches are readily diagnosed using CT, and no other study is usually needed unless the anomaly is complex or is associated with congenital heart disease.

Aberrant Right Subclavian Artery

An aberrant right subclavian artery is a relatively common anomaly (1/100 patients). It does not usually produce a recognizable mediastinal abnormality on chest radiographs and thus is usually detected incidentally on CT scans obtained for another reason. Its main significance is that it should not be misinterpreted as something else.

In patients with this anomaly, the aortic arch is often somewhat higher than normal. The aberrant right subclavian artery arises from the medial wall of the descending aorta, as its last branch (Fig. 3-1). It passes to the right, behind the esophagus, and then ascends on the right toward the thoracic inlet. It lies more posteriorly than is normal for the subclavian artery, often anterolateral to the spine. At its point of origin, the artery may be dilated, or, thinking of it in a more complicated way, the artery may arise from an *aortic diverticulum* (termed *diverticulum of Kommerell*). This may cause compression of the esophagus and symptoms of dysphagia. In some patients, the diverticulum or the anomalous artery becomes aneurysmal (Fig. 3-2).

Right Aortic Arch

There are two primary types of right aortic arch: *right arch associated with aberrant left subclavian artery* and *mirror-image right arch*. Right arch with an aberrant left subclavian artery is most common and is present in about 1 in 1000 people. It is the reverse of a left arch with an aberrant right subclavian artery (Fig. 3-3). However, an associated aortic diverticulum is more common in the presence of a right arch. With this anomaly, there is a low frequency (5% to 10%) of associated congenital heart lesions, and they are usually simple, such as an atrial septal defect. Mirror-image right arch is relatively uncommon and is almost always (98%) associated with congenital heart disease (usually complex anomalies such as tetralogy of Fallot). The CT appearance of a mirror-image arch is well described by its name; it is the mirror image of a normal left arch, with a left innominate artery present. With both types of right arch the descending aorta is usually left-sided, crossing from right to left in the lower mediastinum.

Double Aortic Arch

Double aortic arch is relatively uncommon, but because a plain radiograph shows a mediastinal abnormality (representing the right arch), it is often evaluated using CT. This anomaly is uncommonly associated with congenital heart disease, but because a complete vascular ring is present, symptoms of dysphagia are common. In this anomaly, the ascending aorta splits into right and left arches. The right arch, which is usually higher and larger than the left, passes to the right of the trachea and esophagus, crosses behind these structures, and rejoins the left arch, which occupies a relatively normal position (Fig. 3-4). Each arch is smaller than normal and smaller than the descending aorta. Each arch also gives

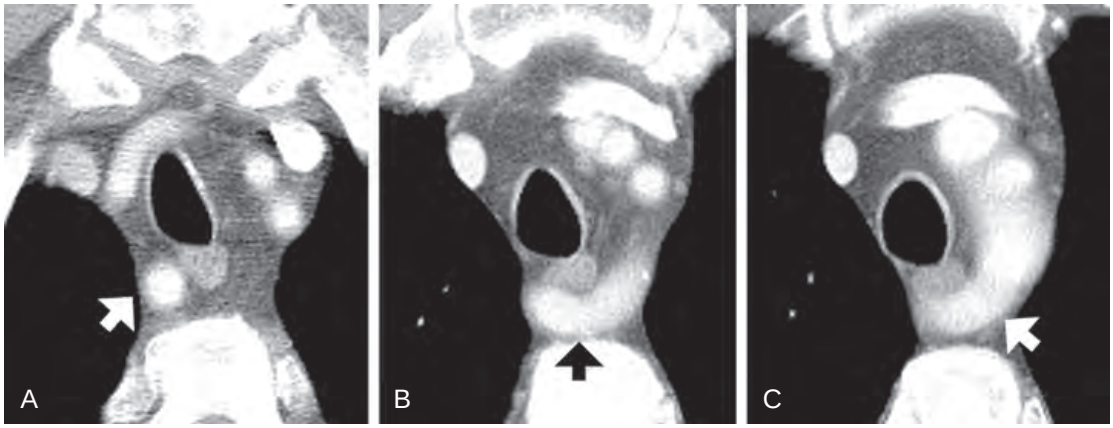

FIGURE 3-1 ■ Aberrant right subclavian artery. *A,* An aberrant right subclavian artery (*arrow*) is located posteriorly in the right superior mediastinum. *B,* At a level 7 mm below *A,* the anomalous artery (*arrow*) passes posterior to the esophagus. *C,* At 7 mm below *B,* the origin (*arrow*) of the anomalous artery from the posterior superior aortic arch is visible.

FIGURE 3-2 ■ Aneurysm of an aberrant right subclavian artery. *A,* As in Figure 3-1A, an aberrant right subclavian artery is situated in the right mediastinum. It is dilated and its lumen is partially filled with a clot. *B* and *C,* At lower levels, the aberrant artery is located posterior to the esophagus, and its origin (*arrow*) from the posterior superior aortic arch is visible.

rise to a subclavian and a carotid artery, and no innominate artery is present. This results in a symmetric appearance to the great vessels in the supra-aortic mediastinum that is highly suggestive of the diagnosis.

Aortic Coarctation and Pseudocoarctation

Coarctation, and its rare variant pseudocoarctation, can be readily diagnosed using CT; but even if this is possible, catheterization is usually necessary to measure intra-arterial pressures and thus the significance of the vascular obstruction.

The site of narrowing in coarctation is generally at the aortic isthmus, distal to the origin of the left subclavian artery and near the ligamentum arteriosum (*juxtaductal coarctation*). On CT, the narrowed segment is often visible because it is decidedly smaller than the aorta above and below this level (Fig. 3-5). This size difference reflects not only the narrowed segment at the coarctation but also some dilatation of the prestenotic and poststenotic aorta. Long narrowing of the aortic arch (hypoplasia) is less common. Images reconstructed in the plane of the aortic arch can show coarctation to better advantage. One word of caution: The degree of narrowing at the site of coarctation may be overestimated if the reformatted plane is slightly off the sagittal plane of the aorta. Dilatation of internal mammary arteries or intercostal arteries (usually the third through eighth) acting as collateral pathways can be seen.

In pseudocoarctation, the aortic arch is kinked anteriorly and its lumen is somewhat narrowed, but a significant pressure gradient across the kink and collateral vessels are not present. The aortic arch is higher than normal and initially descends in an abnormally anterior position, well in front of the spine. At a level near the carina, however,

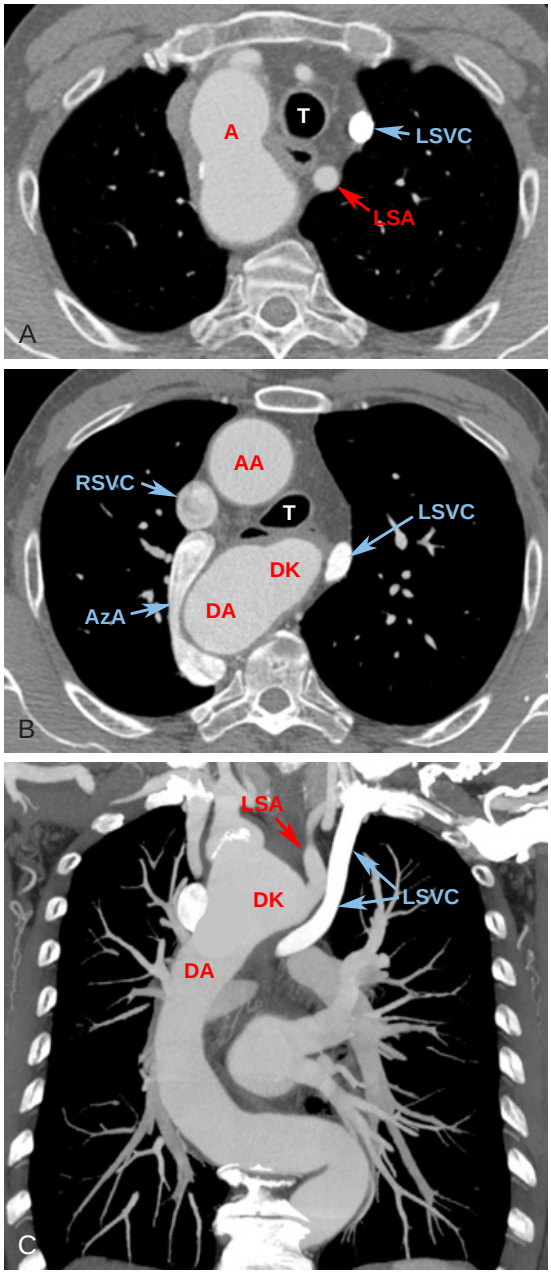

FIGURE 3-3 ■ Right aortic arch with an aberrant left subclavian artery and diverticulum of Kommerell. *A,* In a patient with no evidence of congenital heart disease and with a right aortic arch (A), an aberrant left subclavian artery (LSA) is visible in the left mediastinum. This patient also has a persistent left superior vena cava (LSVC). T, trachea. *B,* At a lower level, the ascending aorta (AA) and descending aorta (DA) are visible; a retroesophageal diverticulum of Kommerell (DK) gives rise to the left subclavian artery seen at higher levels. The LSVC, RSVC, and a dilated AzA are also visible at this level. In this patient the LSVC drained into the azygos vein. *C,* A thick coronal maximum-intensity projection reconstruction through the DA shows the DA and DK giving rise to the aberrant LSA.

the aorta again angles posteriorly, forming a second arch, and assumes its normal position anterolateral to the spine. This anomaly is usually not associated with symptoms.

Both coarctation and pseudocoarctation are associated with congenital bicuspid aortic valve (30% to 85% of patients with coarctation); this may result in aortic stenosis. In some patients, CT shows aortic valve calcification, allowing this diagnosis to be suggested.

Aortic Aneurysm

If the ascending aorta measures more than 4 cm in diameter, it is usually referred to as dilated or ectatic. Although a diagnosis of "aortic dilatation" as opposed to "aortic aneurysm" is somewhat arbitrary, this chapter uses "aortic dilatation" or "ectasia" to refer to a generalized dilatation of relatively mild degree (4 cm), with the implication that it is not necessarily a serious problem. "Aneurysm," in contrast, refers to a more focal abnormality or more severe dilatation of the entire aorta (5 cm). If the aorta is more than 6 cm, treatment is usually considered. At the risk of oversimplification, for the ascending aorta, a diameter of 4 cm = aortic dilatation, 5 cm = aortic aneurysm, and 6 cm = surgery.

In some patients with an (atherosclerotic) aortic aneurysm, the diagnosis can be made and the aneurysm distinguished from a solid mass because of peripheral intimal calcification visible on unenhanced scans. Thrombus within an aneurysm or hematoma adjacent to a leaking aneurysm may appear higher in attenuation than aortic blood on unenhanced scans. With contrast infusion, the lumen of the aorta and the aneurysm and the thickness of the aortic wall can be defined clearly (Fig. 3-6).

With atherosclerotic aneurysms, the aortic wall is often thickened and calcification is commonly visible. There may be visible areas of plaque or thrombus within the lumen of the aneurysm (Fig. 3-7); these may also be calcified. Plaque often appears low in attenuation relative to soft tissue or the aortic wall because of its fat content or because of some opacification of the aortic wall itself. Plaque can also be seen in patients with atherosclerosis who do not have aortic dilatation. Focal ulceration of a plaque or thrombus (Fig. 3-7) may occur and should be distinguished from a penetrating atherosclerotic ulcer (PAU), if possible (see later discussion).

Aneurysms are often described as fusiform or saccular, depending on their appearance. Aneurysms localized to the ascending aorta may occur with atherosclerosis, Marfan's syndrome, cystic medial necrosis, syphilis, or aortic valvular

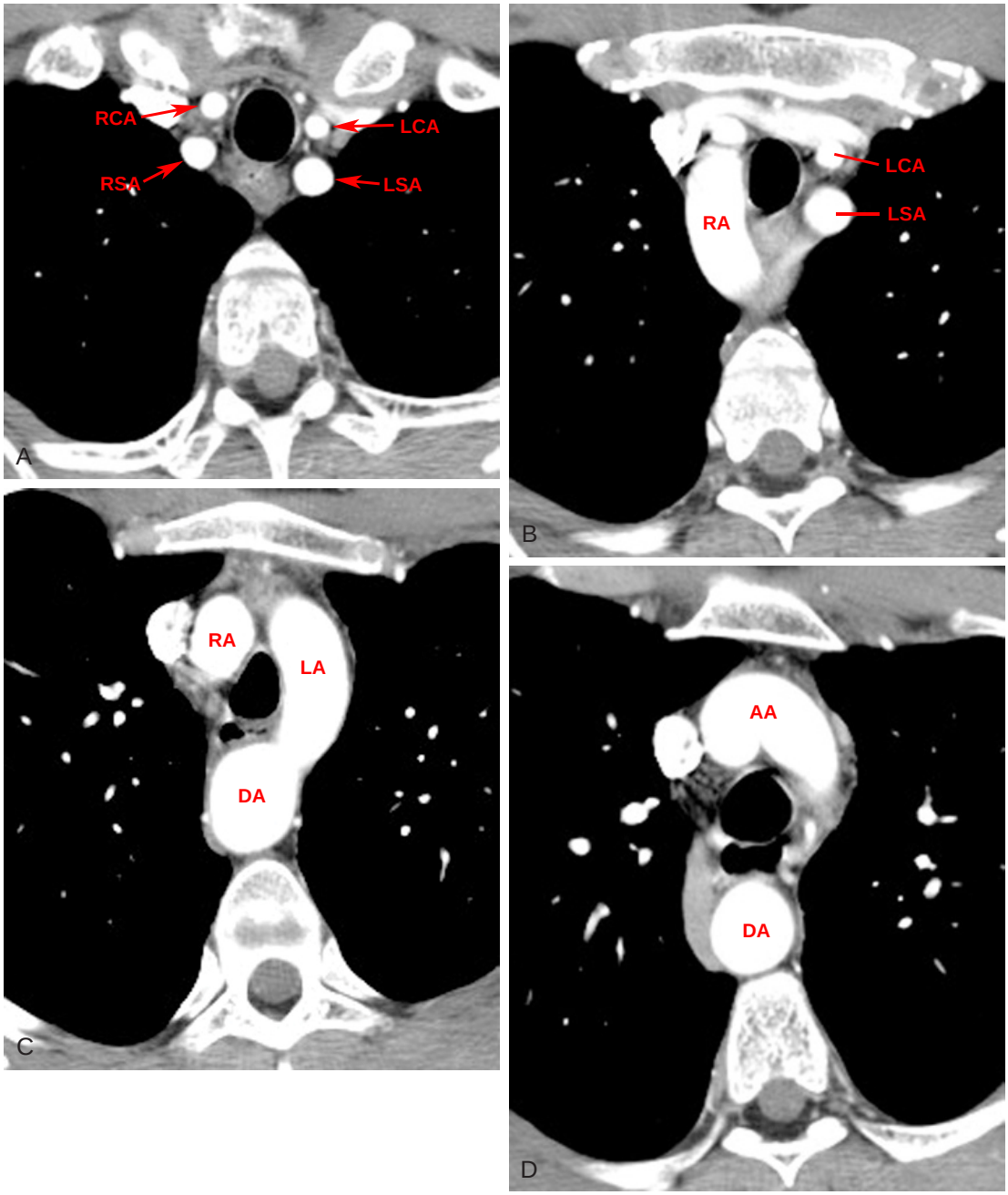

FIGURE 3-4 ■ Double aortic arch. *A*, In the upper mediastinum, the subclavian and carotid arteries appear bilaterally symmetric. LCA, left carotid artery; LSA, left subclavian artery; RCA, right carotid artery; RSA, right subclavian artery. *B*, At a level below *A*, the right arch (RA) is visible to the right of the trachea. On the left side of the mediastinum, the left carotid artery (LCA) and left subclavian artery (LSA), which arise from the left arch, are visible. The RA is characteristically higher and larger than the left. *C*, At a level below *B*, the left arch (LA) is now visible. The anterior right arch (RA) and descending aorta (DA) are also visible at this level. *D*, At a level below *C*, the ascending aorta (AA) and descending aorta (DA) are visible. The ascending aorta has a double-barreled appearance at this level.

disease. An aneurysm near the ligamentum arteriosum may be atherosclerotic in origin, a ductus aneurysm (aneurysm at the site of the ductus arteriosus or a ductus diverticulum), mycotic, related to coarctation, or post-traumatic (i.e., a pseudoaneurysm). Mycotic aneurysms are usually focal, and they may be associated with periaortic inflammation (visible as edema of periaortic fat) or abscess (with localized fluid collections); gas bubbles may be seen within soft tissues. Descending aortic aneurysms are usually atherosclerotic.

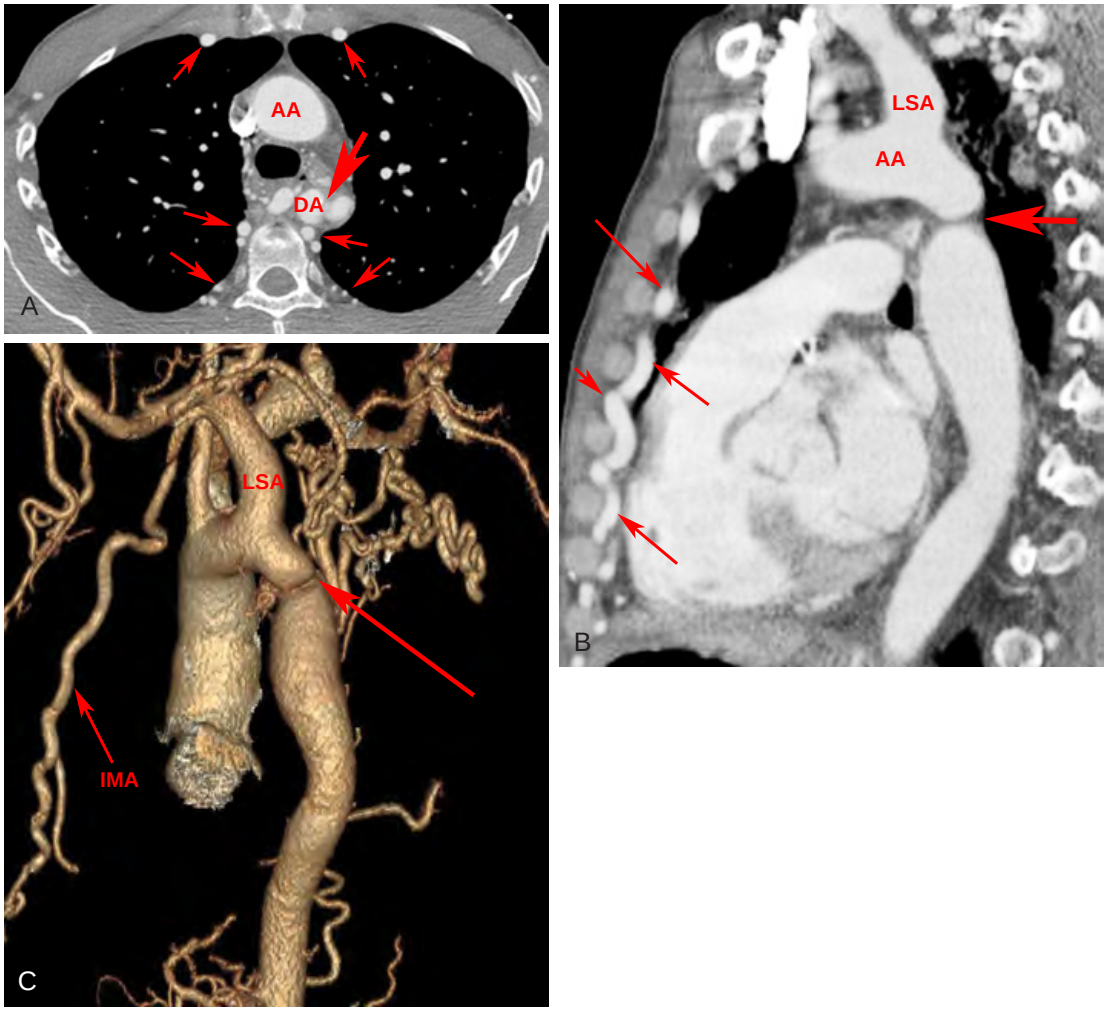

FIGURE 3-5 ■ Aortic coarctation. Multidetector computed tomography with contrast enhancement in a patient with coarctation. *A,* The descending aorta (DA), at the level of the coarctation (*large arrow*), is significantly smaller than the ascending aorta (AA). The internal mammary and intercostal arteries (*arrows*) are dilated, serving as collateral pathways. *B,* Sagittal reconstruction along the plane of the aorta shows marked narrowing at the site of the coarctation (*large arrow*). The left subclavian artery (LSA) is large, because it serves as a collateral pathway, reconstituting flow in the descending aorta. The dilated left internal mammary artery is visible anteriorly (*small arrows*). AA, aortic arch. *C,* Three-dimensional reconstruction of the aorta and its branches showing the coarctation (*large arrow*). The left subclavian artery (LSA) giving rise to the dilated left internal mammary artery (IMA) can also be seen.

Aortic Trauma

Spiral CT has assumed an important role in the diagnosis of aortic injuries, usually associated with a fall or automobile accident. Traumatic aortic laceration, rupture, or pseudoaneurysm occurs most commonly in the following areas: (1) at the aortic root, (2) at the level of the ligamentum arteriosum, or (3) at the diaphragm and aortic hiatus. Patients with aortic root injury often die at the scene of injury; in patients who reach the hospital, injuries at the level of the ligamentum are most common (Fig. 3-8).

Mediastinal hematoma (fluid with a density of about 50 Hounsfield units, HU) contiguous with the aorta is invariably visible on CT in patients with aortic laceration or rupture (Fig. 3-8); the absence of hematoma effectively excludes this diagnosis. The presence of hematoma at the location of a sternal or vertebral fracture does not predict aortic injury.

Contrast-enhanced multidetector CT (MDCT) with thin slices (e.g., 1.25 mm) is highly accurate in diagnosing acute aortic laceration or rupture, with a sensitivity of nearly 100%. The site of rupture or tear may have the appearance of an aortic wall irregularity, dissection, or focal aneurysm (Fig. 3-8); extravasation of contrast is rarely seen, and if present requires immediate attention. It has been suggested that aortography

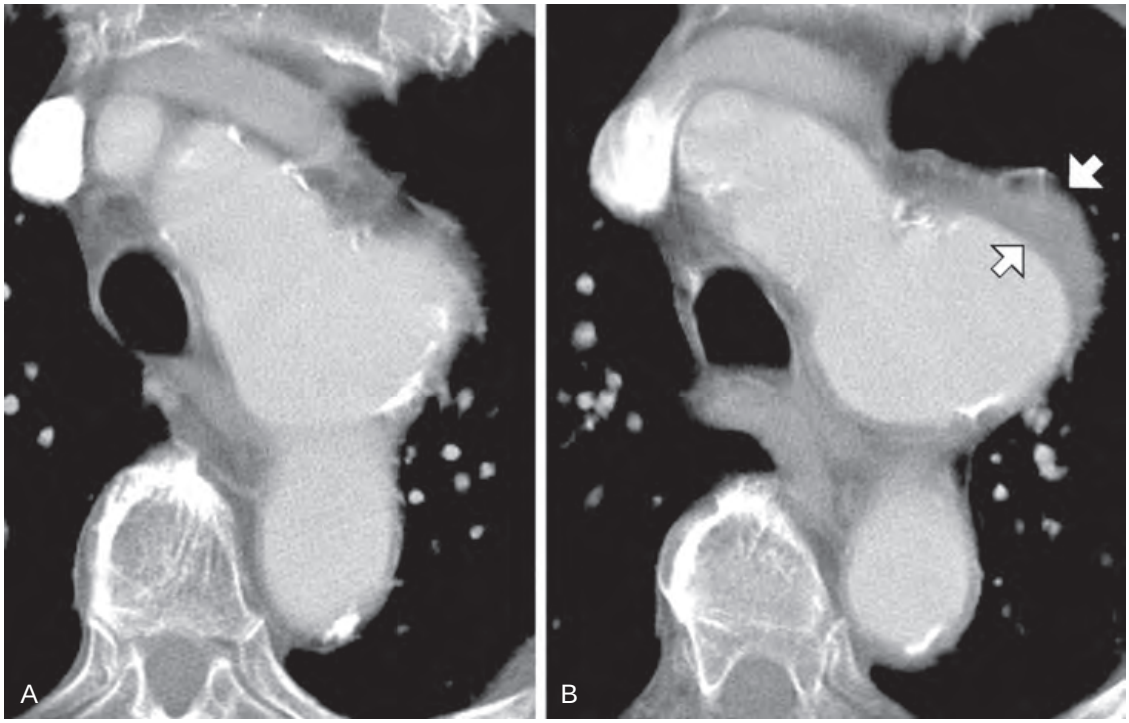

FIGURE 3-6 ■ Aortic aneurysm. *A* and *B,* A focal, saccular aneurysm of the aortic arch shows some clots lining its lumen (*arrows*).

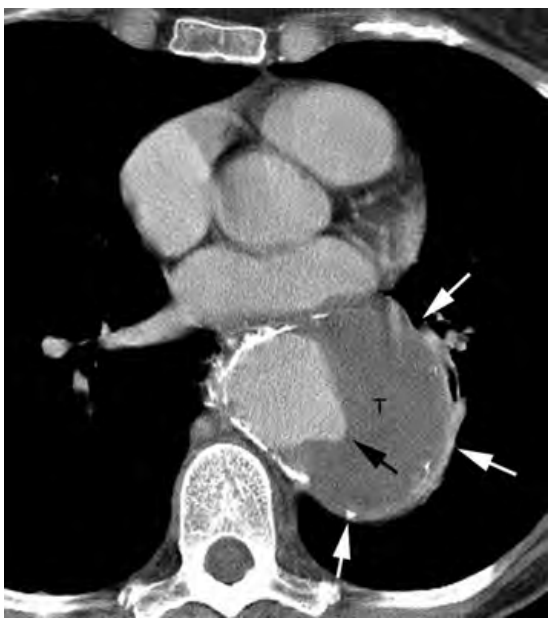

FIGURE 3-7 ■ Aortic aneurysm containing a thrombus. A focal, saccular aneurysm of the descending aorta (*white arrows*) shows calcification of its wall. The aneurysm contains a large thrombus (T) with focal ulceration (*black arrow*).

is not needed if (1) no mediastinal hematoma is visible on CT or (2) no recognizable aortic abnormality in patients with a visible mediastinal hematoma is apparent. Aortography may be necessary in some patients with inadequate CT studies or questionable CT findings, or may be obtained at the time a stent graft is placed for treatment.

Chronic post-traumatic pseudoaneurysm is usually located in the region of the aortopulmonary window, below the takeoff of the left subclavian artery and near the ligamentum arteriosum (Fig. 3-9). Calcification of the wall of the pseudoaneurysm may be present.

Acute Aortic Syndromes

Acute aortic syndrome is a term describing several aortic abnormalities, which present with acute chest pain and are often associated with similar predisposing conditions. These include aortic dissection, intramural hematoma (IMH), and penetrating atherosclerotic ulcer (PAU). They have in common the presence of penetration of the aortic intima or disruption of the media.

Aortic Dissection

Aortic dissection is often associated with hypertension, weakness of the aortic wall (e.g.,

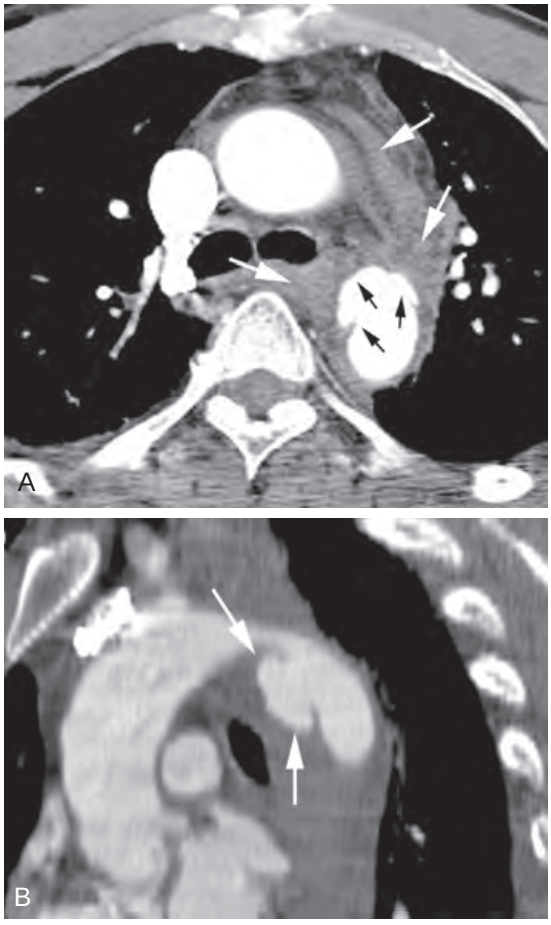

FIGURE 3-8 ■ Acute traumatic aortic rupture with a pseudoaneurysm. *A,* In a patient involved in a motor vehicle accident, contrast-enhanced CT shows mediastinal hematoma (*white arrows*) contiguous with the aorta. There is irregularity of the proximal descending aorta, with a pseudoaneurysm anteriorly (*black arrows*). *B,* A sagittal reconstruction along the aorta shows a pseudoaneurysm (*arrows*) involving the proximal descending aorta. This location is most common.

Marfan's syndrome or cystic medial necrosis), or trauma. Patients usually have acute chest pain. The goal in diagnosing dissection is the demonstration of an intimal flap, displaced inward from the edge of the aorta, separating the true and false channels. CT is ideally suited to this because of its cross-sectional format.

Two schemes for the classification of aortic dissections have been proposed by Daily and DeBakey. Daily's classification, commonly known as the Stanford classification, is most frequently used because of its simplicity and relevance to treatment.

Through use of the Stanford classification, aortic dissections are divided into types A and B. Type A dissections involve the ascending aorta (Fig. 3-10); approximately two-thirds of acute

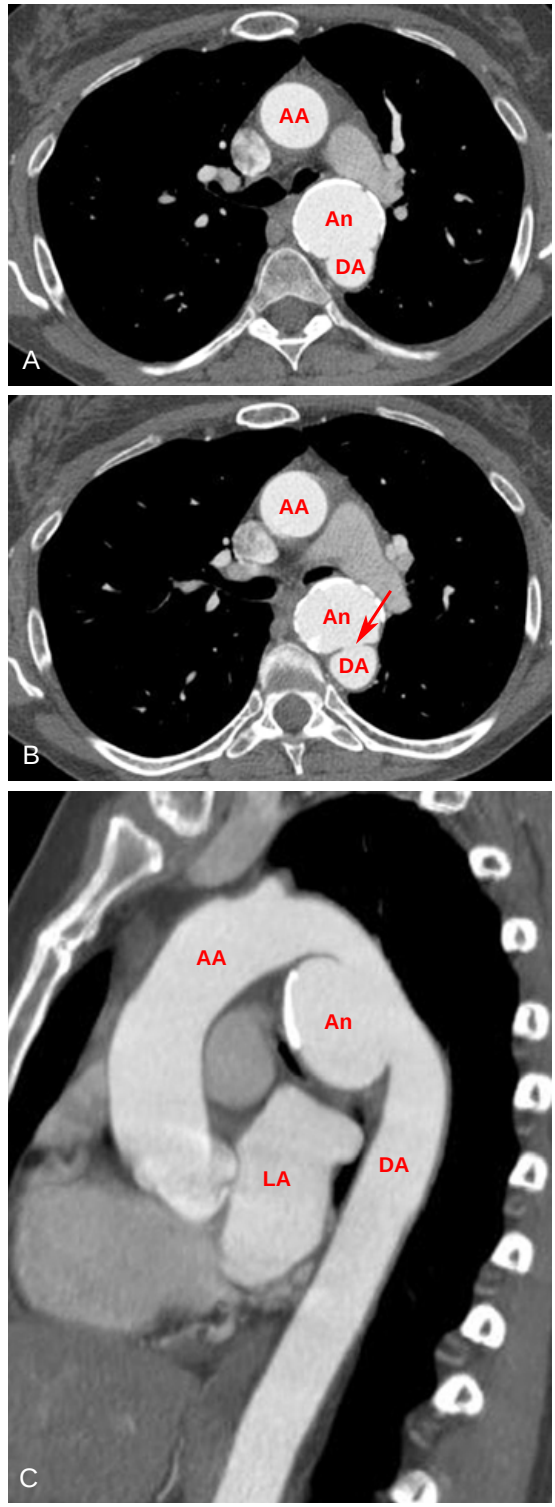

FIGURE 3-9 ■ Chronic post-traumatic pseudoaneurysm. A contrast-enhanced computed tomography scan in a patient who had previously been in a motor vehicle accident. *A,* A focal pseudoaneurysm (An) extends anteriorly from the proximal descending aorta (DA), with dense calcification of its wall. AA, ascending aorta. *B,* At a slightly lower level, a defect (*arrow*) in the anterior wall of the descending aorta represents the site of rupture. *C,* A sagittal reconstruction in the plane of the aortic arch shows the pseudoaneurysm in a typical location. LA, left atrium.

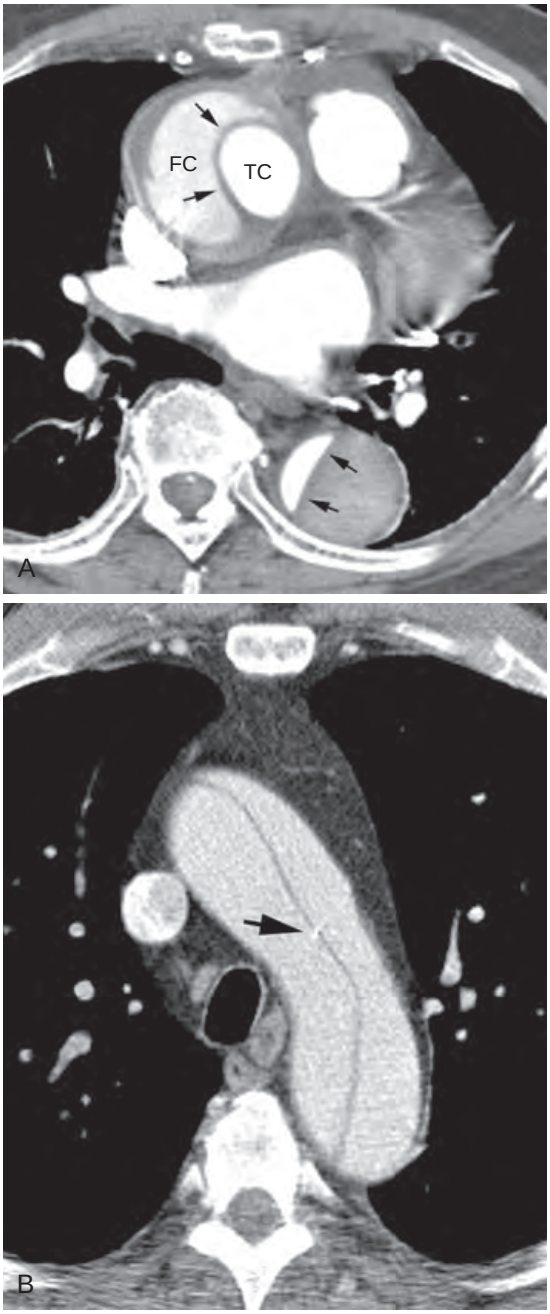

FIGURE 3-10 ■ Type A aortic dissection in two patients. *A,* A patient with acute chest pain shows a type A dissection involving the ascending and descending aorta. The intimal flap (*black arrows*) is lower in attenuation than the contrast-opacified blood. In the ascending aorta, the true channel (TC) is more densely opacified and is smaller. The false channel (FC) is less densely opacified, is more irregular in appearance, and contains a thrombus. The ascending aorta is dilated. In the descending aorta, the true channel is more densely opacified and is more compressed, whereas the false channel is poorly opacified and is located lateral and posterior to the true channel. *B,* The intimal flap is visible in the aortic arch. Calcification of the intima (*arrow*) is visible.

dissections are type A. Because of the possibility of retrograde dissection and rupture into the pericardium (resulting in tamponade) or occlusion of the coronary or carotid arteries, these dissections are usually treated surgically with grafting of the region of the tear. Electrocardiogram (ECG)-gated MDCT can provide exceptional detail in patients with a type A dissection (Fig. 3-11). Type B dissections do not involve the aortic arch but typically arise distal to the left subclavian artery (Fig. 3-12). These are generally treated medically (by normalization of blood pressure) instead of surgically. Placement of an endovascular stent graft is now also used for treatment of type B dissection.

DeBakey's classification includes three types. Type I (involvement of the entire aorta, both ascending and descending) is most common. Type II dissections, which are often associated with Marfan's syndrome, involve the ascending aorta only and, together with type I, correspond to Daily's type A. Type III dissections involve the descending aorta only and are related to hypertension or trauma; this type is equivalent to Daily's type B.

CT is highly sensitive and specific (>95%) in diagnosing dissection and in determining its location and type and the aortic branches involved; consequently, it is an excellent screening and diagnostic procedure in patients with a suggestive clinical presentation. Transesophageal echocardiography may be performed in some patients with suspected acute dissection; it is highly sensitive but has lower specificity (70%). The accuracy of magnetic resonance imaging is similar to that of CT, and magnetic resonance imaging may be performed in patients unable to have radiographic contrast agents; it may also be performed before surgery in patients shown to have a type A dissection. CT or magnetic resonance imaging can be used to follow up patients with dissection after treatment to watch for redissection or extension of the dissection.

In patients with suspected dissection, CT should be performed with rapid contrast infusion. Using a spiral technique, it is easy to scan through the great vessels, aortic arch, and descending aorta (1.25- or 2.5-mm detector width for MDCT) during rapid contrast infusion (at 2.5 to 3.5 mL/second) and to continue the scans to the level of the aortic bifurcation in the abdomen. A scanning delay of approximately 20 to 30 seconds should be used after the start of injection, or scanning should be timed by the scanner. Contrast-enhanced scans are usually preceded by unenhanced scans through the thorax to look for IMH (see later discussion).

In a patient with dissection, the intimal flap is usually delineated by contrast medium filling

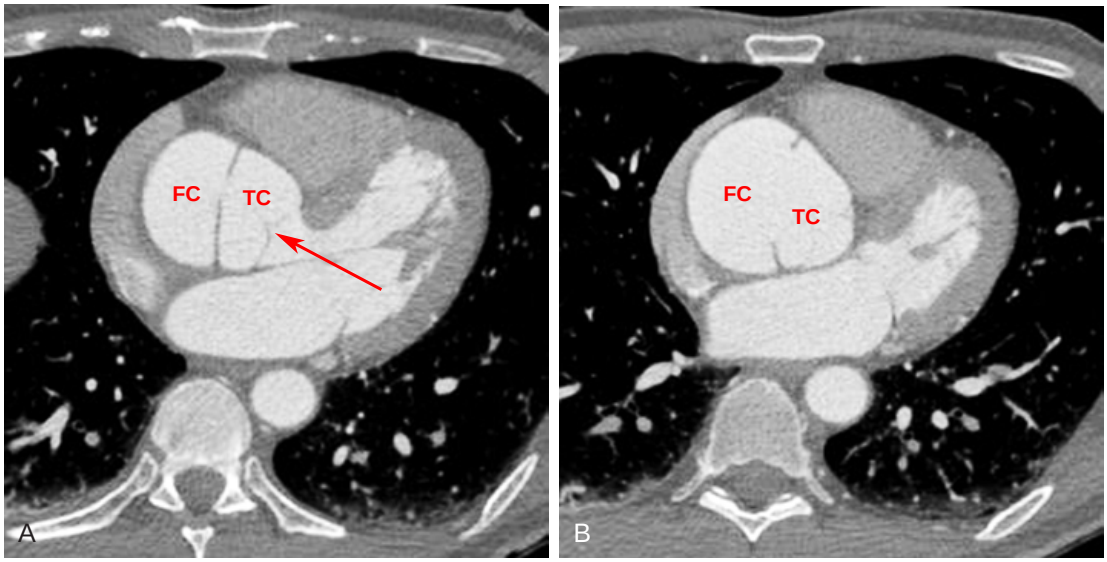

FIGURE 3-11 ■ Type A aortic dissection. Electrocardiogram-gated multidetector computed tomography shows a type A dissection involving the aortic root. *A,* At the level of the left ventricular outflow tract and aortic valve (*arrow*), the true channel (TC) or lumen and false channel (FC) are identified, with the intimal fenestration at the site of origin of the dissection seen as a hole or defect in the intraluminal flap. The aorta is dilated. *B,* At a higher level, a large fenestration in the intimal flap is visible.

both the true and false channels. A fenestration in the aortic intima may be visible at the site of origin of the dissection (Fig. 3-12). The true and false channels can often be distinguished based on the following CT findings (Figs. 3-10*A*, 3-11, and 3-12), although this may be difficult or impossible in some cases:

1. If the aortic root or ascending aorta is normal in appearance, trace the opacified aortic lumen on adjacent slices to see which of the distal channels it communicates with. This represents the true channel.
2. The false channel tends to be located lateral to the true channel at the level of the aortic arch and spirals posteriorly in the descending aorta. Because of this characteristic location, the left renal artery is the abdominal branch most likely to arise from the false channel.
3. The true lumen is usually smaller.
4. The false channel is usually more irregular in contour, and it may contain strands of tissue termed *cobwebs* within the contrast stream.
5. The false channel is more likely to contain a thrombus.
6. Blood flow is slower and opacification is often delayed in the false channel.
7. Aortic wall calcification may be seen lateral to the true channel.

The false channel may be opacified or thrombosed. Thrombosis of the false channel is associated with better prognosis. The false channel may dilate, and sometimes it may rupture. Overall, the aortic diameter may be increased at the site of a dissection because of dilatation of the false channel.

Artifacts, arising because of cardiac motion or vascular pulsations during the scan, may mimic an intimal flap. They are commonly seen at the level of the aortic root and in the descending aorta, adjacent to the left heart border. Typically, they are less sharply defined than a true intimal flap, may extend beyond the edges of the aorta, or are inconsistently seen from one level to the next.

Two other abnormalities may closely mimic the clinical presentation of dissection. Consequently, these may be seen on CT scans obtained to exclude dissection in patients with acute aortic syndrome. These are IMH and PAU.

Intramural Hematoma

IMH results from hemorrhage into the aortic wall. Acute IMH may closely mimic the presentation of dissection (acute chest pain in a patient with hypertension). It is thought to occur because of bleeding from the vasa vasorum, although in some cases it may represent a sealed-off dissection.

On contrast-enhanced scans, the IMH appears as a smooth, crescentic, or, less commonly, concentric thickening of the aortic wall (Figs. 3-13 and 3-14). On unenhanced scans, the IMH

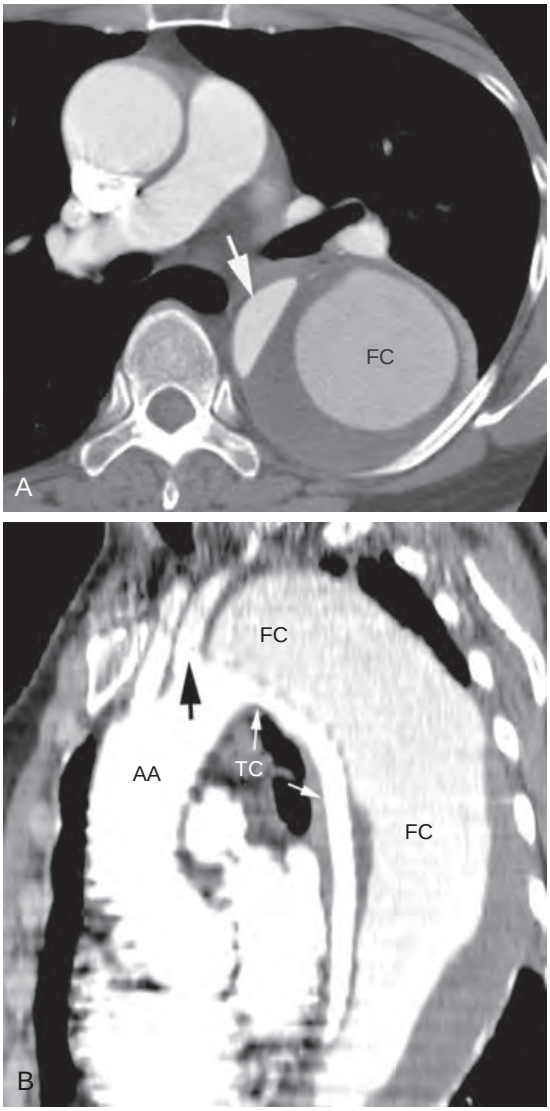

FIGURE 3-12 ■ Type B aortic dissection. *A,* Enhanced spiral computed tomography shows a dissection in the descending aorta. The false channel (FC) is larger, located posterolaterally, less opacified, and lined by a thrombus. The true channel (*arrow*) is more compressed. The ascending aorta is normal in appearance. *B,* A sagittal reconstruction shows the large FC originating distal to the left subclavian artery (*black arrow*). The true channel (TC) is small and more densely opacified; it is evident that it communicates directly with the normal ascending aorta (AA). The intimal flap separating the true and false channels is visible.

appears denser than unenhanced blood in the aortic lumen; because of this characteristic appearance, CT in a patient with suspected dissection should be preceded by unenhanced scans through the thorax. If unenhanced scans are not obtained prospectively, delayed unenhanced scans may be obtained. Inward displacement of intimal calcification can also be seen on unenhanced scans.

It should be remembered that the normal aortic wall is a few millimeters in thickness. On unenhanced scans, it appears to have the same density as blood in the aortic lumen in healthy subjects. In patients with anemia (hematocrit, ≤ 35%), the normal aortic wall may appear denser than blood. This should not be confused with IMH. As a rough rule, the CT density of unenhanced blood in the aortic lumen (in HU) is about the same as the hematocrit.

The smooth crescentic or concentric wall thickening seen with IMH is usually different in appearance from dissection with a thrombosed channel. Thrombosed dissection uncommonly appears crescentic or concentric in shape. A thrombus lining an aneurysm can also mimic IMH, but it is usually more irregular in contour. The presence of acute chest pain as a presenting symptom also suggests an acute IMH rather than a thrombus within a chronic dissection or aneurysm.

An IMH may rupture, progress to frank dissection (by rupture into the aortic lumen), result in an aneurysm, or resolve. Treatment is similar to that for dissection occurring in the same location (i.e., type A or B), and IMH is often classified as type A or B, as is dissection (Figs. 3-13 and 3-14). A type A IMH is treated surgically because of potential complication (Fig. 3-14).

Penetrating Atherosclerotic Ulcer

In patients with atherosclerosis, ulceration of an atherosclerotic plaque may, over time, penetrate the aortic wall, resulting in PAU. The descending aorta is most often involved, because atherosclerosis is most common there. PAU may lead to chest pain similar to that for dissection or IMH.

True PAU penetrates the intima and extends into (or through) the aortic wall (Fig. 3-15); its appearance is similar to that of a penetrating gastric ulcer (Fig. 3-16). Calcification of the aortic wall or enhancement of the wall after contrast infusion may help in diagnosing wall penetration. PAU may result in localized IMH (Fig. 3-17), dissection (which is usually localized), pseudoaneurysm, or, sometimes, rupture. Surgical treatment may be necessary in some cases, particularly in patients presenting with chest pain, even if the PAU is limited to the descending aorta. Incidental PAU may not require treatment.

Ulceration of an atheroma or thrombus (Figs. 3-7 and 3-18) may mimic the appearance of PAU, but it is more superficial and does not involve the aortic wall itself.

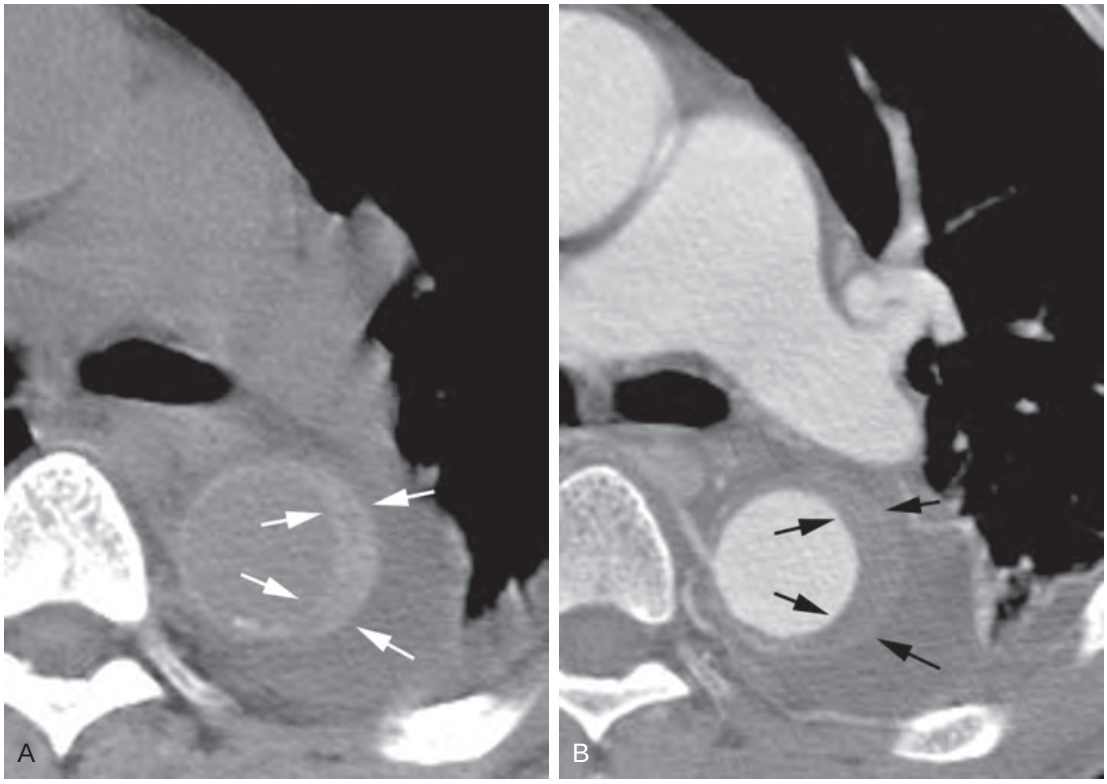

FIGURE 3-13 ■ Intramural hematoma (type B). *A,* In a man with acute chest pain, unenhanced CT shows crescentic thickening of the aortic wall (*arrows*). This is higher in attenuation than blood in the aortic lumen. *B,* Contrast-enhanced spiral computed tomography shows crescentic thickening of the aortic wall (*arrows*). On the enhanced scan, the high attenuation of the hematoma is difficult to appreciate.

SUPERIOR VENA CAVA AND GREAT VEINS

Congenital Abnormalities

Azygos Lobe

An azygos lobe is a common anomaly and is present in about 1 in 200 patients. It results in a typical appearance on plain radiographs and CT that is easily recognized and produces a characteristic alteration in normal mediastinal anatomy. In patients with this anomaly, the azygos arch is located more cephalad than normal, at, near, or above the junction of the brachiocephalic veins. Above this level, the azygos fissure is visible within the lung, marginating the azygos lobe (Fig. 3-19).

Persistent Left Superior Vena Cava

The only other frequent venous anomaly is persistent left superior vena cava (LSVC), which represents failure of the embryonic left anterior cardinal vein to regress. This anomaly is difficult to recognize on plain films; however, in some patients, there is a slight prominence of the left superior mediastinum, or a left-sided venous catheter may be inadvertently placed in the LSVC. It is present in about 0.3% of healthy subjects, at approximately the same frequency as for an azygos lobe; it is usually unassociated with symptoms or other abnormalities but is more frequent (4.4%) in patients with congenital heart disease.

On CT in patients with this anomaly, the LSVC is positioned lateral to the left common carotid artery in the supra-aortic mediastinum (Fig. 3-3). It descends along the left mediastinum, passing downward, anterior to the left hilum, and usually enters the coronary sinus posterior to the left atrium. In 65% of patients, the left brachiocephalic vein is absent, a right vena cava is also present, and the two vessels are about the same size and in the same relative position on opposite sides of the mediastinum. If the left brachiocephalic vein is also present, joining the right and left superior venae cavae, the right SVC will be larger than the left.

An LSVC will exhibit dense opacification after contrast medium injection into the left arm. If contrast medium is injected on the right and the vein is not opacified, its tubular shape and

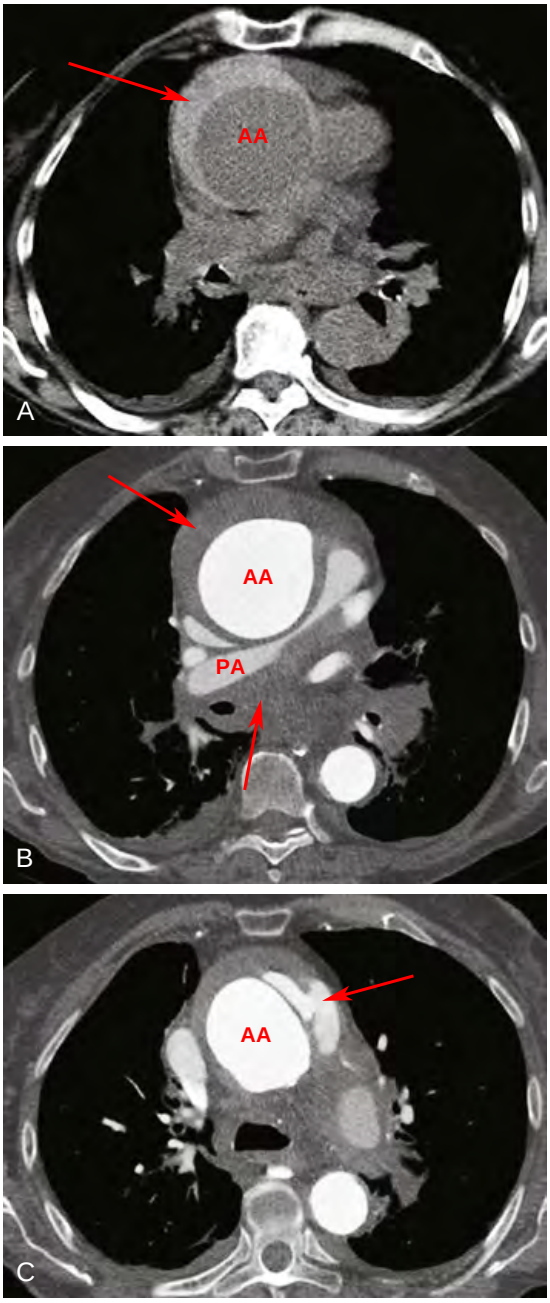

FIGURE 3-14 ■ Intramural hematoma (type A) with aortic rupture. *A*, In an elderly woman with acute chest pain, the ascending aorta (AA) is dilated and an intramural hematoma (IMH) (*arrow*) is visible because of its high attenuation. *B*, At a higher level, the AA is dilated and high-attenuation blood (*arrows*) is seen in relation to the IMH and free in the mediastinum. The right pulmonary artery (PA) is markedly compressed by the dilated aorta and mediastinal hematoma. *C*, Cephalad to *B*, contrast opacification of a portion of the IMH is seen, as well as leakage into the mediastinum. High-attenuation blood is visible throughout the mediastinum. This patient died shortly after computed tomography was performed.

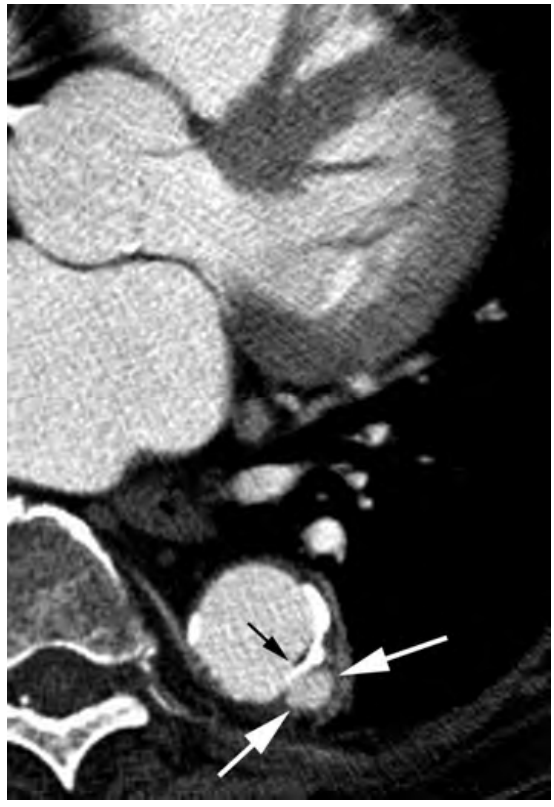

FIGURE 3-15 ■ Penetrating atherosclerotic ulcer. Enhanced spiral computed tomography in a man with chest pain shows contrast opacification of a focal ulceration extending into the aortic wall (*white arrows*). Calcification (*black arrow*) shows the location of the intima.

FIGURE 3-16 ■ Penetrating atherosclerotic ulcer. Enhanced multidetector computed tomography in a patient with chest pain shows contrast opacification of a focal ulceration of the medial wall of the aortic arch (*arrow*). On an unenhanced image this was associated with a focal intramural hematoma.

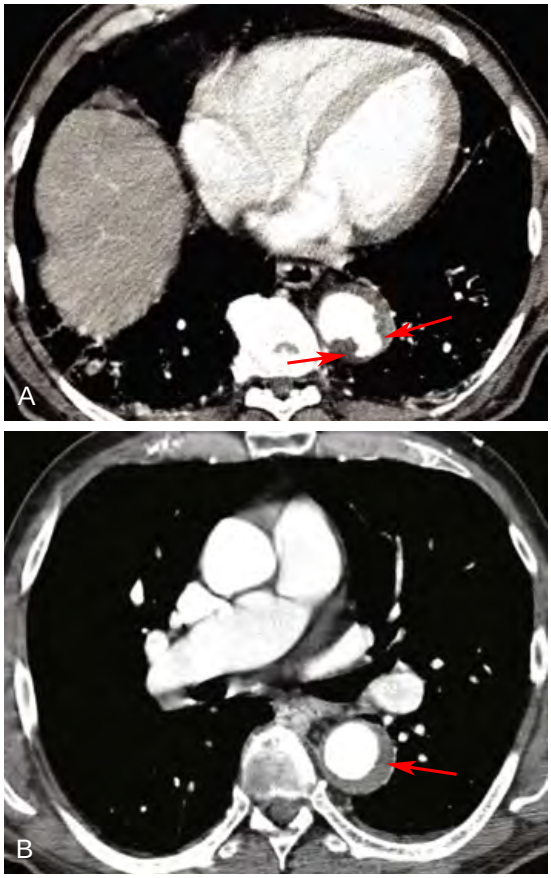

FIGURE 3-17 ■ Penetrating atherosclerotic ulcer associated with an intramural hematoma. *A,* Enhanced multidetector computed tomography in a patient with chest pain shows a focal ulceration in the descending aorta (*arrows*). On this single image, this could represent an ulcerated thrombus, although when associated with chest pain, a penetrating atherosclerotic ulcer should be expected. *B,* At a higher level, an intramural hematoma (*arrow*) results in crescentic thickening of the aortic wall.

FIGURE 3-18 ■ Ulceration of an atheromatous plaque. A sagittal reconstruction through the aortic arch and descending aorta shows extensive ulceration of an atheromatous plaque. None of the ulcers projects through the aortic wall. This patient was asymptomatic.

characteristic position are usually enough for a definite diagnosis.

Azygos or Hemiazygos Continuation of the Inferior Vena Cava

Embryogenesis of the inferior vena cava is one of the most complicated sequences I know of and several vessels must develop and regress in turn for it to form normally. During fetal development, the vessels that form the azygos and hemiazygos veins normally communicate with the suprarenal inferior vena cava, but this communication usually breaks down. If it does not, then azygos or hemiazygos continuation of the inferior vena cava is said to be present.

These lesions may be associated with other congenital anomalies, including polysplenia (in patients with hemiazygos communication) or asplenia (with azygos communication), or they may be isolated abnormalities. Typical findings include marked dilatation of the azygos arch and posterior azygos vein (Fig. 3-20). If hemiazygos continuation is present, the dilated azygos vein will be seen to cross the mediastinum, from right to left, behind the descending aorta, to communicate with a dilated hemiazygos vein. A normal-appearing inferior vena cava is often visible at the level of the heart and diaphragm, draining the hepatic veins. Either anomaly may be associated with duplication of the abdominal inferior vena cava. Rarely, a dilated hemiazygos vein drains into the left brachiocephalic vein instead of joining the azygos.

Superior Vena Cava Syndrome

Obstruction of the superior vena cava (SVC), or either of the brachiocephalic veins, is a common clinical occurrence, and symptoms of venous obstruction may require CT. In some patients undergoing CT for diagnosis of a mediastinal

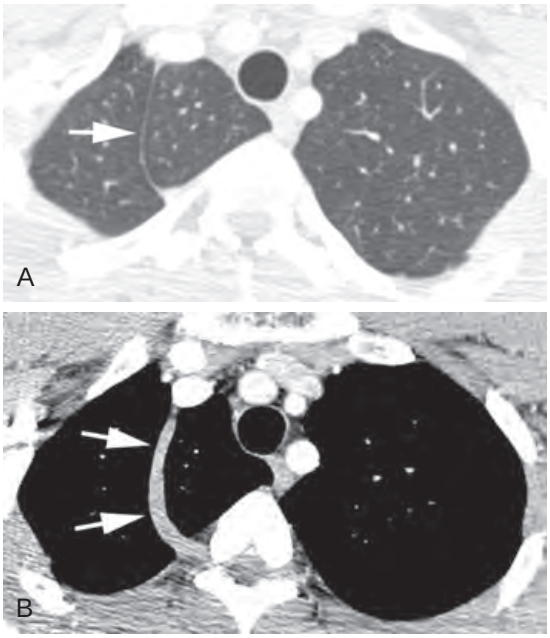

FIGURE 3-19 ■ Azygos lobe. *A,* Within the upper lung, the azygos fissure (*arrow*) distinguishes the azygos lobe medially from the remainder of the upper lobe. *B,* At a lower level, the azygos arch (*arrows*) passes from an anterior to a posterior position. In this patient, it arises from the right brachiocephalic vein.

mass or lung cancer, CT will also show findings of vena cava obstruction.

SVC obstruction can be seen in a variety of diseases, most commonly bronchogenic carcinoma, although in some parts of the United States, granulomatous mediastinitis as a result of histoplasmosis is a common cause. Other causes of SVC obstruction include sarcoidosis, fibrosing mediastinitis, tuberculosis, and mediastinal radiation for neoplasm. Because of the frequent use of subclavian catheters, venous thrombosis resulting in obstruction is not uncommon.

On CT in patients with SVC obstruction (Figs. 3-21 and 3-22), a number of characteristic findings are present. Beginning peripherally, as the contrast medium bolus is injected, it is common to see opacification of a number of small venous collateral vessels in the shoulder, axilla, upper chest wall, and upper mediastinum. However, it should be remembered that some filling of small veins in the chest wall and axilla can be seen in the absence of a venous abnormality (perhaps because of poor positioning of the patient's arm for injection). Unless other findings of venous obstruction (e.g., large collateral veins) are present, this finding should not be of great concern.

In patients with obstruction of the SVC, flow of contrast medium from the arm is delayed and the scan sequence must be delayed accordingly, or mediastinal vascular opacification will be poor. Collateral vessels, which are characteristically dilated in patients with obstruction of the SVC, include the intercostal veins, the internal mammary veins, the left superior intercostal vein (which results in the "aortic nipple" sometimes visible on chest radiographs), and the hemiazygos vein. The azygos vein and azygos arch usually form the final common pathway for venous return from all these collateral vessels, bypassing the area of obstruction and draining blood into the lower SVC, just above the right atrium.

In patients with thrombosis of the SVC or brachiocephalic veins, a thrombus is sometimes visible in the vessel lumen, outlined by contrast medium. One word of caution, however: If contrast medium is injected into only one arm, as is typical, streaming of unopacified blood from one brachiocephalic vein into the SVC can mimic the appearance of an SVC clot.

PULMONARY ARTERIES

Dilatation of the main pulmonary artery can be seen as a result of pulmonic stenosis, a left-to-right shunt, or pulmonary hypertension. A main pulmonary artery diameter measuring 3.5 cm or more (lateral to the ascending aorta), or exceeding the diameter of the ascending aorta, suggests abnormal dilatation, usually associated with pulmonary hypertension (Fig. 3-23*A*). Associated right ventricular dilatation or hypertrophy may be observed (Fig. 3-23*B*). With pulmonic stenosis, the main and left pulmonary arteries are dilated, whereas the right pulmonary artery is relatively normal in size. With shunts or pulmonary hypertension, both pulmonary arteries are large.

Pulmonary artery aneurysms are rare; they may be mycotic aneurysms or caused by catheter-related complications, Takayasu's arteritis, Williams syndrome, prenatal varicella, or Behçet's syndrome.

Pulmonary Embolism

Contrast-enhanced CT is commonly used to diagnose pulmonary embolism (PE; Figs. 3-24 and 3-25). PE diagnosis is one of the most important uses of chest CT in clinical practice. Because of CT, the use of radionuclide imaging and pulmonary arteriography has decreased precipitously in recent years.

MDCT is highly advantageous because thin slices and rapid scanning are possible. With MDCT, an appropriate technique involves (1) 1.25-mm detector rows, (2) a pitch of about 1.5,

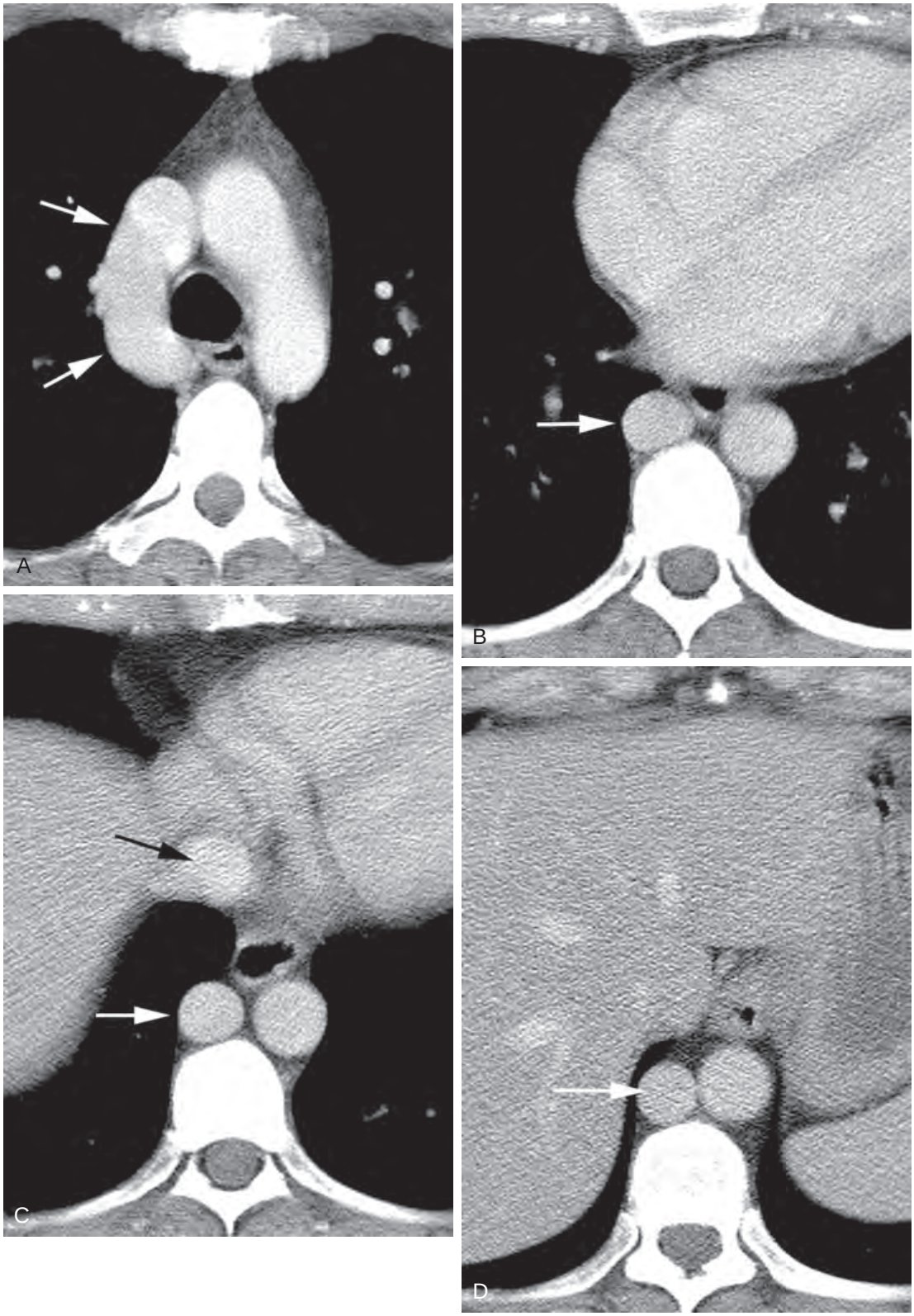

FIGURE 3-20 ■ Azygos continuation of the inferior vena cava. The azygos arch (*white arrows*, *A*) and the posterior azygos vein (*white arrow*, *B* to *D)* are markedly dilated. A normal-appearing inferior vena cava is visible at the level of the heart and diaphragm (*black arrow*, *C*), draining the hepatic veins, but it is not seen below this level.

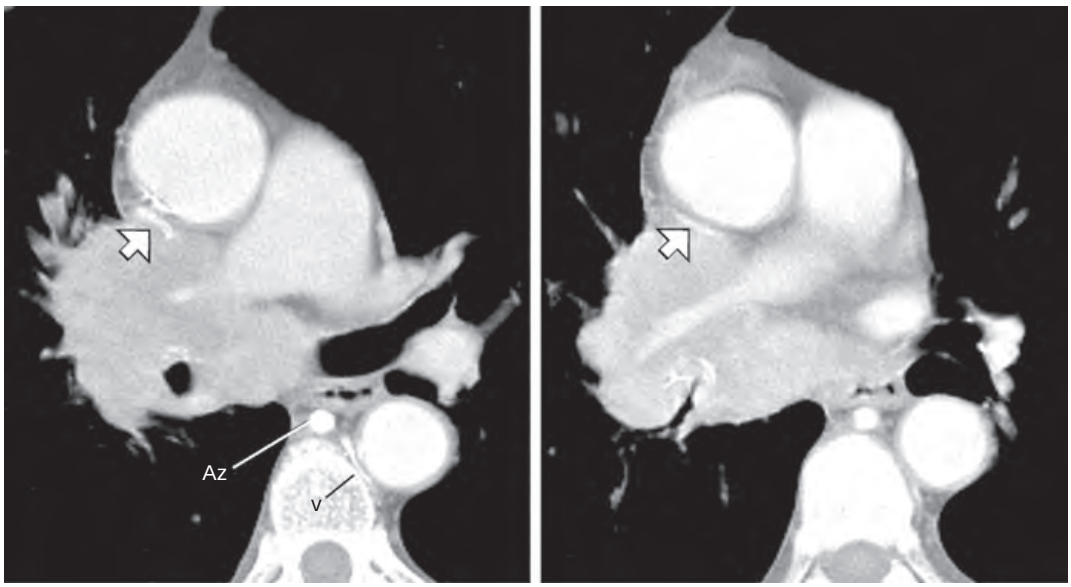

FIGURE 3-21 ■ Superior vena cava (SVC) obstruction in bronchogenic carcinoma. *A* and *B,* In a patient with a large right hilar mass and mediastinal invasion, the SVC (*arrows*) is nearly obstructed. The azygos vein (Az) and a left intercostal vein (V) are opacified because they are serving as collateral pathways to bypass the obstruction.

FIGURE 3-22 ■ Superior vena cava syndrome in metastatic carcinoma. Computed tomography with contrast enhancement in a patient with metastatic carcinoma and symptoms of superior vena cava syndrome. The superior vena cava contains a large tumor thrombus (*large arrow*). The internal mammary vein and azygos vein (*small arrows*) are opacified because they are serving as collateral pathways. The right upper lobe is consolidated because of post-obstructive pneumonia. Pleural effusions are present.

(3) a single breath hold of 5 seconds, (4) coverage of the entire thorax (volume of 25 cm), (5) contrast medium injection at a rate of 5 mL/second, with the injection started 20 seconds before scanning or timed by the scanner, and (6) reconstruction at 1.25-mm intervals.

A filling defect visible within a pulmonary artery is usually diagnostic of PE (Figs. 3-24 and 3-25), but large filling defects mimicking PE can also be seen in patients with intraluminal pulmonary artery masses. These may occur with pulmonary artery angiosarcoma or endovascular tumor embolism (e.g., in sarcomas, hematoma, and renal cell carcinoma) with tumor masses growing within the artery lumen; these are much less common than PE.

An acute PE is usually centered in the lumen of the artery, outlined by the injected contrast agent (Figs. 3-24 and 3-25). If the vessel is seen in cross-section, this appearance is termed the *doughnut sign.* If the vessel is visible along its length, it is termed the *railroad track sign.* Some clots may completely obstruct an artery; if this is the case, the vessel may appear expanded at the point of obstruction. The clot usually measures 60 HU or less in attenuation; the opacified blood outlining it measures considerably more (i.e., 200 HU).

Acute pulmonary emboli are usually long or "worm-shaped," and they are usually visible on a number of scans when oriented perpendicular to the scan plane (i.e., the vessel is seen in cross-section) or are seen along their length if the artery lies in the scan plane. An apparent filling defect visible on only one or two scans (for a vessel seen in cross-section) is likely an artifact. Contrast streaming artifacts in patients with slow blood flow or poor opacification can result in apparent filling defects, but they will usually be ill-defined, and the apparent defect will have an attenuation higher than that of a clot. Generally speaking, if an apparent filling defect appears brighter than muscle on the same scan, it is a flow artifact rather than a PE. Measuring the attenuation of an

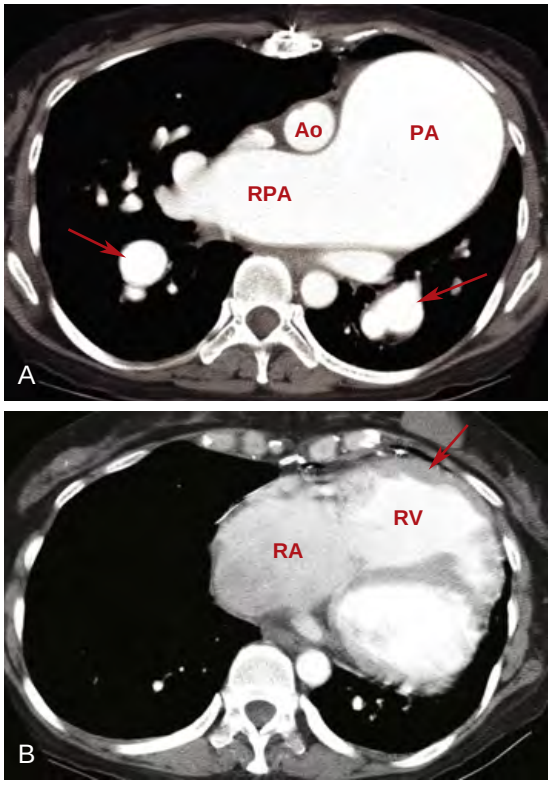

FIGURE 3-23 ■ Marked dilatation of the pulmonary artery in a patient with Eisenmenger's syndrome and pulmonary hypertension. *A,* The main pulmonary artery (PA) greatly exceeds the diameter of the ascending aorta (Ao), indicating the presence of pulmonary hypertension. The right pulmonary artery (RPA) and interlobar pulmonary arteries (*arrows*) are also dilated. *B,* Computed tomography at a lower level shows dilatation of the right ventricle (RV) and right atrium (RA). The RV wall (*arrow*) is markedly hypertrophied (thickened) because of pulmonary hypertension. This is an extreme example of PA dilatation.

apparent filling defect can also help in deciding if it is an artifact; flow artifacts usually have an attenuation greater than 100 HU.

A *chronic PE* is usually adherent to the vessel wall and is located peripherally, with contrast in the center of the vessel lumen (Fig. 3-26). This is the opposite of what is seen with acute PE. *Pulmonary artery webs* (wispy or thin linear filling defects) can indicate a chronic embolism or may be seen as a clot that is resolving. Enlargement of the main pulmonary artery because of pulmonary hypertension can be seen with chronic PE.

The sensitivity and specificity of spiral CT in diagnosing acute PE involving the main pulmonary artery branches are considered to be 100%; its overall sensitivity and specificity exceed 90% for segmental emboli. The sensitivity of MDCT in detecting subsegmental clots is less, but MDCT is more sensitive in detecting small clots than other imaging modalities used clinically.

It should be kept in mind that isolated subsegmental emboli are relatively uncommon (other large clots, more easily seen, are usually also present), and isolated subsegmental clots may not be significant from a hemodynamic point of view. A number of studies have shown that if a CT (even a single-detector CT with 3-mm-thick slices and slow scanning) is read as showing "no PE," patient outcome is very good, with 3-month survival without recurrent PE of about 99% or more. This is just as good as when other modalities are used for diagnosis.

When single-detector CT was first introduced for PE diagnosis, there was concern among physicians that CT was not sufficiently sensitive to use for PE diagnosis. However, at present, because of advances in MDCT technology, many

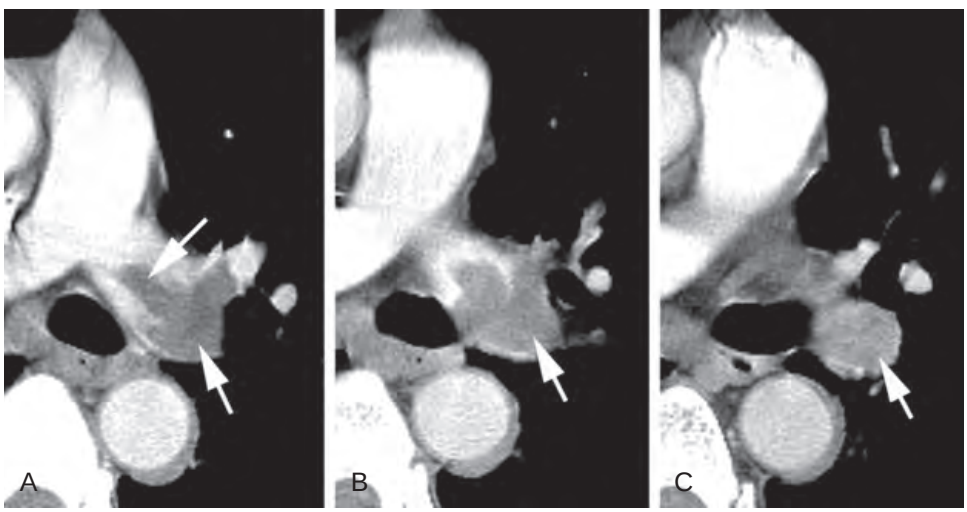

FIGURE 3-24 ■ Acute pulmonary embolism in the left main pulmonary artery. *A* to *C,* A clot fills the left main and interlobar pulmonary artery (*arrows*) and is outlined by contrast medium in *A.*

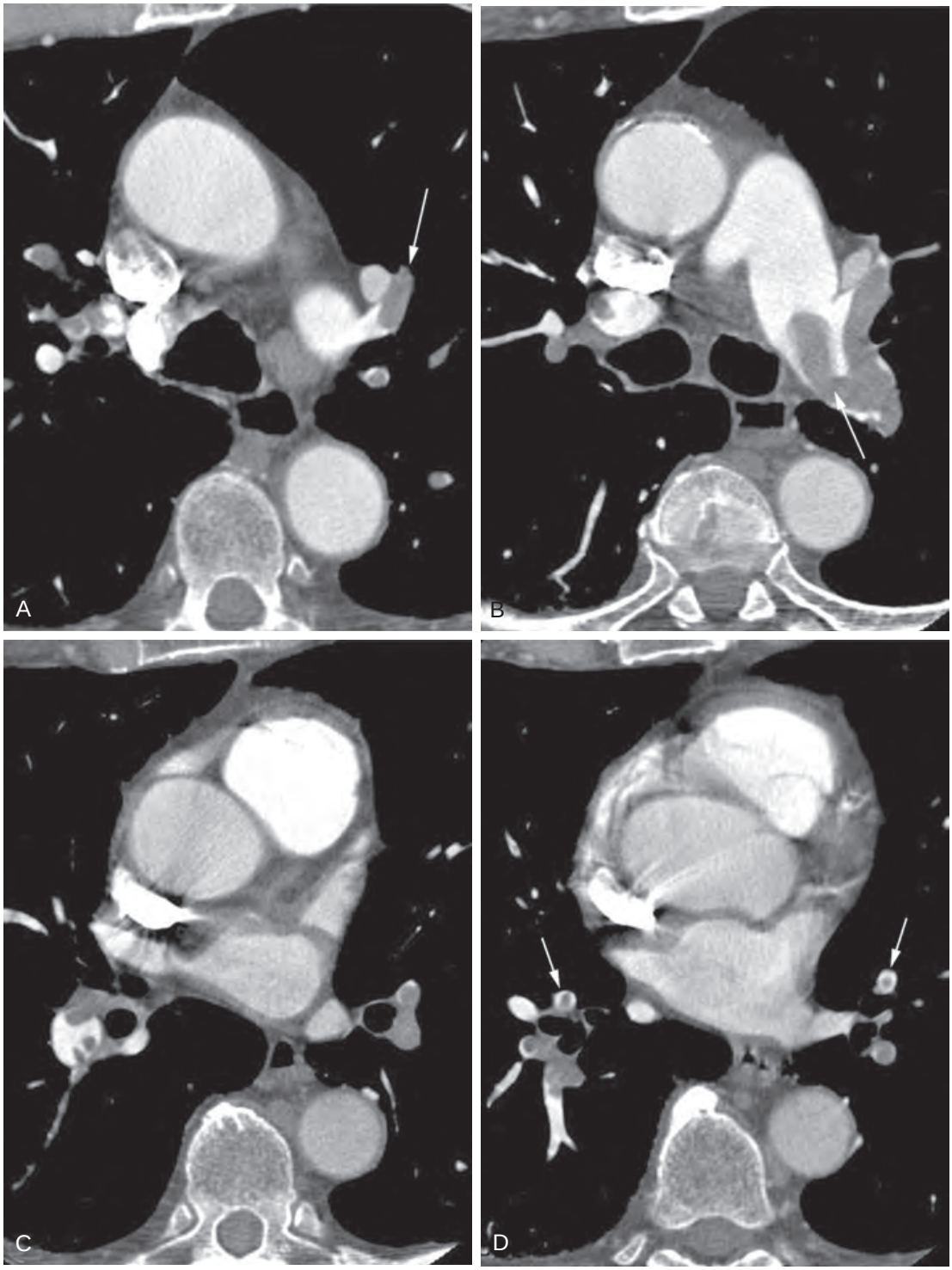

FIGURE 3-25 ■ Multidetector computed tomography (1.25-mm slices) in acute pulmonary embolism. *A* to *D*, Multiple clots (*arrows*) are visible within large central, lobar, segmental, and subsegmental pulmonary artery branches. They are outlined by contrast medium, showing examples of the "railroad track sign" *(arrow, B)* and "doughnut sign" *(arrows, D).* Some vessels are completely obstructed and the clots are not outlined by contrast medium (*arrow*, *A*).

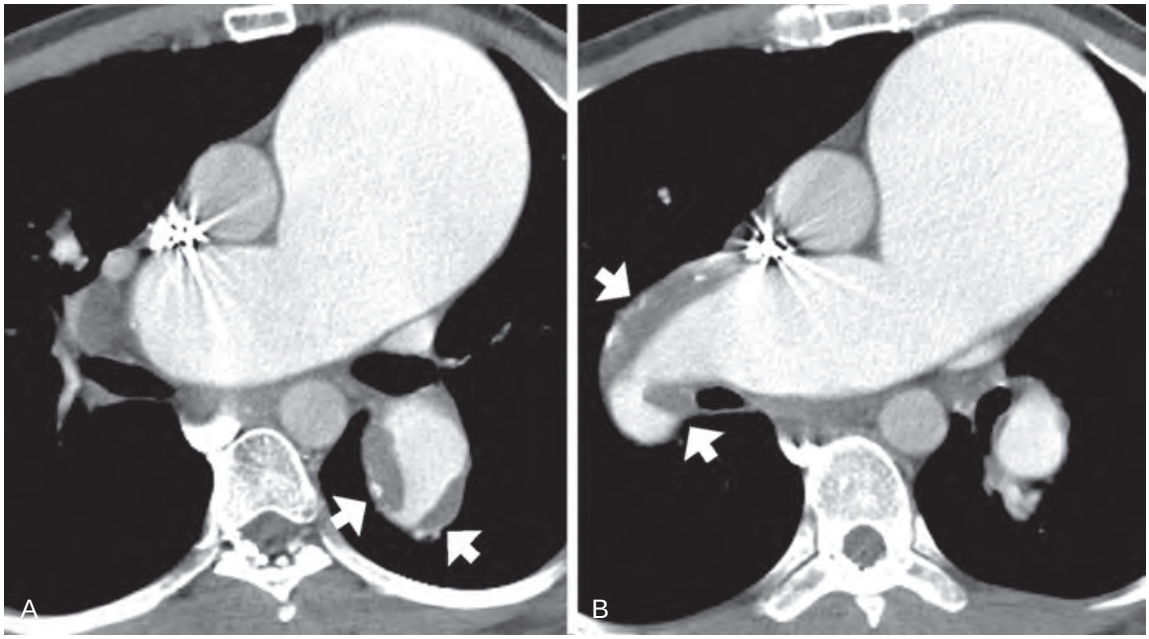

FIGURE 3-26 ■ Chronic pulmonary embolism and pulmonary hypertension in a patient with Marfan's syndrome. *A* and *B,* The main pulmonary artery is dilated because of pulmonary hypertension. A thrombus (*arrows*) is adherent to the vessel wall. Some calcification of the vessel wall is also seen.

investigators now feel that CT is *too sensitive*, and likely to overdiagnose PE (i.e., detect subsegmental clots that are clinically insignificant and do not require treatment). Incidental (asymptomatic) subsegmental PE is commonly seen on MDCT (Fig. 3-27). The necessity for treatment of isolated subsegmental PE is controversial and based on very few data; it may be unnecessary in stable patients without other significant abnormalities.

It should also be kept in mind that only about 5% of patients having CT for clinically suspected PE actually have PE as a cause of their symptoms, even when D-dimer is used in screening. The remainder of these patients have other abnormalities associated with acute chest pain, dyspnea, and hypoxemia. These include atelectasis, pneumonia, pulmonary edema, pleural effusions, cancer, and diffuse lung diseases. MDCT is very helpful in the diagnosis of these abnormalities.

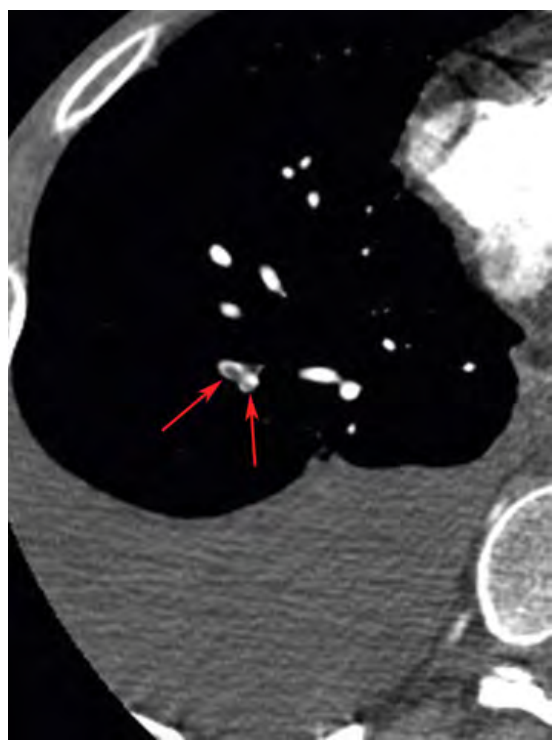

FIGURE 3-27 ■ Isolated subsegmental pulmonary embolism, likely incidental and clinically insignificant. Multidetector computed tomography obtained in a patient with chest pain and shortness of breath shows a definite clot (*arrows*) draped over both limbs of a branching subsegmental artery. This was the only clot visible. This small pulmonary embolism is likely insignificant. The patient's symptoms were likely related to his pleural effusion.

THE HEART AND PERICARDIUM

CT is not commonly used for evaluation of cardiac abnormalities, but some knowledge of cardiac anatomy on CT is necessary for proper interpretation of scans and identification of paracardiac abnormalities or masses and the effect they have on the heart. Occasionally, incidental cardiac abnormalities are detected on CT. Coronary artery calcification or stenosis can be assessed

FIGURE 3-28 ■ Old myocardial infarct with a left ventricular thrombus. Multidetector computed tomography in a patient with a prior myocardial infarct shows thinning of the septal and left ventricular myocardium (*small red arrows*). Subendocardial calcification is present. A clot (*large red arrow*) fills the apex of the ventricle.

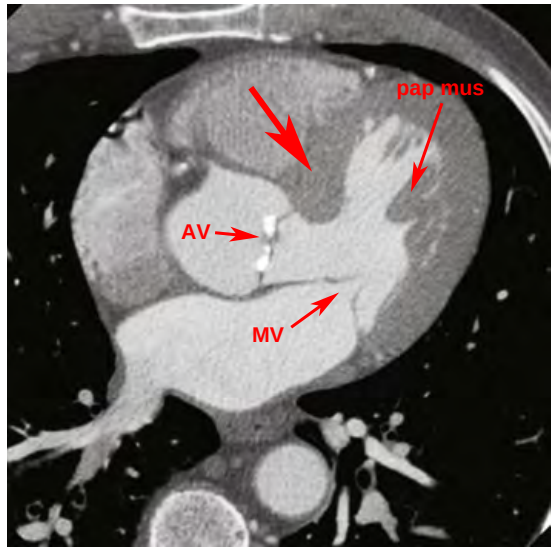

FIGURE 3-29 ■ Aortic valve calcification with focal septal hypertrophy. Multidetector computed tomography shows dense calcification of the aortic valve (AV), with focal hypertrophy (thickening) of the ventricular septum (*large arrow*). The mitral valve (MV) appears normal. Normal papillary muscle (pap mus) should not be confused with a thrombus.

using CT, and CT is excellent for evaluating pericardial abnormalities.

Cardiac Pathology

With the development of rapid MDCT techniques, the use of CT in evaluating cardiac abnormalities has increased, and CT can show a number of abnormalities in patients with ischemic heart disease or other cardiac abnormalities. However, echocardiography, magnetic resonance imaging, and angiography remain the modalities of choice in most patients with suspected cardiac disease.

In patients with an acute myocardial infarction, after bolus injection of contrast medium, infarcted myocardium can show less opacification than normal myocardium and, to some degree, infarct size can be quantitated. Ventricular thrombus can also be shown in patients with an acute myocardial infarction.

In patients with a prior infarct, CT can be valuable in showing ventricular aneurysm, thinning of the myocardium, subendocardial fat or calcification, and thrombus (Fig. 3-28). A warning: Normal papillary muscle, which appears as a filling defect (Fig. 3-29), should not be confused with a clot.

Myocardial wall thickening can be seen in patients with ventricular hypertrophy (Figs. 3-23*B* and 3-29) and patients with hypertrophic cardiomyopathy. CT is sensitive in detecting valve and annular calcification (Fig. 3-29). The severity of aortic valve calcification correlates with aortic stenosis.

Intracardiac tumors can be shown with contrast-enhanced CT but are generally uncommon and are usually evaluated using other techniques. Lung cancer with invasion of the pulmonary vein can result in a left atrial mass. *Lipomatous hypertrophy of the atrial septum* is seen on CT as an incidental finding in about 2% of cases; it appears as a fat-attenuation thickening of the septum (Fig. 3-30) and often mimics a mass on echocardiography. It is generally without clinical significance but has been associated with atrial arrhythmia. It should not be confused with a true cardiac tumor.

Coronary Arteries

Coronary artery calcification is often identified on CT scans at and below the level of the aortic root (Fig. 3-31). The *left main coronary artery* is about 1 cm in length; it arises from the aorta at about the 4-o'clock position and gives rise to the *left anterior descending coronary artery* (LAD) extending anteriorly and inferiorly and the *circumflex coronary artery* (CCA) extending posteriorly and inferiorly. Calcification of the left main coronary is said to be present if calcium is seen proximal to its point of bifurcation into the left anterior descending and circumflex arteries. The *right coronary artery* (RCA) arises from the

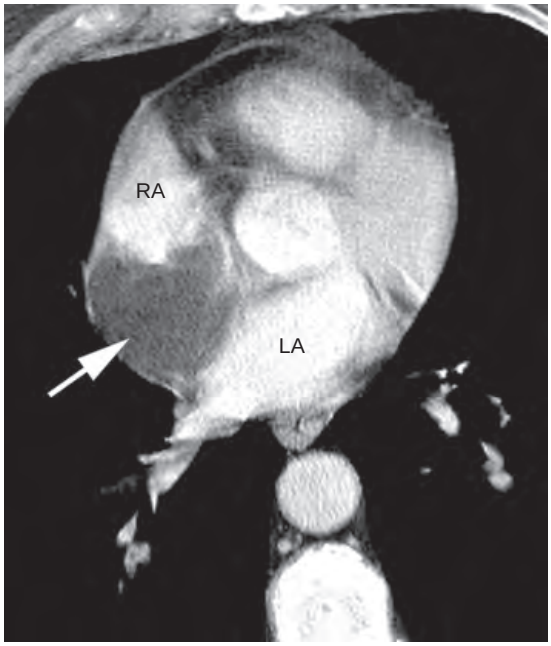

FIGURE 3-30 ■ Lipomatous hypertrophy of the atrial septum. A focal low-attenuation (fatty) mass is visible in the region of the atrial septum (*arrow*), compressing both the right atrium (RA) and left atrium (LA). This abnormality is usually of no consequence, and this patient had no cardiac symptoms.

anterior aorta (at about the 11-o'clock position) slightly caudal to the left main artery and extends anteriorly and inferiorly in the atrioventricular groove. Left anterior descending artery calcification almost always predominates.

The extent of coronary artery calcification correlates to some degree with the presence of significant coronary artery obstruction and cardiac death. The likelihood and extent of coronary artery calcification also correlate with patient age. Although the absence of visible coronary artery calcification does not exclude the possibility of obstructive coronary artery plaque, it makes it unlikely.

Dedicated CT may be performed to evaluate the coronary arteries for detection of artery calcification, stenosis, or occlusion. Calcification is graded using a computerized numerical scoring system, and the extent of calcification can be correlated with age and sex. Coronary CT angiography (CTA) is accomplished using ECG gating, contrast enhancement, and various reconstructions (including curved planar reconstruction) to demonstrate the coronary arteries along their length, regardless of their actual three-dimensional course (Fig. 3-31). Both calcificied plaque (hard plaque) and noncalcified (soft) plaque can be demonstrated.

Scoring of coronary artery calcification is not performed on routine chest CT scans, but if calcification is present, the coronary arteries involved and the severity or extent of calcification (expressed in general terms such as localized or extensive) can be reported. Several rules are generally followed in interpreting routine scans showing coronary artery calcification, although these should not be engraved in stone:

- In patients over 70 years of age, the presence of coronary calcification is common and does not necessarily predict significant coronary artery disease. Coronary calcification is not usually mentioned in the CT report.
- In men under 60 and women under 70 years of age, coronary artery calcification is less common and is usually mentioned in the report, along with the arteries involved (i.e., LAD, RCA, and/or CCA).
- In men between the ages of 60 and 70 years, coronary calcification is usually mentioned if it is more than limited.

Pericardial Abnormalities

Pericardial Effusion, Thickening, and Fibrosis

Pericardial effusion results in thickening of the normal pericardial stripe. When fluid begins to accumulate, this condition occurs first in the dependent portions of the pericardium, typically posterior to the left ventricle (Fig. 3-32). As the effusion increases in size, it is visible lateral and anterior to the right atrium and right ventricle; when large, it appears as a concentric opacity surrounding the heart. Large effusions can also extend into the superior pericardial recess. The presence of tamponade, associated with pericardial effusion, may be more directly related to the speed at which the fluid accumulates and the distensibility of the pericardium than the size of the effusion alone.

Pericardial thickening or fibrosis, usually as a result of inflammation, can produce a similar thickening of the pericardial stripe. With contrast medium infusion, enhancement of the thickened pericardium may be seen, which thus distinguishes it from effusion. Pericardial thickening may also be denser than fluid collections, even without contrast infusion. Thickening may be smooth, or focal and nodular. Calcification can occur, particularly as a result of tuberculosis, purulent pericarditis, or hemopericardium.

In the presence of symptoms of constrictive pericarditis, the CT appearance of a normal pericardium rules out the diagnosis, whereas a thickened pericardium allows a presumptive diagnosis of constriction to be made. In the presence of pericardial metastases, CT can show an effusion (Fig. 3-32) or nodular masses may be visible, particularly after contrast medium infusion.

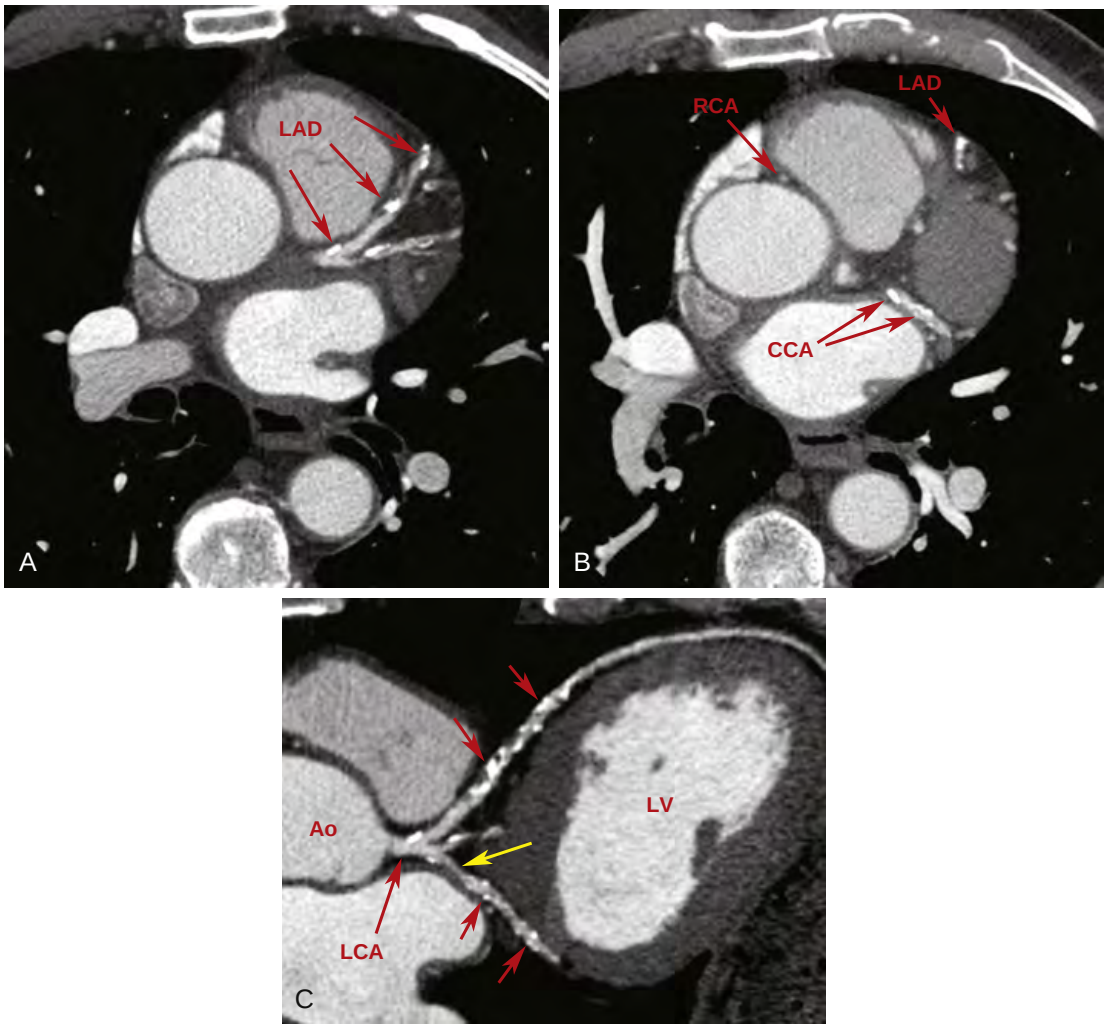

FIGURE 3-31 ■ Coronary artery calcification and computed tomography angiography. *A,* Electrocardiogram-gated contrast-enhanced computed tomography shows calcification of the left anterior descending (LAD) coronary artery and a branch. *B,* At a lower level, calcification (*arrows*) of the LAD artery and circumflex coronary artery (CCA) is visible. The right coronary artery (RCA) is noncalcified. *C,* A curved reconstruction showing the left coronary artery (LCA) and the LAD artery and CCA along their axes. Multiple calcifications are visible (*red arrows*). A noncalcified stenosis of the CCA (*yellow arrow*) is also shown. Ao, aorta; LV, left ventricle.

FIGURE 3-32 ■ Pericardial effusion from metastatic lung cancer. Fluid accumulates first in the dependent portions of the pericardium, posterior to the left ventricle. In this patient, most of the fluid has accumulated in this region.

SUGGESTED READING

Araoz PA, Haramati LB, Mayo JR, Barbosa EJ Jr, Rybicki FJ, Colletti PM: Panel discussion: Pulmonary embolism imaging and outcomes. *AJR Am J Roentgenol* 198:1313–1319, 2012.

Batra P, Bigoni B, Manning J, et al.: Pitfalls in the diagnosis of thoracic aortic dissection at CT angiography. *Radiographics* 20:309–320, 2000.

Bechtold RE, Wolfman NT, Karstaedt N, Choplin RH: Superior vena caval obstruction: Detection using CT. *Radiology* 157:485–487, 1985.

Castaner E, Andreu M, Gallardo X, et al.: CT in nontraumatic acute thoracic aortic disease: Typical and atypical features and complications. *Radiographics* 23:S93–S110, 2003.

Dillon EH, van Leeuwen MS, Fernandez MA, Mali WPTM: Spiral CT angiography. *AJR Am J Roentgenol* 160:1273–1278, 1993.

Gavant ML, Flick P, Menke P, Gold RE: CT aortography of thoracic aortic rupture. *AJR Am J Roentgenol* 166:955–961, 1996.

Gavant ML, Menke PG, Fabian T, et al.: Blunt traumatic aortic rupture: Detection with helical CT of the chest. *Radiology* 197:125–133, 1995.

Gefter WB, Hatabu H, Holland GA, et al.: Pulmonary thromboembolism: Recent developments in diagnosis with CT and MR imaging. *Radiology* 197:561–574, 1995.

Goodman LR, Lipchik RJ: Diagnosis of pulmonary embolism: Time for a new approach [editorial]. *Radiology* 199:25–27, 1996.

Gotway MB, Patel RA, Webb WR: Helical CT for the evaluation of suspected acute pulmonary embolism: Diagnostic pitfalls. *J Comput Assist Tomogr* 24:267–273, 2000.

Hayashi H, Matsuoka Y, Sakamoto I, et al.: Penetrating atherosclerotic ulcer of the aorta: Imaging features and disease concept. *Radiographics* 20:995–1005, 2000.

Hoff JA, Chomka EV, Krainik AJ, et al.: Age and gender distributions of coronary artery calcium detected by electron beam tomography in 35,246 adults. *Am J Cardiol* 87:1335–1339, 2001.

Mayo JR, Remy-Jardin M, Müller NL, et al.: Pulmonary embolism: Prospective comparison of spiral CT with ventilation-perfusion scintigraphy. *Radiology* 205:447–452, 1997.

McMahon MA, Squirrell CA: Multidetector CT of aortic dissection: A pictorial review. *Radiographics* 30:445–460, 2010.

Moores LK, Jackson WL Jr, Shorr AF, Jackson JL: Meta-analysis: Outcomes in patients with suspected pulmonary embolism managed with computed tomographic pulmonary angiography. *Ann Intern Med* 141:866–874, 2004.

Nienaber CA, Powell JT: Management of acute aortic syndromes. *Eur Heart J* 33:26–35, 2012.

Pannu HK, Flohr TG, Corl FM, Fishman EK: Current concepts in multi-detector row CT evaluation of the coronary arteries: Principles, techniques, and anatomy. *Radiographics* 23:S111–S125, 2003.

Remy-Jardin M, Pistolesi M, Goodman LR, et al.: Management of suspected acute pulmonary embolism in the era of CT angiography: A statement from the Fleischner Society. *Radiology* 245:315–329, 2007.

Sadigh G, Kelly AM, Cronin P: Challenges, controversies, and hot topics in pulmonary embolism imaging. *AJR Am J Roentgenol* 196:497–515, 2011.

Tello R, Costello P, Ecker C, et al.: Spiral CT evaluation of coronary artery bypass graft patency. *J Comput Assist Tomogr* 17:253–259, 1993.

Trerotola SO: Can helical CT replace aortography in thoracic trauma [editorial]? *Radiology* 197:13–15, 1995.

Webb WR, Gamsu G, Speckman JM, et al.: CT demonstration of mediastinal aortic arch anomalies. *J Comput Assist Tomogr* 6:445–451, 1982.

Webb WR, Gamsu G, Speckman JM, et al.: CT demonstration of mediastinal venous anomalies. *AJR Am J Roentgenol* 159:157–161, 1982.

Wiener RS, Schwartz LM, Woloshin S: When a test is too good: How CT pulmonary angiograms find pulmonary emboli that do not need to be found. *BMJ* 347:f3368, 2013.

Zeman RK, Berman PM, Silverman PM, et al.: Diagnosis of aortic dissection: Value of helical CT with multiplanar re-formations and three-dimensional rendering. *AJR Am J Roentgenol* 164:1375–1380, 1995.

CHAPTER 4

MEDIASTINUM: LYMPH NODE ABNORMALITIES AND MASSES

W. Richard Webb

LYMPH NODE GROUPS

Mediastinal lymph nodes are generally classified by location, and most descriptive systems are based on a modification of Rouvière's classification of lymph node groups.

Anterior Mediastinal Nodes

Internal mammary nodes are located in a retrosternal location near the internal mammary artery and veins (Fig. 4-1). They drain the anterior chest wall, anterior diaphragm, and medial breasts.

Paracardiac nodes (diaphragmatic, epiphrenic, and pericardial) surround the heart on the surface of the diaphragm and communicate with the lower internal mammary chain (Fig. 4-2). Like internal mammary nodes, they are most commonly enlarged in patients with lymphoma and metastatic carcinoma, particularly breast cancer.

Prevascular nodes lie anterior to the great vessels (Figs. 4-1, 4-3, and 4-4*A*). They may be involved in a variety of diseases, notably lymphoma, but their involvement in lung cancer is less common.

Middle Mediastinal Nodes

Lung diseases (e.g., lung cancer, sarcoidosis, tuberculosis, and fungal infections) that secondarily involve lymph nodes typically involve middle mediastinal lymph nodes.

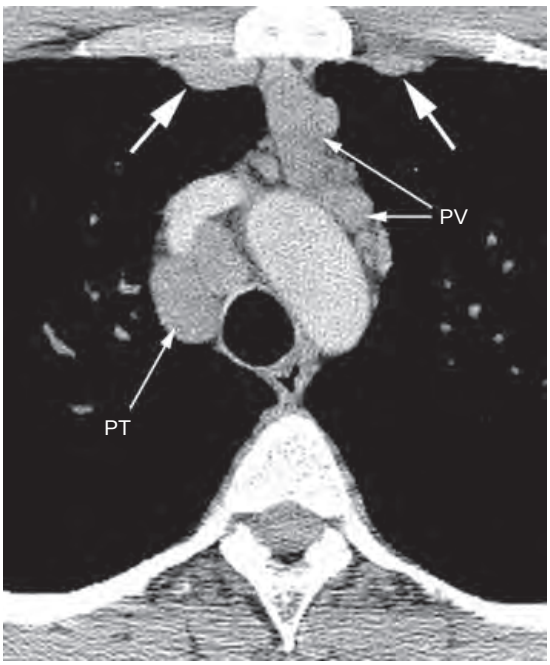

FIGURE 4-1 ■ Internal mammary node enlargement in sarcoidosis. Bilateral internal mammary nodes (*large arrows*) are enlarged, as are pretracheal (PT) and prevascular (PV) nodes.

FIGURE 4-2 ■ Paracardiac node enlargement. In a patient with lymphoma, enlargement of the paracardiac nodes (*large arrows*) is visible. These lie anterior to the pericardium (*small arrows*).

Pretracheal or *paratracheal nodes* occupy the pretracheal (or anterior paratracheal) space (Figs. 4-1, 4-3, and 4-4*A*). These nodes form the final pathway for lymphatic drainage from most of both lungs (except the left upper lobe). Because of this, they are commonly abnormal regardless of the location of the lung disease.

Aortopulmonary nodes are considered by Rouvière to be in the anterior mediastinal group, but because they serve the same function as right paratracheal nodes, they are illustrated in Figures 4-3*C*, 4-4*B*, and 4-4*C*. The left upper lobe is drained by this node group.

Subcarinal nodes are located in the subcarinal space, between the main bronchi (Fig. 4-4*B* to *D*), and drain the inferior hila and both lower lobes. They communicate in turn with the right paratracheal chain.

Peribronchial nodes surround the main bronchi on each side (Figs. 4-4*B* and *C*). They communicate with bronchopulmonary (hilar; Figs. 4-4*C* and *D*), subcarinal, and paratracheal nodes.

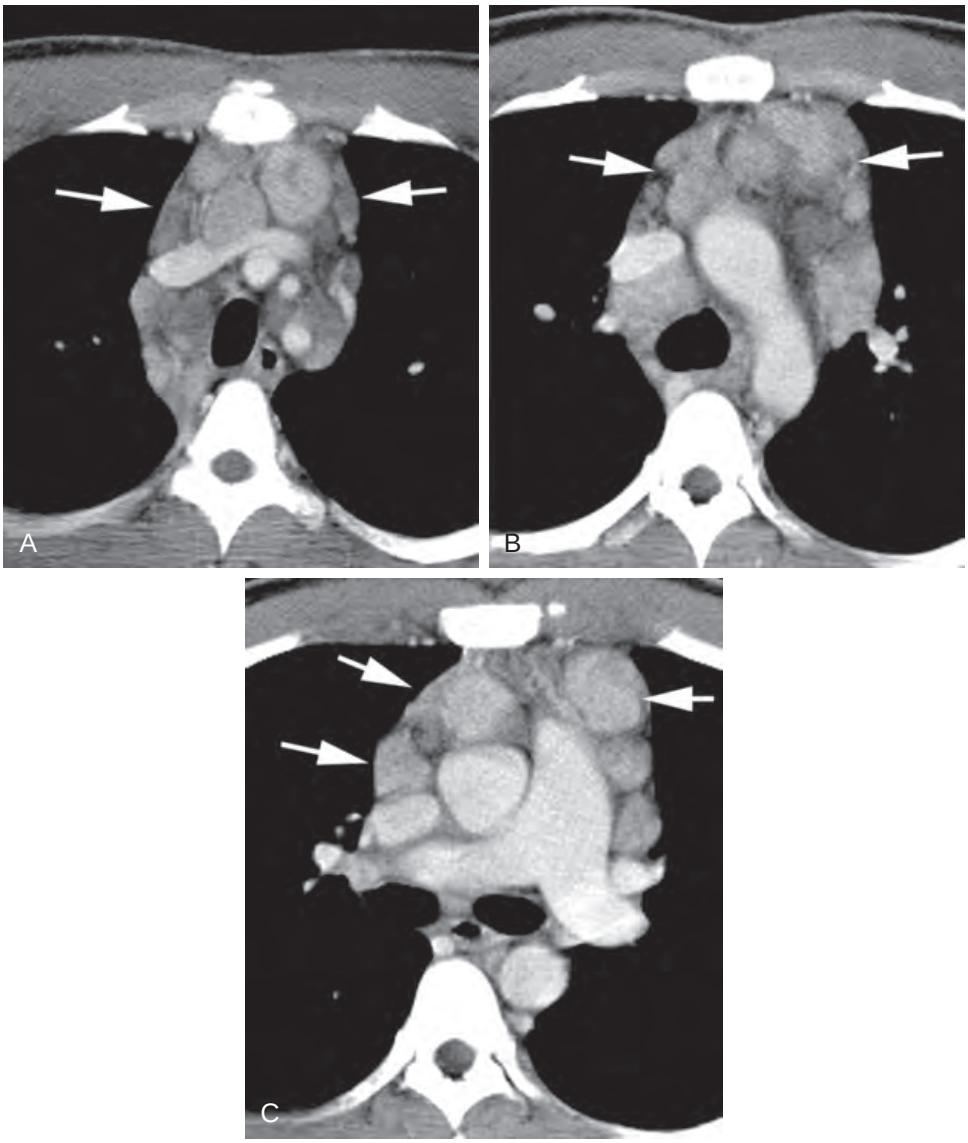

FIGURE 4-3 ■ Prevascular lymph node enlargement in Hodgkin's lymphoma. Enlarged prevascular or anterior mediastinal lymph nodes (*arrows*) are seen anterior to the brachiocephalic veins and great vessels (*A*), anterior to the aortic arch and superior vena cava (*B*), and anterior to the superior vena cava, aortic root, and main pulmonary artery (*C*). Enlarged pretracheal lymph nodes are also visible at all three levels. In *C*, prevascular nodes are contiguous with nodes lateral to the main pulmonary artery, usually considered to be in the aortopulmonary window. Some nodes appear low in attenuation and are probably necrotic.

Posterior Mediastinal Nodes

Paraesophageal nodes lie posterior to the trachea or are associated with the esophagus, or both (Fig. 4-5). Subcarinal nodes are not included in this group.

Inferior pulmonary ligament nodes are located below the pulmonary hila, medial to the inferior pulmonary ligament. On computed tomography (CT), they are usually seen adjacent to the esophagus on the right and the descending aorta on the left. Below the hila, they are difficult to distinguish from paraesophageal nodes. Together with the paraesophageal nodes, they drain the medial lower lobes, esophagus, pericardium, and posterior diaphragm.

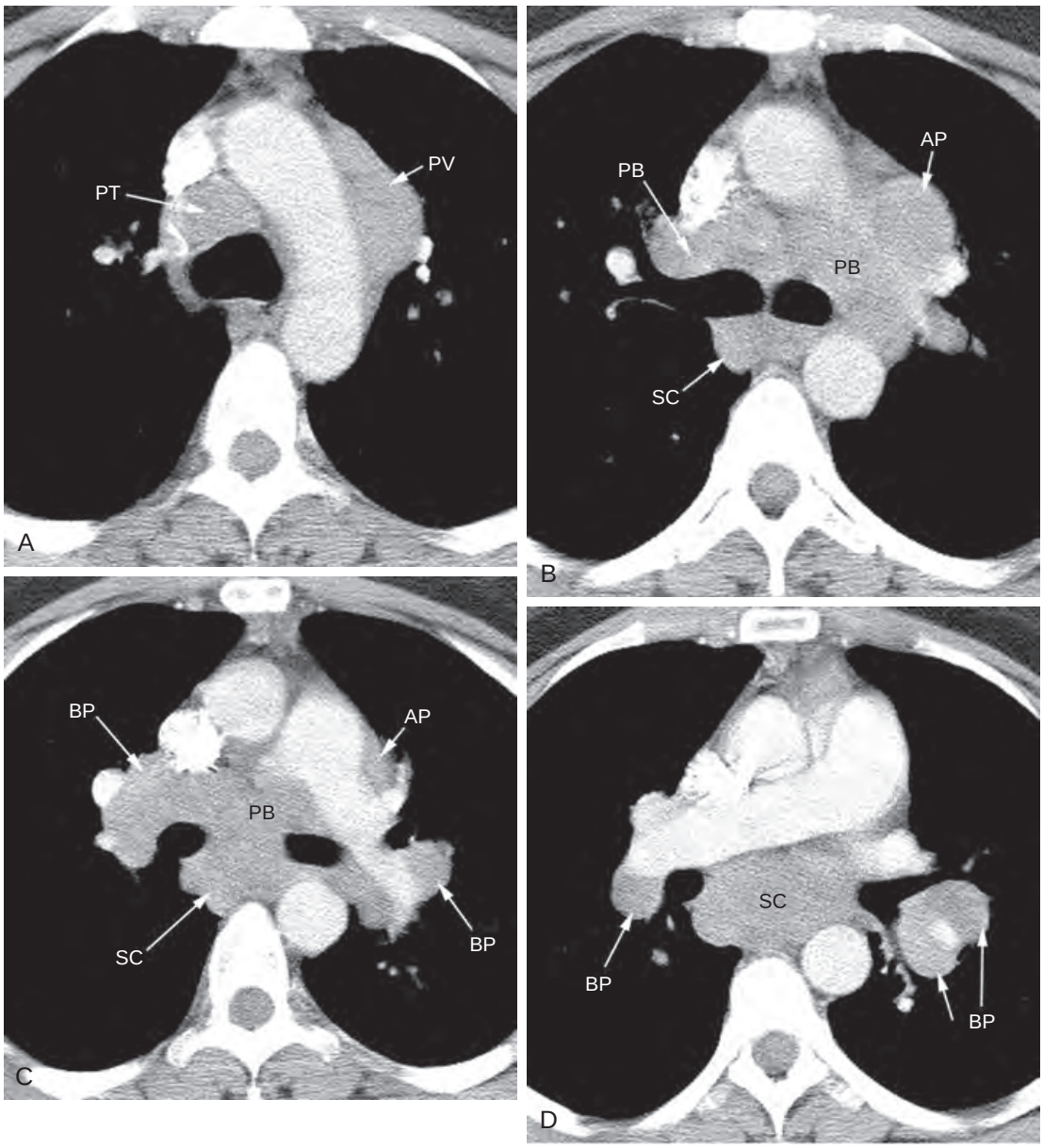

FIGURE 4-4 ■ Lymph node enlargement in a patient with sarcoidosis. *A*, At the aortic arch level, enlarged pretracheal (PT) and prevascular (PV) nodes are visible. *B*, At the level of the tracheal carina, lymph nodes lateral to the left pulmonary artery are termed *aortopulmonary* (AP). Lymph nodes adjacent to the main bronchi are termed *peribronchial* (PB). Subcarinal (SC) lymph nodes are located posterior to the carina. *C*, At a lower level, aortopulmonary, peribronchial, and SC nodes are again visible. Hilar lymph nodes are termed *bronchopulmonary* (BP). *D*, Below *C*, large subcarinal and bronchopulmonary nodes are again visible.

Paravertebral nodes lie lateral to the vertebral bodies, posterior to the aorta on the left (Fig. 4-5). They drain the posterior chest wall and pleura. They are most commonly involved, together with the retrocrural or retroperitoneal abdominal nodes, in patients with lymphoma or metastatic carcinoma.

FIGURE 4-5 ■ Paravertebral lymph node enlargement in metastatic testicular carcinoma. Large lymph nodes on the right (*large arrow*) can be considered paraesophageal or inferior pulmonary ligament nodes. They appear inhomogeneous and are necrotic. An enlarged left paravertebral lymph node (*small arrows*) is also visible posterior to the aorta.

Lymph Node Stations

In the 1970s, the American Joint Committee on Cancer (AJCC) and Union Internationale Contre le Cancer (UICC) introduced a numeric system for localization of intrathoracic lymph nodes for the purpose of lung cancer staging. Lymph nodes were described relative to regions in the mediastinum termed *lymph node stations*. The AJCC/UICC node-mapping system was modified in 1983 by the American Thoracic Society to more precisely define anatomic and CT criteria for each station, and the American Thoracic Society classification system has been in common usage since its development. In 1997, the AJCC/UICC published a further revision intended to be a compromise between the AJCC and American Thoracic Society classifications. Detailed knowledge of these lymph node stations is not necessary in clinical practice.

In 2009, the International Association for the Study of Lung Cancer (IASLC) introduced a simplified and more practical (and easily remembered) system for classifying lymph nodes, based on lung cancer survival statistics, in conjunction with a revision of the lung cancer staging system (Table 4-1). This classifies mediastinal nodes into four groups or zones known as (1) the upper zone (paratracheal and prevascular nodes), (2) the aortopulmonary zone (aortopulmonary window nodes), (3) the subcarinal zone (subcarinal nodes), and (4) the lower zone (paraesophageal and inferior pulmonary ligament nodes). Hilar lymph nodes and more peripheral peribronchial nodes represent two

TABLE 4-1 **International Association for the Study of Lung Cancer (IASLC) Lymph Node Zones compared to AJCC/UICC Node Stations**

IASLC Nodal Groups	AJCC/UICC Description	AJCC/UICC Station
Mediastinal zone		
Upper zone	Right upper paratracheal	2R
	Left upper paratracheal	2L
	Prevascular	3
	Right lower paratracheal	4R
	Left lower paratracheal	4L
Aortopulmonary zone	Subaortic	5
	Paraaortic	6
Subcarinal zone	Subcarinal	7
Lower zone	Paraesophageal	8
	Pulmonary ligament	9
Hilar/interlobar zone	Hilar	10
	Interlobar	11
Peripheral zone	Lobar	12
	Segmental	13
	Subsegmental	14

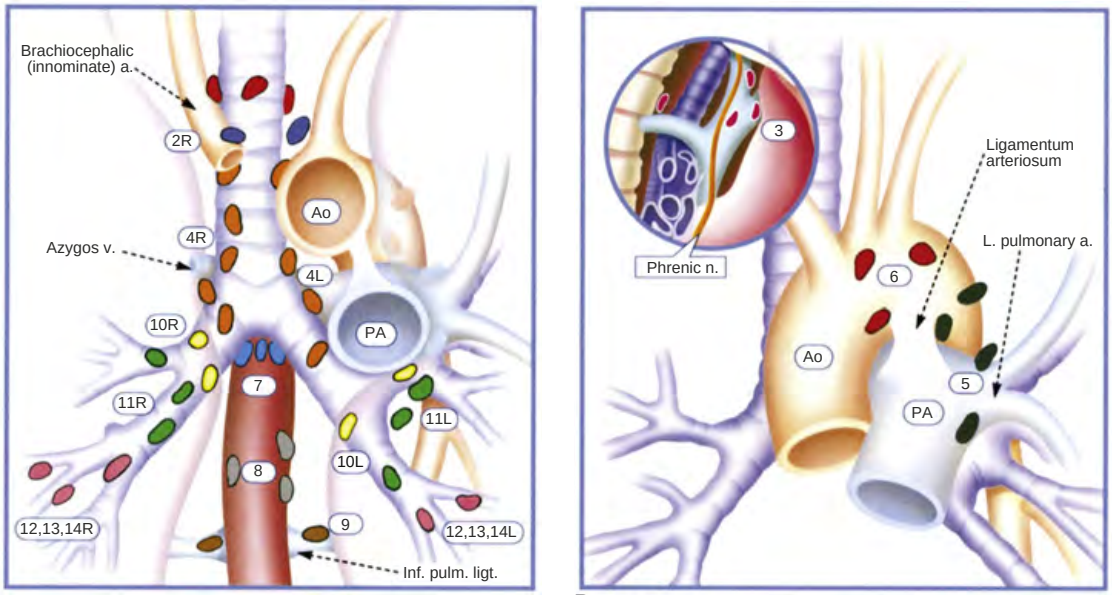

FIGURE 4-6 ■ American Joint Committee on Cancer and Union Internationale Contre le Cancer lymph node stations. *A* and *B*, Ao, aorta; PA, pulmonary artery; a., artery; v., vein; Inf. pulm. ligt., inferior pulmonary ligament; n., nerve; L. pulmonary a., left pulmonary artery. (Reproduced from Mountain CF, Dresler CM: Regional lymph node classification for lung cancer staging. Chest 111:1718–1723, 1997, with permission.)

additional groups. Table 4-1 provides a comparison of IASLC zones and AJCC/UICC lymph node stations, and a diagrammatic representation of AJCC/UICC lymph node stations (Fig. 4-6) is provided for localization of node zones.

CT APPEARANCE OF LYMPH NODES

Lymph nodes are generally visible as discrete, round or elliptical in shape, and of soft-tissue attenuation, surrounded by mediastinal fat and distinguishable from vessels by their location. They often occur in clusters (Fig. 4-7). In some locations, nodes that contact vessels may be difficult to identify without contrast infusion. Normal lymph nodes may show a fatty hilum (Fig. 4-7).

Internal mammary nodes, paracardiac nodes, and paravertebral nodes are not usually seen on CT in healthy subjects, but in other areas of the mediastinum, normal nodes are often visible. The expected size of normal nodes varies with their location, and a few general rules apply. Subcarinal nodes can be quite large in healthy subjects. Pretracheal nodes are also commonly visible, but these nodes are typically smaller than normal subcarinal nodes. Nodes in the supraaortic mediastinum are usually smaller than lower pretracheal nodes, and left paratracheal nodes are usually smaller than right paratracheal nodes.

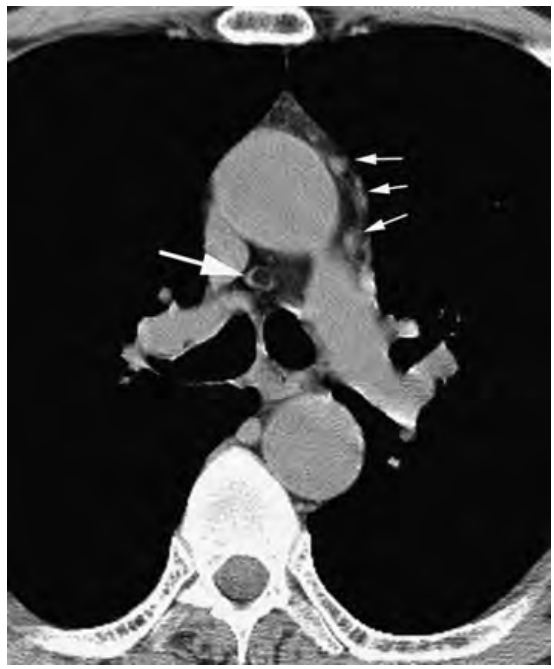

FIGURE 4-7 ■ Normal mediastinal nodes. Small lymph nodes are visible in the aortopulmonary window (*small arrows*) with a short-axis diameter of less than 1 cm. A normal-sized pretracheal lymph node (*large arrow*) has a fatty hilum and contains a large amount of fat. This is a benign appearance.

TABLE 4-2 **Upper Limits of Normal for the Short-Axis Node Diameter**

Node Group	Short-Axis Node Diameter* (mm)
Supra-aortic paratracheal	7
Subaortic paratracheal	9
Aortopulmonary window	9
Prevascular	8
Subcarinal	12
Paraesophageal	8

*Mean normal node diameter plus two standard deviations.

Measurement of Lymph Node Size

The *short axis* or *least diameter* (i.e., the smallest node diameter seen in cross-section) is generally used when measuring the size of a lymph node. Measuring the short axis is better than measuring the *long axis* or *greatest diameter* because it more closely reflects the actual node diameter when nodes are obliquely oriented relative to the scan plane and shows less variation among healthy subjects. Different values for the upper limits of normal short-axis node diameter have been found for different mediastinal node groups (Table 4-2). However, except for the subcarinal regions, a short-axis node diameter of 1 cm or less is generally considered normal for clinical purposes. In the subcarinal region, 1.5 cm is usually considered to be the upper limit of normal.

Lymph Node Enlargement

Except in the subcarinal space, lymph nodes are considered to be enlarged if they have a short-axis diameter greater than 1 cm. In most cases, they are outlined by fat and are visible as discrete structures (Fig. 4-3). However, in the presence of inflammation or neoplastic infiltration, abnormal nodes can be matted together, giving the appearance of a single large mass or resulting in infiltration and replacement of mediastinal fat by soft-tissue opacity.

The significance given to the presence of an enlarged lymph node must be tempered by knowledge of the patient's clinical situation. For example, if the patient is known to have lung cancer, then an enlarged lymph node has a 70% likelihood of tumor involvement. However, the same node in a patient without lung cancer is much less likely to be of clinical significance. In the absence of a known disease, an enlarged node must be regarded as likely to be hyperplastic or reactive. In addition, the larger a node is, the more likely it is to represent a significant abnormality. Mediastinal lymph nodes larger than 2 cm often have tumor involvement, although this may also be seen in patients with sarcoidosis or other granulomatous diseases.

Lymph Node Calcification

Calcification can be dense, involving the node in a homogeneous fashion, stippled, or egg-shell-like in appearance. The abnormal nodes are often enlarged but can also be of normal size. Multiple calcified lymph nodes are often visible, usually in contiguity.

Lymph node calcification usually indicates prior granulomatous disease, including tuberculosis, histoplasmosis and other fungal infections, and sarcoidosis (Fig. 4-8). The differential diagnosis also includes silicosis, coal workers' pneumoconiosis, treated Hodgkin's disease, metastatic neoplasm, typically mutinous adenocarcinoma, thyroid carcinoma, or metastatic osteogenic sarcoma. Egg-shell calcification is most often seen in patients with silicosis or coal workers' pneumoconiosis, sarcoidosis, and tuberculosis.

Low-Attenuation or Necrotic Lymph Nodes

Enlarged lymph nodes may appear to be low in attenuation (Fig. 4-5), often with an enhancing rim if contrast has been injected. Typically, low-attenuation nodes reflect the presence of necrosis. They are commonly seen in patients with active tuberculosis, fungal infections, and neoplasms, such as metastatic carcinoma and lymphoma.

Lymph Node Enhancement

Normal lymph nodes may show some increase in attenuation after intravenous contrast infusion. Pathologic lymph nodes with an increased vascular supply may increase significantly in attenuation. The differential diagnosis of densely enhanced mediastinal nodes is limited and includes metastatic neoplasm (e.g., lung cancer, breast cancer, renal cell carcinoma, papillary thyroid carcinoma, sarcoma, and melanoma), Castleman's disease (Fig. 4-15), angioimmunoblastic lymphadenopathy, infections such as tuberculosis, and sometimes sarcoidosis.

DIFFERENTIAL DIAGNOSIS OF MEDIASTINAL LYMPH NODE ENLARGEMENT

Lung Cancer

Approximately 35% of patients diagnosed with lung cancer have mediastinal node metastases

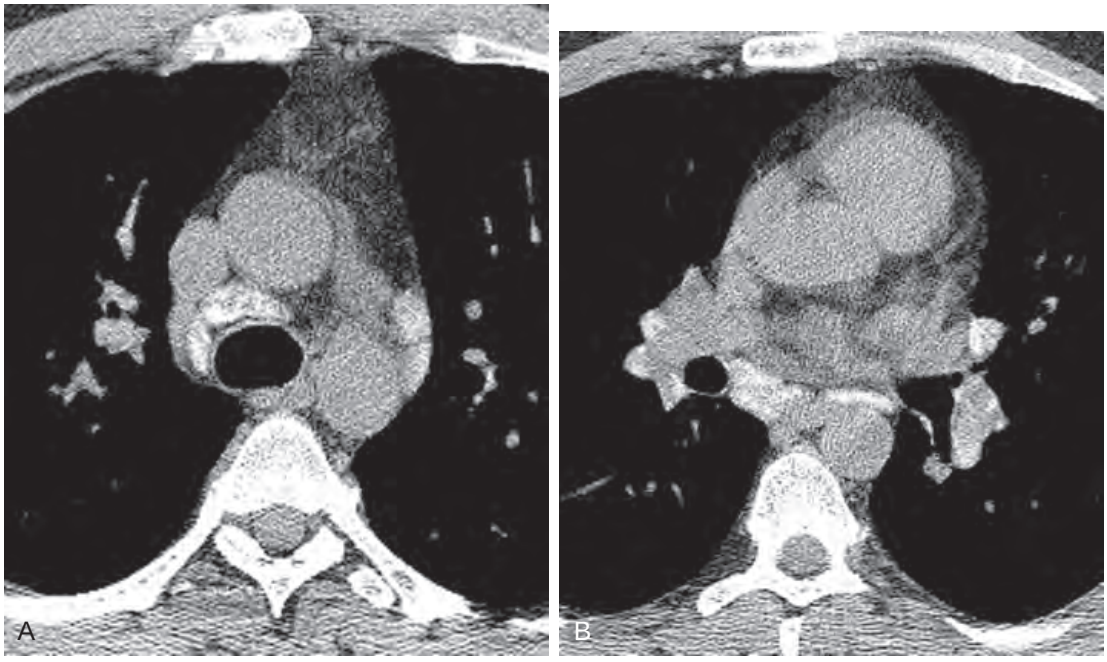

FIGURE 4-8 ■ Lymph node calcification in sarcoidosis. *A* and *B*, Enlarged lymph nodes show homogeneous and stippled calcification. Pretracheal, aortopulmonary, subcarinal, and hilar lymph nodes are involved.

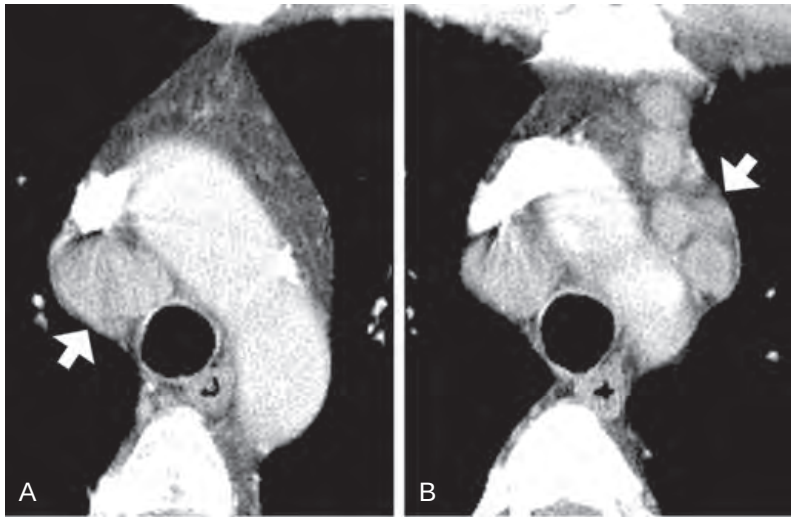

FIGURE 4-9 ■ Lymph node enlargement in a patient with a right-sided bronchogenic carcinoma. *A*, Lymph node enlargement in the pretracheal space (*arrow*) is ipsilateral, N2, and potentially resectable. These nodes are large, and thus are likely involved by tumor. *B*, Lymph node enlargement in the prevascular space (*arrow*) is contralateral, N3, and is considered unresectable.

(Fig. 4-9). Lung cancer most often involves the middle mediastinal node groups. Left upper lobe cancers typically metastasize to aortopulmonary window nodes, whereas tumors involving the lower lobes on either side tend to metastasize to the subcarinal and right paratracheal groups. Right upper lobe tumors typically involve paratracheal nodes.

Lung Cancer Staging

In patients with non–small-cell bronchogenic carcinoma, although the genetics, cell type, and histologic characteristics of the tumor affect prognosis, the anatomic extent of the tumor (tumor stage) is usually most important in determining the therapeutic approach. The most

TABLE 4-3 **TNM Classification of Lung Cancer (TNM 7, 2009)**

T (primary tumor)	
T0	No evidence of a primary tumor
T1	A tumor that is:
	a. 3 cm or less in greatest diameter
	T1a ≤ 2 cm
	T1b > 2 cm but ≤ 3 cm
	b. Surrounded by lung or visceral pleura
	c. Without invasion proximal to a lobar bronchus (i.e., not involving main bronchus)
T2	A tumor with any of the following features:
	a. Larger than 3 cm and ≤ 7 cm in greatest diameter
	T2a > 3 cm but ≤ 5 cm
	T2b > 5 cm but ≤ 7 cm
	b. Invades the visceral pleura
	c. Involves a main bronchus ≥ 2 cm distal to the carina
	d. Associated with atelectasis or obstructive pneumonia, extending to the hilum, but involving less than the entire lung
T3	A tumor with any of the following features:
	a. Larger than 7 cm ($T3_{>7}$)
	b. Associated with additional tumor nodule(s) in the same lobe ($T3_{Satell}$)
	c. Invades chest wall, diaphragm, phrenic nerve, mediastinal pleura, or parietal pericardium ($T3_{Inv}$)
	d. Involves the main bronchus < 2 cm distal to the carina, without involvement of the carina ($T3_{Centr}$)
	e. Associated with atelectasis or obstructive pneumonia of an entire lung ($T3_{Centr}$)
T4	A tumor of any size with any of the following features:
	a. Invasion of the heart, great vessels, trachea, carina, recurrent laryngeal nerve, esophagus, or vertebral body ($T4_{Inv}$)
	b. Additional tumor nodule(s) in another ipsilateral lobe ($T4_{Ipsi\ Nod}$)
N (regional lymph nodes)	
N0	No regional lymph node metastases
N1	Metastases to ipsilateral peribronchial, perihilar, or intrapulmonary nodes, including direct extension
N2	Metastases to ipsilateral mediastinal nodes or subcarinal nodes
N3	Metastases to contralateral hilar or mediastinal lymph nodes, or scalene or supraclavicular lymph nodes
M (distant metastases)	
M0	Metastases absent
M1	Metastases present
M1a	Intrathoracic metastases, with either
	a. Tumor nodules in the contralateral lung ($M1a_{Contr\ Nod}$)
	b. Tumor with pleural nodules or malignant pleural effusion ($M1a_{Pl\ Dissem}$)
	(pleural effusion not obviously associated with metastases has no effect on stage)
M1b	Distant metastases

Modified from Rami-Porta R, Crowley JJ, Goldstraw P: The revised TNM staging system for lung cancer. Ann Thorac Cardiovasc Surg 15:4–9, 2009, and Detterbeck FC, Boffa DJ, Tanoue LT: The new lung cancer staging system. Chest 136:260–271, 2009.

widely used anatomic staging classification is the TNM classification revised in 2009.

This classification is based on consideration of the following characteristics: (1) the size, location, and extent of the primary tumor (T); (2) the presence or absence of lymph node metastases (N); and (3) the presence or absence of distant metastases (M) (Tables 4-3 and 4-4). Based on this classification, excellent correlations are found between tumor stage and survival after treatment.

For radiologic purposes, precise classification of tumor stage is not usually necessary. However, differentiation of potentially resectable stages (stages I to IIIa) and stages usually considered unresectable (stages IIIb to IV) is important (Table 4-4). The criteria for resectability are generally accepted but are not absolute; different

TABLE 4-4 **Lung Cancer Stage Based on TNM Classification (TNM 7, 2009)**

Stage Groups	T	N	M
Ia	T1a,b	N0	M0
Ib	T2a	N0	M0
IIa	T1a,b	N1	M0
	T2a	N1	M0
	T2b	N0	M0
IIb	T2b	N1	M0
	T3	N0	M0
IIIa	T1–3	N2	M0
	T3	N1	M0
	T4	N0,1	M0
IIIb	Any T	N3	M0
	T4	N2	M0
IV	Any T	Any N	M1a,b

Modified from Rami-Porta R, Crowley JJ, Goldstraw P: The revised TNM staging system for lung cancer. Ann Thorac Cardiovasc Surg 15:4–9, 2009, and Detterbeck FC, Boffa DJ, Tanoue LT: The new lung cancer staging system. Chest 136:260–271, 2009.

surgeons may have different criteria for what is resectable. In particular, the resectability of some stage IIIa tumors is controversial; stage IIIa tumors may be treated with chemotherapy or radiation prior to resection.

The next section discusses the impact of mediastinal lymph node metastases and mediastinal invasion on lung cancer staging. Chapters 5 and 7 discuss other aspects of lung cancer staging.

Mediastinal Node Metastases in Lung Cancer

In the TNM lung cancer staging system, ipsilateral mediastinal node metastases and subcarinal node metastases are termed *N2* and are considered potentially resectable (although this is not always the case); contralateral nodes are termed *N3* and are considered unresectable (Fig. 4-9).

In patients with lung cancer, the likelihood that a mediastinal node is involved by tumor is directly proportional to its size. However, although large nodes are most likely to be involved by tumor (Fig. 4-9), they can be benign; similarly, although small nodes are usually normal, they can harbor metastases. Although a short-axis measurement of greater than 1 cm is used in clinical practice to identify abnormally enlarged nodes, it is important to realize that no node diameter clearly separates benign nodes from those involved by tumor.

Using a short-axis node diameter of 1 cm as the upper limit of node size, CT will detect mediastinal lymph node enlargement in about 60% of patients with node metastases (CT sensitivity), whereas about 70% of patients with normal nodes will be classified normal on CT (CT specificity). Although CT is not highly accurate in diagnosing node metastases, it is commonly used to guide subsequent procedures or treatment.

In patients without node enlargement on CT, thoracotomy may be performed without prior mediastinoscopy, although this varies with the surgeon. Although some such patients will be found to have microscopic or small intranodal metastases, their presence does not necessarily indicate that surgery was inappropriate. Some patients with ipsilateral intranodal mediastinal metastases (N2) can have successful treatment results after surgical excision of nodes and radiation or chemotherapy.

In contrast, if mediastinal lymph node enlargement is seen on CT, about 70% of patients will have node metastases; benign hyperplasia of mediastinal lymph nodes accounts for the other 30%. Patients with large mediastinal nodes usually have node sampling at mediastinoscopy or by CT-guided needle biopsy before surgery. If node metastases are found at mediastinoscopy, surgery is not generally performed, even though the nodes would be classified as N2; it has been shown that patients with node metastases diagnosed at mediastinoscopy have a poor prognosis after surgery. It should be kept in mind that in patients with enlarged nodes on CT and mediastinal lymph node metastases, the metastases are not always in the nodes that appear large; that is, in some cases, CT can be right for the wrong reason.

Positron emission tomography (PET) scanning is more accurate than CT in the assessment of mediastinal lymph nodes in lung cancer and has assumed a significant role in preoperative staging. PET has a sensitivity of about 80% for diagnosis of mediastinal node metastases (vs. 60% for CT) and a specificity of about 90% (vs. 70% for CT). PET is usually combined with CT (PET-CT) because of the poor anatomic detail provided by PET alone.

Mediastinoscopy is slightly more sensitive than CT, has much higher specificity (100%; that is, no normal nodes are called abnormal based on mediastinoscopy), and has higher accuracy for diagnosing mediastinal node metastases. However, the mediastinoscopist cannot evaluate all mediastinal compartments or lymph node groups, and a significant percentage (up to 25%) of patients with bronchogenic carcinoma who have a negative mediastinoscopy result are found to have mediastinal nodal metastases at surgery.

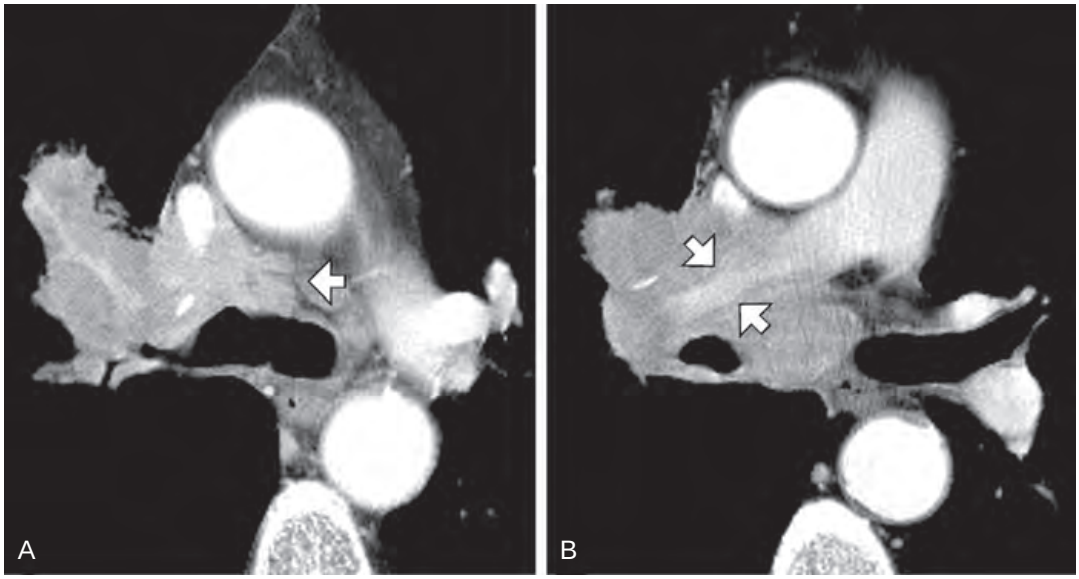

FIGURE 4-10 ■ Mediastinal invasion by bronchogenic carcinoma. A right hilar tumor has resulted in extensive mediastinal invasion anterior to the carina (*arrow, A*) and is surrounding and narrowing the right pulmonary artery (*arrows, B*). There is extensive replacement of fat by tumor, the tumor surrounds and compresses the pulmonary artery and compresses the vena cava, and fat planes are invisible adjacent to the great vessels.

Using a standard transcervical approach, the mediastinoscopist can only evaluate pretracheal lymph nodes, nodes in the anterior subcarinal space, and lymph nodes extending anterior to the right main bronchus. Lymph nodes in the anterior mediastinum (prevascular space), aortopulmonary window, and posterior portions of the mediastinum (e.g., posterior subcarinal space and azygoesophageal recess) are inaccessible using this technique, although some can be evaluated using a left parasternal mediastinoscopy (Chamberlain procedure). CT and PET-CT, in contrast, allow evaluation of all these areas, show where any enlarged nodes are, and can serve to guide needle aspiration biopsy or parasternal mediastinotomy if enlarged lymph nodes are visible in areas that cannot be evaluated using a standard approach.

Mediastinal Invasion by Lung Cancer

In addition to node metastasis, bronchogenic carcinoma can involve the mediastinum by direct extension, so-called mediastinal invasion. In current surgical practice, invasion of the mediastinal pleura, parietal pericardium, diaphragm, or chest wall, termed *T3* in the lung cancer staging system, does not prevent surgery. However, significant invasion of mediastinal fat or other mediastinal structures, such as the heart, great vessels, trachea, esophagus, or vertebral body, may prevent resection; such lesions are classified as *T4* (Fig. 4-10). Some T4 tumors with no node metastases or hilar node metastases are considered resectable following chemotherapy or radiation.

How accurate is CT in predicting mediastinal invasion? An obvious finding is that a lung mass not contacting the mediastinum is not invasive, and this is an important use of CT.

CT findings of mediastinal invasion (Fig. 4-10) include the following:

1. Replacement of mediastinal fat by a tumor of soft-tissue attenuation
2. Compression or displacement of mediastinal vessels by tumor
3. A tumor contacting more than 90° of the circumference of a structure, such as the aorta or pulmonary artery (the greater the extent of circumferential contact, i.e., 180°, the greater is the likelihood of invasion)
4. Obliteration of the mediastinal fat plane normally seen adjacent to most mediastinal structures
5. A tumor contacting more than 3 cm of the mediastinum
6. Obtuse angles where a tumor contacts the mediastinum
7. Mediastinal pleural or pericardial thickening

A definite diagnosis of invasion can be made if a tumor infiltrating mediastinal fat is visible. Other findings of mediastinal invasion are less accurate. If none of these findings is present, the tumor is likely resectable.

Lymphoma and Leukemia

Mediastinal lymph nodes are commonly involved in patients with lymphoma. A small percentage are first recognized because of mediastinal masses noted on chest radiographs, but these patients will often have systemic signs and symptoms, including fever, night sweats, weight loss, weakness, and fatigue.

Hodgkin's Disease

Hodgkin's disease (HD) has a predilection for thoracic involvement, both at the time of diagnosis and if the disease recurs. HD occurs in patients of all ages but peaks in incidence in the third and fifth decades of life.

More than 85% of patients with HD eventually develop intrathoracic disease, typically involving the superior mediastinal (prevascular, pretracheal, and aortopulmonary) lymph nodes (Figs. 4-3 and 4-11). An important rule is that intrathoracic lymphadenopathy not associated with superior mediastinal node enlargement is unlikely to be Hodgkin's lymphoma.

In one study, it was uncommon for CT to show evidence of mediastinal adenopathy if the chest radiograph was normal, but if the chest radiograph was abnormal, CT detected additional sites of adenopathy in many cases (Table 4-5).

FIGURE 4-11 ■ Hodgkin's lymphoma. Extensive enlargement of mediastinal and hilar lymph nodes is visible. A left lung nodule reflects pulmonary involvement.

CT was most helpful in diagnosing subcarinal, internal mammary, and aortopulmonary window node enlargement. Cardiophrenic angle (paracardiac) lymph nodes are present in about 10% of patients and are seen well on CT (Fig. 4-2). Adenopathy in this location is less common in other diseases. In a significant percentage of patients, the additional node involvement shown by CT changes therapy.

Enlargement of a single node group can be seen with HD, most commonly in the prevascular (anterior) mediastinum. This often indicates the presence of nodular sclerosing histology, which accounts for 50% to 80% of adult HD. In patients with lymphoma, mediastinal lymph nodes may become matted, being visible as a single large mass (Fig. 4-12) rather than individual discrete nodes. Mediastinal nodes or masses in patients with Hodgkin's lymphoma can appear cystic or fluid-filled on CT (Fig. 4-12). Calcification is unusual and of limited extent, except after treatment.

Non-Hodgkin's Lymphoma

Non-Hodgkin's lymphoma (NHL) is a diverse group of diseases that vary in radiologic manifestation, clinical presentation, course, and prognosis. In comparison with HD, these tumors are less common and generally occur in an older group of patients (40 to 70 years of age). At the time of presentation, the disease is often generalized (85% are stage III or IV), and chemotherapy is most appropriate. For this reason, precise anatomic staging is less crucial than with HD.

In one series, 43% of patients with NHL had intrathoracic disease and 40% had involvement of only one node group, which is much more common than in patients with HD (Fig. 4-13). In addition, posterior mediastinal nodes were more frequently involved. Lung involvement was present in only 4%; in some patients, lung infiltration may be rapid.

NHL may occur as a primary mediastinal mass. The most common cell types presenting in this fashion are *lymphoblastic lymphoma* (60% of

TABLE 4-5 **Mediastinal Lymph Node Enlargement in Hodgkin's Disease**

Site	Abnormal (%)	Visible on CT (%)	Visible on Radiographs (%)
Pretracheal	64	64	57
Aortopulmonary window	62	62	48
Subcarinal	46	44	9
Internal mammary	38	38	4
Posterior medial	18	12	11
Paracardiac	13	10	7

cases; Fig. 4-13) and *large B-cell lymphoma*. These resemble the appearance of mediastinal HD, with a large anterior mediastinal mass predominating, and occur in a similar age group, being most common in young patients.

CT, as in patients with HD, can show evidence of intrathoracic disease when it is unrecognizable on plain radiographs and can affect management in patients with localized (stage I or II) disease.

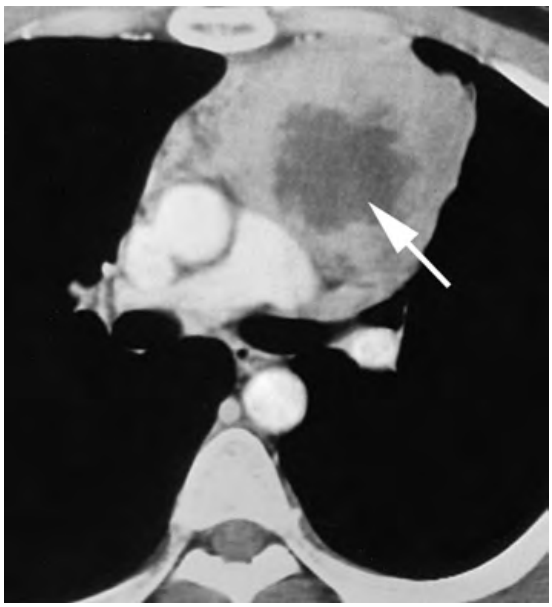

FIGURE 4-12 ■ Anterior mediastinal Hodgkin's lymphoma with necrosis. The anterior mediastinal mass contains an irregular area of cystic necrosis (*arrow*).

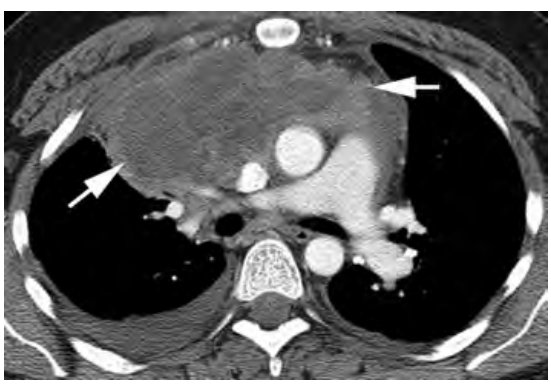

FIGURE 4-13 ■ Lymphoblastic non-Hodgkin's lymphoma (NHL) involving the anterior mediastinum. A bulky mediastinal mass (*arrows*) contains areas of low attenuation, likely caused by necrosis. Mediastinal vascular structures are displaced posteriorly. Bilateral pleural effusions are present. Involvement of a single lymph node group is common with NHL. Lymphoblastic NHL commonly presents as an anterior mediastinal mass, similar to Hodgkin's disease.

Leukemia

Leukemia, particularly the lymphocytic varieties, can cause hilar or mediastinal lymph node enlargement, pleural effusion, and occasionally infiltrative lung disease. Lymphadenopathy is generally confined to the middle mediastinum, and the larger masses seen with some lymphomas generally do not occur.

Metastases

Extrathoracic primary tumors can result in mediastinal node enlargement, either with or without hilar or lung metastases (Figs. 4-5 and 4-14). Node metastases can be present because of inferior extension from neck masses (thyroid carcinoma and head and neck tumors), extension along lymphatic channels from below the diaphragm (testicular carcinoma, renal cell carcinoma, and gastrointestinal malignancies), or dissemination via other routes (breast carcinoma and melanoma). Middle mediastinal (paratracheal) or paravertebral mediastinal nodes are most commonly involved when the tumor is subdiaphragmatic. With breast carcinoma, internal mammary node metastases occur.

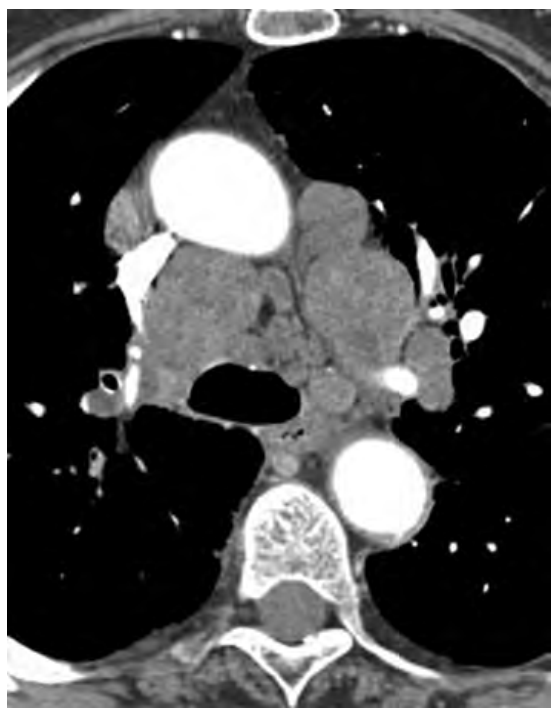

FIGURE 4-14 ■ Extensive mediastinal lymph node metastases in colon carcinoma. Enlarged lymph nodes are visible in the pretracheal space, prevascular space, and aortopulmonary window. Hilar lymph nodes are also enlarged.

Sarcoidosis

Mediastinal lymph node enlargement is common in patients with sarcoidosis, occurring in 60% to 90% of cases. Typically, node enlargement is extensive, involving the hila as well as the mediastinum, and masses appear bilateral and symmetrical in most patients (Figs. 4-1, 4-4, and 4-8); this sometimes allows differentiation of sarcoidosis from lymphoma, which more typically produces asymmetrical enlargement. In addition, lymph nodes can be quite large in patients with sarcoidosis, but large isolated masses, as seen in some patients with lymphoma, are uncommon. Paratracheal lymph nodes are typically involved. Even though it is commonly stated that sarcoidosis does not involve anterior mediastinal lymph nodes, this involvement is often visible on CT; paravertebral node enlargement is seen occasionally (Table 4-6).

Infections

A variety of infectious agents can cause mediastinal lymph node enlargement during the acute stage of the infection. These include a number of fungal infections (commonly histoplasmosis and coccidioidomycosis), tuberculosis, bacterial infections, and viral infections. Typically, there will be symptoms and signs of acute infection, and chest radiographs will show evidence of pneumonia.
The lymph node enlargement will often be asymmetrical, involving hilar and middle mediastinal nodes. In patients with tuberculosis, enlarged nodes typically show rim enhancement and central necrosis after contrast medium injection; this appearance is nearly diagnostic in patients with an appropriate history. Lymph node calcification occurs in patients with chronic fungal or tuberculous infection.

Castleman's Disease (Angiofollicular Lymph Node Hyperplasia)

An unusual disease of unknown cause, Castleman's disease occurs in two forms. The more common localized form is characterized by enlargement of hilar or mediastinal lymph nodes, usually middle or posterior mediastinal nodes. A single smooth or lobulated mass, which can be large, is typically visible on CT, and dense opacification after contrast medium infusion is commonly visible. Localized Castleman's disease is usually asymptomatic and has a benign course.
The rare diffuse form of Castleman's disease results in generalized lymph node enlargement involving mediastinal and hilar nodes, and often axillary, abdominal, and inguinal node groups (Fig. 4-15). It is often associated with systemic symptoms and has a progressive course despite treatment. As with the localized form, marked node enhancement can be seen.

TABLE 4-6 **Sarcoidosis: Frequency of Enlarged Nodes Seen on CT in Patients with Nodes**

Node Group	Frequency (%)
Hilar	90
Right paratracheal	100
Aortopulmonary window	90
Subcarinal	65
Anterior mediastinal	50
Posterior mediastinal	15

DIAGNOSIS OF MEDIASTINAL MASSES

Differential diagnosis of a mediastinal mass on CT is usually based on several factors. The location of the mass is fundamental in differential diagnosis. Although most mediastinal masses can occur in different parts of the mediastinum, most have characteristic locations (Table 4-7). Location is used in this chapter to classify masses. Lymph node masses, such as lymphoma, already discussed in this chapter, and abnormalities discussed in other chapters (e.g., aortic aneurysm) are not covered again but are included in Table 4-7.

Other considerations in differential diagnosis include whether a single mass or multifocal abnormalities are present (i.e., involving several areas of the mediastinum), the shape of the mass (round or lobulated), and findings such as pleural effusion. Attenuation of a mass (fat, fluid, soft-tissue, or a combination of these, and the presence, character,

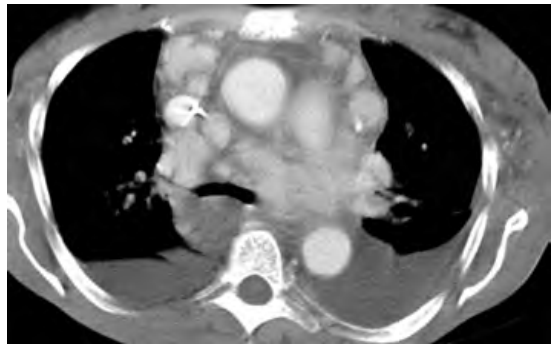

FIGURE 4-15 ■ Diffuse Castleman's disease. Extensive enhancing mediastinal lymphadenopathy in a patient with the diffuse form of Castleman's disease. The enhancement is typical. Enlarged axillary, abdominal, and inguinal lymph nodes were also visible. Bilateral pleural effusions are also present.

TABLE 4-7 **Differential Diagnosis of Mediastinal Masses Based on Common Sites of Origin**

- Prevascular space (anterior mediastinum)
  - Thymic masses
    - Thymoma
    - Thymic carcinoma
    - Thymic neuroendocrine tumor
    - Thymolipoma
    - Thymic cyst
    - Thymic hyperplasia
    - Thymic lymphoma
  - Germ cell tumors
    - Teratoma and dermoid cyst
    - Seminoma
    - Nonseminomatous germ cell tumors
  - Thyroid abnormalities (goiter and neoplasm)
  - Parathyroid tumor or hyperplasia
  - Lymph node masses (particularly Hodgkin's lymphoma)
  - Vascular abnormalities (aorta and great vessels)
  - Mesenchymal abnormalities (e.g., lipomatosis, lipoma)
  - Foregut cyst
  - Lymphangioma
  - Hemangioma
- Retrosternal space (anterior mediastinum)
  - Lymph node masses
- Pretracheal space (middle mediastinum)
  - Lymph node masses
    - Lung carcinoma
    - Sarcoidosis
    - Lymphoma (particularly Hodgkin's disease)
    - Metastases
    - Infections (e.g., tuberculosis)
  - Foregut cyst
  - Tracheal tumor
  - Mesenchymal masses (e.g., lipomatosis, lipoma)
  - Thyroid abnormalities
  - Vascular abnormalities (aorta and great vessels)
  - Lymphangioma and hemangioma
- Aortopulmonary window (middle mediastinum)
  - Lymph node masses
    - Lung carcinoma
    - Sarcoidosis
    - Lymphoma
    - Metastases
    - Infections (e.g., tuberculosis)
  - Mesenchymal masses (e.g., lipomatosis, lipoma)
  - Vascular abnormalities (aorta or pulmonary artery)
  - Chemodectoma
  - Foregut cyst
- Subcarinal space and azygoesophageal recess (middle mediastinum)
  - Lymph node masses
    - Lung carcinoma
    - Sarcoidosis
    - Lymphoma
    - Metastases
    - Infections (e.g., tuberculosis)
  - Foregut cyst
  - Dilated azygos vein
  - Esophageal masses
  - Varices
  - Hernia
- Paravertebral masses (posterior mediastinum)
  - Neurogenic tumor
    - Nerve sheath tumors
    - Sympathetic ganglia tumors
    - Paraganglioma
  - Meningocele
  - Foregut cyst
  - Neurenteric cyst
  - Thoracic spine abnormalities
  - Extramedullary hematopoiesis
  - Fluid collections and pseudocyst
  - Vascular abnormalities
  - Hernias
  - Esophageal masses
  - Varices
  - Mesenchymal masses (e.g., lipomatosis, lipoma)
  - Lymph node masses
    - Lymphoma (particularly non-Hodgkin's)
    - Metastases
  - Dilated azygos or hemiazygos vein
  - Hernia
  - Lymphangioma and hemangioma
  - Thymic mass or germ cell tumor
- Anterior cardiophrenic angle masses
  - Lymph node masses (particularly lymphoma and metastases)
  - Pericardial cyst
  - Fat pad
  - Morgagni hernia
  - Thymic masses
  - Germ cell tumors

TABLE 4-8 **Attenuation Characteristics of Mediastinal Masses***

Mass	Air	Fat	Water	Tissue	>Tissue	Calcium
Thymoma	N	N	O	A	N	O
Thymolipoma	N	A	N	C	N	N
Lymphoma (thymic)	N	N	O	A	N	R
Dermoid cyst/teratoma	N	O	O	A	N	O
Germ-cell tumor	N	N	R	A	N	R
Thyroid tumor	N	N	O	A	C	C
Lipoma	N	A	N	N	N	N
Hygroma	N	C	C	C	N	N
Cysts (congenital)	R	N	C	O	N	R
Hernia	O	O	N	O	N	N
Lung cancer (nodes)	N	N	O	A	N	N
Tuberculosis (nodes)	N	N	C	A	N	C
Sarcoidosis (nodes)	N	N	R	A	N	O
Castleman's (nodes)	N	N	N	A	N	O
Neurogenic tumor	N	O	C	C	N	O
Neurenteric cyst	R	N	A	N	N	N
Meningocele	N	N	A	N	N	N
Hematopoiesis	N	O	N	A	N	N

*ACORN: A, always; C, common; O, occasionally; R, rare; N, never ("never" does not mean it never happens, but rather that it is so unlikely that practically the radiologist should "never" consider the diagnosis, and if the differential diagnosis turns out to be wrong, will "never" be blamed).

and amount of calcification) is also very important in differential diagnosis (Table 4-8).

PREVASCULAR SPACE MASSES

Masses in the prevascular space, when large, tend to displace the aorta and great arterial branches posteriorly (Fig. 4-13), but distinct compression or narrowing of these relatively thick-walled structures is unusual. Within the supra-aortic mediastinum, displacement, compression, or obstruction of the brachiocephalic veins is not uncommon. In the subaortic mediastinum, posterior displacement or compression of the superior vena cava is typical only with right-sided masses. On the left, compression of the main pulmonary artery can be seen.

Although we are taught that the differential diagnosis of anterior mediastinal masses includes the "4 Ts" (thymoma, teratoma, thyroid tumor, and terrible lymphoma), the differential diagnosis should be extended to include (1) thymoma and *other thymic tumors*; (2) teratoma and *other germ-cell tumors*; (3) thyroid masses; (4) lymphoma and *other lymph node masses*; and (5) parathyroid masses, cysts, fatty masses, and lymphangioma (hygroma).

Thymic Tumors

Tumors of various histology arise from cells of thymic origin, including thymoma, thymic carcinoma, thymic carcinoid tumor, thymolipoma, thymic cyst, lymphoma, and leukemia. Thymic hyperplasia may mimic a mass.

Thymoma

Thymoma is a tumor of thymic epithelial origin and is a common cause of anterior mediastinal mass in adults. Occasionally, these lesions arise in the middle or posterior mediastinum. It is extremely difficult to determine if thymomas are benign or malignant by histologic criteria, but the World Health Organization (WHO) has developed an alphanumeric histologic classification system (i.e., A, AB, B1-3, C) that correlates with the presence of invasion, metastasis, and survival. Thymomas are generally classified as *invasive* or *noninvasive* based on their appearance at surgery. Approximately 30% of thymomas are pathologically and surgically invasive. Invasion of mediastinal structures or the pleural space is most typical. Distant metastases are not common with invasive thymoma.

From 10% to 30% of patients with myasthenia gravis will be found to have a thymoma, whereas a larger percentage of patients with thymoma (30% to 50%) have myasthenia. Other syndromes associated with thymoma include red blood cell hypoplasia and hypogammaglobulinemia.

On CT, thymomas are usually visible in the prevascular space (Fig. 4-16), but they can also be seen in a paracardiac location. They appear as a

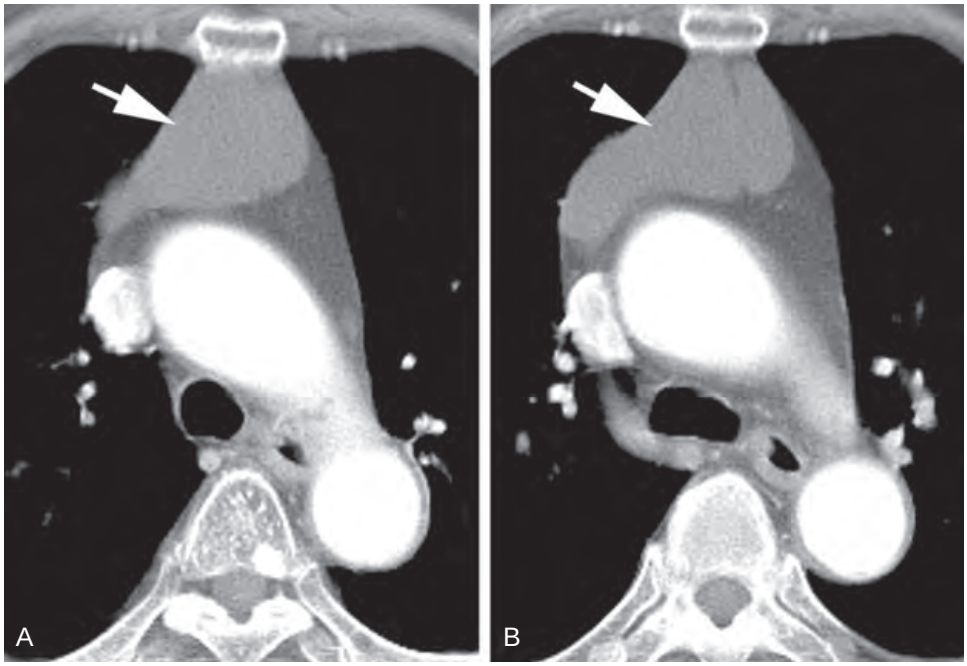

FIGURE 4-16 ■ Thymoma. *A* and *B,* At two levels, a large but well-marginated mass involves the right thymic lobe (*arrows*). A noninvasive thymoma was found at surgery. The left thymic lobe is replaced by fat.

localized mass distorting or replacing the normally arrowhead-shaped thymus. Typically, they are unilateral. Calcification and cystic degeneration can be present. On CT, bilaterality, large size, lobulated contours, poor definition of the tumor margin, and associated pleural effusion or nodules suggest the presence of an invasive thymoma, but a definite diagnosis is difficult to make on CT.

In patients suspected of having thymoma because of myasthenia gravis, CT can demonstrate tumors that are invisible on plain radiographs. However, small thymic tumors may not be distinguishable from a normal or hyperplastic gland with CT.

Thymic Carcinoma

Similar to invasive thymoma, thymic carcinoma arises from thymic epithelial cells. However, unlike invasive thymoma, thymic carcinoma can be diagnosed as malignant on the basis of histology. It is classified as C in the WHO system previously described. This tumor is aggressive and is more likely to result in distant metastases than invasive thymoma. Thymic carcinoma cannot be distinguished accurately from thymoma on CT unless metastases are visible.

Thymic Neuroendocrine Tumor

Thymic neuroendocrine tumors, which may be further classified as carcinoid, atypical carcinoid, or small-cell neuroendocrine carcinoma, are usually malignant and aggressive. This type of lesion does not differ significantly from thymoma in its CT appearance, but it has a worse prognosis. Approximately 40% of patients have Cushing's syndrome as a result of tumor secretion of adrenocorticotropic hormone, and nearly 20% have been associated with multiple endocrine neoplasia syndromes I and II.

Thymolipoma

Thymolipoma is a rare, benign thymic tumor consisting primarily of fat but also containing strands or islands of thymic tissue. The tumor is generally unaccompanied by symptoms and can be large when first detected, usually on chest radiographs. Because of its fatty content and pliability, it tends to drape around the heart and can simulate cardiac enlargement. On CT, its fatty composition, with wisps of soft tissue within it, can permit a preoperative diagnosis (Fig. 4-17).

Thymic Cyst

Thymic cysts are either congenital or acquired and can be diagnosed using CT if they are thin-walled and their contents have an attenuation close to that of water. In some cases, they will show soft-tissue attenuation. Calcification of the cyst margin can occur. Notably, thymoma can

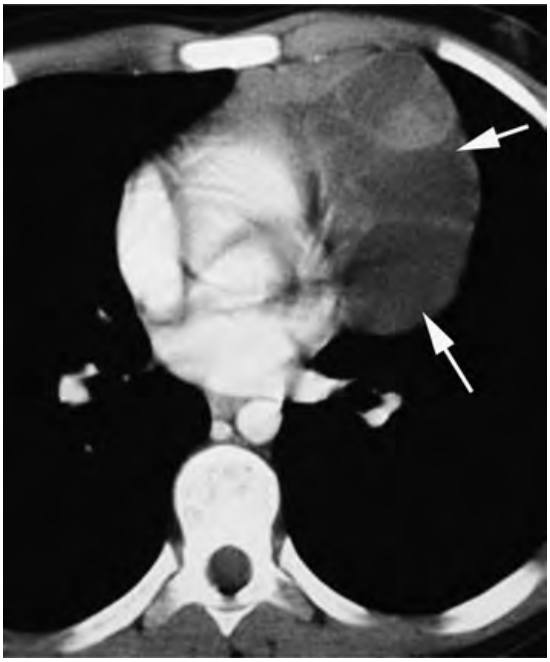

FIGURE 4-17 ■ Thymolipoma. A large, low-attenuation, anterior mediastinal mass (*arrows*) is composed primarily of fat but also contains strands of soft tissue. The mass is somewhat droopy in appearance.

have cystic components but also demonstrates solid areas or a thick or irregular wall.

An important general rule in diagnosing mediastinal masses is that cysts can appear solid, and solid (malignant) masses can have cystic or necrotic components. A true cyst has a thin wall; a mass with cystic degeneration usually has a thick, irregular wall.

Thymic Hyperplasia and Thymic Rebound

Thymic hyperplasia may result in thymic enlargement or a focal thymic mass. It is associated with myasthenia gravis. Distinction from thymoma on CT may be impossible.

The thymus may appear enlarged and relatively dense (containing little fat) in patients with thymic hyperplasia. In young patients, the thymus may show significant rebound hyperplasia 3 months to a year after cessation of chemotherapy for malignancy. This can result in a distinctly enlarged thymus.

Thymic Lymphoma

Anterior mediastinal lymph node enlargement (Figs. 4-3 and 4-9) or thymic involvement (Fig. 4-18) is present in more than half of patients with HD. In patients with thymic involvement, lymphoma can present as a single spherical or lobulated mass or as thymic enlargement. In such cases, lymphoma can be indistinguishable from thymoma or other causes of prevascular mass. However, if the abnormality is multifocal (indicating its origin from nodes) or is associated with other sites of lymph node enlargement, the diagnosis is made more easily (Fig. 4-18). Cystic areas of necrosis may be visible at CT in patients with lymphoma (Fig. 4-12). Except in rare cases, calcification does not occur in the absence of radiation. HD limited to the prevascular mediastinum is typically of the nodular sclerosing cell type.

Germ-Cell Tumors

Several different tumors originating from rests of primitive germ cells can occur in the anterior mediastinum. These include teratoma, dermoid cysts, seminoma, choriocarcinoma, and endodermal sinus tumor. These tumors are less common than thymoma. Approximately 80% of germ-cell tumors are benign. Germ-cell tumors are usually considered in three categories: teratoma and dermoid cysts, seminoma, and nonseminomatous germ-cell tumors.

Teratoma and Dermoid Cyst

Teratomas can be cystic or solid and are most commonly benign. A teratoma contains tissues of ectodermal, mesodermal, and endodermal origins. A dermoid cyst is a specific type of teratoma derived primarily from epidermal tissues, although other tissues are usually present. Teratomas are classified histologically as mature or immature. Mature teratomas are benign; immature teratomas usually behave in a malignant fashion in adults but may be benign in children.

Teratomas occur in a distribution similar to that of thymomas; they rarely originate in the posterior mediastinum. Benign lesions are often round, oval, and smooth in contour; as with thymoma, an irregular, lobulated, or ill-defined margin suggests malignancy. On average, these tumors are larger than thymomas, but they can be any size. Calcification can be seen (Fig. 4-19) but is nonspecific except in the unusual instance when a bone or tooth is present within the mass. They may appear cystic or contain visible fat, a finding that is of great value in differential diagnosis (Fig. 4-19). A fat–fluid level can also be seen.

Seminoma

Seminoma occurs almost entirely in young men. It is the most common malignant mediastinal germ-cell tumor, accounting for 30% of such

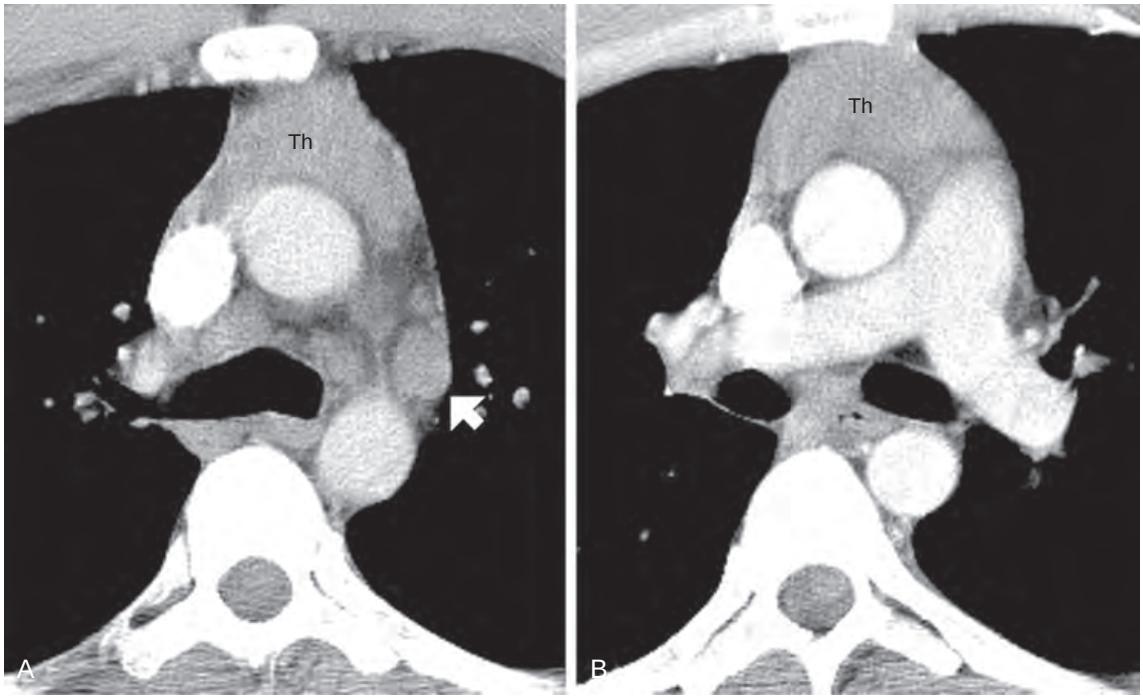

FIGURE 4-18 ■ Lymphoma with thymic and mediastinal lymph node enlargement. *A* and *B,* The thymus (Th) is symmetrically enlarged. This appearance could represent thymoma or another primary thymic tumor. However, enlarged lymph nodes in the aortopulmonary window (*arrow, A*) and pretracheal space are a clue to the diagnosis.

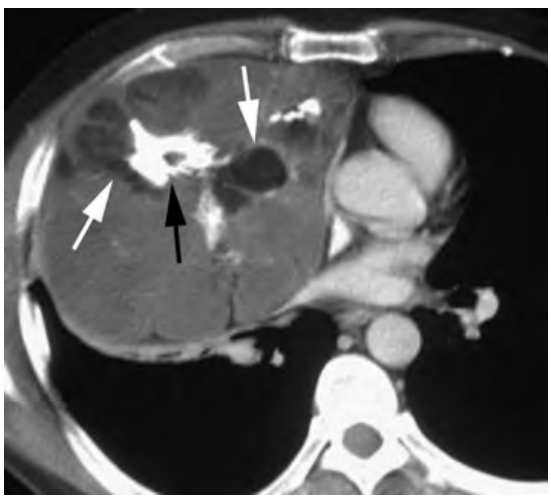

FIGURE 4-19 ■ Mature teratoma. A lobulated anterior mediastinal mass contains low-attenuation fat (*white arrows*), an important finding in diagnosis, and calcium (*black arrow*).

cases. On CT, seminoma presents as a large, smooth or lobulated homogeneous soft-tissue mass, although small areas of low attenuation can be seen. Obliteration of fat planes is common, and pleural or pericardial effusion may be present. Seminomas are radiosensitive, and the 5-year survival rate for affected patients is 50% to 75%.

Nonseminomatous Germ-Cell Tumors

Nonseminomatous germ-cell tumors, namely embryonal carcinoma, endodermal sinus (yolk sac) tumor, choriocarcinoma, and mixed types, are often grouped together because of their rarity, similar appearance, aggressive behavior, and poor prognosis. The tumors are usually unresectable at the time of diagnosis because of local invasion or distant metastasis. Unlike seminoma, radiotherapy is of limited value.

On CT, these tumors often show heterogeneous opacity, including ill-defined areas of low attenuation secondary to necrosis and hemorrhage or cystic areas. They often appear infiltrative, with obliteration of fat planes, and may be spiculated. Calcification may be seen.

Thyroid Masses

A small percentage of patients with a thyroid mass have some extension of the mass into the superior mediastinum, and, rarely, a completely intrathoracic mass can arise from ectopic mediastinal thyroid tissue. In most patients, such masses represent a goiter (Fig. 4-20), but other diseases (Graves' disease and thyroiditis) and neoplasms can result in an intrathoracic mass. Masses are often asymmetrical.

Most patients with intrathoracic goiter are asymptomatic, but symptoms of tracheal or

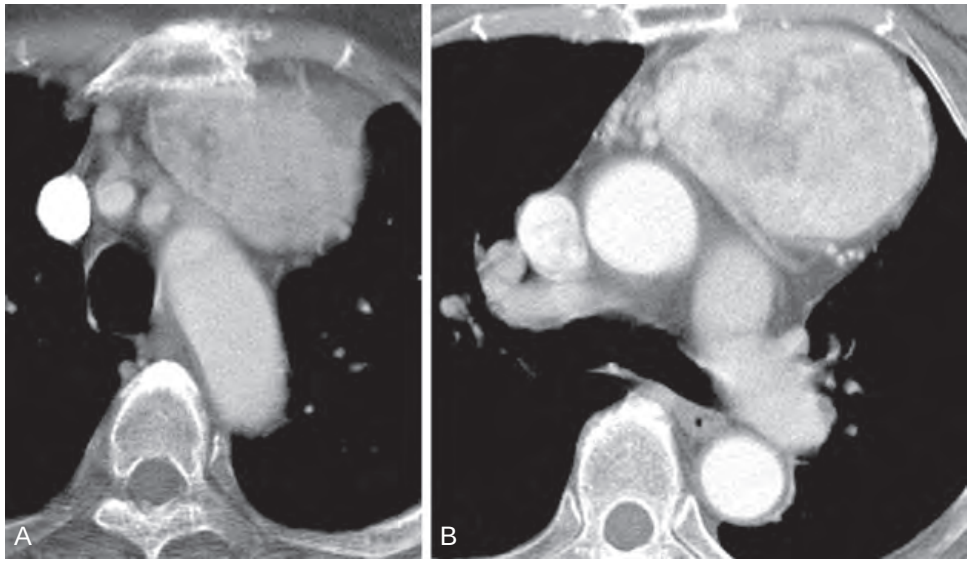

FIGURE 4-20 ■ Mediastinal goiter. *A,* A large inhomogeneous mass is visible in the anterior mediastinum. *B,* It shows enhancement after contrast medium infusion. At higher levels, the mass was contiguous with the inferior thyroid.

esophageal compression can be present. CT usually shows anatomic continuity of the visible mass with the cervical thyroid gland. The location of the mass on CT is somewhat variable, and it can be anterior or posterior to the trachea. Masses anterior to the trachea splay the brachiocephalic vessels, whereas masses that are primarily posterior and lateral to the trachea displace the brachiocephalic vessels anteriorly. A location anterior to the great vessels is somewhat unusual (Fig. 4-20). Calcifications and low-attenuation cystic areas are common in patients with goiter. In addition, because of their high iodine content, the CT attenuation of goiters, Graves' disease, and thyroiditis can be greater than that of soft-tissue and thyroid tumors, but less dense than normal thyroid tissue.

As a rule, if a thyroid mass is suspected clinically, CT should be performed without contrast injection. This allows subsequent injection of radioactive iodine for diagnosis. Injection of iodinated radiographic contrast agents delays radionuclide imaging.

Mesenchymal Abnormalities

Lipomatosis and Lipoma

A diffuse accumulation of unencapsulated fat in the mediastinum, so-called mediastinal lipomatosis, can occur in patients with Cushing's syndrome, after long-term corticosteroid therapy, or as a result of exogenous obesity. It produces no symptoms. CT shows a generalized increase in anterior mediastinal fat surrounding the great vessels, with some lateral bulging of the mediastinal pleural reflections. On CT, fat has a characteristic low attenuation, measuring from –50 to –100 Hounsfield units (HU).

As with other mesenchymal tumors, lipomas can occur in any part of the mediastinum but are most common anteriorly. Because of their pliability, they rarely cause symptoms. A lipoma, although of the same attenuation as lipomatosis, is localized. Most fatty masses are benign. Liposarcoma, teratoma, and thymolipoma, which are other masses that can contain fat, also contain soft-tissue elements and thus can be distinguished from lipoma or lipomatosis.

Lymphangioma (Hygroma)

Lymphangiomas are classified histologically as simple, cavernous, and cystic. Simple lymphangiomas are composed of small, thin-walled lymphatic channels with considerable connective tissue stroma. Cavernous lymphangiomas consist of dilated lymphatic channels, whereas cystic lymphangiomas (hygromas) contain single or multiple cystic masses filled with serous or milky fluid and having little, if any, communication with normal lymphatic channels. Most commonly, these lesions are detected in children and may extend into the neck. However, they can be seen in adults as well. On CT, the mass can appear as a single cyst, be multicystic, or envelop, rather than displace, mediastinal structures. Discrete cysts may not be visible; calcification does not occur. Abnormal vessels that are opacified by contrast medium may be present.

RETROSTERNAL SPACE MASSES

Enlargement of internal mammary nodes results in a convexity in the expected position of this node chain (Fig. 4-1). Other than lymph node enlargement, masses in this region are unusual. Metastases and lymphoma are most common. The anterior mediastinal masses previously listed can project into this space.

PRETRACHEAL SPACE MASSES

Masses that occupy the pretracheal compartment characteristically replace or displace normal pretracheal fat. Because the pretracheal space is limited by the relatively immobile aortic arch anteriorly and to the left, large masses extend preferentially to the right, displacing and compressing the superior vena cava anteriorly and laterally. In the presence of a pretracheal mass, the superior vena cava appears crescentic and convex laterally. Lateral displacement of the superior vena cava results in most of the mediastinal widening visible on plain films. Large masses also displace the trachea posteriorly, but tracheal cartilage usually prevents significant tracheal narrowing. Masses in this compartment are almost always of lymph node origin, but masses more typical in other parts of the mediastinum may involve the pretracheal space.

AORTOPULMONARY WINDOW MASSES

Masses in the aortopulmonary region typically replace mediastinal fat; when large, they displace the mediastinal pleural reflection laterally. Displacement or compression of the aorta, pulmonary artery, and trachea is sometimes seen.

Aortopulmonary window masses are almost always the result of lymph node enlargement (Figs. 4-3 and 4-4). Other masses occurring in this region include aortic abnormalities (aneurysm or pseudoaneurysm) and chemodectoma.

SUBCARINAL SPACE AND AZYGOESOPHAGEAL RECESS

Large masses in the subcarinal space can (1) produce a convexity of the azygoesophageal recess, (2) splay the carina, (3) displace the carina anteriorly, (4) displace the esophagus to the left, and/or (5) displace the right pulmonary artery anteriorly and compress its lumen. The most common masses involving this compartment are lymph node masses, cysts, and esophageal lesions.

Bronchogenic and Esophageal Duplication Cysts

Congenital bronchogenic cysts result from anomalous budding of the foregut during development. Most commonly, they are visible in the subcarinal space, but they can occur in any part of the mediastinum. They appear as single smooth masses that are round or elliptical (Fig. 4-21) and occasionally show calcification of their walls or contents. Air–fluid levels occurring because of communication with the trachea or bronchi are rare. When large, bronchogenic cysts can produce symptoms due to compression of mediastinal structures. A rapid increase in size can occur because of infection or hemorrhage.

Esophageal duplication cysts are indistinguishable from bronchogenic cysts, but they always contact the esophagus. They usually appear as well-defined solitary masses and occasionally contain an air–fluid level when they communicate with the esophagus.

CT can be of great value in diagnosing a mediastinal cyst. If a mass is thin-walled and is of fluid attenuation (approximately 0 HU), it can be assumed to represent a benign cyst. However, high CT numbers (20–40 HU) suggesting a solid mass can also be found in patients with foregut duplication cysts. These cysts contain a thick gelatinous material or blood. In such patients, surgery is usually required for diagnosis, but magnetic resonance imaging may sometimes help.

Esophageal Lesions

Esophageal lesions are discussed in Chapter 17.

PARAVERTEBRAL MASSES

Paravertebral masses may be seen to replace paravertebral fat. On the left, the normal concave mediastinal pleural reflection, posterior to the aorta, becomes convex in the presence of a significant mass. On the right, a paravertebral convexity is visible in a region where little tissue normally exists (Fig. 4-5).

Neurogenic Tumors

Neurogenic tumors are divided into three groups arising from (1) peripheral nerves or a nerve sheath (neurofibroma or neurilemmoma), (2) sympathetic ganglia (ganglioneuroma or neuroblastoma), and (3) paraganglionic cells (pheochromocytoma or chemodectoma). Tumors in each of these three groups may be benign or malignant. Although neurogenic tumors can occur at any age, they are

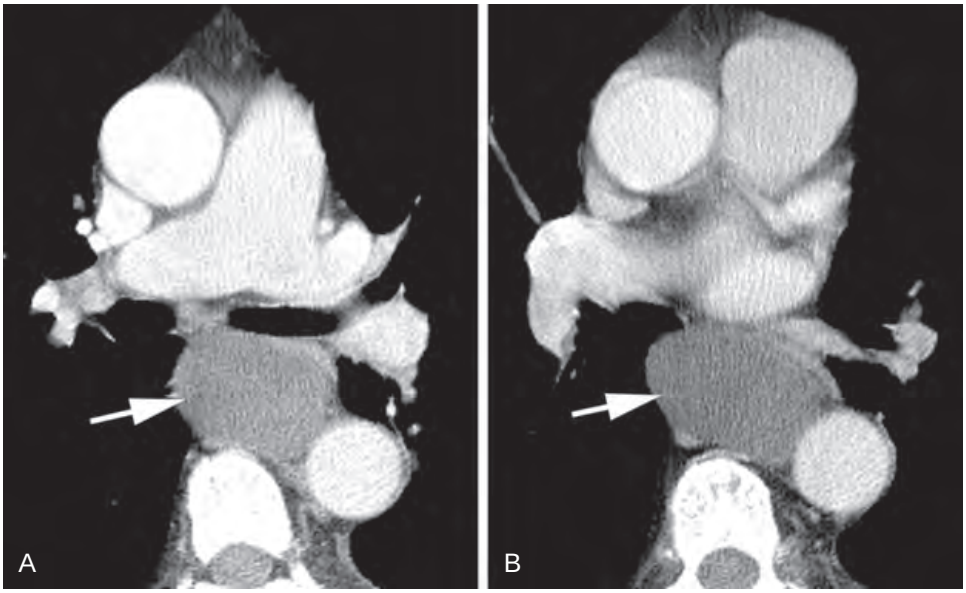

FIGURE 4-21 ■ Bronchogenic cyst. *A* and *B*, A large, oval, low-attenuation cyst (*arrows*) is visible in the subcarinal region and azygoesophageal recess. This location is typical.

most common in young patients. Neuroblastoma and ganglioneuroma are most common in children, whereas neurofibroma and neurilemmoma more frequently affect young adults.

Radiographically, neurogenic tumors appear as well-defined round or oval soft-tissue masses, typically in a paravertebral location (Fig. 4-22). Although the different tumors are by no means always distinguishable, a ganglioneuroma tends to be elongated, lying adjacent to the spine, whereas neurofibroma and neurilemmoma are smaller and more spherical in shape. Although neural tumors are frequently of soft-tissue attenuation, they can be low in attenuation because of the presence of lipid-rich Schwann cells, fat, or cystic regions. Although benign tumors tend to be sharply marginated and fairly homogeneous, and malignant tumors tend to be infiltrating and irregular, these findings are not sufficiently reliable for diagnosis. Calcification can occur, particularly in neuroblastoma; the presence of calcium does not help in distinguishing benign from malignant lesions.

A neurofibroma arising in a nerve root can be dumbbell-shaped, that is, partially inside and partially outside the spinal canal. In such cases, the intervertebral foramen may be enlarged. CT can be helpful in determining the extent of the mass and associated vertebral abnormalities, and can distinguish the mass from an aortic aneurysm or other vascular lesion if an intravenous contrast agent is given. CT after injection of myelographic contrast medium may be useful in demonstrating intraspinal extension.

FIGURE 4-22 ■ Neurofibromas in neurofibromatosis. A smooth, paravertebral, posterior mediastinal mass is visible (*large white arrow*). The neural foramen is slightly enlarged (*black arrow*). Multiple other neurofibromas are also present, some of which are relatively low in attenuation (*small white arrows*).

Anterior or Lateral Thoracic Meningocele

A thoracic meningocele represents anomalous herniation of the spinal meninges through an

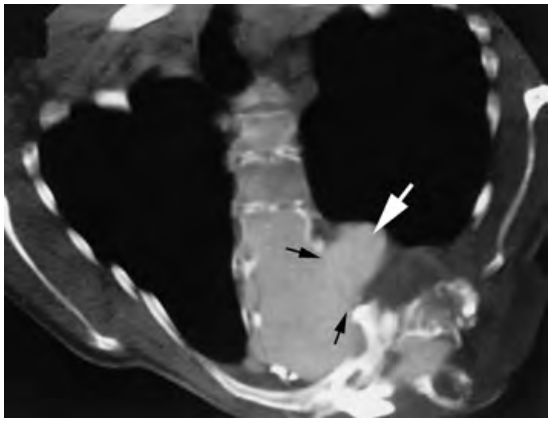

FIGURE 4-23 ■ Lateral thoracic meningocele. In a patient with neurofibromatosis and scoliosis, a meningocele (*white arrow*) is associated with a large foraminal defect (*black arrows*). Myelographic contrast material opacifies the meningocele.

intervertebral foramen or a defect in the vertebral body. It results in a soft-tissue mass visible on chest radiographs. In most patients, this abnormality is associated with neurofibromatosis; most cases are detected in adults. It is said that meningocele is the most common cause of a posterior mediastinal mass in patients with neurofibromatosis, but I doubt it.

Meningoceles are described as lateral or anterior, depending on their relationship to the spine. They are slightly more common on the right. Findings that suggest the diagnosis include rib or vertebral anomalies at the same level or an association with scoliosis. The mass is often visible at the apex of the scoliotic curve. CT after intraspinal contrast medium injection shows filling of the meningocele and is diagnostic (Fig. 4-23); magnetic resonance imaging may also be diagnostic.

Neurenteric Cyst

A neurenteric cyst, which is rare, is composed of both neural and gastrointestinal elements and is frequently attached to both the meninges and the gastrointestinal tract. It appears as a homogeneous posterior mediastinal mass and rarely contains air because of communication with the abdominal viscera. As with meningocele, it is frequently associated with a vertebral anomaly or scoliosis. As opposed to meningocele, it frequently causes pain and is generally diagnosed at a young age.

Diseases of the Thoracic Spine

Tumors (either benign or malignant), infectious spondylitis, or vertebral fracture with associated hemorrhage can produce a paravertebral mass. Frequently, the abnormality is bilateral and fusiform, allowing it to be distinguished from solitary masses such as a neurogenic tumor. Associated abnormalities of the vertebral bodies or disks assist in diagnosis and should be sought. Preservation of disks in association with vertebral body destruction suggests neoplasm or tuberculosis; disk destruction suggests infection other than tuberculosis.

Extramedullary Hematopoiesis

Extramedullary hematopoiesis can result in paravertebral masses in patients with severe anemia (usually congenital hemolytic anemia or thalassemia). These masses are of unknown origin but perhaps arise from lymph nodes, veins, or an extension of rib marrow. Masses can be multiple and bilateral and are most commonly associated with the lower thoracic spine. They have no specific CT characteristics. With resolution they may appear as fat density.

Fluid Collections and Pseudocyst

Occasionally, posterior pleural fluid collections can simulate a paravertebral mediastinal mass. Mediastinal extension of a pancreatic pseudocyst through the aortic or esophageal hiatus can occur, but it is rare.

Vascular Abnormalities

Posteriorly located aortic aneurysms can occupy this part of the mediastinum. Azygos and hemiazygos vein dilatation also produces abnormalities in this region. Dilated azygos or hemiazygos veins, because they are visible on a number of contiguous slices, are easily distinguished from a focal mass.

PARACARDIAC MASSES

Compression of the atria or right ventricle can be seen in the presence of a paracardiac mass, but left ventricular compression is uncommon because of the thickness of its wall and the relatively high pressure of its contents. A variety of masses can be seen in this location. Large anterior mediastinal masses often project posteriorly into a paracardiac location.

Anterior Cardiophrenic Angle Masses

Although a number of the mediastinal masses already described can occur at the level of the

anterior cardiophrenic angle, differential diagnosis of lesions occurring in this location includes several specific entities. These include a pericardial cyst, a large epicardial fat pad, a Morgagni hernia, and enlargement of paracardiac lymph nodes (Fig. 4-2).

Pericardial Cyst

Most commonly, pericardial cysts touch the diaphragm, 60% in the anterior right cardiophrenic angle and 30% in the left cardiophrenic angle; 10% occur higher in the mediastinum. Most patients are asymptomatic. The cysts typically appear as smooth, round, homogeneous masses (Fig. 4-24). They range up to 15 cm in diameter. Although they are usually low in attenuation (i.e., near 0 HU), they may have similar attenuation to soft tissue.

Fat Pad

Deposition of fat in either cardiophrenic angle is not uncommon, particularly in obese patients, and can simulate a mass on plain radiographs. CT, of course, is diagnostic.

Morgagni Hernia

Hernias of abdominal contents through the anteromedial diaphragmatic foramen of Morgagni can result in a cardiophrenic angle mass; 90% of these occur on the right. The hernia usually contains omentum or liver; bowel is less common. When the hernia contains fat, CT can confirm its benign nature but does not allow its differentiation from a fat pad. When it contains liver, CT may allow diagnosis by showing hepatic vessels or bile ducts. If bowel is present in the hernia sac, gas is usually visible.

DIFFUSE MEDIASTINAL ABNORMALITIES

Mediastinitis

Mediastinal infections (mediastinitis) can be acute or chronic.

Acute Mediastinitis

Acute mediastinitis usually results from esophageal perforation or spread of infection from adjacent tissue spaces, including the pharynx, lungs, pleura, and lymph nodes. The primary symptoms are substernal chest pain and fever. CT shows mediastinal widening, replacement of normal fat by fluid attenuation, or localized fluid collections. Gas bubbles may be seen (Fig. 4-25).

Granulomatous Mediastinitis

In patients with histoplasmosis, tuberculosis, or sarcoidosis, chronic mediastinal lymph node enlargement and associated fibrosis can result in so-called granulomatous mediastinitis. In these patients, the large nodes and associated fibrous tissue form a mediastinal mass that can compress the superior vena cava, pulmonary arteries or veins, bronchi, and esophagus.

The node enlargement tends to be asymmetrical, except in patients with sarcoidosis. Fibrosis

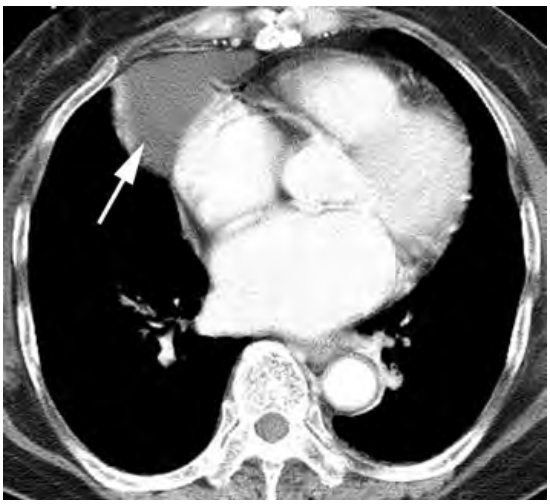

FIGURE 4-24 ■ Pericardial cyst. A fluid-attenuation mass (i.e., 0 HU) is visible in the right cardiophrenic angle (*arrow*). This appearance and location are typical of a pericardial cyst.

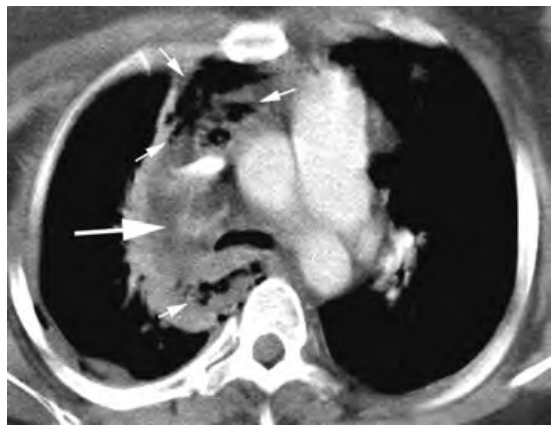

FIGURE 4-25 ■ Acute mediastinitis caused by esophageal perforation by a car antenna. There is mediastinal widening, increased attenuation of mediastinal fat as a result of inflammation (*large arrow*), and multiple collections of air (*small arrows*).

can replace normally visible mediastinal fat. Calcification of the nodes can be seen in some patients, indicating the benign nature of the disease process. Compression of the main bronchi (usually the left) or pulmonary arteries (usually the right) can sometimes be recognized.

Fibrosing Mediastinitis

In some patients, similar mediastinal fibrosis is not associated with obvious granulomatous disease. This occurrence is less common than granulomatous mediastinitis. In a few patients, this is associated with fibrosis elsewhere (retroperitoneal fibrosis). Symptoms and radiographic findings are similar to those for granulomatous mediastinitis, but calcification does not occur.

Mediastinal Hemorrhage

Mediastinal hemorrhage usually results from trauma such as venous or arterial laceration, from aortic rupture or dissection, or from anticoagulation (see Chapter 3). Superior mediastinal widening associated with blurring of normal mediastinal contours is usually present. Mediastinal fluid visible on CT is high in attenuation (> 50 HU). Blood can dissect extrapleurally over the lung apex, resulting in a so-called apical cap. In some patients, blood will also be present in the left pleural space. Contrast-enhanced CT may be of value in diagnosing associated aortic aneurysm, dissection, or rupture.

Suggested Readings are available on Expert Consult.

SUGGESTED READING

Ahn JM, Lee KS, Goo JM, et al.: Predicting the histology of anterior mediastinal masses: Comparison of chest radiography on CT. *J Thorac Imaging* 11:265–271, 1996.

Bashist B, Ellis K, Gold RP: Computed tomography of intrathoracic goiters. *AJR Am J Roentgenol* 140:455–460, 1983.

Brown LR, Aughenbaugh GL: Masses of the anterior mediastinum: CT and MR imaging. *AJR Am J Roentgenol* 157:1171–1180, 1991.

Castellino RA, Blank N, Hoppe RT, et al.: Hodgkin disease: Contributions of chest CT in the initial staging evaluation. *Radiology* 160:603–605, 1986.

Castellino RA, Hilton S, O'Brien JP, et al.: Non-Hodgkin lymphoma: Contribution of chest CT in the initial staging evaluation. *Radiology* 199:129–132, 1996.

Dales RE, Stark RM, Raman S: Computed tomography to stage lung cancer: Approaching a controversy using meta-analysis. *Am Rev Respir Dis* 141:1096–1101, 1990.

Detterbeck FC, Boffa DJ, Tanoue LT: The new lung cancer staging system. *Chest* 136:260–271, 2009.

Freundlich IM, McGavran MH: Abnormalities of the thymus. *J Thorac Imaging* 11:58–65, 1996.

Glazer GM, Gross BH, Quint LE, et al.: Normal mediastinal lymph nodes: Number and size according to American Thoracic Society mapping. *AJR Am J Roentgenol* 144:261–265, 1985.

Glazer HS, Aronberg DJ, Sagel SS: Pitfalls in CT recognition of mediastinal lymphadenopathy. *AJR Am J Roentgenol* 144:267–274, 1985.

Glazer HS, Kaiser LR, Anderson DJ, et al.: Indeterminate mediastinal invasion in bronchogenic carcinoma: CT evaluation. *Radiology* 173:37–42, 1989.

Glazer HS, Molina PL, Siegel MJ, Sagel SS: Pictorial essay: Low-attenuation mediastinal masses on CT. *AJR Am J Roentgenol* 152:1173–1177, 1989.

Glazer HS, Siegel MJ, Sagel SS: Pictorial essay: High-attenuation mediastinal masses on unenhanced CT. *AJR Am J Roentgenol* 156:45–50, 1991.

Glazer HS, Wick MR, Anderson DJ, et al.: CT of fatty thoracic masses. *AJR Am J Roentgenol* 159:1181–1187, 1992.

Jolles H, Henry DA, Roberson JP, et al.: Mediastinitis following median sternotomy: CT findings. *Radiology* 201:463–466, 1996.

Kawashima A, Fishman EK, Kuhlman JE, et al.: CT of posterior mediastinal masses. *Radiographics* 11:1045–1067, 1991.

McLoud TC, Bourgouin PM, Greenberg RW, et al.: Bronchogenic carcinoma: Analysis of staging in the mediastinum with CT by correlative lymph node mapping and sampling. *Radiology* 182:319–323, 1992.

Mountain CF, Dresler CM: Regional lymph node classification for lung cancer staging. *Chest* 111:1718–1723, 1997.

Müller NL, Webb WR, Gamsu G: Paratracheal lymphadenopathy: Radiographic findings and correlation with CT. *Radiology* 156:761–765, 1985.

Müller NL, Webb WR, Gamsu G: Subcarinal lymph node enlargement: Radiographic findings and CT correlation. *AJR Am J Roentgenol* 145:15–19, 1985.

Quint LE, Glazer GM, Orringer MB, et al.: Mediastinal lymph node detection and sizing at CT and autopsy. *AJR Am J Roentgenol* 147:469–472, 1986.

Rami-Porta R, Crowley JJ, Goldstraw P: The revised TNM staging system for lung cancer. *Ann Thorac Cardiovasc Surg* 15:4–9, 2009.

Rosado-de-Christenson ML, Templeton PA, Moran CA: Mediastinal germ-cell tumors: Radiologic and pathologic correlation. *Radiographics* 12:1013–1030, 1992.

CHAPTER 5

THE PULMONARY HILA

W. Richard Webb

Computed tomography (CT) is helpful in the diagnosis of endobronchial lesions, hilar and parahilar masses, and hilar vascular lesions.

TECHNIQUE

The hila are adequately assessed using spiral CT with a 5-mm slice thickness (it takes about 15 contiguous 5-mm slices to image the hila), but thinner slices are helpful in identifying bronchial abnormalities. Scans with a 1.25-mm thickness are routinely obtained for most chest CT indications and are used in this chapter to illustrate normal anatomy. Contrast infusion is optimal for imaging the hila.

Scans are usually viewed with a mean window level of –600 to –700 Hounsfield units (HU) and a window width of 1000 or 1500 HU (lung window) for accurate assessment of hilar contours and bronchial anatomy. Scans are also viewed at a mean window value of 0 to 50 HU and a window width of 400 to 500 HU (soft-tissue or mediastinal window) to obtain information about hilar structures, lymph nodes, and masses. Both are necessary.

DIAGNOSIS OF HILAR MASS OR ADENOPATHY

A detailed understanding of cross-sectional hilar anatomy is needed in order to detect and accurately localize hilar abnormalities on CT. Contrast enhancement simplifies the identification of hilar masses or lymph node enlargement.

Lobar and segmental bronchi (Fig. 5-1) are consistently seen on CT and reliably identify successive hilar levels. Their recognition is key to interpretation of hilar CT. In general, hilar anatomy and contours at the same bronchial levels are relatively constant from one patient to the next. The bronchi should be looked at first when reading a CT scan of the hila. Bronchial anatomy is less variable than the branching patterns of arteries or veins.

In some locations, normal hilar contours are consistent enough that a diagnosis of hilar adenopathy or mass can be made on the basis of an abnormality in hilar contour alone, seen using a lung window. In other locations, contours vary according to the size and position of the hilar pulmonary arteries and veins. In these locations, contrast opacification of the pulmonary vessels is essential for accurate diagnosis.

A hilar mass or lymph node enlargement may be suggested by a local or generalized alteration in hilar contour; a visible mass or lymph node enlargement; bronchial narrowing, obstruction, or displacement; or thickening or obliteration of the walls of bronchi that normally contact the lungs.

As a general rule, any nonvascular (nonenhancing) hilar structure larger than 5 to 10 mm (short axis) should be regarded with suspicion and may represent an enlarged lymph node. However, normal amounts of soft tissue larger than this and representing fat and normal nodes are visible in some hilar regions. Mild lymph node enlargement is commonly present in patients with inflammatory lung disease (e.g., pneumonia), and such lymph node enlargement should not be of great concern.

NORMAL AND ABNORMAL HILAR ANATOMY

There are two ways to read hilar CT. The first way is to look at each hilum separately, identifying each important structure, and the second is to compare one side with the other at successive scan levels, looking for points of similarity and dissimilarity. In fact, it is a good idea to do both.

I suggest that as you read the next section, you first learn about right hilar anatomy, skipping what is written about the left hilum. When you finish, and are somewhat oriented, you should start over, reading about both hila, comparing their anatomy, noting what is symmetrical and what is not, and learning how the left hilum differs from the right. Also, you should learn to trace each lobar bronchus from its origin to its segmental branches, because this should be done during interpretation of CT.

Although the hila are not symmetrical structures, they have a number of similarities, and identifying

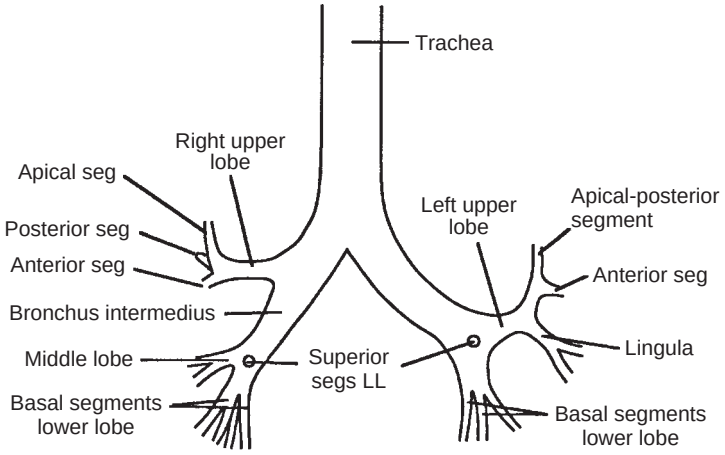

FIGURE 5-1 ■ Normal bronchial tree. All the bronchi shown are visible on CT in most patients. Those bronchi that appear horizontal (such as those of the right upper lobe) or nearly vertical are usually seen better than those that have an oblique course relative to the scan plane (such as the right middle lobe or lingular bronchi). LL, lower lobe; seg, segment.

these can be of value. These similarities are emphasized in the following description. To reinforce the normal appearances and their significance, and expected alterations in anatomy occurring because of mass or node enlargement, abnormal findings are discussed for each hilar level described.

Some variation exists among patients in the relative levels of the hila; therefore, there is some variation in the levels at which right and left hilar structures are visible on CT. The right-to-left relations illustrated in Figure 5-1 and described in the following text may or may not be present in individual cases, although side-to-side variation will usually be minor (1 or 2 cm).

Because recognizing lobar and segmental bronchial anatomy is fundamental to interpreting hilar CT, it is reviewed briefly in Table 5-1. Each of the segments listed is commonly, but not invariably, visible.

TABLE 5-1 Lobar and Segmental Bronchial Anatomy

Right Upper Lobe Segments	Left Upper Lobe Segments
Apical	Apical-posterior
Posterior	Anterior
Anterior	Superior lingular
	Inferior lingular
Right Middle Lobe Segments	
Medial	
Lateral	
Right Lower Lobe Segments	**Left Lower Lobe Segments**
Superior	Superior
Anterior	Anteromedial
Medial	Lateral
Lateral	Posterior
Posterior	

Upper Hila

Right Hilum

CT at the level of the distal trachea or carina shows the apical segmental bronchus of the right upper lobe in cross-section, surrounded by several vessels of similar size (Fig. 5-2*A* to *C*). On either side, a mass or lymphadenopathy is easily recognized. Anything larger than the expected pulmonary vessels is abnormal (Figs. 5-3 and 5-4). Comparison with the opposite side at this level is helpful.

Left Hilum

The apical-posterior segmental bronchus and associated arteries and veins have a similar appearance to the right side at this level (Fig. 5-2*B* and *C*), as does lymph node enlargement (Fig. 5-3*A*).

Right Upper Lobe Bronchus and Left Upper Lobe Segments

Right Hilum

Approximately 1 cm distal to the carina, the right upper lobe bronchus is usually visible along its length, with its anterior and posterior segmental branches both generally seen at the same level (Fig. 5-5*A* to *C*). The anterior segment, usually

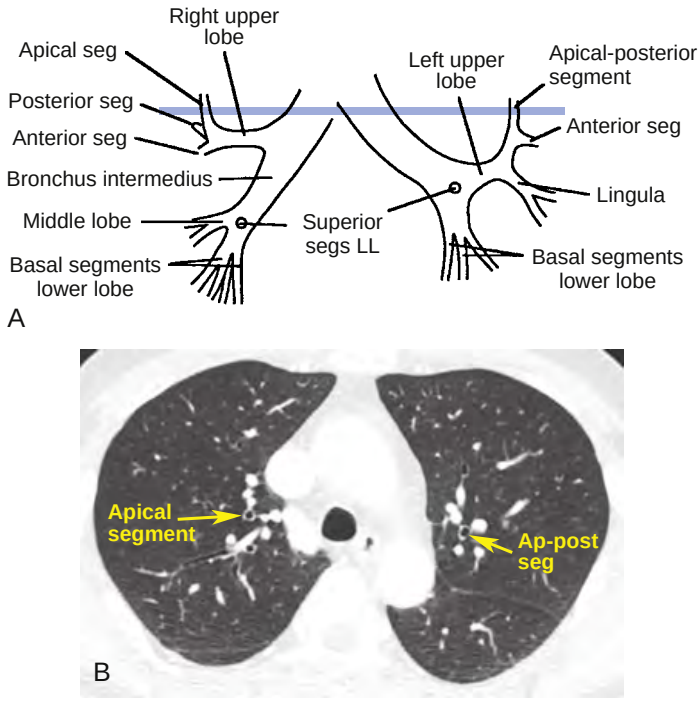

FIGURE 5-2 ■ Upper hilar level: normal anatomy. *A,* Approximate scan level shown in *B.* LL, lower lobe; seg, segment. *B,* CT with lung window settings at a level slightly above the carina shows the apical segmental bronchus of the right upper lobe in cross-section, with several adjacent vessels of similar size. On the left, the apical-posterior (Ap-post) segmental bronchus of the left upper lobe and associated arteries and veins have a similar appearance.

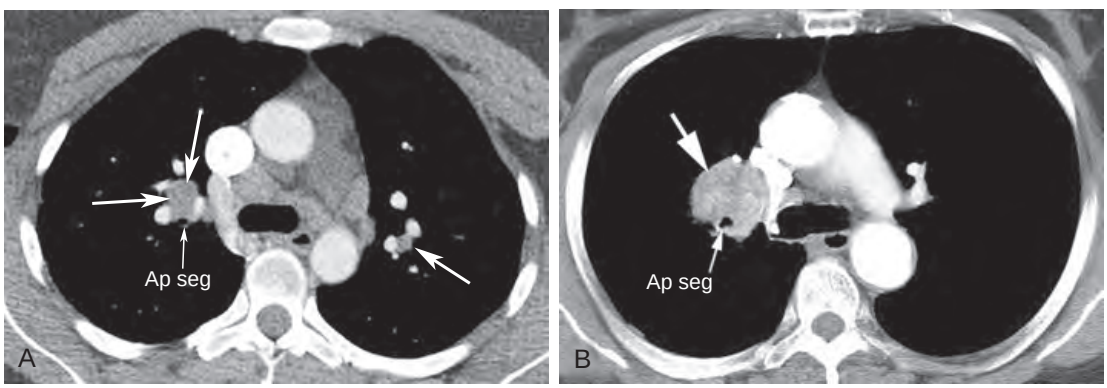

FIGURE 5-3 ■ Abnormal upper hila in two patients. *A,* In a patient with sarcoidosis and bilateral hilar adenopathy, a contrast-enhanced scan through the upper hila shows lymph node enlargement (*arrows*). On the right, a large node is visible anterior to the apical segmental (Ap seg) bronchus of the right upper lobe. On the left, an enlarged lymph node is visible lateral to pulmonary vessels. *B,* In a patient with a right upper lobe carcinoma, lymph node enlargement (*arrow*) is visible anterior to the apical segment bronchus of the right upper lobe.

lying in or near the scan plane, is commonly seen over a length of 1 or 2 cm. The posterior segment bronchus usually angles slightly cephalad, out of the scan plane, and may not be seen as well. If it is not seen at the level of the upper lobe bronchus, you should look for it at the next higher level. In some normal subjects, the origin of the apical segment can be seen at this level as a round lucency, usually at the point of bifurcation (or, in this case, trifurcation) of the right upper lobe bronchus.

Anterior to the right upper lobe bronchus, the truncus anterior (pulmonary artery supplying most of the upper lobe) produces an oval opacity of variable size but often about the same size as the right main bronchus visible at the same level (Fig. 5-5*C*). An upper lobe vein branch (posterior vein), lying in the angle between anterior and

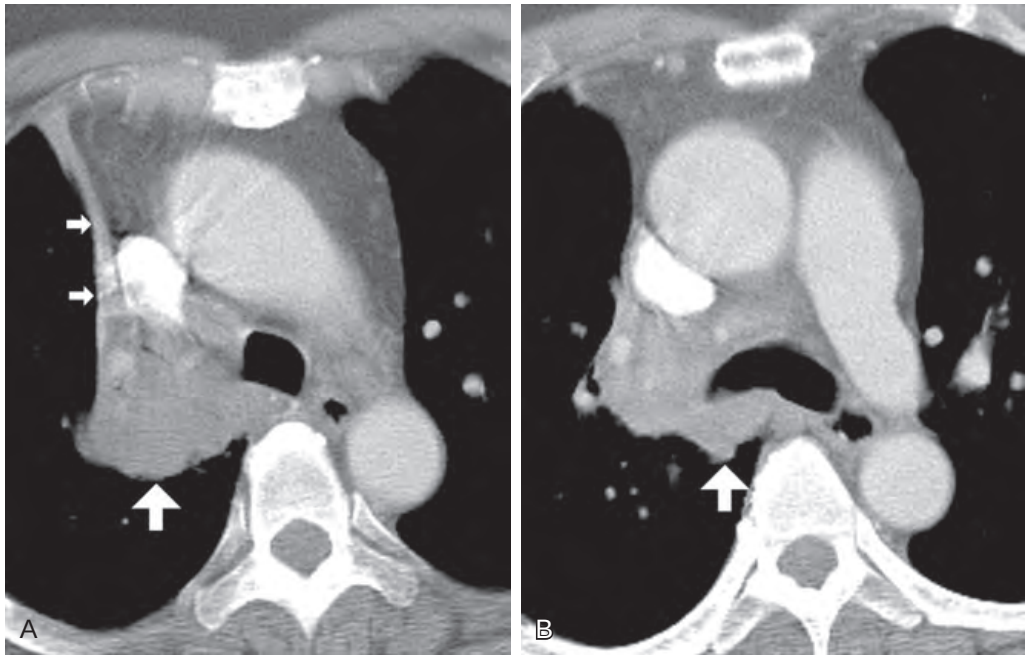

FIGURE 5-4 ■ Abnormal upper right hilum in bronchogenic carcinoma. *A,* A large mass (*large arrow*) encompasses the region of the apical segmental bronchus of the right upper lobe. A thin linear opacity (*small arrows*) along the right mediastinum reflects collapse of the right upper lobe. *B,* Below the level shown in *A,* the mass results in obstruction of the right upper lobe bronchus. The mass (*arrow*) is also visible posterior to the right main bronchus.

posterior segmental branches, is present and is visible in almost all patients. The posterior wall of the right upper lobe bronchus is usually outlined by lung and appears smooth and 2 to 3 mm in thickness.

Within the anterior right hilum at this level, a mass or lymph node enlargement can be identified if a soft-tissue opacity larger than the expected size of the truncus anterior is visible (Fig. 5-6). This, of course, could be confirmed by contrast medium injection. Laterally, in the angle between the anterior and posterior segmental bronchi, anything larger than the expected vein is abnormal (Fig. 5-6). Posteriorly, thickening of the wall of the upper lobe bronchus or main bronchus (Fig. 5-7) or a focal soft-tissue opacity behind it will almost always be abnormal. An anomalous pulmonary vein branch may sometimes be seen posterior to the bronchus; it is seen at multiple adjacent levels.

Left Hilum

On the left side, at or near this level, the apical-posterior and anterior segmental bronchi of the left upper lobe are usually visible (Fig. 5-5*A* to *C*). The apical-posterior segment is seen in cross-section as a round lucency, whereas the anterior segment is directed anteriorly, roughly in the scan plane, at about the 1-o'clock position. In some subjects, the anterior segmental bronchus is seen at a lower level. These bronchi lie lateral to the main branch of the left pulmonary artery, which produces a large convexity in the posterior hilum at this level, and the superior pulmonary vein, which results in an anterior convexity. In many normal subjects, the artery supplying the anterior segment of the left upper lobe is seen medial to the anterior segment bronchus. Lymphadenopathy can be seen in relation to all these structures and is most easily recognized after contrast infusion (Fig. 5-6*A* and *B*).

Right Bronchus Intermedius and Left Upper Lobe Bronchus

Right Hilum

Below the level of the right upper lobe bronchus, the bronchus intermedius is visible as an oval lucency at several adjacent levels (Fig. 5-8). Its posterior wall is sharply outlined by lung. Anterior and lateral to the bronchus, the hilar silhouette may vary in appearance, primarily because of variations in the sizes and positions of pulmonary veins. A collection of fat and normal-sized nodes, sometimes measuring more than 10 mm in diameter, is commonly seen at the level of the bifurcation of the right pulmonary artery, anterior and lateral to the bronchus intermedius (Fig. 5-8). A mass involving the posterior hilum can be

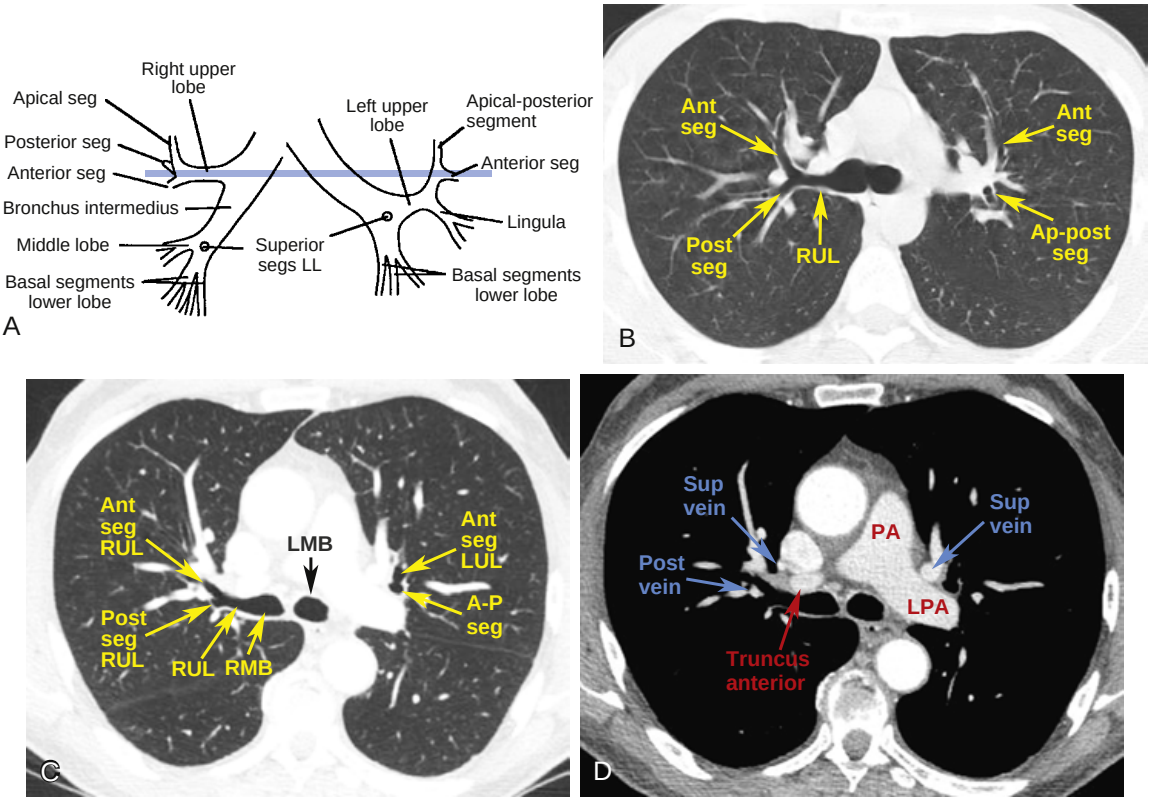

FIGURE 5-5 ■ Right upper lobe bronchus and left upper lobe segments level: normal anatomy. *A*, Approximate level of scans shown in *B* to *D*. LL, lower lobe; seg, segment. *B*, Right hilum: CT with 2.5-mm slice thickness shows the right upper lobe bronchus (RUL) along its length, together with its anterior (ant seg) and posterior segmental (post seg) branches arising from the RUL in a Y-shaped pattern. Left hilum: On the left side, the apical-posterior (Ap-post seg) and anterior segmental bronchi of the left upper lobe are both visible. The apical-posterior segment is seen in cross-section, whereas the anterior segment is directed anteriorly. *C* and *D*, 1.25-mm slices at this level in a different patient than for the scan shown in *B*. Right hilum: The right upper lobe bronchus (RUL) arises from the right main bronchus (RMB) just below the carina. The anterior (Ant seg) and posterior segmental (Post seg) bronchi arise from the RUL. The posterior wall of the RUL bronchus contacts lung and is a few mm thick. The truncus anterior is anterior to the RUL bronchus. An upper lobe vein branch (Post vein) lies in the angle between the anterior and posterior segmental branches. A superior vein branch (Sup vein) lies anteriorly. Left hilum: The left main bronchus (LMB) is within the mediastinum. In this patient, the anterior segmental bronchus (LUL) is seen at the point at which it separates from the apical-posterior segment (A-P seg). *D*. The left upper lobe segmental bronchi lie lateral to the main branch of the left pulmonary artery (LPA), which produces a convexity in the posterior hilum, and the superior pulmonary vein, which results in an anterior convexity. The artery supplying the anterior segment of the left upper lobe is seen medial to the anterior segment bronchus and adjacent to the vein. PA, main pulmonary artery.

readily diagnosed without contrast medium injection because of thickening of the posterior bronchial wall (Fig. 5-7); thickening of the posterior wall of the bronchus intermedius is a common finding in patients with a right hilar mass, particularly when it results from lung cancer.

Diagnosis of anterior or lateral hilar masses at this level generally requires contrast administration (Figs. 5-9 and 5-10). Normal soft tissue and nodes (Fig. 5-8) should not be mistaken for a hilar mass.

Left Hilum

The left upper lobe bronchus is usually visible at the level of the bronchus intermedius on the right. It is typically seen along its axis, extending anteriorly and laterally from its origin at an angle of 10° to 30° (Fig. 5-8). The apical-posterior and anterior segmental bronchi of the left upper lobe usually arise from a common trunk that originates from the upper aspect of right upper lobe bronchus. The left superior pulmonary veins are anterior and medial to the left upper lobe (LUL) bronchus at this level, and the descending branch of the left pulmonary artery forms an oval soft-tissue opacity posterior and lateral to it. Normal lymph nodes (< 5 mm in diameter) are commonly visible medial to the artery and lateral to the bronchus. Because only the oval artery occupies the lateral hilum, lobulation of the lateral hilum

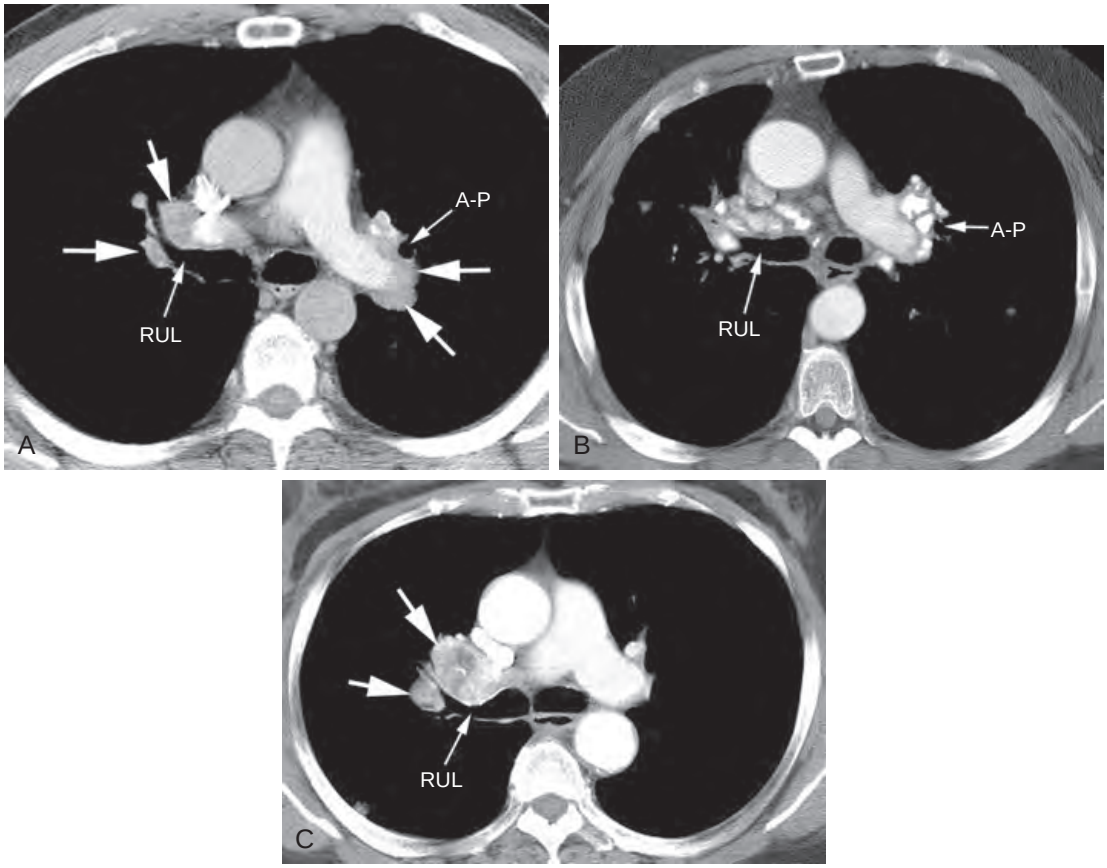

FIGURE 5-6 ■ Hilar adenopathy in three patients shown at the same level as in Figure 5-5*C* and *D*. *A,* In a patient with sarcoidosis, there is extensive adenopathy (*arrows*) at the level of the right upper lobe bronchus (RUL) and the apical-posterior segmental bronchus (A-P) of the left upper lobe. On the right, nodes are visible as unopacified structures anteriorly and laterally. The soft-tissue opacity seen in the position of the posterior vein on the right is too large to represent a vessel. On the left side, there are enlarged nodes (*arrows*) in both the lateral and posterior hilum, which are distinguishable from the opacified left pulmonary artery. *B,* CT at the level of the RUL bronchus and the A-P segmental bronchus of the left upper lobe shows extensive lymph node calcification secondary to sarcoidosis. The calcified lymph nodes are similar in location to those shown in *A*. *C,* Lymph node enlargement (*arrows*) at the level of the RUL bronchus in the same patient as shown in Figure 5-3*B*.

(more than one convexity) indicates a mass or lymphadenopathy (Figs. 5-9, 5-10, and 5-11).

Although the lung contacts and sharply outlines the posterior wall of the bronchus intermedius at several levels, the left posterior bronchial wall is usually outlined by the lung only at this level, that is, at the level of the left upper lobe bronchus. In approximately 90% of individuals, the lung sharply outlines the posterior wall of the left main or upper lobe bronchus, medial to the descending pulmonary artery (Figs. 5-8 and 5-12*B* and *C*); this is termed the *left retrobronchial stripe*. As on the right, the bronchial wall should measure 2 to 3 mm in thickness. Thickening of this stripe, or a focal soft-tissue opacity behind it, indicates lymph node enlargement or bronchial wall thickening (Figs. 5-9 and 5-11). In 10% of normal individuals, however, the lung does not contact the bronchial wall because the descending pulmonary artery is medially positioned against the aorta. This should not be misinterpreted as abnormal.

Usually the lingular bronchus is also seen on the left at the level of the bronchus intermedius (Fig. 5-12*A* to *D*). The lingular bronchus is usually visible at a level near the undersurface of the left upper lobe bronchus, from which it originates; its two segments (superior and inferior) can sometimes be seen (Fig. 5-12). The superior segmental bronchus of the lower lobe is often visible at this level, arising posteriorly. The pulmonary artery and veins appear the same as at the level of the left upper lobe bronchus (Fig. 5-8). Normal lymph nodes are commonly visible medial to the artery. At this level, significant lobulation of the lateral hilar contour indicates a mass or adenopathy (Fig. 5-13).

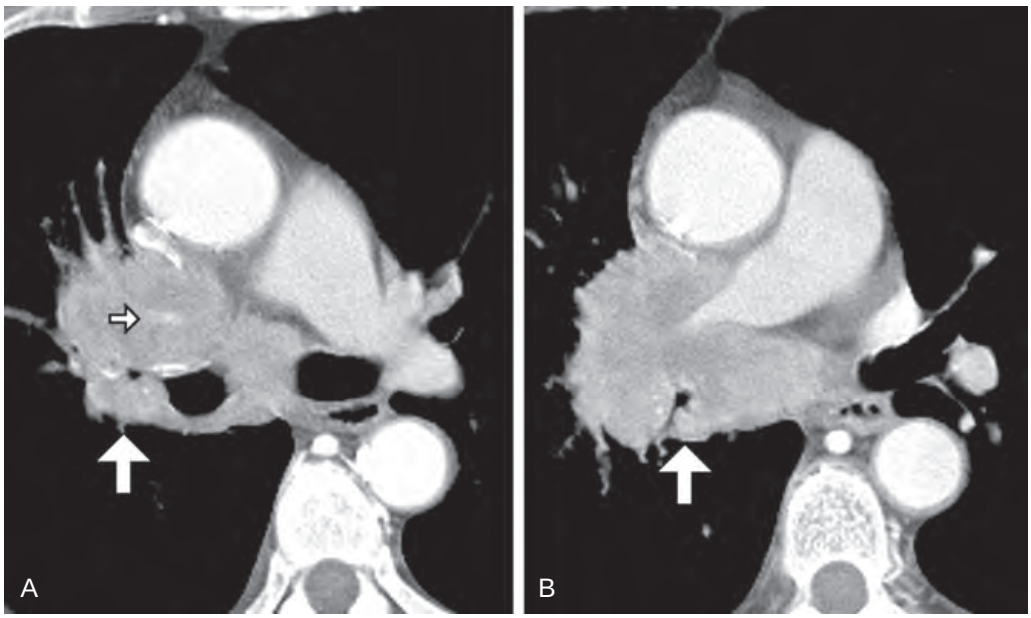

FIGURE 5-7 ■ Bronchogenic carcinoma with a right hilar mass. *A,* A large carcinoma causes narrowing of the right upper lobe bronchus and obstruction of the anterior and posterior segmental bronchi. The truncus anterior (*small arrow*), anterior to the bronchus, is markedly narrowed and surrounded by tumor. The posterior walls of the right upper lobe bronchus (*large arrow*) and right main bronchus are thickened. *B,* At a lower level, the bronchus intermedius is narrowed and its posterior wall is thickened (*arrow*). The mass also invades the mediastinum, surrounding and narrowing the right pulmonary artery.

Right Middle Lobe Bronchus and Left Lower Lobe Bronchus

Right Hilum

On the right, at the level of the lower bronchus intermedius, the middle lobe bronchus arises anteriorly and extends anteriorly, laterally, and inferiorly at an angle of about 30° to 45° (Fig. 5-14). Because of its obliquity, only a short segment of its lumen is visible at each level on CT, and this appearance should not be misinterpreted as bronchial obstruction. Often, the superior segmental bronchus of the lower lobe arises posterolaterally at this level (Fig. 5-14).

At the level of the origin of the middle lobe bronchus, the superior pulmonary veins lie anterior and medial to the bronchus, whereas the descending (interlobar) branch of the right pulmonary artery lies beside and behind it (Fig. 5-12). Normal lymph nodes (<5 mm in diameter) are commonly visible lateral to the artery and bronchus. Because of this separation of the artery and veins, the lateral hilum at this level (representing the artery) is oval, without prominent lobulation. Any lobulation of significant size suggests hilar adenopathy or a mass (Figs. 5-15 to 5-17).

The left hilum at the level of the left upper lobe bronchus or lingular bronchus (Fig. 5-12) can appear as the mirror image of the right hilum at the level of the right middle lobe bronchus, and comparison of the two sides is common practice. However, the left upper lobe bronchus or lingular bronchus is usually visible 1 to 2 cm above the right middle lobe bronchus.

Left Hilum

At the level of the right middle lobe bronchus, the basal bronchial trunk of the left lower lobe is usually visible (Fig. 5-14), although in some patients the superior segmental bronchus of the left lower lobe or segments of the left lower lobe may be visible.

Lower Lobe Bronchi (Basal Segments)

Right and Left Hilum

At this level, the hila are relatively symmetrical and comparison of one side to the other can be helpful. The main lower lobe bronchial trunk on each side (Fig. 5-14*B* and *C*), which eventually gives rise to the basal segmental bronchi, branches in a variable fashion. It is common for the lower lobe bronchial trunk on the right to divide into

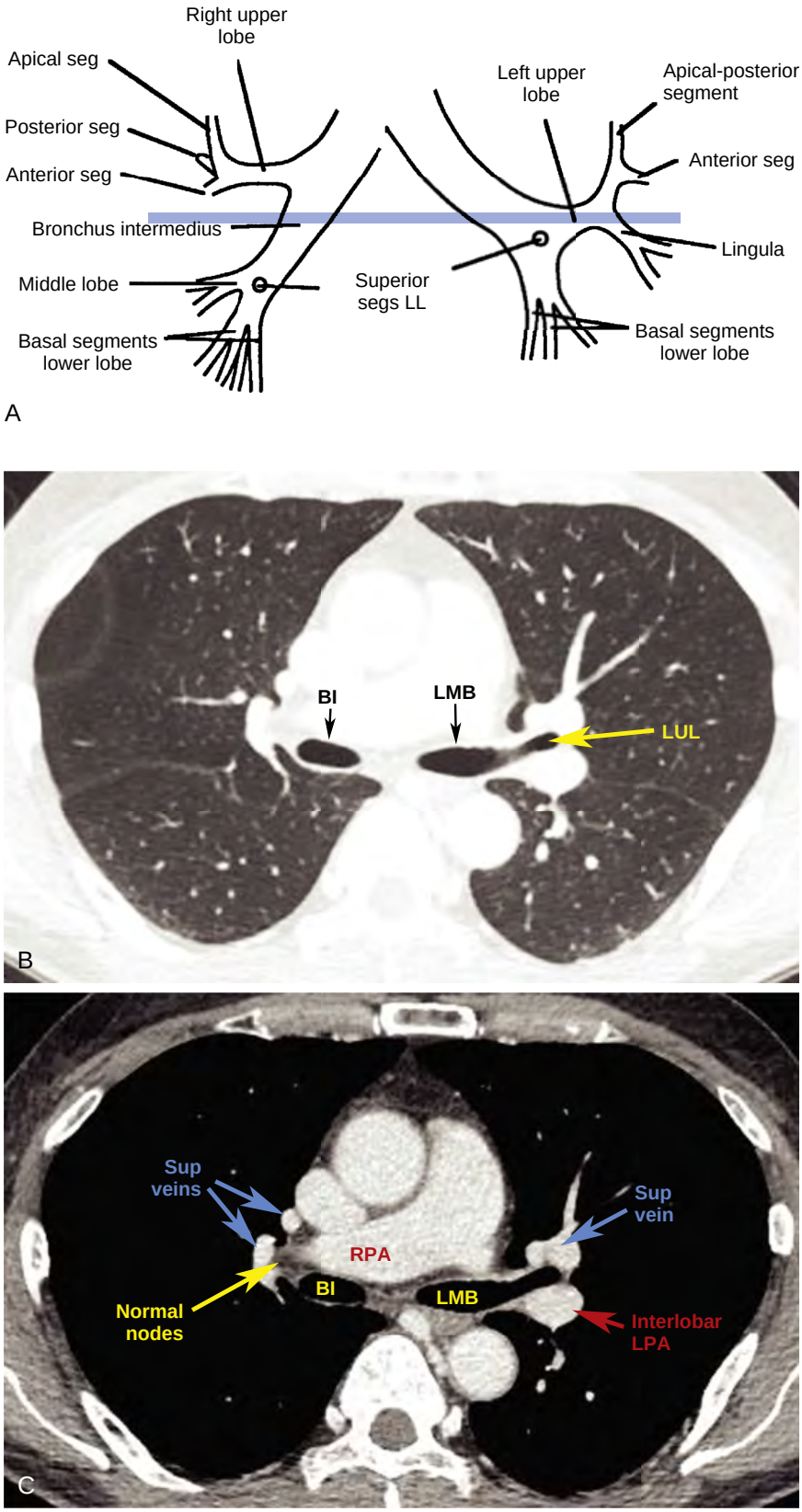

FIGURE 5-8 ■ Normal bronchus intermedius and left upper lobe bronchus level. *A*, Approximate level of the scans shown in *B* and *C*. LL, lower lobe; seg, segment. *B* and *C*, The bronchus intermedius (BI) is visible as an oval lucency with its posterior wall sharply outlined by the lung. Anterior and lateral to the bronchus, the hilum is made up of the right pulmonary artery (RPA) and superior pulmonary veins (sup veins). Normal lymph nodes and fat are visible in the anterolateral hilum, between the opacified pulmonary artery and veins. On the left, the left main bronchus (LMB) and left upper lobe (LUL) bronchus are visible. The left superior pulmonary vein is anterior to the bronchi, and the interlobar or descending branch of the left pulmonary artery (LPA) forms an oval soft-tissue opacity posterior to the LUL.

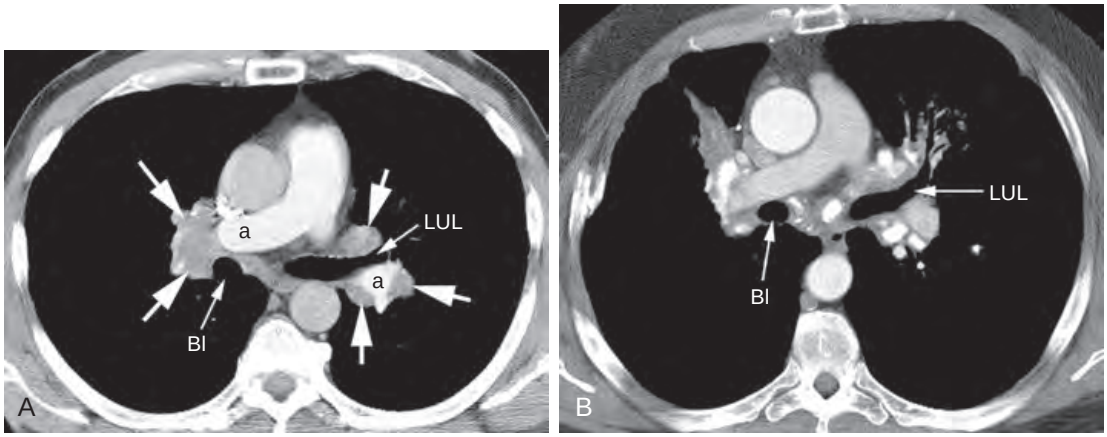

FIGURE 5-9 ■ Abnormal bronchus intermedius and left upper lobe bronchus level in two patients with sarcoidosis. *A,* On the right, a scan at the level of the bronchus intermedius (BI) shows enlargement of the normal node group (*arrows*) shown in Figure 5-8*B,* situated lateral to the pulmonary artery (a). On the left, a scan at the level of the left upper lobe (LUL) bronchus shows enlarged lymph nodes (*arrows*) in the anterior hilum and surrounding the opacified pulmonary artery (a). Enlarged lymph nodes are situated posterior to the LUL bronchus. *B,* A scan at the level of the bronchus intermedius and LUL bronchus shows multiple calcified lymph nodes.

FIGURE 5-10 ■ Abnormal bronchus intermedius and left upper lobe bronchus level. In a patient with non-Hodgkin's lymphoma and bilateral hilar adenopathy (*arrows*), enlarged lymph nodes are clearly distinguished from opacified pulmonary vessels.

two basal bronchial branches or trunks at a level above the origins of the basal segmental bronchi.

At the level of the lower lobe bronchial trunk, on either side, the anterior bronchial wall is usually outlined by lung, with pulmonary artery branches lateral to the bronchus and veins posterior and medial to the bronchus (Fig. 5-14*B* and *C*). Enlarged lymph nodes can be identified anterior to the bronchus at this level.

The basal segmental branches of the lower lobe bronchi vary in appearance, depending on their courses (Fig. 5-18). On the right, the four segmental branches (medial, anterior, lateral, and posterior) are usually visible; on the left are three basal segments (anteromedial, lateral, and posterior). These segments are much better seen with thin slices. It is not unusual to have trouble identifying all specific basal lower lobe segments, but this is not generally of clinical significance.

The segmental bronchi are accompanied by pulmonary artery branches that are slightly larger than the bronchi; the bronchi and arteries are nearly perpendicular to the scan plane and thus are seen in cross-section (Fig. 5-18). The inferior pulmonary veins pass behind and medial to the bronchi to enter the left atrium and, unlike the arteries, tend to be seen along their axis. Hilar masses or lymph node enlargement can be diagnosed on the basis of contour abnormalities or asymmetries between the hila. Soft-tissue densities that seem too large to be the pulmonary artery or vein branches should be regarded with suspicion (Figs. 5-19, 5-20, and 5-21). The largest nodes seen at this level tend to be anterior.

BRONCHIAL ABNORMALITIES

The excellent contrast and spatial resolution of CT allow for accurate assessment of bronchial lesions, and CT is often performed to guide bronchoscopy in patients who have a suspected hilar or bronchial abnormality. Accurate indicators of

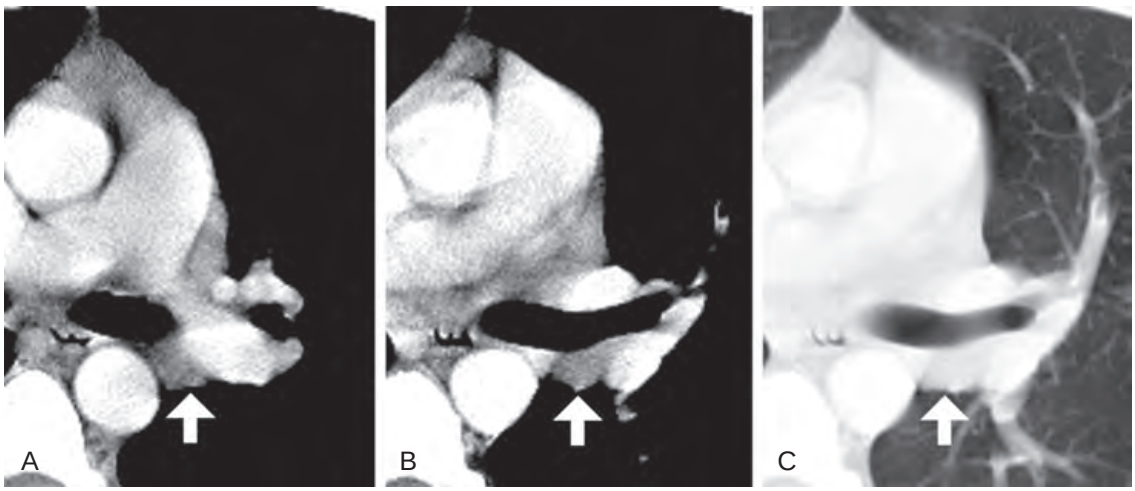

FIGURE 5-11 ■ Left hilar adenopathy (left upper lobe bronchus level). *A*, Lymph node enlargement (*arrow*) is visible in the posterior hilum, behind the left upper lobe bronchus, and between the aorta and left pulmonary artery. *B* and *C*, The enlarged lymph node (*arrows*) lies posterior to the bronchus (i.e., in the region of the retrobronchial stripe) and prevents the lung from outlining its posterior wall.

bronchial pathology are (1) bronchial wall thickening, (2) an endobronchial mass, and (3) narrowing or obstruction of the bronchial lumen.

Bronchial wall thickening is most easily assessed on CT in regions where the hilar bronchi lie adjacent to the lung: the posterior walls of the right main and both upper lobe bronchi and the posterior wall of the bronchus intermedius. Smooth bronchial wall thickening can be caused by inflammatory disease, pulmonary edema, or tumor infiltration (Figs. 5-7 and 5-22), whereas localized or lobulated thickening usually indicates tumor infiltration or lymph node enlargement (Fig. 5-11).

An *endobronchial mass* is most easily diagnosed with thin slices. Polypoid endobronchial masses may appear round or lobulated (Figs. 5-24 and 5-25) and in some cases tend to expand the bronchus in which they arise.

Bronchial narrowing and obstruction may be caused by an endobronchial tumor (Fig. 5-23) or compression by an extrinsic mass (Fig. 5-7 and 5-17). Abrupt changes in bronchial caliber on CT usually indicate circumferential tumor infiltration or an endobronchial mass (Fig. 5-23), but it is important to look at adjacent scans to confirm that the apparent bronchial narrowing does not reflect an oblique bronchial course, with the bronchus leaving the scan plane (as with the right middle lobe bronchus). Bronchial abnormalities that are primarily mucosal can be missed using CT because of their minimal thickness.

In general, scans viewed with a lung window setting are best for identifying normal bronchi and detecting bronchial abnormalities, but they often overestimate the degree of bronchial narrowing if thick slices are used. Soft-tissue (mediastinal) window settings are more accurate for assessing bronchial lumen diameter in the presence of an abnormality (and show mass lesions), but they somewhat overestimate luminal diameter. If a bronchial lesion is suspected, both window settings should be used. Thin scans, particularly with multidetector CT, can be of great value in identifying bronchial abnormalities.

DIFFERENTIAL DIAGNOSIS OF HILAR MASS AND HILAR BRONCHIAL ABNORMALITIES

Lung Cancer

The most common cause of a hilar mass or lymph node enlargement is bronchogenic carcinoma. The hilar mass can appear irregular because of local infiltration of the lung parenchyma. In patients with tumors arising centrally (usually squamous cell carcinoma or small-cell carcinoma), bronchial abnormalities (narrowing or obstruction) are commonly visible on CT (Figs. 5-7, 5-17, and 5-23). If the bronchial abnormality involves the tracheal carina, resection may be impossible; bronchoscopy rather than CT, however, is most accurate for making this determination.

When the carcinoma arises in the peripheral lung and the hila are abnormal because of lymph node metastases, the hilar mass or masses may be smoother and more sharply defined than when the hilar mass represents the primary tumor. However, this distinction is not always easily made. Patients with a central mass and bronchial

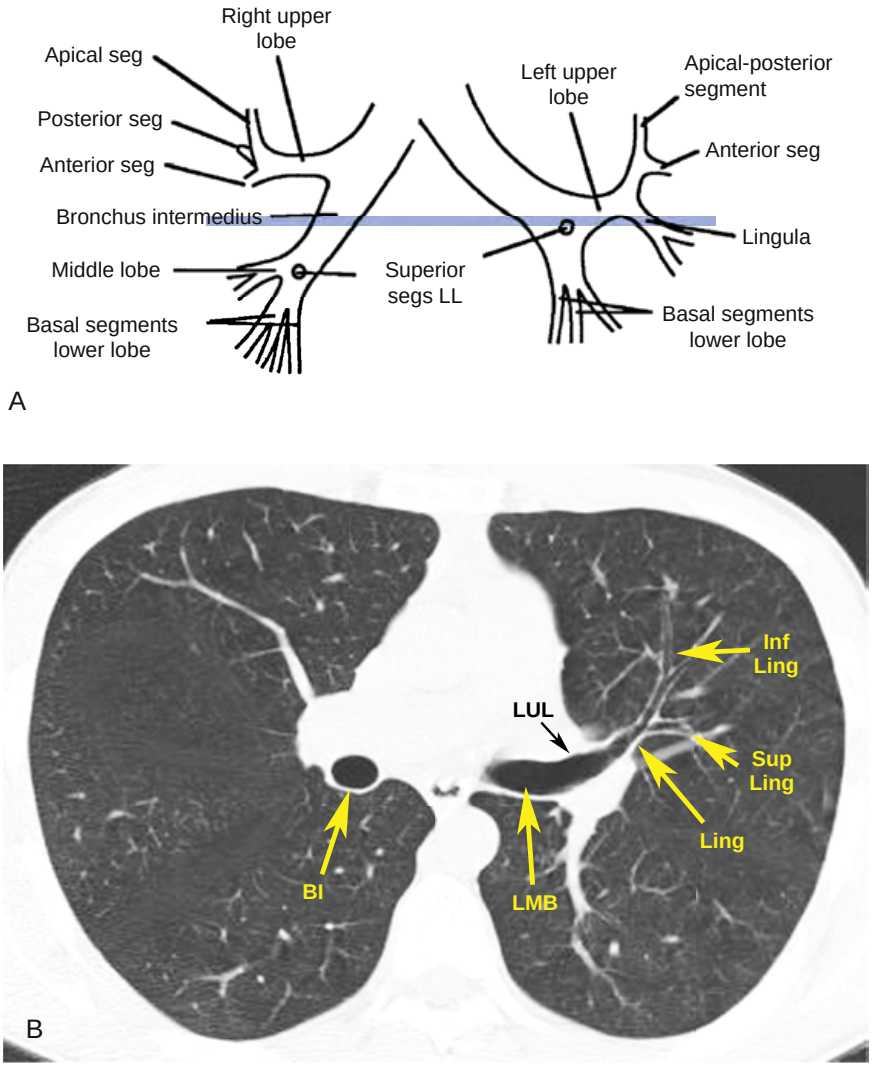

FIGURE 5-12 ■ Normal bronchus intermedius and lingular bronchus level. *A,* Approximate level for scans shown in *B* to *D.* LL, lower lobe; seg, segment. *B,* CT with a 2.5-mm slice thickness. At a level below that in Figure 5-8, the bronchus intermedius (BI) is visible as an oval lucency on the right, with its posterior wall sharply outlined by lung tissue. On the left, the left upper lobe (LUL) bronchus is visible, extending anteriorly and laterally from the left main bronchus (LMB). The left posterior bronchial wall is outlined by the lung at this level. This is termed the *left retrobronchial stripe.* The lingular bronchus (Ling) arises from the lower edge of the LUL and divides into two branches, the superior lingular (sup Ling) and inferior lingular (inf Ling) segments.

obstruction often show peripheral parenchymal abnormalities. In patients with hilar node metastases, a bronchial abnormality seen on CT usually reflects external compression by the enlarged hilar nodes, but bronchial invasion may also be present. Hilar node metastases are present at surgery in 15% to 40% of patients with lung cancer.

In patients with bronchogenic carcinoma, enlarged hilar nodes visible on CT may not be caused by node metastasis. Hyperplastic nodal enlargement often occurs in patients with lung cancer, particularly when there is bronchial obstruction and distal pneumonia or atelectasis. Conversely, a normal-sized hilar node can harbor microscopic metastases. In the lung cancer staging system (Table 4-3), ipsilateral hilar lymph node metastases are termed *N1*. Contralateral hilar lymph node metastases are classified as *N3*.

Other Primary Bronchial Tumors

Other primary bronchial tumors can be associated with a hilar mass. The most common of these is the *carcinoid tumor*. This malignant tumor arises from the main, lobar, or segmental bronchi in 80% to 90% of cases (Fig. 5-24). It tends to grow slowly and to be locally invasive. A well-defined endobronchial mass is

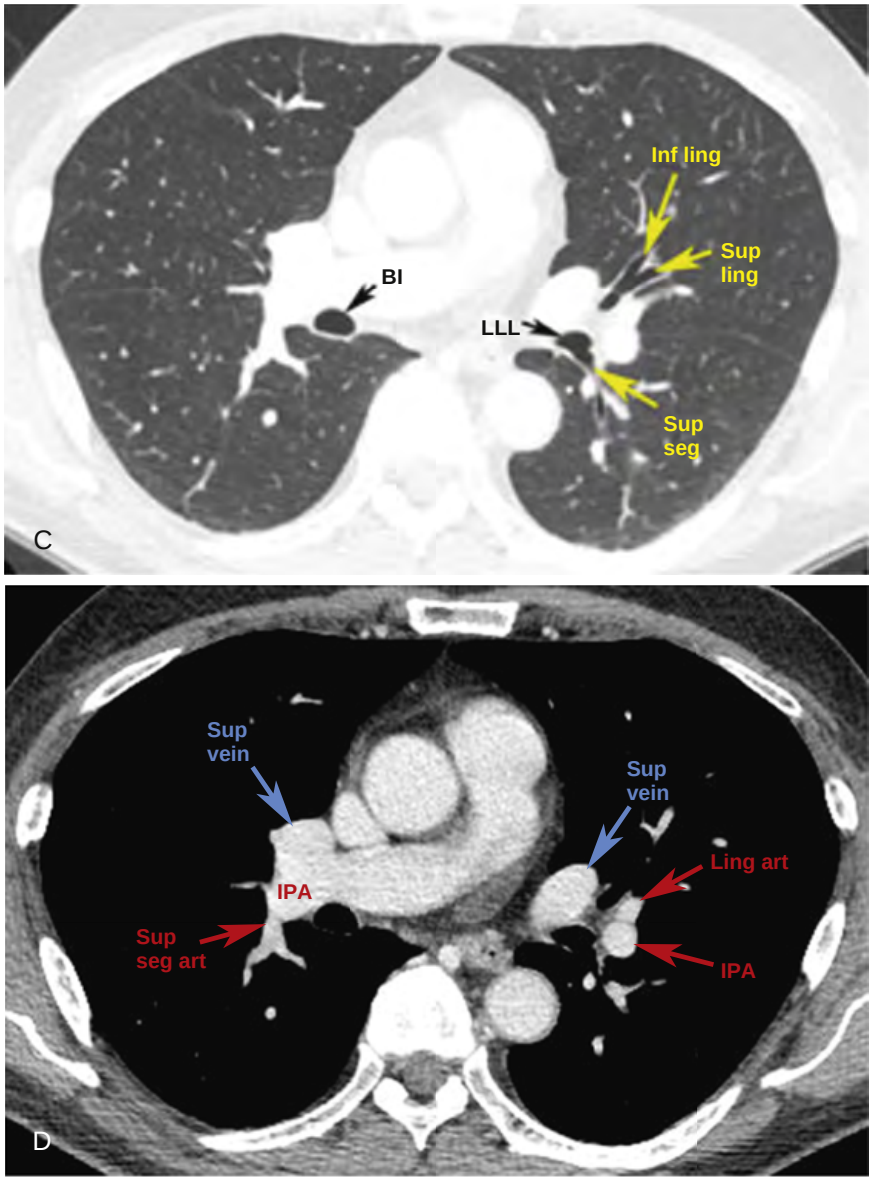

FIGURE 5-12, cont'd ■ *C* and *D*, 1.25-mm slices at a level slightly below that shown in *B*. Right hilum: On the right, the BI is visible as an oval lucency, with its posterior wall sharply outlined by the lung. The interlobar pulmonary artery (IPA) and superior pulmonary veins (sup vein) are anterior and lateral to the bronchus. The artery branch to the superior segment of the right lower lobe (sup seg art) is directed posteriorly. Left hilum: Below the level of the left upper lobe bronchus, the lingular bronchus branches into the superior and inferior lingular segments. The proximal left lower lobe (LLL) bronchus is visible, along with its first branch, the superior segment bronchus (sup seg). The left superior pulmonary vein is anterior and medial to the bronchus, and the descending branch of the left IPA is posterior to the lingular bronchus and lateral to the lower lobe bronchus. The lingular artery (Ling art) accompanies the lingular bronchus.

typical, but a large, exobronchial hilar mass is sometimes seen as well. Carcinoid tumors are highly vascular and usually enhance densely after contrast medium infusion. Carcinoid tumors can be calcified.

Adenoid cystic carcinoma (*cylindroma*) can result in a CT appearance similar to that of a carcinoid tumor, but dense enhancement is not typical. It arises in the trachea more commonly than a carcinoid tumor does.

Benign bronchial tumors, such as hamartoma, fibroma, chondroma, and lipoma, usually appear focal and endobronchial on CT rather than infiltrative, and they are not commonly associated with an extrinsic mass. Obstruction is the primary finding on CT.

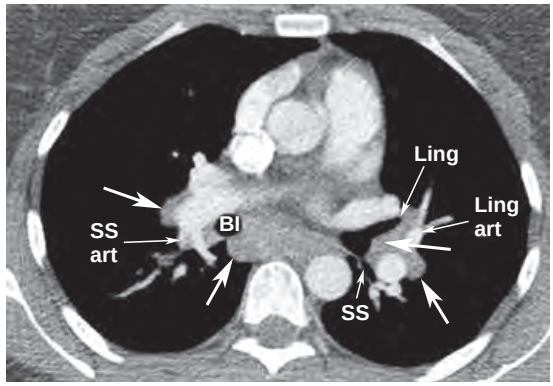

FIGURE 5-13 ■ Abnormal bronchus intermedius and lingular bronchus level in a patient with sarcoidosis. On the right, enlarged lymph nodes (*large arrows*) are visible adjacent to the bronchus intermedius (BI) and pulmonary artery. SS art, superior segment right lower lobe artery. On the left, enlarged lymph nodes (*large arrows*) are visible medial and lateral to the interlobular pulmonary artery and posterior to the lingular bronchus (Ling). SS, superior segment left lower lobe bronchus; Ling art, lingular artery.

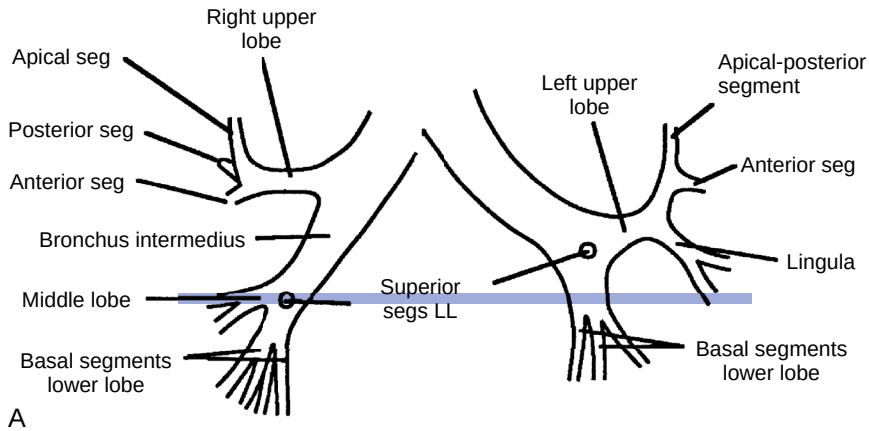

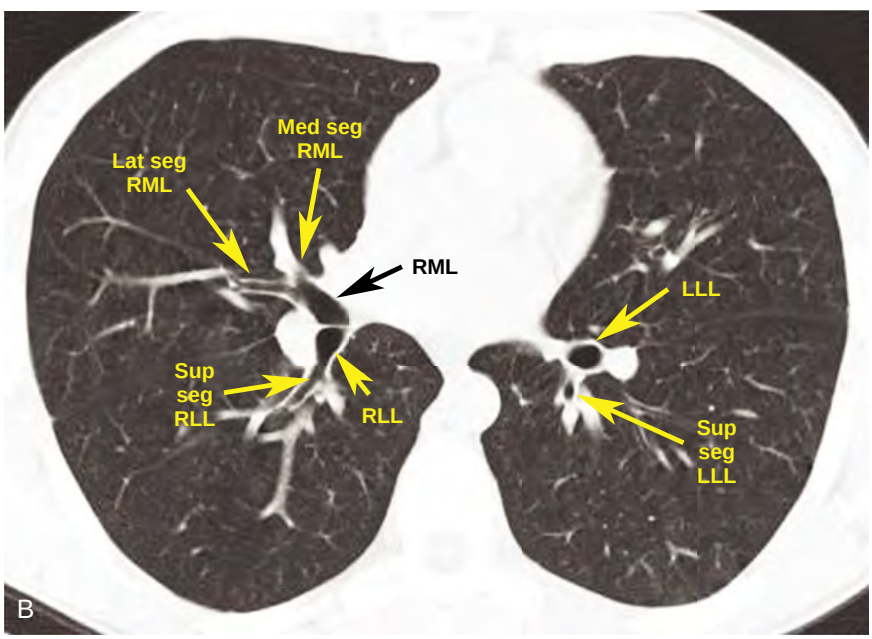

FIGURE 5-14 ■ Normal right middle lobe and left lower lobe bronchus level. *A*, Approximate level for scans shown in *B* to *E*. *B*, CT with a 2.5-mm slice thickness through the right middle lobe (RML) bronchus shows its division into its medial (med seg RML) and lateral (lat seg RML) segmental branches. The middle lobe bronchus extends anteriorly and laterally at an angle of about 45°. The right lower lobe (RLL) bronchus is also visible at this level, giving rise to its superior segment branch (sup seg RLL) posteriolaterally. The interlobar pulmonary artery lies lateral to the bronchi. On the left, the left lower lobe (LLL) bronchus is visible along with a short segment of its superior segmental branch (sup seg LLL). The lower lobe artery is lateral to the LLL bronchus.

Lymphoma

Hilar adenopathy is present in 25% of patients with Hodgkin's lymphoma and 10% of patients with non-Hodgkin's lymphoma (Fig. 5-10). Hilar involvement is usually asymmetrical. Multiple nodes in the hilum or mediastinum are usually involved. Endobronchial lesions can also be seen, or bronchi may be compressed by enlarged nodes, but this is much less common than with lung cancer. There are no specific features of the hilar abnormality seen in patients with lymphoma that allow a definite diagnosis.

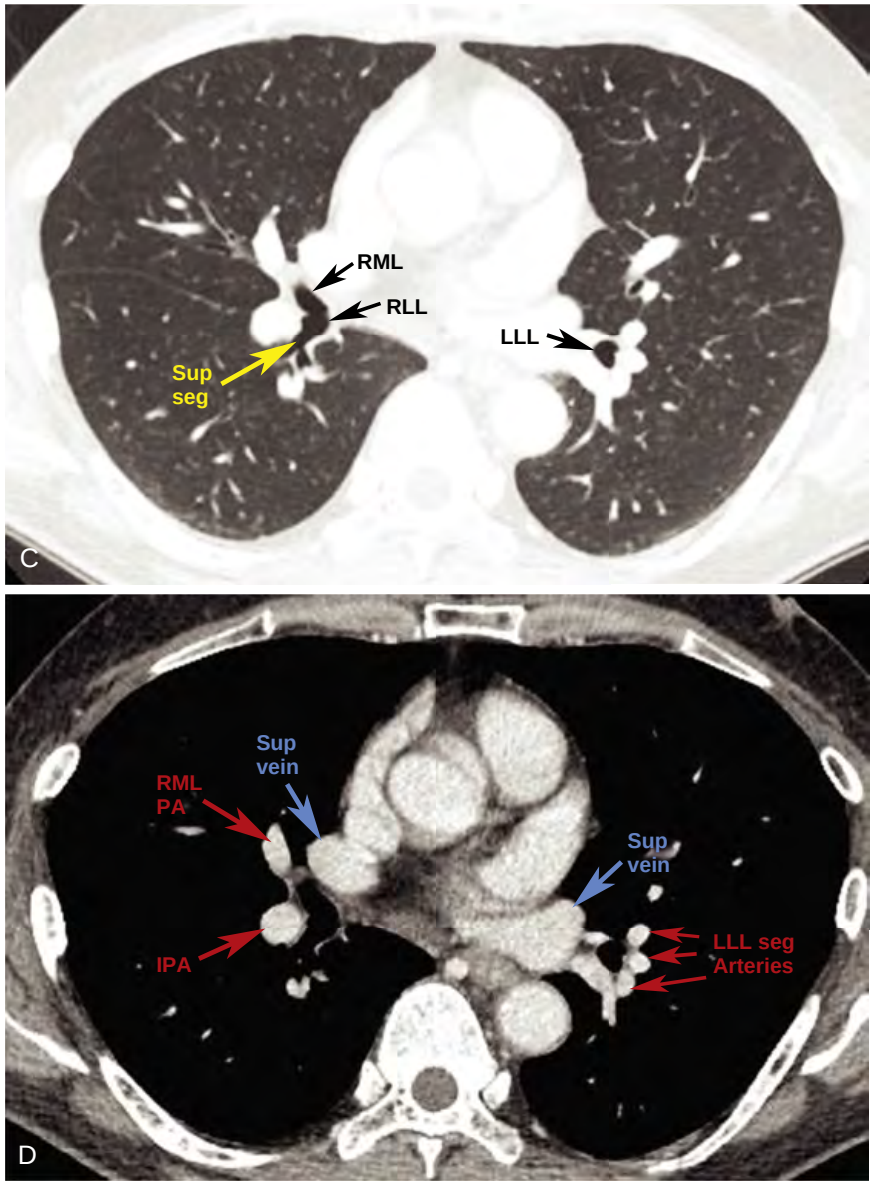

FIGURE 5-14, cont'd ■ *C* and *D*, 1.25-mm slice in a different patient. Right hilum: The RML bronchus is visible, but because it angles caudad, only a short segment of its lumen is visible. The RLL bronchus and its superior segment (sup seg) are also visible, as in *B*. The superior pulmonary vein (sup vein) lies anterior and medial to the RML, whereas the oval descending (interlobar) branch of the right pulmonary artery (IPA) lies beside and behind it. The right middle lobe artery (RML PA) accompanies the RML bronchus. Note that the appearance of the right hilum at this level is quite similar to that of the left hilum at the levels of the left upper lobe and lingular bronchi. Left hilum: The LLL bronchus is visible below the takeoff of the superior segment. It has a double-barreled appearance as it begins to divide into the basal segments of the LLL. As on the right, the superior pulmonary vein (sup vein) is anterior. The basal segmental branches (LLL seg arteries) of the pulmonary artery are lateral.

Continued

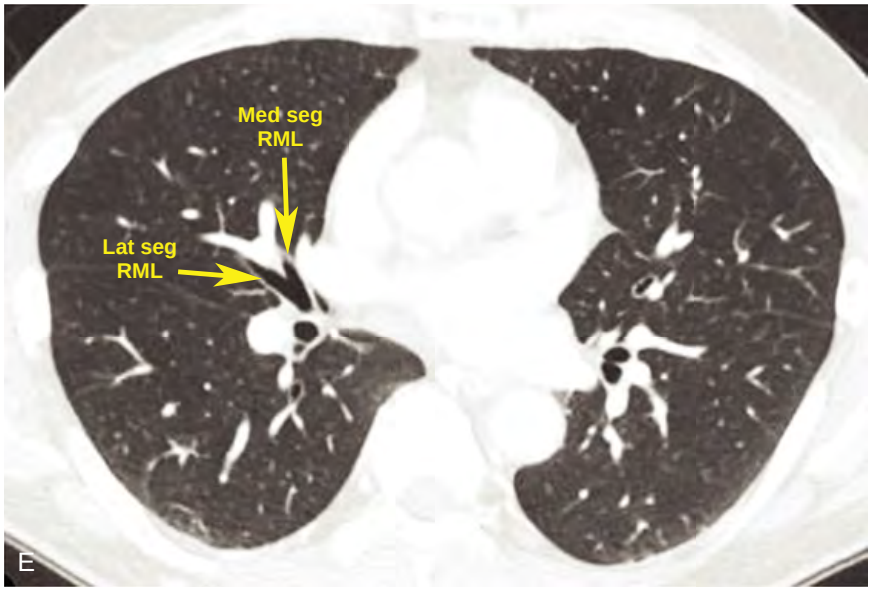

FIGURE 5-14, cont'd ■ E. Slightly below *C*, the RML medial (med seg) and lateral (lat seg) segmental bronchi are visible.

Metastases

Metastases to hilar lymph nodes or bronchi from an extrathoracic primary tumor are not uncommon. Hilar node metastases may be unilateral or bilateral. Endobronchial metastases can also be seen (Figs. 5-25 and 5-26) without the presence of hilar node metastases; these may appear to be focal and endobronchial or infiltrative. Head and neck carcinomas, thyroid carcinoma, genitourinary tumors (particularly renal cell and testicular carcinoma), melanoma, and breast carcinomas are most commonly responsible for hilar or endobronchial metastases.

Inflammatory Disease

Unilateral or bilateral hilar lymphadenopathy and bronchial narrowing can be seen in a number of infectious and inflammatory conditions. Primary tuberculosis usually causes unilateral hilar adenopathy. Fungal infections, most notably histoplasmosis and coccidioidomycosis, cause unilateral or bilateral adenopathy. Sarcoidosis causes bilateral and symmetrical adenopathy in most patients (Fig. 5-9). Silicosis and coal workers' pneumoconiosis are also commonly associated with bilateral hilar lymph node enlargement.

In patients with prior tuberculosis, histoplasmosis, sarcoidosis, or silicosis, calcified hilar nodes are commonly seen (Fig. 5-9). Eggshell (peripheral) calcification of lymph nodes is most commonly seen with silicosis, sarcoidosis, or tuberculosis. Calcified nodes can erode into a bronchus, causing obstruction, that is, so-called *broncholithiasis*.

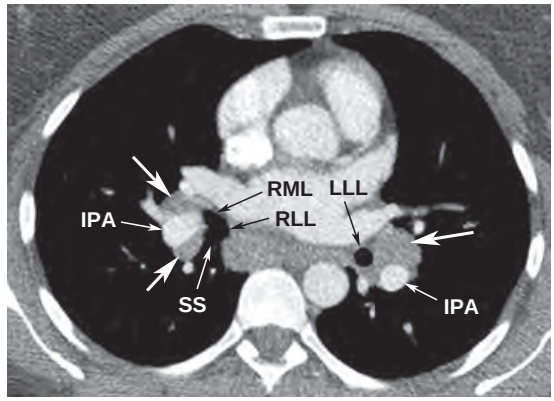

FIGURE 5-15 ■ **Abnormal right middle lobe and left lower lobe bronchus level in a patient with sarcoidosis.** On the right, enlarged lymph nodes (*large arrows*) are seen anterior and posterior to the interlobar pulmonary artery (IPA) and are situated lateral to the right middle lobe (RML), lower lobe (RLL), and superior segment (SS) bronchi. Subcarinal lymph node enlargement is also present. On the left, enlarged nodes (*large arrow*) are lateral to the lower lobe bronchus (LLL) and surround the IPA.

Mucus

Blobs of mucus may simulate one or more endobronchial lesions on CT; these are usually located along the posterior bronchial wall. If this diagnosis is suggested—for instance, if a focal bronchial lesion is seen when it is not expected—a repeat scan can be obtained after the patient

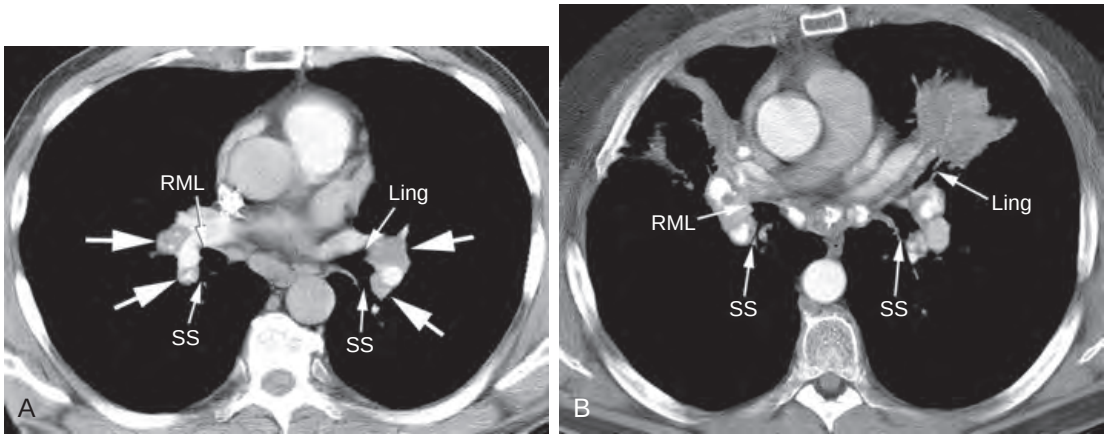

FIGURE 5-16 ■ Abnormal right middle lobe bronchus and lingular level in two patients with sarcoidosis. *A,* On the right, a scan at the level of the origin of the right middle lobe (RML) bronchus shows enlargement of nodes (*large arrows*) anterior and posterior to the pulmonary artery. Several of the nodes show calcification. On the left, a scan at the level of the lingular (Ling) bronchus shows enlarged lymph nodes (*large arrows*) anterior and posterior to the opacified pulmonary artery (as on the right side). *B,* As in *A,* a scan at the level of the RML bronchus and lingular bronchus shows lymph node enlargement (and calcification) anterior and posterior to the pulmonary artery. SS, superior segment bronchus of the lower lobe.

FIGURE 5-17 ■ Right hilar mass (bronchogenic carcinoma). The right middle lobe bronchus is invisible (*small black arrow*) and obstructed. A large right hilar mass (*large white arrow*) is present.

coughs. The abnormality will disappear if it is just mucus. Large mucus plugs can also mimic hilar masses or can be seen as a bronchial abnormality on CT.

PULMONARY VASCULAR DISEASE

CT is useful in differentiating pulmonary vascular disease from hilar adenopathy. Pulmonary hypertension with dilatation of the pulmonary arteries is relatively common and can simulate a hilar mass on plain radiographs (Fig. 5-27). CT can accurately define the size of the pulmonary arteries in patients with arterial dilatation. If the main pulmonary artery is larger than the ascending aorta, pulmonary hypertension is likely present. Rarely, in patients with chronic pulmonary hypertension, pulmonary artery calcification can be seen as a result of atherosclerosis. Other causes of pulmonary artery enlargement are reviewed in Chapter 3.

Encasement or compression of one of the main pulmonary arteries by tumor tissue in patients with a bronchogenic carcinoma can be diagnosed with CT and can be of value in assessing the extent of surgery that will be required for resection. For example, tumor surrounding the left pulmonary artery generally indicates that pneumonectomy rather than lobectomy is required. However, caution must be exercised; narrowing of the pulmonary artery can reflect compression rather than encasement. Adequate assessment requires the use of intravenous contrast. Chapter 3 discusses the CT diagnosis of pulmonary embolism.

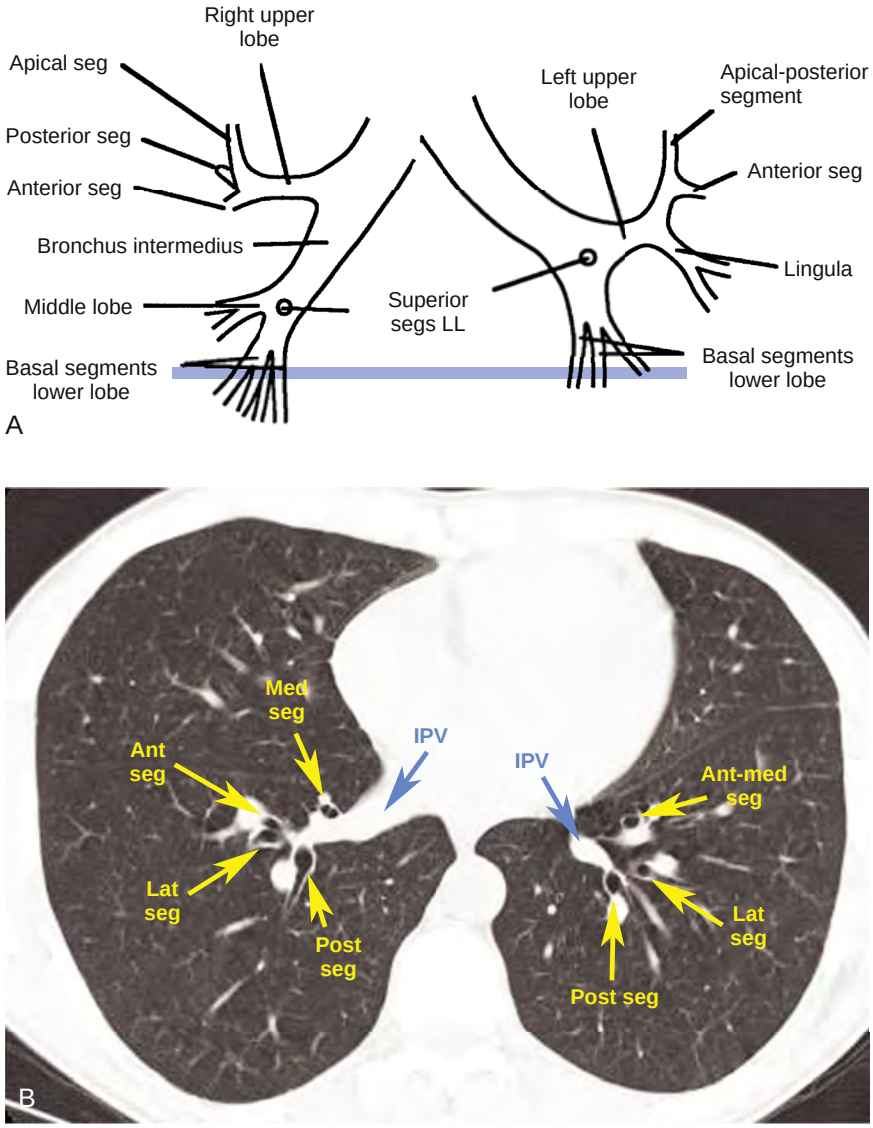

FIGURE 5-18 ■ Normal lower lobe bronchi (basal segments). *A*, Approximate level for the scan shown in B. LL, lower lobe; seg, segment. *B*, On the right, the medial (Med seg), anterior (Ant seg), lateral (Lat seg), and posterior (Post seg) segmental bronchi of the right lower lobe are visible. The basal segmental bronchi arise in a variable fashion. The inferior pulmonary vein (IPV) is posterior and medial to the bronchi, and segmental pulmonary artery branches with a round appearance accompany the bronchi. On the left, the anteromedial (Ant-med seg), Lat seg, and Post seg branches of the left lower lobe bronchus are visible. The vascular anatomy is the same as on the right.

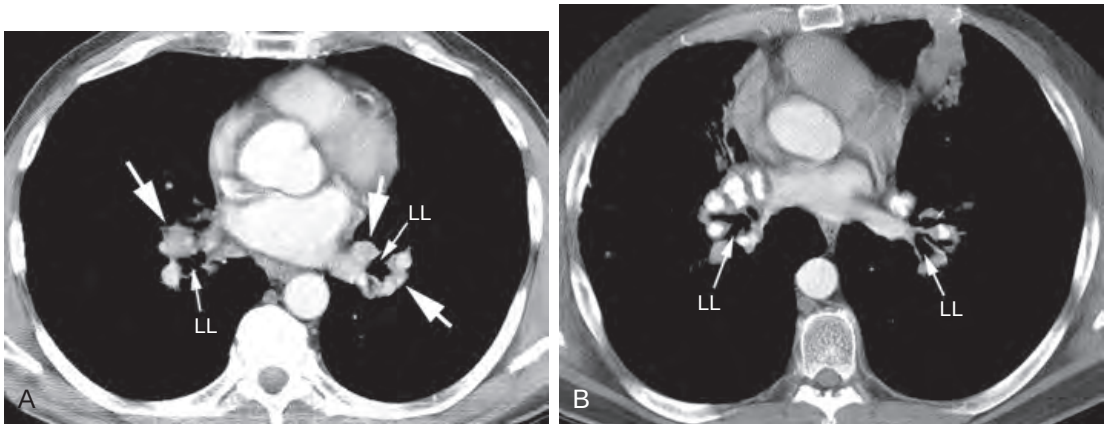

FIGURE 5-19 ■ Abnormal lower lobe bronchial level in two patients with sarcoidosis. *A* and *B*, At the level of the lower lobe (LL) segments, abnormal lymph nodes (*arrows*) are visible anteriorly and adjacent to the vascular branches.

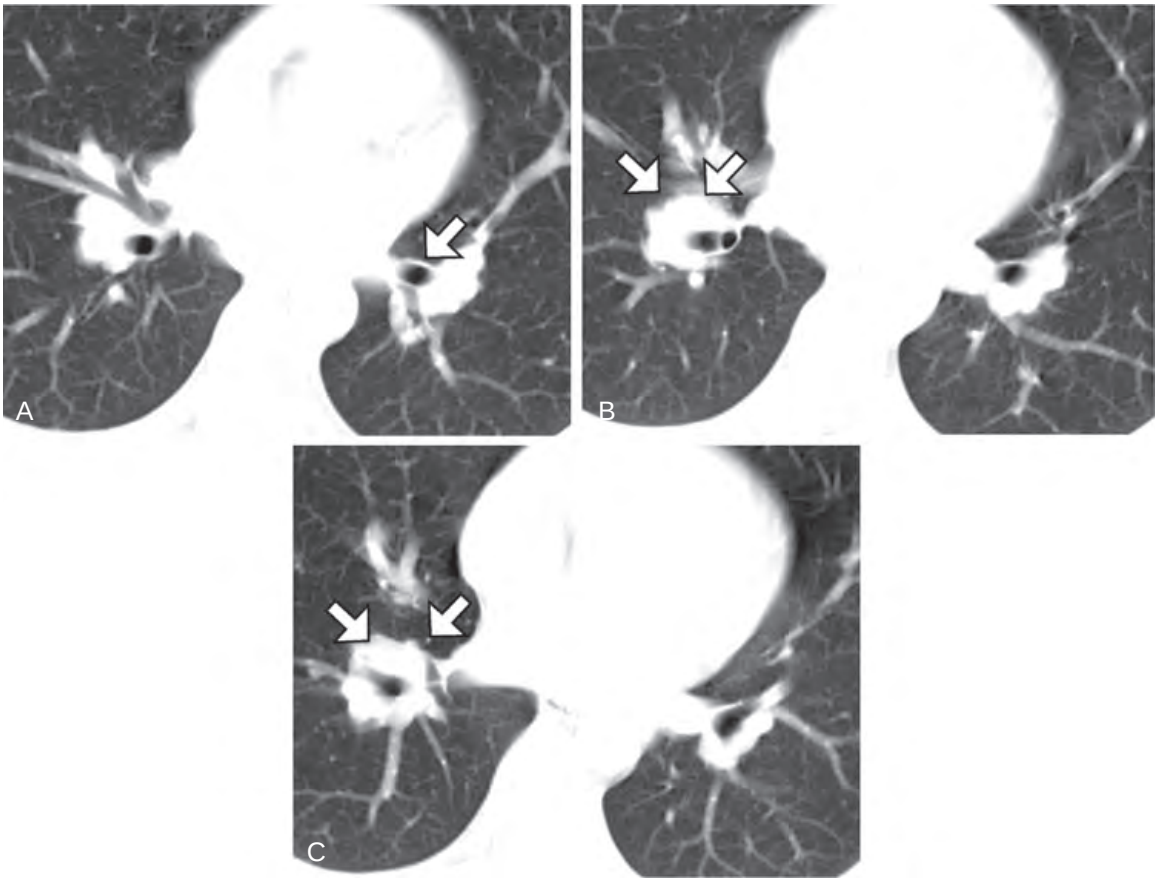

FIGURE 5-20 ■ Right hilar adenopathy, lower lobe bronchi, and basal segments. *A*, Lobulation of the right hilum at the level of the right middle lobe bronchus indicates lymph node enlargement. Note that the lung contacts the anterior wall of the left lower lobe bronchial trunk (*arrow*), and arteries and veins are lateral, posterior, and medial to the bronchus. This appearance is normal. *B*, The right lower lobe bronchial trunk has divided into two branches. Soft tissue anterior to these branches represents lymph node enlargement (*arrows*). On the left, the lower lobe bronchial trunk remains outlined by the lung anteriorly. *C*, At the level of the basal segments, the right and left sides appear asymmetrical. The right bronchial segments are surrounded by soft tissue. Nodes (*arrows*) are anterior to the bronchi.

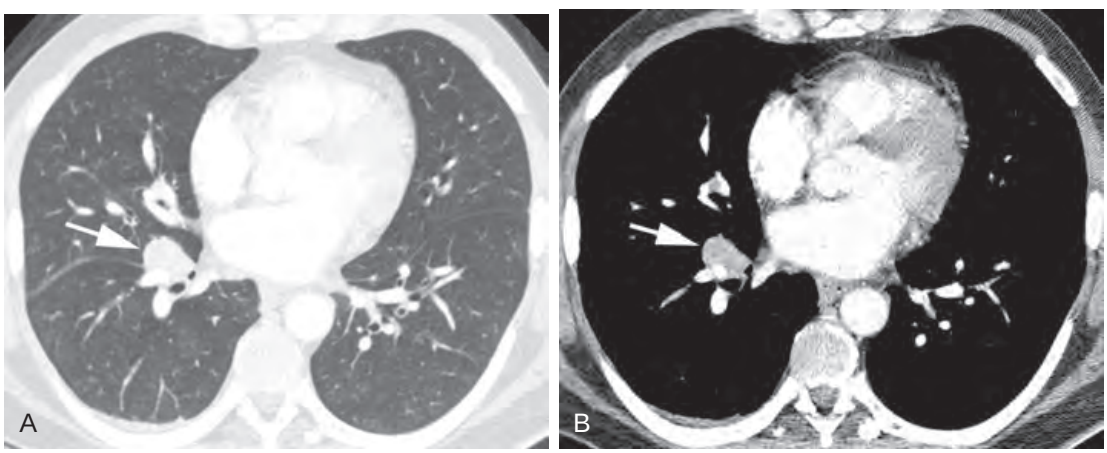

FIGURE 5-21 ■ Right hilar adenopathy, lower lobe bronchi. *A* and *B*, In a patient with non-Hodgkin's lymphoma, an enlarged lymph node (*arrow*) is visible anterior to the right lower lobe bronchial branches.

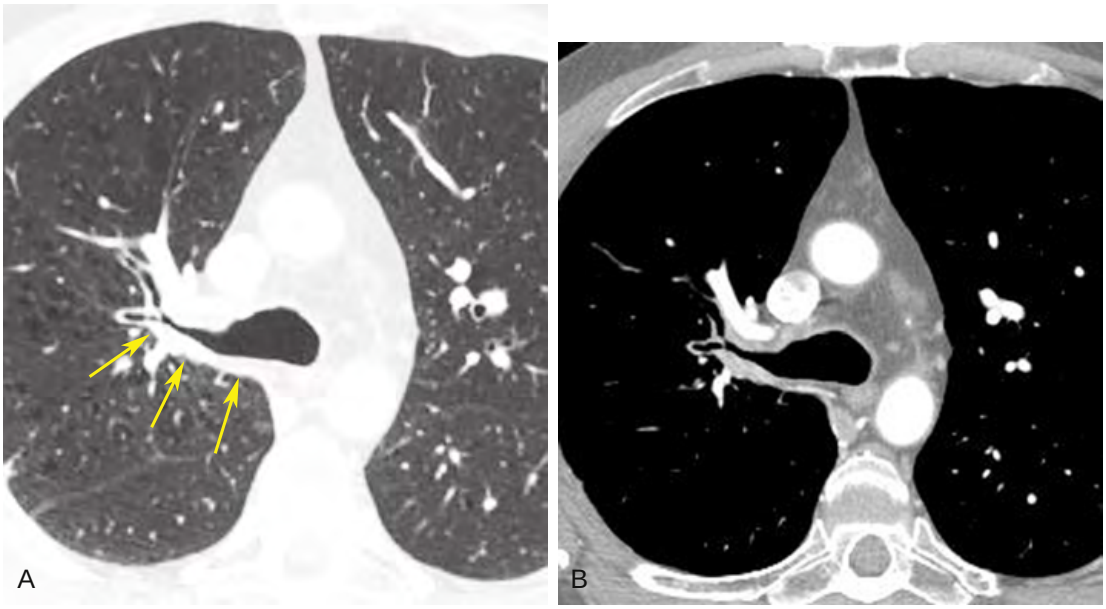

FIGURE 5-22 ■ Bronchogenic carcinoma with bronchial wall thickening. *A* and *B*, There is thickening of the posterior wall of the right upper lobe bronchus and right main bronchus due to tumor infiltration (*arrows*). Irregular narrowing of the lumen of the right upper lobe bronchus is also visible. The wall of the right upper lobe bronchus is normally smooth and thin.

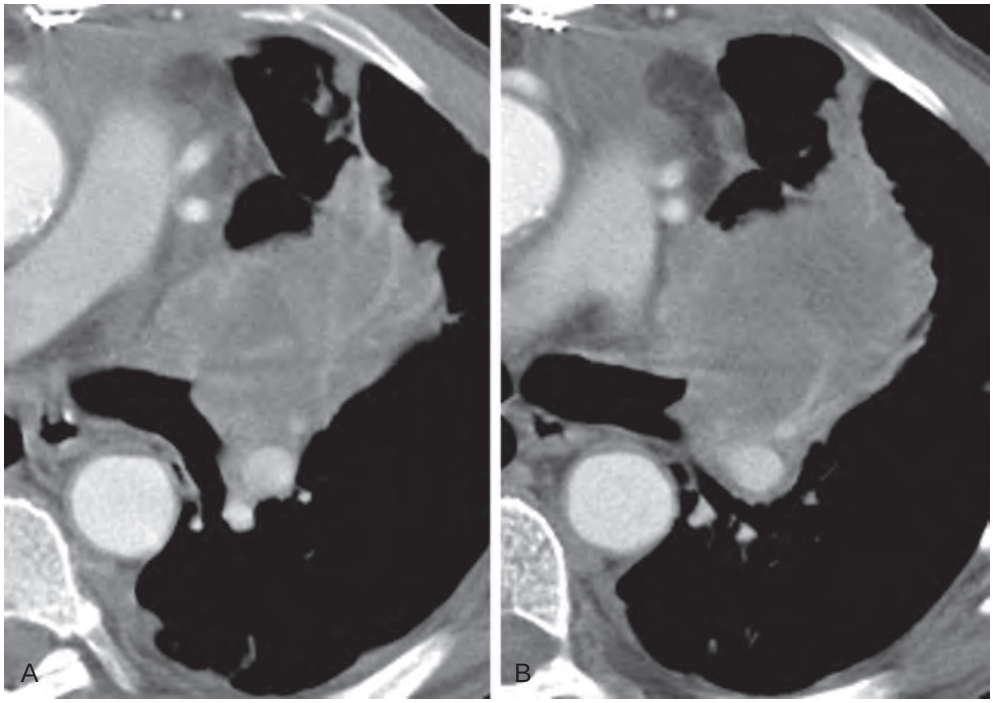

FIGURE 5-23 ■ Bronchogenic carcinoma with left upper lobe bronchus obstruction. *A* and *B*, There is abrupt termination of the left upper lobe bronchus, associated with distal collapse and consolidation of the left upper lobe. This appearance strongly suggests bronchogenic carcinoma.

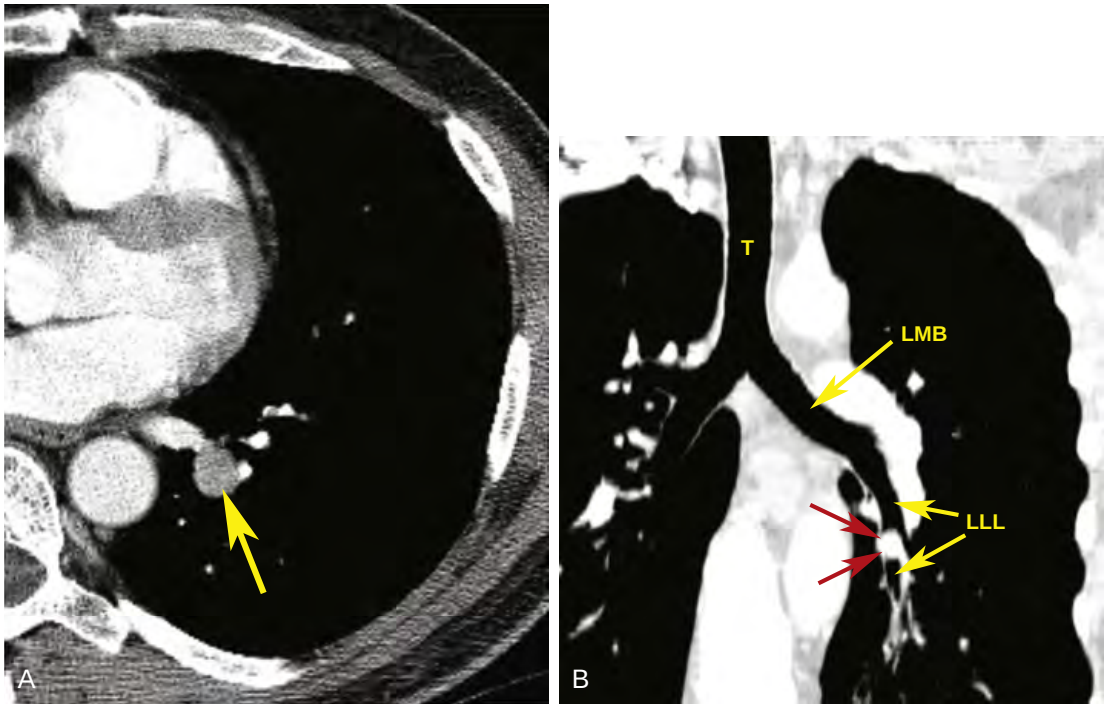

FIGURE 5-24 ■ Endobronchial carcinoid tumor in a young patient with recurrent left lower lobe pneumonia. *A*, Spiral CT with a 1.25-mm slice shows a round mass *(arrow)* in the location of the left lower lobe bronchus. Although it might be mistaken for a vessel, it is much less dense than enhanced arteries and veins. *B*, Coronal reconstruction shows a round mass *(red arrows)* within the left lower lobe bronchus (LLL). T, trachea; LMB, left main bronchus.

FIGURE 5-25 ■ Endobronchial metastasis from colon carcinoma. A focal endobronchial lesion *(arrow)* is visible within the left main bronchus. This represents an endobronchial metastasis.

FIGURE 5-26 ■ Endobronchial metastasis from breast carcinoma. In a patient with a right mastectomy, a focal lesion narrowing the lower lobe bronchus (*small arrow*) is associated with right lower lobe atelectasis (*large arrow*). This represents an endobronchial metastasis.

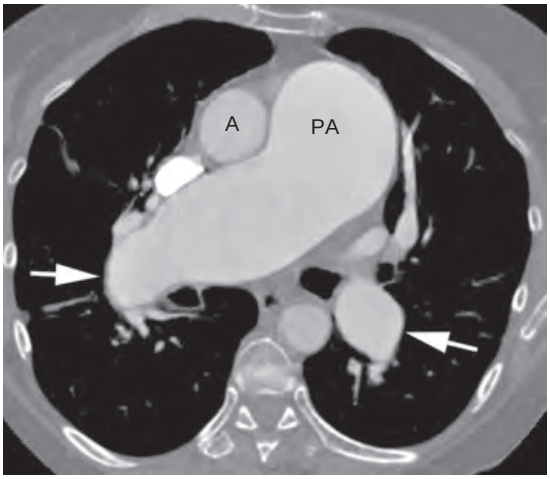

FIGURE 5-27 ■ Pulmonary artery enlargement in pulmonary hypertension. The main pulmonary artery (PA) is larger than the ascending aorta (A), which is a good sign of pulmonary hypertension. Enlargement of the hilar arteries (*arrows*) is also seen.

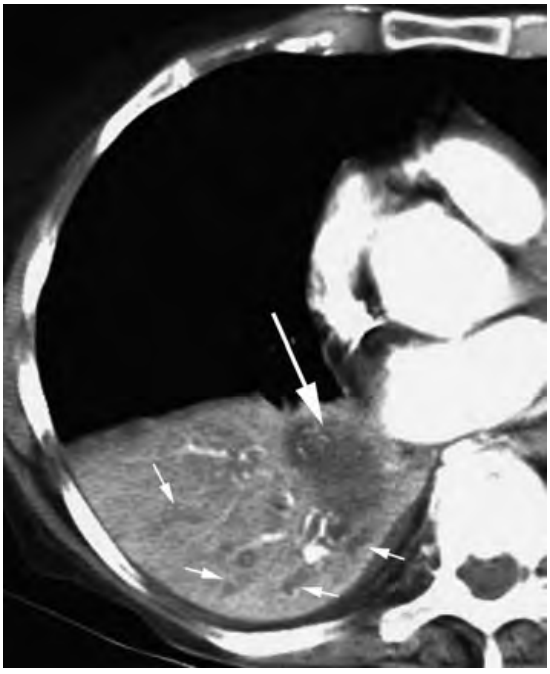

FIGURE 5-28 ■ Hilar mass with atelectasis. In a patient with right hilar carcinoma associated with right lower lobe atelectasis, the hilar mass can be distinguished from the collapsed lung after contrast infusion. The mass (*large arrow*) appears less dense than the opacified and enhanced lung tissue. Low-attenuation, mucus-filled bronchi (*small arrows*) are visible within the consolidated lung. These are associated with bronchial obstruction and are termed *mucous bronchograms.*

MASS VERSUS ATELECTASIS

In patients with a hilar mass and bronchial obstruction, collapse or consolidation of the distal lung can obscure the margins of the mass, making it difficult to diagnose. On plain radiographs, the mass can sometimes be detected because of alterations in the shape of the collapsed or consolidated lobe or lobes (i.e., Golden's S sign). Similarly, alterations in the shape of a collapsed lobe can be seen on CT in the presence of a mass.

If contrast is injected, the collapsed lobe is usually enhanced to a greater degree than the mass causing the collapse (Fig. 5-28). Of additional value in distinguishing mass and lung consolidation are air bronchograms, which are sometimes visible despite bronchial obstruction. These indicate the presence of lung consolidation and are not usually visible with the mass itself. In some patients, low-attenuation, fluid-filled bronchi (i.e., *mucous bronchograms*) are seen within the collapsed lung instead of air bronchograms.

SUGGESTED READING

Glazer GM, Gross BH, Aisen AM, et al.: Imaging of the pulmonary hilum: A prospective comparative study in patients with lung cancer. *AJR Am J Roentgenol* 145:245–248, 1985.

Müller NL, Webb WR: Radiographic imaging of the pulmonary hila. *Invest Radiol* 20:661–671, 1985.

Naidich DP, Khouri NF, Scott WJ, et al.: Computed tomography of the pulmonary hila: I. Normal anatomy. *J Comput Assist Tomogr* 5:459–467, 1981.

Naidich DP, Khouri NF, Stitik FP, et al.: Computed tomography of the pulmonary hila: II. Abnormal anatomy. *J Comput Assist Tomogr* 5:468–475, 1981.

Ng CS, Wells AU, Padley SP: A CT sign of chronic pulmonary arterial hypertension: The ratio of main pulmonary artery to aortic diameter. *J Thorac Imaging* 14:270–278, 1999.

Park CKA, Webb WR, Klein JS: Inferior hilar window. *Radiology* 178:163–168, 1991.

Rami-Porta R, Crowley JJ, Goldstraw P: The revised TNM staging system for lung cancer. *Ann Thorac Cardiovasc Surg* 15:4–9, 2009.

Remy-Jardin M, Duyck P, Remy J, et al.: Hilar lymph nodes: Identification with spiral CT and histologic correlation. *Radiology* 196:387–394, 1995.

Remy-Jardin M, Remy J, Artaud D, et al.: Volume rendering of the tracheobronchial tree: Clinical evaluation of bronchographic images. *Radiology* 208:761–770, 1998.

Sone S, Higashihara T, Morimoto S, et al.: CT anatomy of hilar lymphadenopathy. *AJR Am J Roentgenol* 140:887–892, 1983.

Webb WR, Gamsu G: Computed tomography of the left retrobronchial stripe. *J Comput Assist Tomogr* 7:65–69, 1983.

Webb WR, Gamsu G, Glazer G: Computed tomography of the abnormal pulmonary hilum. *J Comput Assist Tomogr* 5:485–490, 1981.

Webb WR, Glazer G, Gamsu G: Computed tomography of the normal pulmonary hilum. *J Comput Assist Tomogr* 5:476–484, 1981.

Webb WR, Hirji M, Gamsu G: Posterior wall of the bronchus intermedius: Radiographic–CT correlation. *AJR Am J Roentgenol* 142:907–911, 1984.

CHAPTER 6

LUNG DISEASE

W. Richard Webb

On computed tomography (CT), normal lung varies in appearance, depending on the window settings used. With a window mean of –600 to –700 Hounsfield units (HU) and a width of 1000 to 1500 HU, the lungs appear dark, but not as black as the air visible in the trachea or bronchi. This slight difference in attenuation between lung parenchyma and air should be sought in choosing an appropriate window setting. If the lungs are viewed with too high a window mean, soft-tissue structures in the lung (vessels, bronchi, or lung nodules) are difficult to see or are underestimated in terms of their size, and any areas of lucency, such as bullae, may be missed. The lungs, after all, are not simply bags of air, and they should not appear to be so. If too low a window mean is used, the size of soft-tissue structures in the lung will be overestimated.

LOBAR ANATOMY

The lobes are delineated by the major and minor fissures (Fig. 6-1).

Major Fissures

The major fissures are not clearly visible on CT obtained with 5-mm collimation but are easily seen as thin white lines on CT with a 1.25-mm slice thickness (Fig. 6-1). The lung adjacent to the fissures contains few visible vessels and appears relatively avascular. The major fissures are incomplete in many patients (i.e., they do not completely separate the lobes).

Within the lower thorax, the major fissures angle anterolaterally from the mediastinum, contacting the anterior third of the hemidiaphragms. They separate the lower lobes posteriorly from the upper lobe on the left and the middle and upper lobes on the right. In the upper thorax, the major fissures angle posterolaterally. Above the aortic arch, they contact the posterior chest wall.

Minor Fissure

The minor fissure parallels the scan plane and is more difficult to see. However, it is usually visible on thin-section scans as a white line of varying sharpness and thickness, depending on its orientation. The relatively avascular lung on both sides of the fissure is visible on CT in most patients. In some patients, the minor fissure mimics the appearance of the major fissure but is seen anterior to it.

Because the minor fissure often angles caudally, the lower, middle, and upper lobes may all be seen on a single scan. If the minor fissure is concave caudad, it can sometimes be seen in two locations or can appear ring-shaped (Fig. 6-2), with the middle lobe between the fissure lines or in the center of the ring and the upper lobe anterior to the most anterior part of the fissure.

Accessory Fissures

In patients with an azygos lobe, the four layers of the *mesoazygos*, or azygos fissure, are invariably visible above the level of the intrapulmonary azygos vein. The azygos fissure is C-shaped and convex laterally, beginning anteriorly at the right brachiocephalic vein and ending posteriorly at the right anterolateral surface of the vertebral body (Fig. 3-16). Other accessory fissures, most commonly the inferior accessory fissure, are occasionally seen on CT. They are not generally of diagnostic significance.

LOBAR PNEUMONIA

Lobar consolidation resulting from pneumonia (i.e., *lobar pneumonia)* is relatively uncommon. Pneumonia more typically results in patchy consolidation, a pattern often referred to as *lobular pneumonia* or *bronchopneumonia*. The term *consolidation* is used on CT to describe the presence of homogeneous lung opacity due to replacement of air within alveoli, with obscuration of the underlying vessels and bronchial walls; *air bronchograms* (visible air-filled bronchi) are typical, but not invariably present. On enhanced CT, vessels with a normal appearance and course can often be seen within consolidated lung. In contrast, a mass, or space-occupying lesion, usually displaces vessels or bronchi, or they may be invisible because of

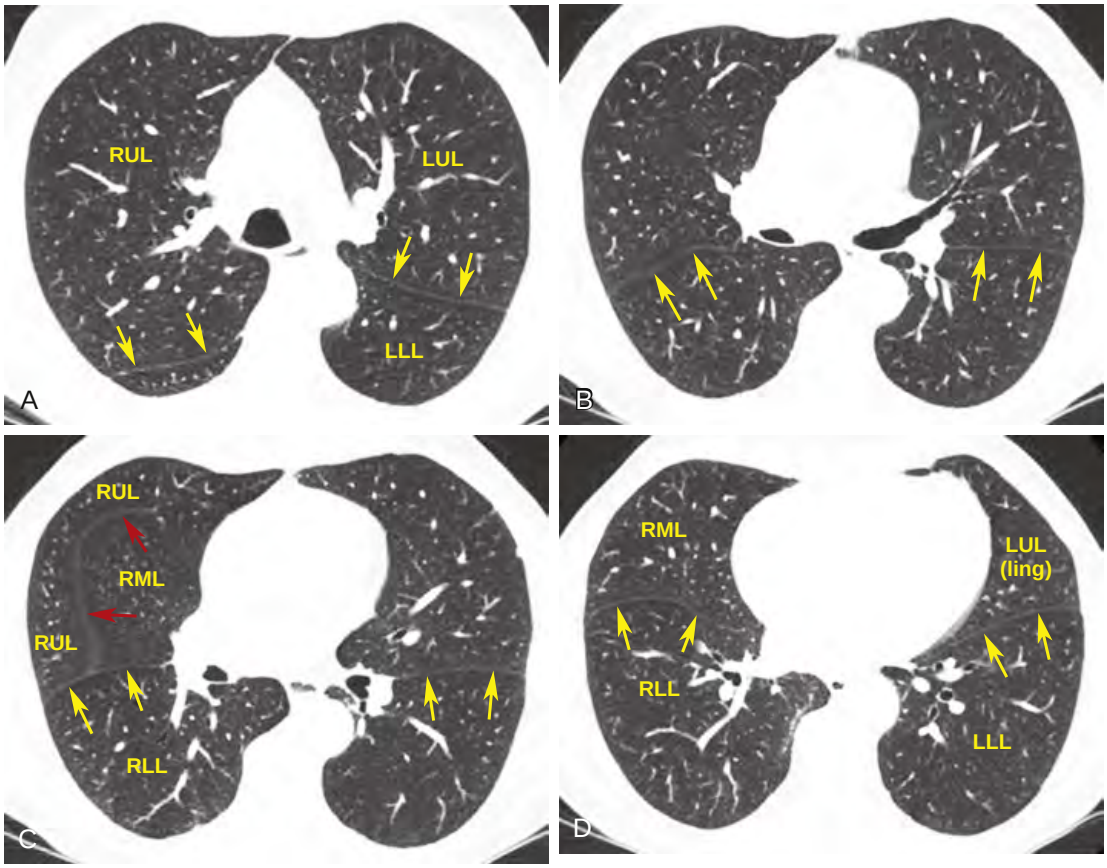

FIGURE 6-1 ■ Normal fissures. *A*, At a level slightly below the aortic arch, the major fissures (*arrows*) are visible as thin lines. They angle posterolaterally. On the right, the major fissure separates the right upper lobe (RUL) from the superior segment of the right lower lobe. On the left, it separates the left upper (LUL) and left lower (LLL) lobes. *B*, Several centimeters lower, the major fissures (*arrows*) are more anteriorly positioned. *C*, The major fissures (*yellow arrows*) remain visible. The minor fissure (*red arrows*) separates the right middle lobe (RML) medially from the right upper lobe laterally and anteriorly. *RLL*, right lower lobe. *D*, At a lower level, the major fissures angle anterolaterally (*arrows*). Their bowed appearance is normal. The RML is located anterior to the right major fissure. On the left, the lingular (ling) portion of the left upper lobe is anterior to the fissure.

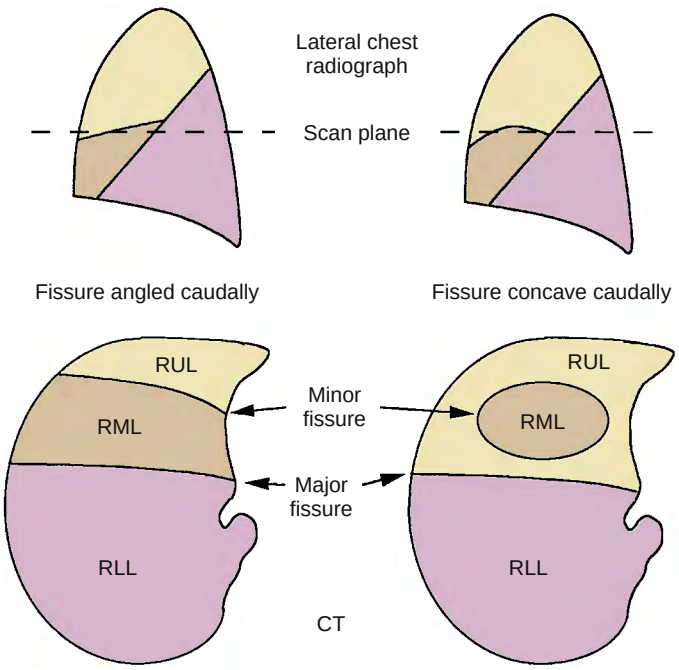

FIGURE 6-2 ■ Possible appearances for the minor fissure. Depending on the orientation of the minor fissure, its appearance and the relations of the lobes of the right lung can vary. If the minor fissure angles downward, both the middle and upper lobes can be seen on a single scan. If the minor fissure is concave caudad, it may appear ring-shaped or curved, as in Figure 6-1*C*. RLL, right lower lobe; RML, right middle lobe; RUL, right upper lobe.

invasion or obstruction. In addition to pneumonia, other causes of lobar consolidation include obstructive pneumonia (with a central bronchial obstruction), invasive mucinous adenocarcinoma, and in rare cases a vascular abnormality (e.g., pulmonary embolism).

In a patient with lobar pneumonia, the volume of the consolidated lobe is normal or sometimes increased (Fig. 6-3). Usually the organisms responsible lead to an exuberant inflammatory exudate that easily spreads from one alveolus to another and results in an expanding sphere of pneumonia that stops when it reaches a fissure. If lobar pneumonia is imaged early in its evolution, it may appear as a rounded, poorly marginated area of consolidation. This is sometimes referred to as *round pneumonia.*

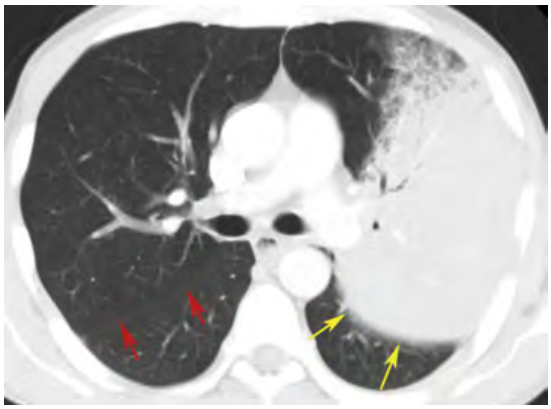

FIGURE 6-3 ■ Lobar left upper lobe pneumonia. Pneumococcal pneumonia results in homogeneous consolidation of the posterior left upper lobe, marginated by the left major fissure. The fissure is bowed posteriorly (*yellow arrows*). The right major fissure is also seen (*red arrows*).

Typical organisms that should be considered in the differential diagnosis of lobar pneumonia include *Streptococcus pneumoniae*, *Klebsiella pneumoniae*, *Legionella*, *Mycoplasma*, *Mycobacterium tuberculosis*, other bacteria, and some viral and fungal infections. Pulmonary infections may also present with other CT patterns; these are discussed later in this chapter and include single or multiple nodules, masses, and cavities; bronchiectasis and tree-in-bud nodules; patchy consolidation; ground-glass opacity (GGO); centrilobular nodules; and miliary (random) nodules.

ATELECTASIS: TYPES AND PATTERNS OF LOBAR COLLAPSE

Atelectasis most commonly occurs because of bronchial obstruction (obstructive atelectasis), pleural effusion or other pleural processes that allow the lung to collapse (passive or relaxation atelectasis), or lung fibrosis (cicatrization atelectasis). These conditions can have different appearances. General signs of volume loss on CT are the same as those on chest radiographs. Mediastinal shift (particularly of the anterior mediastinum), elevation of the diaphragm, and displacement of fissures are well seen on CT.

Obstructive Atelectasis

Obstructive atelectasis often occurs because of lung cancer or another tumor, and the bronchi should be examined closely. Lobar atelectasis commonly results; typically, the affected lobe is partially or completely consolidated (Fig. 6-4). Air bronchograms are usually, but not always,

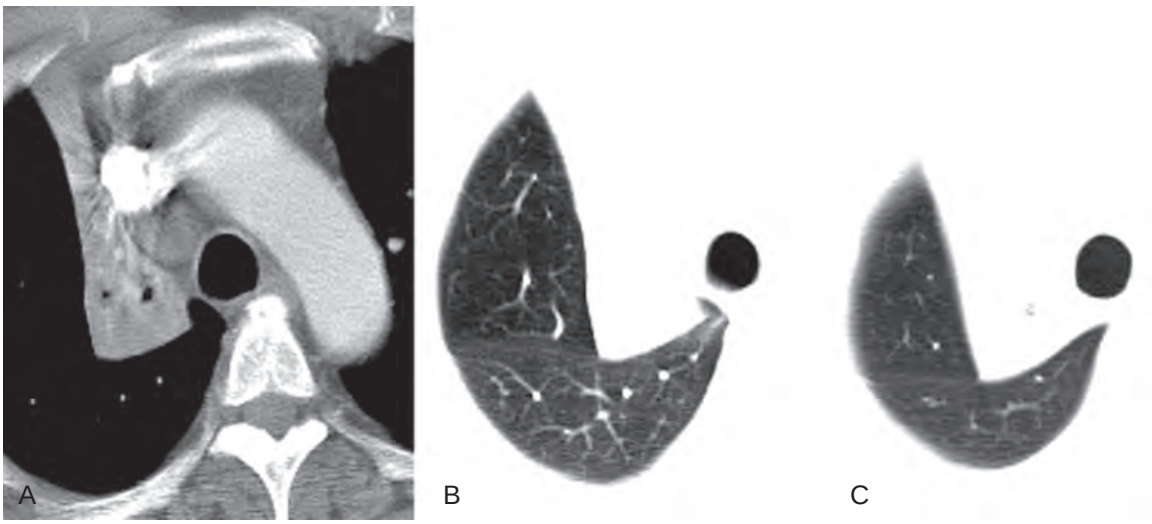

FIGURE 6-4 ■ Right upper lobe collapse. *A,* In a patient with carcinoma obstructing the right upper lobe bronchus, air bronchograms and opacified vessels are visible. *B* and *C,* The collapsed upper lobe has a triangular shape. The middle lobe borders the lateral aspect of the collapsed lobe, whereas the lower lobe is posterior to it.

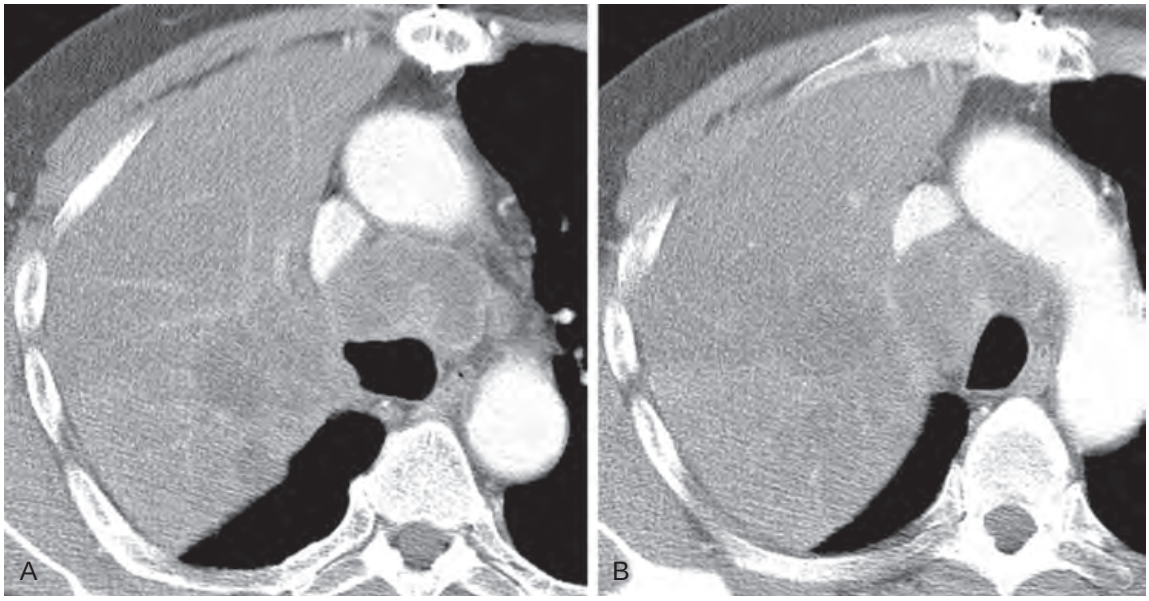

FIGURE 6-5 ■ Lung carcinoma with obstructive pneumonia. *A* and *B*, The right upper lobe is consolidated, but no volume loss is present. No air bronchograms are seen, but opacified vessels are visible. Large, low-density, necrotic mediastinal lymph nodes are also present.

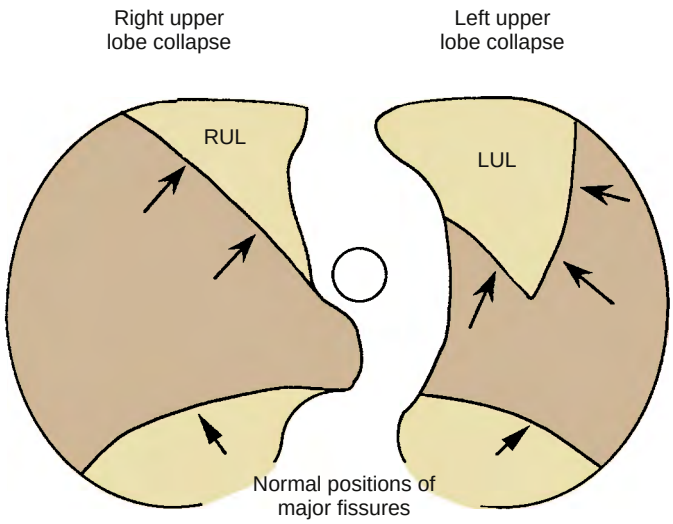

FIGURE 6-6 ■ Typical patterns of upper lobe collapse. LUL, left upper lobe; RUL, right upper lobe. The major fissures are displaced anteriorly and medially (*arrows*) from their normal positions.

absent. *Mucus bronchograms* (low-density fluid or mucus within obstructed bronchi) can sometimes be seen on CT. The air- or mucus-filled bronchi can be dilated in the presence of atelectasis, simulating bronchiectasis. If contrast infusion is used, opacified vessels are often visible within the consolidated and collapsed lobe (a collapsed lung is not simply airless; the alveoli are filled with fluid). If little volume loss is present, the term *obstructive pneumonia* is often used (Fig. 6-5).

On CT, atelectasis can be diagnosed when displacement of fissures is seen. Typical patterns of lobar collapse can be identified (Figs. 6-6 and 6-7).

Right Upper Lobe Collapse

The major fissure rotates anteriorly and medially as the upper lobe progressively flattens against the mediastinum (Figs. 6-4 and 6-6). The fissure can be bowed anteriorly. In the presence of a hilar mass, an appearance similar to Golden's S sign, as seen on plain radiographs, is visible. In some patients, the lobe assumes a triangular shape (Fig. 6-4).

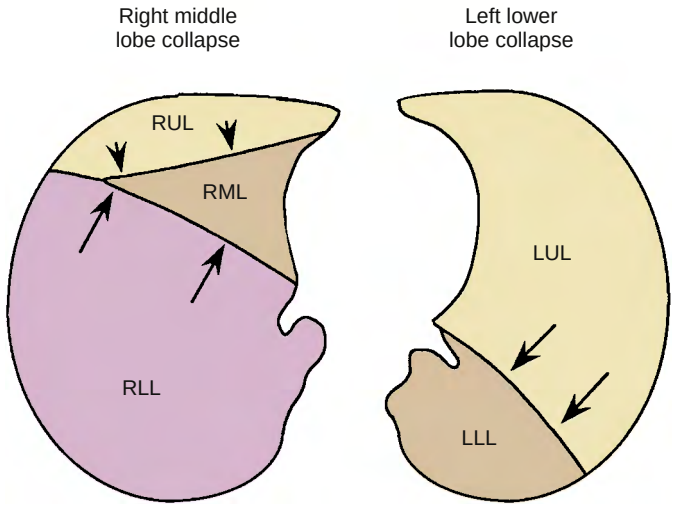

FIGURE 6-7 ■ Typical patterns of middle and lower lobe collapse. LLL, left lower lobe; LUL, left upper lobe; RLL, right lower lobe; RML, right middle lobe; RUL, right upper lobe.

Left Upper Lobe Collapse

As on the right, the major fissure rotates anteromedially. However, above the hilum, the superior segment of the lower lobe may displace part of the upper lobe away from the mediastinum, giving the posterior margin of the collapsed lobe a V shape, (Fig. 6-6). A similar appearance is sometimes seen on the right (Fig. 6-4).

Middle Lobe Collapse

As the middle lobe loses volume, the minor fissure rotates downward and medially. The collapsed lobe assumes a triangular shape, with one side of the triangle abutting the mediastinum (Fig. 6-7). The upper lobe can be seen anterolaterally, bordering the collapsed lobe, with the lower lobe bordering it posterolaterally. These aerated lobes usually separate the collapsed middle lobe from the lateral chest wall.

Lower Lobe Collapse

On either side, the major fissure rotates posteromedially (Fig. 6-7). The collapsed lobe contacts the posterior mediastinum and posteromedial chest wall and maintains contact with the medial diaphragm.

Passive Atelectasis

In the presence of pleural effusion, the lung tends to retract or collapse toward the hilum, and fluid entering the fissures allows the lobes to separate. On injection of contrast, the lung is opacified and is clearly distinguishable from surrounding fluid. Air bronchograms may be seen within the collapsed lobes. Rounded atelectasis is a form of passive atelectasis. *Linear, disk, or plate-like atelectasis* at the lung bases may be seen as a result of limited diaphragmatic motion.

Rounded Atelectasis

Rounded atelectasis represents focal, collapsed, and often folded lung. It is common and almost always occurs in association with pleural thickening or pleural effusion.

Rounded atelectasis is most common in the posterior paravertebral regions and may be bilateral in patients with bilateral pleural abnormalities. Areas of rounded atelectasis, which appear as a mass or mass-like consolidation, are usually several centimeters in diameter. Bending or bowing of adjacent bronchi and arteries toward the edge of the area of rounded atelectasis, because of volume loss or folding of lung, is characteristic (Fig. 6-8); this finding has been termed the *comet tail sign*. Air bronchograms can sometimes be seen within the mass. Rounded atelectasis is densely opacified after contrast infusion.

Four findings must be present to make a confident diagnosis of rounded atelectasis on CT; if these are present, follow-up is usually sufficient (Fig. 6-8). If one of these findings is lacking, caution is required in making the diagnosis, and close follow-up or biopsy may be necessary. These four findings are:

1. Ipsilateral pleural thickening or effusion
2. Significant contact between the lung lesion and the abnormal pleural surface
3. The so-called *comet tail* sign
4. Volume loss in the lobe in which the opacity is seen

Rounded atelectasis may be associated with asbestos-related pleural thickening occurring adjacent to regions of thickened pleura, but it often has an

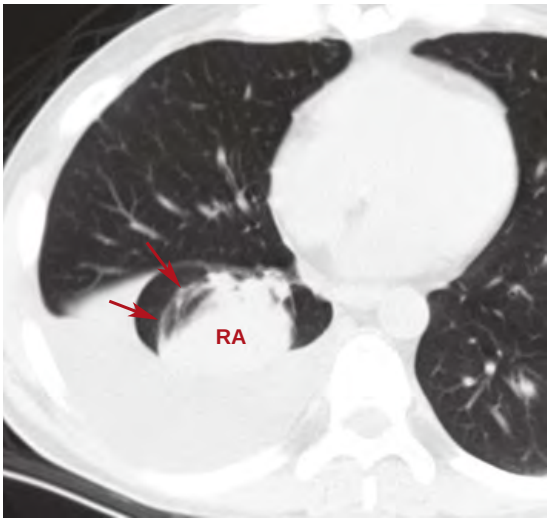

FIGURE 6-8 ■ Rounded atelectasis. Rounded atelectasis (RA) is present in a patient with a large right pleural effusion. The atelectatic lung shows vessels (*arrows*) curving into its edge, the *comet tail sign*. The lesion shows extensive pleural contact and there is posterior displacement of the major fissure, indicating lower lobe volume loss.

atypical appearance in such cases. Areas of atelectasis or focal fibrosis in patients exposed to asbestos can be irregular, may not have extensive pleural contact, and may not be associated with the comet tail sign. Biopsy is often warranted in this setting.

Cicatrization Atelectasis

Cicatrization atelectasis occurs in the presence of pulmonary fibrosis and may be associated with tuberculosis, radiation, or chronic bronchiectasis. In this condition, there is no evidence of bronchial obstruction. Rather, air bronchograms and bronchial dilatation (bronchiectasis) are usually visible within the area of collapse. The volume loss is often severe.

CONGENITAL LESIONS

Pulmonary Agenesis and Aplasia

Pulmonary agenesis consists of the complete absence of lungs, bronchi, and a vascular supply. With pulmonary aplasia, a rudimentary bronchus is present, ending in a blind pouch, but lung parenchyma and pulmonary vessels are absent (Fig. 6-9).

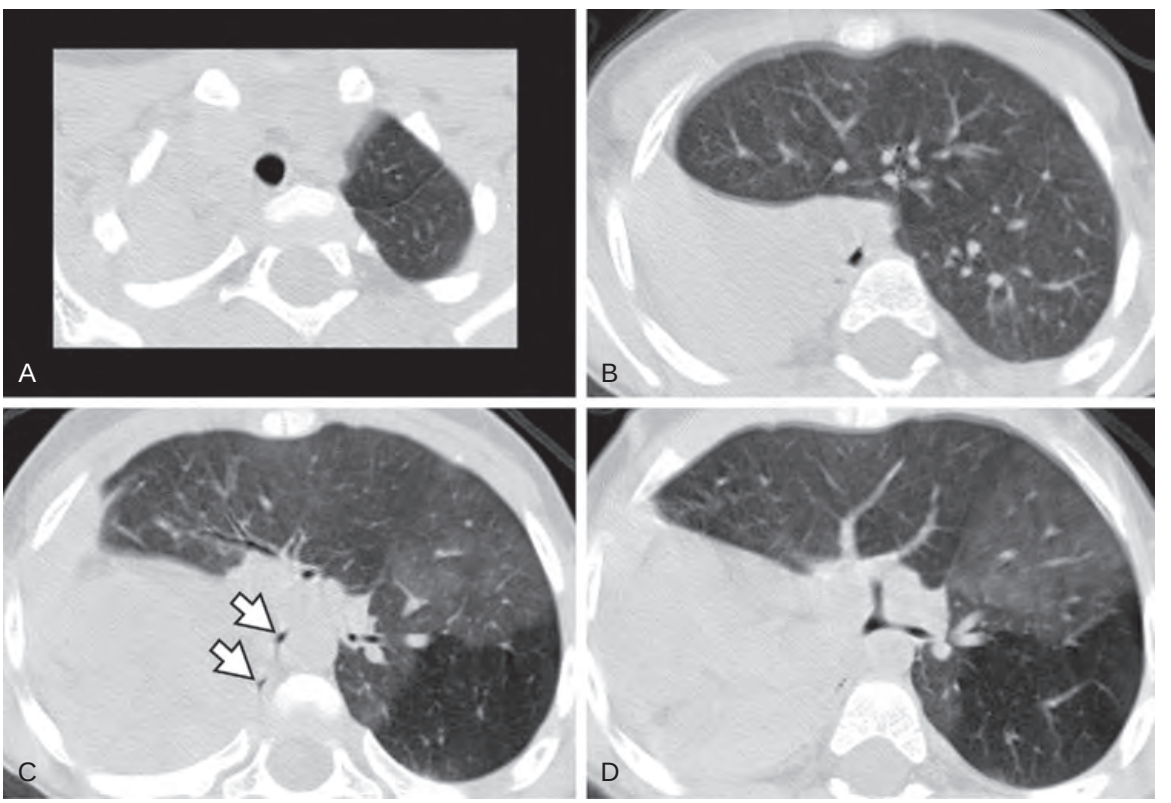

FIGURE 6-9 ■ Pulmonary aplasia in a child. *A* to *D*, The right lung is completely absent, with a mediastinal shift to the right and herniation of the left lung across the midline. The presence of rudimentary bronchi on the right (*arrows*, *C*) indicates that this represents aplasia rather than agenesis.

Tracheal Bronchus

Tracheal bronchus represents the origin of all or part (usually the apical segment) of the right upper lobe bronchus from the trachea (Fig. 6-10); its incidence is less than 1%. A left tracheal bronchus is much less common. Tracheal bronchus is common in cloven-hoofed animals such as pigs, sheep, goats, camels, and giraffes; it may be associated with recurrent infection (in humans).

Bronchial Atresia

Bronchial atresia is characterized by local narrowing or obliteration of a lobar, segmental, or subsegmental bronchus. It is most common in the left upper lobe, followed by the right upper and right middle lobes. Mucus commonly accumulates in dilated bronchi distal to the obstruction, resulting in a tubular, branching, or ovoid mucus plug or *mucocele*. Air trapping in the lobe or segment distal to the obstruction occurs because of collateral ventilation. Obstructed distal lung often appears hyperlucent and hypovascular.

Bronchogenic Cyst

The appearance of a mediastinal bronchogenic cyst is described in Chapter 4. Pulmonary bronchogenic cysts are typically well defined, round or oval, and of fluid or soft-tissue attenuation; previously infected cysts can contain air or an air–fluid level. When a cyst contains air, its wall appears very thin, although consolidation of surrounding lung may be present. These cysts are most common in the lower lobes.

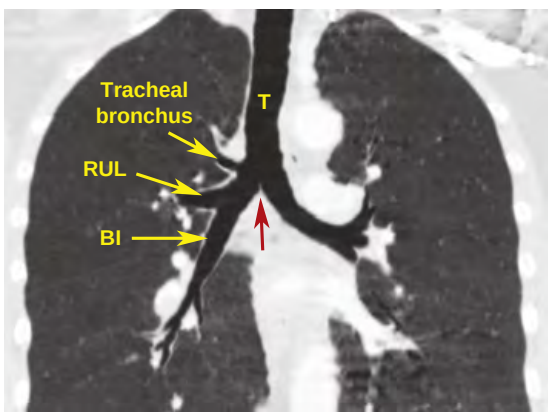

FIGURE 6-10 ■ Tracheal bronchus. Coronal reconstruction through the trachea (T) and bronchi. The tracheal bronchus arises from the lateral wall of the trachea above the carina (*red arrow*). The main right upper lobe (RUL) bronchus is visible at a lower level. BI, bronchus intermedius.

Arteriovenous Fistula

Pulmonary arteriovenous fistulas can be single (65%) or multiple (35%) and are often associated with Osler–Weber–Rendu syndrome (65%). On CT, an arteriovenous fistula can appear as a single dilated vascular sac, visible as a smooth, sharply defined round or oval nodule (most common) or a tangle of dilated tortuous vessels seen as a lobulated or serpiginous mass. In each type, the feeding pulmonary artery (or arteries) and the draining pulmonary vein (or veins) are dilated and should be easily seen on CT (Fig. 6-11). An arteriovenous fistula with a single feeding artery and draining vein (*simple fistula*) is most common; a *complex fistula* has multiple supplying vessels. In most cases, the fistula is immediately subpleural in location. These characteristic findings are generally sufficient for making a specific diagnosis on scans without contrast infusion, even for fistulas only a few millimeters in diameter.

Although contrast medium is not usually needed for diagnosis, an arteriovenous fistula shows rapid and dense opacification after bolus contrast injection, followed by rapid washout of the contrast (Fig. 6-11). As would be expected, opacification occurs just after opacification of the right ventricle and pulmonary artery. For fistulas larger than 3 mm, catheter embolization is the treatment of choice.

Sequestration

Pulmonary sequestration represents a focal lung anomaly, fed by an anomalous systemic artery or arteries, and without normal bronchial or pulmonary artery supply. It can appear cystic or solid on CT. Between 70% and 90% are located posteromedially on the left. In many cases of sequestration, the feeding systemic artery is visible on contrast-enhanced CT (Figs. 6-12 and 6-13). Descriptions follow of the two types.

Intralobar Sequestration

Intralobar sequestration is most common and is usually diagnosed in adults. It is contained within the pleura of a lobe, usually the left lower lobe. Recurrent or chronic infection is common. Venous drainage is usually by means of the pulmonary veins, although systemic (azygos) vein drainage may also be seen. Intralobar sequestration typically contains air but can be quite variable in appearance. On CT, intralobar sequestration can appear as follows:

1. A region of hyperlucent lung (Fig. 6-12*A*)
2. A cystic or multicystic structure (sometimes with air–fluid levels)
3. Consolidated or collapsed lung (Fig. 6-13)
4. A combination of these findings

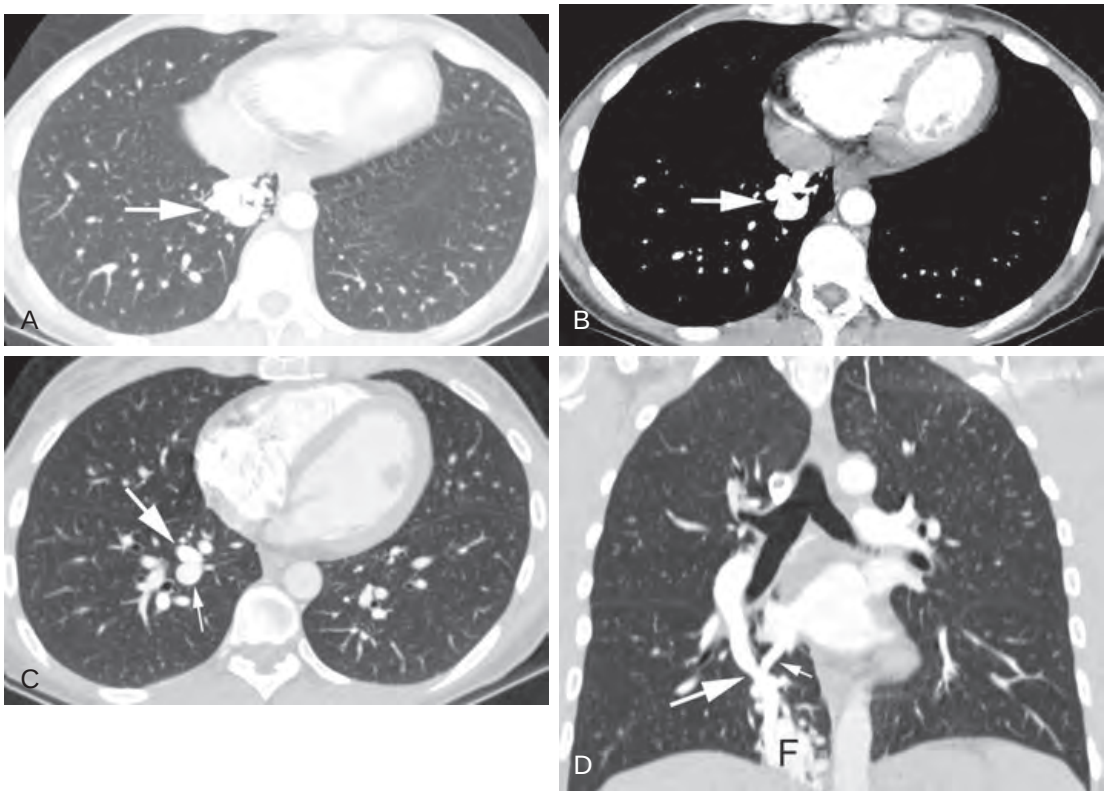

FIGURE 6-11 ■ Arteriovenous fistula. *A,* Contrast-enhanced multidetector computed tomography with a 1.25-mm slice thickness (lung window) shows a lobulated and serpiginous mass at the right lung base typical of an arteriovenous fistula (*arrow*). *B,* With a soft-tissue window setting, dense enhancement is visible (*arrow*). *C,* At a more cephalad level, the feeding artery (*large arrow*) and draining vein (*small arrow*) are visible. *D,* A coronal reformation shows the feeding artery (*large arrow*), draining vein (*small arrow*), and subpleural fistula (F).

Areas of lucent lung in association with, or representing part of, an intralobar sequestration are common (Fig. 6-12*A*). Normal bronchi are not seen in the sequestration, and if the sequestration is aerated, the vascular branching pattern within it may appear abnormal.

Extralobar Sequestration

Extralobar sequestration is usually diagnosed in infants or children, and infection is rare. It has its own pleural envelope. It almost always appears as a solid mass and rarely contains air. Venous drainage is usually through systemic veins.

Hypogenetic Lung (Scimitar) Syndrome

Hypogenetic lung (scimitar) syndrome, a rare anomaly almost always occurring on the right side, is characterized by four features that coexist to varying degrees:

1. Hypoplasia of the lung with abnormal segmental or lobar anatomy
2. Hypoplasia of the ipsilateral pulmonary artery
3. Anomalous pulmonary venous return (the *scimitar vein*) from the right upper lobe or the entire right lung, usually to the vena cava or right atrium
4. Anomalous systemic arterial supply to a portion of the hypoplastic lung, usually the lower lobe

On CT, the hypoplastic lung is recognizable because of dextroposition of the heart and mediastinal shift to the right (Fig. 6-14). The hypoplastic lung may also show abnormal bronchial anatomy, deficient bronchial divisions, or mirror-image bronchial or pulmonary artery branching. When the anomalous (scimitar) vein is present, it is clearly visible on CT, often draining into the right atrium or inferior vena cava. Hypoplasia of the pulmonary artery is usually recognizable by the decreased size of vessels in the hypoplastic lung. This entity may be associated with congenital heart disease.

Anomalous Pulmonary Venous Return

An anomalous pulmonary vein branch is present in about 0.5% of the population and is usually

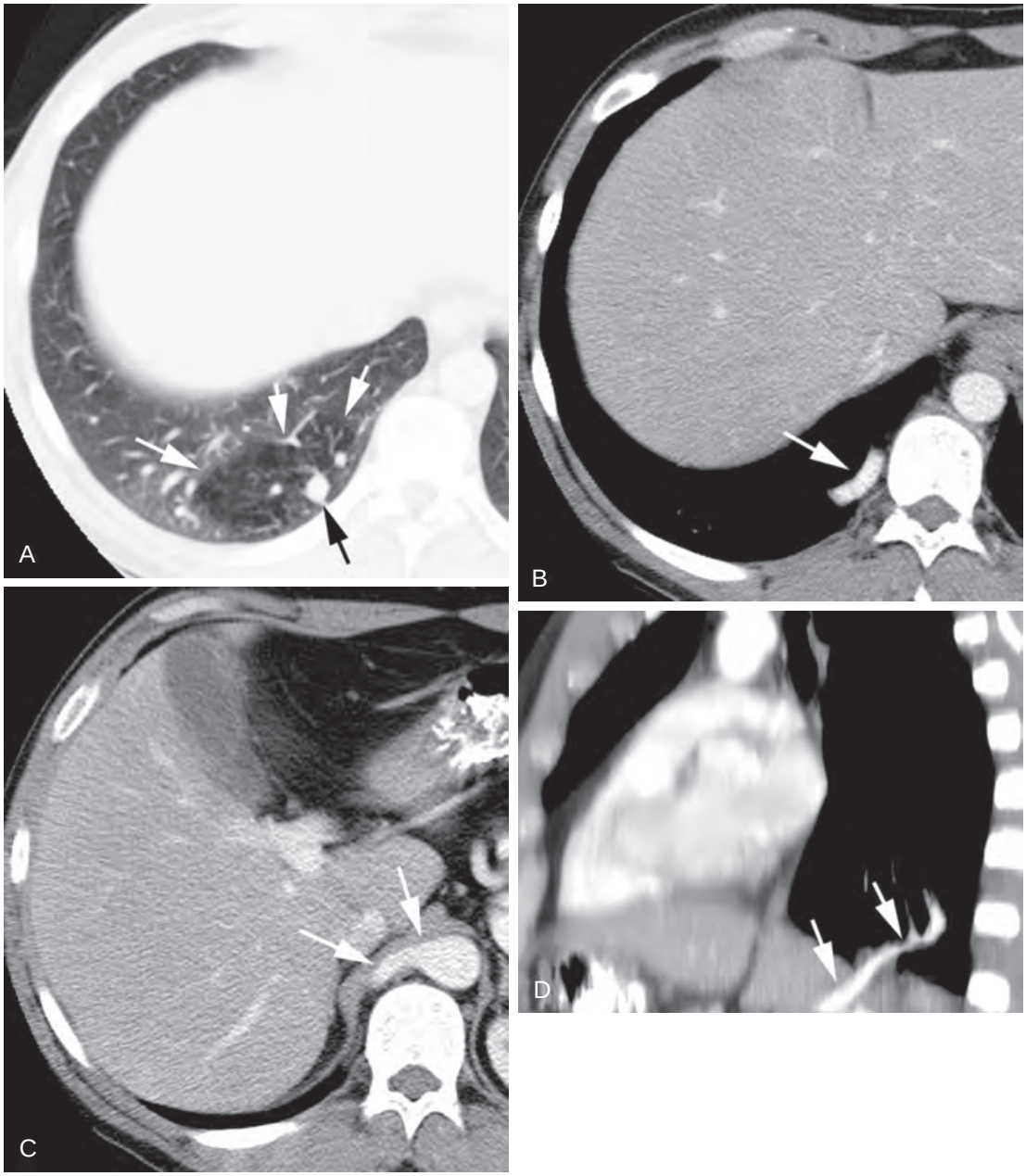

FIGURE 6-12 ■ Intralobar sequestration appearing as hyperlucent lung. *A,* Contrast-enhanced computed tomography (lung window) in a patient with intralobar sequestration shows an area of lucent lung (*white arrows*) at the right base. An abnormal vessel (*black arrow*) is visible within the area of lucency. *B,* Soft-tissue window at a lower level shows the abnormal vessel (*arrow*). *C,* A scan near the lung base shows that the abnormal vessel arises from the aorta (*arrows*). *D,* Sagittal reformation shows the abnormal vessel (*arrows*), originating in the abdomen, that supplies the posterior lower lobe.

asymptomatic. The anomalous vein may drain into various vascular structures. On the right, the most common are the superior vena cava, azygos vein, inferior vena cava, and right atrium. On the left, drainage may be via the left brachiocephalic vein, the persistent left superior vena cava, or the coronary sinus. Drainage may also be below the diaphragm. These can be seen as an isolated anomaly or in association with congenital heart disease.

SOLITARY PULMONARY NODULES AND FOCAL LUNG LESIONS

CT is often used to evaluate a solitary nodule, mass, or focal lesion detected on chest radiographs. It is used to (1) confirm the presence of a parenchymal lesion, (2) determine its morphology, (3) detect the presence of calcium or fat within the nodule, (4) identify nodule opacification after

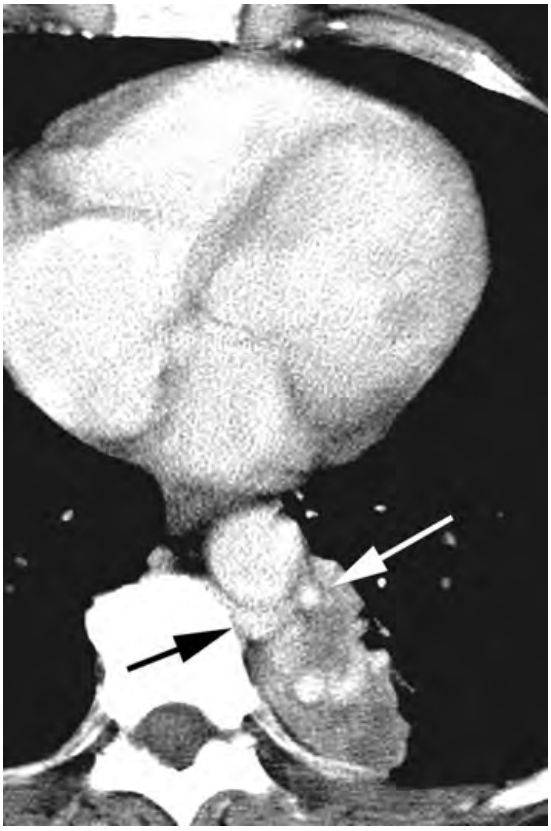

FIGURE 6-13 ■ Intralobar sequestration appearing as consolidated lung. Contrast-enhanced computed tomography (lung window) in a patient with intralobar sequestration shows an area of consolidation adjacent to the aorta in the left lower lobe. An anomalous artery (*white arrow*) arises from the descending aorta and supplies the sequestration. The draining vein (*black arrow*) communicates with the hemiazygos vein.

contrast infusion, and (5) plan percutaneous biopsy. CT is also used to detect lung nodules in patients being screened for lung cancer and to follow nonspecific lung nodules when a more aggressive approach is not warranted.

To make a semantic point, the term *nodule* is usually used to refer to a focal lung lesion 3 cm or less is diameter. *Mass* is used for a lesion larger than 3 cm. These measurements also distinguish a T1 tumor (≤ 3 cm) from a T2 tumor (> 3 cm) in the lung cancer staging system (Table 4-3).

With multidetector CT, scans obtained using a 1.25-mm slice thickness are optimal, but lung cancer screening may be done with thicker slices (i.e., 2 to 5 mm) and a low-dose technique. A high-resolution reconstruction algorithm should generally be used for image reconstruction.

Morphology of Focal Lesions and Lung Nodules

The differential diagnosis of a solitary nodule or mass is long (Table 6-1). However, lung cancers and some other focal lesions can have characteristic appearances on CT, which may be diagnostic or suggest a limited differential.

Lung Cancer

Adenocarcinoma is the most common cell type of lung cancer presenting as a lung nodule, but any cell type can present in this manner. Although a definite diagnosis of lung cancer cannot be made on CT, findings that strongly suggest malignancy in a patient with a solitary nodule include the following:

1. An irregular or spiculated nodule margin, usually caused by fibrosis or invasion of surrounding lung (90% of nodules with a spiculated edge are malignant; Fig. 6-15)
2. A lobulated contour (Fig. 6-16)
3. Air bronchograms (Fig. 6-15) or cystic or "bubbly" air-containing regions within the nodule (seen in 65% of cancers but only 5% of benign lesions)
4. A nodule exceeding 5 mm that is of GGO or of mixed GGO and solid attenuation (two-thirds are malignant; Fig. 6-17)
5. Cavitation (Fig. 6-16) with a nodular cavity wall or a wall exceeding 15 mm in greatest thickness (90% are cancers)
6. A diameter exceeding 2 cm (95% are cancers)

A spiculated edge and the presence of air bronchograms or cystic air-containing regions are particularly common with adenocarcinoma. Lobulation of the nodule also suggests the diagnosis of carcinoma but may also be seen with other lesions, particularly hamartoma.

Both primary lung carcinomas and metastases can cavitate. Typically, a cavitary carcinoma has a thick, irregular, and nodular wall (Fig. 6-16), but some metastatic tumors, particularly sarcomas and those of squamous cell origin, can be thin-walled. A cavitary nodule with a thin wall (< 5 mm) is most likely (90%) benign.

It is now recognized that many adenocarcinomas present as a nodule of GGO or a nodule with both GGO and solid components (Fig. 6-17). The term *ground-glass opacity* is used to describe hazy increased lung attenuation that does not obscure underlying vessels or bronchial walls.

The classification of pulmonary adenocarcinomas has recently been revised and is summarized in Table 6-2. New histologic subtypes of adenocarcinoma include *adenocarcinoma in situ* (*AIS*), *minimally invasive adenocarcinoma* (*MIA*), *lepidic predominant adenocarcinoma* (*LPA*), and *invasive mucinous adenocarcinoma*.

Each of the newly described histologic subtypes of adenocarcinoma may show GGO on CT. AIS usually appears as a pure GGO nodule. (Fig. 6-17*A*). MIA and LPA usually present as a

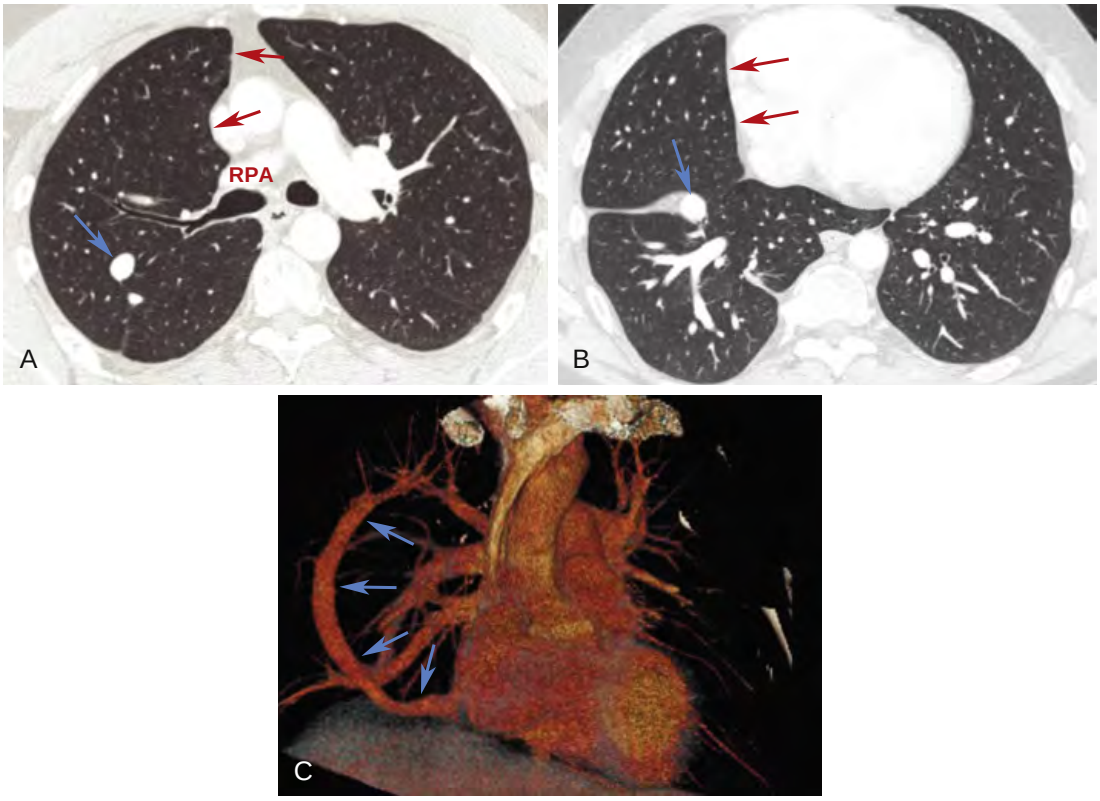

FIGURE 6-14 ■ Hypogenetic lung syndrome. *A*, At the level of the right upper lobe bronchus, the right lung is reduced in volume and the mediastinum is shifted toward the right (*red arrows*). The right pulmonary artery (RPA) appears small when compared to the left. The scimitar vein (*blue arrow*) is visible within the right lung. *B*, At the level of the heart, a rightward mediastinal shift (*red arrows*) is again seen, with the scimitar vein (*blue arrow*) visible in relation to a thickened major fissure. *C*, A three-dimensional reconstruction shows the anomalous vein (*blue arrows*) draining into the right atrium. Its curved shape resembles a Turkish scimitar.

TABLE 6-1 Differential Diagnosis of a Solitary or Multiple Pulmonary Nodule(s)

- Congenital lesions and normal variants
  - Arteriovenous fistula *
  - Bronchogenic cyst
  - Mucoid impaction (bronchial atresia)
  - Sequestration
- Malignant neoplasm
  - Carcinoma *
  - Lymphoma *
  - Lymphoproliferative disease *
  - Metastatic neoplasm *
  - Lung sarcoma (e.g., chondrosarcoma, liposarcoma, fibrosarcoma)
- Benign neoplasms and neoplasm-like conditions
  - Hamartoma
  - Lymphoproliferative disease *
  - Benign tumors (e.g., chondroma, lipoma, fibroma)
- Infection and parasites
  - Angioinvasive aspergillosis *
  - *Dirofilaria immitis* (dog heartworm)
  - *Echinococcus* *
  - Focal (round) pneumonia *
  - Granulomatous infection or granuloma (tuberculosis, nontuberculous mycobacteria, fungus) *
  - Lung abscess *
  - Mycetoma (aspergilloma) *
- Inflammatory (non-infectious) conditions
  - Organizing pneumonia *
  - Rheumatoid nodule *
  - Sarcoidosis *
  - Granulomatosis with polyangiitis (Wegener's granulomatosis) *
- Airways and inhalational disease
  - Mucoid impaction (mucous plug) in bronchiectasis *
  - Conglomerate mass or progressive massive fibrosis (e.g., silicosis) *
  - Lipoid pneumonia *
- Vascular lesions
  - Hematoma
  - Infarction*
  - Septic embolism *
- Miscellaneous
  - Amyloidosis *
  - Rounded atelectasis

*Also commonly presents with multiple nodules.

nodule of mixed GGO and solid attenuation (e.g., the halo sign; Fig. 6-17*B*). The term *halo sign* is used to describe a nodule with a soft-tissue attenuation center surrounded by a less dense halo of GGO. These three types of adenocarcinoma have a better prognosis (100% 5-year survival for AIS and MIA; 75% for LPA) than solid (homogeneously dense) adenocarcinomas, which generally represent invasive tumors (5-year survival 50%). A premalignant lesion, *atypical adenomatous hyperplasia* (*AAH*), typically presents as a GGO nodule 5 mm or less in diameter.

AIS, MIA, and LPA were formerly termed *bronchioloalveolar carcinoma* (*BAC*). These tumors are characterized, at least in part, by *lepidic growth*, which is defined as tumor growth along alveolar walls, using the alveolar walls as a scaffold, without invasion being present. AIS is characterized by pure lepidic growth and MIA by lepidic growth with ≤ 5 mm of invasion; LPA shows lepidic growth with more than 5 mm of invasion. *Invasive mucinous adenocarcinoma* was formerly referred to as diffuse or multifocal BAC because it usually presents with multiple nodules or multifocal GGO or consolidation; it is described later in this chapter.

Although pulmonary adenocarcinoma typically presents as a solitary nodule, up to 20% of patients with adenocarcinoma have multiple synchronous cancers. These are often of GGO.

FIGURE 6-15 ■ Spiculated adenocarcinoma. High-resolution computed tomography in a patient with a left lower lobe nodule shows a spiculated mass (*small white arrows*) suggestive of carcinoma. When a linear opacity contacts the pleural surface (*black arrow*), the resulting opacity is termed a *pleural tail.* Note that the nodule contains several air bronchograms (*large white arrow*).

Hamartoma

CT can be valuable in diagnosing pulmonary hamartoma. Hamartomas appear smooth and rounded or lobulated in contour. Using CT with thin slices, about two-thirds of hamartomas can be correctly diagnosed because of visible fat (60%; Fig. 6-18*A*) that is either focal or diffuse (Fig. 6-12), fat and calcification (30%), or diffuse calcification (10%). Usually, fat is easily seen on scans; CT numbers range between –40 and –120 HU. Calcification may have a "popcorn" appearance because of calcification of nodules of cartilage (Fig. 6-18*B*).

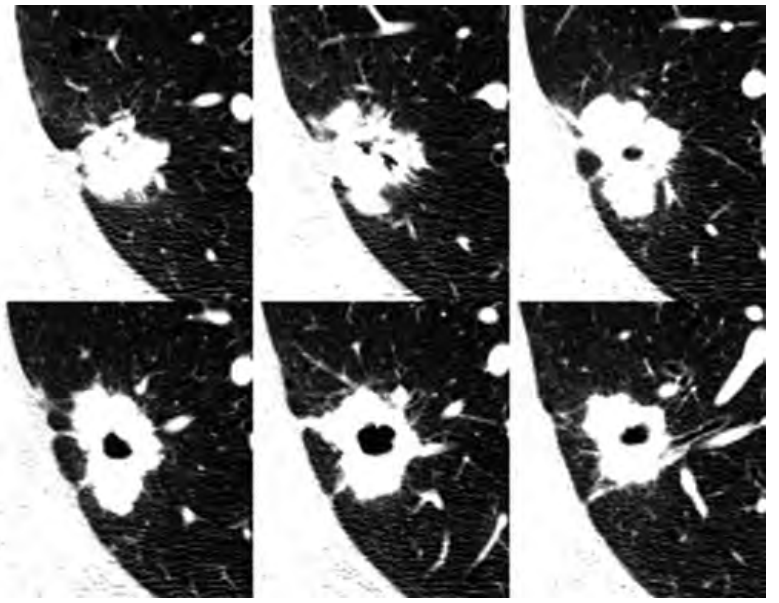

FIGURE 6-16 ■ Spiculated adenocarcinoma with an irregular cavity. Six scans through a nodule were obtained with the spiral technique and 1-mm collimation. The nodule has a lobulated and spiculated margin and contains a thick-walled cavity. Pleural tails are also visible.

Pulmonary Infarction and Septic Embolism

Infarcts can result in a focal pulmonary opacity. Septic emboli are usually multiple. In either instance, nodules typically (1) are peripheral or abut a pleural surface, (2) are round or wedge-shaped, and (3) have a pulmonary artery branch leading to them (the *feeding vessel sign*). Some are associated with a halo sign because of surrounding hemorrhage. In patients with septic embolism, cavitation of lung nodules is common. Using contrast-enhanced CT, associated clots may be identified in the proximal pulmonary artery in patients with pulmonary infarction, but a visible clot is not typical of septic embolism.

The Halo Sign and Angioinvasive Aspergillosis

The halo sign seen on CT was first described in patients with angioinvasive aspergillosis (Fig. 6-19). As indicated in the previous discussion, the term *halo sign* is used to describe a nodule with a soft-tissue attenuation center surrounded by a less dense halo of GGO. In immunosuppressed patients, particularly those with treated leukemia and low white blood cell counts, this appearance is typical and highly suggestive of angioinvasive aspergillosis. Often treatment is begun without confirmation of the diagnosis. In patients with angioinvasive aspergillosis, the halo sign reflects the presence of a septic infarction (the dense center) surrounded by hemorrhage (the halo).

Although suggestive of angioinvasive aspergillosis in the proper clinical setting, the halo sign is nonspecific and can be seen with other infections (tuberculosis, *Legionella*, nocardiosis, and

TABLE 6-2 Classification of Pulmonary Adenocarcinoma (2011)

Premalignant
Atypical adenomatous hyperplasia (AAT)
Preinvasive
Adenocarcinoma in situ (AIS) *
Minimally invasive adenocarcinoma (MIA) *
Invasive adenocarcinoma
Lepidic predominant adenocarcinoma (LPA) *
Invasive adenocarcinoma (various cell types)
Variants of invasive adenocarcinoma
Invasive mucinous adenocarcinoma *
Various cell types

*Newly described histologic types.

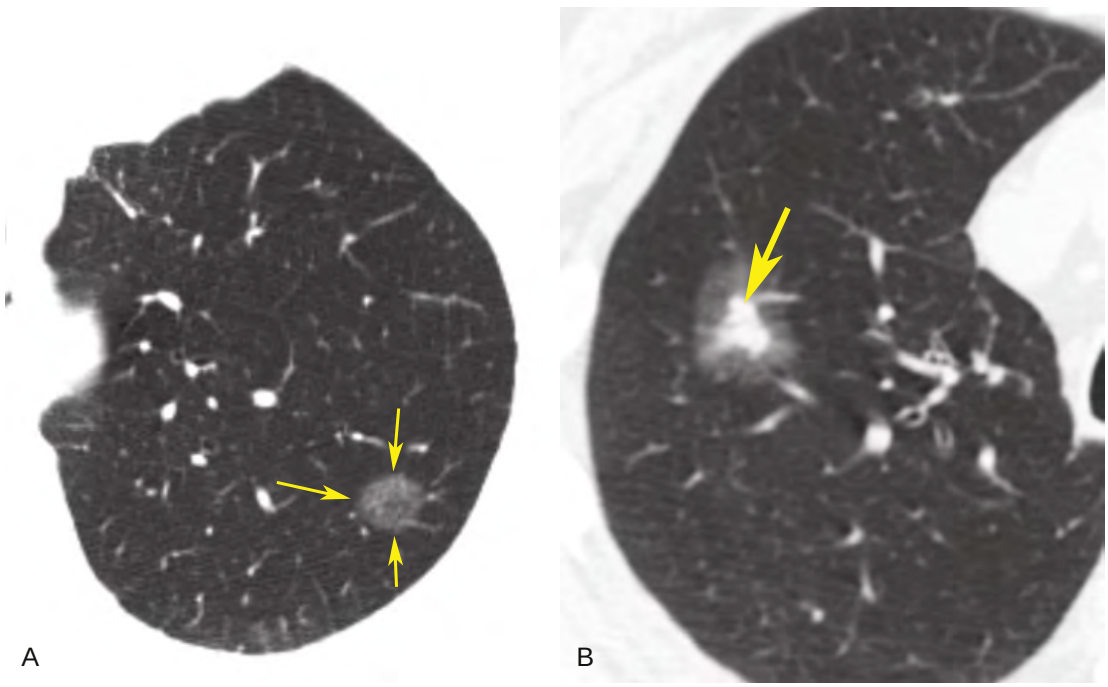

FIGURE 6-17 ■ Two adenocarcinomas associated with ground-glass opacity. *A,* A nodule consisting of pure ground-glass opacity represents an adenocarcinoma in situ (AIS). *B,* A nodule with a dense center (*arrow*) surrounded by a *halo* of ground-glass opacity (the halo sign) represents a lepidic predominant adenocarcinoma (LPA). The soft-tissue attenuation center measures more than 5 mm.

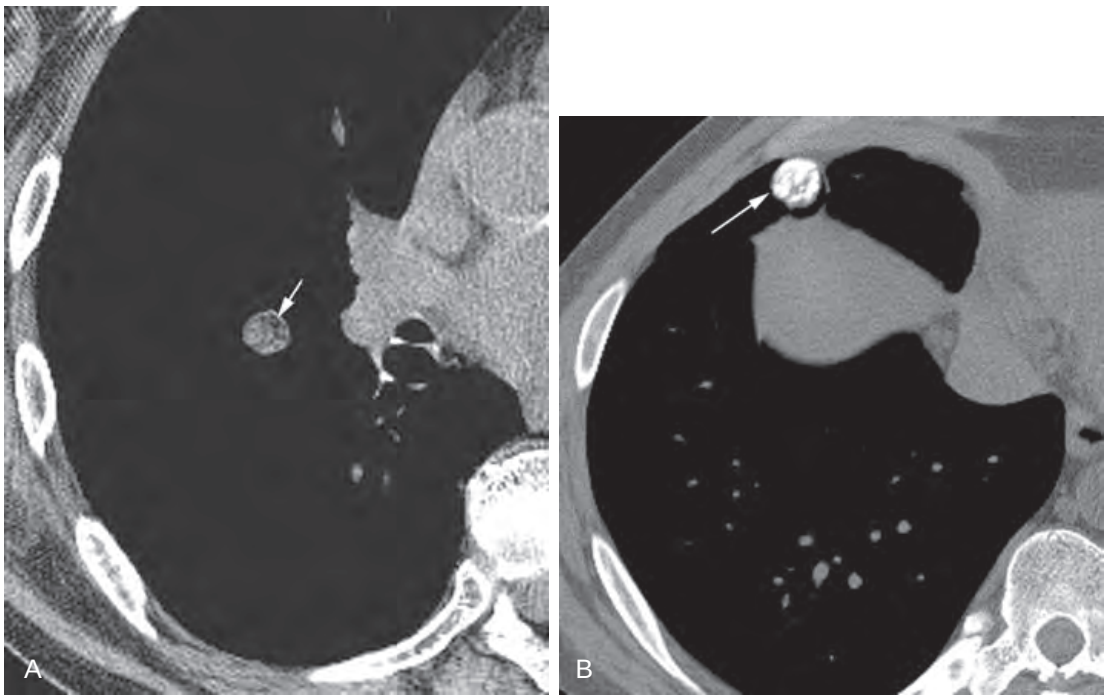

FIGURE 6-18 ■ Hamartoma: common appearances in two patients. *A*, High-resolution computed tomography with soft-tissue (mediastinal) window settings in a patient with a small lung nodule detected on plain films. The nodule is round and sharply defined. It contains areas of low attenuation (*arrow*), indicating the presence of fat. This appearance is diagnostic of hamartoma. *B*, In another patient with hamartoma (*arrow*), a rounded and sharply defined nodule shows "popcorn" calcification. This appearance is seen in some patients with hamartoma.

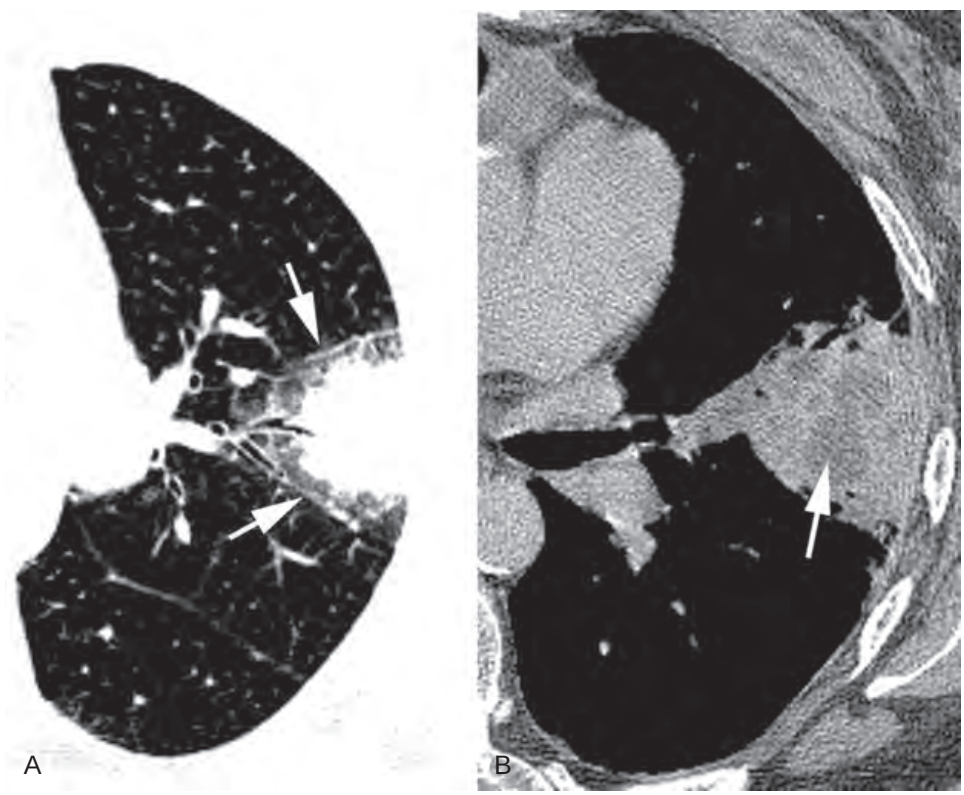

FIGURE 6-19 ■ Invasive aspergillosis with the halo sign. *A*, In an immunosuppressed patient with leukemia, an ill-defined lung mass is surrounded by a less dense *halo* (*arrows*). This finding is highly suggestive of this diagnosis in a patient with the appropriate history. *B*, A soft-tissue window at the same level shows central necrosis (*arrow*).

cytomegalovirus infection), with some tumors (particularly adenocarcinomas, lymphoma, and Kaposi's sarcoma), and in patients with pulmonary infarction and Wegener's granulomatosis. Although the histologic appearance of the halo varies with the entity, it often represents hemorrhage (aspergillosis, Kaposi's sarcoma, infarction, Wegener's granulomatosis), inhomogeneous inflammation (infections), or lepidic tumor growth (adenocarcinoma).

The Air-Crescent Sign and Mycetoma

The presence of a lung mass capped by a crescent of air is termed the *air-crescent sign* (Figs. 6-20 and 6-21). It usually indicates the presence of a mass within a cavity. The air-crescent sign is most typical of mycetoma, but it may also be seen in the later stages of angioinvasive aspergillosis, some bacterial infections with lung infarction, cavitary tumors, a clot or neoplasm within a cavity, and echinococcal cysts.

In patients with a preexisting pulmonary cyst or cavity, a mycetoma or fungus ball can form as a result of saprophytic infection, usually by *Aspergillus* (Fig. 6-21). On CT, a round or oval mass (the fungus ball) can be seen in a dependent location within the cavity and is typically mobile. The mass is capped by a crescent of air. Thickening of the cavity wall is common. In patients with a developing mycetoma, the fungus ball can contain multiple air collections. The same appearance can be seen in semi-invasive (chronic necrotizing) aspergillosis, in which the fungus also invades the wall of the cyst or cavity. Hemorrhage and hemoptysis are common associations. With angioinvasive aspergillosis, septic infarction of the lung can result in an air-crescent sign as the patient recovers (Fig. 6-20).

Lung Abscess and Cavities

A lung abscess can occur with a variety of bacterial, fungal, and parasitic infections. The hallmark of a lung abscess is necrosis or cavitation within an area of pneumonia or dense consolidation; the necrotic region can appear quite irregular. Necrosis is commonly visible on contrast-enhanced CT as one or more areas of low attenuation within opacified lung. Cavitation is said to be present if air is visible within the lesion, and CT is often obtained to confirm this diagnosis when a plain radiograph is suggestive. An air–fluid level or levels are commonly present with bacterial infection (Fig. 6-22) but are uncommon with cavitary carcinoma, tuberculosis, or fungal infection. CT can also be helpful in distinguishing a lung abscess from empyema. Chapter 7 contrasts the CT appearances of lung abscesses and empyema.

Granulomatous Lesions, Infections, and Satellite Nodules

Granulomas usually appear rounded and well defined. They may contain calcium. An infection or granulomatous lesion presenting as a lung nodule or mass may be associated with small nodules adjacent to or surrounding it (i.e., *satellite nodules*;

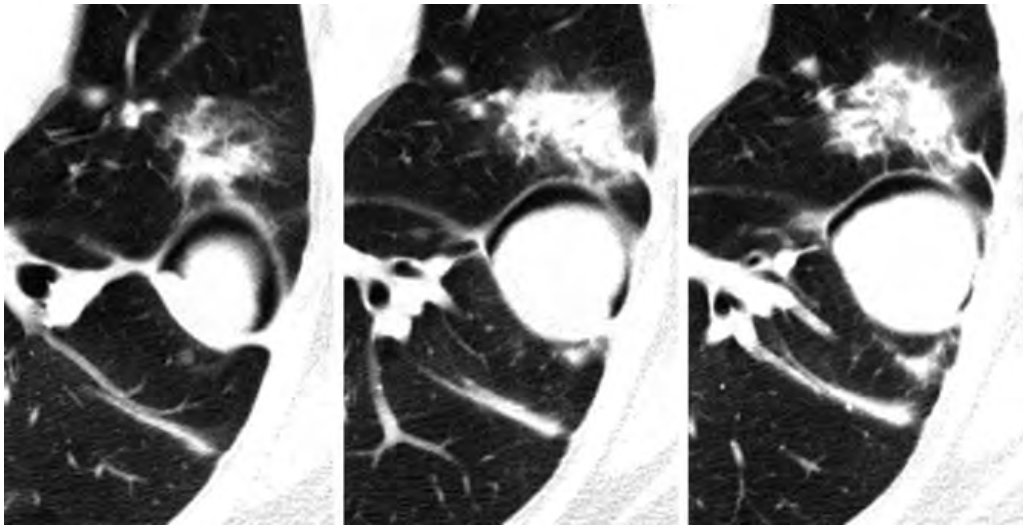

FIGURE 6-20 ■ Invasive aspergillosis with an air-crescent sign. A crescent of air outlines a mass within a cavity. In invasive aspergillosis, the mass represents a ball of infarcted lung and the cavity represents the space the lung used to occupy. This is distinct from aspergilloma, in which an air-crescent sign reflects fungus within a preexisting cavity. Focal consolidation due to acute infection is visible anterior to the cavitary lesion.

(Fig. 6-23). In patients with sarcoidosis, this appearance has been referred to as the *galaxy sign*. Satellite nodules may also be seen with lung carcinoma (Table 4-3), but they are evident in only a few percent of cases.

Tuberculosis (TB) and Atypical Mycobacterial Infection

In most patients with TB exposure and a positive PPD, CT is normal. A small lung nodule, calcified or uncalcified and representing the original site of infection, is sometimes visible; associated calcified lymph nodes may be present. Small nodules in the lung apex reflect the presence of hematogenous spread at the time of the original infection. In most patients, these heal without progression.

In a small percentage of individuals, usually children and immunosuppressed patients, primary exposure to TB results in a focal pneumonia (which may involve any lobe). In half of these cases, associated hilar or mediastinal node enlargement is present. Nodes often appear to be low in attenuation on enhanced CT.

Progression of primary TB (often in immunologically incompetent patients) or post-primary reactivation of an earlier infection (usually in the lung apices) can result in cavitary TB (Fig. 6-24). Cavities are usually irregular in shape, with

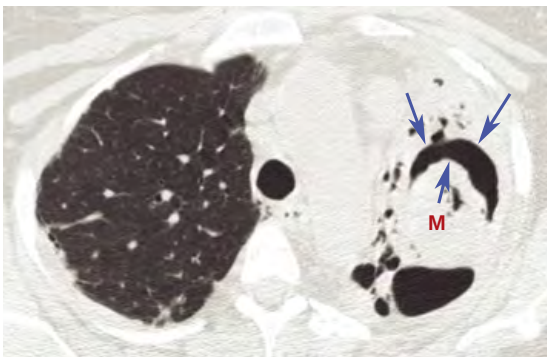

FIGURE 6-21 ■ Mycetoma in a patient with a preexisting cavity. A crescent of air (*arrows*) outlines a mass (mycetoma, M) within a cavity resulting from a prior tuberculosis infection. The mass was mobile and changed position when the patient was prone.

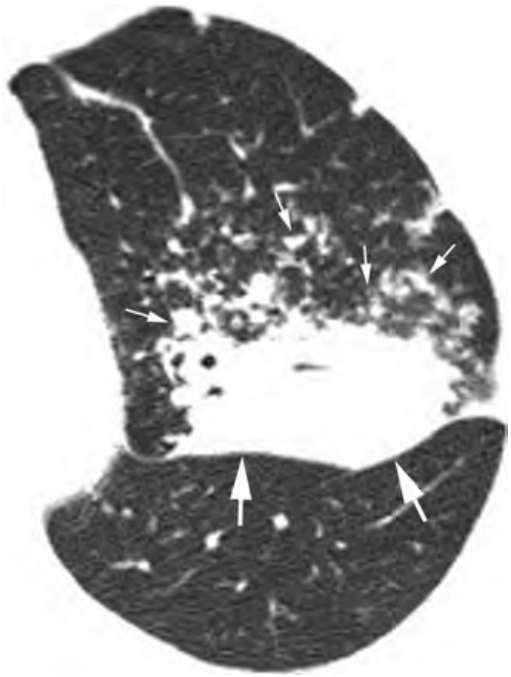

FIGURE 6-23 ■ Satellite nodules in sarcoidosis. High-resolution computed tomography (HRCT) in a patient with sarcoidosis and a left upper lobe mass, marginated posteriorly by the major fissure (*large arrows*). On HRCT, the mass is surrounded by a number of smaller *satellite nodules* (*small arrows*). This appearance is most typical of a granulomatous process. It has also been referred to as the *galaxy sign*.

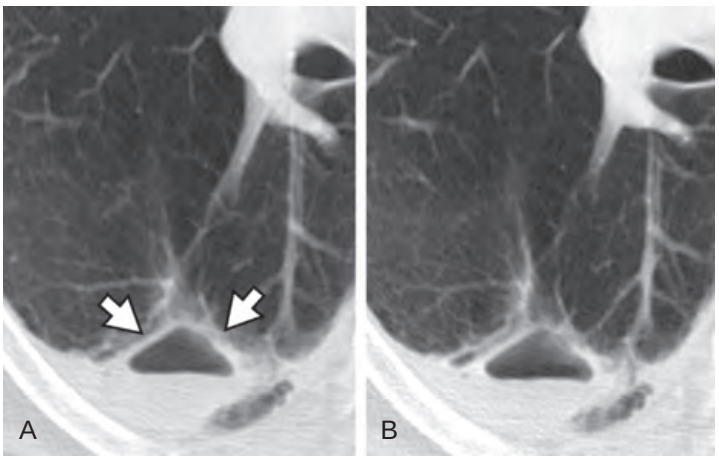

FIGURE 6-22 ■ Lung abscess. *A* and *B*, A thin-walled lung abscess (*arrows*) is visible in the posterior lung and contains an air–fluid level.

irregular walls and multiple septations. Air–fluid levels are typically absent, although hemorrhage or superinfection may produce this finding. Cavities may be multiple and associated with satellite nodules. The spread of infected material through the airways can result in findings of bronchopneumonia (i.e., patchy consolidation, tree-in-bud or centrilobular nodules), often in regions near the cavity or in the lower lobes (Fig. 6-24). Tree-in-bud and centrilobular nodules are described in the section of this chapter devoted to high-resolution computed tomography (HRCT).

Infection with pathogenic atypical mycobacteria can result in identical findings. Fungal infections can also result in findings indistinguishable from TB. If TB is considered in the differential diagnosis, it is generally a good idea to consider fungi as well.

Lipoid Pneumonia

Chronic aspiration of lipid (animal, vegetable, or mineral) can lead to lipoid pneumonia, with fat and variable amounts of fibrosis resulting in focal consolidations or masses. In some patients, most typically those with mineral oil aspiration, CT shows low-attenuation (–50 to –140 HU) consolidation indicative of its lipid content. When fibrosis predominates, the masses are of soft-tissue attenuation. Lipoid pneumonia differs from hamartoma, which may also contain fat, in that masses are larger and less well defined and usually appear more irregular.

Pleural (Fissural) Lesions

Small (a few mm) perifissural nodules are commonly seen on CT and are generally of no concern. Often they are flat or triangular in shape. However, small rounded nodules with minimal fissural contact may represent a significant abnormality, and follow-up may be appropriate.

Occasionally, a pleural abnormality located in a fissure (e.g., a plaque, loculated effusion, or localized fibrous tumor of the pleura) may be misinterpreted as a lung nodule. Looking for the fissures on the CT will sometimes avoid this mistake.

CT Diagnosis of Nodule Calcification

CT may show nodule calcification, indicating that the nodule is benign and that resection is not necessary. About 25% to 35% of benign nodules appearing uncalcified on radiographs show calcification on thin slices.

CT with thin slices is optimum, but dense calcification can also be seen using a 5-mm slice thickness. Soft-tissue window settings are best for proving the presence of calcium.

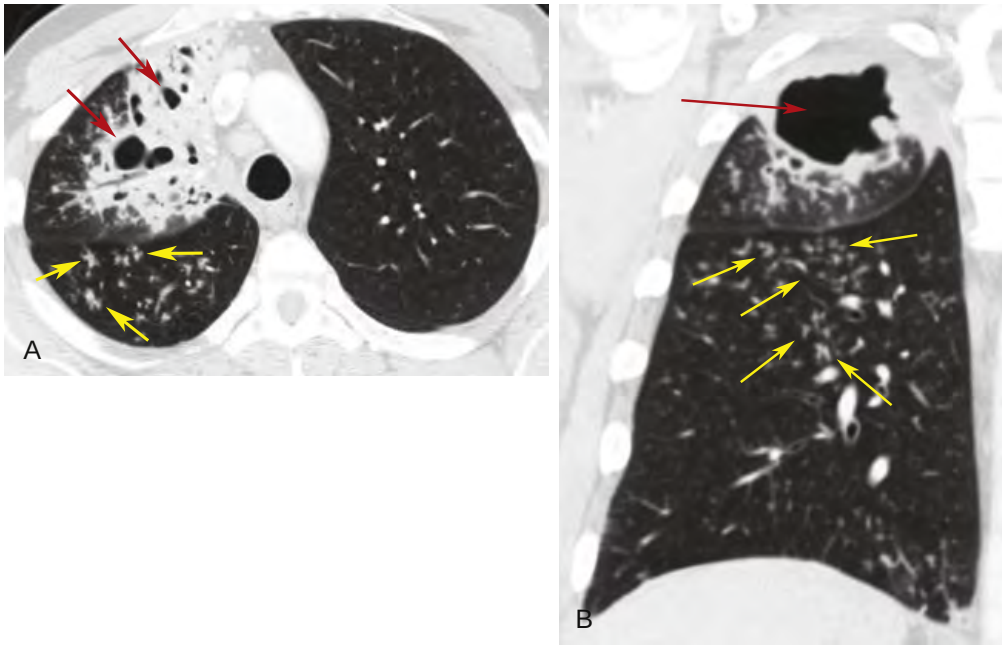

FIGURE 6-24 ■ Tuberculosis with endobronchial spread and tree-in-bud opacity. *A* and *B*, In a patient with active tuberculosis, irregular cavitary lesions (*red arrows*) are visible in the right lung apex. Centrilobular nodules and branching tree-in-bud opacities (*yellow arrows*) in the adjacent lung represent endobronchial spread of infection and are common in active tuberculosis.

When using CT to diagnose "benign" calcification, the radiologist must be sure that the calcification is benign in appearance (Fig. 6-25*A*). To be reasonably sure of a benign diagnosis, one of the following must be seen: (1) diffuse calcification (Fig. 6-25*B*), typical of a granuloma; (2) dense, central (i.e., *bull's-eye*) calcification, most typical of histoplasmosis (Fig. 6-25*C*); (3) central and *popcorn* calcification, typical of hamartoma (Fig. 6-18*B*); or (4) concentric rings of calcification (*target* calcification; Fig. 6-25*D*), typical of histoplasmosis. Nodules that show visible calcification will generally have CT numbers exceeding 100 to 200 HU.

About 5% to 10% of carcinomas contain some calcium, either as a result of tumor calcification or because the carcinoma has engulfed a

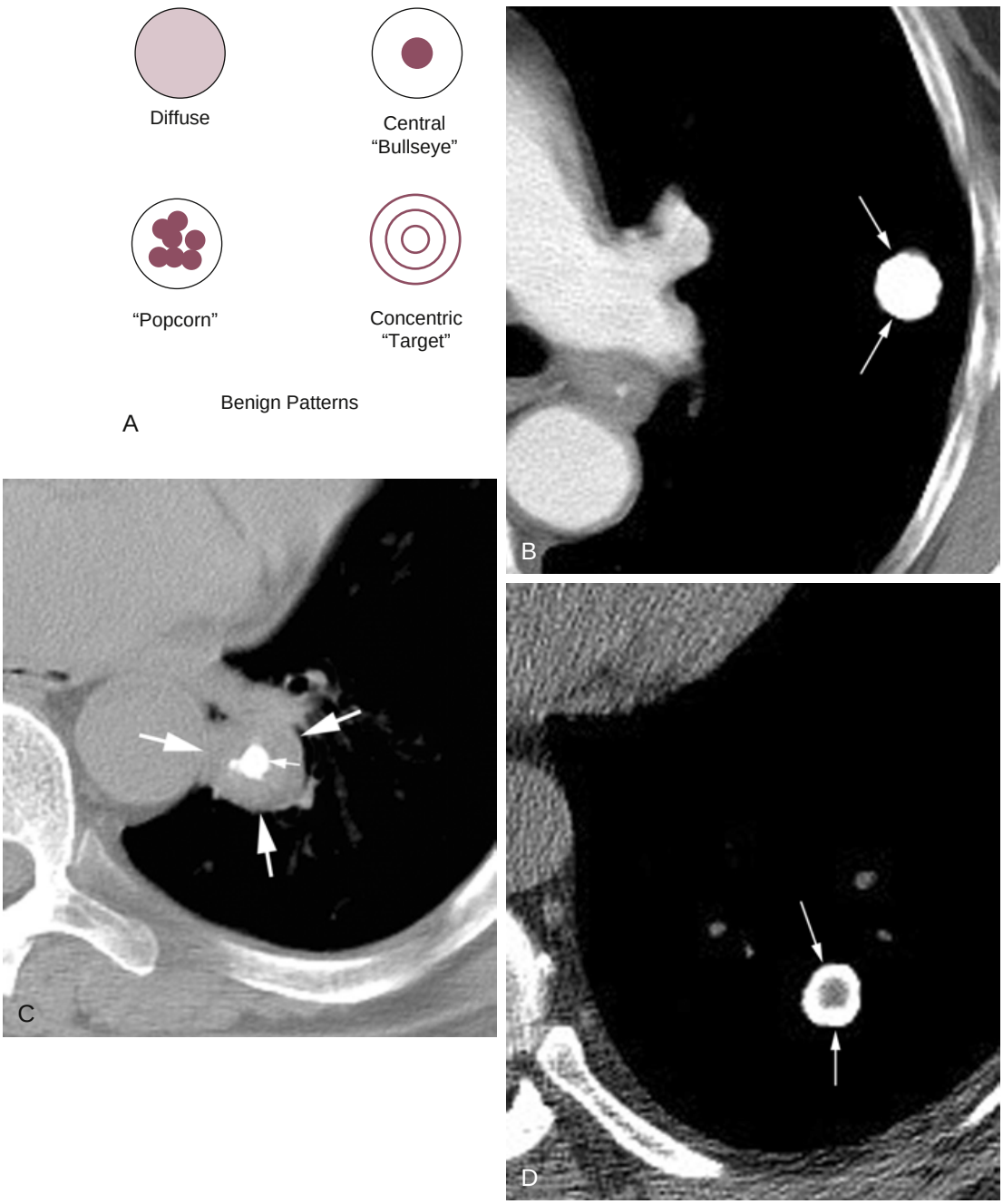

FIGURE 6-25 ■ Benign patterns of calcification. *A*, Patterns of calcification typically associated with benign nodules. *B*, Diffuse nodule calcification (*arrows*) in tuberculoma. *C*, A left lower lobe nodule (*large arrows*) shows dense central (bull's-eye) calcification (*small arrow*). *D*, A concentric ring of calcification (*arrows*) outlines a lung nodule.

preexisting granuloma. Calcification in malignancies is typically punctate or stippled, or is eccentric within the nodule (Fig. 6-26). Although these patterns of calcification may also be seen in benign lesions, when one is interpreting CT, they should be considered to be indeterminate or potentially associated with malignancy (Fig. 6-26*A*). A caveat is that sarcomas and carcinoid tumors may be associated with dense calcification that is either homogeneous or "chunky."

Nodule Opacification

Lung cancers have a greater tendency to be enhanced after contrast infusion than many benign lesions do. Using a specific protocol, contrast enhancement greater than 15 HU is sensitive in detecting cancers, but some benign lesions, such as benign tumors and active granulomatous lesions, are also enhanced. This technique is not commonly used in clinical practice and has largely been replaced by positron emission tomography (PET) combined with CT (CT-PET).

FIGURE 6-26 ■ Indeterminate calcification. *A,* Patterns of calcification that may be seen in either benign or malignant nodules. *B,* Thin-slice computed tomography in a patient with an adenocarcinoma in the lingula shows a nodule with eccentric calcification. Eccentric calcification can be seen in carcinomas.

Nodule Growth Rate and CT Follow-Up of Lung Nodules

The growth rate of a nodule, measured as the time required for doubling of volume (corresponding to a 26% increase in nodule diameter), may be used to determine its likelihood of being malignant. A pulmonary nodule that doubles in volume in less than 1 month or more than 16 months is usually benign. However, the overlapping growth rates of benign and malignant lesions make it difficult to use doubling time as an absolute indicator of malignancy. In the author's opinion, malignancy should be suspected if any growth occurs, no matter how slow; some lung cancers have a doubling time exceeding 1000 days. Carcinomas appearing on CT as a nodule of GGO or mixed GGO and soft tissue have slower growth rates and doubling times than those of invasive adenocarcinomas that appear solid on CT.

Small, nonspecific pulmonary nodules are very commonly seen on CT obtained for other reasons. CT is commonly used to follow a newly detected lung nodule(s) to determine the presence or absence of growth, when the nodule size or appearance or clinical factors do not indicate that a more aggressive approach is needed. It is generally agreed that a solitary pulmonary nodule that does not grow over a 2-year period is very likely benign and does not require resection.

The Fleischner Society has recently published recommendations for the CT follow-up of nonspecific lung nodules appearing solid on CT (Table 6-3) and solitary or multiple nodules that are entirely or partially GGO (Tables 6-4 and 6-5). These have been widely adopted.

In general, for an incidentally detected nodule (or nodules) that appears solid on CT, if the patient has no risk factors for lung cancer (e.g., is not a smoker) and the nodule is ≤ 4 mm in diameter, no follow-up is required (Table 6-3). If the patient is a smoker, then follow-up CT at 1 year is sufficient. For lung nodules larger than 4 mm, follow-up CT is obtained at shorter intervals, and if the nodule exceeds 8 mm, a more aggressive approach may be taken (Table 6-3). If the patient has a known cancer, then a nodule of any size will be followed; the follow-up interval is generally determined by clinical considerations.

For nodules of GGO or mixed GGO and solid attenuation, an initial follow-up at 3 months is recommended (since some GGO nodules resolve), and if the nodule persists, then follow-up for at least 3 years is recommended. PET scanning has high sensitivity (97%) and specificity (80%) in diagnosing cancers that are 1 cm or larger and appear solid on CT. Its sensitivity in the diagnosis of carcinomas appearing as a GGO

TABLE 6-3 Fleischner Society Recommendations for CT Follow-up (FU) of Solid Nodules *

Nodule Size	Low-Risk Patient	High-Risk patient
≤ 4 mm	No FU CT needed (FU is optional)	FU CT at 12 months; if unchanged, no further FU
> 4–6 mm	FU CT at 12 months; if unchanged, no further FU	FU CT at 6–12 months, then at 18–24 months if no change
> 6–8 mm	FU CT at 6–12 months, then at 18–24 months if no change	FU CT at 3–6 months, then at 9–12 and 24 months if no change
> 8 mm	Options: FU CT at 3, 9, and 24 months; positron emission tomography; biopsy; video-assisted thoracic surgery	

*Nodule size is average of length and width. Low-risk patient, minimal or absent history of smoking or other known risk factors; high-risk patient, history of smoking or other known risk factors.

TABLE 6-4 Fleischner Society Recommendations for CT Follow-up (FU) of Solitary Ground-Glass Opacity (GGO) or Part-GGO Nodules

Nodule Type	Recommendation	Additional Remarks
Solitary pure GGO ≤ 5 mm	No FU CT required	Use 1-mm slices to confirm nodule is pure GGO
Solitary pure GGO > 5 mm	FU CT at 3 months; if persistent, yearly FU for at least 3 years	Positron emission tomography of limited value and not recommended
Solitary part-solid nodules	FU CT at 3 months; if persistent and solid component < 5 mm, yearly FU for at least 3 years; if persistent and solid component ≥ 5 mm, then biopsy or resection	Consider positron emission tomography if nodule > 1 cm

TABLE 6-5 Fleischner Society Recommendations for CT Follow-up (FU) of Multiple Ground-Glass Opacity (GGO) or Part-GGO Nodules

Nodule Type	Recommendation	Additional Remarks
Multiple pure GGO ≤ 5 mm	FU CT at 2 and 4 years	Consider alternate cause for GGO nodules
Multiple pure GGO > 5 mm; no dominant lesion	FU CT at 3 months; if persistent, yearly FU for at least 3 years	Positron emission tomography of limited value and not recommended
Dominant part-solid nodule(s)	FU CT at 3 months; if persistent, then biopsy or resection, particularly if solid component ≥ 5 mm	Consider lung-sparing surgery in patients with a dominant lesion suspicious for lung cancer

nodule is low. It is not generally recommended in evaluation of a GGO nodule.

In obtaining follow-up CT to assess a small lung nodule(s) for change in size, it is important to obtain scans with the same slice thickness and view them with the same window settings as in the original study. With spiral CT and volumetric imaging, nodules are not usually missed, but it is possible if the patient breathes during the study. When looking for or comparing nodule size, it is important to look at exactly the same levels on the two scans. Identifying and matching the pattern of branching vessels in the peripheral lung in the region of the nodule is the only way of knowing exactly what level is being viewed. If the same vessels are visible on both the original and follow-up scans and the nodule looks different, then the nodule is different. If a different branching pattern is visible, then an apparent difference in nodule size may not be real.

On occasion, a lung cancer can show a transient decrease in size on follow-up. A single

follow-up scan showing a decrease in nodule size is not sufficient to call the nodule benign. A second scan showing a continued decrease in size or resolution should be obtained.

CT Lung Cancer Screening

CT is used to screen patients at high risk of lung cancer because of smoking history. Comparing CT screening to screening with chest radiographs, more lung cancers, smaller lung cancers, and more early-stage (stage 1) cancers are detected using CT. However, false positives are common (up to 70% of screened patients in some parts of the country show at least one lung nodule).

The results of the National Lung Cancer Screening Trial (NLST) have recently been reported. In this study, more than 52,000 high-risk patients were randomly screened using low-dose CT with 2- to 3-mm-thick slices or chest radiographs and followed with annual screenings for up to 5 years. On initial CT screening, 27% of subjects had at least one nodule ≥4 mm in size, and about 40% had at least one nodule detected by CT during the study. CT, compared to chest radiographs, was more sensitive (94% vs. 74%) and less specific (74% vs. 91%) in detecting cancer. Overall, about 1.1% of CT-screened subjects were found to have lung cancer. Subjects screened using CT had a 20% reduction in lung cancer mortality and a reduction in overall mortality of 6.7% (the more important result).

Use of CT to Guide Biopsy of a Lung Nodule

Bronchoscopy is most accurate in diagnosing central masses that have an endobronchial component, whereas needle biopsy is best for peripheral lung lesions. For lesions in the central half of the lung, if an endobronchial abnormality is seen on CT or a *bronchus sign* (bronchial narrowing or obstruction at the site of a nodule, or a bronchus within the mass lesion) is visible, bronchoscopy directed to the proper site may be attempted. If there is no evidence of an abnormal bronchus on CT or if the nodule is peripheral, needle biopsy should be performed first. CT is usually used for needle aspiration biopsy of lung nodules. It allows precise localization of the needle tip within the nodule and allows the least dangerous approach to the nodule to be chosen (avoiding bullae, large vessels, etc.).

Thoracoscopic biopsy or resection of peripheral lung nodules can be assisted by CT-guided localization techniques. These may involve injection of methylene blue into lung adjacent to the nodule or placement of a hooked wire within the nodule.

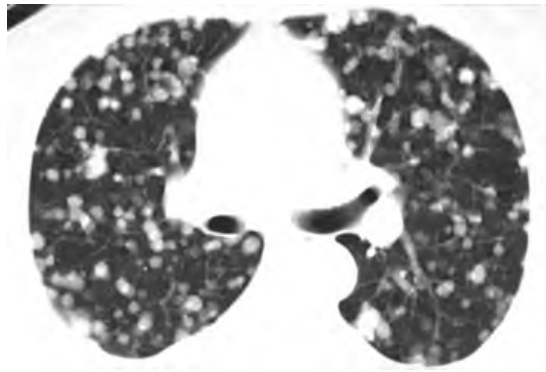

FIGURE 6-27 ■ Pulmonary metastases. Computed tomography shows multiple nodules with a diffuse distribution. Despite their small size, the nodules are sharply defined. This pattern of nodules is termed *random.*

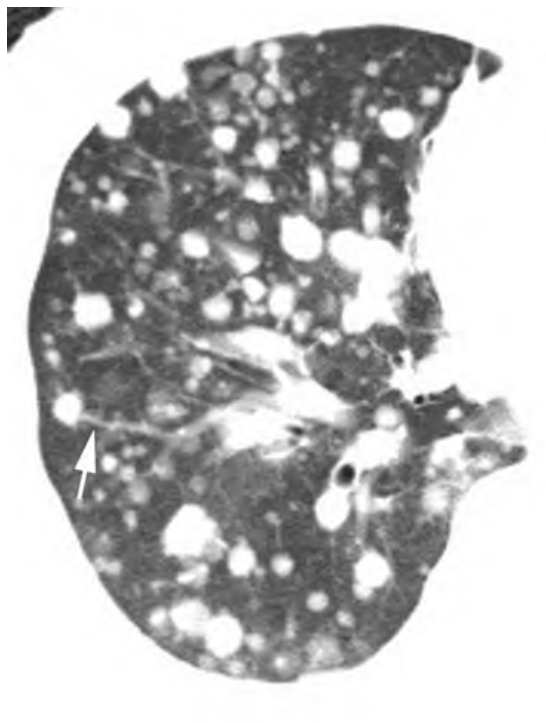

FIGURE 6-28 ■ Pulmonary metastases with the feeding vessel sign. Multiple well-defined nodules represent metastases from a renal cell carcinoma. Involvement of the peripheral lung is typical. A few of these nodules (*arrow*) appear to be related to a pulmonary vessel, the so-called *feeding vessel sign.*

MULTIPLE LUNG NODULES AND MASSES

CT is much more sensitive than plain radiographs in detecting lung nodules. Nodules as small as a few millimeters can be easily detected using CT (Figs. 6-27 and 6-28).

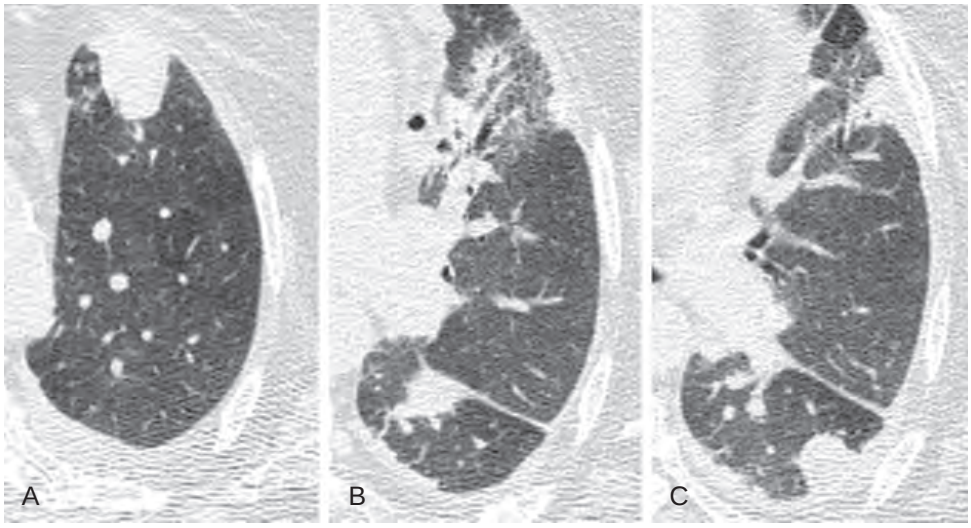

FIGURE 6-29 ■ Nocardiosis with multiple nodules. *A* to *C,* Multiple ill-defined nodules reflect nocardia pneumonia in an immunosuppressed patient.

The differential diagnosis of multiple pulmonary nodules and masses includes many of the entities producing solitary nodules (Table 6-1), such as metastases; lymphoma; bronchogenic carcinoma with synchronous primary tumors; bacterial (Fig. 6-29), fungal, and sometimes viral infections; granulomatous diseases; sarcoidosis; Wegener's granulomatosis; rheumatoid lung disease; amyloidosis; and septic embolism. In most cases, the CT appearance of such nodules is nonspecific. The differential diagnosis of diffuse lung disease characterized by numerous small nodules is reviewed in the section on HRCT and diffuse infiltrative lung disease.

Metastases

Hematogenous pulmonary metastases are typically diffuse or have a predilection for the peripheral and subpleural lung (Figs. 6-27 and 6-28); they may be small or large. Pulmonary metastases are typically round and well defined (Fig. 6-27). Some metastases with a surrounding hemorrhage can be ill defined or associated with the halo sign. Cavitation and calcification can be seen with some metastatic tumors. Pulmonary metastases may be seen to have a connection to a pulmonary artery branch, reflecting their embolic nature (i.e., the *feeding vessel sign*; Fig. 6-28). However, this finding can be present for other causes of pulmonary nodules, such as Wegener's granulomatosis and bland or septic emboli.

Small scattered pulmonary nodules are commonly seen on CT, most of which represent normal subpleural lymphoid aggregates and granulomas. Because nodules of less than 5 mm are too small to biopsy, follow-up CT in 3 months is usually used to assess the significance of small nodules in patients with a known tumor. Metastases typically increase in size in untreated patients.

Invasive Mucinous Adenocarcinoma

In the current classification of pulmonary adenocarcinoma reviewed in the previous discussion, what was formerly referred to as diffuse or multifocal bronchioloalveolar carcinoma is now termed *invasive mucinous adenocarcinoma*. This tumor presents with diffuse or patchy lung consolidation or GGO, or multiple lung nodules that may be centrilobular in location (Fig. 6-30). Although mucinous adenocarcinoma is associated with lepidic growth, the tumor cells secrete mucin, which fills the alveoli and results in the visible consolidation. The presence of visible opacified arteries within an area of consolidation on contrast-enhanced CT (termed the *CT angiogram sign*) has been reported to be suggestive of this tumor, but the same appearance can also be seen for other causes of consolidation, such as pneumonia. Bronchorrhea (excessive watery sputum production) can be associated with invasive mucinous adenocarcinoma.

Lymphoma and Lymphoproliferative Disease

Pulmonary parenchymal involvement is seen in 10% of patients with Hodgkin's disease at the time of presentation. Direct extension from hilar nodes, focal discrete areas of consolidation, or mass-like lesions can be seen. Air bronchograms or areas of cavitation may be visible within the abnormal regions. In patients with untreated

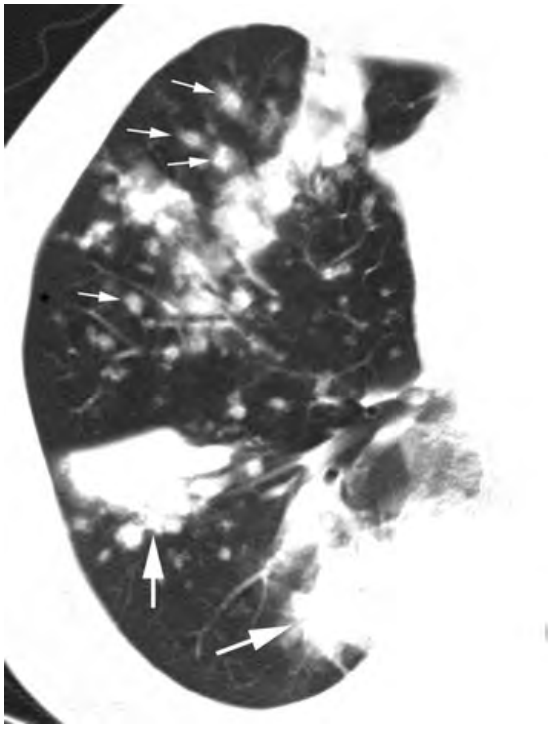

FIGURE 6-30 ■ Invasive mucinous adenocarcinoma with consolidation and multiple nodules. Focal areas of consolidation (*large arrows*) are visible in the right lung. Multiple nodules (*small arrows*) are also visible; these nodules are usually centrilobular in location and reflect endobronchial spread of tumor tissue.

Hodgkin's disease, lung involvement usually does not occur in the absence of radiographically demonstrable mediastinal (and usually ipsilateral hilar) adenopathy.

In patients with non-Hodgkin's lymphoma, pulmonary disease can occur in the absence of lymph node enlargement (i.e., primary pulmonary lymphoma). This is common in patients with acquired immunodeficiency syndrome. Large, ill-defined nodules can be seen.

Other lymphoproliferative diseases, such as *focal lymphoid hyperplasia* and *post-transplantation lymphoproliferative disorder* (*PTLD*), can also result in multiple pulmonary nodules or masses.

Infections

In immunosuppressed patients, multiple nodules or masses suggest a fungal or, less likely, a nontuberculous mycobacterial or bacterial (e.g., nocardia) infection. The nodules may show the halo sign or cavitation. Aspergillus infection is most common among the fungal organisms in immunosuppressed patients.

Community-acquired fungal (e.g., histoplasmosis, coccidioidomycosis, blastomycosis, and cryptococcosis) and nontuberculous mycobacterial infections can be seen in immunocompetent patients. Focal consolidation or a solitary nodule or mass is more common than multiple nodules or masses, except when a massive inoculation of organisms has occurred (e.g., multinodular histoplasmosis in a cave explorer).

Amyloidosis

Patients with localized nodular amyloidosis are usually asymptomatic. Nodular amyloidosis may manifest as single or multiple lung nodules or masses that are usually well defined and round. Bilateral lung nodules are most typical, and they tend to be peripheral or subpleural in location. Nodules range from 0.5 to 5 cm in diameter in most cases but may be as large as 10 cm. Calcification is visible radiographically in 30% to 50% of cases, and may be stippled or dense. Cavitation may be seen in approximately 5% of cases. Nodules may grow slowly or remain stable over a number of years.

Granulomatosis with Polyangiitis (Wegener's Granulomatosis)

Granulomatosis with polyangiitis (Wegener's granulomatosis) is a multisystem disease of unknown cause associated with involvement of the upper respiratory tract (nasal, oral, or sinus inflammation), lower respiratory tract (airway or lung), and kidney. The presence of cytoplasmic antineutrophilic cytoplasmic antibody (c-ANCA) is characteristic and is seen in 90% of cases. Patients are usually between the ages of 30 and 60 years.

Multiple lung masses or cavities 2 to 4 cm in diameter are typical (Fig. 6-31). Usually, fewer than a dozen nodules or masses are visible. A solitary nodule or mass may be seen, but this appearance is less common. With progression of the disease, nodules and masses tend to increase in size and number. With treatment, nodules usually resolve over a period of months. Typically, cavitary nodules and masses become thin-walled and decrease in size with treatment. Complete resolution may occur.

AIRWAY ABNORMALITIES

The Trachea

The trachea extends inferiorly from the thoracic inlet for a distance of 8 to 10 cm before bifurcating into the right and left main bronchi. The trachea is usually round or oval in shape and approximately 2 cm in diameter. In some patients, the trachea appears somewhat triangular, with the

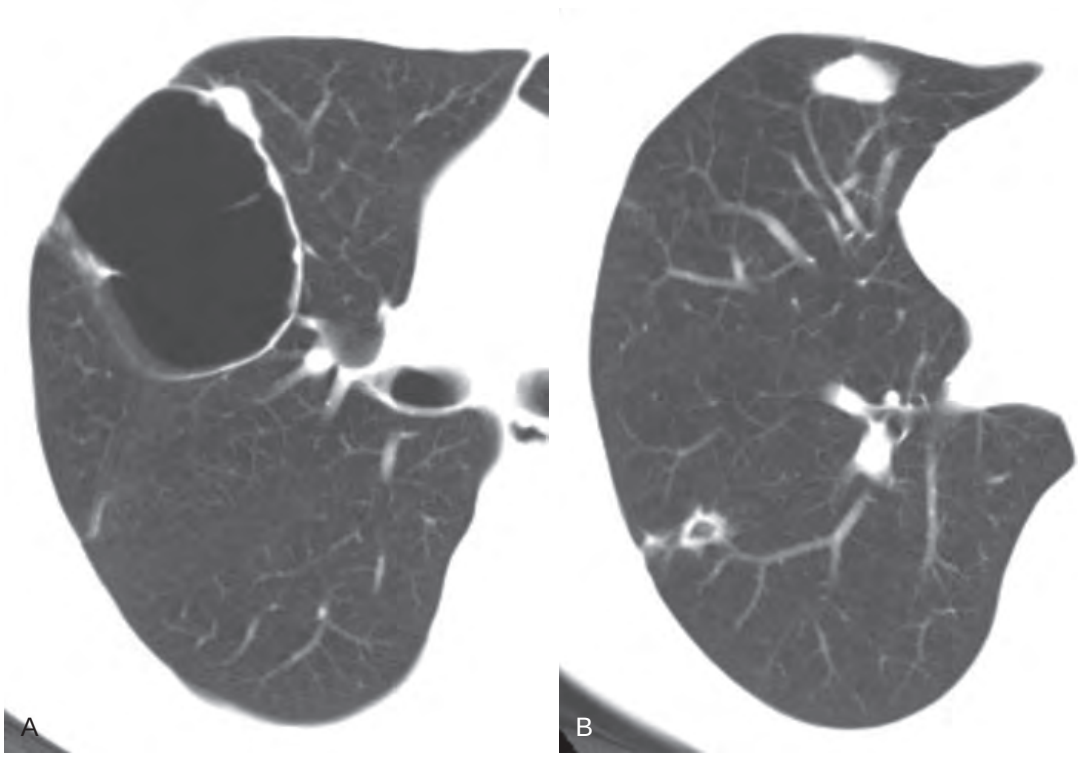

FIGURE 6-31 ■ Granulomatosis with polyangiitis (Wegener's granulomatosis). *A* and *B,* Thin-walled cavities and nodules are present.

apex of the triangle directed anteriorly. This appearance is particularly common at the level of the carina and proximal main bronchi. Tracheal cartilage may be visible as a relatively dense horseshoe-shaped structure within the tracheal wall, with the open part of the horseshoe being posterior; calcification of tracheal cartilage is common in older patients, particularly women. The tracheal wall should measure no more than 2 or 3 mm in thickness. The posterior tracheal membrane, which contains no cartilage, is very thin and may bow anteriorly with expiration.

Tracheal abnormalities are often associated with narrowing of the tracheal lumen. They can be considered as focal or diffuse. Tracheal abnormalities are uncommon and may be asymptomatic unless the tracheal lumen is reduced to a few millimeters in diameter.

Focal Tracheal Abnormalities

Tracheal stenosis occurring because of previous intubation is a relatively common abnormality. It usually results in an hourglass narrowing of the trachea at the former site of the endotracheal tube balloon or tip. Narrowing of the tracheal lumen may be associated with intratracheal soft-tissue masses of reactive (granulation) tissue or collapse of the tracheal wall because of destruction of the tracheal rings and associated fibrosis.

FIGURE 6-32 ■ Tracheal carcinoma (adenoid cystic carcinoma). The tumor is arising from the posterior tracheal wall and narrows the tracheal lumen. An extrinsic mass (*arrows*) is present.

Primary tracheal tumors are rare. The most common primary malignancies, occurring in approximately equal numbers, are squamous cell carcinoma and cylindroma (adenoid cystic carcinoma) (Fig. 6-32). Adenoid cystic carcinoma commonly arises from the posterior tracheal wall and is most common in the upper trachea; squamous cell carcinoma is most common in the distal trachea. CT can be helpful in choosing treatment

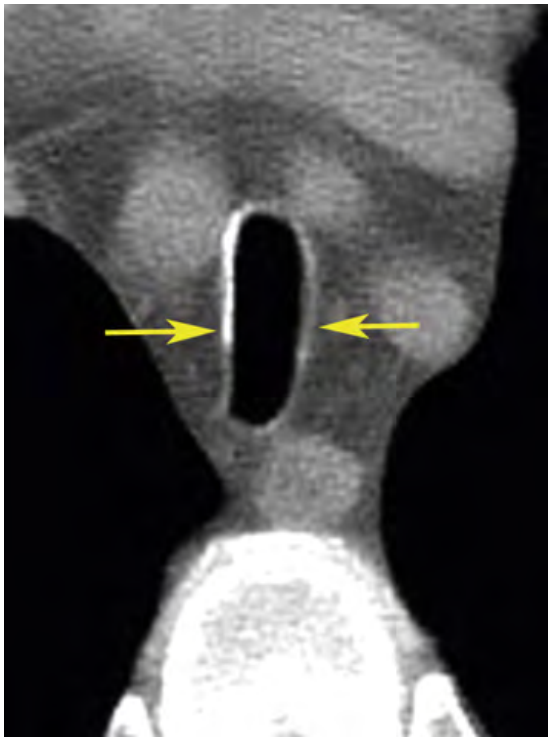

FIGURE 6-33 ■ Saber-sheath trachea. There is side-to-side narrowing of the trachea (*arrows*). The tracheal wall is normal in thickness. Calcification of the tracheal cartilage is present.

in a patient with a tracheal tumor. If there is no mediastinal invasion (as evidenced by a mediastinal mass), the lesion may be curable with a partial tracheal resection.

Mediastinal tumors may compress, displace, or invade the trachea. Unless a tumor can be seen within the tracheal lumen, tracheal invasion is difficult to diagnose with confidence. The trachea can be involved by lung cancer as a result of direct extension from a tumor arising in a main bronchus; bronchogenic carcinomas involving the trachea or carina are usually considered unresectable (T4). Thickening of the carina or tracheal wall contiguous with a bronchial lesion suggests this diagnosis, but bronchoscopy is usually required for a definite diagnosis.

Diffuse Tracheal Abnormalities

Saber-sheath trachea is a common tracheal abnormality occurring in patients with chronic obstructive pulmonary disease. In this condition, there is side-to-side narrowing of the intrathoracic trachea, probably because of the repeated trauma of coughing, with the anterior-to-posterior tracheal diameter being preserved or increased (Fig. 6-33); the extrathoracic trachea is normal. A focal

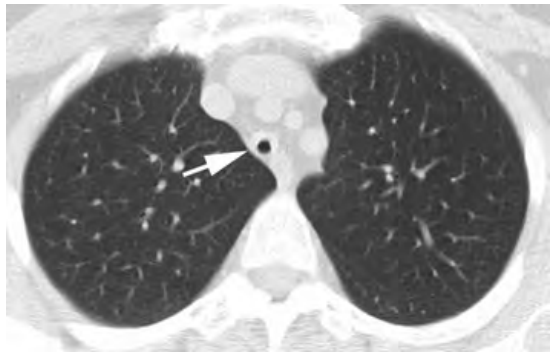

FIGURE 6-34 ■ Tracheal narrowing caused by polychondritis. The trachea is markedly narrowed (*arrow*) in a concentric fashion. This appearance is distinctly different from that of a saber-sheath trachea. In this patient, the trachea was diffusely narrowed, as were the main bronchi.

segment of the trachea at the thoracic inlet may be involved first. The tracheal wall is of normal thickness.

Polychondritis (Fig. 6-34) is an autoimmune disease involving cartilage, including the tracheal cartilage, ears, and joints. It results in thickening of the anterior and lateral tracheal walls (where the cartilage is) because of inflammation and narrowing of the tracheal lumen. The intrathoracic and extrathoracic trachea are both involved.

Granulomatosis with polyangiitis (*Wegener's granulomatosis*) may involve the trachea and main bronchi, with thickening of the tracheal wall and narrowing of its lumen. It is most common in the subglottic trachea but may be diffuse.

Amyloidosis may involve the trachea and main bronchi, with diffuse or multifocal wall thickening and narrowing. Calcification is often present.

Other diseases that in rare cases involve the trachea and main bronchi include TB, scleroma, invasive tracheobronchial aspergillosis, sarcoidosis, and tracheobronchopathia osteochondroplastica.

Central Bronchial Abnormalities

The most common abnormalities of the central bronchi are compression by enlarged mediastinal or hilar lymph nodes or extrinsic masses, and bronchial tumors, as described in Chapters 4 and 5.

Bronchiectasis

Bronchiectasis is defined as irreversible bronchial dilatation. It is commonly associated with chronic infection and sputum production.

Spiral CT obtained with thin slices should be used to diagnose bronchiectasis. In normal patients, a bronchus and its adjacent pulmonary

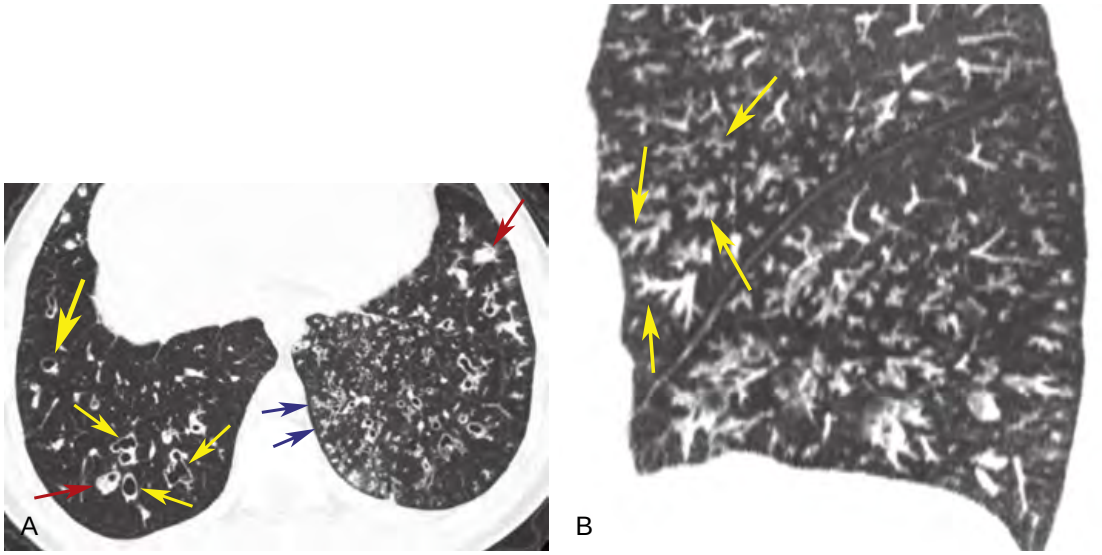

FIGURE 6-35 ■ Bronchiectasis in a patient with ciliary dysmotility. *A,* High-resolution computed tomography shows bronchiectasis at the lung bases. Thick-walled and irregularly dilated bronchi are visible in the right lower lobe (*yellow arrows*). Their appearance would be classified as cylindrical or varicose. The dilated bronchi are considerably larger than the adjacent pulmonary artery and are examples of the *signet ring sign* (*large yellow arrow*). Some bronchi (*red arrows*) are filled with mucus and are of soft-tissue attenuation. Numerous examples of the tree-in-bud pattern (*blue arrows*) are visible in the left lower lobe. *B,* The tree-in-bud pattern (*arrows*) is shown on a sagittal reconstruction through the left lung base.

artery (bronchi and arteries travel together) are about the same size; on average, the lumen of a bronchus measures about 60% of the artery diameter.

In patients with bronchiectasis, the dilated ring-shaped bronchus appears larger than its adjacent artery; together they mimic the appearance of a signet ring, a finding for bronchiectasis termed the *signet ring sign* (Fig. 6-35). By definition, the signet ring sign is present if the internal diameter of a bronchus exceeds the diameter of the adjacent artery. However, this appearance is occasionally seen in healthy subjects, particularly in those over 60 years of age. In patients with true bronchiectasis, because of infection or inflammation, bronchial wall thickening is also usually present, and the bronchus is considerably larger than the artery. Mucus or pus may be seen filling abnormal bronchi in patients with bronchiectasis. More peripheral, small airway abnormalities may also be present; a *tree-in-bud* pattern, corresponding to mucus- or pus-filled dilated bronchioles, may be seen (Fig. 6-35). Bronchiectasis is usually classified by its appearance as *cylindrical*, *varicose*, or *cystic*, but these designations are of little clinical significance. Cystic bronchiectasis may be associated with air–fluid levels in the dilated bronchi.

Bronchiectasis has many causes. Childhood infection, chronic airway infection, immunodeficiency, and cystic fibrosis are common causes. Most patients with bronchiectasis have nonspecific findings, with abnormalities being most severe peripherally and in the lower lobes. Several diseases show other appearances. *Cystic fibrosis* usually shows bilateral bronchiectasis involving the upper lobes and is most severe in the central (parahilar) lung regions. *Allergic bronchopulmonary aspergillosis* (*ABPA*) in patients with asthma also shows central bronchiectasis (Fig. 6-36*A*); mucous plugs are common and are often high in attenuation because of calcium concentrated by the fungus (Fig. 6-36*B*). *Tuberculosis* shows upper lobe bronchiectasis, which is often asymmetrical. Mycobacterium avium *complex* (*MAC*) *infection*, typically in older women (Fig. 6-37), is associated with bronchiectasis preferentially involving the middle lobes and lingua. *Immune deficiency*, *childhood infections*, and *ciliary dysmotility* (e.g., *Kartegener's syndrome*) are typically associated with lower lobe bronchiectasis (Fig. 6-35).

Bronchitis

Bronchial wall thickening without dilatation usually indicates inflammation (e.g., asthma, inflammatory bowel disease, and smoking) or infection and is termed *bronchitis*. When associated with infection, mucus or pus may be seen within the airway lumen, and tree-in-bud and/or nodules may be visible within the peripheral lung.

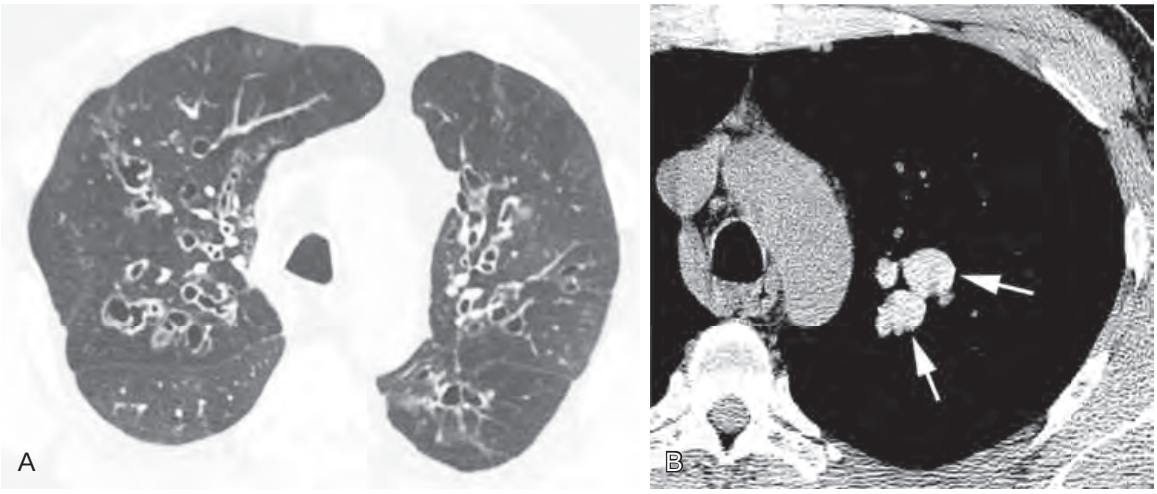

FIGURE 6-36 ■ Bronchiectasis in two patients with allergic bronchopulmonary aspergillosis (ABPA). *A,* High-resolution computed tomography shows bronchiectasis in the central upper lobes. The lung parenchyma appears heterogeneous because of mosaic perfusion. *B,* In another patient, mucous plugs (*arrows*) appear higher in attenuation than soft tissue using a mediastinal window. This finding strongly suggests ABPA.

Bronchiolitis (Small Airways Disease)

There are three patterns of small airway (bronchiolar) abnormalities visible on HRCT; these have distinct appearances, although more than one may be seen in an individual patient.

Cellular bronchiolitis with tree-in-bud nodules. *Tree-in-bud* is a finding that looks like its name (Figs. 6-35 and 6-37). Branching opacities that are too big to represent normal vessels are visible in the lung periphery or in a centrilobular location, often with small nodules associated with the tips of branches. Tree-in-bud reflects the presence of mucus or pus filling dilated centrilobular bronchioles. Common causes include, endobronchial spread of TB or MAC (Fig. 6-24), bacterial bronchopneumonia, chronic airway infection associated with bronchiectasis, and fungal and viral infections; when this finding is present, infection should first be considered. It uncommonly occurs in other conditions, including noninfectious inflammatory bronchiolitis (i.e., follicular bronchiolitis), mucoid impaction of bronchioles (as in ABPA), aspiration, and invasive mucinous adenocarcinoma. Tree-in-bud may also be associated with the next two patterns.

Cellular bronchiolitis with centrilobular nodules. Centrilobular nodules can be seen in patients with infectious or inflammatory bronchiolitis. In patients with infection, centrilobular nodules may be associated with a tree-in-bud pattern. Often the nodules are patchy in distribution. In patients with noninfectious bronchiolitis, centrilobular nodules are often of GGO and

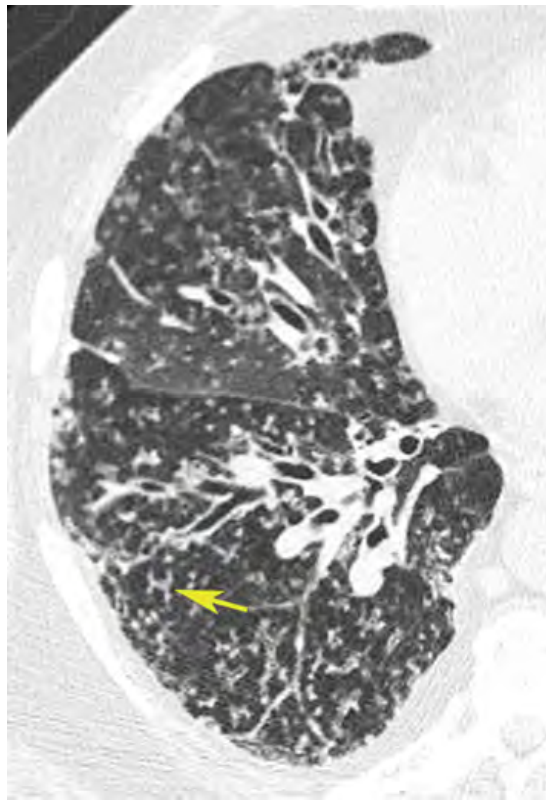

FIGURE 6-37 ■ *Mycobacterium avium* complex (MAC) infection. In an elderly woman, bronchial wall thickening, bronchiectasis, and a tree-in-bud pattern (*arrow*) are visible. This combination is typical of MAC infection. Bronchiectasis is usually most severe in the middle lobe and lingula.

diffuse [e.g., in hypersensitivity pneumonitis (Fig. 6-47) or respiratory bronchiolitis in smokers]. Centrilobular nodules are discussed later.

Constrictive (obliterative) bronchiolitis with mosaic perfusion. In patients with small airway obstruction due to constrictive or cellular bronchiolitis, the lung parenchyma may appear heterogeneous in attenuation, with patchy and geographic areas of relative lucency. This finding is termed *mosaic perfusion*. Mosaic perfusion reflects the presence of a patchy decrease in lung perfusion, and pulmonary vessels within the lucent lung regions appear smaller than vessels in denser regions because of the decrease in blood flow (Fig. 6-38). Mosaic perfusion is most common in airway obstruction, resulting in reflex vasoconstriction. It may also be seen with vascular occlusion, as in chronic pulmonary embolism. When due to airway obstruction, air trapping may be visible on expiratory scans; in some patients with constrictive bronchiolitis, mosaic perfusion is not visible, but expiratory scans show air trapping (Fig. 6-39). This pattern may accompany tree-in-bud and centrilobular nodules in some patients.

FIGURE 6-38 ■ Constrictive bronchiolitis with mosaic perfusion. In a patient with bronchiolitis obliterans resulting from a bone marrow transplantation and graft-versus-host reaction, the lung has a patchy appearance on high-resolution computed tomography. Differences in lung density reflect differences in lung perfusion secondary to abnormal ventilation related to airway obstruction. Note that the vessels look larger in the dense lung regions than in the lucent lung regions; this is an important clue to the presence of mosaic perfusion.

DIFFUSE LUNG DISEASE AND HRCT

HRCT techniques are described in Chapter 1. HRCT involves the use of thin slices and a high-resolution (sharp) algorithm; in patients with suspected diffuse infiltrative or airways disease, images are usually obtained in both the supine and prone positions, and expiratory imaging is performed to detect air trapping (Fig. 6-39).

HRCT is sometimes used to evaluate patients with acute symptoms associated with a diffuse lung abnormality to characterize the disease present and limit the differential diagnosis. Common causes of diffuse lung disease with an acute presentation include pneumonia, aspiration, various causes of pulmonary edema, and diffuse alveolar damage resulting in acute respiratory distress syndrome. In addition, because routine CT is now obtained with thin slices, any chest CT can be regarded as HRCT.

HRCT is more commonly used to evaluate diffuse infiltrative lung diseases, particularly when they are chronic or progressive and the diagnosis is in question. The term *diffuse infiltrative lung disease* is used to describe a variety of conditions, both alveolar and interstitial, that manifest as a generalized parenchymal abnormality. In general, HRCT is used (1) to detect lung disease in patients with symptoms of respiratory distress or abnormal pulmonary function tests who have normal chest radiograph results (approximately

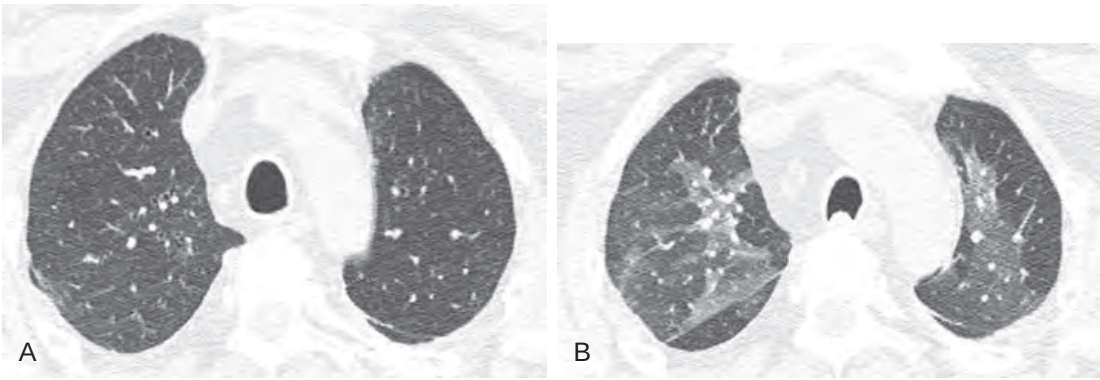

FIGURE 6-39 ■ Constrictive bronchiolitis with air trapping. High-resolution computed tomography in a patient with constrictive bronchiolitis resulting from lung transplant rejection. *A*, The inspiratory scan appears normal, without evidence of mosaic perfusion. *B*, The expiratory scan shows patchy air trapping. The relatively dense lung is normal.

10% to 15% of patients with infiltrative lung disease have normal chest radiograph results); (2) to characterize lung disease in terms of its morphologic pattern (e.g., is there honeycombing?) and perhaps make a specific diagnosis; (3) to assess disease activity; and (4) to localize areas of abnormality in patients who are having a lung biopsy. Compared with plain radiographs, HRCT is more sensitive (94% vs. 80%), more specific (96% vs. 82%), and more accurate in making a diagnosis (by >10%).

HRCT may be obtained using a spiral volumetric technique or individual slices obtained at 1- to 2-cm intervals. In a patient with a diffuse lung disease, particularly when chronic or progressive, scans at 1- to 2-cm intervals provide an adequate sample of the lung anatomy for diagnosis. A spiral technique results in a higher radiation dose but is also more inclusive.

Scans are usually obtained during full inspiration in the supine position. Prone scans are commonly obtained in patients with a suspected interstitial lung disease to avoid misdiagnosis when posterior atelectasis develops with the patient lying supine. Some dependent lung collapse is often seen on CT, and having scans in both positions allows us to differentiate this finding from subtle pathologic processes. Post-expiratory scans at three to five levels are often obtained to detect air trapping associated with small airways disease.

High-Resolution Findings in Healthy Subjects

The lung is a lobular organ made up of numerous secondary pulmonary lobules. Secondary pulmonary lobules (or simply pulmonary lobules) are polygonal in shape and usually measure 1 to 3 cm in diameter. They are marginated by interlobular septa containing veins and lymphatic channels (Fig. 6-40). In the center of the lobule are pulmonary artery and bronchiolar branches.

On HRCT, normal interlobular septa are sometimes visible as very thin, straight lines of uniform thickness that are 1 to 2 cm in length, but usually only a few well-defined septa are visible in healthy subjects. A linear, branching, or dot-like opacity seen within the secondary lobule, or within a centimeter of the pleural surface, represents the centrilobular artery branch. The centrilobular bronchiole is not normally visible. In healthy subjects, the pleural surfaces, fissures, and margins of central vessels and bronchi appear smooth and sharply defined.

Abnormal HRCT Findings

Although the findings described later are typically associated with HRCT, they are applicable to routine CT diagnosis as well.

Thickened Interlobular Septa

Thickening of interlobular septa can be seen in patients with a variety of interstitial lung diseases (Fig. 6-41). Within the central lung, thickened septa can outline lobules that appear hexagonal or polygonal and contain a visible central arterial branch. In the peripheral lung, thickened septa often extend to the pleural surface. Septal thickening can appear smooth, nodular, or irregular in different diseases.

Often, thickened septa in the peripheral lung reflect generalized interstitial thickening and are also associated with (1) thickening of fissures caused by subpleural interstitial thickening, (2) prominent centrilobular structures caused by thickening of the sheath of connective tissue that surrounds them, and (3) thickening of the interstitium surrounding central vessels and bronchi (i.e., peribronchial cuffing).

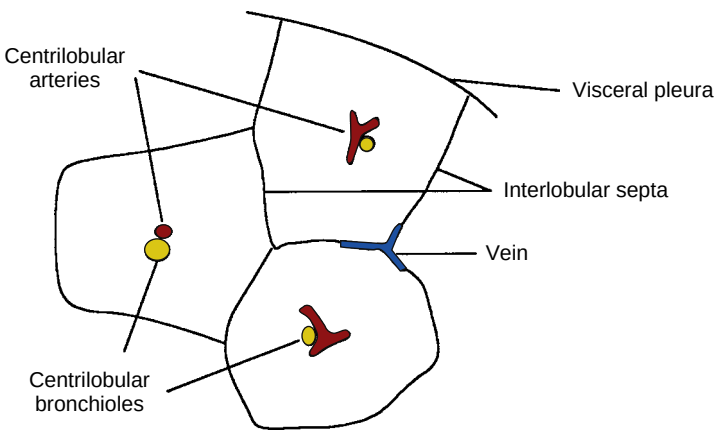

FIGURE 6-40 ■ Normal pulmonary lobules.

Common causes of interlobular septal thickening as the predominant HRCT finding include:

1. Lymphangitic spread of carcinoma (smooth or nodular septal thickening; Fig. 6-41)
2. Interstitial pulmonary edema (smooth thickening)
3. Sarcoidosis (nodular when granulomas are present; irregular in fibrotic or end-stage disease)

Findings of Pulmonary Fibrosis

Honeycombing represents lung fibrosis associated with cystic areas of lung destruction. It results in a characteristic coarse reticular pattern or cystic appearance on HRCT that is typical (Figs. 6-42 and 6-43). Cystic spaces are usually several millimeters to 1 cm in diameter, are marginated by thick, clearly definable walls, and typically appear in rows and clusters in the peripheral and subpleural lung, with adjacent cysts sharing walls. Unless a row or cluster of cysts is visible in the immediate subpleural lung, honeycombing cannot be diagnosed with certainty. The presence of honeycombing on HRCT means that fibrosis is present and is essential for a diagnosis of *usual interstitial pneumonia* (*UIP*). It is a finding that should not be overcalled.

Common causes of fibrosis with honeycombing as the predominant HRCT finding include the following:

1. Idiopathic pulmonary fibrosis (IPF; 60% to 70% of cases; Fig. 6-43)
2. Collagen vascular diseases, particularly rheumatoid arthritis and scleroderma (Fig. 6-42)

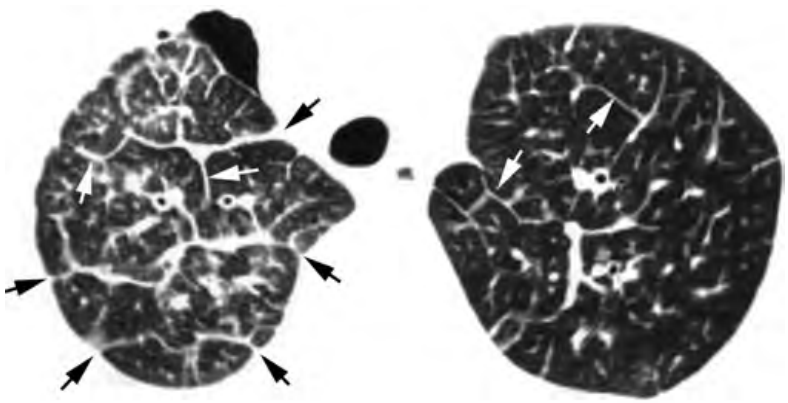

FIGURE 6-41 ■ Thickening of interlobular septa. In a patient with lymphangitic spread of breast carcinoma, high-resolution computed tomography shows evidence of septal thickening (*arrows*) characteristic of this disease. Although the septal thickening is bilateral, it is most severe on the right side. A small right pneumothorax is also present.

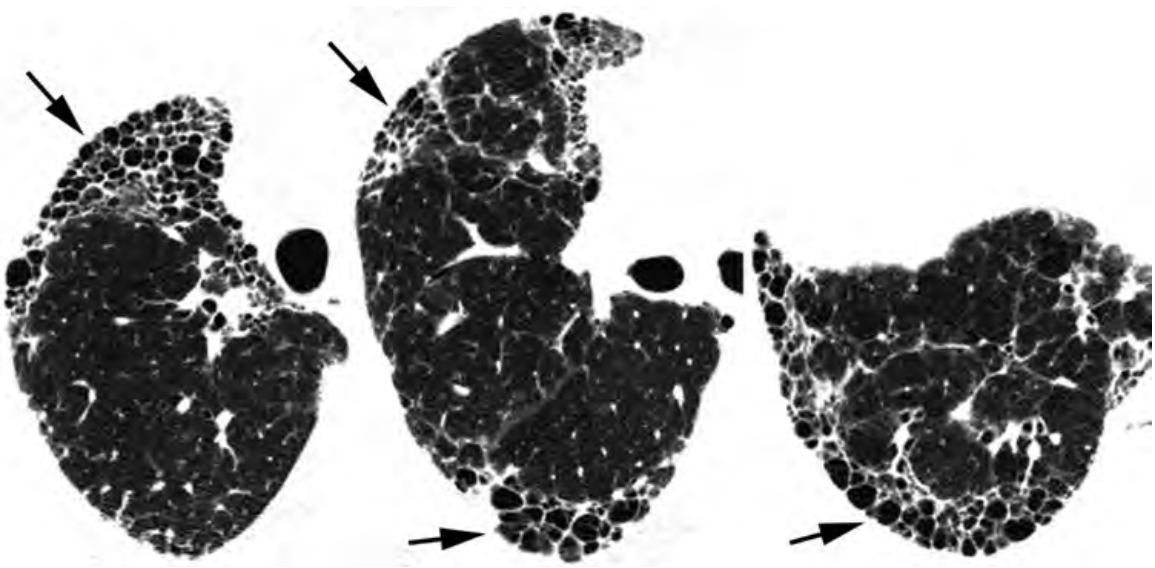

FIGURE 6-42 ■ Pulmonary fibrosis and honeycombing in rheumatoid arthritis. High-resolution computed tomography of the right lung at three levels shows characteristic small, thick-walled cysts (honeycomb cysts) that are most evident peripherally (*arrows*). This appearance is diagnostic of fibrosis.

3. Drug-related fibrosis
4. Asbestosis in association with pleural thickening
5. End-stage hypersensitivity pneumonitis
6. End-stage sarcoidosis (a small percentage of patients)

Reticulation (*a reticular pattern*), appearing as a network of linear opacities, is commonly present in patients with lung fibrosis (Fig. 6-44) and is typically associated with architectural distortion and displacement of vessels or fissures.

Traction bronchiectasis (dilatation of bronchi because of surrounding lung fibrosis) is a common finding in patients with fibrotic lung disease and reticulation. It is commonly present in patients with honeycombing. In traction bronchiectasis, large or small airways are dilated and have a very irregular, corkscrew appearance (Fig. 6-44).

Conglomerate masses of fibrous tissue (i.e., *progressive massive fibrosis*) can be seen in the upper lobes of patients with sarcoidosis or silicosis. Traction bronchiectasis may be seen within the mass.

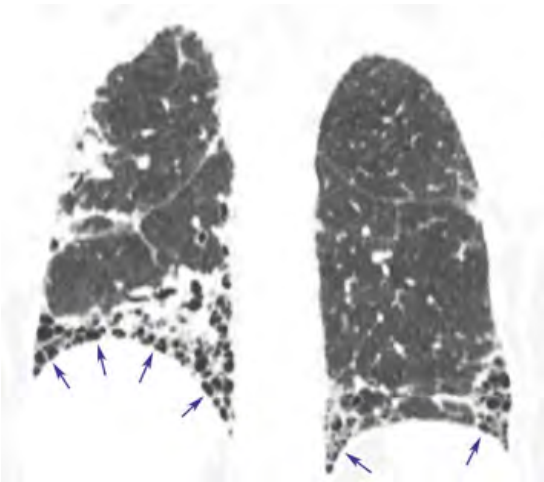

FIGURE 6-43 ■ Pulmonary fibrosis, honeycombing, and a usual interstitial pneumonia (UIP) pattern in idiopathic pulmonary fibrosis (IPF). Coronal high-resolution computed tomography reconstruction shows honeycombing (*arrows*) with a basal and subpleural predominance. This is typical of a UIP pattern.

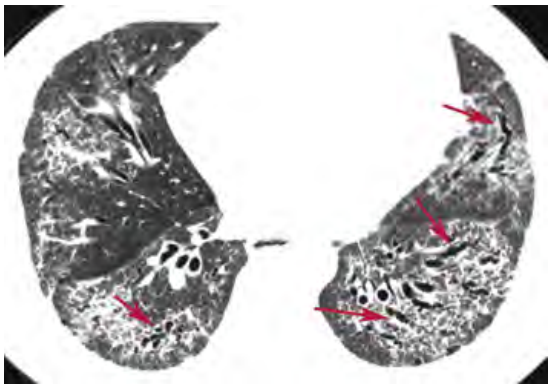

FIGURE 6-44 ■ Pulmonary fibrosis with reticulation and traction bronchiectasis in fibrotic nonspecific interstitial pneumonia (NSIP). High-resolution computed tomography in a patient with fibrotic NSIP associated with collagen vascular disease reveals abnormal lung reticulation associated with irregular dilatation of the bronchi (traction bronchiectasis; *arrows*). Note the relative sparing of the immediate subpleural lung. This is typical of NSIP.

Nodules

Small nodules (a few millimeters to 1 cm in diameter) can be detected on HRCT in patients with granulomatous diseases such as sarcoidosis and miliary tuberculosis, in patients with metastatic tumors, and in patients with small airways disease. Three distributions of lung nodules can be identified on HRCT (Fig. 6-45); recognition of one of these three patterns is invaluable in differential diagnosis.

Perilymphatic nodules occur in lung regions rich in lymphatic channels. They predominate (1) at the pleural surfaces (particularly the fissures), (2) adjacent to large vessels and bronchi, (3) within interlobular septa, and (4) in the centrilobular regions. They are typically patchy in distribution and are most common in sarcoidosis (Figs. 6-45 and 6-46), silicosis, and lymphangitic carcinoma.

Random nodules also involve the pleural surfaces but involve the lung in a diffuse and uniform

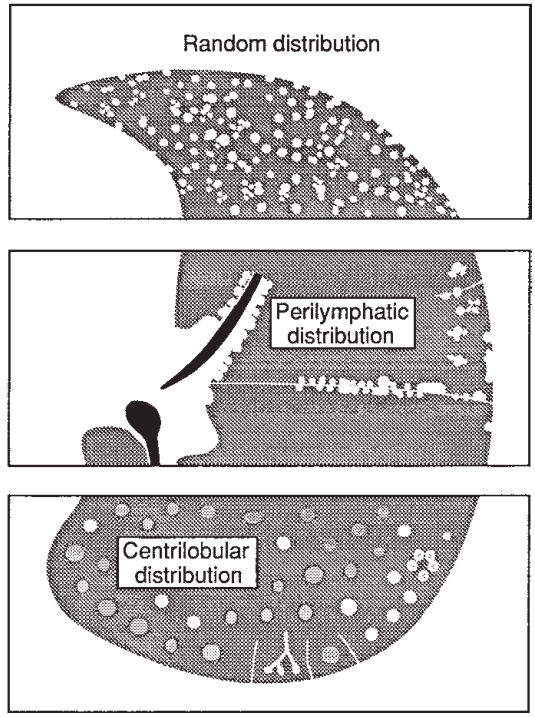

FIGURE 6-45 ■ Distributions of lung nodules. The tree-in-bud pattern is illustrated, along with centrilobular nodules and random distribution.

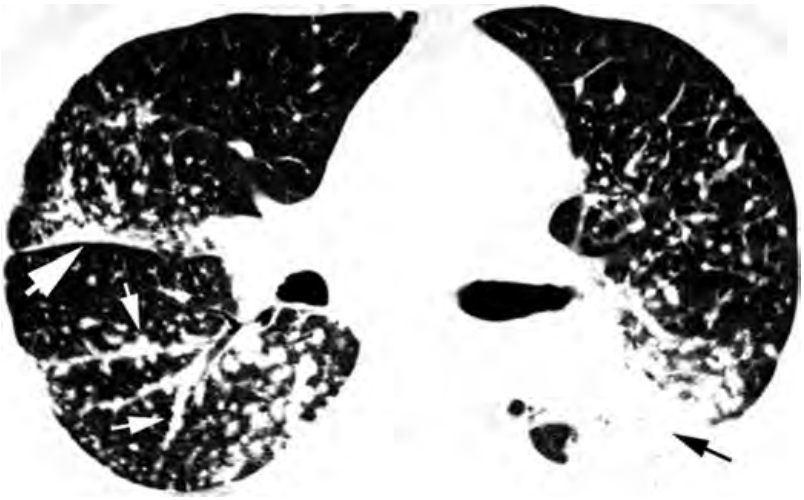

FIGURE 6-46 ■ Perilymphatic nodules (sarcoidosis). Multiple nodules are visible adjacent to the major fissure (*large white arrow*) and central bronchi and vessels (*small white arrows*). This pattern is characteristic of sarcoidosis. Note the patchy distribution, whereby some lung regions are involved whereas others appear normal. A conglomerate mass associated with satellite nodules is visible on the left (*black arrow*).

FIGURE 6-47 ■ Centrilobular nodules in a patient with hypersensitivity pneumonitis. Small, ill-defined nodules of ground-glass opacity are visible. The most peripheral nodules (*arrows*) are about 5 mm from the fissure or the pleural surfaces. The pleural surfaces are spared.

fashion, with a random distribution in relation to lung structures. They are most typical of hematogenous disease, such as miliary TB or fungus and hematogenous metastases (Figs. 6-27 and 6-45). Sarcoidosis uncommonly results in this pattern.

Centrilobular nodules usually spare the pleural surfaces and are centrilobular in location (Fig. 6-47). They tend to be visible in relation to small vessels, with the most peripheral nodules being about 5 mm from the pleural surface. Because lobules are all about the same size, the nodules appear evenly spaced and can mimic a random pattern at first glance; however, pleural nodules are absent with a centrilobular pattern. Centrilobular nodules may be patchy or diffuse and may be of soft-tissue attenuation or GGO. Centrilobular nodules usually reflect diseases that occur in relation to centrilobular bronchioles and are common with endobronchial spread of infection (e.g., TB and bacterial bronchopneumonia), endobronchial spread of tumor tissue (e.g., invasive mucinous adenocarcinoma), and cellular bronchiolitis (e.g., hypersensitivity pneumonitis and respiratory bronchiolitis). Small vessel diseases (vasculitis) and abnormalities (edema or hemorrhage) can also result in centrilobular nodules, but these are much less common. In patients with centrilobular nodules due to infection, a tree-in-bud pattern may also be visible.

In attempting to make a diagnosis for one of these three patterns of multiple nodules, it is easiest to first determine if nodules are visible in relation to the pleural surfaces and fissures. If pleural nodules are absent, the distribution is likely centrilobular; if fissural nodules are present, then the overall distribution of lung nodules determines the pattern present. Nodules with a patchy distribution and occurring in relation to the specific structures listed earlier indicate a perilymphatic distribution; a diffuse and uniform distribution indicates a random pattern. This method can be used to correctly categorize more than 95% of the cases seen.

Consolidation

HRCT findings of air space consolidation have been described. Lung appears homogeneously opaque with obscuration of the pulmonary vessels. Air bronchograms are often present.

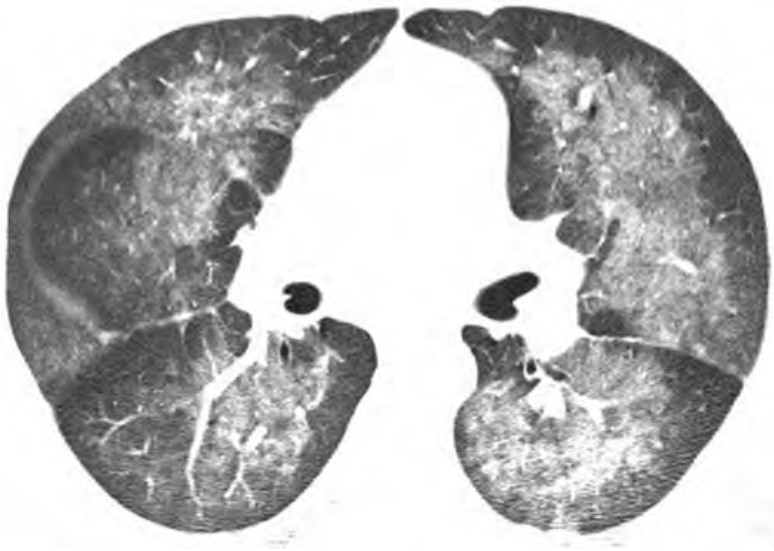

FIGURE 6-48 ■ Ground-glass opacity. Perihilar ground-glass opacity in this patient reflects pulmonary edema and hemorrhage related to an acute reaction to cocaine use. Note the appearance of the major and minor fissures (compare with Fig. 6-2).

The differential diagnosis of consolidation is primarily based on the duration of the symptoms. Consolidation associated with acute symptoms usually represents pneumonia (Fig. 6-3), severe pulmonary edema or hemorrhage, aspiration, or diffuse alveolar damage associated with acute respiratory distress syndrome. In patients with consolidation and chronic symptoms (i.e., longer than 4 to 6 weeks), common causes include organizing pneumonia, invasive mucinous adenocarcinoma (Fig. 6-30), chronic eosinophilic pneumonia, and lipoid pneumonia.

Ground-Glass Opacity

In some patients with minimal interstitial disease, alveolar wall thickening, or minimal air space consolidation, a hazy increase in lung density can be observed on HRCT (Fig. 6-39); this is termed *ground-glass opacity*. GGO is differentiated from consolidation in that areas of increased opacity do not obscure underlying pulmonary vessels.

GGO is nonspecific and can be seen in a variety of diseases. As in patients with consolidation, the differential diagnosis of GGO is primarily based on the duration of symptoms. GGO associated with acute symptoms usually represents an atypical pneumonia (*Pneumocystis jiroveci* or viral pneumonia), edema (Fig. 6-48), hemorrhage, aspiration, or acute hypersensitivity pneumonitis. In patients with chronic symptoms (i.e., longer than 4 to 6 weeks), common causes include subacute hypersensitivity pneumonitis, nonspecific interstitial pneumonia (NSIP), desquamative interstitial pneumonia (DIP), organizing pneumonia, invasive mucinous adenocarcinoma, lipoid pneumonia, and pulmonary alveolar proteinosis.

In all patients with acute symptoms, GGO indicates an active disease. In 60% to 80% of patients with chronic symptoms, this appearance correlates with some type of active lung disease. However, if GGO is seen only in lung regions that also show findings of fibrosis (e.g., honeycombing, reticulation, and traction bronchiectasis), it is likely that the GGO represents fibrosis rather than active disease. GGO in areas of fibrosis is common in patients with usual interstitial pneumonia (UIP) and IPF, representing fibrosis.

Lung Cysts

Lung cysts are thin-walled, air-filled spaces within the lung parenchyma. Cysts are seen in honeycombing, bullous emphysema, and pneumonias resulting in pneumatocele formation (e.g., *Pneumocystis* pneumonia). Several rare lung diseases result in lung cysts as a primary manifestation. These include Langerhans cell histiocytosis, lymphangiomyomatosis (Fig. 6-49), lymphocytic interstitial pneumonia or amyloidosis, particularly in association with Sjögren's syndrome, and Birt–Hogg–Dube syndrome.

HRCT Appearances in Specific Diseases: A Baker's Dozen

Although more than 200 diseases can result in a diffuse pulmonary abnormality, knowledge of relatively few allows correct diagnosis of most cases observed. More than 90% of patients with diffuse lung disease have one of about a dozen diseases. Some of the entities described later are uncommon but have typical HRCT findings or are important to know about.

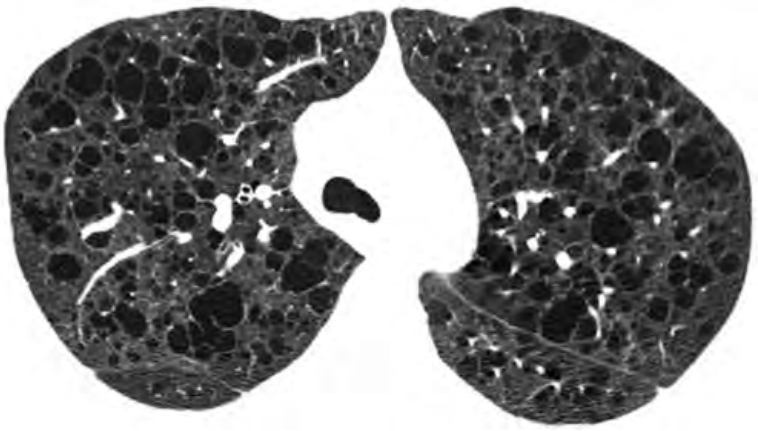

FIGURE 6-49 ■ Lung cysts in lymphangiomyomatosis (LAM). Diffuse, thin-walled, rounded lung cysts are visible in a young woman. This appearance is typical of LAM.

Metastatic Carcinoma

Although lymphangitic and hematogenous spread of carcinoma produce somewhat different patterns, overlap is common and some patients show features of both.

Lymphangitic Spread of Carcinoma. In a patient with an appropriate history of malignancy and progressive dyspnea, the HRCT appearance of lymphangitic spread is diagnostic. It is characterized by the following:

1. Interlobular septal thickening that is smooth or nodular (Fig. 6-41)
2. Peribronchial interstitial thickening (peribronchial cuffing)
3. Thickening of fissures (smooth or nodular)
4. A patchy or unilateral distribution (in some cases)
5. Lymph node enlargement (in some cases)

Hematogenous Spread of Tumor is characterized by the following:

1. A random distribution of small nodules, sometimes with a peripheral predominance (Figs. 6-27 and 6-28)
2. Involvement of fissures and the pleural surfaces
3. A bilateral distribution
4. The presence of large nodules

Usual Interstitial Pneumonia and Idiopathic Pulmonary Fibrosis

Usual interstitial pneumonia (*UIP*) is a histologic pattern characterized by patchy lung fibrosis and honeycombing. UIP may be caused by idiopathic pulmonary fibrosis (IPF), which accounts for two-thirds of cases, collagen vascular diseases (particularly rheumatoid arthritis and scleroderma), drug-related fibrosis, asbestosis, end-stage hypersensitivity pneumonitis (HP), and sometimes sarcoidosis. UIP is one of the *idiopathic interstitial pneumonias*, a category that also includes NSIP, organizing pneunomia (OP), and desquamative interstitial pneumonia (DIP), as described later.

IPF may be diagnosed when a UIP pattern seen on CT or pathology is not associated with known diseases or exposures associated with this histologic pattern. In other words, IPF is idiopathic UIP. Patients with IPF are usually older than 50 years of age and most are men. Progressive dyspnea is typical. The prognosis is very poor.

A UIP pattern on HRCT is characterized by:

1. Subpleural and basal predominance (Fig. 6-43)
2. Reticulation (with traction bronchiectasis)
3. Honeycombing (Figs. 6-42 and 6-43)
4. Absence of inconsistent features, including the following:
   a) Upper, mid-lung, or peribronchial predominance
   b) Extensive GGO (> reticulation in extent)
   c) Profuse micronodules (bilateral, upper lobe)
   d) Discrete cysts not representing honeycombing
   e) Mosaic perfusion or air trapping (bilateral, ≥ three lobes)
   f) Segmental or lobar consolidation

If these four criteria are met, a UIP pattern should be diagnosed on HRCT. If the patient has no known disease (i.e., the UIP pattern is idiopathic), then the patient has IPF. However, if, for example, the patient has a UIP pattern and asbestos exposure, he has asbestosis.

Nonspecific Interstitial Pneumonia

NSIP is a histologic pattern that, despite its name, is specific. It is commonly associated with collagen vascular disease or drug treatment but may be idiopathic as well. It is less common than UIP and IPF but is still relatively common in clinical practice. NSIP occurs in cellular (inflammatory)

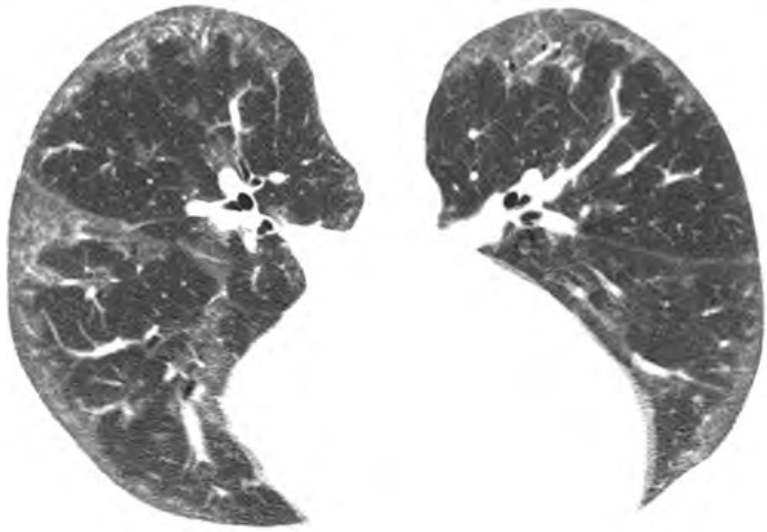

FIGURE 6-50 ■ Cellular nonspecific interstitial pneumonia (NSIP) in a patient with scleroderma. High-resolution computed tomography in the prone position shows peripheral, subpleural ground-glass opacity. This appearance is typical of NSIP.

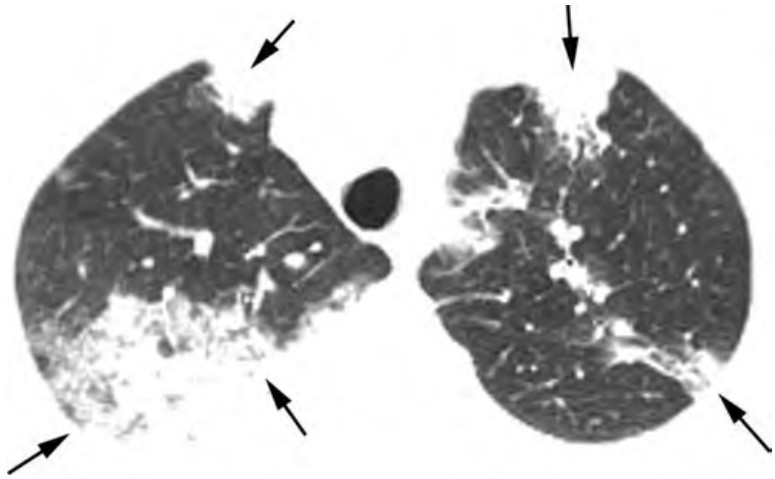

FIGURE 6-51 ■ Organizing pneumonia. Patchy areas of consolidation are noted in the peripheral lung (*arrows*). This appearance in a patient with chronic symptoms is typical.

and fibrotic forms. It often responds to treatment in the cellular stage, with a good prognosis.

NSIP has a variable appearance but often has the following characteristics:

1. Predominance in the peripheral, posterior, and basal lung regions, with a concentric distribution (Figs. 6-44 and 6-50)
2. Sparing of the immediate subpleural lung (seen in 50% of cases), a finding that is highly predictive of NSIP (Figs. 6-44 and 6-50)
3. GGO in cellular NSIP (Fig. 6-50)
4. Reticulation (Fig. 6-44)
5. Traction bronchiectasis (usually but not always in fibrotic NSIP; Fig. 6-44)
6. Rare honeycombing, which, if present, is of limited extent

Collagen Vascular Diseases

Rheumatoid lung disease, scleroderma, and other collagen diseases may result in findings of UIP, NSIP (Figs. 6-42, 6-44, and 6-50), OP, or lymphoid interstitial pneumonia (LIP). Specific collagen diseases are also associated with disease-specific findings or common associations (e.g., rheumatoid nodules, esophageal dilatation in scleroderma).

Organizing Pneumonia

OP is a histologic pattern that can be idiopathic or result from infection, toxic exposure, drug reactions, or collagen diseases. It typically results in progressive dyspnea and low-grade fever, simulating pneumonia. The idiopathic form of this disease is termed cryptogenic OP (COP).

HRCT features are nonspecific and include the following:

1. Patchy or nodular consolidation that is irregular in contour
2. Patchy or nodular GGO (Fig. 6-51)

3. A peripheral and peribronchial distribution
4. The *atoll sign* or *reversed halo sign*, in which a ring of consolidation surrounds GGO, a sign that is uncommonly seen in other diseases

Desquamative Interstitial Pneumonia (DIP) and Respiratory Bronchioloitis–Interstitial Lung Disease (RB-ILD)

These diseases are closely related and are caused by cigarette smoking in almost all cases. In both conditions, alveolar filling with macrophages is typically present. In DIP, lung involvement is extensive; in RB-ILD, involvement is limited to the peribronchiolar regions. Symptoms include cough and dyspnea. Treatment includes smoking cessation or steroid administration. The prognosis is good.

HRCT features include the following:

1. Patchy or diffuse GGO (in DIP)
2. Centrilobular nodules of GGO (in RB-ILD)
3. Air-filled cysts within regions of GGO
4. Air trapping in some
5. Rare findings of fibrosis
6. HP

Hypersensitivity Pneumonitis

Hypersensitivity pneumonitis (HP) is a common lung disease resulting from exposure to one of a number of organic dusts (e.g., bird-fancier's lung). In the acute and subacute stages, interstitial and alveolar infiltrates and ill-defined peribronchiolar granulomas are present. In the chronic stage, fibrosis and honeycombing occur. HP has a good prognosis if treated in the subacute stage using steroids or by removing the offending antigen from the environment. In 50% of cases the antigen cannot be identified.

In the subacute stage, HRCT typically shows the following:

1. Patchy or geographic GGO (80%; Fig. 6-52*A*)
2. Poorly defined centrilobular GGO nodules (50%; Fig. 6-47)
3. Upper or mid-lung predominance, with involvement of the entire cross-section of the lung (i.e., there is no subpleural predominance)
4. Mosaic perfusion caused by bronchiolar obstruction (Fig. 6-52*A*)
5. Air trapping (commonly present on expiratory scans; Fig. 6-52*B*)
6. A combination of patchy GGO and patchy mosaic perfusion (termed the *headcheese sign* because of its resemblance to a sausage of the same name; Fig. 6-52); the headcheese sign is typical of HP

In the chronic or fibrotic stage, HP typically shows the following:

1. Patchy or geographic reticulation and traction bronchiectasis
2. Honeycombing in some cases
3. Upper or mid-lung predominance, with involvement of the entire cross-section of the lung
4. Mosaic perfusion caused by bronchiolar obstruction
5. Air trapping (commonly present on expiratory scans)

Chronic Eosinophilic Pneumonia

Chronic eosinophilic pneumonia is idiopathic and is characterized by filling of alveoli by a mixed

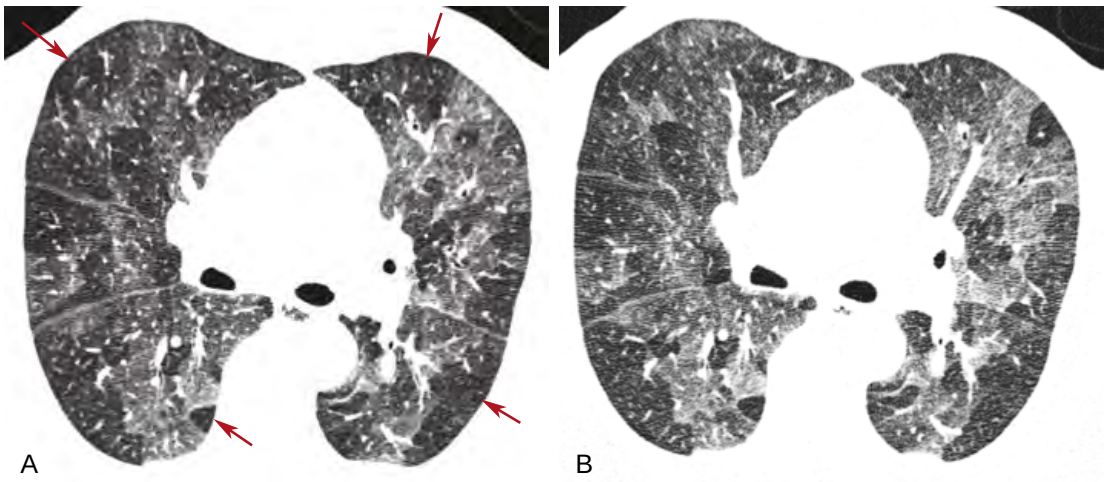

FIGURE 6-52 ■ Ground-glass opacity and mosaic perfusion in hypersensitivity pneumonitis. *A* and *B*, Multiple patchy areas of increased lung attenuation are typical of ground-glass opacity (GGO). Geographic areas of relative lucency reflect mosaic perfusion due to cellular bronchiolitis. This combination of GGO and focal lucencies is typical of hypersensitivity pneumonitis (HP) and is termed the *headcheese sign*.

inflammatory infiltrate consisting primarily of eosinophils. Blood eosinophilia is usually present. Patients present with fever, cough, and shortness of breath; HRCT features are nonspecific and are similar or identical to those of organizing pneumonia, including (1) patchy consolidation or, less often, GGO, (2) a peripheral or peribronchial distribution, and (3) the atoll or reversed halo sign.

Sarcoidosis

Sarcoidosis can have a diagnostic appearance in many patients. Patients may be relatively asymptomatic despite extensive abnormalities. HRCT findings in patients with active and end-stage disease differ.

HRCT findings in patients with active sarcoidosis follow:

1. Perilymphatic nodules, 1 to 10 mm (particularly subpleural and peribronchial; Figs. 6-23 and 6-46); calcification can occur
2. Numerous peribronchial nodules can result in large parahilar masses with satellite nodules (i.e., the galaxy sign); air bronchograms may be present (Fig. 6-23)
3. A patchy distribution, often asymmetrical
4. Upper lobe predominance
5. Hilar and mediastinal node enlargement (helpful in diagnosis but not always present); calcification can be present
6. GGO (uncommon), reflecting the presence of small granulomas

HRCT findings in patients with end-stage sarcoidosis and fibrosis include the following:

1. Irregular septal thickening
2. Architectural distortion
3. Parahilar conglomerate masses containing crowded, ectatic bronchi, often involving the upper lobes
4. Honeycombing (a small percentage)
5. Hilar and mediastinal node enlargement (not always present)

Silicosis and Coal Workers' Pneumoconiosis

Findings for silicosis and coal workers' pneumoconiosis can be similar to those for sarcoidosis, but significant differences are recognizable.

Findings include the following:

1. Perilymphatic nodules, 1 to 10 mm (particularly centrilobular and subpleural), with calcification in some cases
2. Symmetrical distribution
3. Posterior lung predominance
4. Upper lobe predominance
5. Conglomerate masses of nodules or fibrosis in the upper lobes
6. Hilar and mediastinal node enlargement; possible eggshell calcification

Tuberculosis

TB has different appearances, depending on the form of the disease. In primary TB, CT may be normal or may show findings of pneumonia. In patients with disseminated TB, HRCT findings depend on the mode of spread:

Endobronchial Spread

1. Centrilobular nodules (Fig. 6-24)
2. Tree-in-bud nodules (Fig. 6-24)
3. Focal areas of consolidation
4. Bronchial wall thickening or bronchiectasis
5. Usually patchy or focal

Miliary Spread

1. Random nodules of 1 to 5 mm (Fig. 6-45)
2. Usually diffuse

Pulmonary Alveolar Proteinosis

Pulmonary alveolar proteinosis (PAP) is characterized by filling of the alveolar spaces by a lipid-rich proteinaceous material. A majority of cases are idiopathic, but some are associated with exposure to dusts (particularly silica), hematologic or lymphatic malignancies, or chemotherapy. Nocardial or mycobacterial superinfection may occur. HRCT findings can be diagnostic and include (1) patchy or geographic GGO and (2) smooth, interlobular septal thickening in the regions of GGO. This combination is termed *crazy paving*. Although this finding is typical of PAP, it is nonspecific.

Langerhans Cell Histiocytosis

Histiocytosis (Langerhans cell histiocytosis) is associated with centrilobular nodules early in the disease and cystic lesions late in the disease. Nodules and cysts can coexist. The disease is related to smoking and occurs in both men and women. It has the following features:

1. Centrilobular nodules, which may be cavitary
2. Thick- or thin-walled, very irregularly shaped lung cysts
3. Upper lobe predominance
4. Sparing of the costophrenic angles

Lymphangiomyomatosis (LAM)

HRCT in LAM demonstrates thin-walled rounded cysts involving the entire lung, with intervening lung appearing normal. When seen in a female patient with a characteristic history

(i.e., dyspnea, spontaneous pneumothorax, and sometimes chylous pleural effusions), the findings are diagnostic. LAM occurs only in women of child-bearing age, but an identical abnormality can occur in patients with tuberous sclerosis, also almost entirely in women.

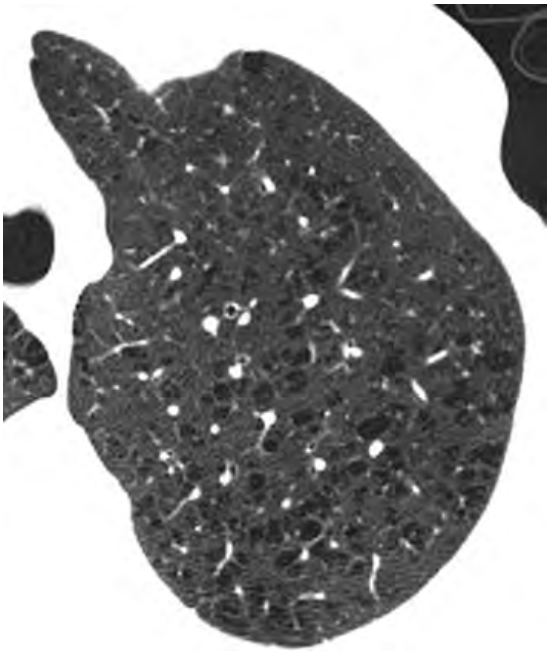

FIGURE 6-53 ■ Centrilobular emphysema. On high-resolution computed tomography, multiple spotty areas of cystic lucency without visible walls are typical of centrilobular emphysema.

HRCT features of LAM include the following:

1. Thin-walled, rounded lung cysts (Fig. 6-49)
2. Normal-appearing intervening lung
3. A diffuse distribution, without sparing of the lung bases
4. Lymph node enlargement or pleural effusion in some patients
5. Renal angiomyolipoma in some patients

EMPHYSEMA

On HRCT or thin-slice spiral CT, emphysema is apparent in areas of low attenuation within surrounding normal lung parenchyma. Emphysema is usually distinguishable from honeycombing or cystic lung disease, because in most cases the lucent areas lack visible walls (Fig. 6-45). On CT, emphysema may be classified as centrilobular, panlobular, paraseptal, or bullous.

Centrilobular emphysema is most common, is usually associated with smoking, and is typically most severe in the upper lobes (Fig. 6-53). Sometimes it appears centrilobular on HRCT, but the presence of spotty upper-lobe lucencies without visible walls is diagnostic.

Panlobular emphysema is much less common and is often related to α_1-antitrypsin deficiency. It is diffuse or most severe at the lung bases and is manifest as an overall decrease in lung attenuation and in the size of pulmonary vessels (Fig. 6-54). Early panlobular emphysema can be quite difficult to detect. Focal lucencies may be absent.

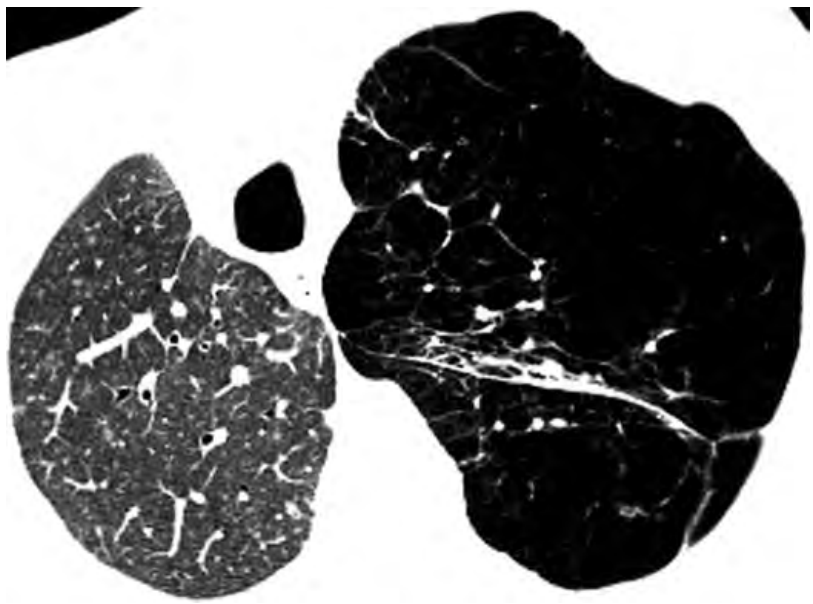

FIGURE 6-54 ■ Panlobular emphysema. Panlobular emphysema in a patient with a right lung transplant. The native left lung, involved by emphysema, is too lucent and the vessels are abnormally small.

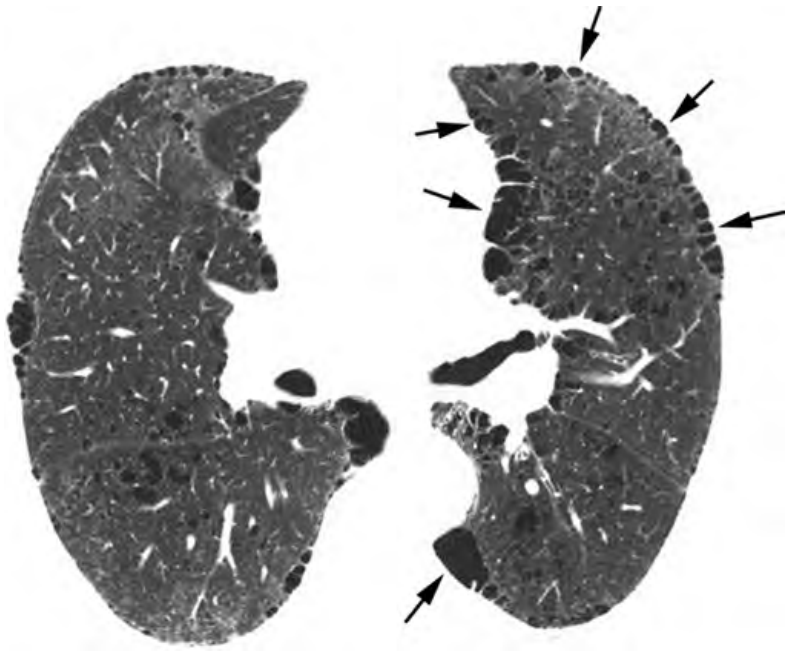

FIGURE 6-55 ■ Paraseptal emphysema. Subpleural lucency (*arrows*) is typical of paraseptal emphysema. Centrilobular emphysema is also present. It is similar in appearance to honey-combing but typically occurs in a single layer, predominates in the upper lobes, and is not associated with findings of fibrosis.

Paraseptal emphysema is common. It involves the subpleural lung adjacent to the chest wall and mediastinum. Emphysematous spaces several centimeters in diameter are typical and their walls are seen easily (Fig. 6-55). It can occur as an isolated abnormality in young patients or may be associated with centrilobular emphysema. It has an upper lobe predominance.

Bullous emphysema is said to be present when bullae predominate. It is most often associated with paraseptal emphysema. Large bullae can be seen, particularly in young men. Bullae sometimes contain fluid as well as air, which may indicate infection.

SUGGESTED READING

Aberle DR, Hansell DM, Brown K, Tashkin DP: Lymphangiomyomatosis: CT, chest radiographic, and functional correlations. *Radiology* 176:381–387, 1990.

Aberle DR, Adams AM, Berg CD, et al.: Reduced lung-cancer mortality with low-dose computed tomographic screening. *N Engl J Med* 365:395–409, 2011.

Akira M, Yamamoto S, Yokoyama K, et al.: Asbestosis: High-resolution CT–pathologic correlation. *Radiology* 176:389–394, 1990.

American Thoracic Society/European Respiratory Society: American Thoracic Society/European Respiratory Society international multidisciplinary consensus classification of the idiopathic interstitial pneumonias. *Am J Respir Crit Care Med* 165:277–304, 2002.

Aquino SL, Gamsu G, Webb WR, Kee SL: Tree-in-bud pattern: Frequency and significance on thin section CT. *J Comput Assist Tomogr* 20:594–599, 1996.

Austin JH, Müller NL, Friedman PJ, et al.: Glossary of terms for CT of the lungs: recommendations of the Nomenclature Committee of the Fleischner Society. *Radiology* 200:327–331, 1996.

Balakrishnan J, Meziane MA, Siegelman SS, Fishman EK: Pulmonary infarction: CT appearance with pathologic correlation. *J Comput Assist Tomogr* 13:941–945, 1989.

Brauner MW, Grenier P, Mompoint D, et al.: Pulmonary sarcoidosis: Evaluation with high-resolution CT. *Radiology* 172:467–471, 1989.

Cartier Y, Kavanagh PV, Johkoh T, et al.: Bronchiectasis: Accuracy of high-resolution CT in the differentiation of specific diseases. *AJR Am J Roentgenol* 173:47–52, 1999.

Church TR, Black WC, Aberle DR, et al.: Results of initial low-dose computed tomographic screening for lung cancer. *N Engl J Med* 368:1980–1991, 2013.

Davis SD: CT evaluation for pulmonary metastases in patients with extrathoracic malignancy. *Radiology* 180:1–12, 1991.

Engeler CE, Tashjian JH, Trenkner SW, Walsh JW: Ground-glass opacity of the lung parenchyma: A guide to analysis with high-resolution CT. *AJR Am J Roentgenol* 160:249–251, 1993.

Foster WL, Gimenez EI, Roubidoux MA, et al.: The emphysemas: Radiologic–pathologic correlations. *Radiographics* 13:311–328, 1993.

Gruden JF, Webb WR, Naidich DP, McGuinness G: Multinodular disease: Anatomic localization at thin-section CT–multireader evaluation of a simple algorithm. *Radiology* 210:711–720, 1999.

Gruden JF, Webb WR, Warnock M: Centrilobular opacities in the lung on high-resolution CT: diagnostic considerations and pathologic correlation. *AJR Am J Roentgenol* 162:569–574, 1994.

Ikezoe J, Murayama S, Godwin JD, et al.: Bronchopulmonary sequestration: CT assessment. *Radiology* 176:375–379, 1990.

Johkoh T, Müller NL, Cartier Y, et al.: Idiopathic interstitial pneumonias: Diagnostic accuracy of thin-section CT in 129 patients. *Radiology* 211:555–560, 1999.

Kuhlman JE, Reyes BL, Hruban RH, et al.: Abnormal air-filled spaces in the lung. *Radiographics* 13:47–75, 1993.

Leung AN, Miller RR, Müller NL: Parenchymal opacification in chronic infiltrative lung diseases: CT–pathologic correlation. *Radiology* 188:209–214, 1993.

Lewis ER, Caskey CI, Fishman EK: Lymphoma of the lung: CT findings in 31 patients. *AJR Am J Roentgenol* 156:711–714, 1991.
Lynch DA, Travis WD, Müller NL, et al.: Idiopathic interstitial pneumonias: CT features. *Radiology* 236:10–21, 2005.
Mahoney MC, Shipley RT, Cocoran HL, Dickson BA: CT demonstration of calcification in carcinoma of the lung. *AJR Am J Roentgenol* 154:255–258, 1990.
McGuinness G, Naidich DP, Leitman BS, McCauley DI: Bronchiectasis: CT evaluation. *AJR Am J Roentgenol* 160:253–259, 1993.
McHugh K, Blaquiere RM: CT features of rounded atelectasis. *AJR Am J Roentgenol* 153:257–260, 1989.
Moore AD, Godwin JD, Müller NL, et al.: Pulmonary histiocytosis X: Comparison of radiographic and CT findings. *Radiology* 172:249–254, 1989.
Müller NL, Colby TV: Idiopathic interstitial pneumonias: High-resolution CT and histologic findings. *Radiographics* 17:1016–1022, 1997.
Müller NL, Miller RR: Computed tomography of chronic diffuse infiltrative lung disease: I. *Am Rev Respir Dis* 142:1206–1215, 1990.
Müller NL, Miller RR: Computed tomography of chronic diffuse infiltrative lung disease: II. *Am Rev Respir Dis* 142:1440–1448, 1990.
Müller NL, Miller RR: Diseases of the bronchioles: CT and histopathologic findings. *Radiology* 196:3–12, 1995.
Naidich DP: High-resolution computed tomography of cystic lung disease. *Semin Roentgenol* 26:151–174, 1991.
Naidich DP, Ettinger N, Leitman BS, McCauley DI: CT of lobar collapse. *Semin Roentgenol* 19:222–235, 1984.
Park JS, Lee KS, Kim JS, et al.: Nonspecific interstitial pneumonia with fibrosis: Radiographic and CT findings in seven patients. *Radiology* 195:645–648, 1995.
Patel RA, Sellami D, Gotway MB, et al.: Hypersensitivity pneumonitis: Patterns on high-resolution CT. *J Comput Assist Tomogr* 24:965–970, 2000.
Primack SL, Hartman TE, Lee KS, Müller NL: Pulmonary nodules and the CT halo sign. *Radiology* 190:513–515, 1994.
Primack SL, Müller NL: Radiologic manifestations of the systemic autoimmune diseases. *Clin Chest Med* 19:573–586, 1998.
Proto AV, Ball JB: Computed tomography of the major and minor fissures. *AJR Am J Roentgenol* 140:439–448, 1983.
Raghu G, Collard HR, Egan JJ, et al.: An official ATS/ERS/JRS/ALAT statement: Idiopathic pulmonary fibrosis: evidence-based guidelines for diagnosis and management. *Am J Respir Crit Care Med* 183:788–824, 2011.
Remy J, Remy-Jardin M, Giraud F, Wattinne L: Angioarchitecture of pulmonary arteriovenous malformations: Clinical utility of three-dimensional helical CT. *Radiology* 191:657–664, 1994.
Siegelman SS, Khouri NF, Scott WW, et al.: Pulmonary hamartoma: CT findings. *Radiology* 160:313–317, 1986.
Silva CIS, Müller NL, Churg A: Hypersensitivity pneumonitis: Spectrum of high-resolution CT and pathologic findings. *AJR Am J Roentgenol* 188:334–344, 2007.
Stern EJ, Frank MS: CT of the lung in patients with pulmonary emphysema: Diagnosis, quantification, and correlation with pathologic and physiologic findings. *AJR Am J Roentgenol* 162:791–798, 1994.
Swensen SJ, Viggiano RW, Midthun DE, et al.: Lung nodule enhancement at CT: Multicenter study. *Radiology* 214: 73–80, 2000.
Templeton PA, Zerhouni EA: High-resolution computed tomography of focal lung disease. *Semin Roentgenol* 26: 143–150, 1991.
Traill ZC, Maskell GF, Gleeson FV: High-resolution CT findings of pulmonary sarcoidosis. *AJR Am J Roentgenol* 168:1557–1560, 1997.
Travis WD, Hunninghake G, King TE, et al.: Idiopathic nonspecific interstitial pneumonia: Report of an American Thoracic Society project. *Am J Respir Crit Care Med* 177:1338–1347, 2008.
Travis WD, Brambilla E, Noguchi M, et al.: International Association for the Study of Lung Cancer/American Thoracic Society/European Respiratory Society international multidisciplinary classification of lung adenocarcinoma. *J Thorac Oncol* 6:244–285, 2011.
Webb EM, Elicker BM, Webb WR: Using CT to diagnose nonneoplastic tracheal abnormalities: Appearance of the tracheal wall. *AJR Am J Roentgenol* 174:1315–1321, 2000.
Webb WR: Radiologic evaluation of the solitary pulmonary nodule. *AJR Am J Roentgenol* 154:701–708, 1990.
Webb WR: High-resolution computed tomography of the lung: Normal and abnormal anatomy. *Semin Roentgenol* 26:110–117, 1991.
Webb WR: High-resolution computed tomography of obstructive lung disease. *Radiol Clin North Am* 32:745–757, 1994.
Zwirewich CV, Vedal S, Miller RR, Müller NL: Solitary pulmonary nodule: High-resolution CT and radiologic–pathologic correlation. *Radiology* 179:469–476, 1991.

CHAPTER 7

PLEURA, CHEST WALL, AND DIAPHRAGM

W. Richard Webb

TECHNICAL CONSIDERATIONS

In general, the pleura and chest wall are well evaluated using routine thoracic computed tomography (CT) techniques. Contrast infusion is helpful in showing pleural thickening and in allowing its differentiation from pleural fluid. Soft-tissue window settings and bone windows are most suitable for evaluating pleural abnormalities, the chest wall, and the diaphragm.

It should be kept in mind that the diaphragm and posterior pleural space extend well below the lung bases, and scans inferior to the diaphragmatic domes must be obtained to evaluate these structures completely. A good general rule is that if ribs are visible, then the pleural space is being viewed. Scanning with the patient in the prone position may be of assistance in evaluating pleural diseases; free pleural effusions shift to the dependent portion of the pleural space when the patient is moved from the supine position to the prone or decubitus position, whereas loculated effusions or fibrosis show little or no change. Prone scans in patients with pleural effusion are most commonly obtained when using CT for placing a chest tube.

PLEURA

Normal Anatomy

Because of the oblique orientation of the lateral ribs, usually only a short segment of each rib is visible on a single CT slice; each progressively more anterior rib represents the one arising at a higher thoracic level (Fig. 7-1). Thus, for example, at any given level, the fifth rib is anterior to the sixth, and the fourth is anterior to the fifth. At the level of the lung apex, the first rib can be identified by its anterior position and by its articulation with the manubrium immediately below the level of the clavicle.

In many patients, a bony spur projects inferiorly from the undersurface of the first rib at its junction with the manubrium. In cross-section, this bony spur can appear to be surrounded by lung and can mimic a lung nodule. This appearance is usually bilateral and symmetrical, providing a clue as to its true nature. As would be expected, it appears calcified.

Costal Pleura

On CT or high-resolution CT (HRCT) in normal subjects, a 1- to 2-mm-thick opaque stripe is commonly seen in the intercostal spaces, between adjacent rib segments (Fig. 7-1). This stripe primarily represents the innermost intercostal muscle. In the paravertebral regions, the innermost intercostal muscle is absent, and a much thinner line (or no line at all) is visible at the pleural surface. The visceral and parietal pleura pass internal to the ribs and innermost intercostal muscles and are separated from them by a thin layer of extrapleural fat, but they are not normally visible on CT.

Intrapulmonary Fissures

Intrapulmonary fissures are described in Chapter 6 (Fig. 6-1). Normal collections of fat extending into the inferior aspects of the major fissures at the diaphragmatic surface can simulate fissural pleural thickening or effusion. These will be low in attenuation at mediastinal window settings.

Inferior Pulmonary Ligament

On each side below the inferior pulmonary vein, the parietal and visceral pleural layers join, forming a fold that extends inferiorly along the mediastinal surface of the lung and ends at the level of the diaphragm. This fold, the *inferior pulmonary ligament*, anchors the lower lobe. On CT images

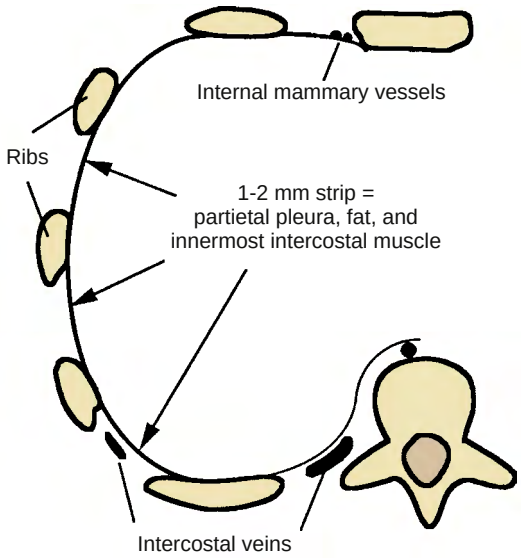

FIGURE 7-1 ■ Normal pleura. A 1- to 2-mm line of opacity at the pleural surface primarily represents the innermost intercostal muscle, combined with the two pleural layers and the endothoracic fascia. In the paravertebral region, this stripe is much thinner or invisible.

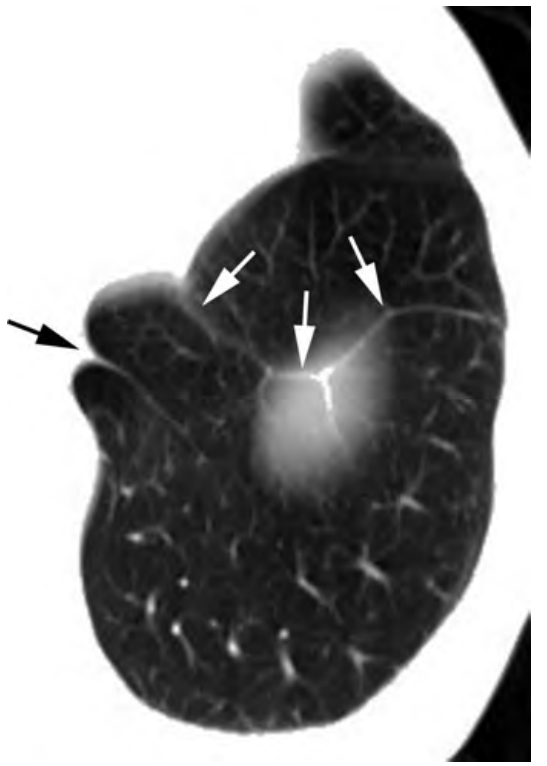

FIGURE 7-2 ■ Inferior pulmonary ligament and phrenic nerve. A small triangular opacity (*black arrow*) arising adjacent to the esophagus represents the left inferior pulmonary ligament. Longer linear densities near the surface of the diaphragm (*white arrows*) represent pleural reflections adjacent to the phrenic nerves.

viewed at lung window settings, it appears as, or is related to, a small triangular opacity of 1 cm or less in size with its apex pointing laterally into the lung and its base against the mediastinum. On each side, it usually lies adjacent to the esophagus (Fig. 7-2). Pleural effusion or pneumothoraces can be limited and marginated by the inferior pulmonary ligament.

A similar opacity can be seen on the right, lateral to the inferior vena cava (and thus anterior to the inferior pulmonary ligament), and on the left arising lateral to the left ventricle, extending inferiorly to the diaphragm and then laterally for several centimeters along the diaphragmatic surface (Fig. 7-2). These represent the phrenic nerve and its pleural reflection. Their only significance is that they are commonly seen and is just as commonly confusing.

Pleural Thickening and Look-Alikes

Pleural thickening is visible on CT as a soft-tissue curvilinear stripe passing internal to the ribs and innermost intercostal muscles. When the pleura is visible on CT, it is thickened. Thickened pleura is enhanced and is best seen after contrast infusion. Usually visible thickened pleura represents the parietal pleural layer.

In the presence of pleural thickening, the extrapleural fat layer is often thickened as well, and the visible pleural line is often separated from the ribs and intercostal muscles by this fat layer. In the paravertebral regions or adjacent to the mediastinum, a distinct opaque stripe is visible in the presence of pleural thickening.

A small *pleural effusion* can mimic the appearance of pleural thickening; however, effusion is usually dependent on location and is crescentic. Thickened pleura can often be distinguished from small pleural fluid collections by contrast infusion; thickened pleura enhances, whereas fluid does not.

Normal *extrapleural fat pads* of a few millimeters in thickness can sometimes be seen internal to the ribs, particularly in the lower posterolateral thorax, and may not be easily distinguishable from pleural thickening or fluid. However, normal fat pads appear low in attenuation and are often symmetrical, whereas pleural abnormalities generally are not.

The *subcostalis muscles* are sometimes visible posteriorly in the lower thorax, as a 1- to 2-mm-thick stripe internal to one or more ribs. In contrast to pleural thickening, these muscles are smooth, uniform in thickness, and bilaterally symmetrical.

Segments of *intercostal veins* are commonly visible in the paravertebral regions and can mimic

focal pleural thickening. Continuity of these opacities with the azygos or hemiazygos veins can sometimes allow them to be identified correctly.

Pleural Effusion and Empyema

Diagnosis of Paradiaphragmatic Fluid Collections

The visceral pleura covers the surface of the lung, and its inferior extent is defined by the inferior extent of the lung in the costophrenic angles. The parietal pleura is contiguous with the chest wall and diaphragm and extends well below the level of the lung bases in the costophrenic angles. Thus, pleural fluid collections in the costophrenic angles can be seen below the lung base and can mimic collections of fluid in the peritoneal cavity.

The parallel curvilinear configuration of the pleural and peritoneal cavities at the level of the perihepatic and perisplenic recesses allows fluid in either cavity to appear as an arcuate or semilunar opacity displacing the liver or spleen away from the adjacent chest wall. The relation of the fluid collection to the ipsilateral diaphragmatic crus (see later discussion) helps to determine its location. Pleural fluid collections in the posterior costophrenic angle lie posterior to the diaphragm and cause lateral displacement of the crus. Peritoneal fluid collections are anterior to the diaphragm and lateral to the crus, displacing it medially. Fluid seen posterior to the liver is within the pleural space; the peritoneal space does not extend into this region (this is the "bare area" of the liver).

A large pleural effusion allows the lower lobe to float anteriorly and lose volume. The posterior edge of the lower lobe, when surrounded by fluid both anteriorly and posteriorly, can appear to represent the diaphragm (a *pseudodiaphragm*), with pleural fluid posteriorly and ascites anteriorly (Fig. 7-3). Sequential scans at more cephalad levels, however, generally allow the correct interpretation to be made. Typically, the arcuate opacity of the atelectatic lower lobe becomes thicker superiorly, is contiguous with the remainder of the lower lobe, and often contains air bronchograms.

Fissural Fluid

Large effusions often extend into the major fissures, displacing the lower lobes medially and posteriorly. A localized collection of pleural fluid in a major or minor fissure can have a confusing appearance on CT scans and can be misinterpreted as representing a parenchymal mass.

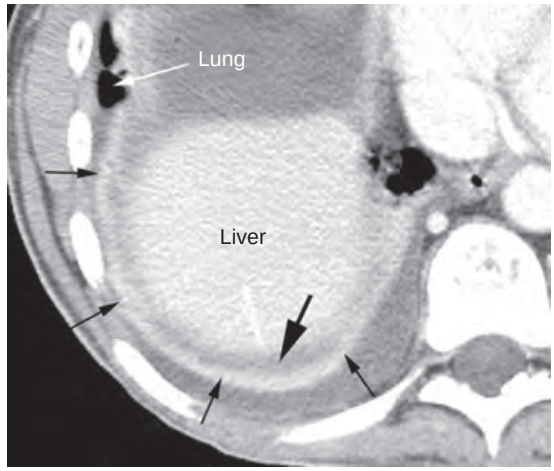

FIGURE 7-3 ■ Subpulmonic effusion and a pseudodiaphragm mimicking ascites. In a patient with a large right pleural effusion, the collapsed posterior lower lobe (*small black arrows*) simulates the diaphragm. Fluid (*large black arrow*) separating this opacity from the liver is in the region of the "bare area" of the liver. Ascites does not occur in this location. An aerated lower lobe (*white arrow*) is seen in association with the anterior aspect of the pseudodiaphragm.

However, careful analysis of contiguous images will usually confirm the relation of the mass to the plane of the fissure. The edges of the fluid collection may be seen to taper, conforming to the fissure and forming a "beak" (Fig. 7-4).

Characterization of Effusion: Exudate versus Transudate

A pleural effusion is usually characterized clinically (based on thoracentesis) as being an *exudate* (a high-protein effusion associated with pleural disease) or a *transudate* (a low-protein effusion associated with alteration in systemic factors governing the formation of pleural fluid) (Table 7-1). Exudates, being high in protein, tend to loculate, and tube drainage may be necessary. CT findings can help in making this diagnosis and assessing the fluid collection.

On CT, a crescentic and dependent fluid collection is likely, but not always, free (a definite diagnosis of free pleural effusion requires demonstration of a shift in effusion in association with a shift in patient position); a crescentic effusion may be a transudate or exudate (Figs. 7-5 and 7-6). Lenticular fluid collections, and collections that are nondependent, are likely loculated, and very likely represent exudate or an empyema (Figs. 7-6 and 7-7). When an effusion is described, its shape (crescentic or lenticular) and location (dependent or nondependent) should first be indicated.

Most effusions appear to be near to water in attenuation, and measured CT numbers cannot

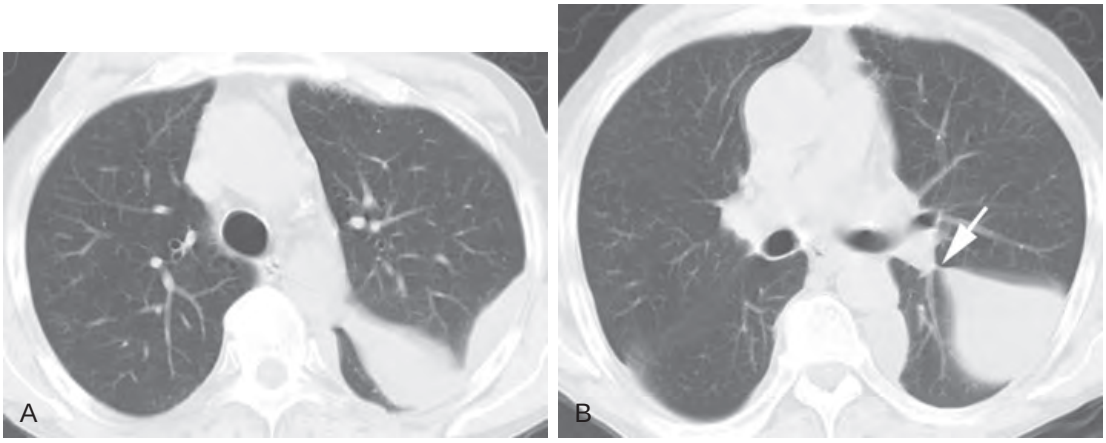

FIGURE 7-4 ■ Fluid in a fissure. *A* and *B*, In this patient, a free left pleural effusion extends into the left major fissure. The fluid tapers medially in relation to the fissure (*arrow*, *B*), forming a "beak." Fissural fluid tends to be "localized" but not loculated.

TABLE 7-1 **Common Causes of Exudates and Transudates**

Exudates	Transudates
Parapneumonic effusion	Congestive heart failure
Empyema	Liver disease
Malignancy	Renal disease
Collagen vascular disease	Overhydration
Pulmonary embolism	Low serum protein
Abdominal disease	
Hemothorax	
Chylothorax	

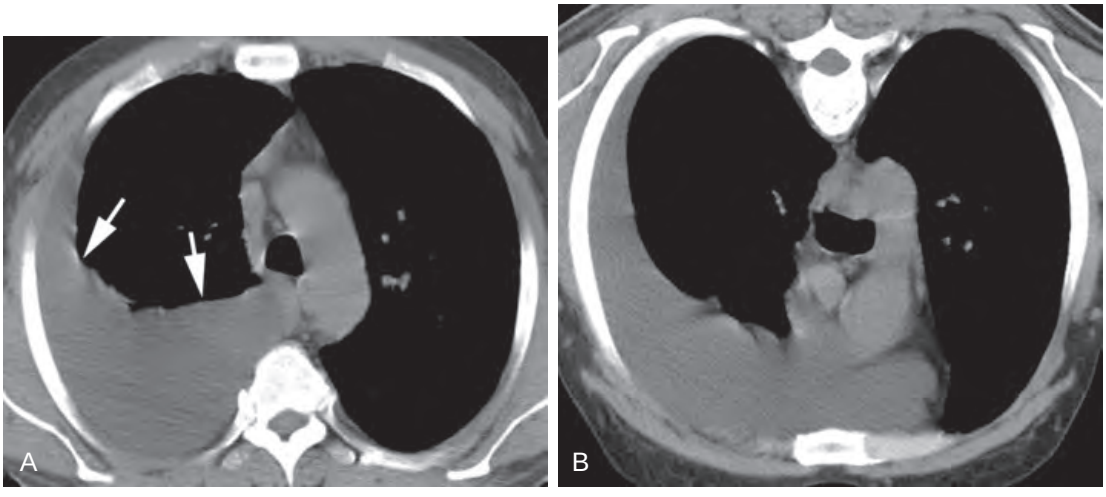

FIGURE 7-5 ■ Free pleural effusion with a gravitational shift. *A*, A large crescentic fluid collection (*arrows*) is visible posteriorly on the right. *B*, With the patient in the prone position, the fluid shifts to the anterior thorax. This indicates it is free rather than loculated. No pleural thickening is seen.

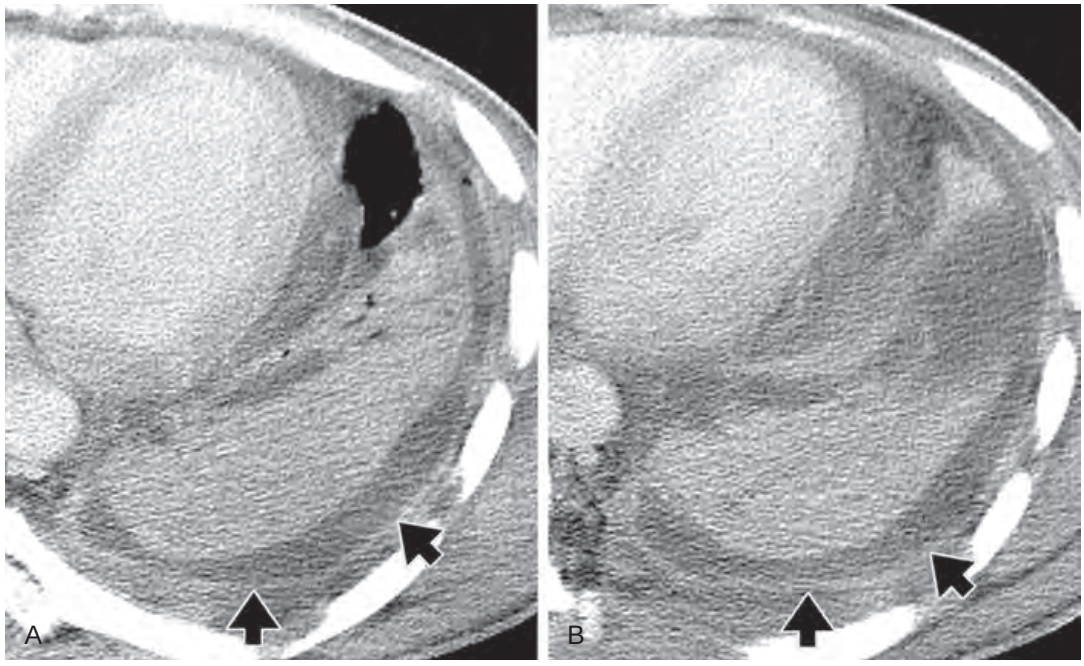

FIGURE 7-6 ■ Crescentic pleural effusion with pleural thickening. *A* and *B*, In this patient, a dependent and crescentic fluid collection is visible. Although this finding suggests that the effusion is free, this is not always the case. The parietal pleura is thickened (i.e., it is visible; *arrows*). This finding indicates the presence of an exudate. The effusion represents an empyema. The left lower lobe is collapsed.

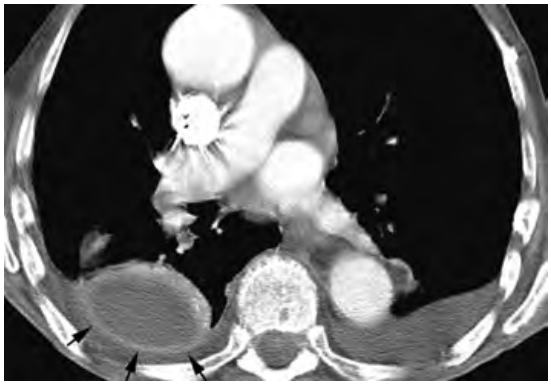

FIGURE 7-7 ■ Pleural effusions, with and without pleural thickening. Bilateral pleural effusions are present. The right pleural effusion is lenticular in shape and is associated with pleural thickening (*arrows*) and the split pleura sign. It represents an empyema. The left pleural effusion is not associated with pleural thickening; this appearance is nonspecific. The left pleural effusion was transudative.

be reliably used to predict the specific gravity of the fluid or its nature (i.e., exudate or transudate). In patients with effusion, the presence of pleural thickening on CT (Figs. 7-6 and 7-7) indicates that the effusion is an *exudate* rather than a *transudate*, with a specificity of nearly 100%. By definition, the pleura is considered thickened on CT if it is visible; contrast enhancement helps greatly in making this diagnosis. Transudates are not associated with pleural thickening (except in the rare case of a patient with preexisting pleural disease who subsequently develops an unrelated transudate).

The absence of pleural thickening on contrast-enhanced CT in a patient with pleural effusion is less helpful; in this situation, the effusion can be an exudate or a transudate (Fig. 7-7). Only about 50% to 60% of exudates are associated with visible pleural thickening on CT. However, the absence of pleural thickening on a contrast-enhanced scan effectively rules out empyema; empyema is almost always associated with parietal pleural thickening on contrast-enhanced CT.

Hemothorax

Hemothorax is defined as a pleural effusion having a hematocrit equal to 50% of the blood hematocrit. It may be traumatic or related to other causes of bleeding. Hemothorax may be dense (>50 Hounsfield units, HU) or may appear inhomogeneous, with some areas, particularly dependent regions, having an attenuation greater than that of the surrounding fluid. A fluid–fluid level (a hematocrit effect) or dependent clot may be seen with hemothorax (Fig. 7-8).

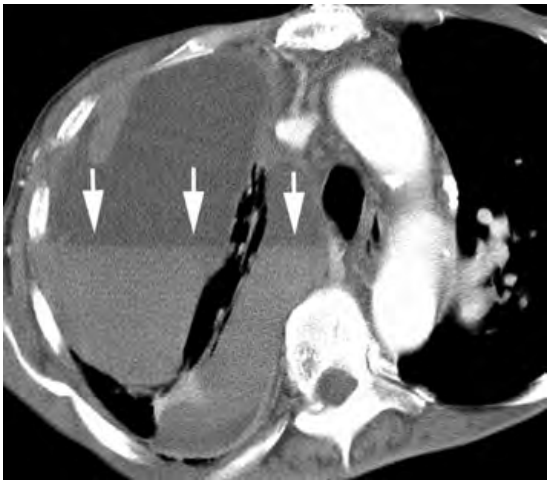

FIGURE 7-8 ■ Hemothorax. A large right pleural effusion shows a distinct fluid–fluid level or hematocrit effect, with dense blood or clot layered posteriorly (*arrows*).

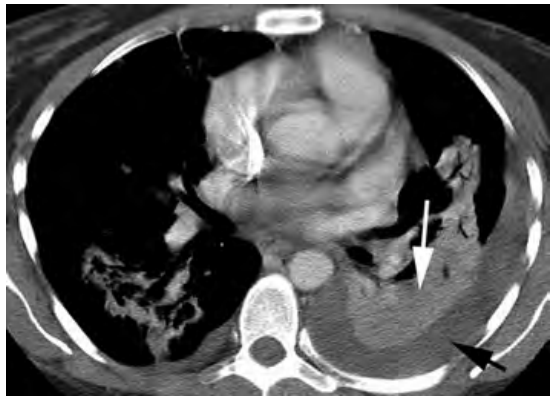

FIGURE 7-9 ■ Parapneumonic pleural effusion. A patient with left lower lobe pneumonia (*white arrow*) also shows a left pleural effusion (*black arrow*). The effusion is dependent and crescentic in appearance; it is not associated with pleural thickening.

Parapneumonic Effusion

Pleural fluid can accumulate in patients with pneumonia, even when the pleural space is uninfected. This is termed a *parapneumonic effusion*, and it results from increased permeability of the visceral pleura associated with the inflammation. The effusion is usually an exudate.

Parietal pleural thickening is present in about half of patients with parapneumonic effusion, whereas visceral pleural thickening is seen in one-fourth of patients. Because loculation is not usually present, the effusion is typically crescentic and dependent (Fig. 7-9).

Empyema

Empyema is diagnosed if pleural fluid contains infectious organisms on smear or culture. Classically, an empyema is associated with the *split pleura sign*. This sign is said to be present when the thickened visceral and parietal pleural layers are split apart by and surround the empyema (Figs. 7-7 and 7-10); these pleural layers are generally of similar thickness.

However, the split pleura sign is not always present in patients with empyema. Although empyema is nearly always associated with parietal pleural thickening on contrast-enhanced CT, visceral pleural thickening (and thus the split pleura sign) is only present in half of cases (Fig. 7-6).

Empyemas can be free or loculated, and crescentic (Fig. 7-6), rounded, elliptical, or lenticular in shape (Figs. 7-6, 7-7, and 7-10). In patients with a dependent and crescentic effusion associated with pleural thickening, simple parapneumonic effusion and empyema cannot be distinguished. Loculated effusions are typically elliptical or lenticular and often nondependent; loculation is not usually present in parapneumonic effusion and predicts empyema. Multiple loculations may be present (Fig. 7-10*B*).

The presence of air within an empyema is almost always caused by recent thoracentesis but may also indicate bronchopleural fistula (Fig. 7-11) or the presence of a gas-forming organism. In the absence of thoracentesis, this finding is usually an indication for tube drainage.

Extension of an empyema to involve the chest wall is termed *empyema necessitatis*. Two-thirds of cases result from tuberculosis, but other responsible organisms include *Actinomyces* and *Nocardia*. CT findings include low-attenuation fluid collections within the chest wall.

Differentiation of Empyema from Lung Abscess

Distinguishing empyema from lung abscess is sometimes important in patients who are clinically infected; empyema is often treated using tube drainage, whereas lung abscess generally is not. CT can be helpful in making this distinction, particularly when contrast medium is infused.

The outer edge of an empyema is sharply demarcated from adjacent lung, and on contrast-enhanced scans the empyema wall appears regular in thickness. When a bronchopleural fistula is present and air is contained within the empyema cavity, or when air is introduced into the empyema at thoracentesis, its inner margin usually appears smooth.

In contrast, lung abscesses are irregularly shaped and often contain multiple areas of low-attenuation necrosis or collections of air and fluid. On contrast-enhanced scans, the abscess

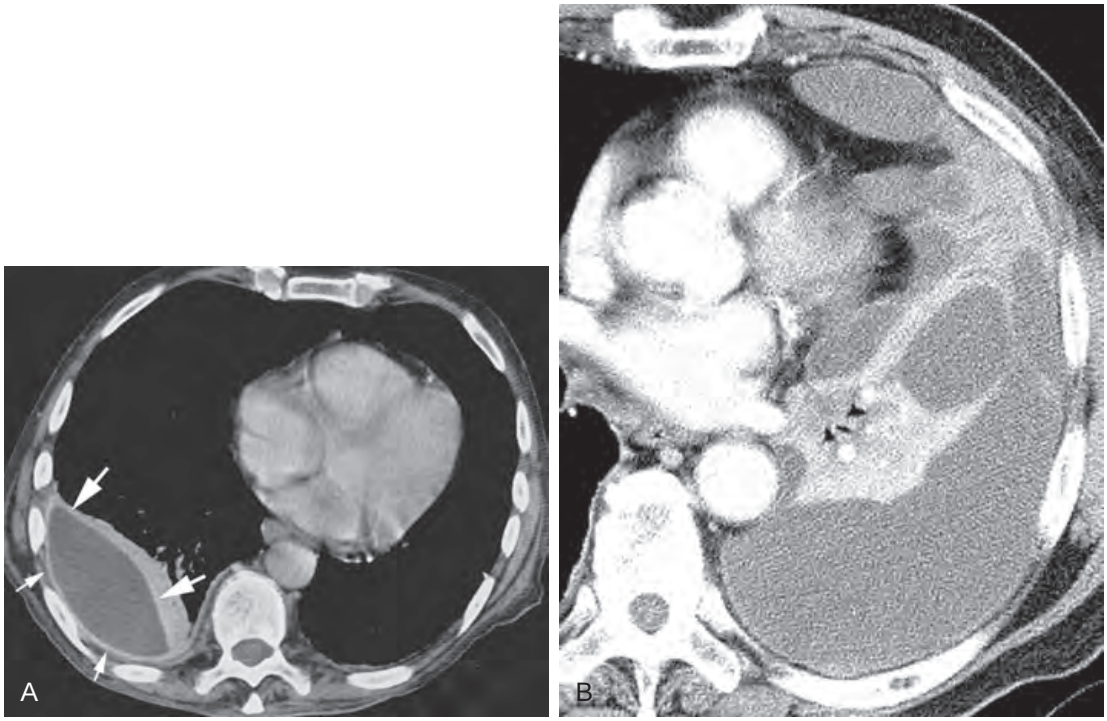

FIGURE 7-10 ■ Empyema in two patients. *A,* A classic empyema is lenticular and well defined. After contrast injection, the thickened visceral (*large white arrows*) and parietal pleura (*small white arrows*) and the split pleura sign are visible. *B,* An empyema associated with a large left pleural effusion, pleural thickening, and multiple loculations.

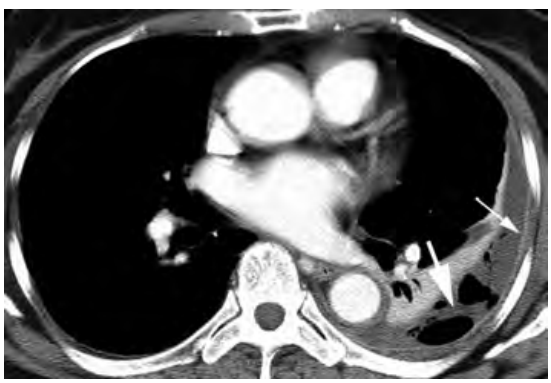

FIGURE 7-11 ■ Empyema and bronchopleural fistula. A crescentic left pleural effusion associated with pleural thickening (*small arrow*). Multiple collections of air (*large arrow*) in the left effusion are caused by a bronchopleural fistula. The presence of multiple discrete air bubbles indicates the presence of a multiseptated pleural effusion.

wall is generally opacified relative to fluid in the abscess cavity. The inner surfaces of an abscess are often irregular and ragged, and their outer edges may be poorly defined because of adjacent pulmonary parenchymal consolidation.

At their point of contact with the chest wall, empyemas can show acute or obtuse angles (Fig. 7-12), whereas abscesses typically have acute angles. Empyemas also tend to compress and displace the lung and vessels, acting as a space-occupying mass, whereas lung abscesses destroy the lung without displacing it (usually).

Thoracostomy Tubes

Infected pleural fluid collections often become loculated and can be difficult to drain. CT is sometimes indicated to evaluate thoracostomy tube position when the tube is functioning poorly. Malpositioned chest tubes can lie within a fissure, within a loculated fluid collection (whereas other collections remain undrained), or outside the empyema.

Pleural Thickening

Organizing Empyema (Pleural Peel)

In patients with chronic empyema, especially if it is tuberculous in origin, ingrowth of fibroblasts can result in pleural fibrosis and the development of chronic pleural thickening. CT may show a thickened pleural peel (Fig. 7-13). The presence of a decreased volume of the affected hemithorax is an important finding (Fig. 7-13). Calcification, which typically is focal in its early stages, may become extensive (Fig. 7-14). Frequently, a thickened layer of extrapleural fat is also visible, separating the parietal pleura and the ribs (this layer is

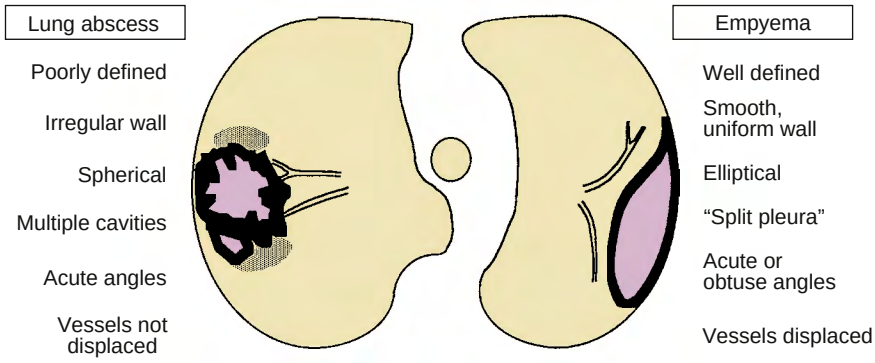

FIGURE 7-12 ■ Empyema versus lung abscess.

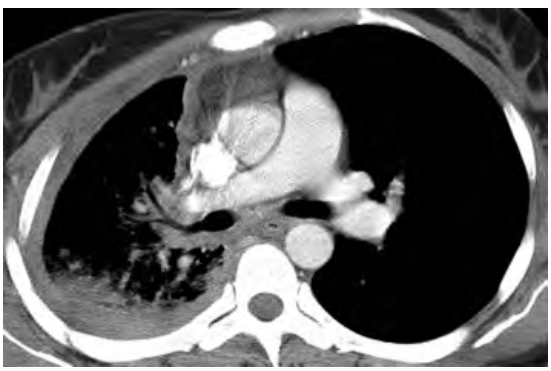

FIGURE 7-13 ■ Pleural peel. A patient with prior empyema shows extensive smooth thickening of the right pleura. Note that the hemithorax is reduced in volume. This is typical of pleural fibrosis.

considerably thicker than the fat pads, which can be seen normally) (Fig. 7-14). Treatment usually requires pleural stripping.

Dense pleural thickening, even with calcification, does not indicate that the pleural disease is inactive. Loculated fluid collections resulting from active infection (Fig. 7-14) may be seen on CT within the thickened pleura.

Pleural Calcification and Talc Pleurodesis

Pleural thickening with calcification may be seen with chronic empyema, particularly if it is tuberculous in nature (Fig. 7-14), and with resolved hemothorax, asbestos exposure (Figs. 7-15 and 7-21), and rarely in pleural sarcomas. Pleurodesis using talc can mimic pleural calcification. The talc is dense and typically accumulates in the posterior and inferior hemithorax (Fig. 7-16).

Asbestos-Related Pleural Disease

Asbestos-related pleural thickening has a typical appearance on CT. Early pleural thickening is discontinuous, with the intervening pleura appearing normal; focal areas of pleural thickening are termed *pleural plaques* (Figs. 7-15 and 7-19). The pleural disease is typically bilateral. Calcification is common. Diffuse pleural thickening, which is probably the result of prior asbestos-related benign pleural effusion, can also be seen. In patients with asbestos-related pleural disease, the pleural thickening, plaques, or calcification typically involve the parietal pleura, but this is difficult to recognize on CT unless the presence of pleural fluid separates the visceral and parietal pleural layers.

The diaphragmatic pleura is commonly involved in patients with asbestos-related pleural disease (Fig. 7-19). However, the diaphragm lies roughly in the scan plane, and detection of uncalcified pleural plaques on the diaphragmatic surface can be difficult. In some patients, diaphragmatic pleural plaques are visible deep in the posterior costophrenic angle, below the lung base; in this location, pleural disease can be localized to the parietal pleura, because only parietal pleura is present. Pleural plaques along the mediastinum have been considered unusual in patients with asbestos-related pleural disease, but they are visible on CT scans in about 40% of these patients. Paravertebral pleural thickening is also common.

Although it is unusual, pleural thickening can involve a fissure and result in a localized fissural pleural plaque. These may simulate a lung nodule on CT unless the plane of the fissure is identified.

Pleural Neoplasms

Pleural Effusion Associated with Malignancy

In patients with malignancy, pleural effusion can result from tumor involvement of the pleura or lymphatic obstruction in the hila or mediastinum.

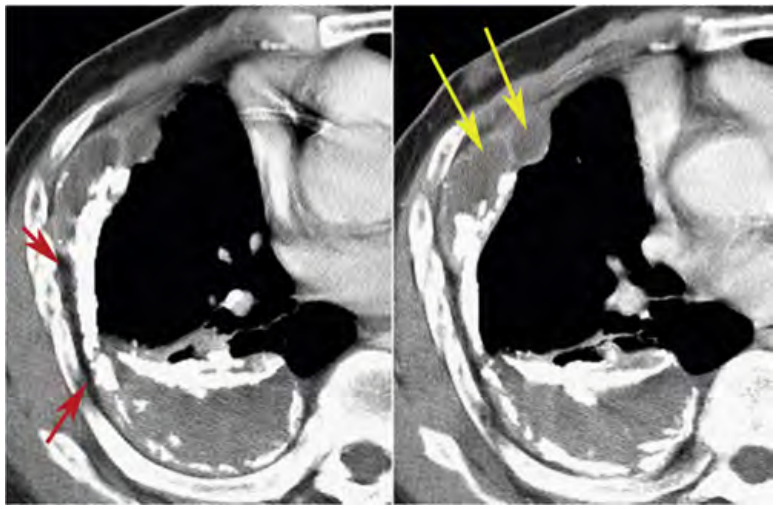

FIGURE 7-14 ■ Calcified pleural thickening associated with tuberculosis. The parietal and visceral pleura are densely calcified. Thickened extrapleural fat (*red arrows*) is visible external to the calcified parietal pleura. Residual fluid is evident in the pleural space, and loculated collections anteriorly (*yellow arrows*) reflect active infection.

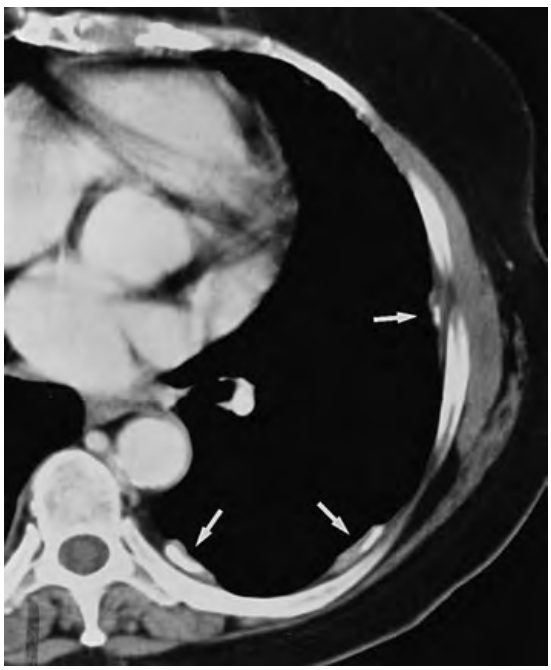

FIGURE 7-15 ■ Asbestos-related pleural plaques. Typical calcified pleural plaques (*arrows*) are visible. They are often internal to the ribs.

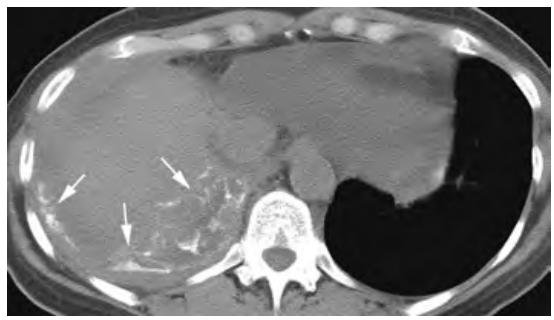

FIGURE 7-16 ■ Talc pleurodesis. Streaky high-attenuation opacities in the posterior right hemithorax represent talc injected for pleurodesis (*arrows*). This appearance mimics pleural thickening with calcification.

FIGURE 7-17 ■ Malignant effusion caused by metastatic carcinoma. A large left pleural effusion is associated with left lung atelectasis, mediastinal displacement to the left, and pleural thickening (*arrows*).

In both instances, an exudate is typically present. Effusions may be large.

The term *malignant effusion* means that malignant cells are present in the fluid. It can occur with pleural metastases or mesothelioma. In patients with malignant effusion, pleural thickening may or may not be visible on contrast-enhanced CT (Fig. 7-17).

CT Findings of Malignancy

Primary and metastatic tumors may involve the pleura, with or without pleural effusion. CT findings that strongly suggest the diagnosis of malignant involvement of the pleura (Fig. 7-18) include:

1. Nodular pleural thickening
2. A pleural thickness of more than 1 cm

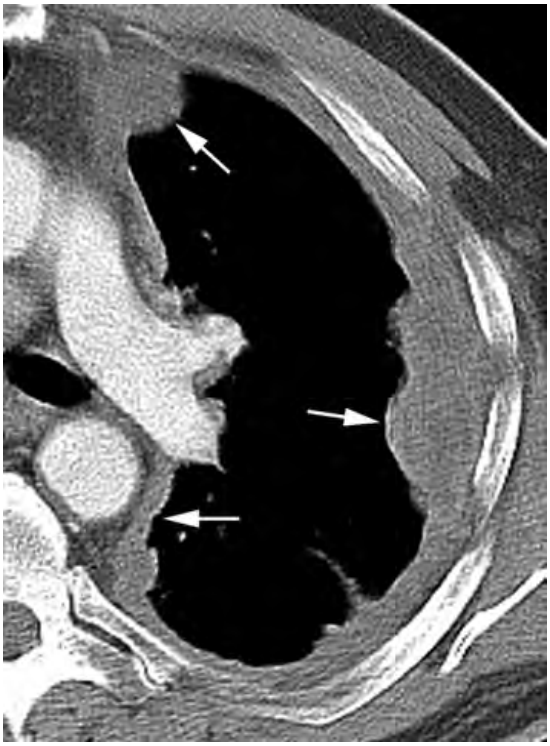

FIGURE 7-18 ■ CT findings of malignancy in mesothelioma. There is circumferential and nodular left pleural thickening (*arrows*). The mediastinal pleura is abnormal, and the pleural thickening exceeds 1 cm. These four findings predict a malignant process.

3. Thickening that concentrically involves the pleura, encasing the lung
4. Thickening of the mediastinal pleura

Mesothelioma

Mesothelioma (also known as diffuse or malignant mesothelioma) is a highly aggressive neoplasm with an extremely poor prognosis. It is characterized morphologically by gross and nodular pleural thickening. However, hemorrhagic pleural effusion is often present and may obscure the underlying pleural thickening, which can be minimal in early cases. Mesothelioma spreads most commonly by local infiltration of the pleura. In most patients, this tumor is related to asbestos exposure; although it is rare in the general population, the incidence in workers heavily exposed to asbestos is about 5%.

In patients with mesothelioma, CT can expedite the initial diagnosis and define the extent of tumor tissue. Usually, irregular or nodular pleural thickening is visible (Fig. 7-18), although a new pleural effusion or diffuse pleural thickening may be the only recognizable finding (Fig. 7-19). Pleural thickening is usually most pronounced in the inferior thorax. Contrast infusion can allow tumor

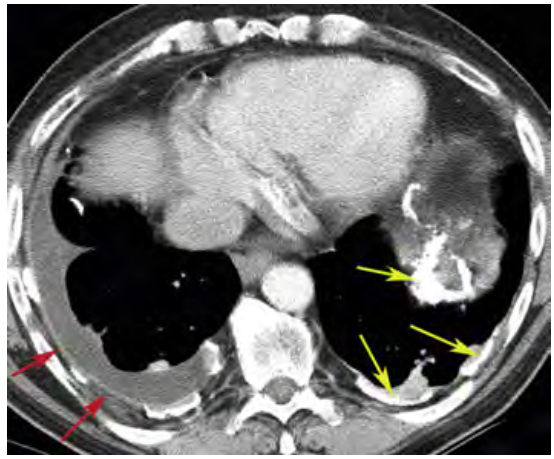

FIGURE 7-19 ■ Mesothelioma in a patient with asbestos exposure. Bilateral calcified pleural plaques (*yellow arrows*) reflect asbestos exposure; note the presence of a calcified plaque on the surface of the left hemidiaphragm. A new right pleural effusion associated with parietal pleural thickening (*red arrows*) is nonspecific but in this patient indicates the presence of mesothelioma.

to be distinguished from associated fluid collections. Scans with the patient in the prone or decubitus position can also help in distinguishing underlying mesothelioma from pleural fluid.

Although mesothelioma is visible most frequently along the lateral chest wall, mediastinal pleural thickening or concentric pleural thickening is seen with extensive disease (Fig. 7-18). The abnormal hemithorax can appear contracted and fixed, with little change in size on inspiration. Thickening of the fissures, particularly the lower part of the major fissures, can reflect tumor infiltration. Malignant mesothelioma typically spreads by local invasion, involving the mediastinum and sometimes the chest wall. Although hematogenous pulmonary metastases or distant metastases occur in about 30% of cases, these are usually clinically insignificant; local invasion usually determines prognosis.

Localized Fibrous Tumor of the Pleura

A localized fibrous tumor of the pleura, previously termed *benign mesothelioma*, is uncommon. It is usually detected incidentally on chest radiographs but can be associated with chest pain, hypoglycemia, and hypertrophic pulmonary osteoarthropathy. About 70% of tumors are benign and 30% are malignant.

A localized fibrous tumor usually arises from the visceral pleura and most commonly involves the costal pleural surface (Fig. 7-20); occasionally, it can be seen within a fissure (Fig. 7-21). On CT, these tumors are solitary, smooth, sharply defined, and often large lesions that contact a pleural surface (Figs. 7-20 and 7-21).

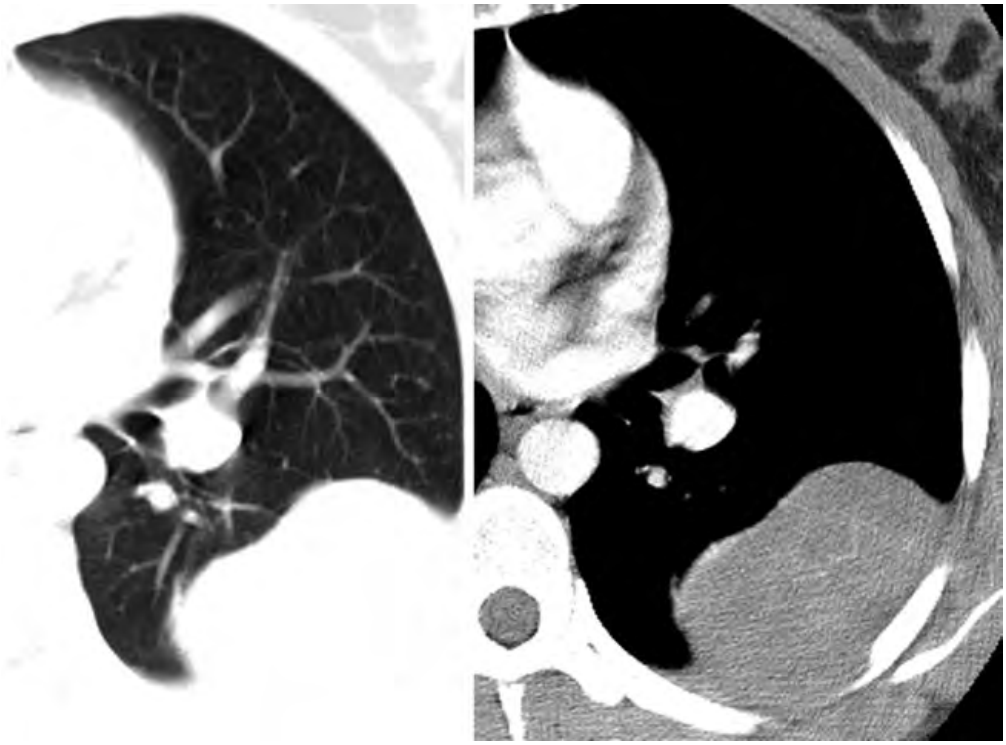

FIGURE 7-20 ■ Localized fibrous tumor of the pleura. The large homogeneous mass is smooth and sharply defined. Slight beak-shaped pleural thickening is seen adjacent to the mass, probably related to a small amount of pleural fluid.

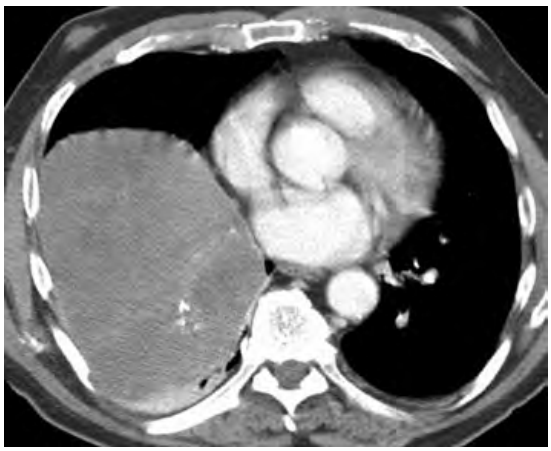

FIGURE 7-21 ■ Localized fibrous tumor of the pleura. A large heterogeneous and calcified mass appears smooth and sharply defined.

Usually, a localized fibrous tumor appears homogeneous on CT, but necrosis can result in a multicystic appearance with or without contrast infusion, and calcification may be present. Large tumors are often heterogeneous in appearance (Fig. 7-21). Although it is generally believed that pleural abnormalities result in obtuse angles at the point of contact between the lesion and the chest wall, localized fibrous tumors may show acute angles with slightly tapered pleural thickening adjacent to the mass (Fig. 7-20). This thickening may reflect a small amount of fluid accumulation in the pleural space at the point at which the visceral and parietal pleural surfaces are separated by the mass. A similar "beak" or "thorn" sign is often visible on plain radiographs in patients with a localized fibrous tumor in a fissure.

Pleural Metastases

Malignant pleural effusion may or may not be associated with visible pleural thickening, but in some cases, pleural metastases result in large pleural nodules visible on CT. In the majority of patients with nodular pleural metastases, pleural effusion is also present. Nodular pleural metastases are more easily seen on contrast-enhanced scans, being higher in attenuation than associated fluid (Figs. 7-22 and 7-23). Invasive thymoma and some other tumors can result in pleural nodules unassociated with pleural effusion.

Pleural metastases can diffusely infiltrate the pleura, resulting in an appearance indistinguishable from that of mesothelioma (Fig. 7-24). Extension into the fissures can also be seen; nodules of tumor within a fissure or thickening of the fissure may be seen (Fig. 7-25).

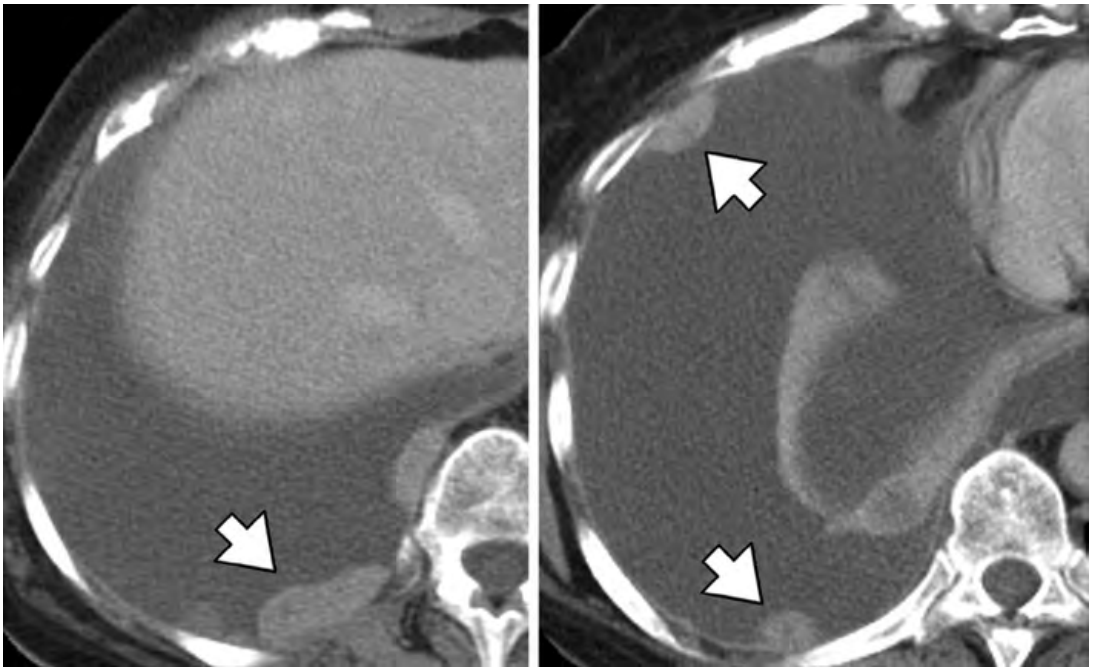

FIGURE 7-22 ■ Pleural metastases from colon carcinoma. On a contrast-enhanced computed tomography scan, focal nodular pleural masses (*arrows*) are visible arising from the parietal pleura. A large pleural effusion is also present.

FIGURE 7-23 ■ Pleural metastasis. Pleural thickening is evident after contrast medium infusion. An enhanced pleural mass (*arrow*) and pleural effusion are visible.

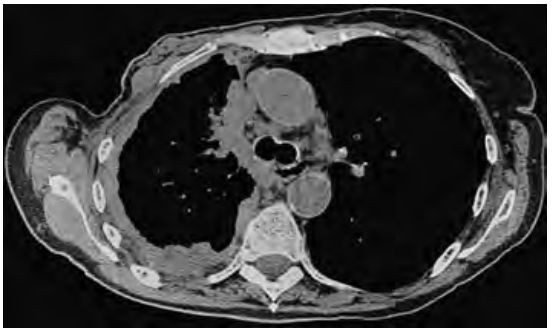

FIGURE 7-24 ■ Pleural metastasis. Diffuse nodular pleural thickening in a patient with breast cancer simulates mesothelioma.

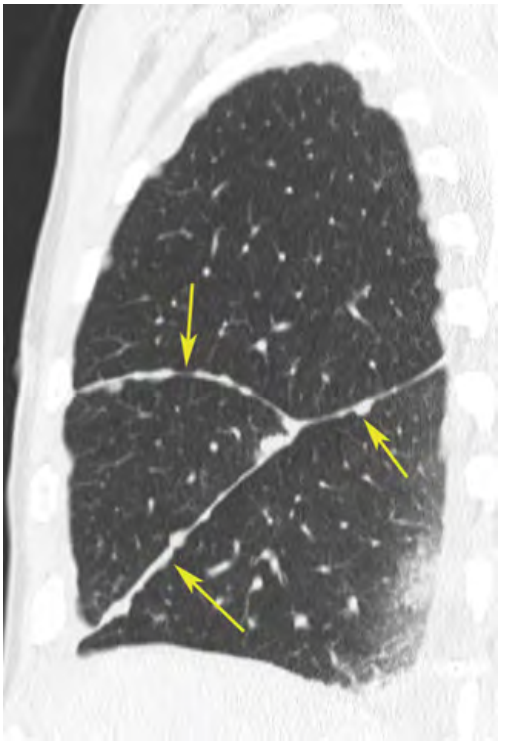

FIGURE 7-25 ■ Pleural metastases with pleural nodules involving the fissures. Nodular thickening of the major and minor fissures (*arrows*) on this sagittal reconstruction is due to pleural metastases from colon carcinoma. A small pleural effusion is visible in the posterior costophrenic angle.

Lymphoma

Pleural effusions occur in 15% of patients with Hodgkin's disease and usually reflect lymphatic or venous obstruction by a mediastinal or hilar tumor rather than by pleural involvement; effusions in Hodgkin's disease tend to resolve after local mediastinal or hilar radiation. Pericardial effusions, however, present in 5% of patients, usually indicate direct involvement of the pericardium. Masses involving the pleura or extrapleural chest wall can sometimes be seen in Hodgkin's or non-Hodgkin's lymphoma.

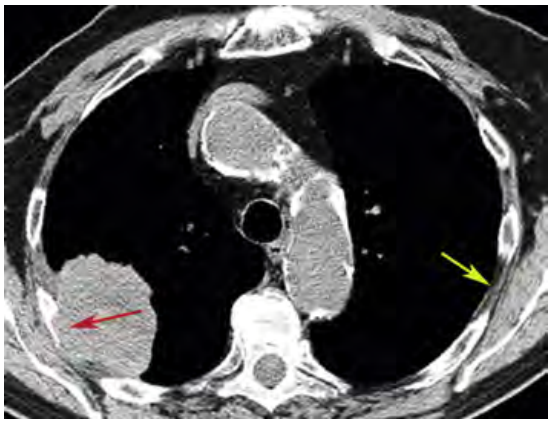

FIGURE 7-26 ■ Lung carcinoma with chest wall invasion. This patient shows a number of findings that predict or are diagnostic of chest wall invasion, including more than 3 cm of contact between the tumor and chest wall, obtuse angles with the pleural surface, and a contact length between the tumor and the chest wall of > 70% of the maximum tumor diameter. Also note (*red arrow*) the obliteration of normal exptrapleural fat, rib destruction, and chest wall mass adjacent to the tumor. Normal fat planes (*yellow arrow*) are shown on the left.

CHEST WALL

Lung Cancer with Chest Wall Invasion

Direct invasion of the chest wall by a peripheral bronchogenic carcinoma is common. In the lung cancer staging system (Table 4-3), tumors invading the chest wall, diaphragm, phrenic nerve, mediastinal pleura, or parietal pericardium are classified as *T3* and are usually resectable. Tumors invading the vertebral body or great vessels at the lung apex are considered *T4*; these may be resectable if lymph node metastases are limited to the hila, often following chemotherapy and/or radiation.

Hodgkin's disease can involve structures of the chest wall by direct invasion from the mediastinum or lung in a small percentage of cases. Malignant mesothelioma is a less common tumor that also can invade the chest wall.

The CT diagnosis of chest wall invasion can be difficult, but a variety of CT findings can help in prediction. The most accurate CT findings of chest wall invasion in order of increasing specificity (Figs. 7-26 and 7-27) are:

1. Obtuse angles at the point of contact between tumor and pleura
2. Extensive contact between the tumor and chest wall (> 3 cm or 70% of the tumor diameter)
3. Obliteration of extrapleural fat planes
4. Infiltration of soft tissues
5. A chest wall mass
6. Bone destruction

Diagnosing chest wall invasion when a tumor simply abuts the pleura should be avoided. Tumors adjacent to the pleura, even when associated with focal pleural thickening and pleural

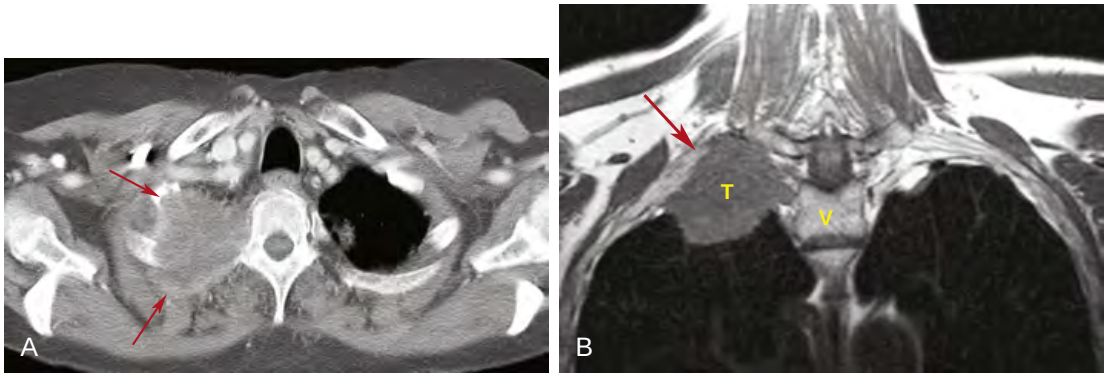

FIGURE 7-27 ■ Pancoast tumor with chest wall invasion. *A*, On computed tomography, a right apical mass is associated with invasion of the chest wall and rib destruction (*arrows*). Although the tumor appears to contact the vertebral body, it appears intact. *B*, Coronal magnetic resonance imaging shows the relationship of the tumor (T) to the vertebral body (V) and the brachial plexus (*arrow*), which appears to be involved.

effusion, may not be invasive. In a patient with bronchogenic carcinoma, pleural effusion can occur for a variety of reasons, including obstructive pneumonia and lymphatic or pulmonary venous obstruction by tumor. Only patients with demonstration of tumor cells in the pleural fluid (malignant effusion) or pleural nodules are considered to have unresectable disease (*M1* in the staging system; Table 4-3).

Superior Sulcus (Pancoast) Tumors

Invasive tumors arising in the superior pulmonary sulcus produce the characteristic clinical findings of Horner's syndrome and shoulder and arm pain; this presentation is termed *Pancoast syndrome*. Previously, tumors of the superior sulcus were considered to have a poor prognosis, but combined therapy with radiation, followed by resection of the upper lobe, chest wall, and adjacent structures, has resulted in 5-year survival rates of up to 30%. In patients being considered for this combined therapy, CT scans can provide information on the anatomic extent of tumor spread that is useful in planning both the radiation therapy and the surgical approach to the tumor. However, magnetic resonance imaging has been shown to be more accurate than CT in showing the apical extent of tumors.

Extension of a tumor posteriorly or laterally at the lung apex primarily involves the chest wall (Fig. 7-27). Although such chest wall invasion does not prevent resection, extensive chest wall and bone involvement makes surgical treatment difficult, and the prognosis for patients with extensive chest wall disease is relatively poor. Invasion of tumor tissue posteromedially involves the ribs or vertebral bodies. This occurs in one-third to half of cases and usually can be seen on CT scans. Anterior and medial extension of a tumor can involve the esophagus, trachea, and brachiocephalic vessels. Invasion of these structures or the vertebral body precludes resection in most cases.

AXILLARY SPACE

As usually defined, the axilla is bordered by the fascial coverings of the following muscles: the pectoralis major and pectoralis minor anteriorly; the latissimus dorsi, teres major, and subscapularis posteriorly; the chest wall and serratus anterior medially; and the coracobrachialis and biceps laterally. However, when patients are scanned with their arms above their heads, the axilla is open laterally.

The axilla contains the axillary artery and vein, branches of the brachial plexus, some branches of the intercostal nerves, and a large number of lymph nodes, all surrounded by fat. The axillary vessels and the brachial plexus extend laterally, near the apex of the axilla, close to the pectoralis minor muscle. In general, the axillary vein lies below and anterior to the axillary artery, whereas the brachial plexus is largely above and posterior to the artery. Although these vessels usually can be seen on CT scans, in many healthy individuals it is impossible to distinguish artery and vein within the axilla, unless the vein is opacified by contrast medium.

Lymphadenopathy

Axillary lymph nodes, which are usually up to 1 cm but occasionally 1.5 cm in diameter, can be seen in normal subjects. Lymph nodes larger than 1 cm (short axis or least diameter) should be considered suspicious when an abnormality is suspected on clinical grounds; lymph nodes 2 cm in diameter are considered pathologic regardless of history. Axillary lymphadenopathy is seen most frequently in patients with lymphoma or metastatic carcinoma. Lymph node masses are detected most easily by observing both axillae for symmetry. Enlarged lymph nodes high within the axilla lie beneath the pectoral muscles (subpectoral nodes) and may not be palpable, but these nodes can be detected by CT. Axillary masses in relation to nerves of the brachial plexus can also be demonstrated using CT.

BREAST

Soft tissues of the breasts are seen on CT scans of female patients in the supine position. Localized breast masses are occasionally visible, but their CT appearance is usually nonspecific. Enhancing masses are suspicious for carcinoma. Breast masses detected incidentally on CT images generally should be evaluated by physical examination and mammography.

Breast Carcinoma

Other than for staging, CT is not used in the routine evaluation of patients with breast cancer. However, CT can aid the planning of radiation therapy by providing an accurate measurement of chest wall thickness and by detecting internal mammary lymph node metastases.

Mastectomy

In women who have had a mastectomy, characteristic alterations in chest wall anatomy are seen,

depending on the surgical procedure performed. CT is sometimes used to evaluate suspected local tumor recurrence and to guide needle biopsy.

Surgery for breast cancer is often limited to lumpectomy, and little is visible on CT except for a local scar. Some residual breast tissue remains when segmental or partial mastectomy is performed. Simple mastectomy consists of removal of the breast. Axillary lymph node dissection may be performed with any of these approaches. Typically, surgical clips are present within the axilla and focal scarring remains visible on CT. Postoperative scarring is visible as irregular soft tissue within the axillary fat. Localized post-operative fluid collections may be seen in the breast or axilla.

A radical mastectomy consists of complete removal of the breast tissue and pectoralis major and pectoralis minor muscles and extensive axillary lymph node dissection. On CT, although most of the pectoralis muscles are absent, residual pectoralis major muscle is sometimes seen at its sternal or costal attachment. This should not be misinterpreted as a recurrent tumor.

Modified radical mastectomy consists of removal of the breast and the pectoralis minor muscle and axillary lymph node dissection. In patients who have undergone a modified radical mastectomy, the amount of pectoralis minor muscle remaining is variable. Without careful clinical correlation, it is sometimes difficult to distinguish postsurgical changes from tumor recurrence.

Keep in mind that if a patient has difficulty in elevating both arms symmetrically for the CT scan because of surgery, asymmetry of the breasts, axilla, and underlying musculature may be present (e.g., the pectoralis muscle may look thicker on one side). This asymmetry should not be misinterpreted as abnormal.

DIAPHRAGM

Anatomy

Because of the transaxial plane of CT, the central portion of the diaphragm does not appear as a distinct structure, and its position can only be inferred by the position of the lung base above and the upper abdominal organs below. However, as the more peripheral portions of the diaphragm extend caudad toward their sternal and costal attachments, the anterior, posterior, and lateral portions of the diaphragm become visible adjacent to retroperitoneal fat (Fig. 7-28). Where the diaphragm is contiguous with the liver or spleen, it is sometimes outlined as a distinct structure because of a subdiaphragmatic fat layer.

FIGURE 7-28 ■ Normal diaphragm. The diaphragm is outlined by retroperitoneal fat. Where it contacts the liver and spleen, it is not usually visible as a discrete structure. The diaphragmatic crura can appear quite lumpy (*arrows*). Here they pass anterior to the aorta to form the aortic hiatus.

Diaphragmatic Crura

The right and left diaphragmatic crura are tendinous structures arising inferiorly from the anterior surfaces of the upper lumbar vertebral bodies and intervening discs and continuous with the anterior longitudinal ligament of the spine. The crura ascend anterior to the spine on each side of the aorta, and then pass medially and anteriorly, joining the muscular diaphragm anterior to the aorta to form the aortic hiatus (Fig. 7-28). The right crus, which is larger and longer than the left, arises from the first three lumbar vertebral levels; the left crus arises from the first two lumbar segments.

The diaphragmatic crura can be mistaken for enlarged lymph nodes or masses because of their rounded appearance; para-aortic lymph nodes can indeed be seen in a similar position. However, on contiguous CT scans, the crura merge gradually with the diaphragm at more cephalad levels. The diameter of the crura also varies with lung volume, increasing in thickness at full inspiration compared with expiration.

Openings in the Diaphragm

The diaphragm is perforated by several openings that allow structures to pass from the thorax to the abdomen. The aortic hiatus is posterior; it is bounded posteriorly by the vertebral body and anteriorly by the crura. Through it pass the aorta, the azygos and hemiazygos veins, the thoracic duct, the intercostal arteries, and the splanchnic nerves. The esophageal hiatus is situated more anteriorly, in the muscular portion of the diaphragm. Through it pass the esophagus, the vagus nerves, and small blood vessels. The

FIGURE 7-29 ■ Bochdalek hernias. In this patient, bilateral Bochdalek hernias (H) consist of retroperitoneal fat. The edges of the diaphragm (*arrows*) outline the defects leading to herniation.

foramen of the inferior vena cava pierces the fibrous central tendon of the diaphragm anterior and to the right of the esophageal hiatus.

Of these three structures, the aortic hiatus is defined most easily. On CT scans, the esophageal foramen is visible as an opening at the junction of the esophagus and stomach. The foramen of the inferior vena cava must be inferred from the position of the inferior vena cava. The foramina of Morgagni and of Bochdalek are not visible on CT scans in normal individuals.

Diaphragmatic Abnormalities

Hernias

Abdominal or retroperitoneal contents can herniate into the chest through congenital or acquired areas of weakness in the diaphragm or through traumatic diaphragmatic ruptures. Hernias of the stomach through the esophageal hiatus are the most common.

Hernias through the foramen of Bochdalek were thought to be uncommon in adults; however, CT has shown that small Bochdalek defects may occur in as many as 5% of healthy adult subjects. This is the most common type of diaphragmatic hernia in infants. Most are left-sided, and although they are often located in the posterolateral diaphragm, they can occur anywhere along the posterior costodiaphragmatic margin (Fig. 7-29). Bochdalek hernias in adults usually contain retroperitoneal fat or, much less commonly, kidney.

Parasternal hernias through the foramen of Morgagni are relatively rare. Most Morgagni hernias occur on the right and, in contrast to Bochdalek hernias, usually contain an extension of the peritoneal sac. Their contents can include omentum, liver, or bowel.

An understanding of the anatomy of the anterior portion of the diaphragm is essential in correctly diagnosing a Morgagni hernia. The presence of bowel anterior to the heart can suggest the presence of a hernia, but this is not usually the case.

Diaphragmatic rupture can result from penetrating or nonpenetrating trauma to the abdomen or thorax. In nearly all cases, the left hemidiaphragm is affected, with ruptures of the central or posterior diaphragm being the most frequent. The diaphragmatic defect may appear as a localized absence of visible diaphragm, associated with thickening of the adjacent visible portion of the diaphragm or ipsilateral crus. Omentum, stomach, small or large intestine, spleen, and kidney may all herniate through a diaphragmatic rent. Reconstruction of CT in the sagittal or coronal plane may help in diagnosis; the hernia may show a "neck" at the site of herniation.

If diaphragmatic rupture is associated with splenic rupture, small bits of splenic tissue may seed the left pleural space. This is termed *thoracic splenosis*. CT can show small, left-sided pleural nodules, usually associated with findings of splenectomy and diaphragmatic injury.

Tumors

Tumors involving the diaphragm usually represent pleural tumors (e.g., mesothelioma), pleural metastases, or upper abdominal tumors with local invasion. Primary diaphragmatic tumors are rare. Pleural lipoma is occasionally seen as an incidental finding.

Diaphragmatic Eventration or Paralysis

Local eventration of the right hemidiaphragm with superior displacement of the liver can be confused radiographically with a peripheral pulmonary or pleural mass. CT scans after infusion of contrast medium can demonstrate opacification of normal intrahepatic vessels in the apparent mass, allowing its identification.

Hemidiaphragm elevation is seen in patients with diaphragmatic paralysis. The ipsilateral diaphragm may appear thinner than the opposite hemidiaphragm if the paralysis is chronic.

SUGGESTED READING

Aberle DR, Gamsu G, Ray CS, Feuerstein IM: Asbestos-related pleural and parenchymal fibrosis: Detection with high-resolution CT. *Radiology* 166:729–734, 1988.

Adler BD, Padley SPG, Müller NL: Tuberculosis of the chest wall: CT findings. *J Comput Assist Tomogr* 17:271–273, 1993.

Aquino SL, Webb WR, Gushiken BJ: Pleural exudates and transudates: Diagnosis with contrast-enhanced CT. *Radiology* 192:803–808, 1994.

Berkmen YM, Davis SD, Kazam E, et al.: Right phrenic nerve: Anatomy, CT appearance, and differentiation from the pulmonary ligament. *Radiology* 173:43–46, 1989.

Choi JA, Hong KT, Oh YW, et al.: CT manifestations of late sequelae in patients with tuberculous pleuritis. *AJR Am J Roentgenol* 176:441–445, 2001.

Dynes MC, White EM, Fry WA, Ghahremani GG: Imaging manifestations of pleural tumors. *Radiographics* 12:1191–1201, 1992.

Federle MP, Mark AS, Guillaumin ES: CT of subpulmonic pleural effusions and atelectasis: Criteria for differentiation from subphrenic fluid. *AJR Am J Roentgenol* 146:685–689, 1986.

Ferretti GR, Chiles C, Choplin RH, Coulomb M: Localized benign fibrous tumors of the pleura. *AJR Am J Roentgenol* 169:683–686, 1997.

Halvorsen RA, Fedyshin PJ, Korobkin M, et al.: Ascites or pleural effusion? CT differentiation: Four useful criteria. *Radiographics* 6:135–149, 1986.

Im J-G, Webb WR, Rosen A, Gamsu G: Costal pleura: Appearances at high-resolution CT. *Radiology* 171:125–131, 1989.

Kawashima A, Libshitz HI: Malignant pleural mesothelioma: CT manifestations in 50 cases. *AJR Am J Roentgenol* 155:965–969, 1990.

Leung AN, Müller NL, Miller RR: CT in differential diagnosis of diffuse pleural disease. *AJR Am J Roentgenol* 154:487–492, 1990.

McLoud TC, Flower CDR: Imaging the pleura: Sonography, CT, and MR imaging. *AJR Am J Roentgenol* 156:1145–1153, 1991.

Müller NL: Imaging the pleura. *Radiology* 186:297–309, 1993.

Naidich DP, Megibow AJ, Hilton S, et al.: Computed tomography of the diaphragm: Peridiaphragmatic fluid localization. *J Comput Assist Tomogr* 7:641–649, 1983.

Naidich DP, Megibow AJ, Ross CR, et al.: Computed tomography of the diaphragm: Normal anatomy and variants. *J Comput Assist Tomogr* 7:633–640, 1983.

Stark DD, Federle MP, Goodman PC, et al.: Differentiating lung abscess and empyema: Radiography and computed tomography. *AJR Am J Roentgenol* 141:163–167, 1983.

Takasugi JE, Godwin JD, Teefey SA: The extrapleural fat in empyema: CT appearance. *Br J Radiol* 64:580–583, 1991.

Waite RJ, Carbonneau RJ, Balikian JP, et al.: Parietal pleural changes in empyema: Appearances at CT. *Radiology* 175:145–150, 1990.

CHAPTER 8

INTRODUCTION TO CT OF THE ABDOMEN AND PELVIS

William E. Brant

The development of multidetector-row computed tomography (MDCT), with up to 128 detector rows at present, has solidified CT as a primary imaging modality for the abdomen and pelvis. The technology of MDCT scanners continues to advance with progressive increases in the number of detectors and decreases in acquisition times. Concern is now focused on the CT radiation dose and overutilization because thin-slice rapid scanning during multiple phases of contrast enhancement has rapidly expanded indications for body CT. Isotropic voxel scanning allows CT data obtained in the axial plane to be reconstructed with the same resolution in any plane. (An isotropic voxel is of the same size in all directions.) Coronal, sagittal, and oblique plane reconstructions have become routine. CT angiography and virtual endoscopy are a reality.

Evaluation of the abdomen and pelvis by CT requires greater attention to patient preparation, technique, and individualization than CT evaluation of any other area of the body. The best-quality studies are produced when the radiologist evaluates the patient clinically, assesses the nature of the imaging problem, and tailors the study to optimize the information that the examination provides.

TECHNICAL CONSIDERATIONS

When a request is presented for an abdomen–pelvis CT scan, the radiologist should assess the clinical problem to be evaluated by reviewing the patient history and all pertinent previous imaging studies available. Medical history of importance to CT examination includes the current indication for the study, the risk of administering contrast agents, including any history of allergic reactions or impaired renal function, the presence of cardiac or other diseases, past abdominal surgeries, a history of prior malignancies and radiation therapy, and findings and availability of previous imaging studies performed elsewhere. Previous imaging studies are reviewed to ensure that all previously identified abnormalities and questionable findings are appropriately reevaluated.

Decisions to be made to individualize the examination include the following:

- Area scanned: anatomic landmarks and scan extent
- Radiation dose (mA and peak kilovoltage, kVp), pitch, scan speed, and rotation time
- Beam collimation (detector width and number of detector rows)
- Type and concentration of contrast medium to be administered: intravenous, oral, rectal, or intracavitary
- Intravenous contrast medium concentration, administration rates, method of administration, and scan timing for arteriography and venography, or for arterial phase, venous phase, and delayed phase enhancement of solid organs and tissues
- Slice thickness, reconstruction intervals, reconstruction planes, and three-dimensional image reconstructions

Most institutions have developed standard protocols for a variety of indications and these depend in part on the scanner manufacturer and number of detector rows. These may be modified as needed to appropriately address the patient problem.

GASTROINTESTINAL CONTRAST AGENTS

Nearly all CT scans of the abdomen require administration of intraluminal contrast agents to demonstrate the lumen of and distend the gastrointestinal tract. Radiopaque agents may be dilute concentrations of barium or iodinated contrast agents. Iodine agent concentrations of 1% to 3% provide optimal intraluminal opacification for CT, compared with the 30% to 60% solutions used for fluoroscopy. Barium mixtures and water-soluble iodinated agents are equally effective as opaque oral contrast agents.

Air and water are excellent as low-attenuation contrast agents. Carbon dioxide is preferred for instillation into the rectum to insufflate the colon for CT colography. Effervescent crystals with a small volume of water may be given orally to distend the stomach with gas. Water serves as an excellent low-density contrast agent for the upper gastrointestinal tract. Urine in the distended bladder provides an excellent contrast for bladder lesions. Patient preparation may include having the patient avoid urination or clamping an indwelling Foley catheter. Low-attenuation barium-based contrast agents are utilized for CT enterography.

INTRAVENOUS CONTRAST AGENTS

Intravenous contrast agents improve the quality of abdominal CT by opacifying blood vessels, increasing the CT attenuation of abdominal organs, confirming perfusion, and improving image contrast between lesions and normal structures. MDCT allows multiphase imaging to demonstrate the passage of contrast through the arterial system, organs and tumors, and the venous system. Delayed images show contrast excretion by the kidneys, late enhancement, or prolonged retention of intravenous contrast agent in organs and lesions. For most applications, intravenous contrast agents are administered by power injectors that provide accurate control of the rate and volume of administration.

Low-osmolar "non-ionic" iodine-based agents are the intravenous contrast media of choice for most abdominal scanning because of their lower rate of adverse reactions. Sterile iodinated contrast agents approved for intravenous injection can be injected into indwelling catheters, drainage tubes, sinus tracts, and fistulas to evaluate the extent of disease. For intravenous administration, iodine concentrations of 60% and 75% are most commonly used. Older ionic contrast agents of higher osmolality are no longer utilized for intravascular injection because of significantly higher rates of adverse reactions. However, these cheaper ionic agents may be used for intracavitary injection, for which adverse reactions are rare. For injection into the bladder for CT cystography or through indwelling catheters for demonstration of fistulas, sinus tracts, or abscess cavities, the contrast is usually diluted to an iodine concentration of 2% to 3%.

While a detailed review of adverse reactions and the safe use of intravenous contrast is beyond the scope of this text, patient safety is always the first priority. Adverse reactions associated with intravenous contrast administration include anaphylaxis, cardiac and respiratory arrest, nephrotoxicity, hives, and many others. The reader is referred to the Suggested Reading section for several excellent reviews on the safe use of iodinated intravenous contrast agents.

HOW TO INTERPRET CT SCANS OF THE ABDOMEN AND PELVIS

When one is just beginning to learn interpretation of body CT, it is very useful to develop a checklist to ensure that all structures are inspected and that all key observations are noted to make accurate and comprehensive diagnoses. Because of the dramatic increase in the number of images obtained by MDCT, image viewing is best performed on a computer workstation utilizing reconstructed digital images obtained directly from the CT scanner. Image display workstations allow rapid scrolling through serial images, convenient changes in window level and window width settings, and rapid image reformatting in multiple anatomic planes and with three-dimensional techniques.

Each CT image of the abdomen contains much more information than can be displayed by any one window width and level setting. Routine soft-tissue windows (window width ~400; window level 30 to 50) define most of the abdominal anatomy. However, the liver may also be inspected using narrower liver windows (window width ~100 to 150; window level 70 to 80) to increase image contrast within the liver and improve the visibility of subtle lesions. The lung bases are included on scans through the upper abdomen and should be inspected using lung windows (window width 1000 to 2000; window level 600 to 700). Lung windows are also used to detect free intraperitoneal air and gas collections. Lastly, inspection of the bones using bone windows (window width ~2000; window level ~600) may yield important clues to pathologic findings within the abdomen and pelvis (Fig. 8-1).

Each organ and structure should be systematically examined on serial images obtained through all phases of the CT examination. No interpretation will be accurate without considering the phase of contrast enhancement (arterial, venous, cortical, nephrogram, delayed, etc.).

- Lung bases: nodules, infiltrates, scars, pleural effusions, atelectasis
- Liver: size, homogeneous parenchymal attenuation, uniform enhancement, portal veins, hepatic veins, hepatic arteries
- Biliary tree and gallbladder: visible bile ducts, wall thickness, presence and

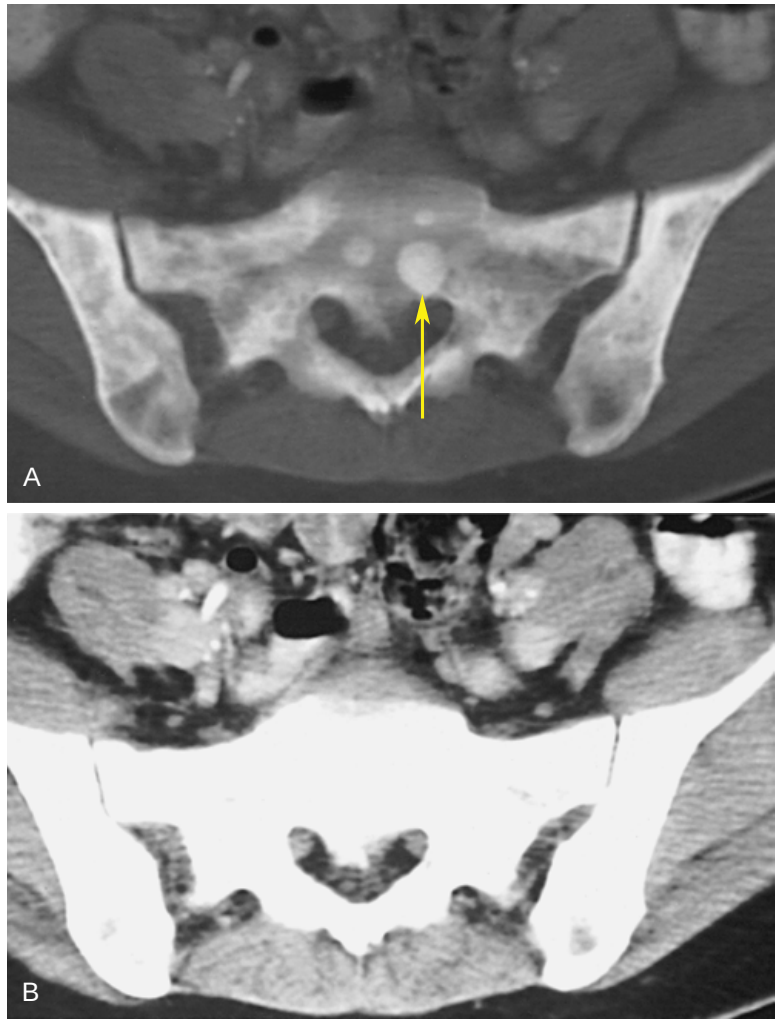

FIGURE 8-1 ■ Bone windows. *A* and *B,* Metastatic lesions (*arrow*) from prostate carcinoma to the sacrum and iliac bones are obvious on a bone window (*A*) but cannot be seen on a routine soft-tissue window (*B*).

distention of the gallbladder, low-density stones, high-density stones
- Spleen: size (normal up to 14 cm), inhomogeneous enhancement early, homogeneous enhancement late, splenules, splenic vein, splenic artery
- Adrenals: Y or V shape, limb thickness less than 1 cm, no convex margins
- Pancreas: size and position, head, neck, body, tail, size of the pancreatic duct, patent splenic vein, lucent peripancreatic fat
- Kidneys: normal size 9 to 13 cm in adults, symmetrical enhancement, calyces and pelvis and ureter, position and orientation
- Lymph nodes: retroperitoneum, mesentery, omentum, porta hepatis, pelvis
- Blood vessels: aorta, inferior vena cava, celiac axis and branches, superior and inferior mesenteric arteries, renal arteries, renal veins, splenic vein, superior mesenteric vein, portal vein
- Stomach: position, distention, contents, wall thickness, fold thickness
- Duodenum and small bowel: position, distention, wall thickness, surrounding fat, mesentery
- Colon and rectum: position, distention, wall thickness, luminal contents, diverticula
- Uterus and ovaries: size, position, endometrium, follicles, appropriateness for the patient's age and phase of the menstrual cycle, uterine and adnexal masses
- Prostate and seminal vesicles: size, contour, definition, calcifications
- Bladder: distention, wall thickness, luminal contents
- Bones: degenerative changes, metastatic disease, mineralization

After diligent use of a checklist, detailed inspection of the images becomes automatic and familiar. It should be remembered that an individual "sees" what he or she looks for and that it

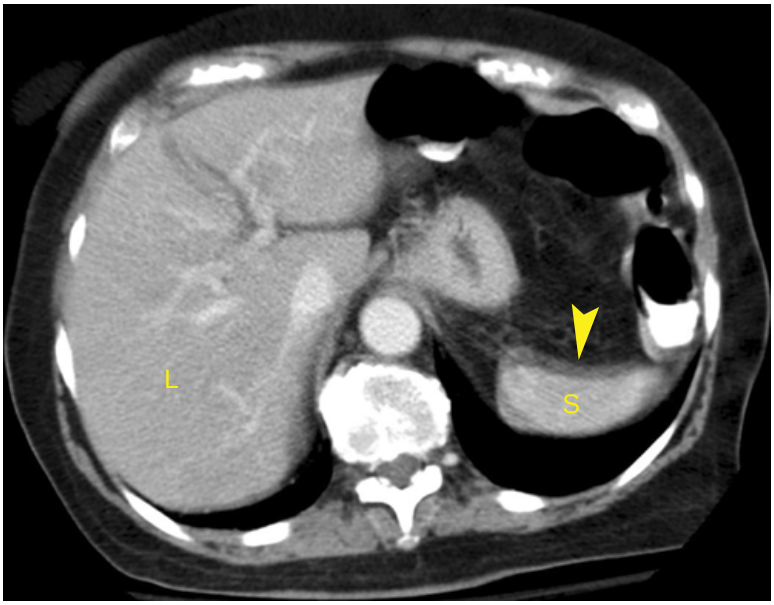

FIGURE 8-2 ■ Motion artifact. Despite a scan acquisition time of less than 1 second, patient breathing motion has caused blurring (*arrowhead*) of the margin of the spleen (S), simulating a subcapsular collection. Careful inspection of the image of the liver (L) reveals indistinctness of the hepatic vessels and the outline of the liver.

is hardest to "see" what is not there, such as an absent gallbladder or ectopic kidney.

ARTIFACTS IN BODY CT

Patient Motion

Patient motion during CT scanning causes anatomic structures to be displaced, distorted, and blurred. Anomalous white bands and dark spots may be displayed on the image as a result of motion during scan acquisition. The rapid scan times of modern MDCT scanners diminish but do not totally eliminate the effect of cardiac motion, vessel pulsation, and bowel peristalsis. Most patients can hold their breath for the 20 seconds or less required to scan the abdomen. Uncooperative patients may breathe or move during scanning, causing severe artifacts and limiting diagnostic information (Fig. 8-2).

Volume Averaging

By design, a CT scanner irradiates a three-dimensional slab of tissue to create a two-dimensional image. All CT images are "volume-averaged" in that a finite thickness of patient tissue is summated to create the two-dimensional image (Fig. 8-3). The effect of this technique is to display the summed average of densities within the slice thickness instead of separate individual densities. For example, volume averaging of opaque oral contrast within the duodenum may create the appearance of a high-density stone

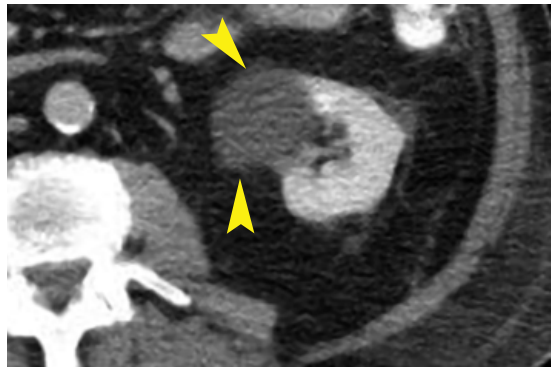

FIGURE 8-3 ■ Volume-averaging artifact. The margin (*arrowheads*) of the cyst extending from the left kidney is blurred because its contour is rounded and the attenuation of the cyst is averaged with the attenuation of the adjacent fat within this 5-mm computed tomography slice.

in the gallbladder when no stone is present. Volume averaging is diminished and spatial resolution is increased by using thin slices. MDCT has the capability to obtain a large number of thin slices over a short period of time to minimize volume-averaging artifacts.

Beam Hardening

Beam hardening refers to an increase in the mean energy of an x-ray beam when it passes through an object. Low-energy x-ray photons are preferentially absorbed, while higher-energy x-ray photons are more likely to pass through the structure. Radiographically dense structures that strongly

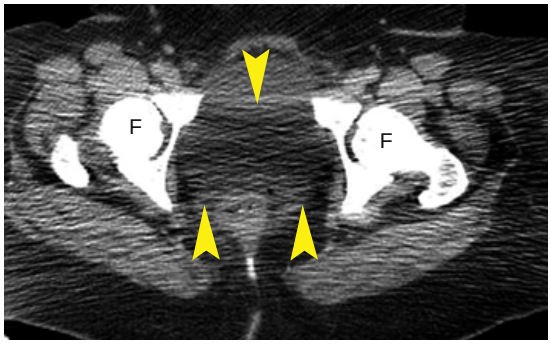

FIGURE 8-4 ■ Beam hardening artifact. The alternating light and dark streaks of a beam hardening artifact (between *arrowheads*) are prominent on this computed tomography image of the pelvis in an obese patient. The dense bone of the femoral heads (F) and acetabula selectively absorbs lower-energy x-ray photons, resulting in higher average energy of the transmitted x-ray beam. The artifact is accentuated by increased absorption of radiation in this "thicker" patient.

absorb x-ray photons harden the beam and may produce streak artifacts on the CT image. This artifact is most commonly seen in body CT between the dense bones of the hips (Fig. 8-4) and those of the shoulders. Dense metallic objects such as surgical clips, bullets, and orthopedic hardware produce dramatic beam hardening and prominent streak artifacts (Fig. 8-5); this phenomenon is further accentuated by motion.

Noise: Quantum Mottle

Image reconstruction in CT requires a large amount of data to produce an adequate image. The data are generated by x-ray photons that course through the patient: some are absorbed and some are transmitted. The latter photons strike the CT detectors; the more transmitted photons, the better are the data. The smaller the

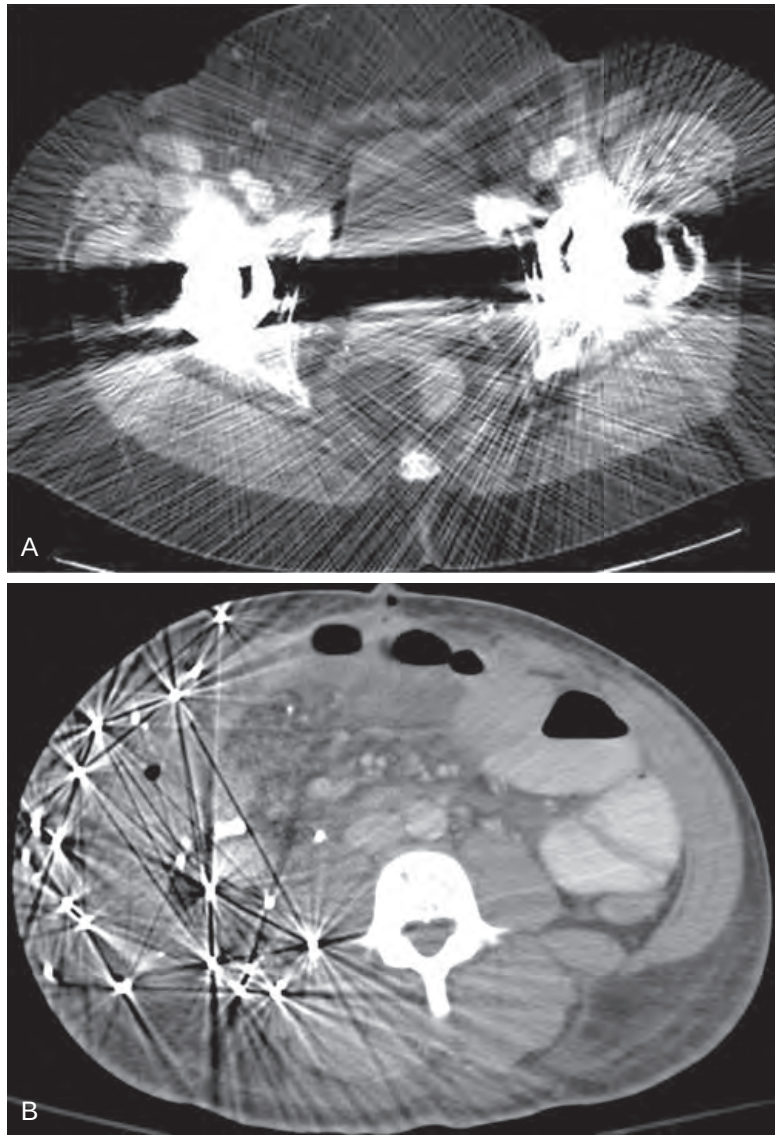

FIGURE 8-5 ■ Metal artifact. *A,* Bilateral metallic hip prostheses ruin a computed tomography image of the pelvis, with dense dark and light bands and streaks. *B,* A similar effect is produced by lead buckshot in a patient with shotgun wounds.

number of x-ray photons that strike the detectors, the more limited are the data. The more photons that are absorbed, the higher is the radiation dose to the patient. The use of MDCT has resulted in valuable multiphase imaging to assess organ and tumor perfusion in arterial, venous, and delayed phases of contrast enhancement. This valuable additional diagnostic information comes at the cost of increased radiation exposure to the patient because the patient is scanned multiple times. Current CT scanners and MDCT scanning protocols are designed to emphasize use of the lowest radiation dose needed to produce an acceptable diagnostic image. This drive to lower radiation doses leads to noisier images. Quantum mottle noise resulting from low-dose techniques with limited numbers of photons produces CT image results with a salt-and-pepper grainy appearance (Fig. 8-6). With MDCT, choices must be made to find a balance between radiation dose to the patient and acceptable noise in the image. The size of the patient significantly affects the radiation exposure needed to produce diagnostic CT images. An obese patient with large axial dimensions requires far higher radiation than a small child. It is essential that CT dose parameters are adjusted to correlate with the size of the patient. Reducing slice thickness to improve resolution and decrease volume averaging effect will reduce the number of photons used to create the image and cause increased noise (quantum mottle artifact) in the image. Thinner slices require higher radiation exposure to produce a diagnostic image.

RADIATION DOSE IN CT

The continuing expansion of the indications for CT for diagnostic imaging combined with the popularity and widespread use of MDCT has caused a dramatic increase in radiation exposure to patients. CT now accounts for more than 40% of all radiation exposure to patients from diagnostic imaging. There may be as many as 65 million CT examinations performed each year in the United States. Approximately 11% of these examinations are performed on infants and children, who are more susceptible to the adverse effects of radiation. The radiation dose profile for MDCT is 27% higher than for single-detector helical CT. The individual doses to the kidneys, uterus, ovaries, and pelvic bone marrow may be 92% to 180% higher with MDCT than with single-detector helical CT. The dose penalty with MDCT increases with decreasing slice thickness and repeat scanning during the different phases of contrast enhancement. These considerations mandate the radiologist and the ordering physician to limit CT to definitive indications, provide dose-efficient CT imaging protocols, offer alternative imaging techniques for young children who are at the greatest risk from radiation, work with manufacturers to limit radiation doses, and educate patients and health care providers on the potential risk of low-dose radiation. Guidelines for imaging of the pregnant patient are provided in the Suggested Reading section.

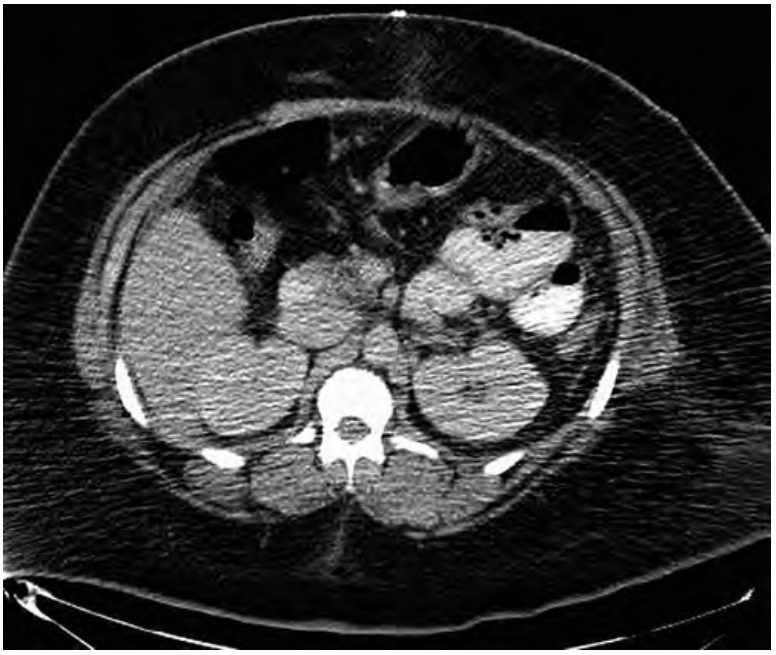

FIGURE 8-6 ■ Quantum mottle artifact. Computed tomography image of the abdomen in an obese patient shows a generalized prominent salt-and-pepper (light and dark dots) appearance. This is called a quantum mottle or noise artifact and is created by a deficiency in the number of photons used to create the image. Low-dose (mA) CT techniques, reduced slice thickness, and large patient size are factors that increase image noise.

SUGGESTED READING

Bettman MA: Frequently asked questions: Iodinated contrast agents. *Radiographics* 24:s3–s10, 2004.

Chintipalli KN, Montgomery RS, Hatab M, et al.: Radiation dose management: Part 1, minimizing radiation dose in CT-guided procedures. *AJR Am J Roentgenol* 198: W352–W356, 2012.

Cody DD, Mahesh M: Technologic advances in multidetector CT with a focus on cardiac imaging. *Radiographics* 27:1829–1837, 2007.

Dalrymple NC, Prasad SR, El-Merhi FM, Chintapalli KN: Price of isotropy in multidetector CT. *Radiographics* 27: 49–62, 2007.

Fält T, Söderberg M, Hörberg L, et al.: Seesaw balancing radiations dose and IV contrast dose: evaluation of a new abdominal CT protocol for reducing age-specific risk. *AJR Am J Roentgenol* 200:383–388, 2013.

Goldberg-Stein SA, Liu B, Hahn PF, Lee SI: Radiation dose management: Part 2, estimating fetal radiation risk from CT during pregnancy. *AJR Am J Roentgenol* 198:W347–W351, 2012.

Hendee WR, O'Connor MKO: Radiation risks of medical imaging: separating fact from fantasy. *Radiology* 264: 312–321, 2012.

Hunt CH, Hartman RP, Hesley GK: Frequency and severity of adverse effects of iodinated and gadolinium contrast materials: retrospective review of 456,930 doses. *AJR Am J Roentgenol* 193:1124–1127, 2009.

Maldijian PD, Goldman AR: Reducing radiation dose in body CT: A primer on dose metrics and key CT technical parameters. *AJR Am J Roentgenol* 200:741–747, 2013.

Pasternak JJ, Williamson EE: Clinical pharmacology, uses, and adverse reactions of iodinated contrast agents: A primer for the non-radiologist. *Mayo Clin Proc* 87:390–402, 2012.

Prince MR, Zhang H, Newhouse JH: Science to practice: A new insight into nephrotoxicity after contrast medium administration. *Radiology* 265:651–653, 2012.

Thrall JH: Radiation exposure in CT scanning and risk: Where are we? *Radiology* 264:325–328, 2012.

Wang CL, Cohan RH, Ellis JH, et al.: Frequency, outcome, and appropriateness of treatment of nonionic iodinated contrast media reactions. *AJR Am J Roentgenol* 191: 409–415, 2008.

Wang PI, Chong ST, Kielar AZ, et al.: Imaging of pregnant and lactating patients: Part 1, evidence-based review and recommendations. *AJR Am J Roentgenol* 198:778–784, 2012.

Wang PI, Chong ST, Kielar AZ, et al.: Imaging of pregnant and lactating patients: Part 2, evidence-based review and recommendations. *AJR Am J Roentgenol* 198:785–792, 2012.

CHAPTER 9

PERITONEAL CAVITY, VESSELS, NODES, AND ABDOMINAL WALL

William E. Brant

PERITONEAL CAVITY

Anatomy

The various recesses and spaces of the peritoneal cavity are easiest to recognize on computed tomography (CT) when ascites is present. Identifying the precise compartment in which an abnormality resides goes a long way toward determining the nature of the abnormality and deciding on a plan for intervention. The peritoneum is a thin membrane that produces serous fluid, which lubricates the abdominal and pelvic cavity. The parietal peritoneum lines the abdominal wall and covers the retroperitoneum. The visceral peritoneum covers the organs and bowel. Whereas all the spaces of the peritoneal cavity potentially communicate with one another, diseases such as abscesses tend to loculate within one or more specific locations. The right subphrenic space communicates with the anterior subhepatic and posterior subhepatic (Morison's) space around the liver. The left subphrenic space communicates freely with the left subhepatic space. The right and left subphrenic spaces are separated by the falciform ligament and do not communicate directly. The lesser sac is the isolated peritoneal compartment between the stomach and the pancreas. It communicates with the rest of the peritoneal cavity (greater sac) through the small opening of the foramen of Winslow.

The right subphrenic and subhepatic spaces communicate freely with the pelvic peritoneal cavity via the right paracolic gutter. The phrenicocolic ligament prevents free communication between the left subphrenic/subhepatic spaces and the left paracolic gutter. Free fluid, blood, infection, and peritoneal metastases commonly settle in the pelvis because it is the most dependent portion of the peritoneal cavity, and the pelvic recesses communicate freely with both sides of the abdomen.

The small-bowel mesentery is a double layer of peritoneum that suspends the jejunum and ileum and contains branches of the superior mesenteric artery and vein, as well as mesenteric lymph nodes. The mesentery extends like a fan obliquely across the abdomen from the ligament of Treitz in the left upper quadrant to the region of the right sacroiliac joint. Disease originating from above the ligament is directed toward the right lower quadrant. Disease originating from below the ligament has open access to the pelvis.

The greater omentum is a double layer of peritoneum that hangs from the greater curvature of the stomach and descends in front of the abdominal viscera. The greater omentum encloses fat and a few blood vessels. It serves as fertile ground for implantation of peritoneal metastases.

Fluid in the Peritoneal Cavity

Fluid in the peritoneal cavity originates from many different sources and varies greatly in composition. *Ascites* refers to accumulation of serous fluid within the peritoneal cavity and results from cirrhosis, hypoproteinemia, congestive heart failure, or venous obstruction. Exudative ascites is associated with inflammatory processes such as pancreatitis, peritonitis, and bowel perforation. Neoplastic ascites is caused by intraperitoneal tumor tissue. Chylous ascites is caused by obstruction or traumatic injury to the thoracic duct or cisterna chyli. Urine and bile may spread through the peritoneal cavity owing to obstruction or injury to the urinary or biliary tracts. *Hemoperitoneum* is an important sign of abdominal injury in blunt trauma. When the anatomy of the peritoneal cavity is known, recognition of fluid density within its recesses on CT is easy. Paracentesis is required for precise differentiation of the exact type of fluid present in the peritoneal cavity. However, CT can offer some clues.

- Free intraperitoneal fluid occupies and distends the recesses of the peritoneal cavity. Bowel loops tend to float to the central abdomen. The diaphragm may be elevated or even inverted by a large volume of ascites.
- Serous ascites has an attenuation value close to that of water (–10 to +15 Hounsfield units, HU) and tends to accumulate in the greater peritoneal space, sparing the lesser sac.
- Hemoperitoneum has a higher attenuation value (average 45 HU) that is usually greater than 30 HU. Blood tends to accumulate in greatest amounts about the site of hemorrhage.
- Exudative ascites due to pancreatitis tends to preferentially accumulate within the lesser sac. Exudative ascites and neoplastic ascites have intermediate attenuation values that overlap those of both serous ascites and blood. With peritonitis (Fig. 9-1), the peritoneum appears thickened and is enhanced following intravenous contrast administration.
- Loculations of peritoneal fluid due to benign or malignant adhesions may simulate cystic abdominal masses. Tense loculated ascites may accumulate in confined spaces such as the lesser sac and compress and displace bowel loops. Loculated ascites, however, tends to conform to the general shape of the recesses it occupies. Cystic masses make their own space, cause greater displacement of adjacent structures, and have more varied internal consistency.
- *Pseudomyxoma peritonei* is an unusual complication of mucocele of the appendix or of mucinous cystadenocarcinoma manifest by filling of the peritoneal cavity with gelatinous mucin. The mucinous fluid is typically loculated and causes scalloping and a mass effect on the liver and involved bowel (Fig. 9-2). Septations, mottled densities, and calcification within the fluid may be seen on CT. Soft-tissue peritoneal implants are sometimes apparent.

Free Air in the Peritoneal Cavity

Free air within the peritoneal cavity is an important sign of a perforated viscus but may be surprisingly difficult to recognize on CT when the pneumoperitoneum volume is small.

- The diagnosis is based on recognizing that the air is outside the bowel lumen (Fig. 9-3). Images should be routinely examined using lung windows (window level –400 to –600 HU; window width 1000 to 2000 HU) for free intraperitoneal air. Free intraperitoneal air is easiest to recognize anterior to the liver and in nondependent recesses that do not contain bowel. The very thin wall of distended bowel may be difficult to appreciate. A clue is that the air within bowel appears confined, whereas free intraperitoneal air is not confined. Rolling the patient into a decubitus position and rescanning will assist in interpretation of difficult cases.
- Before ascribing pneumoperitoneum to bowel perforation, a thoracic source, such as a pneumothorax or mechanical ventilation, or an iatrogenic source, such as recent paracentesis or a recent surgical procedure, should also be considered.

Peritoneal Carcinomatosis

Diffuse metastatic seeding of the peritoneal cavity occurs commonly with abdominopelvic tumors. The most common tumors to spread by

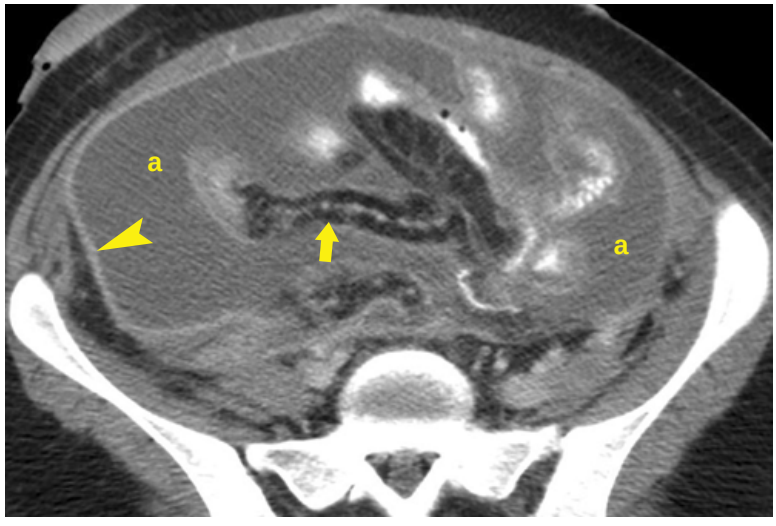

FIGURE 9-1 ■ Peritonitis and ascites. Ascites (a) resulting from pancreatitis occupies and distends peritoneal recesses. Small-bowel loops float within the fluid suspended on fat-filled mesentery (*arrow*). The parietal peritoneum (*arrowhead*) is thickened and is enhanced following intravenous contrast administration, indicating peritoneal inflammation.

FIGURE 9-2 ■ Pseudomyxoma peritonei. High-attenuation gelatinous ascites (a) is loculated in peritoneal recesses and causes scalloping and a mass effect on adjacent organs. The cause was metastatic spread of mucinous adenocarcinoma of the stomach to the peritoneum.

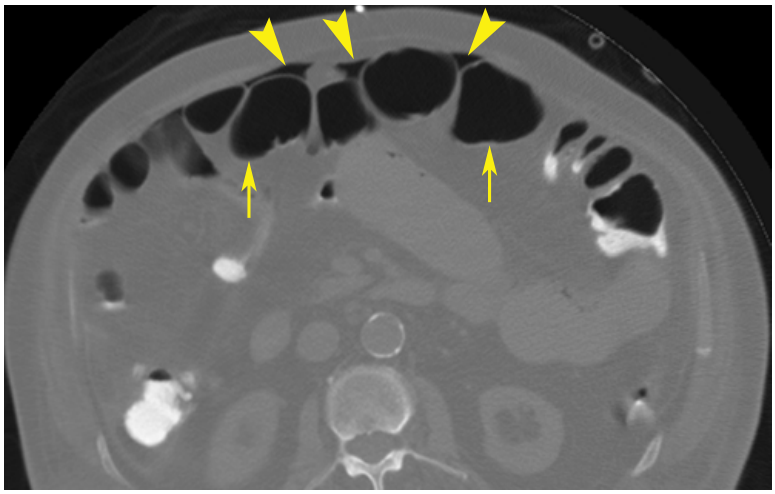

FIGURE 9-3 ■ Pneumoperitoneum. Small pockets of free intraperitoneal air are recognized by a characteristic triangular and linear appearance (*arrowheads*) between bowel loops in nondependent areas of the abdomen. Note the more rounded appearance of air within the bowel confined by the thin bowel wall (*arrows*).

this method are ovarian carcinoma in females, and stomach, pancreas, and colon carcinoma in both genders. The preferential sites for tumor implantation are the pouch of Douglas, the right paracolic gutter, and the greater omentum. CT findings with peritoneal tumor seeding include the following:

- Ascites is usually present and is commonly loculated.
- Tumor nodules appear as soft-tissue masses on, or thickening of, the parietal peritoneum (Fig. 9-4). Implants and involved peritoneum may show contrast enhancement.
- *Omental cake* describes the thickened nodular appearance of tumor involving the greater omentum. The tumor cake displaces the bowel away from the anterior abdominal wall (Fig. 9-5).
- Tumor nodules and enlarged lymph nodes may be seen in the mesentery (Fig. 9-6).
- Thickening and nodularity of the bowel wall are due to serosal tumor implantations.
- Minute implants, which may be painfully obvious and diffuse at surgery, are commonly missed by CT owing to their small size. The presence of ascites in patients with a known abdominopelvic tumor, especially ovarian carcinoma, should be regarded as suspicious for peritoneal seeding. Calcification of tumor implants may aid in their CT identification. Calcified peritoneal carcinomatosis is most commonly associated with serous adenocarcinoma of the ovary, colon, or stomach.
- Tuberculous peritonitis mimics peritoneal carcinomatosis and may cause calcification

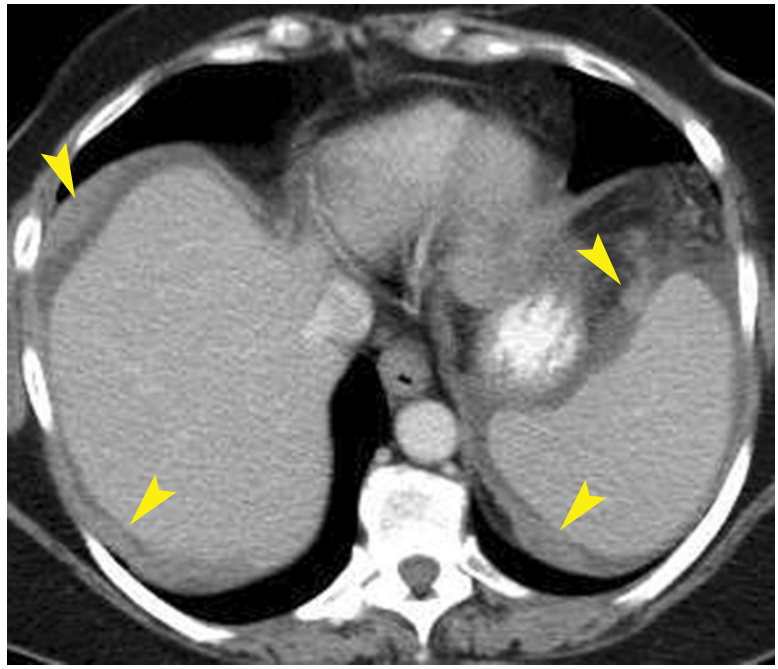

FIGURE 9-4 ■ Peritoneal metastases. Metastases (*arrowheads*) from ovarian carcinoma to the peritoneum appear as focal areas of peritoneal thickening and nodules.

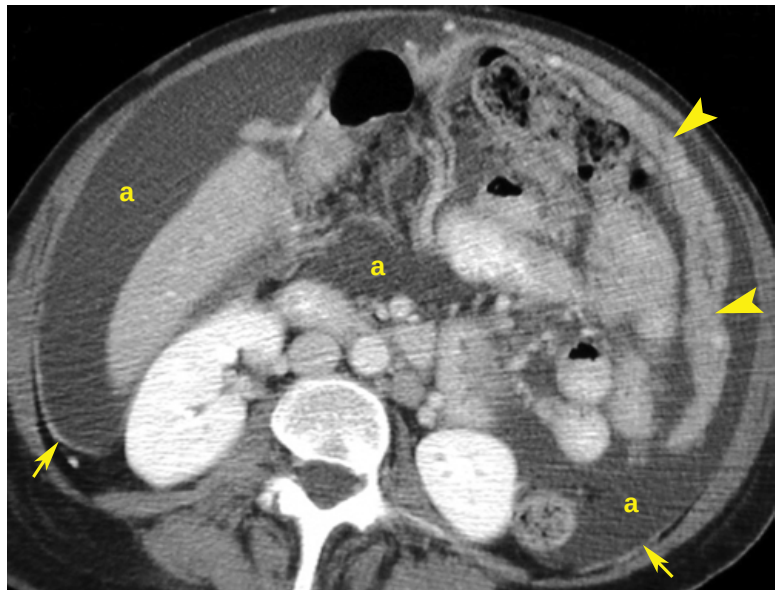

FIGURE 9-5 ■ Omental cake. Ascites (a) is present throughout the peritoneal cavity. The parietal peritoneum (*arrows*) is thickened and is enhanced following intravenous contrast administration, indicating that the ascites is neoplastic or inflammatory. Omental cake (*arrowheads*) manifests as a layer of irregular soft tissue that displaces the bowel away from the anterior abdominal wall.

of the peritoneum. Thickening of the peritoneum caused by tuberculous peritonitis is diffusely smooth, while that due to peritoneal carcinomatosis is irregular and nodular.

Peritoneal Mesothelioma

While most malignant mesotheliomas originate in the pleura, 20% to 40% of mesotheliomas arise within the abdomen. Peritoneal mesothelioma is a rare tumor with a rapidly fatal course. Asbestos exposure is a significant risk factor.

CT shows an enhancing solid tumor in the mesentery or omentum or on peritoneal surfaces (Fig. 9-7). It may cause diffuse irregular thickening of the peritoneum, multiple small nodules, or an infiltrating mass. Multilocular cystic forms of the tumor also occur. Ascites is present in most cases.

Abscess

CT is commonly performed to search for abdominal and pelvic abscesses and plan for their percutaneous or surgical drainage. Once an

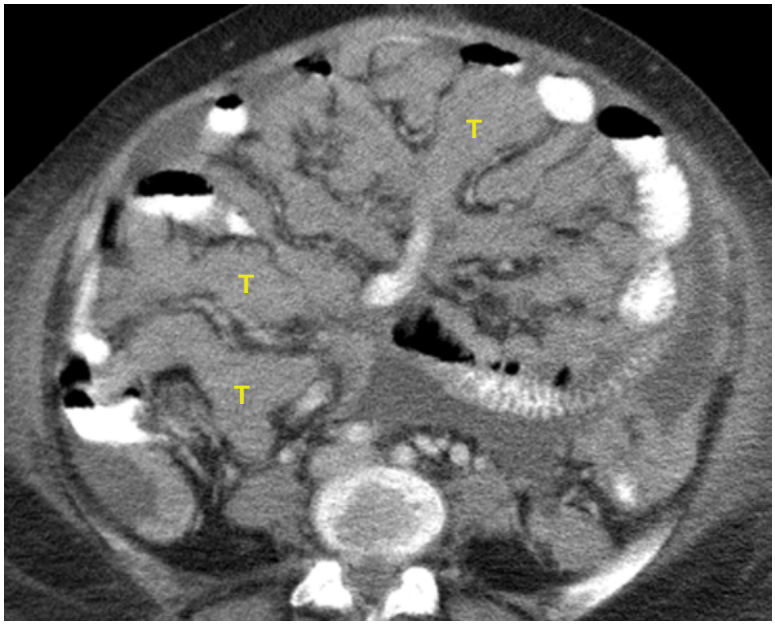

FIGURE 9-6 ■ Mesenteric carcinomatosis. Tumor nodules (T) from intraperitoneal spread of ovarian cancer cause diffuse thickening of the folds of the small-bowel mesentery.

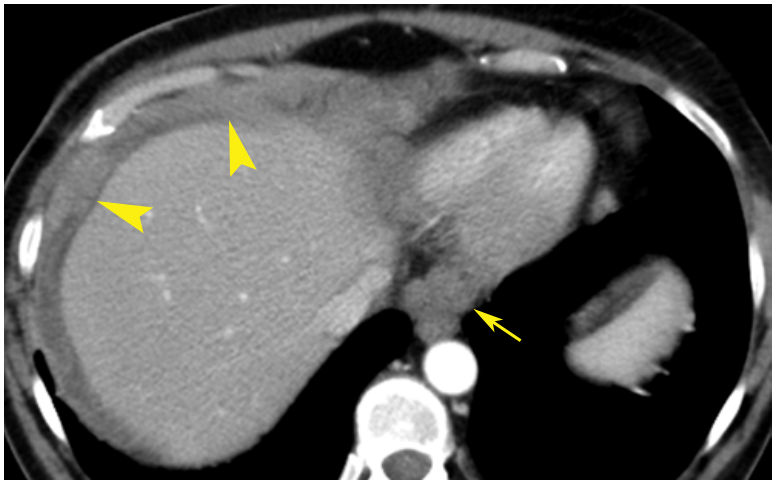

FIGURE 9-7 ■ Peritoneal mesothelioma. Tumor nodules (*arrowheads*) on peritoneal surfaces are apparent. The appearance is indistinguishable from peritoneal carcinomatosis, but biopsy confirmed peritoneal mesothelioma. Adenopathy (*arrow*) is seen adjacent to the esophagus.

abscess is found, percutaneous aspiration confirms the diagnosis and provides material for culture. Image-directed catheter placement is commonly used for drainage ("pus busting"). Most abscesses occur as complications of abdominal trauma, surgery, pancreatitis, or bowel perforation (ruptured appendicitis, diverticulitis). Intraperitoneal abscesses are commonly located in the pelvic cavity and the subphrenic and subhepatic spaces. CT features of abscess include the following.

- Most abscesses appear as loculated fluid collections displacing the bowel and adjacent organs. Internal debris, fluid–fluid levels, and septations are often present within the collection, and sometimes air–fluid levels or bubbles of air (Fig. 9-8) are seen.
- Definable walls with irregular thickening are usually identifiable.
- Any nearby fascia is thickened and fat planes are infiltrated or obliterated due to inflammation.
- Ascites, pleural effusions, and lower-lobe pulmonary infiltrates commonly accompany abdominal abscesses.
- Any fluid collection within the abdomen is suspect in patients in whom abscess is suggested clinically. Fine-needle aspiration is a safe and definitive way to exclude or confirm the diagnosis.

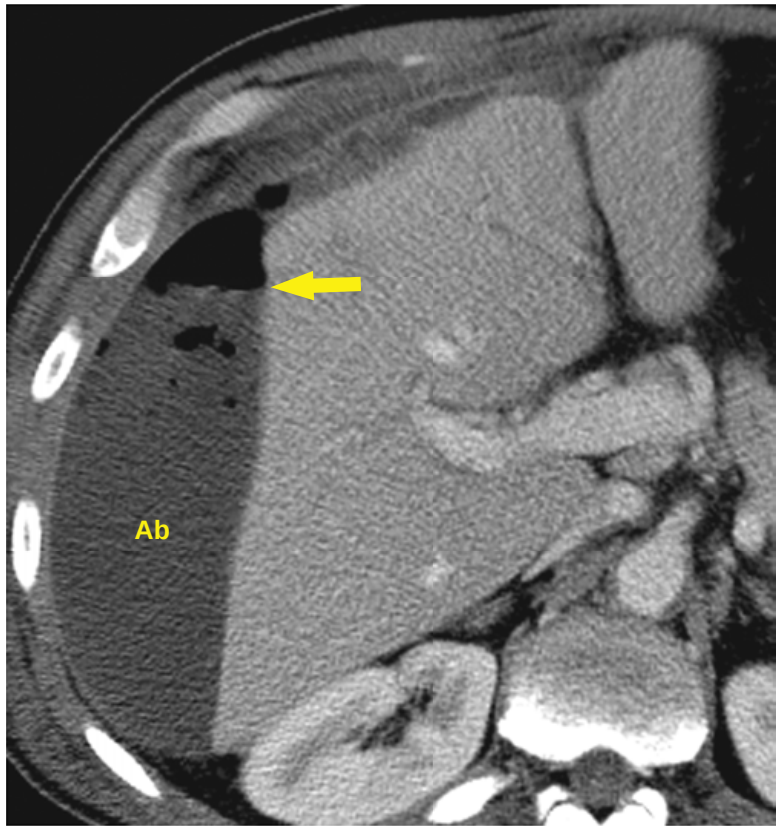

FIGURE 9-8 ■ Subphrenic abscess. A postoperative abscess (Ab) is seen as a fluid collection between the diaphragm and the liver. Mass impression on the liver is evidence of fluid loculation. An air–fluid level (*arrow*) is evident, caused by gas-producing *Escherichia coli*. This abscess was successfully treated utilizing percutaneous catheter drainage guided by computed tomography.

Cystic Abdominal and Pelvic Masses

Cystic masses in the abdomen and pelvis commonly present challenges in diagnosis. Differential considerations include:

- Abscess
- Loculated ascites
- Pancreatic pseudocyst
- Ovarian/paraovarian cyst/cystic tumor (see Chapter 18)
- Lymphocele is a cystic mass containing lymphatic fluid that occurs as a complication of surgery or trauma that disrupts lymphatic channels. It may be of any size and appear days to years after surgery.
- Cystic lymphangioma is a congenital counterpart of lymphocele believed to arise due to congenital obstruction of lymphatic channels (Fig. 9-9). Most are thin-walled and multiloculated. Attenuation ranges from water to fat density. Mesenteric cysts are cystic lymphangiomas of the mesentery. Omental cysts are less common cystic lymphangiomas of the greater omentum.
- Enteric duplication cysts are lined with gastrointestinal mucosa and are usually attached to normal bowel.
- Cystic teratoma may arise in the retroperitoneum, mesentery, or omentum. CT shows a complex cystic and solid mass with areas of water and fat attenuation and calcification.
- Peritoneal inclusion cyst (see Chapter 18)
- Spinal meningeal cyst (see Chapter 18)

VESSELS

Anatomy

The abdominal aorta descends anterior to the left side of the spine to its bifurcation at the level of the iliac crest. The normal aorta does not exceed 3 cm in diameter and tapers progressively as it proceeds to its bifurcation. The inferior vena cava lies to the right of the aorta. Its shape varies from round to oval to slit-like, depending on the breath-holding technique and intravascular fluid balance. The common iliac arteries and veins appear oval in cross-section as they diverge from the midline. The common iliac vessels bifurcate at the pelvic brim, which is identified by noting the shape of the sacrum change from convex anteriorly (the sacral promontory) to concave. The external iliac vessels course anteriorly to the inguinal triangle, whereas the internal iliac

FIGURE 9-9 ■ Cystic lymphangioma. A coronal computed tomography image shows a well-defined cystic mass (C) that is centered in the mesentery and displaces loops of the small bowel without causing bowel obstruction. Pathology following surgical removal revealed a mesenteric cystic lymphangioma.

(hypogastric) vessels have many small branches in the posterior pelvis. The iliac arteries normally do not exceed 1.5 cm in diameter.

The celiac axis originates from the anterior aspect of the aorta at the level of the aortic hiatus in the diaphragm. The superior mesenteric artery originates anteriorly from the aorta 1 cm below the celiac axis. The renal arteries arise from the lateral aspect of the aorta within 1 cm of the superior mesenteric artery. The inferior mesenteric artery is a tiny anterior branch off the aorta just above the bifurcation.

Anatomic Variations

A number of vascular anomalies must be recognized to avoid misinterpretation as abnormalities. Above the popliteal fossa, the veins of the lower limbs and abdomen are usually solitary and slightly larger than the accompanying artery.

- Duplication of the inferior vena cava (IVC) (Fig. 9-10) may be identified extending between the left common iliac vein and the left renal vein on the left side of the aorta.
- Left renal veins may course posterior instead of anterior to the aorta (retroaortic left renal vein; Fig. 9-11), or duplicated left renal veins may course both anterior and posterior to the aorta (circumaortic left renal veins).
- The intrahepatic segment of the IVC may be absent, with drainage continuing to the superior vena cava via the azygos system (azygos continuation of the IVC).

Technical Considerations

Thin-section multidetector CT (MDCT) combined with three-dimensional reconstruction techniques has made CT angiography (CTA) a useful diagnostic and surgical planning tool. Compared to conventional catheter angiography, CTA is less invasive and less costly, can be performed more quickly, and is capable of demonstrating important nonvascular abnormalities that would be missed by the conventional approach.

CT venography of the lower limbs may be combined with CTA of the pulmonary arteries to allow complete evaluation for venopulmonary thromboembolism. CT venography has sensitivity of 89% to 100% and specificity of 94% to 100% for venous thrombosis. Optimal venous enhancement of the lower limbs is obtained at

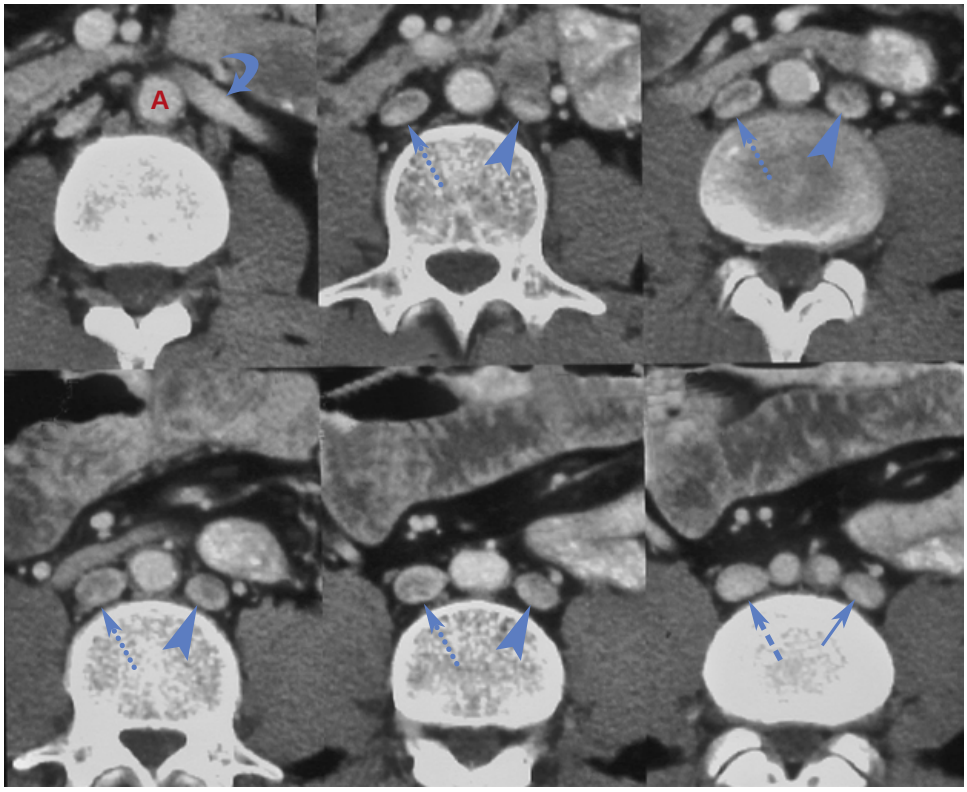

FIGURE 9-10 ■ Duplication of the inferior vena cava (IVC). The persistent left IVC (*blue arrowheads*) extends as a continuation of the left common iliac vein (*blue arrow*) along the left side of the aorta (A) to end in the left renal vein (*blue curved arrow*). The normal right IVC (*dotted blue arrows*) extends from the right common iliac vein (*dashed blue arrow*) to follow its normal course through the liver. Blood flow from the left IVC flows into the right IVC via the left renal vein.

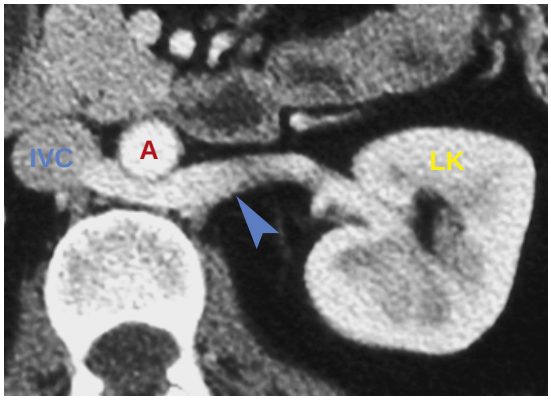

FIGURE 9-11 ■ Retroaortic left renal vein. The left renal vein (*arrowhead*) courses posterior instead of anterior to the aorta (A) to join the inferior vena cava (IVC). LK, left kidney.

3 minutes 30 seconds following intravenous contrast injection into the upper extremity. Images are viewed at a slice thickness of 1.75 to 2.5 mm. Three-dimensional reconstructions provide an overall picture.

Abdominal Aortic Aneurysm

Aneurysms are defined as circumscribed dilatations of an artery. A true aneurysm involves all three layers of the arterial wall (intima, media, and adventitia). Most are due to atherosclerotic disease that weakens the vessel wall and allows the lumen to dilate as a result of high intra-aortic blood pressure. Risk factors for abdominal aortic aneurysms (AAA) include age over 60 years, smoking, hypertension, and Caucasian ethnicity.

- Fusiform, saccular, or spherical dilatation of the aorta is the key finding (Fig. 9-12) for AAA. Care must be taken to avoid overestimation of aortic size because the vessel is tortuous and imaged obliquely.
- An outer-to-outer diameter for the abdominal aorta of >3 cm is evidence of AAA. Risk of rupture depends largely on the size of the aneurysm. The risk is about 5% for AAA of <5 cm, 16% for those >6 cm, and 76% for those >7 cm. Risk of rupture is also affected by the rate of aneurysm expansion, continued smoking, and persisting hypertension.

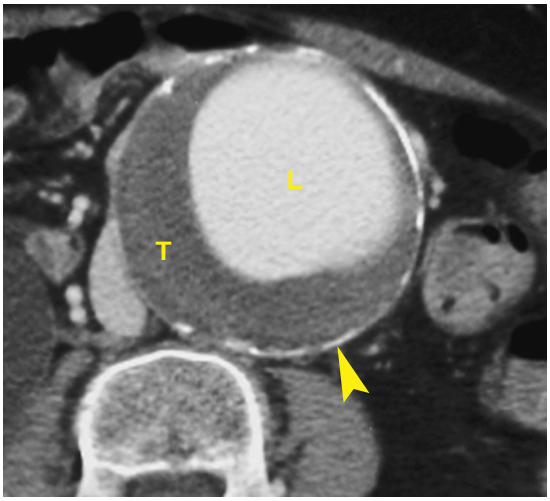

FIGURE 9-12 ■ Aneurysm of the abdominal aorta. A large aortic aneurysm is evident. The aorta exceeds 5 cm in diameter. A large amount of thrombus (T) partially surrounds the contrast-enhanced patent lumen (L). Note the atherosclerotic calcification (*arrowhead*) in the wall of the aneurysm.

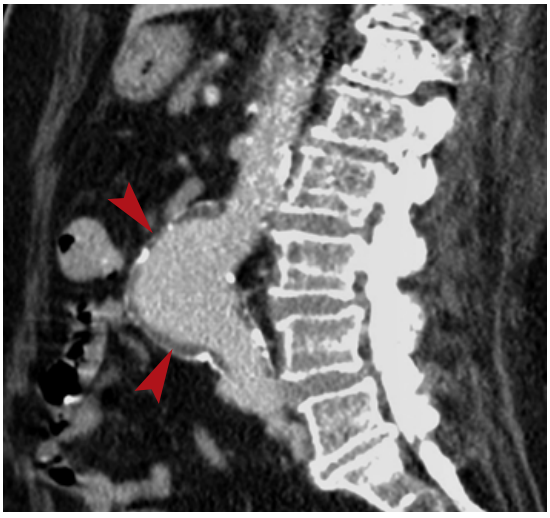

FIGURE 9-13 ■ Saccular aneurysm of the abdominal aorta. Sagittal image shows focal saccular dilatation of the abdominal aorta (*arrowheads*). Note the atherosclerotic calcifications throughout the aorta of this 81-year-old woman.

- Failure of the aorta to taper distally is another sign of aneurysm (Fig. 9-13). Distal dilatation is evidence of aneurysm even if the diameter is <3 cm.
- Iliac artery aneurysms are defined by a vessel diameter >1.5 cm (Fig. 9-14).
- The patent lumen is enhanced by intravenous contrast. A thrombus within the aneurysm remains of low density. Atherosclerotic plaques may be of low attenuation or may be calcified.

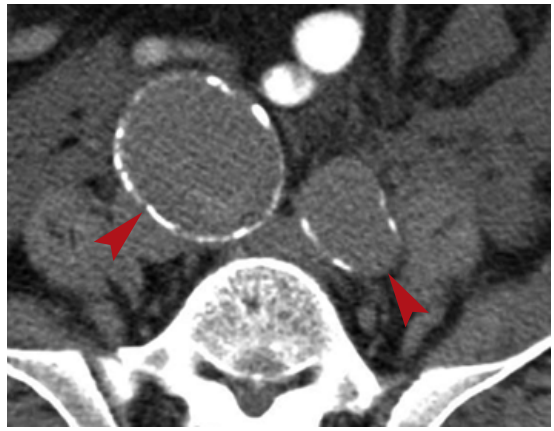

FIGURE 9-14 ■ Aneurysms of both common iliac arteries. Computed tomography without intravenous contrast reveals bilateral aneurysms of the iliac arteries (*arrowheads*) measuring 4 cm on the right and 2.5 cm on the left.

- Calcification is commonly present in the wall of the aorta and the wall of the aneurysm. Occasionally, a long-standing intraluminal thrombus may also be calcified.
- The proximal extent of the AAA must be defined for treatment planning. Most (90%) begin below the origin of the renal arteries (infrarenal AAA). An origin above the renal arteries must be identified because more complicated surgical repair is required.
- Inflammatory and fibrotic changes may be seen in the perianeurysmal soft tissues. These likely result from an immune response to atherosclerotic plaque and do not represent a chronic leak of the aneurysm. The inflammatory tissue may be enhanced following intravenous contrast administration. The inflammatory mass may envelop and obstruct the ureters. Patients presenting with unexplained renal failure deserve ultrasound evaluation of the kidneys and abdominal aorta.

Rupture of an Abdominal Aortic Aneurysm

Acute rupture of an AAA is highly lethal (mortality reported as 77% to 94%). The classic presentation is abdominal pain, hypotension, and a pulsatile abdominal mass. Because ruptured AAAs are commonly confused clinically with other diseases, CT is used to confirm the diagnosis. Unenhanced CT is adequate to demonstrate characteristic findings of a ruptured AAA. Rapid intervention is needed.

- An AAA, usually large, is evident.
- An adjacent periaortic hemorrhage dissects tissue planes of the pararenal and perirenal

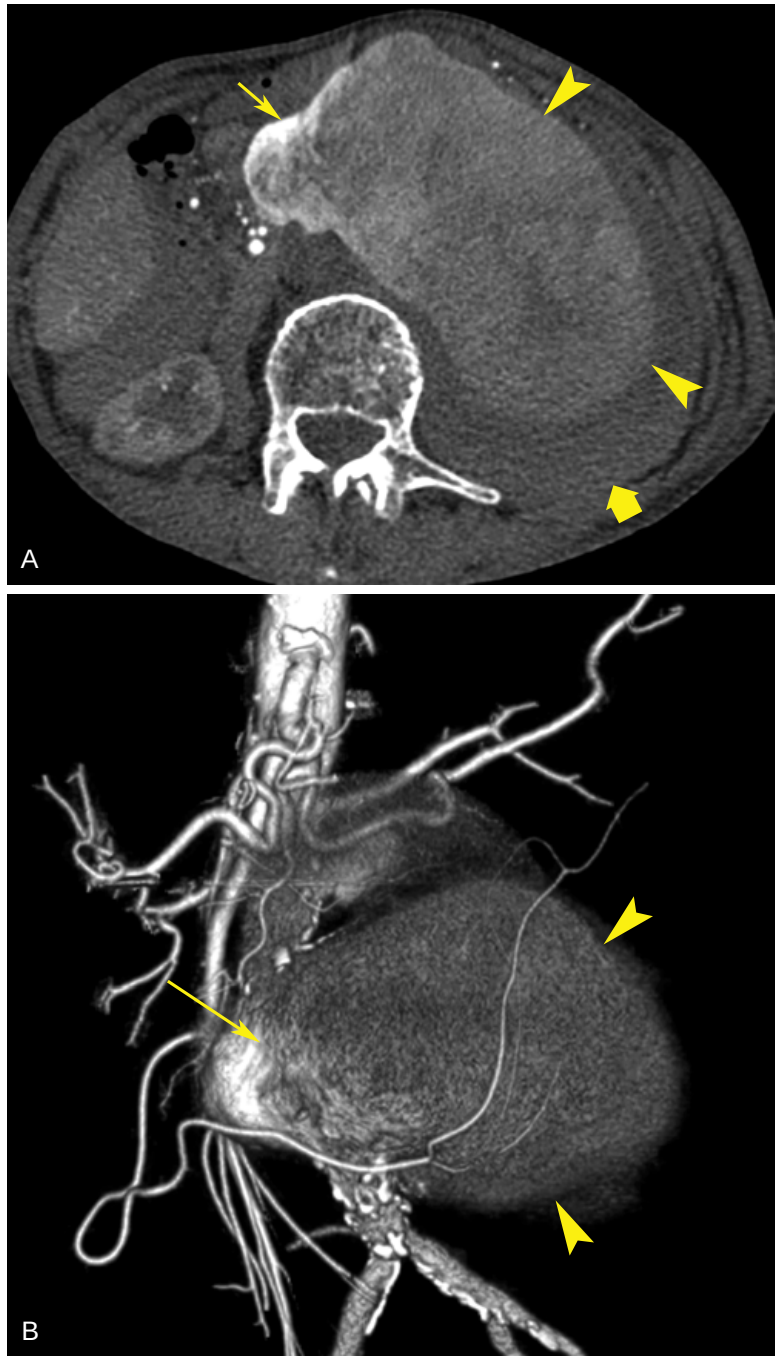

FIGURE 9-15 ■ Rupture of an aortic aneurysm. *A,* Axial post-contrast computed tomography demonstrates a prominent active retroperitoneal hemorrhage of high attenuation (*arrowheads*) extending into a lower-attenuation thrombus (*fat arrow*). Note the disruption (*skinny arrow*) of the wall of the aortic aneurysm. *B,* Three-dimensional maximum-intensity projection reconstruction shows the active hemorrhage (*arrowheads*) extending into the retroperitoneal thrombus from the rent (*skinny arrow*) in the aneurysm.

retroperitoneum (Fig. 9-15), resulting in a retroperitoneal hematoma adjacent to the AAA.

- The *draped aorta sign* refers to the absence of visualization of the posterior wall of an AAA. The wall is indistinct and follows the contour of the adjacent vertebral bodies.
- Active arterial bleeding may be demonstrated with intravenous contrast administration. Streaks and puddles of contrast are seen outside the aorta within the retroperitoneal hematoma.
- Iliac artery aneurysms, especially those larger than 3.5 cm, may also be sites of rupture, producing similar findings.
- The *hyperattenuating crescent sign* refers to a crescent-shaped area of high attenuation within the wall or the intraluminal thrombus of AAA (Fig. 9-16). The sign is indicative of impending rupture of an AAA. It is

caused by acute blood dissecting into the intraluminal thrombus and dissecting to the weak outer wall of the aneurysm. Progressive damage of the wall leads to rupture.

Infected Aneurysms

Infected aneurysms are rare, difficult to suspect clinically, and highly prone to rupture (53% to 75% rupture incidence). Infected aneurysms are also called *mycotic aneurysms*; however, this term does not imply a fungal infection. Most infected aneurysms occur as a result of bacterial infection of the intima in a normal arterial wall or in a preexisting aneurysm, commonly in association with bacterial endocarditis. Urgent surgical repair is needed.

- The aneurysm is saccular in shape with a lobulated contour in nearly all cases (Fig. 9-17). It may be found anywhere in the aorta or branch arteries. Gas is occasionally present in the soft tissues.
- Periarterial soft-tissue stranding and fluid are commonly present.
- Findings of osteomyelitis may be seen in the vertebral body adjacent to an infected AAA.

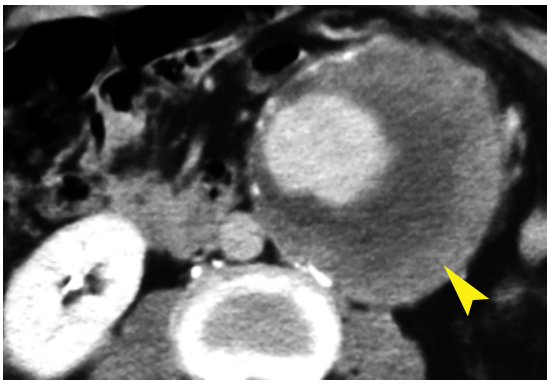

FIGURE 9-16 ■ Hyperattenuating crescent sign. Routine follow-up computed tomography revealed a rapid increase in size for this aortic aneurysm. The crescent of increased density (*arrowhead*) in the periphery of the aneurysm is highly indicative of impending rupture.

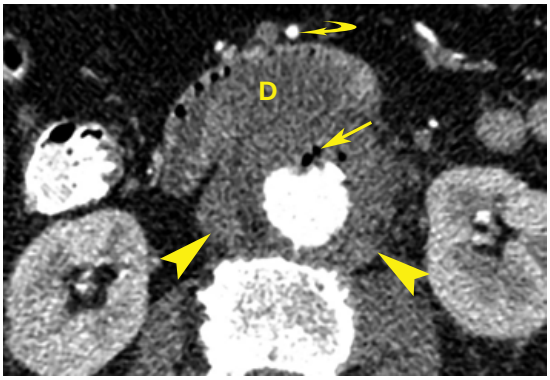

FIGURE 9-17 ■ Mycotic aneurysm. This mycotic aneurysm (*arrowheads*) contains bubbles of gas (*straight arrow*) and threatens rupture into the third portion of the duodenum. The contrast-enhanced superior mesenteria artery (*curved arrow*) is visible anterior to the retroperitoneal third portion of the duodenum.

Aortic Dissection

Dissection of blood into the media through a tear in the intima results in a dilated segment of artery with two lumina. Branch vessels may be occluded by the process or may be fed by the new (false) lumen or the original (true) lumen. Most dissections begin in the thoracic aorta but commonly extend into the abdominal aorta.

- The key finding is an intimal flap separating the true and false lumens (Fig. 9-18).
- Thrombosis of the false lumen may preclude visualization of the intimal flap.
- Differentiation of the true and false lumens is important in treatment planning. The false lumen is usually larger and commonly contains a thrombus. A thrombus is generally not seen in the true lumen. The junction of the flap with the outer wall of the false lumen produces an acute angle called the *beak sign*. Intimal calcifications may be seen on the intimal flap and in the wall of the true lumen.
- Intimal plaque calcification is internally displaced.

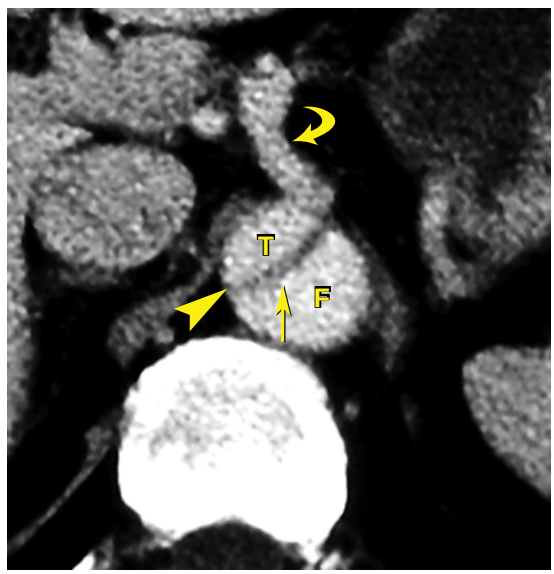

FIGURE 9-18 ■ Aortic dissection. A dissection of the thoracic aorta extends into the abdominal aorta. The intimal flap (*straight arrow*) is readily apparent within the enhancing aorta. The true lumen (T) supplies the celiac axis (*curved arrow*). The false lumen (F) is identified by the so-called beak sign (*arrowhead*).

- The true lumen may be compressed by the expanding hematoma in the false lumen.
- Branch vessels may be compressed or occluded, resulting in ischemia or infarction of the organs supplied.
- *Intramural hematoma* refers to aortic dissection without rupture of the intima. The hematoma results from hemorrhage of the vasa vasorum into the aortic wall that weakens the media without tearing the intima. Noncontrast CT shows high-attenuation blood within the wall of the aorta (Fig. 9-19). Intimal calcifications are displaced toward the aortic lumen. The luminal surface is smooth compared with the irregular surface of more common intraluminal thrombi. Intramural hematomas may resolve or progress to aortic dissection.
- *Penetrating atherosclerotic ulcer* is an atherosclerotic lesion with ulceration that is a precursor to intramural hemorrhage. CT shows a focal ulcer extending into a subintimal hematoma (Fig. 9-20). Treatment is controversial but may involve resection and replacement of the aortic wall with a surgical graft or endoluminal stenting of the affected section of the aorta.

Retroperitoneal Fibrosis

Retroperitoneal fibrosis describes a range of diseases characterized by proliferation of collagen-rich inflammatory tissue that surrounds the infrarenal abdominal aorta, inferior vena cava, and iliac vessels, frequently encasing and obstructing the ureters. Two-thirds of cases are idiopathic. Known causes include drugs (ergot alkaloids), neoplasms (lymphoma, metastases, and sarcoma), retroperitoneal hemorrhages (leaking AAA), and infections (tuberculosis and fungus).

- CT shows an irregular soft-tissue periaortic mass extending from the renal arteries to the iliac vessels. The mass partially surrounds the anterior and lateral aspect of the aorta, characteristically sparing the posterior aspect of the aorta (Fig. 9-21). The aorta is not displaced.
- Encasement of the ureters causes obstruction and hydronephrosis.
- Noncontrast attenuation of the mass is similar to that of muscle. Avid enhancement characterizes early-stage disease, whereas little or no enhancement is present in late, inactive disease.

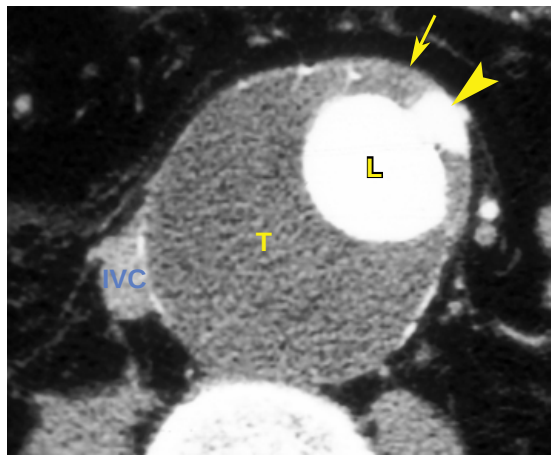

FIGURE 9-20 ■ Penetrating atherosclerotic ulcer. Contrast-enhanced computed tomography reveals a focal contrast-defined ulceration (*arrowhead*) within a high-attenuation intramural thrombus (*arrow*) within an aortic aneurysm. The ulcer communicates with the contrast-enhancing lumen (L) of the aortic aneurysm. A large volume of intraluminal thrombus (T) is also present. The inferior vena cava (IVC) is displaced by the large aneurysm.

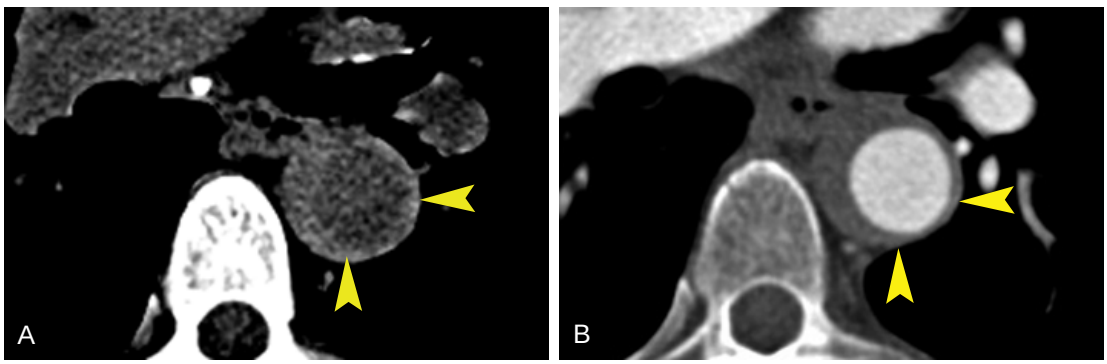

FIGURE 9-19 ■ Intramural hematoma. *A,* Noncontrast computed tomography (CT) demonstrates a high-attenuation hemorrhage (*arrowheads*) in the wall of the descending thoracic aorta that is indicative of intramural hematoma. *B,* Postcontrast CT obscures the high attenuation of an acute intramural hematoma (*arrowheads*), appearing as a bland thrombus.

- Additional findings may include deep vein thrombosis, focal lymphadenopathy, and involvement of the renal vessels.

Deep Venous Thrombosis

Venous thrombi may be bland, septic, or associated with tumor invasion.

- A thrombus appears as a low-attenuation mass within the vein, causing complete or partial obstruction (Fig. 9-22). Dilatation of the vein at the site of thrombosis is evidence that the process is acute.
- Upstream veins may be dilated compared to the contralateral side, and soft tissues may show streaks and strands of edema (thrombophlebitis).
- The wall of the affected vein may show contrast enhancement provided by the vasa vasorum.
- Chronic thrombosis appears as an irregular intraluminal clot that may be calcified. The wall of the affected vein is commonly thickened. The diameter of the lumen may be normal or reduced.
- Flow artifacts and layering of contrast medium may mimic thrombosis. Confirmation with venous compression and Doppler ultrasound may be needed in questionable cases.
- Extrinsic displacement and compression may also be difficult to differentiate from thrombosis. Tumors most likely to extend into the inferior vena cava as a tumor thrombus are renal, hepatic, and adrenal carcinomas.

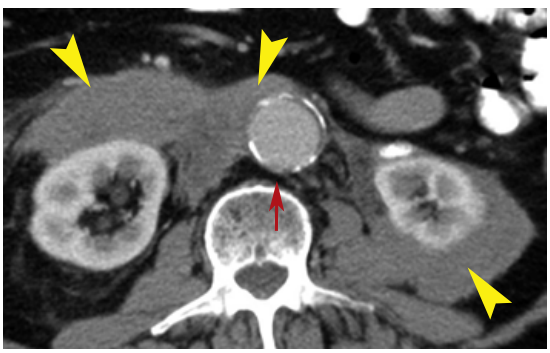

FIGURE 9-21 ■ Retroperitoneal fibrosis. Contrast-enhanced computed tomography reveals a band of soft-tissue attenuation (*arrowheads*) surrounding the left kidney and partially enveloping the aorta and right kidney. The inferior vena cava is compressed and is not visible. Note the characteristic sparing of the posterior aspect of the aorta (*arrow*) by the process of retroperitoneal fibrosis.

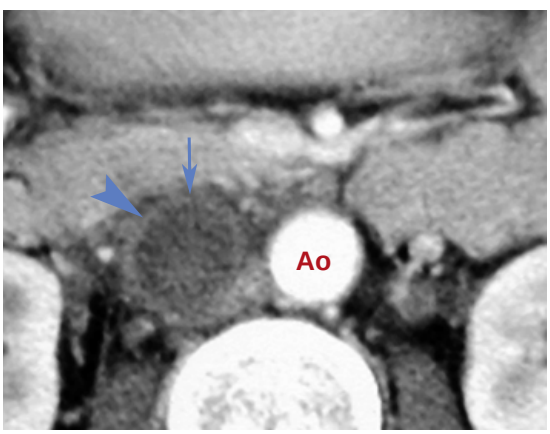

FIGURE 9-22 ■ Thrombosis of the inferior vena cava (IVC). A thrombus fills and distends the IVC (*arrow*). Note the enhancement of the wall (*arrowhead*) of the IVC, which serves as additional evidence that this represents true thrombosis and not a flow defect. Ao, abdominal aorta.

NODES

Anatomy

Normal lymph nodes are oblong and homogeneous in CT attenuation. Most are oriented parallel to their accompanying vessels. Abdominoaortic nodal groups surround the aorta and inferior vena cava and are commonly involved in abdominal and pelvic malignancy. Visceral nodes drain adjacent organs and include mesenteric, hepatic, splenic, and pancreaticoduodenal nodal groups.

Nodal Metastases

Lymph node metastases are associated with poor prognosis of many abdominal malignancies. Size is the major criterion for diagnosis of abnormal lymph nodes. Nodes are considered to be pathologically enlarged when they exceed 10 mm in short axis in the abdomen or pelvis or 6 mm in the retrocrural and porta hepatis region. Multiple 8- to 10-mm nodes in the abdomen or pelvis are considered suspicious. Benign lymph nodes are usually oval in shape, whereas malignant lymph nodes tend to be spherical in shape. Interpretation must always be made within the corresponding clinical context. Even minimally enlarged nodes should be viewed with suspicion when present in an area where a known malignancy is highly likely to metastasize.

Unfortunately, involvement of nodes with metastatic tumor does not usually change the CT attenuation of the node and in some cases will not enlarge the node sufficiently to be interpreted as pathologic according to size criteria. Nodes may be enlarged due to benign disease (false-positive

interpretation) or be of normal size and yet be involved (false-negative interpretation).

- Fat density within a lymph node is usually a sign of benignancy.
- Calcification of a lymph node usually represents granulomatous disease; however, treated lymphoma and germ cell tumors, as well as some calcifying tumors, may also show nodal calcification.
- Large nodes that are internally heterogeneous represent necrosis that is usually associated with malignancy.
- A cystic change within a lymph node usually represents malignancy, especially for nonseminomatous germ cell tumors.
- Heterogeneous contrast enhancement of a lymph node is a sign of malignant involvement.

Lymphoma

Lymphomas are divided into Hodgkin's and non-Hodgkin's types, and account for 5% to 6% of all malignancies. Hodgkin's lymphoma accounts for about 40% of lymphomas and tends to spread in an orderly, contiguous manner. Non-Hodgkin's lymphoma is a mixed group of diseases with a confusing array of changing names and classifications. Noncontiguous spread and involvement of the gastrointestinal tract are characteristic of non-Hodgkin's lymphoma. CT features of lymphoma in the abdomen and pelvis include the following:

- Multiple enlarged individual nodes (>10 mm in short axis) are evident.
- Coalescence of enlarged nodes to form rounded, multilobular nodal masses that may encase vessels, displace organs, and obstruct ureters are apparent (Fig. 9-23).
- Conglomerate nodal masses are typical of lymphoma and are rarely seen with metastatic disease or other conditions.
- Positron emission tomography (PET)-CT provides improved accuracy for lymphoma staging compared to CT alone.
- Calcification of lymphomatous nodes usually occurs only after treatment.
- Signs of extranodal spread of lymphoma to solid organs of the abdomen include diffuse increased organ size, multiple hypodense nodules, solitary intraparenchymal masses, organ invasion by external nodal masses, and diffuse nodular wall thickening in the gastrointestinal tract.

Acquired Immunodeficiency Syndrome

Medications have dramatically slowed the progression of acquired immunodeficiency syndrome (AIDS). However, manifestations of AIDS on CT are dominated by signs of intra-abdominal opportunistic infections, AIDS-related lymphoma, and Kaposi's sarcoma. Most CT findings are a manifestation of a complicating disease rather than human immunodeficiency virus (HIV) infection alone. The most common findings on CT include the following:

- Lymphadenopathy involving the retroperitoneal, pelvic, and mesenteric nodes is caused by disseminated *Mycobacterium avium-intracellulare* infection (30%), AIDS-related lymphoma (30%), Kaposi's sarcoma, or other infection. Lymph node enlargement is unlikely to be due to HIV infection alone. Unexplained adenopathy warrants biopsy.

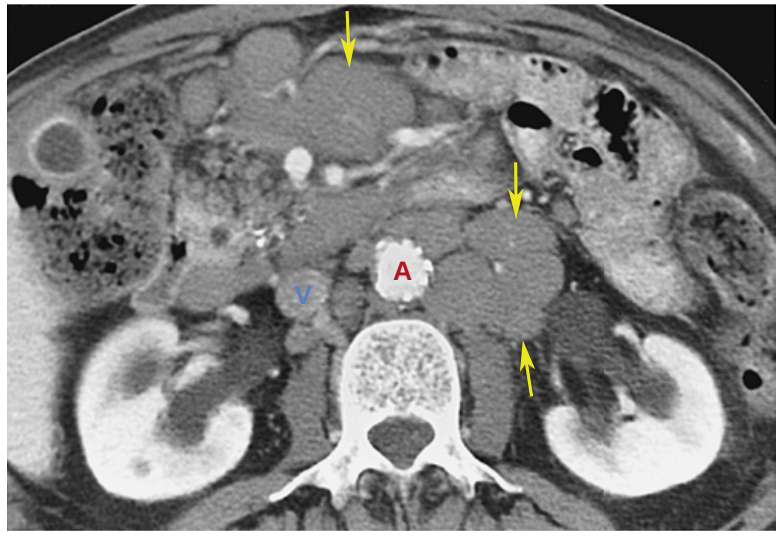

FIGURE 9-23 ■ Lymphoma. Enlarged lymph nodes (*arrows*) surround the aorta (A) and inferior vena cava (V) and are seen in the small-bowel mesentery.

- Hepatosplenomegaly without focal lesions may result from *M. avium-intracellulare* infection, histoplasmosis, and hepatocellular disease.
- Focal, small (<1 cm), low-attenuation lesions in the liver are usually due to *Mycobacterium tuberculosis*, AIDS-related lymphoma, Kaposi's sarcoma, or histoplasmosis.
- Focal, small (<1 cm), low-attenuation lesions in the spleen are caused by *M. tuberculosis*, *M. avium-intracellulare*, coccidiomycosis, candidiasis, bacillary peliosis, Kaposi's sarcoma, AIDS-related lymphoma, and *Pneumocystis carinii* infection.
- Focal bowel wall thickening or a focal bowel mass is nearly always caused by AIDS-related lymphoma.
- Calcification in the spleen, lymph nodes, and liver usually results from *P. carinii* infection.
- Nephromegaly with a striated nephrogram after contrast agent administration is a sign of HIV nephropathy.
- *Mycobacterial* infections cause lymph node enlargement, small, low-density lesions in solid organs, hepatosplenomegaly, and bowel wall thickening.
- *P. carinii* infections cause punctate or nodular calcifications in solid organs and lymph nodes, and low-attenuation lesions in the spleen.
- Kaposi's sarcoma causes adenopathy and hepatosplenomegaly. Less common findings include focal bowel wall thickening, low-density nodules in the liver, and intrahepatic low-density bands in the periportal region.
- AIDS-related lymphoma must be suspected for any solid mass anywhere in the abdomen. Additional findings include multiple sites of adenopathy, bowel involvement with wall thickening and focal masses, and focal masses in the spleen, liver, and kidney.

ABDOMINAL WALL

Anatomy

CT is an excellent imaging technique for evaluation of abnormalities of the abdominal wall. The muscles of the abdominal wall are outlined by subcutaneous and extraperitoneal fat. The rectus abdominis muscles are anterior within the rectus sheath. The flanks are defined by three muscle layers formed by the external and internal oblique and transversus abdominis muscles. The posterior muscles are the latissimus dorsi, quadratus lumborum, and paraspinal muscles.

Abdominal Wall Hernia

Obesity makes hernias of the abdominal wall difficult to diagnose clinically. Hernias may cause intermittent pain or bowel obstruction. Hernia sacs contain fat, which is usually omentum, bowel, and occasionally ascites. Complications include bowel obstruction, incarceration, strangulation, traumatic injury, and hernia recurrence after surgical repair.

- *Incisional hernias* are common ventral hernias with protrusion of the abdominal contents through the abdominal wall after it has been weakened by a surgical incision (Fig. 9-24).
- *Inguinal hernias* are classified as indirect or direct. Indirect hernias are congenital lesions seen to protrude anterior to the spermatic cord (males) or round ligament (females) and lateral to the inferior epigastric vessels (Fig. 9-25). Direct inguinal hernias are always acquired and arise medial to the inferior epigastric vessels.

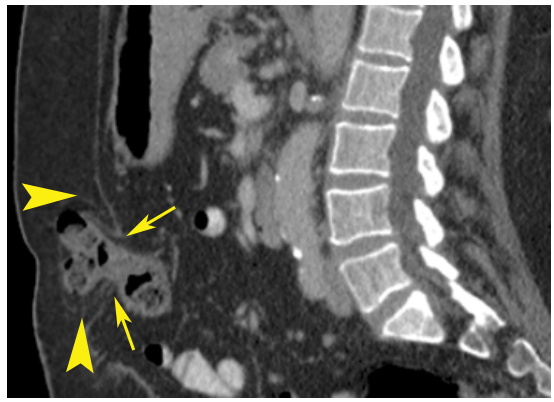

FIGURE 9-24 ■ Incisional hernia. A sagittal plane reconstruction shows a loop of small intestine herniating through a defect in the anterior abdominal wall at the site of a previous surgical incision. The hernia sac is seen as a thin membrane (*arrowheads*). A defect in the anterior abdominal wall is evident (*arrows*).

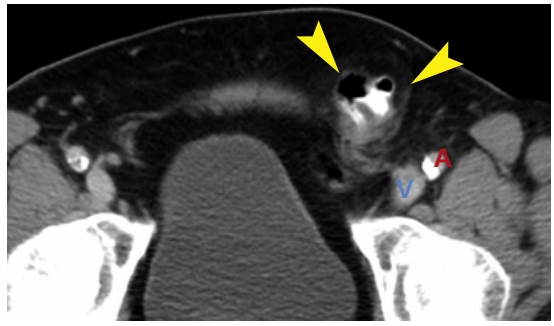

FIGURE 9-25 ■ Inguinal hernia. Bowel (*arrowheads*) protrudes through the left internal inguinal ring and into the inguinal canal. The left femoral vein (V) and left femoral artery (A) serve as anatomic landmarks. Both femoral arteries show atherosclerotic plaques.

- *Paraumbilical hernias* protrude through the linea alba in the region of the umbilicus (Fig. 9-26).
- *Spigelian hernias* are uncommon but carry a high risk of bowel incarceration and strangulation. They protrude through the linea semilunaris at the lateral edge of the rectus abdominis (Fig. 9-27). They are difficult to recognize clinically and often require imaging diagnosis by CT or other modalities.
- *Lumbar hernias* occur through defects in the posterior fascia or lumbar muscles below the 12th rib and above the iliac crest. The hernia sac may contain retroperitoneal fat, bowels loops, a kidney, or another organ.

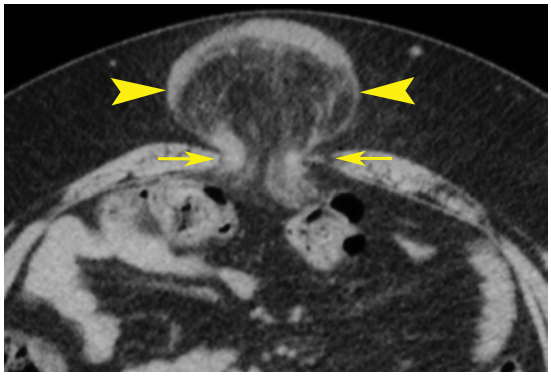

FIGURE 9-26 ■ Paraumbilical hernia. Computed tomography of a very obese woman reveals a paraumbilical hernia (*arrowheads*) containing greater omentum of fat density. A defect (*arrows*) in the anterior abdominal wall at the level of the umbilicus is apparent.

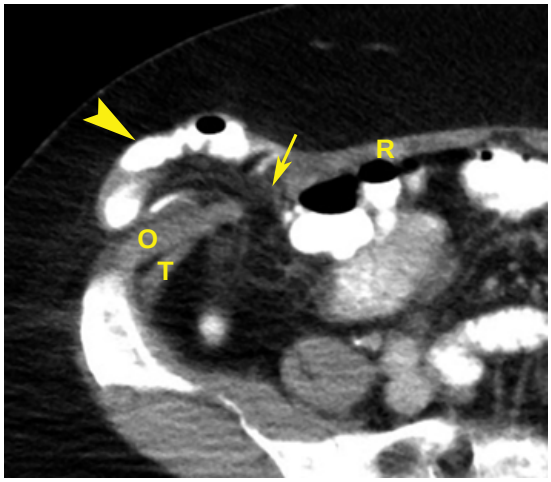

FIGURE 9-27 ■ Spigelian hernia. Magnified view of the right lower quadrant from an axial computed tomography slice shows a defect (*arrow*) in the anterior abdominal wall at the lateral edge of the rectus muscle (R). The small bowel (*arrowhead*) extends through the defect into the subcutaneous tissues. The internal and external oblique muscles (O) are fused and retracted. The transversus abdominis muscle (T) is evident.

- *Richter hernias* involve only a portion of the antimesenteric wall of the bowel in the hernia sac. The entire circumference of the bowel wall is not compromised. However, if the involved portion of the bowel wall becomes strangulated and infarcts, bowel perforation occurs, making this a dangerous type of hernia. Laparoscopic port sites are common locations for Richter hernias.

Abdominal Wall Hematomas

Bleeding into the abdominal musculature may be a complication of bleeding disorders or anticoagulant therapy, or may result from trauma. Hematomas enlarge the involved muscle, are acutely hyperdense, and progressively decrease in attenuation with time (Fig. 9-28). Hematomas or seromas are commonly visualized in surgical wounds during the postoperative period. Infection results in abscess formation, with increased stranding densities in subcutaneous fat, gas formation, and fluid levels. Confirmation of infection requires percutaneous aspiration.

Abdominal Wall Tumors and Subcutaneous Nodules

Fatty tissue provides an optimal background for CT demonstration of nodules and masses in the subcutaneous tissues. Diagnostic considerations include the following:

- Hematogenous metastases to the skin are characteristic of malignant melanoma (Fig. 9-29). Other primaries to consider include

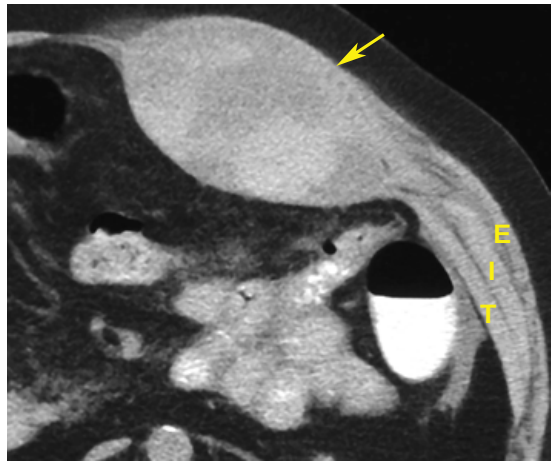

FIGURE 9-28 ■ Rectus hematoma. The left rectus muscle (*arrow*) is markedly enlarged and shows irregular high attenuation indicative of intramuscular hematoma. Bleeding occurred as a complication of dialysis. The flank muscles are well shown. T, transversus abdominis; I, internal oblique; E, external oblique.

FIGURE 9-29 ■ Subcutaneous metastasis. A soft-tissue nodule (*arrow*) with spiculated margins is seen in the subcutaneous fat. Biopsy confirmed metastatic melanoma. Surgical clips (*arrowhead*) are present in the right inguinal region from a previous lymph node dissection. The primary lesion had been removed from the right thigh 2 years previously.

breast, stomach, ovary, renal, and lung carcinomas. Nodules are usually well defined and enlarge over time.

- Desmoid tumors are locally invasive dysplastic tumors of connective tissue that involve the muscles and fascia of the anterior abdominal wall. Local recurrence is common after surgical removal. Familial desmoid tumors occur in Gardner syndrome.
- Benign fibromas, hemangiomas, and lipomas arising in the anterior abdominal wall are relatively common.
- Injection hematomas and granulomas are usually seen in the lower anterior abdominal wall.
- Sebaceous cysts vary in size and are attached to the skin surface.
- Enlarged subcutaneous vessels are round, oval, or tubular in shape. They may be related to portal hypertension or venous thrombosis. Contrast administration shows enhancement.
- Endometriomas result from endometrium implants in surgical scars. They characteristically bleed and become painful during menstruation.

SUGGESTED READING

Agarwal A, Yeh BM, Breiman RS, et al.: Peritoneal calcification: Causes and distinguishing features on CT. *AJR Am J Roentgenol* 182:441–445, 2004.

Aggarwal S, Qamar A, Sharma V, Sharma A: Abdominal aortic aneurysm: A comprehensive review. *Exp Clin Cardiol* 16:11–15, 2011.

Aguirre DA, Santosa AC, Casola G, Sirlin CB: Abdominal wall hernias: Imaging features, complications, diagnostic pitfalls at multi-detector row CT. *Radiographics* 25:1501–1520, 2005.

Caiafa RO, Vinuesa AS, Izquierdo RS, et al.: Retroperitoneal fibrosis: Role of imaging in diagnosis and follow-up. *Radiographics* 33:535–552, 2013.

Ganeshalingam S, Koh D-M: Nodal staging. *Cancer Imaging* 9:104–111, 2009.

Gidwaney R, Badley RL, Yam BL, et al.: Endometriosis of abdominal and pelvic wall scars: Multimodality imaging findings, pathologic correlation, and radiologic mimics. *Radiographics* 32:2031–2043, 2012.

Golledge J, Eagle KA: Acute aortic dissection. *Lancet* 372:55–66, 2008.

Katz DS, Loud PA, Bruce D, et al.: Combined CT venography and pulmonary angiography: A comprehensive review. *Radiographics* 22:S3–S24, 2002.

Kim S, Kim TU, Lee JW, et al.: The perihepatic space: comprehensive anatomy and CT features of pathologic conditions. *Radiographics* 27:129–143, 2007.

Kwee TC, Kwee RM, Nievelstein RAJ: Imaging in the staging of lymphoma: A systematic review. *Blood* 111:504–516, 2008.

Levy AD, Arnaiz J, Shaw JC, Sobin LH: Primary peritoneal tumors: Imaging features with pathologic correlation. *Radiographics* 28:583–607, 2008.

Levy AD, Shaw JC, Sobin LH: Secondary tumors and tumor-like lesions of the peritoneal cavity: Imaging features with pathologic correlation. *Radiographics* 29:347–373, 2009.

Moyle PL, Kataoka MY, Nakai A, et al.: Nonovarian cystic lesions of the pelvis. *Radiographics* 30:921–938, 2010.

Pickhardt PJ, Bhalla S: Unusual nonneoplastic peritoneal and subperitoneal conditions: CT findings. *Radiographics* 25:719–730, 2005.

Rakita D, Newatia A, Hines JJ, et al.: Spectrum of CT findings in rupture and impending rupture of abdominal aortic aneurysms. *Radiographics* 27:497–507, 2007.

Thomas AG, Vaidhyanath R, Kirke R, Rajesh A: Extranodal lymphoma from head to toe: Part 2, the trunk and extremities. *AJR Am J Roentgenol* 197:357–364, 2011.

Tirkes T, Sandrasegaran K, Patel AA, et al.: Peritoneal and retroperitoneal anatomy and its relevance for cross-sectional imaging. *Radiographics* 32:437–451, 2012.

CHAPTER 10

ABDOMINAL TRAUMA

William E. Brant

Multidetector computed tomography (MDCT) is the imaging method of choice for the diagnosis of intra-abdominal injury following blunt abdominal trauma. Treatment is directed by characterization of the precise nature of the injury or by reliable demonstration of the absence of significant injury. CT is particularly valuable when physical examination of the abdomen is equivocal or unreliable, such as in the case of head trauma or impairment of consciousness caused by drugs or alcohol. CT has the advantage that evaluation of the entire abdomen and pelvis is possible in a single comprehensive study. The sensitivity of CT in detecting intra-abdominal injury exceeds 90%.

Candidates for trauma CT of the abdomen are patients who have experienced significant blunt abdominal trauma and who are hemodynamically stable. Patients who are hemodynamically unstable, who have signs of peritonitis, or who have experienced penetrating abdominal trauma are candidates for immediate exploratory surgery, which should not be delayed by CT. Patients with a history of blunt abdominal trauma who do not have physical examination evidence of traumatic injury to the abdomen receive little benefit from trauma CT.

At many institutions, limited ultrasound examination is used for rapid screening of the abdomen and pelvis to detect the presence of free intraperitoneal fluid (FAST scan, focused abdominal sonography for trauma). If fluid is present, trauma CT of the abdomen and pelvis is performed. If fluid is absent and the clinical assessment reveals low risk, trauma CT may be deferred, although not all significant intra-abdominal injuries are associated with hemoperitoneum. The sensitivity of ultrasound in detecting free intraperitoneal fluid is 63%. This limitation is primarily caused by a lack of bladder-filling, which impairs visualization of fluid in the cul de sac. Routine filling of the bladder with 200 to 300 mL of sterile saline improves the sensitivity to 84%. In females of reproductive age and in children, free fluid limited to the cul de sac is most likely physiological.

SCAN TECHNIQUE

Intravenous contrast is the most critical component in the performance of trauma CT of the abdomen. Solid organ enhancement confirms the presence of blood flow and provides optimal detection of lacerations and hematomas, which may be isodense in unenhanced organs. All trauma CT scans must include both the abdomen and the pelvis. Extensive hemorrhage may settle dependently in the pelvis and be barely detectable on scans confined to the abdomen. All CT images should be viewed with lung windows to detect pneumothorax and pneumoperitoneum, bone windows to detect bone injuries, and routine soft-tissue windows to reveal organ injury.

The use of oral contrast prior to trauma CT scans remains controversial, with an increasing number of institutions switching to CT scanning without oral contrast in the setting of trauma. Extended patient preparation with oral contrast may inappropriately delay CT scanning. Patients may vomit or aspirate an oral contrast medium. Oral contrast may interfere with the performance of angiography if it is needed in the treatment of active hemorrhage. Oral contrast is often poorly distributed through the bowel because of ileus induced by trauma. At the author's institution, routine CT scans for acute trauma patients are performed without oral contrast. A number of studies have documented no significant change in the accuracy of trauma CT without the use of oral contrast. Water may serve as an effective agent to distend to the stomach and proximal bowel without the disadvantages of positive contrast agents. When possible and if it does not cause a delay in obtaining a CT scan, 400 to 700 mL of water may be given orally or via a nasogastric tube.

For trauma CT scans, helical MDCT is performed with a 70-second delay following intravenous injection of 150 mL of iodinated contrast agent by power injector at 3.5 mL/second. Images are viewed at a slice thickness of 2.5 to 5.0 mm. Delayed scans through the kidneys at 5 to 10 minutes are performed to evaluate for rupture of

the collecting system if the initial scan shows perirenal fluid or other signs of renal injury. The entire abdomen and pelvis are scanned from the dome of the diaphragm through the ischial tuberosities. If the chest is also being evaluated using trauma CT, the scan is continued through the abdomen and pelvis without overlap. In select cases, an arterial-phase scan at 25 to 30 seconds after intravenous contrast injection may be added to assess for active hemorrhage. Indications for an arterial-phase scan include severe mechanism of injury, clinical suspicion of active bleeding, and known displaced fractures of the pelvis.

CT cystography should be performed if bladder injury is suspected because of gross hematuria, significant trauma to the pelvis, presence of pelvic fractures, or stranding or fluid around the bladder. The bladder must be actively distended to a minimum of 250 mL to demonstrate or exclude bladder rupture. Passive filling of the bladder by intravenous contrast is not sufficient to exclude bladder injury. CT cystography is performed by instilling 250 to 300 mL of 3% to 5% iodinated contrast agent into the bladder via a Foley catheter. Scans are obtained through the pelvis before and after contrast instillation, with images reconstructed at a thickness of 3 to 5 mm. Scans after bladder drainage are not necessary.

TRAUMA CT AND PREGNANT PATIENTS

In pregnant patients, radiation exposure is an appropriate concern. However, trauma is a leading cause of nonobstetric maternal mortality and fetal loss. Pregnancy itself increases the risk of intra-abdominal traumatic injury. Maternal death nearly always results in fetal death. While each case should be evaluated individually, in the setting of major abdominal trauma to a pregnant patient, the risk of a missed or delayed diagnosis of major traumatic injury far outweighs the low risk of radiation exposure. Care should be taken to ensure that the lowest possible radiation dose is used to obtain a diagnostic trauma CT scan.

CT FINDINGS OF TRAUMATIC INJURY

CT findings of traumatic injury within the abdomen or pelvis include the following:

- *Hemoperitoneum.* Blood within the peritoneal cavity is a highly reliable sign of intra-abdominal injury (Fig. 10-1). Fresh unclotted blood measures 30 to 45 Hounsfield units (HU), compared to 0 to 15 HU for ascites or serum. Separation of clotted blood and serum may result in visible fluid layers (*hematocrit effect*). Fresh blood flows from the area of injury to dependent peritoneal recesses in the abdomen and pelvis. Small volumes of low-attenuation fluid (10 to 15 HU) may be considered a normal finding in children, adult males, and females during their menstrual cycle.
- *Sentinel clot.* A focal collection of clotted blood (>60 HU) is an accurate marker of injury to an adjacent organ (Figs. 10-1*A* and 10-2). Occasionally, a sentinel clot is the only positive finding of specific organ injury. Such a clot of higher density stands out in relief compared to lower-density unclotted blood or serum.
- *Active bleeding.* Active hemorrhage may be detected by scanning during the arterial phase of dynamic intravenous contrast administration. Active extravasation is seen as hyperdense foci within areas of lower-density liquid blood (Fig. 10-3). The attenuation of active hemorrhage ranges from 85 to 370 HU and is usually within 20 HU of the attenuation of nearby arteries such as the aorta. On delayed images, the focal contrast collection fades into the surrounding hematoma. This finding is a sign of life-threatening hemorrhage and often necessitates immediate angiographic or surgical therapy.
- *Free air* in the peritoneal cavity is a sign of transmural bowel laceration (Fig. 10-4). Unfortunately, this sign is neither sensitive nor specific. Extraluminal air is found in only 32% to 55% of cases of bowel laceration. Free air may also result from diagnostic peritoneal lavage, barotrauma, or mechanical ventilation. Additional findings of bowel injury must be present before definitively ascribing this finding to bowel perforation. Free air is best detected with lung windows.
- *Free contrast* in the peritoneal cavity may occur on extravasation of oral contrast through a bowel perforation or leakage of contrast-opacified urine from the urinary tract (Fig. 10-5). Extraluminal oral contrast is found in only 14% of bowel transections. Additional findings such as bowel wall thickening and blood in the mesentery confirm bowel injury as the source of such extraluminal contrast. Extravasated contrast-containing urine should be seen on delayed images after the ureter and bladder fill with contrast agent.
- *Subcapsular hematomas* appear as crescent-shaped collections that flatten and indent

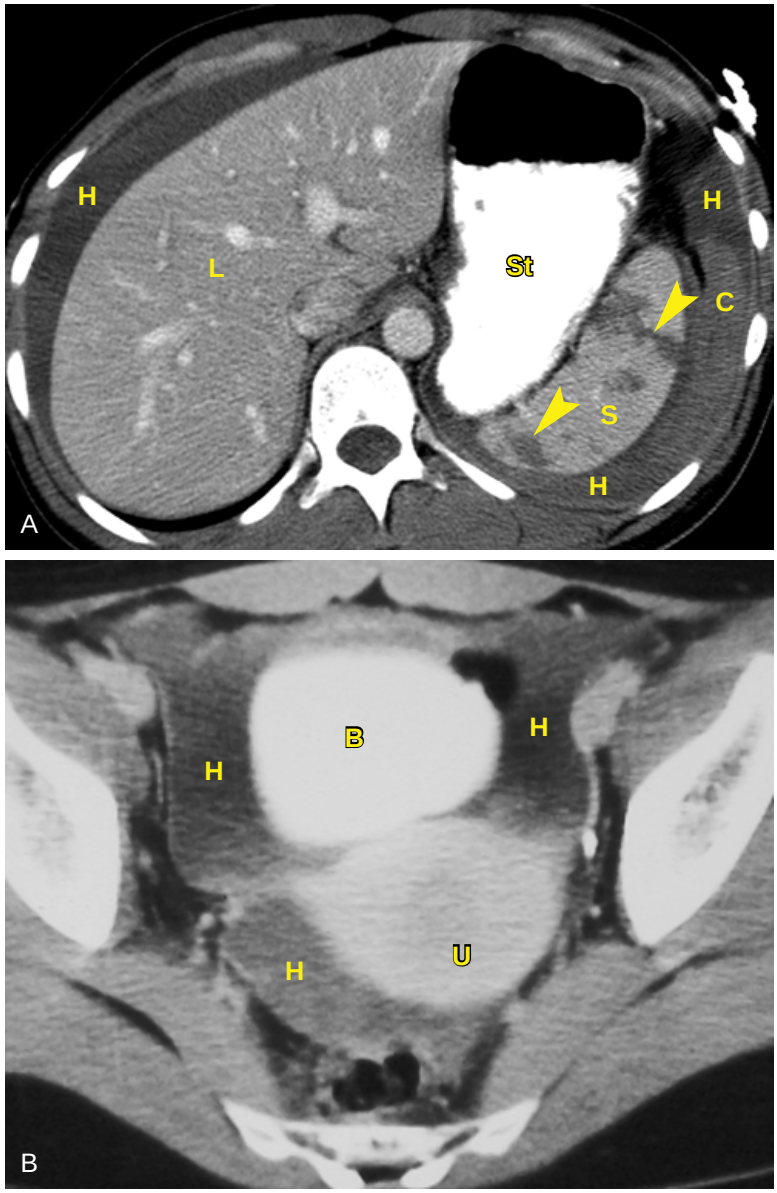

FIGURE 10-1 ■ Hemoperitoneum. *A,* Contrast-enhanced computed tomography (CT) through the upper abdomen shows hemoperitoneum (H) enveloping the liver (L) and spleen (S). Multiple lacerations of the spleen are evident as low-attenuation clefts (*arrowheads*) through the enhanced splenic parenchyma. A higher-attenuation blood clot (C) is seen adjacent to the spleen. This patient received oral contrast, which distended the stomach (St). *B,* CT image of the pelvis shows blood (H) settling in the peritoneal recesses of the pelvis surrounding the bladder (B) and uterus (U).

the organ parenchyma (Fig. 10-6). The density is lower than that of contrast-enhanced parenchyma. The outer border of the collection is sharply defined by the organ capsule. The inner margin compresses the adjacent parenchyma.

- *Intraparenchymal hematomas* are seen as irregularly shaped, rounded, low-density collections within contrast-enhanced parenchyma (Fig. 10-7). Small intraparenchymal hematomas are commonly called *contusions.*
- *Lacerations* are jagged, linear, often branching, defects in organ tissue that are defined by lower-density blood within the laceration (Fig. 10-8). Most lacerations extend through the organ capsule and are associated with hemoperitoneum.
- *Shattered organs* are disrupted by multiple lacerations (Fig. 10-9) and are frequently associated with multiple infracted segments of parenchyma. Portions of enhancing and nonenhancing organ parenchyma may be widely dispersed by hematoma.

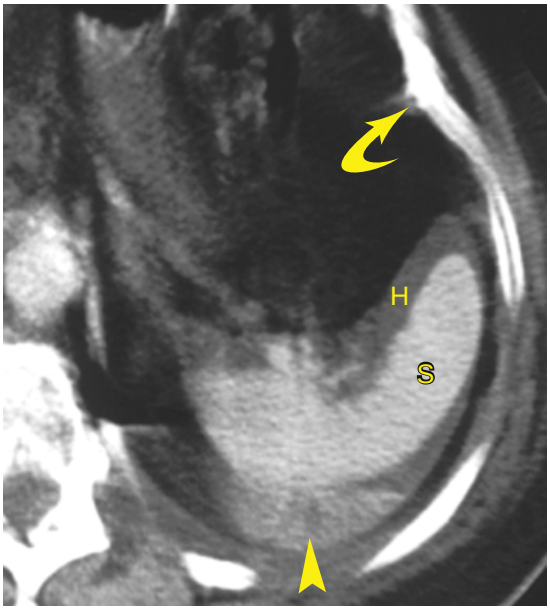

FIGURE 10-2 ■ Sentinel clot. A high-attenuation blood clot (*arrowhead*) serves as a marker of a poorly visible laceration of the spleen (S). Lower-attenuation blood (H) is seen in the recesses of the peritoneal cavity around the spleen. A rib fracture (*curved arrow*) is also present.

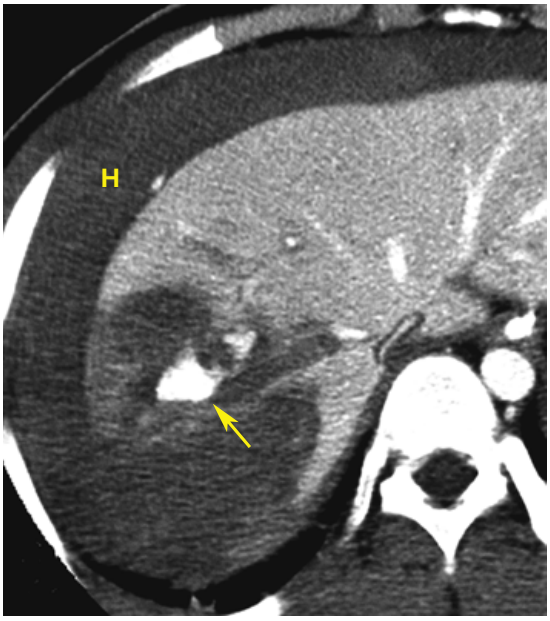

FIGURE 10-3 ■ Active hemorrhage. Contrast-enhanced trauma computed tomography of the liver shows a focus of active hemorrhage (*arrow*) seen as an amorphous extravascular collection of contrast within a low-attenuation hepatic hematoma. Extensive hemoperitoneum (H) is evident.

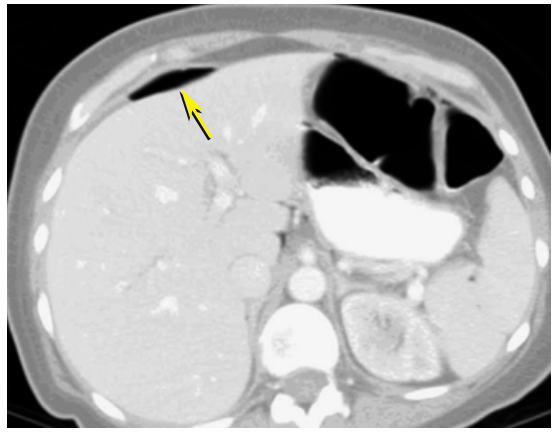

FIGURE 10-4 ■ Pneumoperitoneum. Computed tomography of the abdomen shown with lung windows demonstrates an extraluminal collection of air (*arrow*) anterior to the liver. This patient had a traumatic laceration of the jejunum. Serial images were inspected to provide assurance that no bowel containing gas in the lumen was in this area.

- *Absence of parenchymal enhancement* is an indication of a loss of vascular supply (Fig. 10-10). The supplying artery may be lacerated or thrombosed. The entire organ, or only a portion of it, may be affected.
- *Infarctions* are seen as sharply demarcated, often wedge-shaped, areas of decreased contrast enhancement that extend to the organ capsule (Fig. 10-11). Infarctions are caused by thrombosis or lacerations of segmental arteries.

Spleen Trauma

The spleen is the most frequently injured intraabdominal organ. Current management strives to avoid splenectomy. Patients who undergo splenectomy have a significantly increased risk of infection and overwhelming sepsis. Patients who are hemodynamically stable may be treated conservatively with close observation. *Delayed rupture of the spleen* may occur up to 10 days following trauma (Fig. 10-12). Delayed rupture is associated with low-grade splenic injuries including intraparenchymal and subcapsular hematomas. Surgery is reserved for patients who have active bleeding or large nonperfused portions of the spleen or who have formed pseudoaneurysms. Up to 40% of patients with splenic injury have associated fractures of the left lower ribs. Extraperitoneal hemorrhage may be present in association with splenic injury and intraperitoneal hemorrhage. Blood tracks into the anterior pararenal space along the splenic vessels and pancreas. With rapid bolus administration of intravenous contrast and rapid MDCT scanning, early

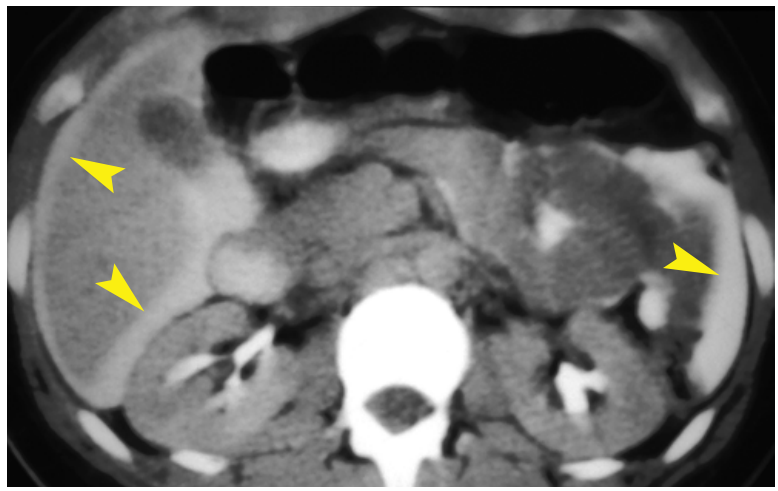

FIGURE 10-5 ■ Free intraperitoneal contrast agent. An image through the upper abdomen reveals high-density contrast agent in the peritoneal recesses (*arrowheads*). This patient had an intraperitoneal rupture of the bladder. Contrast medium excreted in the urine extravasated through the hole in the bladder into the peritoneal cavity.

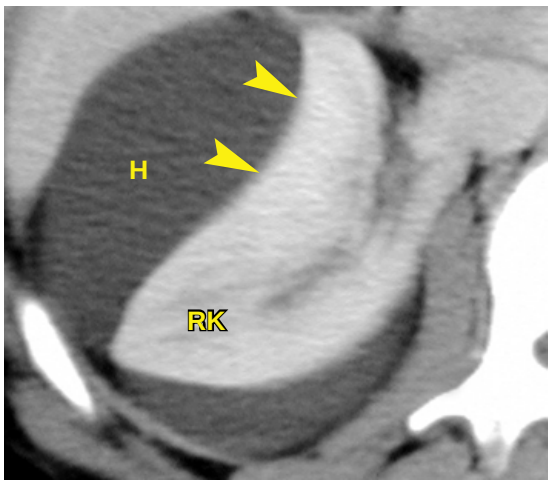

FIGURE 10-6 ■ Subcapsular hematoma. The contour (*arrowheads*) of the right kidney (RK) is compressed and distorted by a hematoma (H) confined within the restricted space bounded by the renal capsule. This finding is indicative of a subcapsular location for the hematoma.

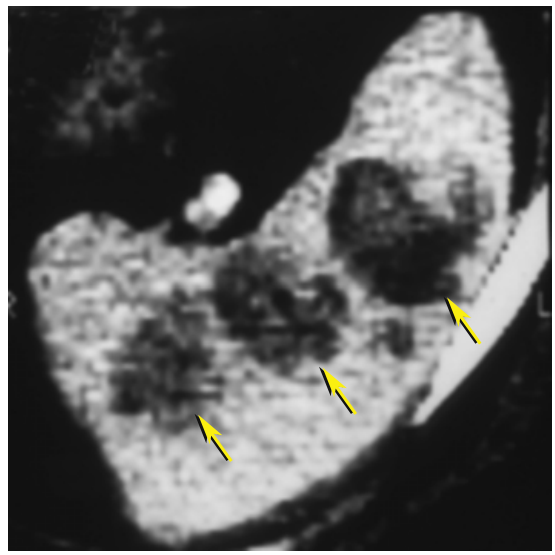

FIGURE 10-7 ■ Intraparenchymal hematomas. Multiple intraparenchymal hematomas (*arrows*) are seen as low-attenuation defects within the contrast-enhanced splenic parenchyma.

irregular enhancement of the spleen (Fig. 10-13) is a common normal finding. Contrast diffuses relatively slowly through the pulp of the spleen. These defects in enhancement must not be mistaken for splenic injury or other abnormalities. Delayed images will demonstrate uniform splenic enhancement.

Liver Trauma

The liver is the second most commonly injured abdominal organ. However, liver laceration is associated with important complications and twice the morbidity of spleen laceration. Up to 45% of patients with liver injury also have spleen injury. When the liver capsule is intact, the liver will usually heal within 1 to 6 months. Liver lacerations tend to parallel the course of the hepatic arteries.

- *Periportal low attenuation* (Fig. 10-14) may be found, with blood tracking adjacent to portal vessels or with dilated periportal lymphatics associated with elevated central venous pressure caused by vigorous fluid resuscitation. Injuries to the biliary tree or intrahepatic lymphatic system are additional causes of periportal low attenuation. This nonspecific finding does not preclude nonsurgical management of liver trauma.
- Diffuse fatty infiltration makes identification of lacerations and hematoma more difficult. Hematomas may appear as high-density

FIGURE 10-8 ■ Liver laceration. Traumatic laceration (*arrows*) of the liver is seen as a jagged, low-attenuation defect against the enhanced liver parenchyma. Blood and fluid within the laceration are responsible for the low attenuation of the laceration. Contrast enhancement of the liver accentuates the lesion.

FIGURE 10-9 ■ Shattered spleen. Multiple lacerations (*arrows*) are seen as jagged defects in the parenchyma of the spleen (S).

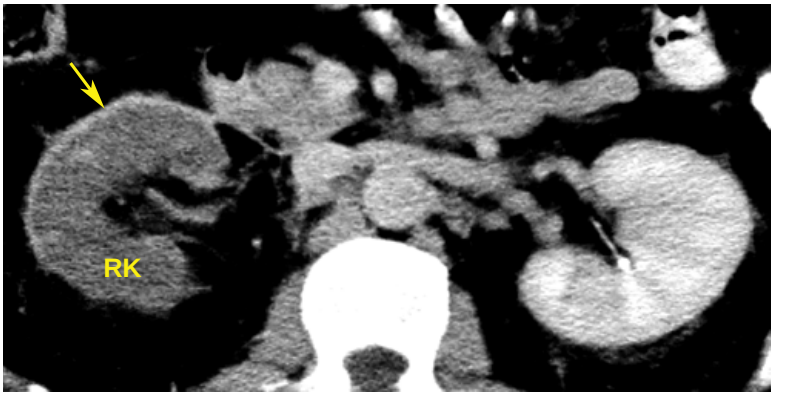

FIGURE 10-10 ■ Renal pedicle injury. The right kidney (RK) shows a diffuse lack of enhancement compared to the left kidney. Failure of an organ to enhance on intravenous contrast administration is evidence of injury to its vascular supply. In this case the main right renal artery thrombosed because of a traumatic tear in the intima. Faint enhancement of the periphery of the kidney is seen, demonstrating the *cortical rim sign* (*arrow*). Arteries supplying the renal capsule do not arise from the main renal artery and thus remain patent when the main renal artery is occluded. These capsular branches provide blood supply to a thin rim of peripheral cortex. The cortical rim sign becomes apparent approximately 8 hours after the vascular insult.

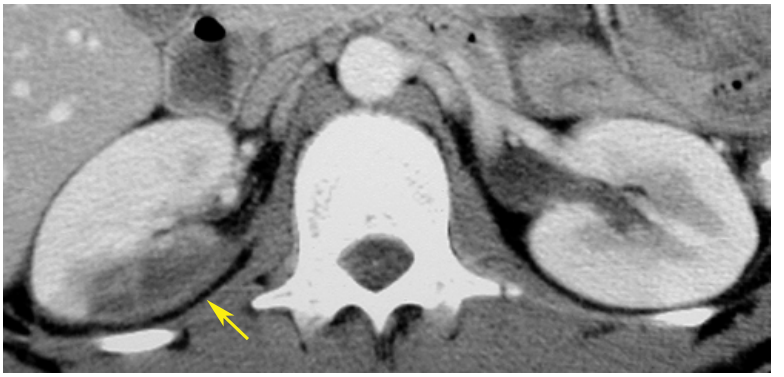

FIGURE 10-11 ■ Renal infarction. A wedge-shaped portion (*arrow*) of the right kidney has failed to enhance. This is evidence of renal infarction resulting from occlusion or tearing of a branch renal artery. The left kidney exhibits normal enhancement.

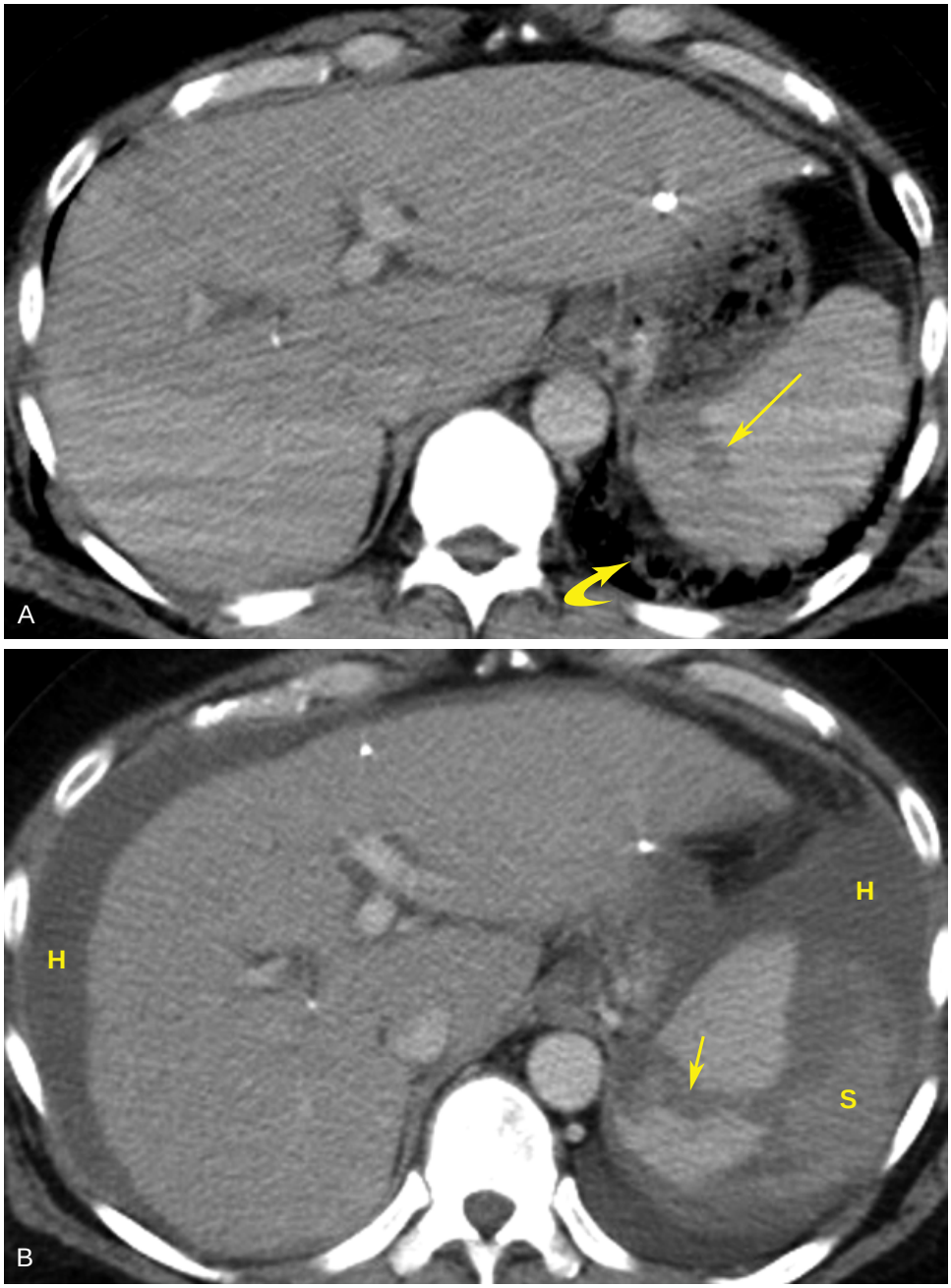

FIGURE 10-12 ■ Delayed rupture of the spleen. *A,* An initial post-trauma computed tomography (CT) scan shows a small intrasplenic hematoma (*straight arrow*) and atelectasis (*curved arrow*) in the left lower lobe of the lung. No hemoperitoneum is present. *B,* On the third day after trauma, the patient experienced increasing pain in the left upper quadrant and generalized abdominal pain. A subsequent CT scan revealed completed rupture of the spleen (*arrow*) with generalized hemoperitoneum (H) and a sentinel clot (S) adjacent to the spleen.

rather than low-density tissue relative to enhanced liver parenchyma.

- Delayed complications affect up to 20% of liver injuries. Bile in liver hematomas delays healing and may result in bilomas. Vascular injury may result in pseudoaneurysms or arterioportal fistulas. A mass effect of bilomas or hematomas may cause obstructive jaundice. Other complications include persistent bile leakage, liver abscess, biliary strictures, and delayed hemorrhage.
- Liver injuries in the superomedial bare area of the liver may be associated with retroperitoneal hematomas rather than hemoperitoneum.

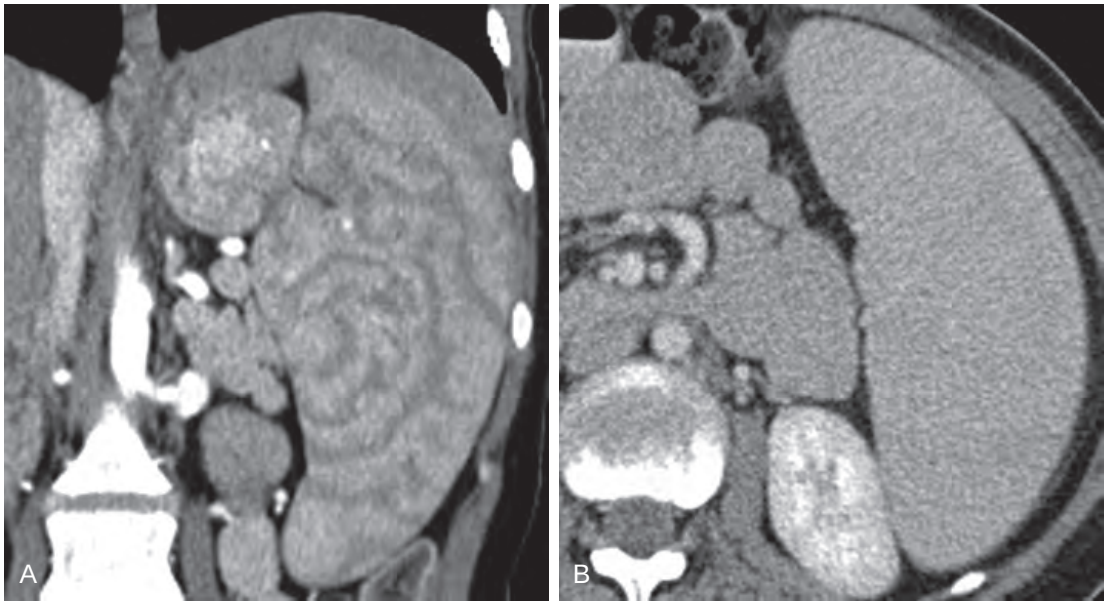

FIGURE 10-13 ■ Early mottled enhancement of the spleen. *A,* Coronal plane multislice CT image obtained during arterial enhancement shows irregular enhancement of the splenic parenchyma, with multiple linear defects caused by normal slow diffusion of contrast through the splenic pulp. *B,* Delayed image of the spleen in the same patient shown in axial projection reveals uniform splenic enhancement.

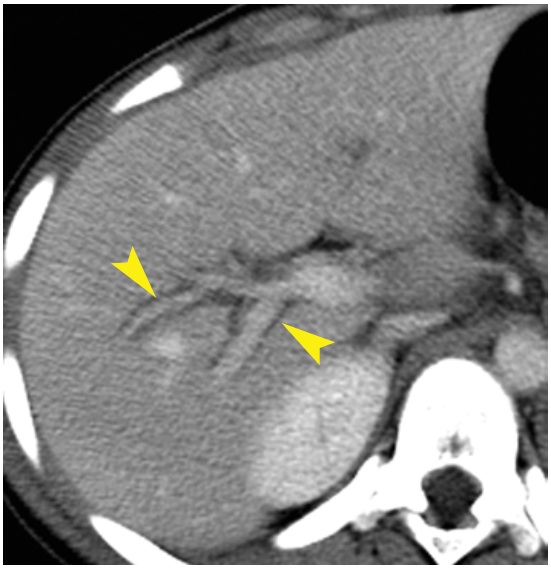

FIGURE 10-14 ■ Periportal low attenuation. Post-contrast trauma computed tomography image of a 10-year-old child shows linear low attenuation (*arrowheads*) adjacent to the enhancing portal veins. A careful search must be made for additional evidence of liver laceration. In this case the periportal low attenuation was caused by aggressive intravenous hydration.

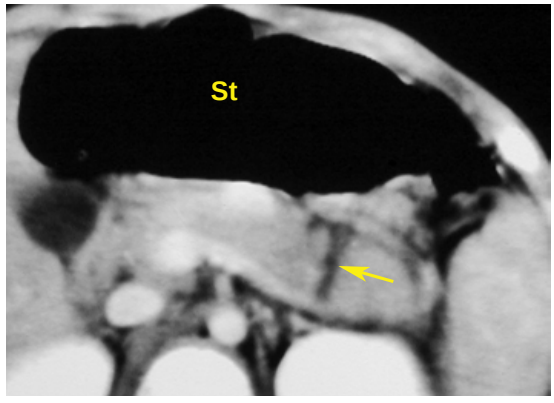

FIGURE 10-15 ■ Pancreas laceration. Trauma computed tomography for a 2-year-old girl shows a laceration (*arrow*) extending between the body and tail of the pancreas. St, stomach filled with air.

Pancreas Trauma

Injury to the pancreas is uncommon but carries high morbidity and is frequently clinically occult. Penetrating trauma, including knife and gunshot wounds, causes most (75%) pancreatic injuries. Blunt abdominal trauma, often associated with child abuse, is the most common cause of pancreatitis in children. The body of the pancreas is compressed against the spine and is prone to contusion, laceration (Fig. 10-15), transection, pancreatitis, and focal hemorrhagic necrosis.

- Tissue displacement may be minimal, making pancreatic lacerations difficult to identify. Fluid tracking adjacent to the splenic vein, unexplained thickening of the anterior renal fascia, and fluid in the lesser sac or anterior pararenal space are CT clues to possible pancreatic injury. The sensitivity of CT for pancreatic injury is 67% to 90%.

- Complications of traumatic injury to the pancreas are common, with mortality as high as 20%. Complications include pseudocyst formation, necrotizing pancreatitis, abscess, and fistula.

Bowel and Mesentery Trauma

Injuries to the bowel and mesentery occur in about 5% of patients following blunt abdominal trauma. CT findings associated with these injuries are often subtle and are easily overlooked. Delays in diagnosis increase the risk of sepsis and peritonitis. The accuracy of CT in the diagnosis of bowel and mesentery injuries is 77% to 93%.

- Bowel segments most commonly injured are the proximal jejunum near the ligament of Treitz and the distal ileum near the ileocecal valve. The duodenum may be injured by a blow to the mid-abdomen from a steering wheel or the handlebars of a bicycle.

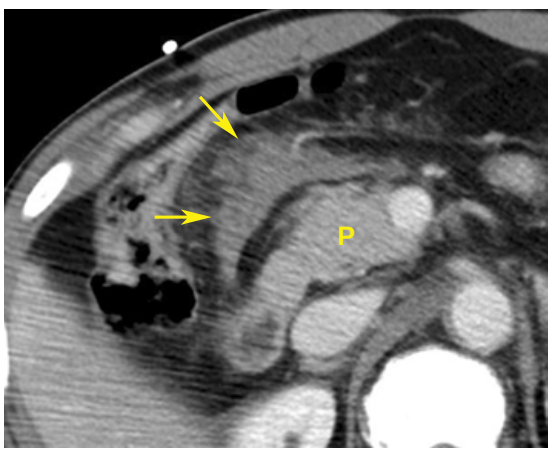

FIGURE 10-16 ■ Mesenteric hematoma. Hemorrhage (*arrows*) into the mesentery is seen as an amorphous density enveloping the mesenteric blood vessels. The head of the pancreas (P) is adjacent to the hematoma. In this case the mesenteric hematoma was an isolated injury.

- As previously mentioned, free intraperitoneal air or oral contrast is highly suggestive, but not a specific sign of bowel injury. Many cases of bowel injury lack these findings.
- Hemoperitoneum in the absence of detection of a solid organ injury warrants a diligent search for subtle abnormalities of the bowel and mesentery. Fluid between bowel loops is highly suggestive of a bowel injury.
- A focal mesenteric hematoma (Fig. 10-16) in association with focal thickening of the bowel wall indicates a high likelihood of a significant bowel injury requiring surgery.
- A focal mesenteric hematoma without focal thickening of the bowel wall is a nonspecific finding associated with both lesions that require surgery and those that do not. An isolated mesenteric hematoma does not require surgery.
- Thickening of the bowel wall may be circumferential or eccentric (Fig. 10-17). A high-density hematoma within the bowel wall is highly indicative of bowel injury. Wall thickening of >3 mm with a well-distended lumen is considered to be abnormal.
- Intense enhancement of the bowel wall associated with bowel wall thickening and free intraperitoneal fluid is strongly indicative of bowel perforation and peritonitis.
- Retroperitoneal air or oral contrast is highly indicative of laceration of the duodenum.
- Wall thickening of the transverse duodenum is highly indicative of intramural duodenal hematoma (Fig. 10-18). The stomach and proximal duodenum may be obstructed.
- Laceration or transection of the jejunum or ileum results in peritonitis and dilatation of small bowel within about 12 hours. Free air is seen in only about 50% of cases. Subtle findings include focal wall thickening and a sentinel clot. The radiologist should check for discontinuity of bowel loops.

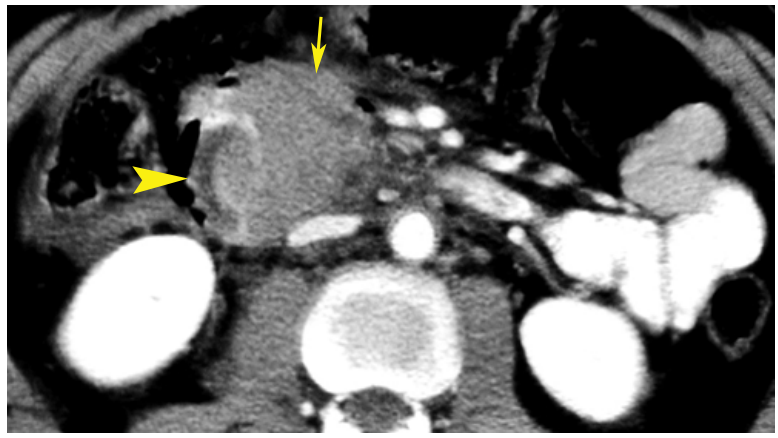

FIGURE 10-17 ■ Torn duodenum. The descending duodenum is filleted open by an extended longitudinal tear. A large hematoma (*arrow*) occupies its lumen and extends around the retroperitoneal vessels. The duodenal wall (*arrowhead*) is thickened. This is a retroperitoneal injury without hemoperitoneum.

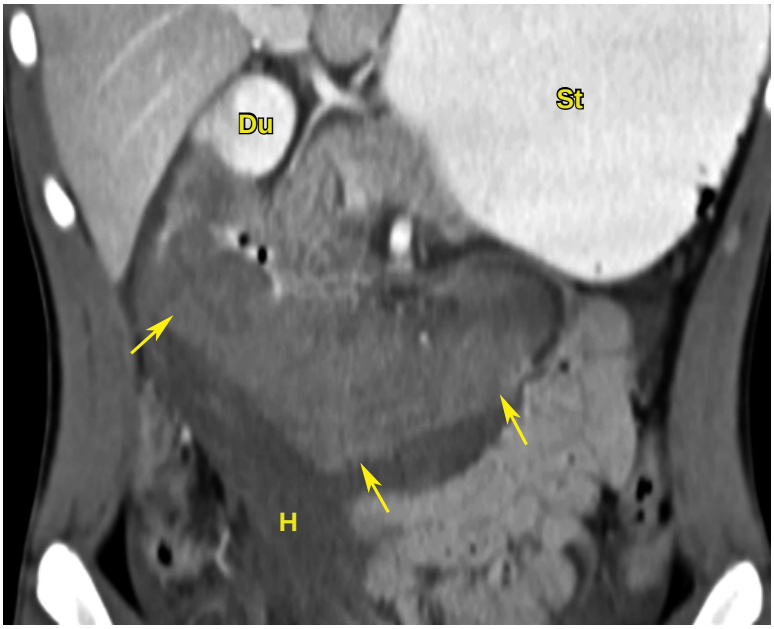

FIGURE 10-18 ■ Duodenal hematoma. Coronal post-contrast computed tomography image shows marked distention of the oral-contrast-filled stomach (St) and duodenal bulb (Du) by a large intramural hematoma (*arrows*) that thickens the wall and obstructs the lumen of the descending and transverse duodenum. Hemorrhage (H) extends into the retroperitoneum.

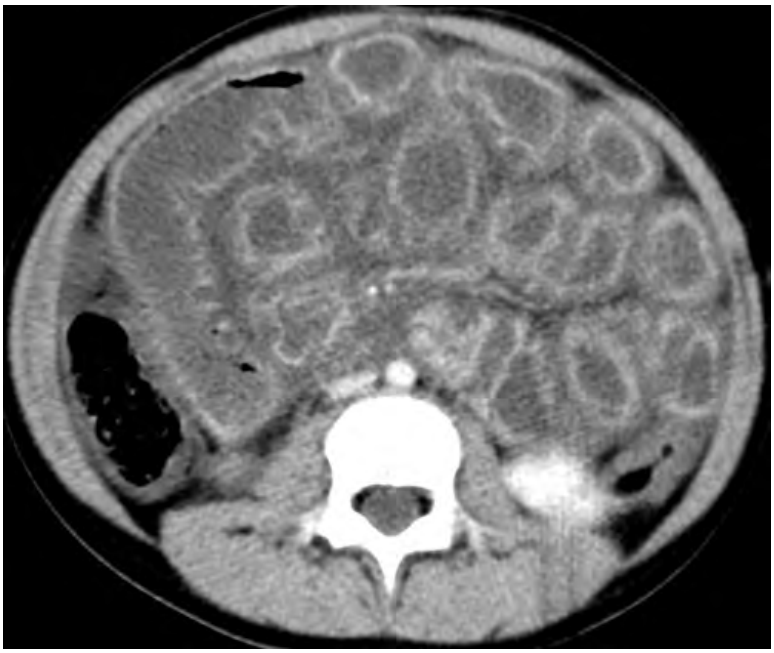

FIGURE 10-19 ■ Shock bowel. Post-contrast computed tomography image of the mid-abdomen of a 7-year-old girl injured in a motor vehicle collision shows diffuse distention of the small bowel with striking enhancement of the bowel wall. The lumen of the small bowel is distended with fluid, and ascites is present.

- Colonic injury may result in intraperitoneal or extraperitoneal findings.
- *Shock bowel* results from severe hypotension and hypoperfusion in trauma patients. CT findings include diffuse dilatation of the small bowel, with wall thickening and increased contrast enhancement of the bowel wall (Fig. 10-19). The colon remains normal. The IVC is flattened, and the kidneys show intense contrast enhancement of the parenchyma.
- Fluid overload resulting from aggressive fluid resuscitation may cause diffuse edema of the small bowel wall associated with dilatation of the IVC, periportal edema, and normal enhancement of the bowel wall and renal parenchyma.

Renal Trauma

The kidneys are injured in 8% to 10% of patients with blunt trauma injuries to the abdomen. Minor

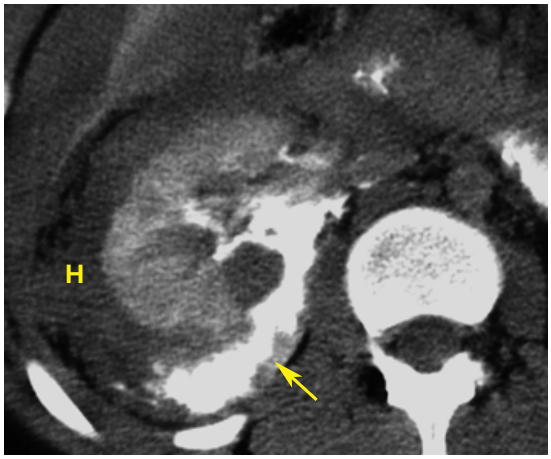

FIGURE 10-20 ■ Tear of the renal collecting system. A delayed image through the right kidney shows extravasation of contrast (*arrow*) from the renal pelvis into the perirenal space already distended with blood (H) and urine. Early post-contrast images showed no early contrast extravasation, excluding active bleeding.

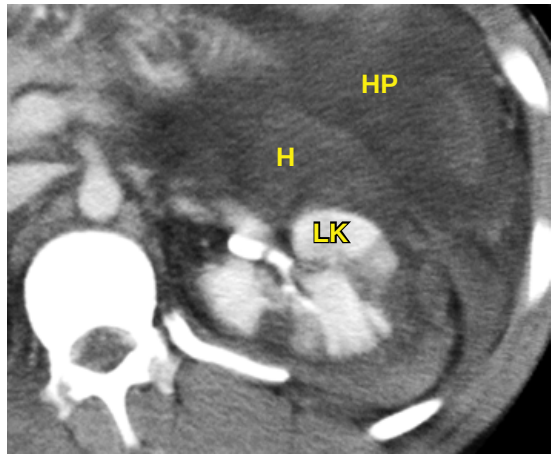

FIGURE 10-21 ■ Shattered kidney. The left kidney (LK) exhibits multiple lacerations and foci of parenchyma that are not enhanced, indicating devascularization. A large perirenal hematoma (H) is present. Hemoperitoneum (HP) caused by a spleen laceration is also evident. This severely damaged kidney was surgically removed.

injuries are most common (75% to 85%) and are managed without surgery. Minor injuries include contusions, subcapsular hematomas, minor lacerations with limited perinephric hematomas, and small cortical infarcts. Hematuria is a reliable sign of injury to the urinary tract.

- Injury to the renal collecting system is diagnosed on delayed images by extravasation of contrast-opacified urine into the renal sinus and medial perirenal space (Fig. 10-20). Deep renal lacerations may be associated with urine leakage into the lateral perirenal space. Urinary extravasation will heal spontaneously as long as there is no obstruction to normal antegrade urine flow. Obstruction requires stent placement or surgical repair.
- Catastrophic injuries require surgical intervention. These include shattered kidneys and injuries to the renal vascular pedicle. Shattered kidneys (Fig. 10-21) have multiple lacerations, severe impairment of contrast excretion, extensive hemorrhage, lacerations of the renal collecting system with urine leakage, and often active arterial bleeding. Devitalized kidney segments may be present.
- Thrombosis of the main renal artery is caused by stretching of the renal pedicle with tearing of the intima, which is less elastic than the media and adventitia. The intimal flap initiates thrombosis, which propagates distally. The entire kidney, or a segmental portion of it, fails to enhance (Fig. 10-10). Abrupt termination of enhancement of the renal artery may be visualized with high-quality helical CT. Most occlusions occur in the proximal 2 cm of the renal artery. This injury usually occurs in the absence of perirenal hematoma. The *cortical rim sign* is a delayed finding of renal arterial occlusion, appearing a minimum of 8 hours after acute thrombosis in the renal artery (Fig. 10-10). Only the periphery of the kidney, supplied by collaterals to the renal capsule, enhances. The bulk of the kidney supplied by the renal artery, which lacks collateral pathways, does not enhance.
- Avulsion of the renal artery is rare and usually life-ending. Patients with avulsion who survive to be examined have absent renal enhancement and large perinephric hematomas and may show arterial extravasation.
- Ureteropelvic junction (UPJ) injuries are caused by sudden deceleration, which tears the UPJ. Urinomas are seen medially or occasionally surrounding the kidney, but no perinephric hematoma is usually present. Complete transections at the UPJ show contrast in the renal pelvis but not in the distal ureter. UPJ lacerations are characterized by visualization of contrast in both the renal pelvis and the distal ureter. Absence of CT visualization of contrast in the ureter is an indication for retrograde pyelography.

Bladder Trauma

Rupture of the bladder occurs in up to 10% of patients with pelvic fractures. In most cases (80%) the bladder is lacerated by a spicule of fractured bone, and urine (and contrast) leaks into extraperitoneal spaces. Rupture of the bladder into the

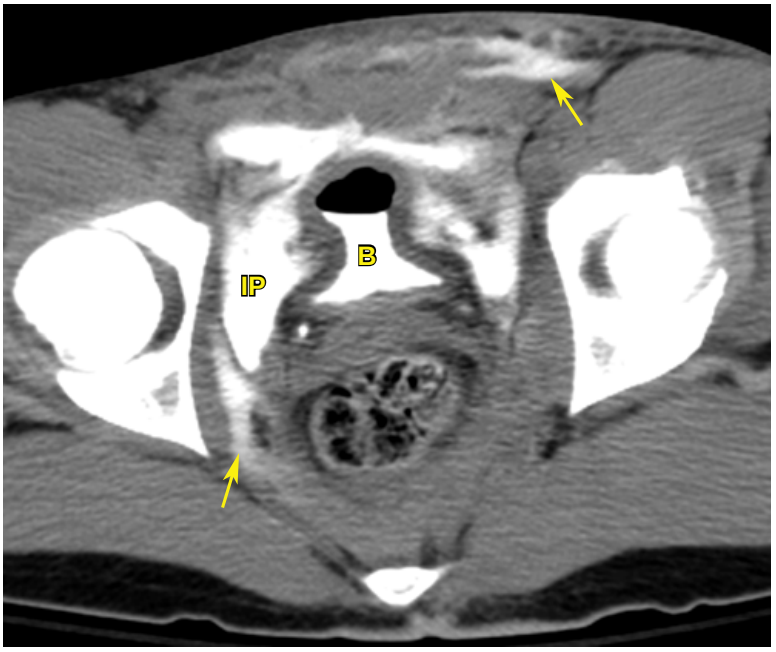

FIGURE 10-22 ■ Intraperitoneal and extraperitoneal bladder rupture. A computed tomography cystogram demonstrates free spillage of contrast from the bladder (B) into the peritoneal cavity (IP) and extraperitoneal spaces (*arrows*).

peritoneal cavity (20%) occurs as a result of a blow to the lower abdomen when the bladder is distended. The sudden increase in intracystic pressure ruptures the bladder at its dome, resulting in leakage of urine into the peritoneal cavity. Both types of bladder rupture are effectively demonstrated by CT following contrast administration either intravenously or via a bladder catheter. However, the bladder must be distended to a volume of at least 250 mL to reliably demonstrate small ruptures.

- The presence of free fluid or hematoma in the pelvis, or fractures of the pubic rami, sacrum, or ileum, suggests possible bladder injury. CT cystography should be considered.
- *Extraperitoneal bladder rupture* is characterized by contrast leakage into the retropubic space with extension along fascial planes into the abdominal wall, scrotum, thigh, and retroperitoneum. The contrast collections tend to be linear and poorly defined. Extraperitoneal bladder ruptures usually heal without surgery.
- *Intraperitoneal bladder rupture* is characterized by contrast leakage into the peritoneal cavity surrounding loops of bowel and extending along the paracolic gutters. The contrast collections are sharply defined by visceral and parietal peritoneum. Intraperitoneal bladder rupture usually requires surgical repair.
- Combined extraperitoneal and intraperitoneal ruptures occur in about 5% of patients (Fig. 10-22).
- *Bladder contusions* appear as focal areas of thickening of the bladder wall. Hemorrhage in the bladder wall may produce focal high attenuation.
- *Urethral injuries* should be suspected in patients with pelvic fractures, bladder injuries, and pelvic hematomas. Clinical findings include blood at the urethral meatus and an inability to void. Urethral injuries are diagnosed from retrograde urethrograms.

Adrenal Trauma

Hemorrhage into the adrenal gland is seen in about 2% of adults with severe trauma. Posttraumatic hemorrhage has a striking propensity to involve the right adrenal gland (90% of cases). The predilection for the right adrenal gland has been attributed to compression of the gland between the liver and the spine. Hemorrhage is bilateral in 25% of cases. Bilateral hemorrhage places the patient at risk of developing adrenal insufficiency.

- Acute hemorrhage produces a hyperdense (50 to 75 HU) round to oval mass replacing the affected adrenal gland (Fig. 10-23).
- Fat adjacent to the adrenal gland is infiltrated with streaks of soft-tissue density representing bleeding into the periadrenal fat.
- The hemorrhage decreases in density and shrinks over time. Calcification may develop in the gland within a few months.

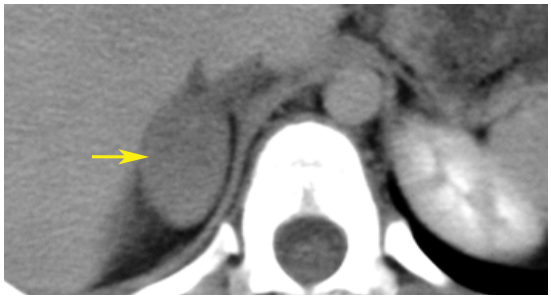

FIGURE 10-23 ■ Adrenal hemorrhage. A solid mass (*arrow*) replaces the right adrenal gland in a patient with multiple injuries incurred in a motor vehicle accident. Follow-up computed tomography revealed that the right adrenal gland returned to a normal appearance, confirming post-traumatic right adrenal hemorrhage.

Hypoperfusion Complex

Persistent hypovolemic shock caused by blood loss from traumatic injury is manifest on CT by:

- Flattening of the infrahepatic inferior vena cava and renal veins
- Decreased size of the abdominal aorta
- Shock bowel seen as diffuse thickening and hyperenhancement of the wall of the small bowel
- Decreased enhancement of the renal medulla on delayed post-contrast images
- Decreased enhancement of the spleen

SUGGESTED READING

Alonso RC, Nacenta SB, Martinez PD, et al.: Kidney in danger: CT findings of blunt and penetrating renal trauma. *Radiographics* 29:2033–2053, 2009.

Brofman N, Atri M, Hanson JM, et al.: Evaluation of bowel and mesenteric blunt trauma with multidetector CT. *Radiographics* 26:1119–1131, 2006.

Daly KP, Ho CP, Persson DL, Gay SB: Traumatic retroperitoneal injuries: Review of multidetector CT findings. *Radiographics* 28:1571–1590, 2008.

Hamilton JD, Kumaravel M, Censullo ML, et al.: Multidetector CT evaluation of active extravasation in blunt abdominal and pelvic trauma patients. *Radiographics* 28:1603–1616, 2008.

Kanki A, Ito K, Tamada T, et al.: Dynamic contrast-enhanced CT of the abdomen to predict clinical prognosis in patients with hypovolemic shock. *AJR Am J Roentgenol* 197:W980–W984, 2011.

Körner M, Krötz MM, Degenhart C, et al.: Current role of emergency US in patients with major trauma. *Radiographics* 28:225–244, 2008.

Linsenmaier U, Wirth S, Reiser M, Körner M: Diagnosis and classification of pancreatic and duodenal injuries in emergency radiology. *Radiographics* 28:1591–1601, 2008.

Lubner M, Menias C, Rucker C, et al.: Blood in the belly: CT findings of hemoperitoneum. *Radiographics* 27:109–125, 2007.

Millo NZ, Plewes C, Rowe BH, Low G: Appropriateness of CT of the chest, abdomen, and pelvis in motorized blunt force trauma patients without signs of significant injury. *AJR Am J Roentgenol* 197:1393–1398, 2011.

Ramchandani P, Buckler PM: Imaging of genitourinary trauma. *AJR Am J Roentgenol* 192:1514–1523, 2009.

Sadro C, Bernstein MP, Kanal KM: Imaging of trauma: Part 2, abdominal trauma and pregnancy — a radiologist's guide to doing what is best for the mother and baby. *AJR Am J Roentgenol* 199:1207–1219, 2012.

Smith J: Focused assessment with sonography in trauma (FAST): Should its role be reconsidered? *Postgrad Med J* 86:285–291, 2012.

Soto JA, Anderson SW: Multidetector CT of blunt abdominal trauma. *Radiology* 265:678–693, 2012.

Stuhlfaut JW, Soto JA, Lucey BC, et al.: Blunt abdominal trauma: Performance of CT without oral contrast material. *Radiology* 233:689–694, 2004.

Tsang BD, Panacek EA, Brant WE, Wisner DH: Effect of oral contrast administration for abdominal computed tomography in the evaluation of acute blunt trauma. *Ann Emerg Med* 30:7–13, 1997.

CHAPTER 11

LIVER

William E. Brant

ANATOMY

The Couinaud (pronounced "kwee-NO") international classification system divides the liver into eight independent segments (Fig. 11-1 and Table 11-1). Each segment is a self-contained unit that can be surgically resected without damaging the remainder of the liver. Each segment has its own dual vascular inflow (hepatic artery and portal vein), its own biliary drainage, and a shared vascular outflow (hepatic veins). The portal triads (bile ducts, hepatic arteries, and portal veins) course through the center of each segment, whereas the hepatic veins define the periphery of the segment and the plane of surgical dissection. This segmental anatomy provides a useful and widely accepted method for identification of the location of lesions seen on computed tomography (CT) and other imaging studies.

The right, middle, and left hepatic veins enter the intrahepatic inferior vena cava (IVC) just before it pierces the diaphragm about 2 cm below the right atrium. Whereas the right hepatic vein usually enters the IVC separately, the middle and left hepatic veins often (65% to 85%) form a common trunk before joining the IVC. In most patients, these three major hepatic veins drain the entirety of the liver except for the caudate lobe. Short hepatic veins separately drain the caudate lobe directly into the IVC. As an anatomic variant, accessory hepatic veins drain segment V or VI independently into the IVC.

The portal vein is formed by the junction of the splenic vein with the superior mesenteric vein just anterior to the IVC and just posterior to the neck of the pancreas. It ascends behind the duodenum in company with the hepatic artery and common bile duct to the porta hepatis, where it divides into a short, fatter right portal vein and a longer, thinner left portal vein.

The hepatic artery has variable anatomy. In its "classic" form (55%), the right and left hepatic arteries branch from a proper hepatic artery that is a continuation of the common hepatic artery arising from the celiac axis. In 10% of individuals, the left hepatic artery arises as a branch of the left gastric artery. In 11%, the right hepatic artery arises from the superior mesenteric artery (SMA). In this case the "replaced" right hepatic artery passes through the portocaval space from the SMA to the right hepatic lobe.

Division of the liver into eight segments is based on a concept of three vertical planes and one transverse plane. A vertical plane through the middle hepatic vein, IVC, and gallbladder fossa divides the liver into right and left lobes. A vertical plane through the right hepatic vein divides the right lobe into anterior (VIII and V) and posterior (VII and VI) segments. A vertical plane through the left hepatic vein divides the left lobe into medial (IVa and IVb) and lateral (II and III) segments. A transverse plane through the left portal vein divides the left lobe into superior (IVa and II) and inferior (IVb and III) segments. An oblique transverse plane through the right portal vein divides the right lobe into superior (VIII and VII) and inferior (V and VI) segments (Table 11-1).

Segment I is the caudate lobe, which is separated from the rest of the liver by the fissure of the ligamentum venosum anteriorly and the IVC posterolaterally. It is supplied by branches of both right and left hepatic arteries and portal veins and drains venous blood directly into the IVC via numerous small hepatic veins. The papillary process of the caudate lobe extends toward the lesser sac and may appear separate from the rest of the caudate lobe, simulating a mass or an enlarged lymph node.

Segment II and *segment III* make up the lateral division of the left lobe. The plane of the left portal vein divides segments II and III. Segment II makes up the left superior and lateral contour of the liver. Segment III makes up the left inferior and lateral contour of the liver. *Segment IV* makes up the medial division of the left lobe. The plane of the left portal vein divides the medial segment of the left lobe into segments IVa (superior) and IVb (inferior). Segment IV was previously called the quadrate lobe.

The anterior segments (V and VIII) of the right lobe are separated from the posterior segments (VI and VII) by the plane of the right hepatic vein. The lateral contour of the anterior right lobe is formed by *segment VIII* superiorly

and *segment V* inferiorly. *Segment VII* lies posterior to segment VIII, and *segment VI* lies posterior to segment V. The plane of the right portal vein separates anterior segments VIII and V and separates posterior segments VII and VI.

Unfortunately, natural anatomic variations in blood supply do not adhere perfectly to the concept of flat geometric planes dividing the segments (Fasel et al, 1998). In reality, the vascular territorial boundaries between segments have more variable and curving undulations to their borders than is indicated by the concept of flat planes. In addition, many three-dimensional drawings in the literature are misleading regarding the location of the lobes. Segment VII is posterior to and hidden by segment VIII in a frontal projection, rather

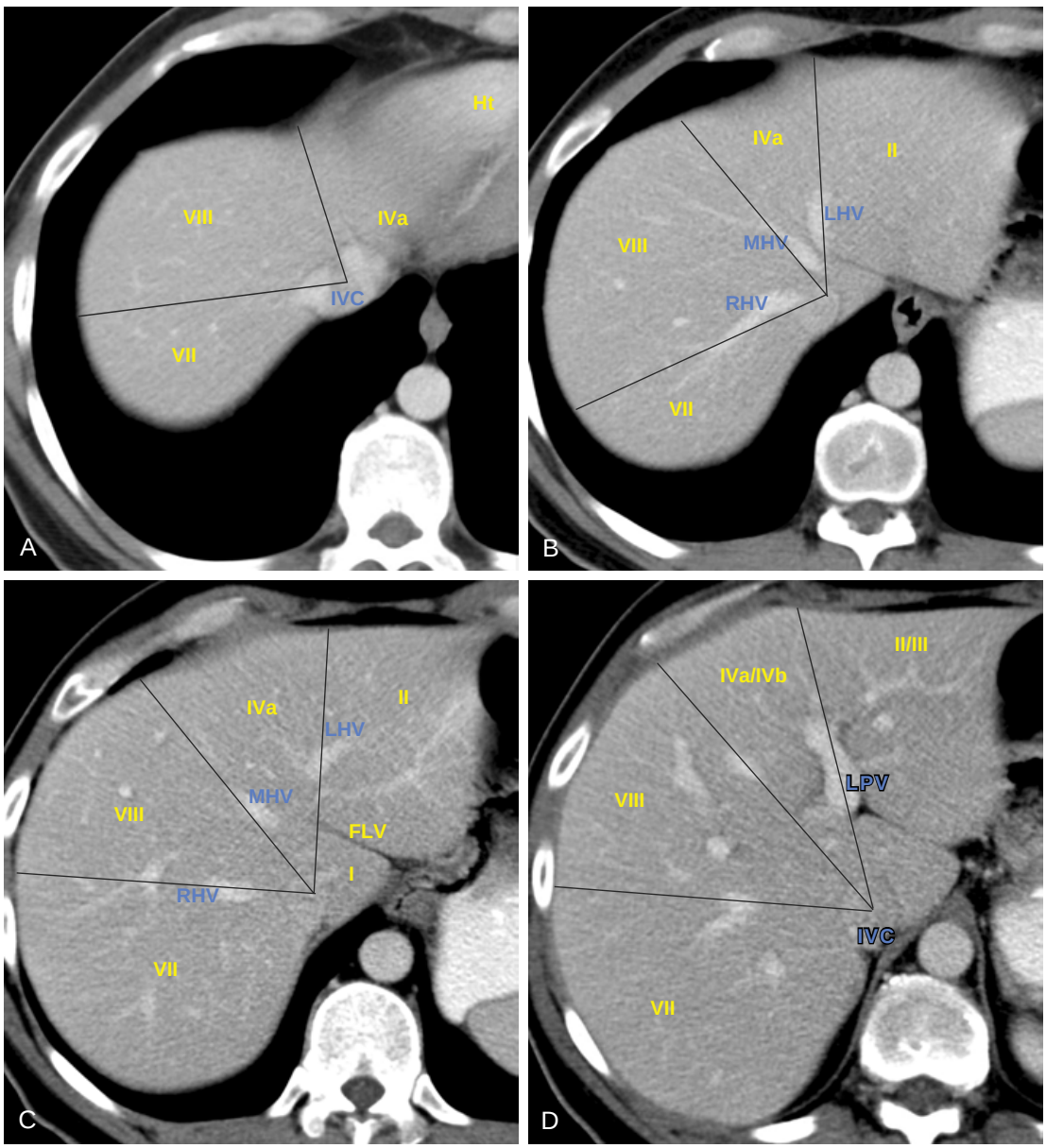

FIGURE 11-1 ■ Anatomic segments of the liver. *A* to *I*, A series of postcontrast computed tomography images reveals anatomic landmarks and the segmental anatomy of the liver. Segments are labeled I through VIII. The vertical planes defined by the right (RHV), middle (MHV), and left (LHV) hepatic veins are shown as straight lines. Other key landmarks are identified. The *arrow* in *F* indicates the posterior branch of the right portal vein (RPV), and the *arrowhead* indicates the anterior branch of the RPV. This patient has had a cholecystectomy. Note the difficulty in applying straight geometric planes to curving vessels. GBF, gallbladder fossa; Ht, heart; FLV, fissure of the ligamentum venosum; FLT, fissure of the ligamentum teres; IVC, inferior vena cava; LPV, left portal vein; MPV, main portal vein.

Continued

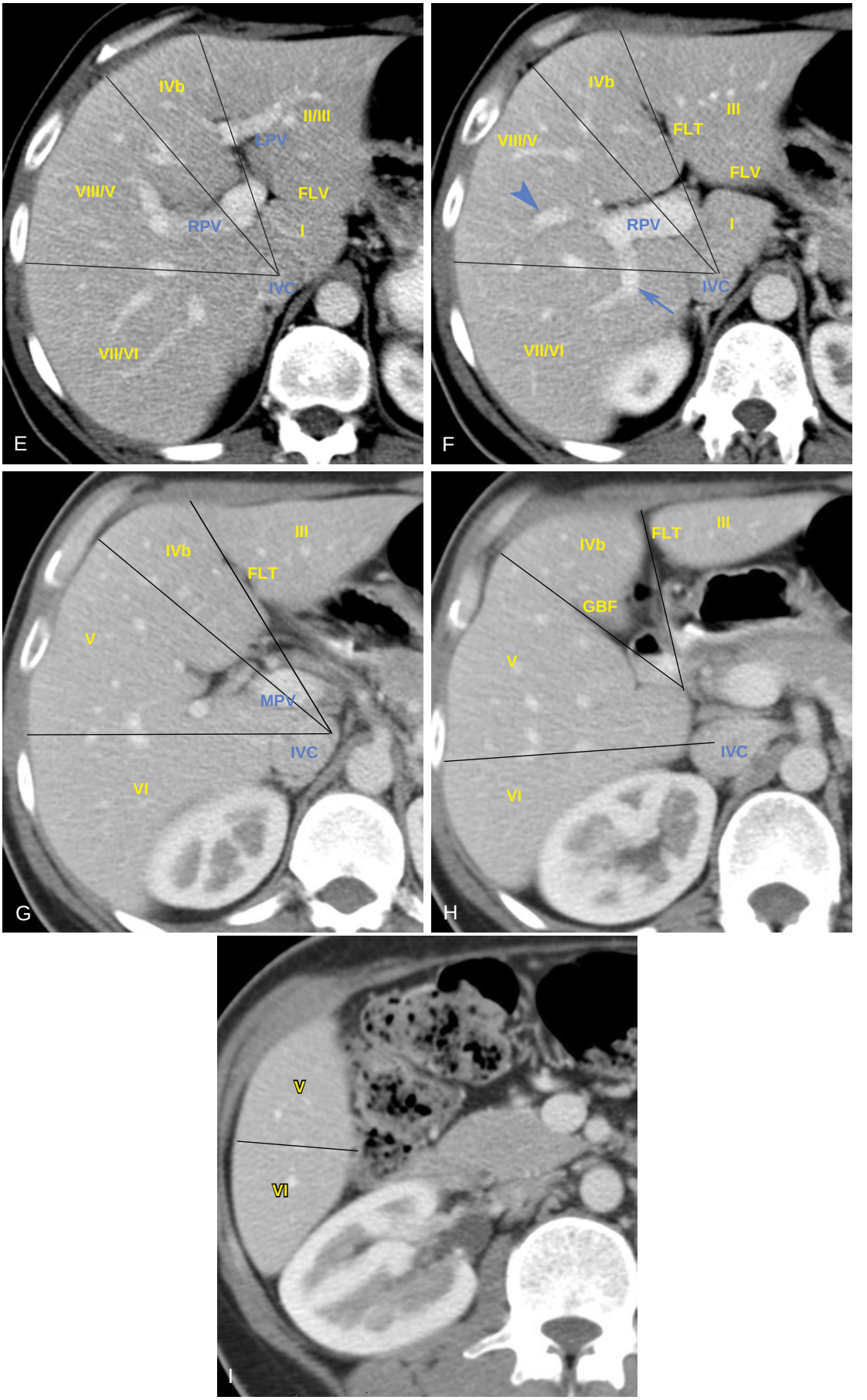

FIGURE 11-1, cont'd

TABLE 11-1 **Nomenclature for Anatomic Segments of the Liver**

Couinaud Segment	Anatomic Description	Traditional Nomenclature
I	Caudate lobe	Caudate lobe
		Left lobe
II	Left lateral superior subsegment	Lateral segment
III	Left lateral inferior subsegment	Lateral segment
IVa	Left medial superior subsegment	Medial segment
IVb	Left medial inferior subsegment	Medial segment
		Right lobe
V	Right anterior inferior subsegment	Anterior segment
VIII	Right anterior superior subsegment	Anterior segment
VI	Right posterior inferior subsegment	Posterior segment
VII	Right posterior superior subsegment	Posterior segment

than lateral to segment VIII as shown in some drawings. Likewise, segment VI is posterior, not lateral, to segment V. The axial images in Figure 11-1 are an attempt to localize the segments as demonstrated by CT. Radiologists should correlate the anatomic description of the lobes in Table 11-1 with their location as shown in Figure 11-1 to learn the segments. It should be recognized that anatomic variations in blood supply make localization of lesions to specific segments somewhat inaccurate. In addition, many liver lesions will involve two or more segments.

Several fissures and ligaments deserve special mention either because they are particularly prominent or because they define important perihepatic spaces. The falciform ligament consists of two closely applied layers of peritoneum extending from the umbilicus to the diaphragm in a parasagittal plane. The caudal free end of the falciform ligament contains the ligamentum teres, which is the remnant of the obliterated umbilical vein. The reflections of the falciform ligament separate over the posterior dome of the liver to form the coronary ligaments that define the "bare area" of the liver not covered by peritoneum. The coronary ligaments reflect between liver and diaphragm and prevent access of intraperitoneal fluid from covering the "bare area" of the liver. The absence of fluid over the bare area is an important sign in the differentiation of ascites from pleural effusion on CT. The remainder of the falciform ligament and ligamentum teres continues into the liver to form a prominent fat-filled fissure that defines the left intersegmental fissure dividing the medial and lateral segments of the left lobe.

The fissure of the ligamentum venosum contains the remnant of the ductus venosus, which in fetal life carries oxygenated blood from the umbilical vein to the IVC. This fissure is commonly fat-filled and prominent on CT and separates the caudate lobe and the left lobe.

The lesser omentum suspends the lesser curve of the stomach and the duodenal bulb from the inferior surface of the liver, attaching within the fissure of the ligamentum venosum. The lesser omentum is subdivided into the gastrohepatic ligament and the hepatoduodenal ligament. The gastrohepatic ligament contains coronary veins that serve as an important sign of portal hypertension when they become dilated. The right free edge of the hepatoduodenal ligament carries the portal vein, hepatic artery, and common bile duct between the porta hepatis and the duodenum. The hepatoduodenal ligament provides the anterior border of the foramen of Winslow, which opens into the lesser sac.

The normal liver is homogeneous in attenuation, measuring 55 to 65 Hounsfield units (HU) on unenhanced CT. The unenhanced liver parenchymal density is normally greater than that of blood vessels and 7 to 8 HU greater than for the splenic parenchyma. Anemia lowers the CT density of blood vessels and may make the liver parenchyma appear falsely increased in density. The contour of the liver is smooth and convex adjacent to the diaphragm, with a sharp inferior border and a concave undersurface. Fissures may be fat-filled and prominent. The right lobe is usually larger than the left lobe and may extend far caudad as a Riedel's lobe, a normal variant. The left lobe is more variable in size, and its lateral segment may extend far to the left and wrap partially around the spleen. Congenital absence of the left lobe is a rare anomaly. *Diaphragmatic slips* are infoldings of the diaphragm that indent the normal smooth contour of the liver (Fig. 11-2). These invaginations of diaphragmatic muscle occur with increasing frequency with age older than 60 years and should not be mistaken for masses in the liver or on the diaphragm.

TECHNICAL CONSIDERATIONS

Multidetector CT (MDCT) allows scanning of the entire liver with thin collimation during a

FIGURE 11-2 ■ Diaphragmatic slips. Folds in the diaphragm (*arrowheads*) in this 78-year-old woman create defects in the liver. These diaphragmatic slips are more common in older patients. They are recognized by their peripheral location and characteristic linear appearance. An enhancing hemangioma (*arrow*) is partially visualized.

single breath hold of 10 to 25 seconds. Acquisition is routinely repeated several times during various phases of contrast medium enhancement.

Dynamic contrast-enhanced liver CT offers the opportunity to accurately characterize lesion enhancement patterns and significantly improve the specificity of diagnosis. Various lesions are detected best, or sometimes only, in specific phases of postcontrast scanning. Intravenous contrast is administered via a power injector at a contrast concentration of 300 mg iodine (I)/mL at a rate of 4 to 5 mL/second for a volume of 100 to 150 mL. Routine scan delays for MDCT are 25 seconds following initiation of contrast injection for the arterial phase and 65 seconds following initiation of contrast injection for the portal venous phase. With MDCT, images are routinely acquired at collimation of 1.25 to 2.50 mm but are viewed at a slice thickness of 5 mm. Image acquisition at thin collimation allows for highly detailed multiplanar reconstructions. Enhancement of the normal liver is homogeneous throughout the parenchyma for all enhancement phases.

- *Noncontrast scans* are commonly obtained to provide a baseline for the degree of lesion enhancement. Many liver lesions are detected, but small lesions are often mistaken for unopacified vessels. Noncontrast scans are superior to postcontrast scans for diagnosis of fatty infiltration and other alterations in parenchymal attenuation.
- *Arterial-phase* acquisition is optimal for visualization of hypervascular lesions supplied by the hepatic artery such as hepatoma, carcinoid metastases, and focal nodular hyperplasia (FNH). Lesions are conspicuous because they enhance more than the surrounding parenchyma. A variety of perfusion abnormalities is seen only on arterial-phase images.
- *Portal venous-phase* imaging yields the best lesion detection overall because parenchymal enhancement is maximum during this phase. Lesions are conspicuous because they are of low attenuation against a background of maximally enhanced liver parenchyma.
- The *equilibrium phase* occurs at 2 to 3 minutes after initiation of contrast injection. During the equilibrium phase, the concentration of contrast agent is approximately equal between the intravascular and extravascular spaces, rendering most liver lesions invisible.
- *Delayed-phase* images, acquired at 10 to 20 minutes after contrast injection, are used to demonstrate delayed contrast fill-in of hemangiomas and to detect fibrotic tumors such as cholangiocarcinoma.

LIVER HEMODYNAMICS AND PERFUSION ABNORMALITIES

The liver has a distinctive dual blood supply, with ~25% of its blood volume normally coming from the hepatic artery and ~75% arriving from the portal vein. While this distribution holds for the liver as a whole, this distribution pattern is not uniform throughout the liver. Alterations in arterial and venous supply to portions of the liver result in transient perfusion abnormalities that can be observed on postcontrast CT. Some perfusion abnormalities result from transient conditions, whereas others are congenital or chronic conditions that cause metabolic alterations in the liver, resulting in abnormalities such as focal steatosis or focal sparing in diffuse fatty liver. Temporary conditions that may cause transient perfusion abnormalities include compression of the liver capsule by ribs or by infoldings of the diaphragm (slips) during breath holding for CT. Variations in vascular supply, termed *third inflow*, are chronic conditions that may result in focal metabolic changes in the liver parenchyma. Third inflow refers to small volumes of the liver that are supplied by aberrant systemic veins, in addition to the usual hepatic artery and portal venous supply.

Perfusion abnormalities usually represent an increase in arterial blood flow to a portion of the

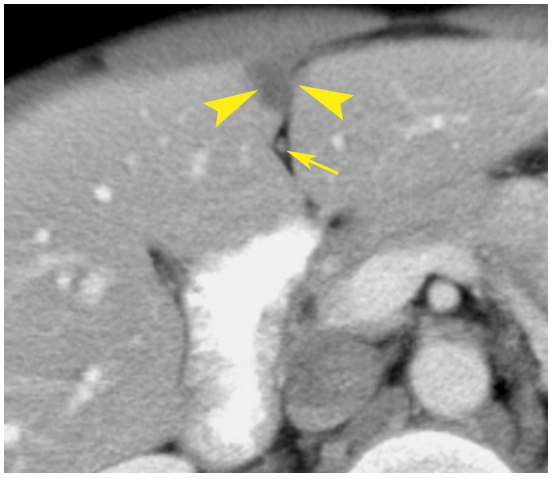

FIGURE 11-3 ■ Pseudolesion caused by third inflow. An early portal venous-phase image shows a low-attenuation nodular focus (*arrowheads*) adjacent to the fissure of the ligamentum teres. This should be recognized as a common pseudolesion related to third inflow. The remnant of the falciform ligament (*arrow*) is seen as a soft-tissue density within the fissure.

liver in response to a focal decrease in portal venous flow. In most cases the perfusion abnormality manifests as increased enhancement of a segment or subsegment of the liver during arterial-phase imaging, with normal parenchymal enhancement during the portal venous phase. When the blood flow anomaly is persistent, resulting metabolic abnormalities manifest as focal steatosis or focal fatty sparing. Most perfusion disorders are asymptomatic but must be recognized to avoid mistaking them for significant lesions.

Third inflow via systemic veins causes perfusion abnormalities in predictable areas of the liver and is thus relatively easy to recognize. Systemic veins communicate with portal venous branches to focally decrease portal venous flow, which results in an increase in hepatic arterial flow in the same area. These are prime areas for focal steatosis or focal fatty sparing.

- The liver parenchyma adjacent to the gallbladder in segments IV and V is sometimes supplied by the cholecystic vein draining the gallbladder.
- The dorsal aspect of segment IV adjacent to the porta hepatis may be supplied by the parabiliary veins draining the distal stomach and head of the pancreas.
- The anterior aspect of segments IV and III adjacent to the fissure of the ligamentum teres is often supplied by the epigastric–paraumbilical veins draining blood from the anterior abdominal wall directly into the liver (Fig. 11-3). This venous plexus may be enlarged and prominently visualized on CT in the presence of an obstruction to either the superior or inferior vena cava. In portal hypertension these collaterals are enlarged and blood flow may reverse to drain out of the liver instead of into the liver.

Extrinsic compression of the liver capsule causes low-attenuation defects with the following features.

- A poorly marginated, low-attenuation defect is seen during the portal venous phase beneath a concave indentation of the liver capsule.
- No abnormalities are seen in the same area on unenhanced, arterial-phase, equilibrium-phase, or delayed images.
- The offending ribs or diaphragmatic slips are evident. Metastatic disease on the peritoneal surface of the liver and subcapsular fluid collections may cause similar perfusion findings.

Tumors may affect perfusion in the adjacent liver parenchyma in several ways.

- Hypervascular tumors may have intratumoral arterioportal shunts. These produce transient, peripheral, wedge-shaped enhancement zones during the arterial phase in the parenchyma peripheral to the tumor and early enhancement of peripheral portal-vein branches before the main portal vein is enhanced. The peripheral enhancement may be mistaken for additional tumor, resulting in overestimation of tumor size.
- Tumor invasion, compression, or induced thrombosis may obstruct the portal vein or its branches. This results in decreased attenuation of the affected parenchyma on noncontrast scans because of edema and transient increased enhancement during the arterial phase arising from increased arterial flow (Fig. 11-4). Thrombi may be seen in portal veins.
- Hypervascular tumors, such as large hepatocellular carcinomas (HCCs), may parasitize and enlarge regional hepatic arteries. The tumor may either "steal" blood from the adjacent parenchyma or cause an increase in arterial blood flow to the adjacent parenchyma. Thus, on arterial-phase imaging, the parenchyma adjacent to large hypervascular tumors may show either increased or decreased enhancement.

DIFFUSE LIVER DISEASE

Fatty Liver

Fatty infiltration of the liver (hepatic steatosis) is one of the most common abnormalities

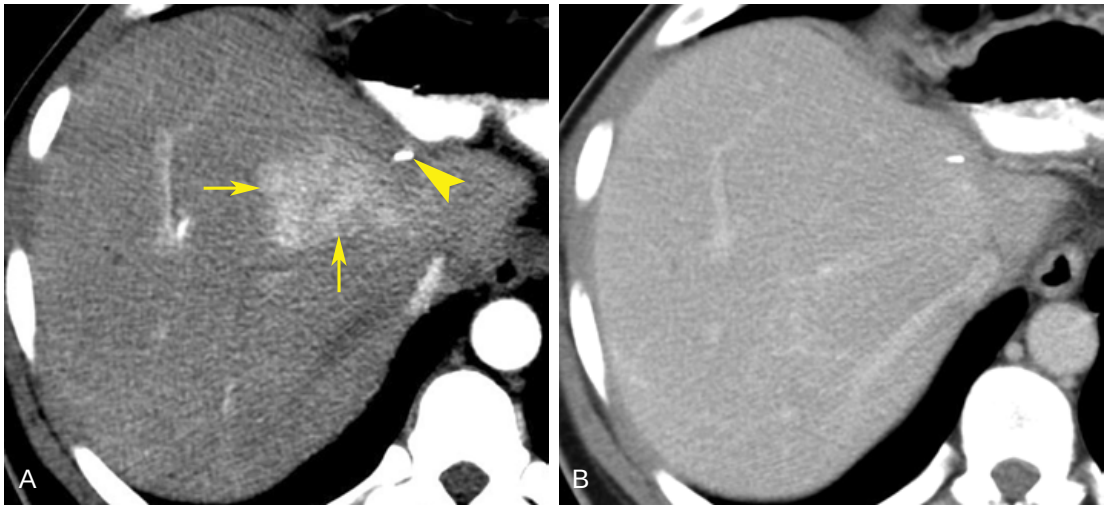

FIGURE 11-4 ■ Transient abnormality in arterial perfusion. *A,* An arterial-phase image of the liver in a patient who has had a left hepatic lobectomy shows a poorly marginated area of bright arterial enhancement (*arrows*). Serial images showed no evidence of a mass in this region. A metallic staple (*arrowhead*) placed during surgery is noted. *B,* A portal venous-phase image through the same region shows normal parenchymal enhancement. This perfusion defect was attributed to postsurgical occlusion of portal venous branches to this area that resulted in a compensatory increase in hepatic arterial flow.

diagnosed by liver CT. Fatty infiltration is a nonspecific response of hepatocytes to a variety of insults, including alcoholism, obesity, diabetes, hyperlipidemia, viral hepatitis, chemotherapy, corticosteroid therapy, hyperalimentation, and malnutrition.

The current obesity epidemic is accompanied by an increasing incidence of nonalcoholic fatty liver disease and nonalcoholic steatohepatitis (NASH). Up to 10% of patients undergoing liver biopsy in the United States have NASH. Up to 80% of obese patients (body mass index >30 kg/m^2) have fatty livers and up to 30% have NASH. NASH leads to liver fibrosis, cirrhosis, and in some cases liver failure. The presence of NASH is associated with an increased risk of atherosclerotic coronary disease. Risk factors for NASH include metabolic syndrome, hypertension, diabetes, insulin resistance, hyperlipidemia, and obesity.

- *Fatty infiltration* lowers the CT attenuation of the involved liver parenchyma. The findings are most accurately assessed on noncontrast CT. The attenuation of normal liver is at least 10 HU greater than that of the spleen. With fatty infiltration, the attenuation of the involved liver is at least 10 HU lower than that of the spleen. Hepatic vessels course through areas of fatty infiltration unaltered. Fatty change is more difficult to judge on postcontrast CT because of the variability in scan timing and the fact that maximum liver enhancement is delayed compared to maximum spleen enhancement. CT attenuation below –40 HU is strong evidence of hepatic steatosis but excludes mild cases.
- In most cases of *diffuse fatty infiltration*, the entire liver is uniformly reduced in density (Fig. 11-5). Vessels stand out in prominent relief but run their normal course through the liver without displacement or narrowing by a mass effect. The liver is usually enlarged, and the parenchyma is minimally enhanced. This pattern is the most common and is the easiest to recognize. In some cases the fatty infiltration is diffuse throughout the liver but is nonuniform and patchy in severity.
- In *focal fatty infiltration*, a geographic or fan-shaped portion of the liver shows fat infiltration, whereas the remainder of the liver is of normal density (Fig. 11-6). The low-density area may extend to the liver surface, but no bulge in contour is seen. Vessels run their normal course through the area of involvement. Margins between fat-infiltrated and normal liver are frequently straight and well defined, reflecting blood-flow territories. Fat infiltration is confined to segments and subsegments. Areas of the liver supplied by third inflow systemic veins are commonly affected; these are adjacent to the gallbladder, the fissure of the ligamentum teres, and the porta hepatis.
- In *multifocal fatty infiltration*, patchy areas of decreased attenuation are scattered throughout the liver (Fig. 11-7). Tumors may be

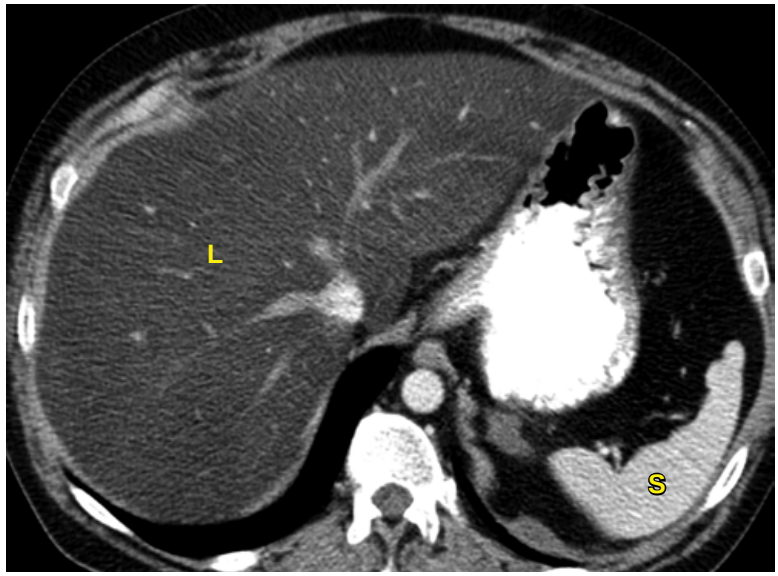

FIGURE 11-5 ■ Diffuse fatty infiltration. The liver parenchyma (L) is diffusely and markedly lower in attenuation than the spleen parenchyma (S), indicating diffuse hepatocellular fatty infiltration. The blood vessels in the liver show normal distribution and tapering without evidence of a mass effect.

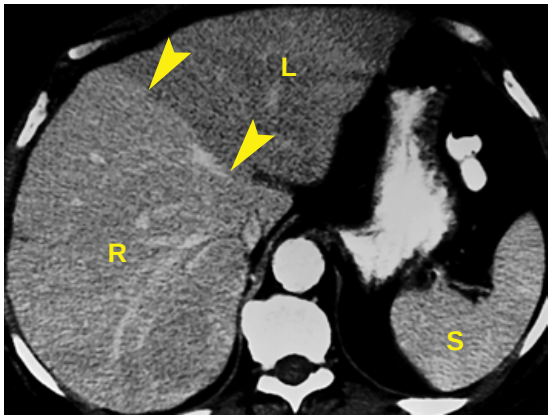

FIGURE 11-6 ■ Focal fatty infiltration. The left lobe of the liver (L) is lower in density than the right lobe of the liver (R) and the spleen (S). A strikingly sharp boundary (*arrowheads*) separates the left and right lobes. This appearance is characteristic of focal fatty infiltration.

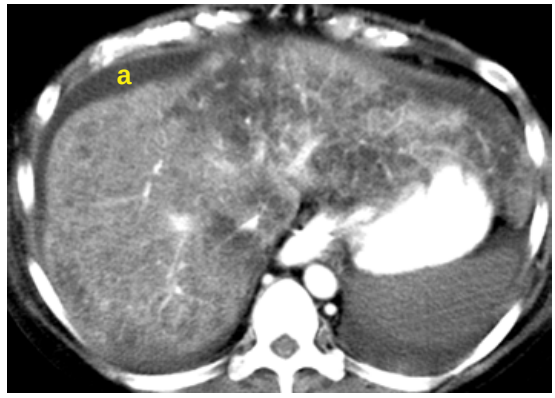

FIGURE 11-7 ■ Multifocal fatty infiltration. Patchy areas of low-attenuation fatty infiltration permeate the liver parenchyma. The intrahepatic blood vessels follow a normal course without a mass effect. Ascites (a) is present.

simulated by islands of fatty infiltration surrounded by normal parenchyma or by islands of normal parenchyma surrounded by fatty infiltration. The pattern tends to be geographic with straight margins rather than rounded masses. Areas of involvement may interdigitate with normal parenchyma.

- In *focal sparing*, islands of normal parenchyma are surrounded by large areas of diffuse fatty infiltration and may simulate neoplasms (Fig. 11-8). As previously mentioned, the focal steatosis pattern and focal sparing are related to chronic perfusion abnormalities such as systemic venous drainage into the liver. Focal sparing is most common in the same areas of the liver most often affected by focal steatosis.

- The following findings are most useful in making a confident diagnosis of fatty infiltration:
  - Angulated geometric margins (nonspherical shape) are present.
  - Interdigitating margins with slender fingers of normal or fatty tissue are evident.
  - Absence of mass effect, vessel displacement, or narrowing by encasement is noted.
  - Rapid change over time. Fatty changes can be seen within 3 weeks after the insult and can resolve within 6 days after removing the insult.
  - Further confirmation of fatty replacement can be provided by other imaging tests. Ultrasonography will show the areas of fatty infiltration as corresponding areas

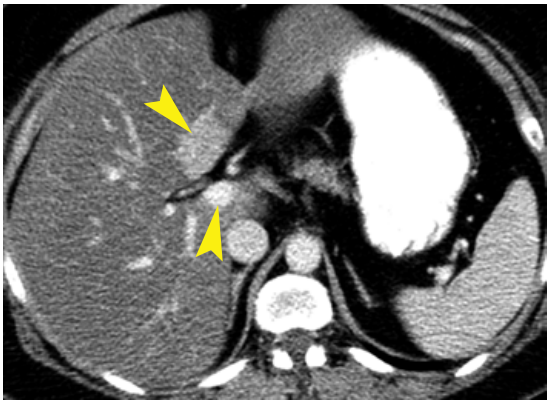

FIGURE 11-8 ■ Focal sparing. Two islands of normal parenchyma (*arrowheads*) in segment IVb and the caudate lobe (segment 1) simulate mass lesions in a liver with extensive fatty infiltration. Most of the liver parenchyma shows fatty infiltration, making these islands of normal parenchyma appear of high attenuation by comparison.

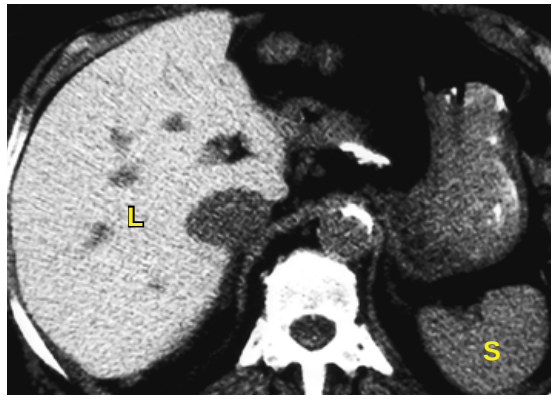

FIGURE 11-9 ■ High-attenuation liver. Noncontrast computed tomography demonstrates markedly high attenuation of the liver (L) compared to the spleen (S) in this patient on chronic amiodarone therapy for cardiac arrhythmias.

of increased parenchymal echogenicity. This gives rise to a "flip-flop" sign: fat is dark on CT and bright on ultrasonography. Chemical shift magnetic resonance with in-phase and out-of-phase images may demonstrate the presence of fat. Percutaneous biopsy is an option in difficult cases.

Increased Liver Attenuation

Normal liver attenuation on unenhanced CT is 55 to 65 HU and is at least 10 HU higher than the attenuation of the spleen. Increased liver attenuation is usually in the range of 75 to 140 HU. Portal and hepatic veins stand out as dark tubular structures against a background of bright liver parenchyma. Causes of increased liver attenuation include the following:

- Iodine: Amiodarone is toxic to the liver and raises its attenuation via deposition of iodine-containing metabolites (Fig. 11-9).
- Gold: Gold therapy may lead to deposition of gold in the liver parenchyma.
- Iron: Hemochromatosis raises liver attenuation via deposition of iron. Primary hemochromatosis is characterized by increased intestinal absorption of iron. Deposition of hemosiderin in hepatocytes and the parenchyma of the pancreas and other organs eventually causes cellular injury and loss of function. In secondary hemochromatosis (also called hemosiderosis), iron overload from multiple blood transfusions is taken up by reticuloendothelial cells in the liver, spleen, and bone marrow. Hemochromatosis commonly progresses to cirrhosis. Magnetic resonance imaging is excellent for confirming the presence of iron excess in the liver.
- Copper: Wilson's disease is associated with increased liver attenuation due to deposition of copper.
- Glycogen: Glycogen storage diseases mildly raise liver attenuation.

Cirrhosis

Cirrhosis is a chronic diffuse liver disease characterized by progressive destruction of the liver parenchyma with distortion of the hepatic architecture by extensive fibrosis and nodular regeneration of liver tissue. The common forms of cirrhosis are Laënnec's cirrhosis caused by alcoholism, postnecrotic cirrhosis related to various types of hepatitis and toxic injury to the liver, and biliary cirrhosis caused by chronic intrahepatic cholestasis. In Western countries, alcohol abuse causes 60% to 70% of cirrhosis cases. Patients with cirrhosis show the following CT findings:

- In the earliest stages of cirrhosis the liver may appear normal on CT.
- Fatty infiltration with hepatomegaly is evidence of active hepatocyte injury.
- Heterogeneous parenchymal attenuation on noncontrast CT is due to patchy fatty infiltration and irregular fibrosis (Fig. 11-10). Contrast enhancement is also heterogeneous and accentuates the diverse appearance of the liver tissue.
- The surface contour of the liver is finely nodular or irregularly lobulated because of areas of parenchymal atrophy and regenerative nodules (Fig. 11-11).
- Atrophy of the right lobe with hypertrophy of the left and caudate lobes is common

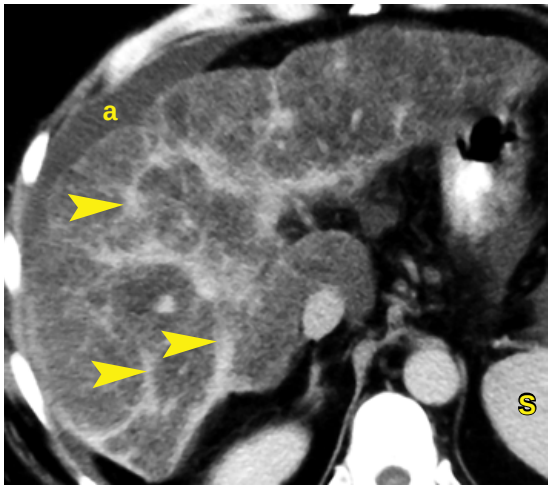

FIGURE 11-10 ■ Advanced cirrhosis with fatty infiltration. Delayed portal venous-phase computed tomography reveals that the liver is misshapen and nodular in contour. Parenchymal density significantly lower than that of the spleen (S) is indicative of fatty infiltration and continuing liver injury. Prominent scars and bands of fibrosis (*arrowheads*) are seen throughout the liver. Ascites (a) is present.

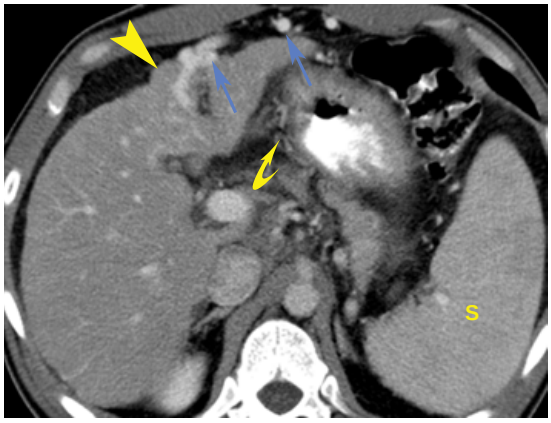

FIGURE 11-11 ■ Cirrhosis with portal hypertension. Postcontrast computed tomography reveals a liver that is nodular in contour (*arrowhead*) with patent enlarged paraumbilical veins (*blue arrows*) and splenomegaly (S), findings indicative of portal hypertension. Mildly enlarged portosystemic collateral vessels (*curved arrow*) are also evident in the gastrohepatic ligament.

and characteristic of alcoholic (Laënnec's) micronodular cirrhosis.

- With progressive cirrhosis the total liver volume decreases, and the liver appears shrunken and deformed (Fig. 11-12).
- The size and prominence of the porta hepatis and intrahepatic fissures increase due to atrophy of adjacent liver tissue.
- Ascites, splenomegaly, and other signs of portal hypertension are commonly present.

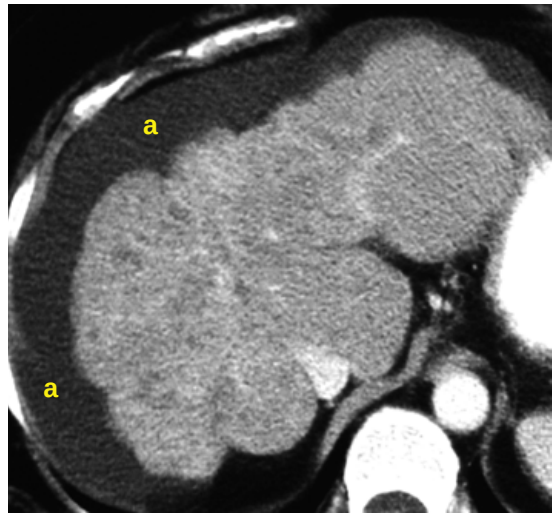

FIGURE 11-12 ■ Advanced cirrhosis. The liver is shrunken with a markedly nodular contour and heterogeneous parenchyma. The hepatic vessels are distorted and poorly visualized. Ascites (a) is present.

- Serous cysts may develop adjacent to intra- and extrahepatic bile ducts. These peribiliary cysts may mimic biliary dilatation when present in a linear configuration. More typically they appear as a row of cysts with thin but visible cyst walls.
- Enlarged lymph nodes (>1 cm) are commonly seen in the porta hepatis and portocaval space in patients with advanced cirrhosis. These are usually benign when associated with the development of cirrhosis and are not indicative of a malignant process.
- Mimics of cirrhosis include the following: treated breast cancer metastases causing retraction of the liver capsule, an irregular liver contour, and heterogeneous parenchymal nodularity; sarcoidosis with noncaseating granulomas causing fine nodularity of the liver surface and parenchymal granularity; miliary metastases causing surface nodularity; and fulminant hepatic failure causing loss of parenchyma with distortion of the liver contour.

Nodules in Cirrhosis

Nodular lesions in cirrhosis may be regenerative nodules, dysplastic nodules, or small HCCs. Regenerative nodules are present in all cirrhotic livers but are visualized on CT in only 25% of cases. They represent a local reparative response to injury, with focal proliferation of hepatocytes and supporting stroma. Dysplastic nodules are premalignant and are nodular collections of hepatocytes that have cellular atypia and

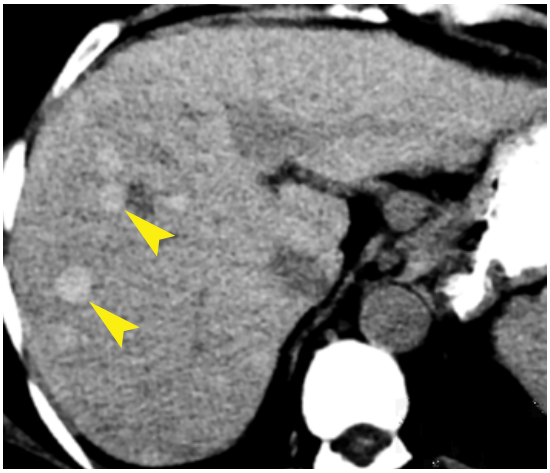

FIGURE 11-13 ■ Siderotic regenerative nodules. Noncontrast computed tomography demonstrates several high-attenuation nodules (*arrowheads*) within a cirrhotic liver. These represent siderotic regenerative nodules with high iron content.

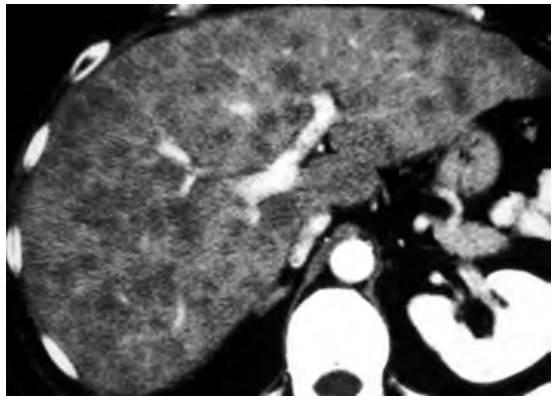

FIGURE 11-14 ■ Regenerative nodules. Portal venous-phase postcontrast computed tomography reveals numerous small (<10 mm), low-attenuation nodules in a cirrhotic liver. This represents unusually prominent visualization of regenerative nodules.

dysplastic features but no frank malignancy. HCCs may develop spontaneously or as a result of progression of focal dysplasia.

- Regenerative nodules are usually not demonstrated on noncontrast CT because they are too small or are isodense with the surrounding tissue. However, they may accumulate iron and show high attenuation on noncontrast CT (Fig. 11-13). These are termed *siderotic nodules*. Siderotic nodules usually disappear on postcontrast CT. Regenerative nodules typically do not enhance on arterial-phase postcontrast CT. On portal venous-phase CT, either regenerative nodules are not seen because of enhancement that is homogeneous with the surrounding tissue, or they appear hypodense because of enhancement that is less than that of the surrounding tissue (Fig. 11-14). Visualized regenerative nodules are typically smaller than 10 mm.
- A unique but very helpful finding is that regenerative nodules often appear larger on portal venous-phase and delayed-phase images than they do on precontrast or arterial-phase CT. This observation is not found for malignant nodules.
- Dysplastic nodules are not often demonstrated on CT. When seen, dysplastic nodules are slightly hypo- or hyperattenuating on non-contrast CT. On post-contrast CT, most dysplastic nodules enhance homogeneously with surrounding liver tissue on both arterial and portal venous phase and are not detectable and show no enhancement on arterial, portal, and equilibrium post-contrast images. Siderotic nodules larger than 10 mm are considered dysplastic. A small number of dysplastic nodules demonstrate homogeneous enhancement on arterial phase, and are isodense with parenchyma on portal venous, equilibrium, and delayed phases. These are distinguishable from HCC only by biopsy.
- Small HCC nodules are hypo- or isointense to the surrounding tissue on noncontrast CT. Hyperintense homogeneous enhancement on arterial-phase CT is the key finding that suggests HCC. The hallmark findings of HCC, considered to be diagnostic without biopsy, are near isointensity on noncontrast CT with hyperenhancement on arterial-phase CT and rapid contrast washout on portal venous-phase CT. Up to 50% of pathologically proven small HCC nodules are not detectable because they are isodense to parenchyma on all phases.
- Diffuse metastatic disease, especially when associated with breast cancer, may mimic cirrhosis with nodules. The patient's medical history usually provides the differentiation. Innumerable small metastases may also be seen with small cell lung carcinoma, melanoma, carcinoid carcinoma, and occasionally pancreatic carcinoma.
- Hemangiomas are rarely seen in cirrhotic livers. The process of parenchymal injury and scarring results in complete fibrosis of most hemangiomas, so they are not detected.
- Hepatic cysts are present at the same frequency as in noncirrhotic livers but are usually easily diagnosed by uniform low attenuation, sharp margination with an imperceptible wall, and lack of contrast enhancement.

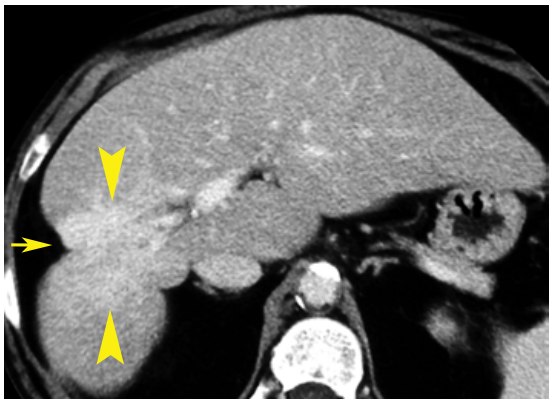

FIGURE 11-15 ■ Confluent fibrosis. Postcontrast axial computed tomography reveals an ill-defined enhancing fibrotic mass (*arrowheads*) extending from the liver periphery toward the porta hepatis and associated marked retraction (*arrow*) of the liver capsule. This is the characteristic appearance of focal confluent fibrosis.

Focal Confluent Fibrosis

Focal confluent fibrosis describes a process of progressive hepatic parenchymal tissue loss with replacement by a fibrotic mass that commonly occurs in cirrhotic livers, especially those related to alcohol abuse.

- The lesion appears as a focal, commonly wedge-shaped, fibrotic mass extending from the porta hepatis to the liver periphery, associated with retraction or flattening of the liver capsule caused by tissue loss (Fig. 11-15). The lesion shows low attenuation on noncontrast CT and delayed but persistent enhancement extending into the equilibrium phase.
- Serial imaging over time shows moderate progression of tissue loss and capsular retraction.

Portal Hypertension

Portal hypertension results from progressive fibrosis of the hepatic vascular bed with the development of portosystemic collateral vessels and eventually hepatofugal flow (i.e., flow away from, instead of into, the liver). Portal hypertension causes major morbidity in the cirrhotic patient because of hepatic encephalopathy and variceal hemorrhage. Portal hypertension can be diagnosed on CT by the presence of the following anatomic signs:

- Portosystemic collateral vessels are enlarged and shunt blood between the portal and systemic veins (Fig. 11-16). Findings include esophageal, paraesophageal, and gastric varices, enlarged paraumbilical veins that connect with enlarged subcutaneous veins around the umbilicus (caput medusae), splenorenal shunts, and perisplenic collaterals. Varices appear as well-defined, round, serpentine structures that enhance homogeneously with contrast during portal venous and delayed phases (Fig. 11-16*B*).
- The portal vein and branches are enlarged (>13 mm) (Fig. 11-16*A*).
- The splenic and superior mesenteric veins are enlarged (>10 mm). With engorgement of the mesenteric veins, the bowel often appears edematous and thick-walled.
- When a splenorenal shunt is present, the left renal vein is enlarged.
- Splenomegaly is usually evident due to splenic congestion.
- Ascites is often present.
- The enlarged collateral vessels characteristic of portal hypertension may be subtle and easily missed or may be mistaken for other structures. A key lesson in radiology is that you see what you look for.

Portal Vein Thrombosis

Thrombosis of the portal vein is found in association with cirrhosis, hepatoma, hypercoagulability, pancreatitis, pancreatic cancer, trauma, or mesenteric inflammation. Portal vein thrombosis can cause or exacerbate portal hypertension. The thrombosis may be partial or complete, and acute or chronic. The thrombus may extend into the splenic and superior mesenteric veins. Signs of portal vein thrombosis include:

- A low-density, nonenhancing, intraluminal thrombus fills, or partially fills, the portal vein (Fig. 11-17).
- The size of the portal vein is often increased (>13 mm).
- If thrombosis is complete, the portal vein does not enhance on postcontrast scans. Failure to visualize the portal vein suggests the diagnosis. If thrombosis is partial, contrast-opacified blood outlines the low-attenuation clot.
- Nonmalignant partial portal-vein thrombosis spontaneously resolves in about half of cases.
- A tumor thrombus within the portal vein may enhance during arterial-phase CT, reflecting blood supply to the tumor within the vein.
- *Cavernous transformation* refers to the development of numerous periportal collateral veins in response to chronic portal-vein thrombosis, usually in patients with cirrhosis. CT reveals a nest of collateral vessels in the porta hepatis.

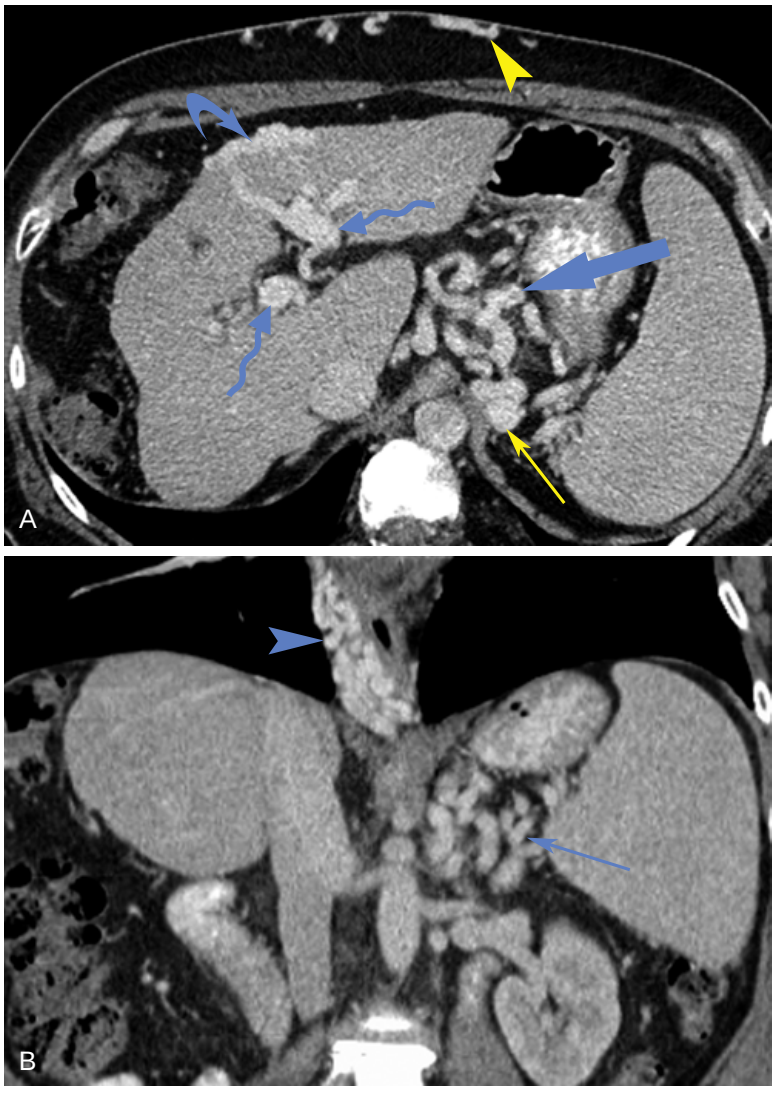

FIGURE 11-16 ■ Portal hypertension. *A,* Axial postcontrast computed tomography (CT) reveals signs of advanced portal hypertension. The right and left portal veins (*blue squiggly arrows*) are enlarged, measuring 15 mm. Dilated and tortuous cardinal veins (*fat straight blue arrow*) are seen in the gastrohepatic ligament and retroperitoneum (*skinny straight yellow arrow*). Paraumbilical collateral veins are patent and dilated, extending through the fissure of the ligamentum teres and falciform ligament (*blue curved arrow*) and as subcutaneous collaterals (*arrowhead*). Visualization of the patent paraumbilical collateral veins is the most specific CT sign of portal hypertension. *B,* Coronal CT image of the same patient reveals dramatic paraesophageal varices (*arrowhead*) and a tangle of retroperitoneal and perigastric collaterals (*arrow*).

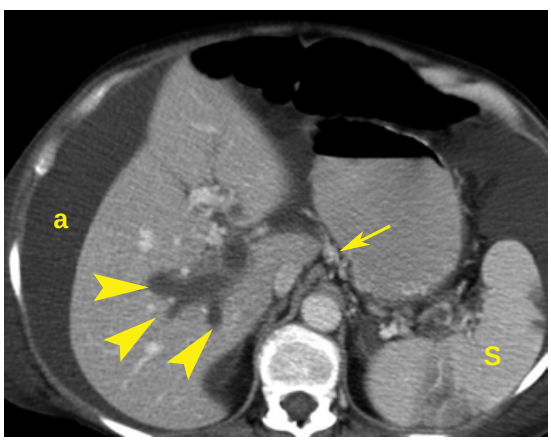

FIGURE 11-17 ■ Portal vein thrombosis. Postcontrast computed tomography shows a low-attenuation thrombus (*arrowheads*) filling and distending the right portal vein and branches. Collaterals have formed in the gastrohepatic ligament (*arrow*). The spleen (S) shows multiple infarctions. The splenic vein (not shown) was also thrombosed. Ascites (a) is present.

- Calcification may be seen within the portal vein when the thrombus is chronic.
- Altered blood flow results in arterial perfusion changes within the liver parenchyma. Where the venous blood flow is decreased, the hepatic arterial blood flow is increased and shows hyperenhancement during arterial-phase CT. Parenchyma with chronic decreased blood flow may atrophy, whereas lesser affected or unaffected parenchyma may show compensatory hypertrophy.

Passive Hepatic Congestion

In the presence of right heart failure, constrictive pericarditis, or pericardial effusion, the volume of returning venous blood exceeds the capacity of the right heart, causing a rise in central venous pressure resulting in dilatation of the IVC and hepatic veins.

Chronic congestion and stasis in the hepatic sinusoids cause ischemic injury to hepatocytes, resulting in fatty infiltration and eventually cirrhosis.

- The hepatic veins and IVC are distended because the failing heart cannot accommodate venous return (Fig. 11-18). Perivascular edema may be present and is seen as low-attenuation zones encircling the portal veins and intrahepatic IVC.
- Contrast media injection into the upper extremities characteristically shows prominent retrograde flow of contrast deep into the hepatic veins. This pathologic finding must be differentiated from bland reflux of contrast into the upper IVC and distal hepatic veins that is sometimes seen with high-volume power injection.
- The hepatic parenchyma may enhance in a mottled mosaic pattern similar to that seen with Budd–Chiari syndrome.
- Cardiomegaly, pleural and pericardial effusions, ascites, and hepatomegaly are frequently present.
- Decreased blood flow, hypoxia, and increased venous pressure lead to diffuse hepatocellular necrosis progressing to cirrhosis. Cardiac cirrhosis may be irreversible even if cardiac function improves.

Budd–Chiari Syndrome

Budd–Chiari syndrome refers to the manifestations of hepatic venous outflow obstruction, which causes elevated pressure in the sinusoids and a decrease in portal venous flow, resulting in severe centrilobular congestion, hepatocellular necrosis, and parenchyma atrophy. Acute thrombosis of the main hepatic veins or IVC is associated with pregnancy, oral contraceptive use, chemotherapy radiation therapy, and polycythemia vera. Neoplastic obstruction of the hepatic veins or IVC occurs with hepatoma and renal cell and adrenal carcinoma. Chronic fibrosis is idiopathic and affects small sublobular and central hepatic veins. Congenital causes include webs or diaphragms that obstruct the IVC. CT findings are variable, depending on the chronicity of the disease.

- In acute Budd–Chiari syndrome (1 to 3 months), the liver is enlarged and shows hypoattenuation, but with normal morphology on noncontrast CT. The IVC and hepatic veins are narrowed. Any thrombus within the veins may show hyperattenuation. After contrast administration, the caudate lobe and liver surrounding the IVC show early arterial enhancement, with decreased enhancement of the liver periphery reflecting sinusoidal congestion. In the portal venous phase, the liver periphery is enhanced while the contrast is washed out of the central liver, resulting in decreased attenuation. This has been termed the "flip-flop" appearance of liver enhancement. The hepatic veins and IVC show low attenuation with enhancement of the vein walls.
- In chronic Budd–Chiari syndrome the caudate lobe is enlarged while the remainder of the liver is dysmorphic, with atrophy and multiple regenerative nodules. The caudate lobe is spared from injury because of its separate hepatic vein drainage. The IVC and hepatic veins are collapsed and usually not visualized. Parenchymal enhancement is inhomogeneous, appearing as a mosaic pattern (Fig. 11-19). Parenchymal nodules of 1 to 4 cm in size show hyperenhancment in the arterial phase that persists into the portal venous phase. Portal hypertension is present and results in splenomegaly and intra- and extrahepatic portosystemic collateral vessels. Characteristic intrahepatic collateral vessels are seen as comma-shaped enhancing vessels. The azygos vein is enlarged and provides an alternate pathway for blood return to the heart.
- Regenerative nodules are prominent and resemble multifocal HCC. The key finding is early washout on the portal venous phase that is characteristic of HCC, while the regenerative nodules in Budd–Chiari syndrome remain relatively hyperdense in the portal venous phase.

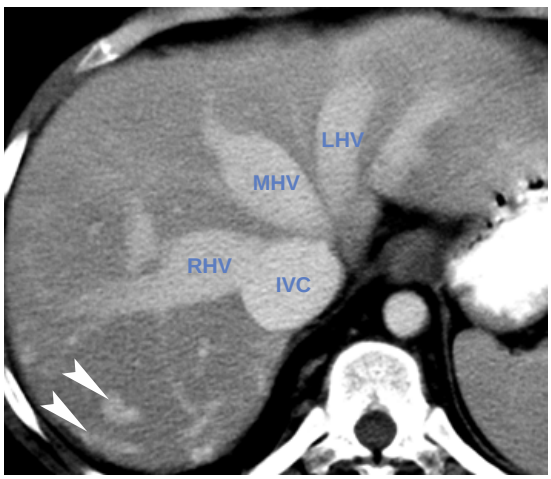

FIGURE 11-18 ■ Passive hepatic congestion. The inferior vena cava (IVC), right hepatic vein (RHV), middle hepatic vein (MHV), and left hepatic vein (LHV) are massively dilated in this patient with chronic right heart failure. Similar in physiology to Budd–Chiari syndrome, the intrahepatic collateral vessels (*arrowheads*) have enlarged and are visualized as enhancing tubular and comma-shaped structures.

Hereditary Hemorrhagic Telangiectasia (HHT)

Also called Osler–Weber–Rendu syndrome, HHT exhibits prominent perfusion abnormalities on CT of the liver. HHT is an autosomal dominant disorder with variable penetrance characterized by multiorgan arteriovenous malformations and telangiectasias (dilated, thin-walled vascular channels). The liver is involved in most cases (~75%). The skin, mucous membranes, lungs, and brain are prominently affected. Patients present in adulthood with hemoptysis, epistaxis, and mucocutaneous telangiectasias. Many patients are asymptomatic when the disease is recognized from imaging findings. CT findings are striking on arterial-phase images (Fig. 11-20).

- Intra- and extrahepatic arteries and the mesenteric arteries are dilated and tortuous.
- Portal and hepatic veins are enlarged and show early contrast opacification reflecting arterioportal (hepatic artery to portal vein), arteriovenous (hepatic artery to hepatic vein), and portovenous (portal vein to hepatic vein) shunting.
- Parenchymal enhancement is strikingly heterogeneous, reflecting shunting, telangiectasias, and vascular masses. Bile ducts may be dilated by vascular compression.
- Telangiectasias appear as hypervascular rounded masses up to 1 cm in size.
- Large, confluent vascular channels (>1 cm) appear as masses showing early and persisting enhancement as contrast pools within the vascular channels.
- Parenchymal perfusion abnormalities and vascular lesions become less conspicuous on portal venous-phase and hepatic-phase images.

FIGURE 11-19 ■ Budd–Chiari syndrome. A portal venous-phase postcontrast image shows a markedly abnormal mottled pattern of liver parenchymal enhancement, with the central liver well enhanced and the peripheral liver poorly enhanced. Venography (not shown) demonstrated occlusion of the intrahepatic inferior vena cava and hepatic veins. The caudate lobe (1) is enlarged.

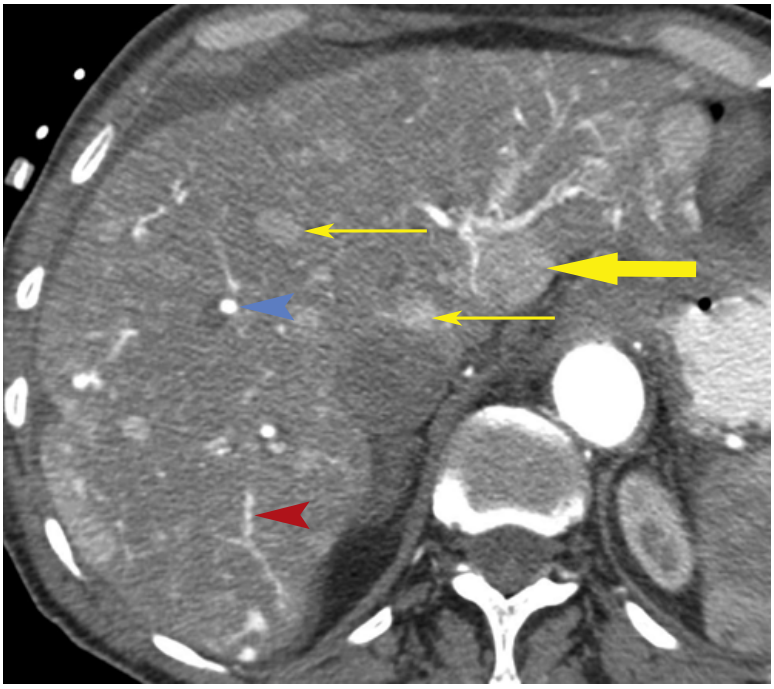

FIGURE 11-20 ■ Hereditary hemorrhagic telangiectasia. Arterial-phase postcontrast computed tomography shows tortuous hepatic arteries (*red arrowhead*), early filling of portal veins (*blue arrowhead*), numerous telangiectasias (*yellow skinny arrows*), and confluent vascular channels (*yellow fat arrow*), findings characteristic of hereditary hemorrhagic telangiectasia.

- The thorax may show cardiomegaly, enlarged pulmonary arteries, and arteriovenous malformations in the lungs. Arteriovenous malformations may also be evident in the pancreas, gastrointestinal tract, and other organs.

Hepatic Sarcoidosis

Sarcoidois is characterized by the presence of noncaseating granulomas scattered diffusely through multiple organs and lymph nodes. The diagnosis is usually made according to the presence of characteristic findings in the chest. The liver is affected pathologically in 94% of cases, although most patients are asymptomatic with respect to their liver disease. About 70% of patients with liver involvement also have spleen involvement.

- The most common CT finding is hepatomegaly.
- Noncontrast CT may reveal innumerable small (<1 mm to 2 cm) hypoattenuating lesions in the liver and spleen. The appearance overlaps that of lymphoma.
- The lesions are hypovascular and show little enhancement during the arterial phase but may become isoattenuating with liver parenchyma on the portal venous phase.
- Diffuse lymphadenopathy is often present (30%) and sometimes massive (nodes >2 cm, 10%).
- A key to differentiating liver sarcoid from lymphoma, metastatic disease, or microabscesses is to note that the patient with sarcoidosis is young, usually black, and generally not clinically ill or symptomatic.

Viral Hepatitis

The various forms of viral hepatitis are the most common cause of liver disease worldwide. Six causative viruses have been identified: A, B, C, E, F, and G. Hepatitis A and B are the most common and are linked to the development of cirrhosis.

- In acute and fulminant viral hepatitis, noncontrast MDCT reveals an enlarged and edematous liver that is heterogeneously low in attenuation.
- On contrast administration the liver parenchyma is irregularly enhanced and remains heterogeneous.
- Fulminant necrosis shrinks the liver volume and shows focal areas of low attenuation.
- Chronic viral hepatitis progresses to hepatic fibrosis, cirrhosis, portal hypertension, ascites, and splenomegaly.

FOCAL LIVER MASSES

Solid Liver Masses

A primary goal of liver imaging is to differentiate significant from insignificant liver masses. Clinically significant liver masses include metastases, hepatocellular carcinoma (hepatoma), and hepatic adenoma. Cavernous hemangioma, hepatic cysts, and FNH are nonsurgical liver masses that must be discriminated.

Metastases

Metastases are the most common malignant tumors in the liver, outnumbering primary malignancy by a ratio of 18 to 1. Metastatic liver disease is a common cause of death in cancer patients. Liver metastases can originate from almost any primary malignancy, but most arise from the gastrointestinal tract, especially the colon. Metastases are usually multiple, but the greatest problems in differentiation occur when they are solitary. A wide spectrum of CT appearance is possible.

- A well-defined, low-density, solid mass with vague peripheral enhancement that produces a target appearance is most common.
- Hypovascular metastases are best seen during the portal venous phase. Metastases from colon cancer are characteristically hypovascular (Fig. 11-21).
- Hypervascular metastases show diffuse enhancement during the arterial phase. The most common hypervascular metastases are from carcinoid carcinoma, choriocarcinoma, melanoma, pancreatic neuroendocrine tumors, pheochromocytoma, renal cell

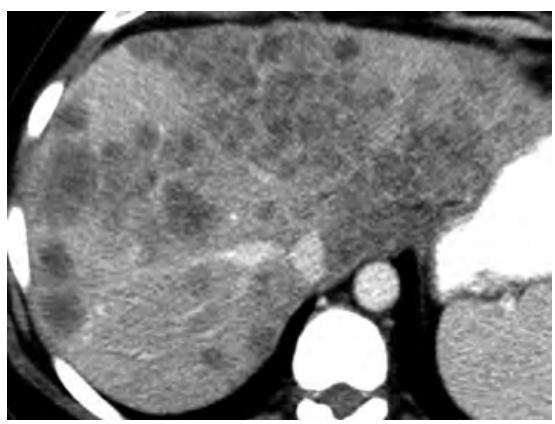

FIGURE 11-21 ■ Metastases. Postcontrast computed tomography shows innumerable ill-defined, low-attenuation nodules throughout the liver. Many nodules show confluent growth. The hepatic vessels are distorted by the mass effect of the metastases from colon carcinoma.

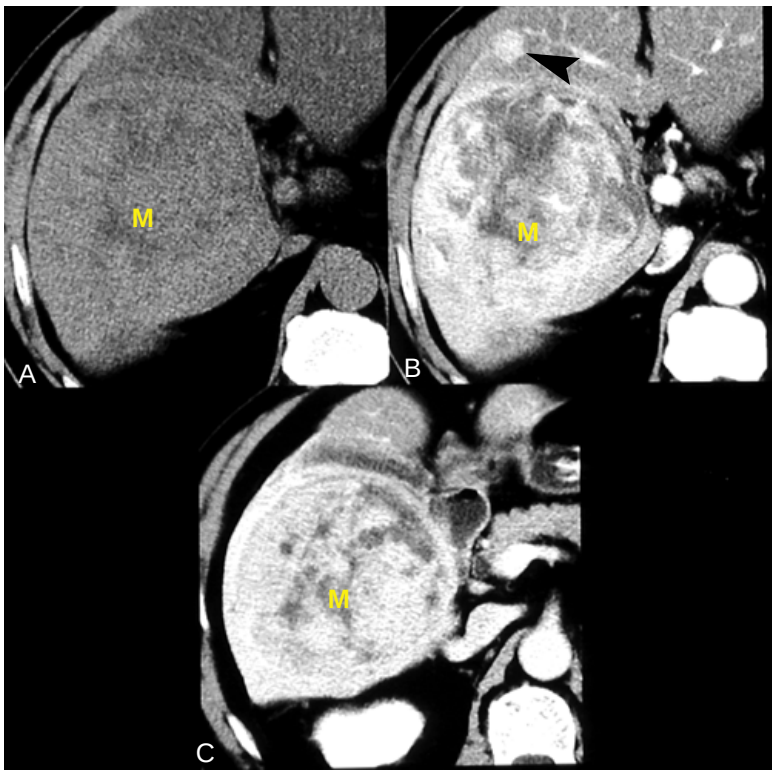

FIGURE 11-22 ■ Hepatocellular carcinoma. *A*, Noncontrast, *B*, arterial-phase, and *C*, portal venous-phase images demonstrate early heterogeneous enhancement of this hepatocellular carcinoma (*M*). The tumor contains areas of hemorrhage and necrosis. A satellite tumor nodule (*black arrowhead*) is seen in the arterial-phase image.

carcinoma, and thyroid carcinoma. About 15% of breast cancer metastases to the liver are hypervascular. If the primary lesion is known to be hypervascular, arterial-phase imaging is required for detection. Hypervascular metastases may not be detectable on portal venous-phase imaging alone.

- Tiny liver nodules that cause perfusion changes in liver parenchyma are likely to be metastases.
- Metastases may appear to be of high density on noncontrast scans, especially when the liver is affected by fatty infiltration.
- Cystic or necrotic tumors are nonenhancing and of low density centrally. Common primaries are mucinous colon and lung carcinoma, melanoma, and carcinoid tumor.
- Metastases may be calcified when the primary neoplasm is mucinous adenocarcinoma, osteosarcoma, or chondrosarcoma.
- Diffusely infiltrating metastases mimic cirrhosis and may not appear as distinct masses.
- In summary, metastases can look like almost every other lesion in the liver and must always be considered a possibility.

Hepatocellular Carcinoma

Hepatoma is the most common primary hepatic malignancy. In Western countries, 80% of HCCs arise in cirrhotic livers. Most patients are older than 50 years. Elevated serum alpha-fetoprotein is a common clinical clue to the diagnosis. Chronic hepatitis B and C are major risk factors for the development of HCC. About 12% of patients with chronic hepatitis develop HCC. HCC occurs in 3% to 6% of patients with other causes for cirrhosis. Detection of HCC on CT is limited by the extensive abnormalities seen with cirrhosis. As many as 40% of all HCCs in cirrhotic livers are missed by CT.

- Three patterns of tumor growth are seen: solitary tumors (50%), diffuse infiltrative tumors (30%), and multinodular tumors (20%). Particularly characteristic is a dominant mass surrounded by satellite lesions.
- Arterial hypervascularity varies with the grade of malignancy and tumor size (Fig. 11-22).
- HCC larger than 2 cm typically shows avid contrast enhancement in the arterial phase with washout in the portal venous or equilibrium phase (Fig. 11-23). CT sensitivity for lesions of this size is 65% according to studies of cirrhotic livers removed for transplantation.
- Small (<2 cm), high-grade tumors typically demonstrate bright homogeneous enhancement on arterial-phase postcontrast images with characteristic washout in the portal

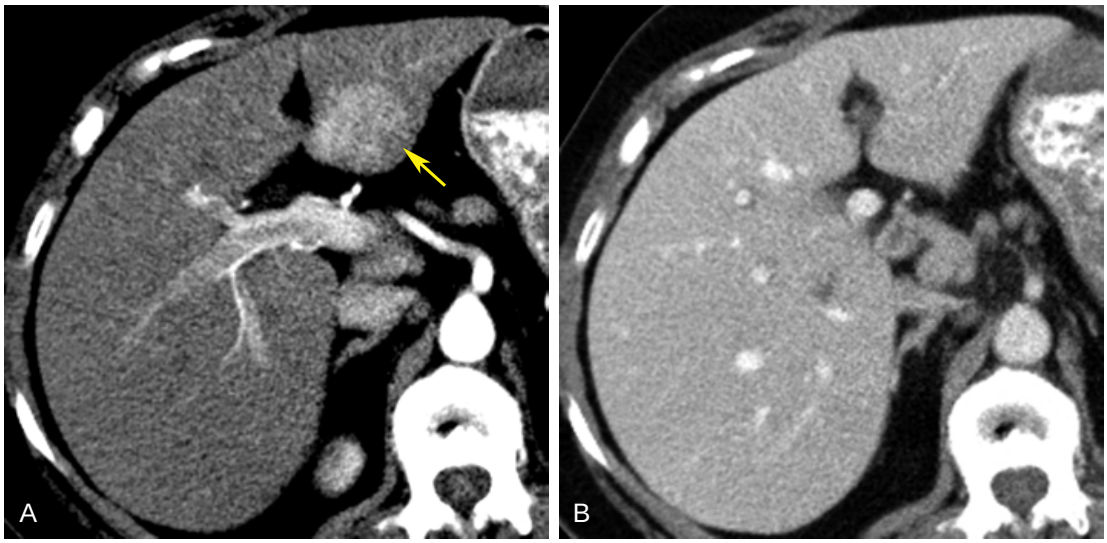

FIGURE 11-23 ■ Hepatocellular carcinoma. *A,* Arterial phase image from a computed tomography examination performed on a patient with chronic hepatitis C shows an avidly enhancing mass (*arrow*) in segment II. *B,* Portal venous-phase image in the same location shows no evidence of the mass. Avid arterial-phase enhancement with rapid washout in the portal venous phase is characteristic of hepatocellular carcinoma.

venous phase. This finding is the hallmark for detection of small HCC and is considered diagnostic without biopsy. However, CT sensitivity is low at 40% to 44%. False-positive nodules with these enhancement characteristics are usually dysplastic nodules (85%).

- Small (<2 cm), low-grade tumors show typical enhancement (arterial-phase hyperenhancement with portal venous-phase washout) on CT in only about 12% of cases. Small nodules that show no arterial-phase enhancement and remain low in attenuation on in portal venous and equilibrium phases are usually considered to be regenerative or dysplastic nodules. However, because some (up to 8% in some studies) prove to be low-grade HCC, follow-up to monitor growth or morphologic change is recommended. Transformation to malignancy is suggested by the development of a focus of arterial hyperenhancement within a hypoattenuating nodule ("nodule-in-nodule" appearance).
- Well-differentiated HCC may best be visualized on portal venous-phase CT scans.
- Areas of tumor necrosis are common, and calcification is present in 25% of cases. A prominent fibrous capsule that is low in attenuation on noncontrast CT and enhances on portal venous-phase and delayed-phase images is uncommon but characteristic.
- Tumor invasion of the hepatic and portal veins is frequent (Fig. 11-24). A liver tumor seen in association with portal vein thrombosis is very likely to be HCC, although peripheral cholangiocarcinomas may also invade the portal vein.
- Fat deposition may occur within HCC. Small, well-differentiated HCC may show diffuse fatty changes that lower the attenuation of the nodule on noncontrast CT. Larger tumors tend to show patchy focal fatty metamorphosis.
- Extrahepatic spread of HCC is most common to the lungs, abdominal lymph nodes, bones, and adrenal glands. Direct invasion by tumor may involve the diaphragm.

FIGURE 11-24 ■ Hepatocellular carcinoma invading the portal vein. Portal venous-phase postcontrast computed tomography shows a large, heterogeneous tumor (M) replacing the right hepatic lobe with a tumor thrombus (*arrowhead*) extending into the portal vein.

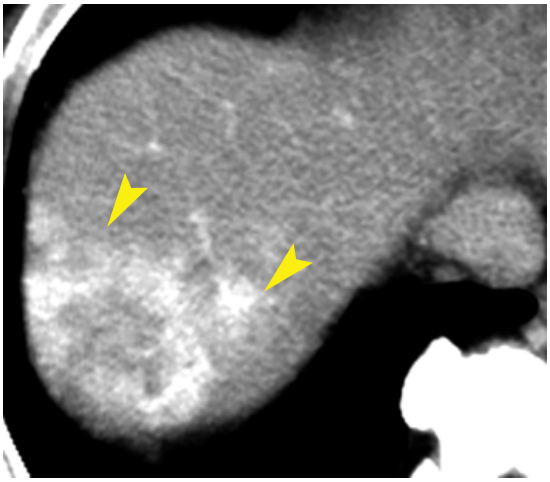

FIGURE 11-25 ■ Cholangiocarcinoma. Arterial-phase computed tomography shows a poorly defined hyperenhancing mass (*arrowheads*) in the right dome of the liver. Pathology confirmed cholangiocarcinoma. The imaging appearance of this mass is indistinguishable from hepatocellular carcinoma.

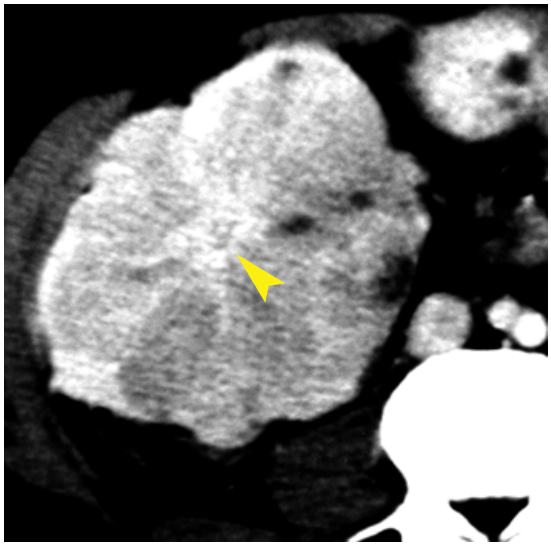

FIGURE 11-26 ■ Fibrolamellar carcinoma. A portal venous-phase image shows a fibrolamellar carcinoma in a 37-year-old man, replacing most of the right lobe of the liver. An enhancing central scar (*arrowhead*) with enhancing radiating fibrous bands is faintly visualized.

Peripheral Mass-Forming Cholangiocarcinoma

Peripheral intrahepatic cholangiocarcinoma is the second most common primary malignant tumor after HCC. Therefore, it should be considered along with HCC in the differential diagnosis of focal solid tumors of the liver. It is an adenocarcinoma arising from the epithelium of the peripheral bile ducts. Cholangiocarcinoma represents 10% to 20% of all primary malignant liver tumors.

- Tumors appear as solid mass lesions with sharply rounded, lobulated, or ill-defined margins. Capsular retraction may be present.
- Dilatation of bile ducts peripheral to the mass favors cholangiocarcinoma over HCC.
- Both cholangiocarcinoma and HCC may invade the portal vein.
- Most tumors are of low attenuation on noncontrast scans. Some are isoattenuating.
- On arterial-phase CT, most tumors remain hypodense. A few show hyperenhancement (Fig. 11-25). On portal venous-phase CT, all tumors become hypointense (>96%) or isointense. Enhancement may be heterogeneous (60%) or homogeneous. Peripheral ring-like enhancement may be seen for larger tumors (>3 cm). This ring-like enhancement tends to wash out and be replaced by progressive central enhancement on delayed images (74%). This marked delay in homogeneous enhancement is most characteristic of cholangiocarcinoma.

Fibrolamellar Carcinoma

Fibrolamellar carcinoma is a rare entity distinct from HCC. This is a slow-growing tumor that usually arises in normal liver. Patients are younger than most HCC patients (usually <40 years), and there is no elevation of serum alpha-fetoprotein. The prognosis is good if the tumor is completely resected.

- A large hepatic mass (often >12 cm) within a normal liver in a young adult or adolescent is characteristic.
- Noncontrast CT reveals a large, low-attenuation, lobulated mass with well-defined margins.
- On postcontrast scans the lesion is prominently and heterogeneously enhanced during both arterial and portal venous phases. The enhancement becomes more homogeneous and remains evident on delayed scans.
- Fibrous tissue extends through the mass, separating the tumor into islands and commonly coalescing into a central scar (Fig. 11-26). The scar is visible on CT in up to 60% of cases. The scar is best seen on delayed scans and may be calcified (33% to 55%). Typically, enhancement of the scar is not present in arterial and portal venous phases but may be evident on delayed scans.
- Cirrhosis, vascular invasion, and multifocal disease, which are common for HCC, are rare in fibrolamellar carcinoma.

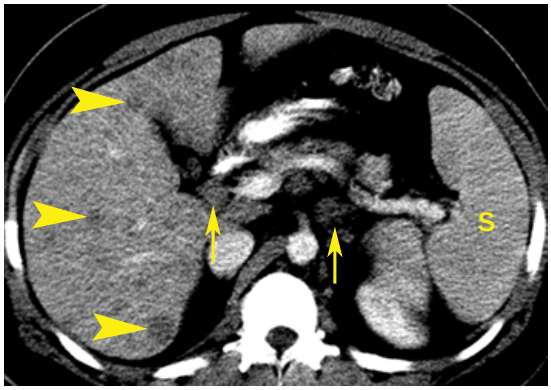

FIGURE 11-27 ■ Secondary hepatic lymphoma. A late portal venous-phase computed tomography image reveals multiple subtle, low-attenuation nodules in the liver in this patient with non-Hodgkin's lymphoma. Numerous enlarged lymph nodes (*arrows*) are visualized, and the spleen (S) is enlarged.

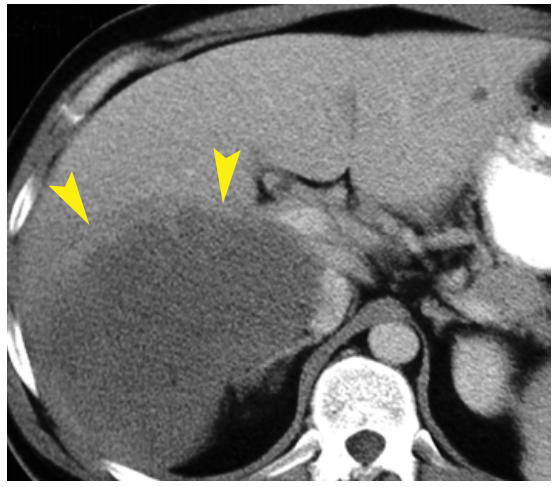

FIGURE 11-28 ■ Primary hepatic lymphoma. Portal venous-phase computed tomography reveals a large, homogeneous, poorly enhancing mass (*arrowheads*) largely replacing the right lobe. Chest–abdomen–pelvis CT showed no additional evidence of lymphoma. A biopsy confirmed primary hepatic lymphoma.

- Fibrolamellar carcinoma may be difficult to differentiate from FNH. Heterogeneous enhancement of the tumor with delayed enhancement of the central scar is a feature that differentiates fibrolamellar carcinoma from FNH.
- Enlarged lymph nodes are present near the porta hepatis in 50% of cases.

Lymphoma

Secondary lymphoma involves the liver in more than half of all patients with both Hodgkin's and non-Hodgkin's lymphoma; however, CT detection of involvement is uncommon. Secondary lymphoma is diffuse or multiple, whereas rare primary liver lymphoma is usually solitary.

- Diffuse infiltration may cause only hepatomegaly without altering the parenchymal density.
- Multiple, well-defined, large, homogeneous, low-attenuation nodules are the most characteristic of secondary lymphoma, especially Hodgkin's lymphoma (Fig. 11-27). Lesions may show a target appearance with enhancement.
- The spleen is also usually involved, and abdominal adenopathy is usually present with secondary lymphoma.
- Primary liver lymphoma presents as a solitary, large, multilobulated mass (Fig. 11-28). Enhancement is usually weak.

Hepatic Adenoma

Hepatocellular adenoma is a rare benign tumor seen most often in young women (90%) who use oral contraceptives, men who take anabolic steroids, and patients with type 1 glyocogen storage disease. It is a significant lesion because of the risk of major hemorrhage associated with its presence. Hepatic adenomas are composed of neoplastic well-differentiated hepatocytes and are lacking in bile ducts and portal triads. Kupffer cells are occasionally present but are nonfunctional. Most patients are asymptomatic and have normal results for liver function tests. Surgical removal is often recommended because of the risk of rupture and malignant transformation. The imaging findings are as follows:

- On unenhanced CT, many adenomas, consisting of well-differentiated hepatocytes, are isoattenuating to normal liver parenchyma.
- However, in some tumors the hepatocytes become filled with fat and the lesion approaches the density of fat. The lipid content of adenomas tends to be more diffuse, whereas that in larger HCCs tends to be focal and patchy. Patients typically do not have cirrhosis or viral hepatitis, and alpha-fetoprotein levels are not elevated.
- Hemorrhage may be most apparent on noncontrast scans. Fresh hemorrhages are of high attenuation, whereas old hemorrhages appear as heterogeneously low in attenuation. Intratumoral hemorrhage is common and is seen in 25% to 40% of adenomas.
- Calcification is seen in 10% of tumors.
- Arterial-phase postcontrast scans show early homogeneous enhancement (Fig. 11-29). The contrast washes out relatively rapidly, and the tumors become near-isodense with

liver parenchyma on portal venous-phase and delayed-phase postcontrast scans.
- Because Kupffer cells are few in number and dysfunctional, uptake of technetium-99m sulfur colloid is absent within the tumor on radionuclide scans.
- Tumors are solitary in 70% to 80% of cases. Lesions vary in size from 1 to 15 cm.
- Multiple tumors are seen in patients with type 1 glycogen storage disease and hepatic adenomatosis (Fig. 11-29). *Hepatic adenomatosis* is defined as having 10 or more adenomas in the liver. Adenomatosis occurs with equal frequency in men and women.
- Tumors lack the central scar that is often present in FNH.

Focal Nodular Hyperplasia

In contrast to hepatic adenoma, FNH contains all the histologic elements of normal liver, including Kupffer cells. It is the second most common benign liver tumor after cavernous hemangioma. Fibrous bands and central stellate fibrous scars are characteristic. Hemorrhage and necrosis are rare. Most patients are asymptomatic, and the tumor is discovered incidentally. Because the tumor is benign and without malignant potential or risk of rupture, no treatment is indicated. FNH is now considered a response of liver parenchyma to a preexisting vascular malformation such as an arteriovenous malformation or telangiectasia.

- Typically, FNH is discovered incidentally as an asymptomatic solitary solid mass lesion in a young woman.
- On unenhanced CT, lesions are isodense or very slightly hypodense to normal liver parenchyma. The central scar may be hypodense (20%) or invisible (80%).
- The hallmark finding of immediate, intense, homogeneous enhancement is seen on arterial-phase postcontrast CT. The central scar may remain hypodense (Fig. 11-30). Large feeding arteries may be evident.
- On the portal venous phase, the lesion becomes nearly isodense with enhanced parenchyma. Large draining veins result in rapid washout of the contrast agent.
- On delayed-phase postcontrast images, the lesion is usually isodense to parenchyma but the central scar may show enhancement.
- Normal (40%) or increased (10%) radionuclide uptake within the tumor on technetium-99m-labeled sulfur colloid scan is the most specific finding. However, 50% of lesions show up as a nonspecific cold defect.
- Lesions are solitary (80% to 95%) and are usually smaller than 5 cm.

Cavernous Hemangioma

Cavernous hemangioma is the second most common focal mass lesion in the liver, exceeded in frequency only by metastases. It is the most common benign liver neoplasm, found in up to 7% of

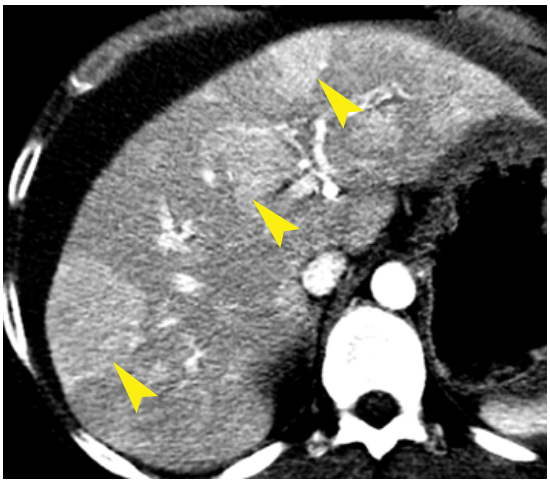

FIGURE 11-29 ■ Multiple hepatic adenomas. An arterial-phase image shows homogeneous enhancement of multiple hepatic adenomas (*arrowheads*) in this woman with hepatic adenomatosis. Ascites is present due to associated impaired liver function.

FIGURE 11-30 ■ Focal nodular hyperplasia. A brightly enhancing mass (*yellow arrow*) in the posterior segment of the right hepatic lobe has a characteristic central low-attenuation scar (*yellow arrowhead*). A large draining vein (*blue arrow*) is evidence of the hypervascular nature of the mass.

individuals. Cavernous hemangiomas are often discovered incidentally during hepatic imaging by ultrasonography or CT. They may be found at any age and are more common in women. Although most are solitary, 10% of affected patients have multiple lesions that may be mistaken for metastases. The tumors consist of large, thin-walled, blood-filled vascular spaces lined by epithelium and separated by fibrous septa. Blood flow through the complex of vascular spaces is very slow, resulting in characteristic prolonged retention of contrast agents on CT. Most lesions are less than 5 cm in size, are asymptomatic, and pose no threat to the patient. The lesions carry no risk of malignant transformation. Larger giant cavernous hemangiomas (20 cm and larger) may cause symptoms due to a pressure effect, hemorrhage, or arteriovenous shunting. About 90% of lesions show classic features on CT.

- On unenhanced CT, a hemangioma appears as a well-defined hypodense mass of the same attenuation as other blood-filled spaces, such as the IVC and portal vein. Isoattentuation with blood vessels is an important diagnostic finding.
- Postcontrast arterial-phase images show early, peripheral, discontinuous nodules of contrast enhancement equal in density to that of the aorta (Fig. 11-31).
- Venous-phase images show progressive fill-in enhancement from the periphery, with the lesion eventually becoming uniformly enhanced.
- Delayed images show prolonged enhancement due to the characteristic slow washout of contrast agent.
- Contrast enhancement usually persists within the lesion for 20 to 30 minutes after contrast injection.
- Because blood flow is slow through the lesion, thrombosis may occur, leading to irregular areas of fibrosis that remain unenhanced through postcontrast CT phases. Occasionally these fibrotic portions of the lesion may show particulate or dense calcification.
- Small hemangiomas, especially those <1 cm, may show immediate homogeneous enhancement during the arterial phase, mimicking HCC and hypervascular metastases. Differentiation is made by observing the slow washout and persistent enhancement during portal venous and delayed phases that is characteristic of hemangioma but not of other hypervascular tumors.
- Most hemangiomas remain stable in size over time.

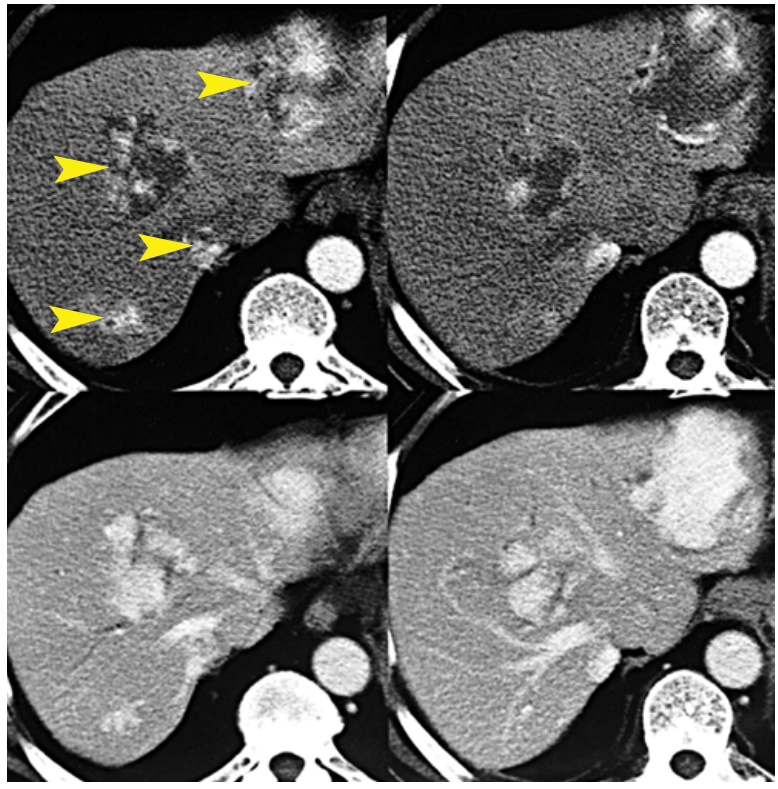

FIGURE 11-31 ■ Cavernous hemangioma. Arterial-phase (top row) and portal venous-phase (bottom row) images demonstrate the characteristic enhancement pattern for multiple cavernous hemangiomas (*arrowheads*). Early contrast medium enhancement appears nodular and at the periphery. Enhancement proceeds centrally to complete opacification, except for areas of fibrous scarring in large lesions.

- When classic findings are observed, the CT examination can be considered diagnostic of cavernous hemangioma with a high degree of confidence. In questionable cases, tagged red blood cell scintigraphy is usually diagnostic.
- Hemangioma is rarely seen in cirrhotic livers. This soft lesion is obliterated by progressive fibrosis.

Cystic Liver Masses

Hepatic Cysts

Simple benign hepatic cysts are unilocular cysts lined by a single thin layer of cuboidal bile-duct epithelium. They are found in up to 20% of the population, most commonly in older patients aged 40 to 70 years. They cause no symptoms and are usually discovered incidentally. They have no malignant potential but must be differentiated from significant lesions. Multiple tiny cysts may mimic early metastases.

- On unenhanced CT, cysts are well defined and of low density with internal attenuation of water (< 20 HU). The cyst wall is not perceptible (Fig. 11-32). Cyst size ranges from a few millimeters to several centimeters. The cysts may be solitary or multiple.
- No enhancement is seen in any phase of postcontrast CT.

FIGURE 11-32 ■ Multiple simple hepatic cysts. Simple hepatic cysts have uniform low internal density and sharp margins with the surrounding hepatic parenchyma. No cyst walls are evident. Intravenous contrast medium does not enhance the lesions.

- Very tiny cysts may not show the low attenuation of water because of volume averaging. A confident diagnosis of a benign cyst can be made by noting uniform low attenuation, sharply defined borders, and stability over time.

Biliary Cystadenomas

Biliary cystadenomas are uncommon cystic neoplasms that arise from mucin-secreting columnar epithelium similar to cystadenomas of the pancreas and ovary. They occur predominantly in middle-aged women and have the potential to develop into cystadenocarcinomas.

- Lesions appear as a complex cystic mass ranging in size from 3 to 40 cm. The lesions have a well-defined, thick fibrous capsule, and most have internal septations. The attenuation of the internal fluid is usually of water density but may be higher if internal hemorrhage has occurred. Calcification may occur in the cyst wall and septa.
- The septa and cyst wall exhibit contrast enhancement.
- Enhancing tumor nodules and papillary projections may be seen in both cystadenomas and cystadenocarcinomas, which cannot be differentiated by imaging. Because of the risk of malignancy, surgical removal is often considered.

Biliary Hamartomas

Biliary hamartomas (von Meyenburg complexes) are multiple small, predominantly cystic lesions that occur throughout the liver and result from failure of involution of embryologic bile ducts. They are considered benign, are asymptomatic, and do not require treatment. However, a few isolated case reports indicate possible degeneration into cholangiocarcinoma.

- Biliary hamartomas are small (<15 mm), often innumerable, hypoattenuating lesions scattered throughout the liver. Lesions may be cystic, solid, or mixed. No communication with the biliary tree is present. Lesions may appear more prominent and numerous on magnetic resonance imaging than on CT.
- Purely cystic lesions show no contrast enhancement. Solid and mixed lesions do enhance to become isodense with hepatic parenchyma on portal venous-phase CT.

Polycystic Liver Disease

Polycystic liver disease occurs in association with autosomal dominant polycystic kidney disease

(70% of cases) or as genetically distinct autosomal dominant polycystic liver disease without renal involvement. Most patients are asymptomatic. Despite massive replacement of the liver parenchyma by cysts, most patients retain normal liver function. Complications are uncommon but include massive hepatomegaly, abdominal pain, intracystic hemorrhage and infection, and portal hypertension. Two types of cysts may be identified:

- Most cysts are peripheral and resemble simple cysts in appearance, with thin walls and internal fluid contents of water attenuation (Fig. 11-33). These cysts are numerous and replace and displace the hepatic parenchyma. They may be large, exceeding 8 cm in diameter.
- Peribiliary cysts are smaller (<1 cm) and multiple, appearing as a string of multiple cysts that parallels the course of the portal triads.
- Infected or hemorrhagic cysts show increased attenuation of the internal fluid, fluid–fluid levels, thickened walls with enhancement, and, rarely, intracystic gas bubbles. Old infected or hemorrhagic cysts may have calcification in the cyst wall.

Pyogenic Abscess

Bacterial hepatic abscess is a localized collection of pus and debris within an area of destroyed parenchyma. Bacterial seeding occurs via the portal vein, hepatic artery, or biliary tree, by direct extension from bowel infection (appendicitis, diverticulitis), or as a result of trauma. Approximately 85% of liver abscesses in the United States are pyogenic, most of which are caused by *Escherichia coli*. Patients are usually clinically septic and are often jaundiced.

- Bacterial abscess is usually solitary but is often multiloculated, with thickened, enhancing walls. The internal fluid measures 0 to 45 HU. When multiple, lesions are often grouped and consist of many microabscesses. Masses are hypodense with a peripheral rim that usually enhances with contrast medium.
- Gas is present within the lesion in 20% of cases (Fig. 11-34).
- Fine-needle aspiration is indicated for bacterial culture. Catheter or surgical aspiration and drainage are needed.
- Biliary obstruction is the most common associated finding.

Amebic Abscess

Amebic abscess occurs in 3% to 7% of patients with amebiasis (*Entamoeba histolytica*). Amebic abscesses account for 6% of liver abscesses in the United States. Amebic serology is positive in 95% of cases. Patients present as acutely ill with a high fever and right upper-quadrant pain. Amebic abscesses are most common in Africa, East Asia, India, South America, and Mexico. Patients with the disease in the United States often have a history of recent travel to these areas.

- The abscess (Fig. 11-35) is usually solitary (85%) and in the right lobe (72%).
- The wall is well defined, thickened (3 to 15 mm), and sometimes nodular, and is enhanced on contrast administration. The liver parenchyma adjacent to the wall of the

FIGURE 11-33 ■ Polycystic liver disease. Noncontrast computed tomography of the liver in a patient with autosomal dominant polycystic kidney disease shows innumerable small hepatic cysts.

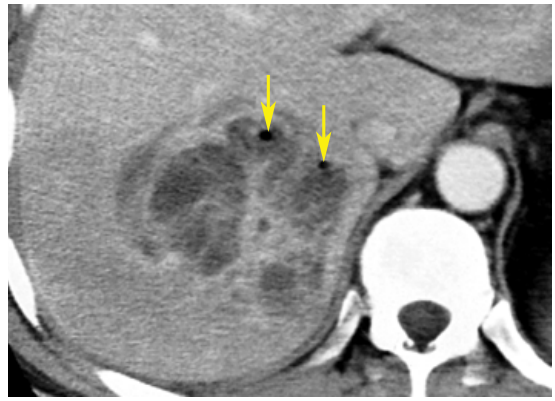

FIGURE 11-34 ■ Pyogenic liver abscess. A liver abscess containing *Escherichia coli* has irregular septations and contains a few bubbles of air (*arrows*). Because of the multiple loculations, this abscess did not respond to a percutaneous catheter for drainage and required surgical debridement.

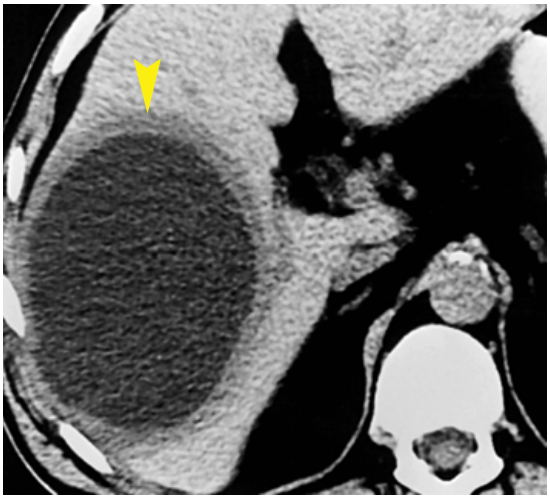

FIGURE 11-35 ■ Amebic abscess. An American living in Thailand returned to the United States with this mass in his liver. Although the internal density is homogeneously low, a distinct thick wall (*arrowhead*) is present and was enhanced on intravenous administration of contrast medium. Serologic titers were positive for amebiasis.

abscess is also commonly enhanced, which leads to a double-rim target appearance. The cavity may show fluid–debris levels, hemorrhage, gas bubbles, and multiple septa.

- Right pleural effusion and right lower-lobe infiltration are often present. The abscess may rupture through the diaphragm, resulting in empyema.

Hydatid Cyst

Hydatid disease is produced by the larval stage of the tapeworm *Echinococcus granulosis*. The liver is the most common site of disease. The disease is not endemic in the United States, so cases are seen in immigrants and travelers to endemic areas, primarily sheep grazing areas in South America, Australia, New Zealand, Africa, the Middle East, and the Mediterranean. The disease is acquired from contaminated food. Most patients have eosinophilia. Serology is positive in only 25% of patients.

- The appearance of a hydatid cyst (Fig. 11-36) depends on its stage of growth. The cyst

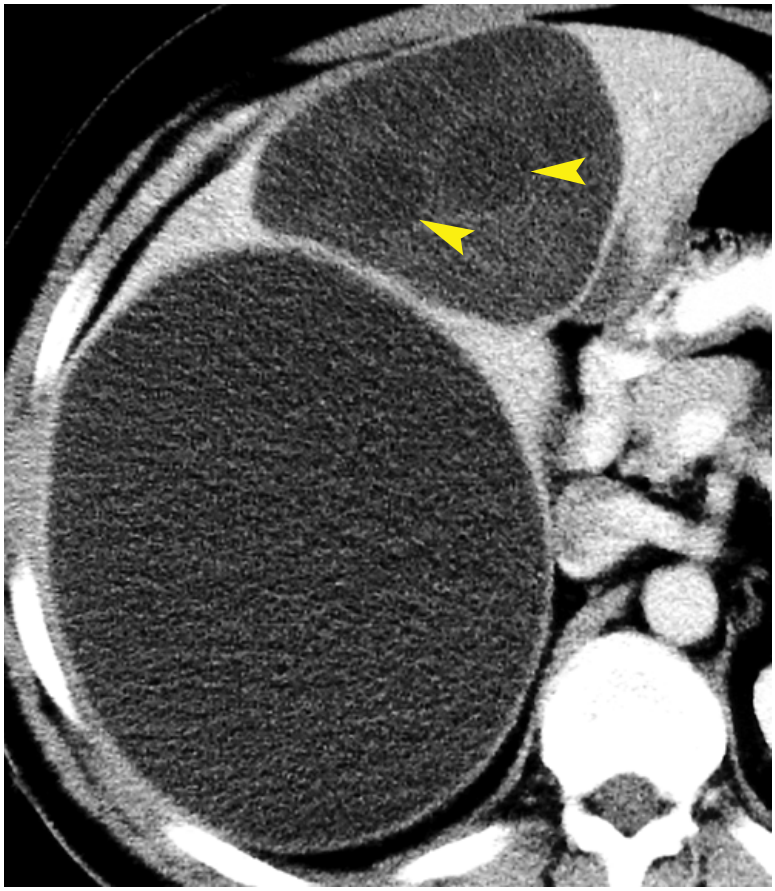

FIGURE 11-36 ■ Hydatid cysts. Two hydatid cysts are seen in the right lobe of the liver. Two daughter cysts (*arrowheads*) are faintly visualized. Ultrasound confirmed the presence of the daughter cysts and revealed thin internal membranes and hydatid sand.

may be unilocular, may contain daughter cysts, or may be completely calcified (dead).
- The cyst wall is usually of high attenuation and is commonly calcified (50%). The attenuation of the internal fluid is usually close to that of water. Layering debris (hydatid sand) is commonly present within the cysts. Detached floating membranes are sometimes evident.
- Daughter cysts present a cyst-within-a-cyst appearance. The daughter cysts may be separated by a hydatid matrix that produces a spoke-wheel appearance.

Fungal Infection: Hepatic Candidiasis

Fungal infection, most commonly with *Candida albicans*, usually occurs only in immune-compromised patients. Infection is spread hematogenously via the portal venous system from the intestinal tract. Complications include cholangitis and rupture of microabscesses.

- CT reveals innumerable hypoattenuating hypovascular lesions (2 to 20 mm in size) throughout the liver. Peripheral ring enhancement may occur, but the lesion does not enhance centrally.
- Similar lesions are commonly present in the spleen and kidneys.
- With healing the lesions may calcify.

SUGGESTED READING

Anderson SW, Kruskal JB, Kane RA: Benign hepatic tumors and pseudotumors. *Radiographics* 29:211–229, 2009.

Assy N, Djibre A, Farah R, et al.: Presence of coronary plaques in patients with nonalcoholic fatty liver disease. *Radiology* 254:393–400, 2010.

Boll DT, Merkle EM: Diffuse liver disease: Strategies for hepatic CT and MR imaging. *Radiographics* 29:1591–1614, 2009.

Boyce CJ, Pickhardt PJ, Kim DH, et al.: Hepatic steatosis (fatty liver disease) in asymptomatic adults identified by unenhanced low-dose CT. *AJR Am J Roentgenol* 194:623–628, 2010.

Brancatelli G, Baron RL, Federle MP, et al.: Focal confluent fibrosis in cirrhotic liver: Natural history studied with serial CT. *AJR Am J Roentgenol* 192:1341–1347, 2009.

Chung J-J, Yu JS, Kim JH, et al.: Nonhypervascular hypoattenuating nodules depicted on either portal or equilibrium phase multiphasic CT images in the cirrhotic liver. *AJR Am J Roentgenol* 191:207–214, 2008.

Colagrande S, Centi N, La Villa G, Villari N: Transient hepatic attenuation differences. *AJR Am J Roentgenol* 183:459–464, 2004.

Fasel JHD, Selle D, Evertsz CJG, et al.: Segmental anatomy of the liver: Poor correlation with CT. *Radiology* 206:151–156, 1998.

Ferral H, Behrens G, Lopera J: Budd–Chiari syndrome. *AJR Am J Roentgenol* 199:737–745, 2012.

Furuta T, Maeda E, Akai H, et al.: Hepatic segments and vasculature: Projecting CT anatomy onto angiograms. *Radiographics*, 29:e37, 2009, 10.1148/rg.e37.

Gore RM, Newmark GM, Thakrar KH, et al.: Hepatic incidentalomas. *Radiol Clin N Am* 49:291–322, 2011.

Hamer OW, Aguirre DA, Casola G, et al.: Fatty liver: Imaging patterns and pitfalls. *Radiographics* 26:1637–1653, 2006.

Hussain SM, Terkivatan T, Zondervan PE, et al.: Focal nodular hyperplasia: Findings at state-of-the-art MR imaging, US, CT, and pathologic analysis. *Radiographics* 24:3–19, 2004.

Jaskolka J, Wu L, Chan RP, Faughnan ME: Imaging of hereditary hemorrhagic telangiectasia. *AJR Am J Roentgenol* 183:307–314, 2004.

Jha P, Poder L, Wang ZJ, et al.: Radiologic mimics of cirrhosis. *AJR Am J Roentgenol* 194:993–999, 2010.

Kim SJ, Lee JM, Han JK, et al.: Peripheral mass-forming cholangiocarcinoma in cirrhotic liver. *AJR Am J Roentgenol* 189:1428–1434, 2007.

Lall CG, Aisen AM, Bansal N, Sandrasegaran K: Nonalcoholic fatty liver disease. *AJR Am J Roentgenol* 190:993–1002, 2008.

Lawrence DA, Oliva IB, Isreal GM: Detection of hepatic steatosis on contrast-enhanced CT images: Diagnostic accuracy of identification of areas of presumed focal fatty sparing. *AJR Am J Roentgenol* 199:44–47, 2012.

Morgan DE, Lockhart ME, Canon CL, et al.: Polycystic liver disease: multimodality imaging for complications and transplant evaluation. *Radiographics* 26:1655–1668, 2006.

Mortele KJ, Segatto E, Ros PR: The infected liver: Radiologic–pathologic correlation. *Radiographics* 24:937–955, 2004.

Prabhaker HB, Rabinowitz CB, Gibbons FK, et al.: Imaging features of sarcoidosis on MDCT, FDG PET, and PET/CT. *AJR Am J Roentgenol* 190:S1–S6, 2008.

Sica GT, Ji H, Ros PR: CT and MR imaging of hepatic metastases. *AJR Am J Roentgenol* 174:691–698, 2000.

Siddiki H, Doherty MG, Fletcher JG, et al.: Abdominal findings in hereditary hemorrhagic telangiectasia: Pictorial essay on 2D and 3D findings with isotropic multiphase CT. *Radiographics* 28:171–183, 2008.

Smith MT, Blatt ER, Jedlicka P, et al.: Fibrolamellar hepatocellular carcinoma. *Radiographics* 28:609–613, 2008.

Torabi M, Hosseinzadeh K, Federle MP: CT of nonneoplastic hepatic vascular and perfusion disorders. *Radiographics* 28:1967–1982, 2008.

Vachha B, Sun MRM, Siewert B, Eisenberg RL: Cystic lesions of the liver. *AJR Am J Roentgenol* 196:W355–W366, 2011.

CHAPTER 12

BILIARY TREE AND GALLBLADDER

William E. Brant

BILIARY TREE

Primary imaging of the biliary tree depends increasingly on computed tomography (CT), magnetic resonance imaging (MRI), and magnetic resonance cholangiopancreatography, with diminishing reliance on invasive endoscopic retrograde cholangiopancreatography. Multidetector CT (MDCT) with thin sections and multiplanar reformations can clearly demonstrate the normal anatomy, anatomic variants, stones, tumors, and inflammatory disease of the biliary system.

Anatomy

The bile ducts arise as biliary capillaries between hepatocytes. Bile capillaries coalesce to form intrahepatic bile ducts. Intrahepatic bile ducts branch in a predictable manner corresponding to the segments of the liver. Interlobular bile ducts combine to form two main trunks from the right and left lobes of the liver. The 3- to 4-cm-long common hepatic duct is formed in the porta hepatis by the junction of the main right and left bile ducts. The cystic duct runs posteriorly and inferiorly from the gallbladder neck to join the common hepatic duct and form the common bile duct (CBD). The 6- to 7-cm-long CBD courses ventral to the portal vein and to the right of the hepatic artery, descending from the porta hepatis along the free right border of the hepatoduodenal ligament to behind the duodenal bulb. Its distal third turns directly caudad, descending in the groove between the descending duodenum and the head of the pancreas just ventral to the inferior vena cava. The CBD tapers distally as it ends in the sphincter of Oddi, which protrudes into the duodenum as the ampulla of Vater. The CBD and the pancreatic duct share a common orifice in 60% of cases and have separate orifices in the remainder. In any case, they are in such close proximity that tumors of the ampullary region generally obstruct both ducts.

Thin-collimation (2.5 to 5 mm) MDCT with dynamic bolus intravenous contrast enhancement reveals normal intrahepatic ducts in about 40% of patients. Normal intrahepatic ducts are 2 mm in diameter in the central liver and taper progressively toward the periphery. The common hepatic duct is usually seen in the porta hepatis, and the CBD is routinely visualized descending adjacent to the descending duodenum. It is fair to use the generic term *common duct* to refer to both the common hepatic and the common bile ducts because the cystic duct junction marking their anatomic partition is not routinely visualized on CT. The normal common duct does not exceed 6 mm in diameter in most adult patients. In elderly patients the normal common duct diameter increases by about 1 mm per decade (i.e., 7 mm is normal for patients in their 70s, and 8 mm is normal for those in their 80s). Contrast medium enhancement improves identification of both normal and dilated bile ducts by enhancing blood vessels and the surrounding parenchyma. Bile ducts are seen as lucent, branching, tubular structures. The bile ducts may be difficult to differentiate from blood vessels without contrast agent administration.

Technique

Evaluation for biliary obstruction is the most common reason to perform CT of the bile ducts. Water is preferred as an oral contrast agent in this clinical setting because high-density contrast in the duodenum may cause streaks and obscure stones in the adjacent CBD.

- The patient should drink 300 mL of water over 15 to 20 minutes just prior to CT examination.
- Thin sections (0.625 to 2.5 mm) using MDCT provide high-resolution images of the bile ducts.
- Multiphase imaging is commonly utilized. Stones may be seen best on noncontrast images. Scanning during the arterial phase

is best for demonstrating pancreatic lesions. Delayed imaging at 15 to 20 minutes after intravenous contrast administration reveals the delayed enhancement characteristic of cholangiocarcinomas.
- Isotropic voxel imaging allows for high-resolution image reconstruction in multiple anatomic planes and in three dimensions.

Biliary Obstruction

CT is about 96% accurate in determining the presence of biliary obstruction, 90% accurate in determining its level, and 70% accurate in determining its cause. The major causes of biliary obstruction are gallstones, tumors, strictures, and pancreatitis (Table 12-1). A rare but interesting cause of biliary obstruction is *Mirizzi syndrome*. A gallbladder stone impacted in the cystic duct induces cholangitis or erodes into the common duct to cause obstructive jaundice. Tumors include cholangiocarcinoma, pancreatic carcinoma, ampullary carcinoma, and benign tumors of the bile duct such as biliary cystadenomas and granular cell tumors.

TABLE 12-1 **Causes of Obstructive Jaundice in Adults**

Gallstone impacted in the bile duct
Bile duct stricture
Trauma, surgery, or instrumentation
Chronic pancreatitis
Primary sclerosing cholangitis
Recurrent pyogenic cholangitis
AIDS-associated cholangitis
Malignancy
Pancreatic carcinoma
Duodenal or ampullary carcinoma
Cholangiocarcinoma
Metastases
Parasites (*Ascaris, Clonorchis, Fasciola*)
AIDS-related cholangiopathy
Choledochal cyst

CT diagnosis of biliary obstruction depends on demonstration of dilated bile ducts. The biliary tree dilates proximal to the point of obstruction, whereas bile ducts distal to the obstruction remain normal or are reduced in size. When cirrhosis, cholangitis, or periductal fibrosis prohibits dilatation of the bile ducts in obstructive jaundice, CT will be falsely negative. The CT findings of biliary obstruction are as follows:
- Multiple branching, round or oval low-density tubular structures, representing dilated intrahepatic biliary ducts, course toward the porta hepatis. (Figs. 12-1 and 12-2).
- Dilatation of the common duct in the porta hepatis is seen as a tubular or oval fluid density of greater than 7 mm in diameter.
- Dilatation of the CBD in the pancreatic head is seen as a round fluid-density tube larger than 7 mm.
- Enlargement of the gallbladder to greater than 5 cm in diameter is evident when the obstruction is distal to the cystic duct.

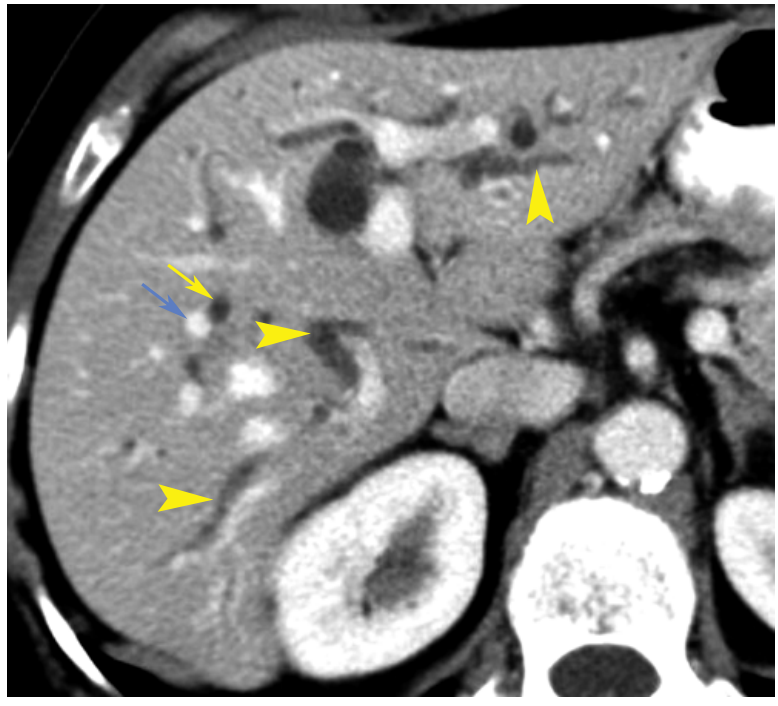

FIGURE 12-1 ■ Dilated bile ducts. Postcontrast image shows dilated bile ducts (*arrowheads*) as low-attenuation round and oval structures or tortuous tubes. Note that in cross-section the dilated bile duct (*yellow arrow*) is slightly larger in diameter than the adjacent portal vein (*blue arrow*). The diameter of normal intrahepatic bile ducts should not be greater than 40% of the diameter of the adjacent portal vein.

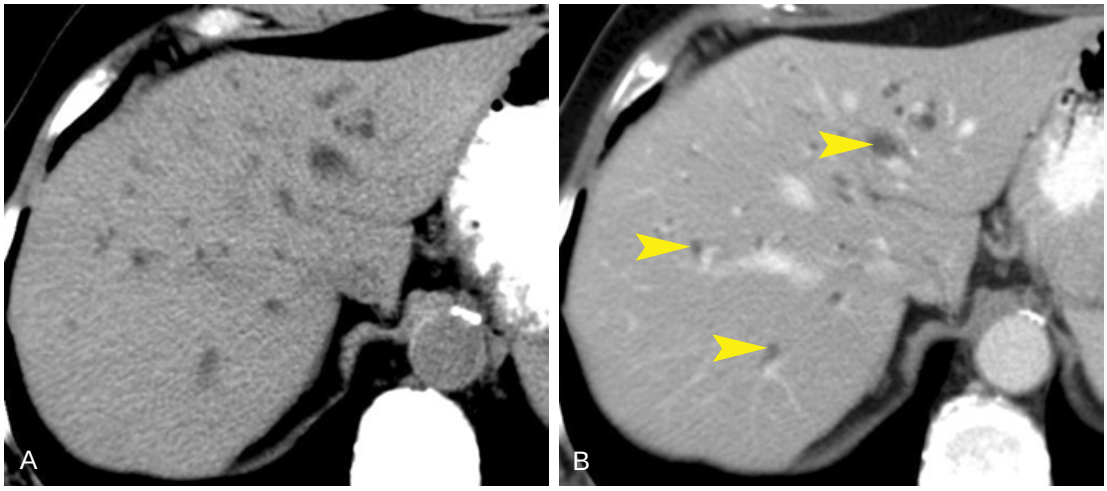

FIGURE 12-2 ■ Dilated bile ducts. *A*, On noncontrast computed tomography, dilated bile ducts are difficult to recognize, appearing as ill-defined foci of low attenuation that are hard to differentiate from unopacified blood vessels. *B*, Following intravenous contrast administration, the dilated bile ducts (*arrowheads*) are much better defined and the blood vessels are now easy to see.

Clues to the cause of biliary obstruction are illustrated in Figure 12-3.

- Abrupt termination of a dilated CBD is characteristic of a malignant process (Fig. 12-4) even in the absence of a visible mass. Common tumors causing biliary obstruction are pancreatic carcinoma, ampullary carcinoma, and cholangiocarcinoma. A small mass may be recognized at the point of biliary obstruction by careful inspection of noncontrast, arterial-phase, portal venous-phase, and delayed-phase postcontrast CT images.
- Gradual tapering of a dilated duct is seen most commonly with benign disease such as an inflammatory stricture and pancreatitis (Fig. 12-5). Calcifications in the pancreas are a clue to the presence of chronic pancreatitis.
- The presence of choledocholithiasis (Fig. 12-6) may be difficult to recognize because of the wide variation in the CT appearance of gallstones.

Choledocholithiasis

Stones in the biliary tree are a common cause of pancreatitis, jaundice, biliary colic, and cholangitis. However, stones in the bile ducts may also be asymptomatic. Most stones (95%) in the bile ducts form in the gallbladder, although stones may also develop primarily within the bile ducts, especially when the gallbladder has been removed or is chronically obstructed. CT demonstrates approximately 75% of stones in the CBD.

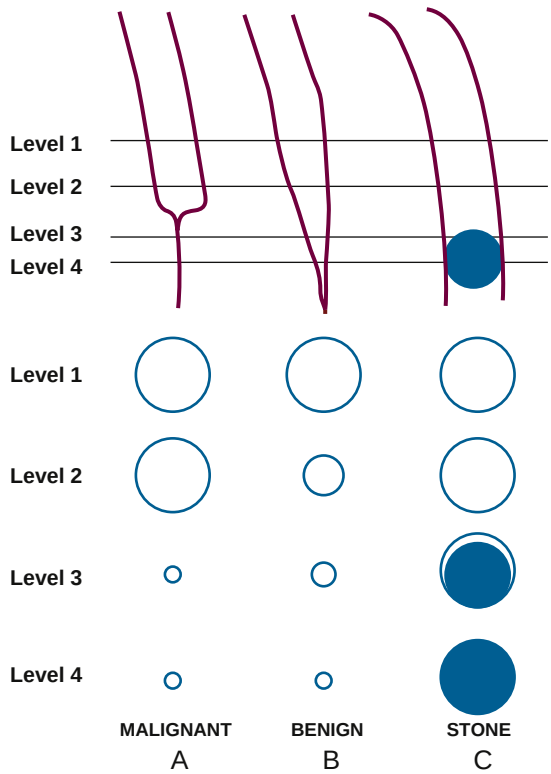

FIGURE 12-3 ■ Clues to the cause of biliary obstruction. *A*, Malignant tumors cause abrupt termination of the distal common bile duct. *B*, Inflammatory strictures and pancreatitis cause progressive tapering of the distal common bile duct. *C*, Impacted gallstones may be seen as rounded structures in the distal common bile duct. The computed tomography density of gallstones varies from calcified to fat density.

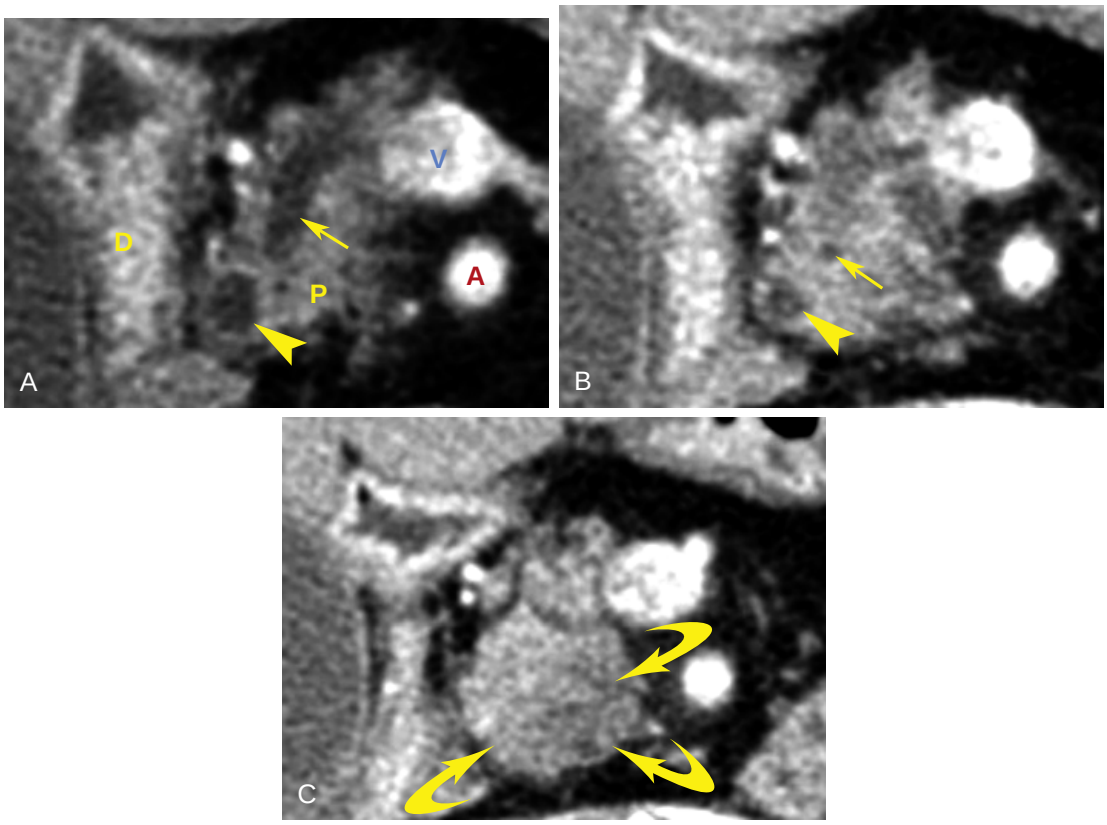

FIGURE 12-4 ■ Malignant tumor obstructing the common bile duct (CBD). Magnified images of sequential slices from contrast-enhanced computed tomography, proceeding from superior to inferior. *A*, The CBD (*arrowhead*) in the head of the pancreas (P) is mildly dilated to 10 mm. The nearby pancreatic duct (*arrow*) is also dilated. D, duodenum; A, superior mesenteric artery; V, superior mesenteric vein. *B*, The CBD (*arrowhead*) and pancreatic duct (*arrow*) become narrowed as they encounter the tumor in the head of the pancreas. *C*, Both ducts disappear within the subtly defined tumor (*curved arrows*). Pathology confirmed pancreatic adenocarcinoma.

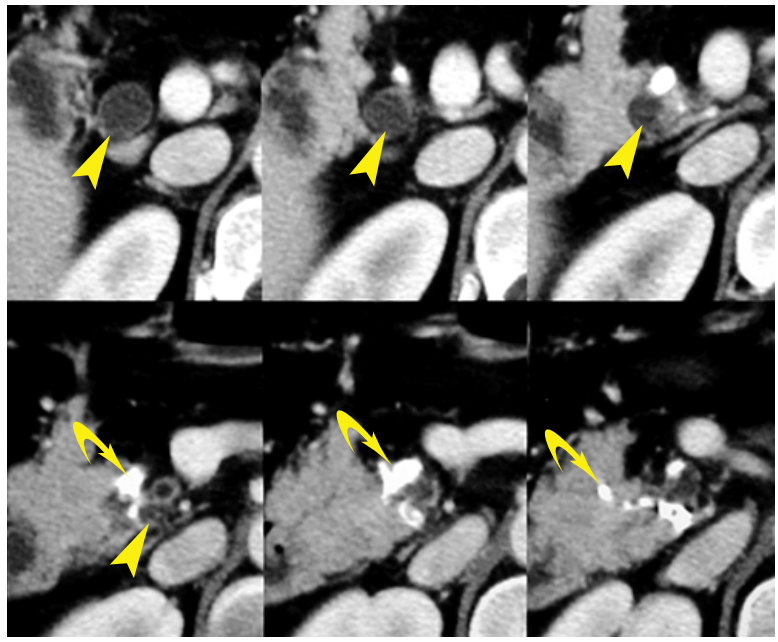

FIGURE 12-5 ■ Benign stricture of the common bile duct (CBD) due to chronic pancreatitis. Magnified sequential postcontrast computed tomography images demonstrate progressive tapering of the distal CBD (*arrowheads*) as it passes through the head of the pancreas. The pancreatic head is deformed, and multiple calcifications (*curved arrows*) and cystic changes indicate chronic pancreatitis.

- Gallstones in the bile ducts are seen as structures of calcified (calcium bilirubinate stones), soft tissue (mixed stones), or fat (cholesterol stones) density (Fig. 12-6). Stones may be isodense with bile and not visualized by CT (15% to 25% of gallstones). Stones may also contain nitrogen gas and show foci of air attenuation.
- The stone may appear as a central density surrounded by a rim or crescent of lower density bile, the so-called target or crescent sign.
- Low-attenuation stones may be defined by a higher-attenuation outer rim, the so-called rim sign.
- Abrupt termination of the CBD proximal to the ampulla is suggestive of a stone in the CBD.

Cholangiocarcinoma

Cholangiocarcinoma is a slow-growing adenocarcinoma arising from the epithelium of the bile ducts. It may occur as a complication of a choledochal cyst, primary sclerosing cholangitis (PSC), Caroli disease, intrahepatic stone disease, or clonorchiasis. Prognosis is poor, with recurrence rates of 60% to 90% after surgical resection. Cholangiocarcinoma exhibits mass-forming, periductal-infiltrating, and intraductal patterns of growth. Tumors occur in the periphery of the liver (10%), in the hilum (25%), and in the extrahepatic bile ducts (65%). The tumors are hypovascular and markedly fibrotic, resulting in poor contrast enhancement and limited CT detection especially on early postcontrast scans. Delayed scans at 10 to 20 minutes after contrast injection are recommended for optimal tumor detection.

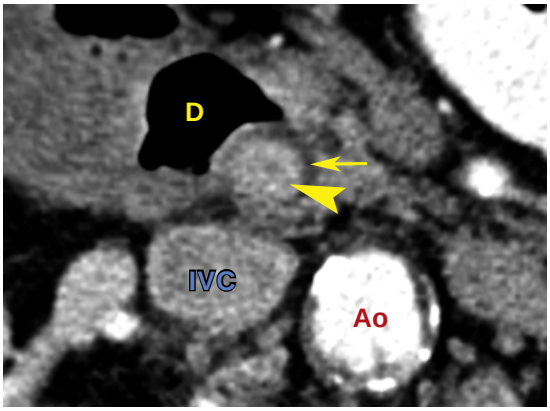

FIGURE 12-6 ■ Stone in the common bile duct (CBD). Magnified image of the distal CBD near the ampulla in a patient with biliary obstruction shows a gallstone (*arrowhead*) as a slightly high-attenuation focus in the CBD. A thin rim of bile (*arrow*) partially surrounds the obstructing stone. D, duodenum; IVC, inferior vena cava; Ao, aorta.

- Intrahepatic mass-forming cholangiocarcinoma appears as a homogeneous tumor with irregular borders and remarkably low attenuation. The mass is highly fibrotic and often shows only weak peripheral enhancement on early postcontrast images (Fig. 11-25). Delayed images (up to several hours) may show central or diffuse enhancement. Bile ducts peripheral to the tumor are usually obstructed and dilated.
- Periductal-infiltrating lesions grow along the bile ducts in an elongated, branching pattern. Irregular narrowing of the duct produces obstruction. Tumor-involved ducts are narrowed with thick walls, whereas peripheral ducts are dilated with thin walls. The visible tumor mass is minimal. Cholangiocarcinomas occurring at the confluence of the right and left hepatic bile ducts are frequently small and infiltrating, causing early biliary obstruction (Fig. 12-7). These have been termed *Klatskin tumors*.
- Intraductal tumors are polypoid or sessile papillary lesions that extend superficially along the bile duct mucosa. Some of these tumors produce large amounts of mucin, which disproportionately dilates the biliary system.
- Extrahepatic cholangiocarcinomas may appear as a duct-obstructing, polypoid tumor nodules of 1 to 2 cm in diameter (Fig. 12-8), an abrupt stricture with wall thickening of up to 1 cm, or single or multiple intraductal, frondlike masses.

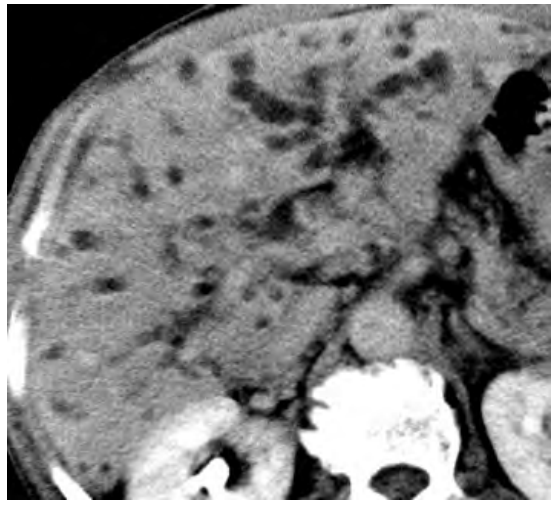

FIGURE 12-7 ■ Cholangiocarcinoma: infiltrating hilar. An infiltrating cholangiocarcinoma at the junction of the right and left bile ducts (a Klatskin tumor) causes generalized dilatation of the intrahepatic biliary tree. The primary tumor is not visualized with computed tomography.

Cholangitis

Cholangitis refers to inflammation of the bile ducts.

- *Primary sclerosing cholangitis* (PSC) is an idiopathic inflammatory condition characterized by progressive fibrosis of the bile ducts that leads to obstruction, cholestasis, and biliary cirrhosis. PSC is strongly associated (70% of cases) with ulcerative colitis and other inflammatory bowel diseases. CT of PSC demonstrates multiple segmental strictures with thickening (2 to 5 mm) of the bile duct walls alternating with normal-caliber or slightly dilated duct segments that produce a beaded appearance (Fig. 12-9). Stones are seen in the ducts in 30% of patients.
- *Acute pyogenic cholangitis* occurs when bacteria contaminate an obstructed biliary system. Liver abscesses and sepsis may occur. Patients present with acute abdominal pain, fever, and intermittent jaundice. CT findings include periductal edema, bile duct dilatation, and inhomogeneous enhancement of the liver parenchyma (Figs. 12-10 and 12-11).
- *Recurrent pyogenic cholangitis* (sometimes termed Oriental cholangitis) refers to recurrent episodes of acute pyogenic cholangitis associated with pigmented stones and multifocal biliary strictures and dilatations. Infestations with *Clonorchis sinensis* and *Ascaris lumbricoides*, malnutrition, and portal vein bacteremia all play a role in its etiology. The condition is endemic in Southeast Asian and Chinese populations and is seen predominantly in immigrants in Western countries. Dilated bile ducts with enhancing thickened walls are filled with stones and pus (Fig. 12-12). Marked dilatation of the CBD is characteristic.
- *AIDS-related cholangiopathy* is associated with opportunistic infection with *Cryptosporidium* or cytomegalovirus. Intrahepatic bile ducts show focal narrowing and dilatation similar to PSC. Striking thickening and enhancement of the walls of the bile ducts and gallbladder are often evident. The distal CBD is commonly strictured.
- *Autoimmune pancreatitis* is observed in a subset of patients with involvement of the

FIGURE 12-8 ■ Cholangiocarcinoma: intraductal polypoid. Magnified image of the distal common bile duct (CBD) shows polypoid cholangiocarcinoma (*arrowhead*) that caused obstructive jaundice with marked dilatation of the CBD. Note the similarity in appearance to the low-attenuation stone shown in Figure 12-6.

FIGURE 12-9 ■ Primary sclerosing cholangitis. Postcontrast computed tomography shows patchy irregular dilatation of the intrahepatic bile ducts. Only the focally dilated portions of the bile ducts are evident. The strictured portions are not seen but can be inferred from this pattern of dilated ducts.

biliary tree. Focal or diffuse strictures of the CBD may occur in association with upstream biliary dilatation. Imaging features of autoimmune pancreatitis are present (see Chapter 13).

Choledochal Cyst

Choledochal cysts are congenital dilatations of any portion of the biliary tree. Most are discovered in childhood. Adult patients with undetected biliary cysts may present with pancreatitis, cholangitis, jaundice, or unexplained abdominal pain, nausea, or vomiting. Complications include gallstones and cholangiocarcinoma. CT demonstrates cystic structures in the course of the intrahepatic bile ducts or CBD and separate from the gallbladder. Todani classifies choledochal cysts into five types.

- Type I (~77%), a classic choledochal cyst, is localized cystic dilatation of the CBD (Fig. 12-13). This may appear large and saccular, or small and fusiform.
- Type II (~1.5%) is a diverticulum arising from the CBD or common hepatic duct. The remainder of the biliary system is normal.

FIGURE 12-10 ■ Acute pyogenic cholangitis. Postcontrast computed tomography in a patient with a liver transplant presenting with acute abdominal pain and fever shows marked periductal and periportal edema (*arrowheads*). Further evaluation revealed a stricture at the biliary anastomosis. A bile culture yielded *Escherichia coli*.

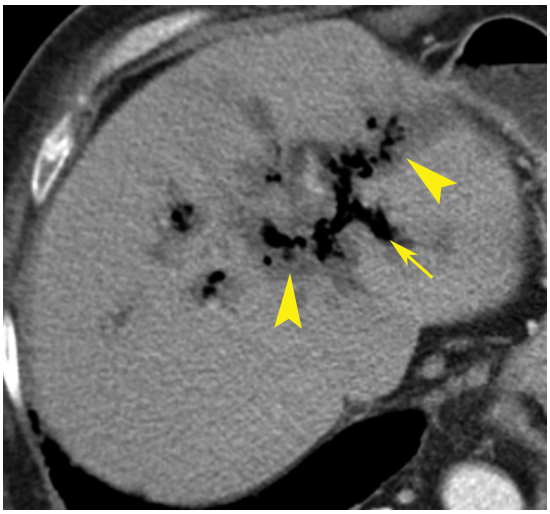

FIGURE 12-11 ■ Acute pyogenic cholangitis. A patient with an obstructing pancreatic tumor developed acute pain and fever after endoscopic retrograde cholangiography. Noncontrast computed tomography reveals gas (*arrow*) within the biliary tree and marked periductal/periportal edema (*arrowheads*). Urgent biliary drainage was needed. A bile culture yielded gas-producing *Escherichia coli*.

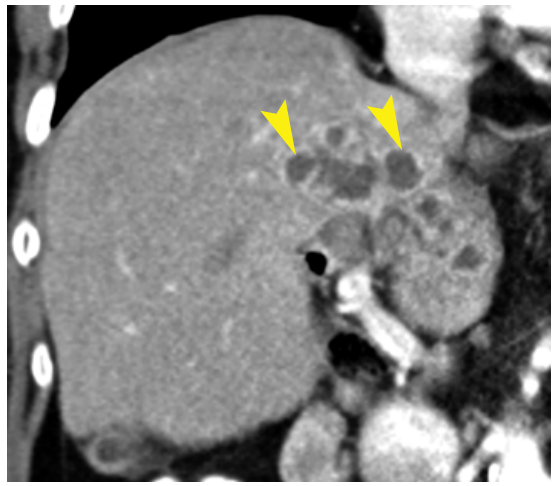

FIGURE 12-12 ■ Recurrent pyogenic cholangitis. Coronal reconstruction of postcontrast computed tomography shows multiple cystic masses (*arrowheads*) with enhancing walls. These represent infected, dilated, obstructed bile ducts and hepatic abscesses. The patient was a Korean immigrant.

FIGURE 12-13 ■ Choledochal cyst, type I. The common bile duct (C) is massively dilated, which is characteristic of a type I choledochal cyst. The neck of the gallbladder (GB) is seen adjacent to the dilated common bile duct.

- Type III (~1.5%), a choledochocele, is a rare bulbous dilatation of the intramural portion of the distal CBD that protrudes into the lumen of the duodenum. Choledochoceles are most commonly detected in adults. Stones are commonly present in the biliary tree.
- Type IV is divided into IV-A (~20%), cystic dilatation of the intrahepatic bile ducts associated with saccular dilatation of the CBD, and IV-B (extremely rare), multiple cystic dilatations of the extrahepatic bile ducts with normal intrahepatic bile ducts.
- Type V is Caroli disease.

Caroli Disease

Caroli disease is a rare congenital anomaly of the biliary tract characterized by saccular dilatation of the intrahepatic biliary tree, cholangitis, and gallstone formation in the absence of cirrhosis or portal hypertension. Patients are at greatly increased risk of bile duct carcinoma (7% of patients). *Caroli syndrome* is the combination of Caroli disease and congenital hepatic fibrosis.

- CT demonstrates cystic dilatation of the intrahepatic biliary tree with focal areas of tubular and saccular enlargement (Fig. 12-14).

Gas or Contrast Material in the Biliary Tree

Gas or contrast material in the biliary tree (Fig. 12-15) is an abnormal finding that must be explained. Most often the cause is iatrogenic. The differential diagnosis is listed in Table 12-2.

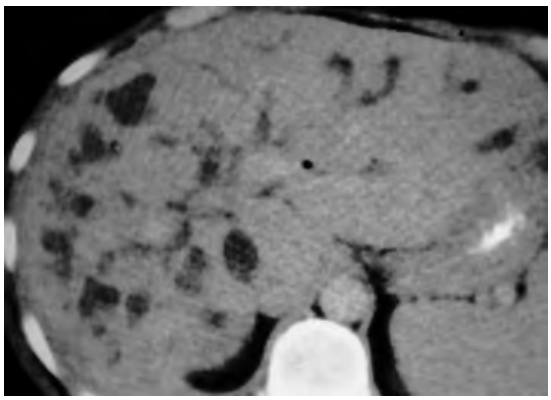

FIGURE 12-14 ■ Caroli disease. Abnormally dilated intrahepatic bile ducts are seen as a tubular and rounded cystic lucencies in the liver.

GALLBLADDER

Anatomy

The gallbladder lies in the fossa formed by the junction of the right and left lobes of the liver. Although the position of the fundus varies, the neck and body of the gallbladder are invariably positioned in the porta hepatis and major interlobar fissure. The gallbladder is in close proximity to the duodenal bulb and hepatic flexure of the colon. The normal gallbladder is 3 to 5 cm in diameter and 10 cm in length and has a capacity of roughly 50 mL. *Agenesis* of the gallbladder is extremely rare (<0.02%) and *duplication* of the gallbladder occurs in about 1 in 4000 individuals. Folds in the gallbladder, producing a Phrygian cap deformity, are common (incidence of 1% to 6%) and are not clinically significant.

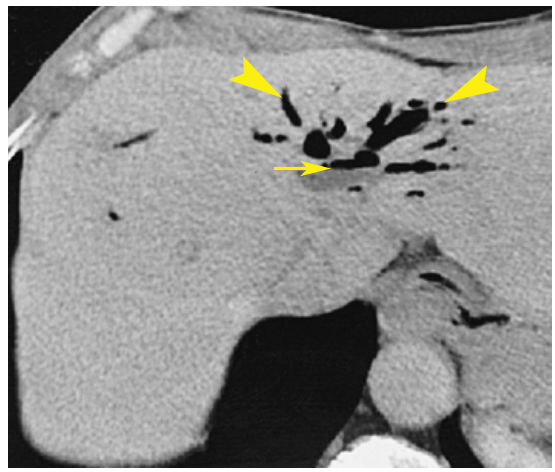

FIGURE 12-15 ■ Air in the biliary tree. Air is seen in the bile ducts (*arrowheads*) of the left lobe of the liver in this patient who underwent choledochojejunostomy as part of a Whipple procedure. Air fills the left hepatic bile ducts in a supine patient and the right hepatic bile ducts in a prone patient. Note the air–bile level (*arrow*).

TABLE 12-2 **Causes of Reflux of Gas or Bowel Contrast into the Biliary Tree**

Iatrogenic
Sphincterotomy
Choledochojejunostomy
Gallstone fistula
Cholecystoduodenal fistula
Perforated ulcer
Choledochoduodenal fistula
Carcinoma
Choledochoenteric fistula

Ultrasonography rather than CT is the primary modality for imaging the gallbladder. However, significant gallbladder pathology may be diagnosed by CT imaging, especially when screening acutely ill patients. Normal bile is of fluid density (0 to 20 Hounsfield units, HU) on CT. Higher-density bile suggests bile stasis (sludge), hemorrhage, or infection (pus). The gallbladder wall enhances avidly with bolus administration of contrast agent.

Gallstones

Although gallstones may be detected by CT, the sensitivity of CT detection is only about 85%, which is much less than that of ultrasonography or MRI. Gallstones vary in CT density from negative Hounsfield units, indicating the fat attenuation of cholesterol stones, to high positive HU for calcified stones (Fig. 12-16). Fissured stones may contain linear streaks of nitrogen gas. Some gallstones may not be seen on CT because they are isodense with bile or because they are too small. Contrast agents in adjacent bowel loops may obscure, or mimic, gallstones.

Acute Cholecystitis

Acute cholecystitis is usually diagnosed clinically, by ultrasonography or by radionuclide hepatobiliary scan. CT is typically used if a patient has unexplained right upper-quadrant pain or atypical symptoms, or is suspected of having complicated cholecystitis. *Gangrenous cholecystitis* may lead to perforation, an abscess, a fistula, or peritonitis. *Acalculous cholecystitis* (approximately 5% to 10% of cases) occurs most commonly in critically ill patients, especially after surgery, trauma, or burns, or in patients on hyperalimentation. Acalculous cholecystitis is induced by biliary stasis, ischemia, and bacteremia. *Emphysematous cholecystitis* is a severe form of cholecystitis that tends to occur in the elderly and in diabetics. It may produce deceptively mild symptoms but carries high morbidity and mortality. The CT findings in acute cholecystitis are as follows:

- CT reveals that gallstones are present in the gallbladder in 75% of cases of acute cholecystitis (Fig. 12-17).
- The gallbladder is usually distended to 4 to 5 cm in diameter, reflecting cystic duct obstruction.

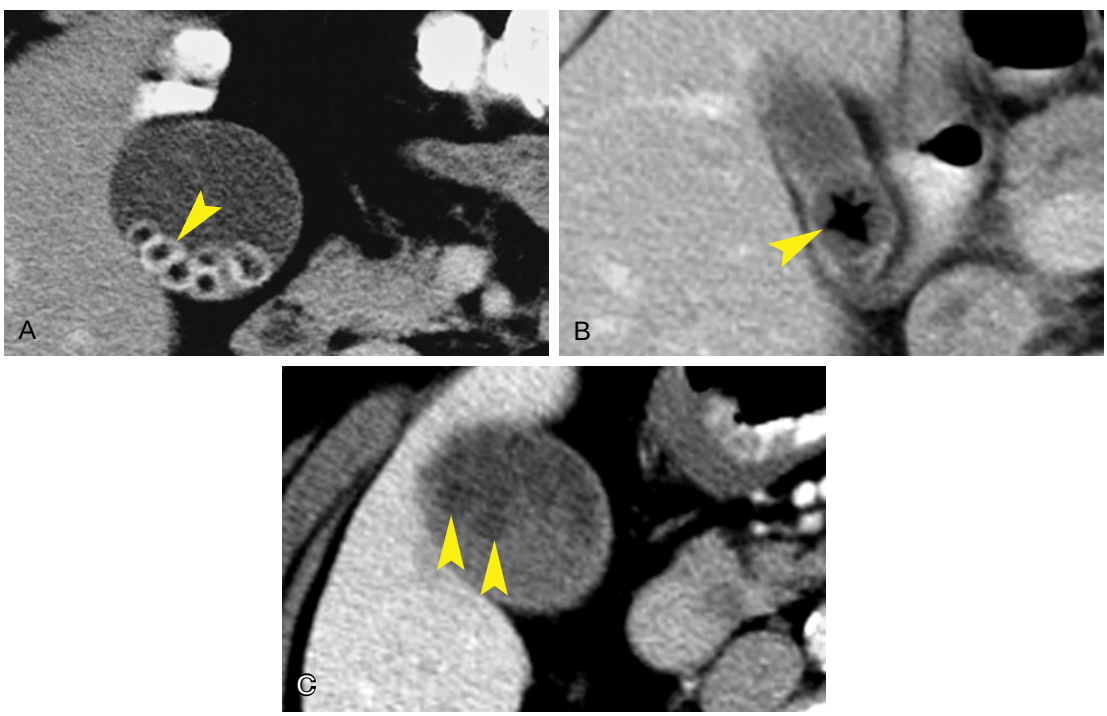

FIGURE 12-16 ■ Gallstones. *A,* Gallstones (*arrowhead*) settle dependently in the gallbladder. These stones consist of low-attenuation centers of high cholesterol content and calcified outer margins. *B,* A gallstone with a very faintly calcified rim contains nitrogen gas (*arrowhead*). *C,* Very low-attenuation gallstones (*arrowheads*) are suspended within the gallbladder and are faintly visible because of their cholesterol content. Gallstones may be entirely of the same attenuation as bile and may be undetectable by computed tomography.

- The gallbladder wall is thickened (>3 mm) and appears indistinct due to inflammation and edema. The wall commonly enhances avidly reflecting inflammatory hyperemia.
- A transient early-phase increase in the attenuation of the liver adjacent to the gallbladder is strong evidence of hyperemia and inflammation.
- A halo of subserosal edema in the gallbladder wall and stranding in the pericholecystic tissues reflect inflammation of the wall.
- Pericholecystic fluid collection is associated with perforation and abscess.
- Increased bile attenuation (above 20 HU) is caused by biliary stasis, intraluminal pus, hemorrhage, or cellular debris.
- The CT findings for *acalculous cholecystitis* are identical to those for calculous cholecystitis except that gallstones are absent. This condition occurs only in patients with the predisposing conditions listed.
- Air in the gallbladder wall or lumen is seen with *emphysematous cholecystitis*, a severe form of acute cholecystitis caused by gas-forming organisms and associated with high mortality (Fig. 12-18).

Porcelain Gallbladder

Calcification of the gallbladder wall (Fig. 12-19), in association with chronic cholecystitis, is termed porcelain gallbladder. The calcification may be broad and continuous or multiple and punctate. Gallstones are nearly always present. Gallbladder carcinoma may develop in 20% to 25% of patients with porcelain gallbladder. Cholecystectomy is often recommended even when the patient is asymptomatic.

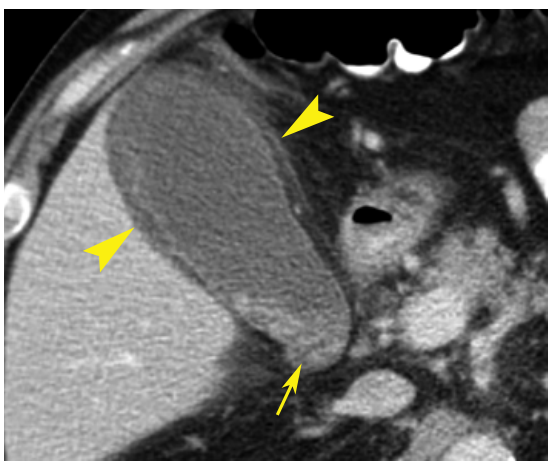

FIGURE 12-17 ■ Acute cholecystitis. The gallbladder is distended, its wall is shaggy and poorly defined, and edema (*arrowheads*) extends from the gallbladder wall into pericholecystic tissues. Multiple small gallstones (*arrow*) are layered dependently within the gallbladder. Surgery in this case confirmed uncomplicated acute cholecystitis.

Gallbladder Carcinoma

Gallbladder carcinoma is the most common malignancy of the biliary system. Most patients are aged 50 years and older. Because of the presence of gallstones and chronic cholecystitis, clinical and imaging evaluations commonly overlook early disease. Because of advanced disease at diagnosis, the typical 5-year survival is only 5%. Newer, more aggressive surgical techniques may improve the 5-year survival to 50%. Chronic cholelithiasis related to gallstones is the major

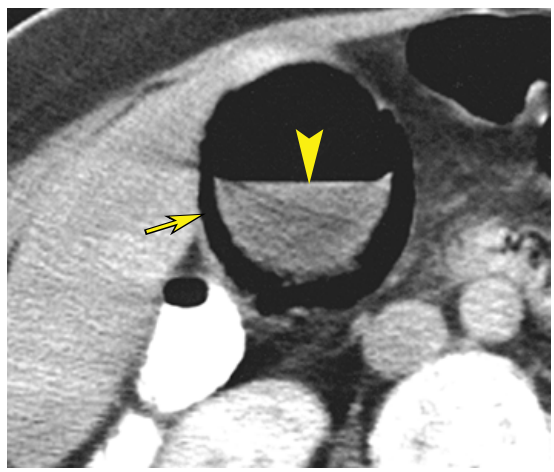

FIGURE 12-18 ■ Emphysematous cholecystitis. Gas infiltrates the wall (*arrow*) of the gallbladder and forms an air–fluid level (*arrowhead*) with bile in the gallbladder lumen.

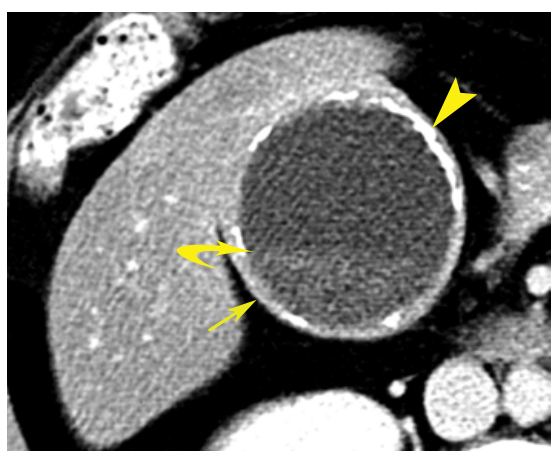

FIGURE 12-19 ■ Porcelain gallbladder. The wall of the gallbladder (*arrow*) is thickened and calcified (*arrowhead*). A faint fluid level (*curved arrow*) is seen in the gallbladder lumen, indicating chronic bile stasis.

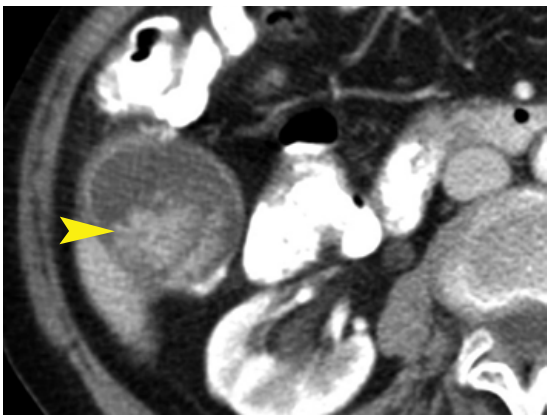

FIGURE 12-20 ■ Gallbladder carcinoma. An enhancing frond-like polypoid mass (*arrowhead*) within the gallbladder lumen is characteristic of gallbladder carcinoma. Gallstones (not shown) were also present in the gallbladder.

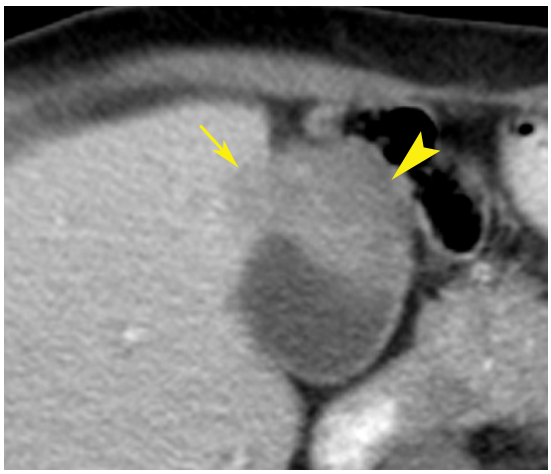

FIGURE 12-21 ■ Gallbladder carcinoma invasion of the liver. Adenocarcinoma (*arrowhead*) arising within the gallbladder extends directly into the liver parenchyma (*arrow*).

risk factor for this tumor. CT reveals three major patterns of disease.

- A polypoid soft-tissue mass is present within the gallbladder lumen (~25% of cases; Fig. 12-20). The cancerous polyps are usually larger than 1 cm and exhibit early contrast enhancement and washout.
- Focal or diffuse thickening of the gallbladder wall, often >1 cm, is evident (~7% of cases).
- A mass containing gallstones replaces the gallbladder and invades the adjacent liver (~68% of cases).
- Associated findings include gallstones, biliary dilatation, metastases in the liver, invasion of the liver (Fig. 12-21), bowel, and adjacent structures, and calcification of the gallbladder wall.

SUGGESTED READING

Catalano OA, Sahani DV, Forcione DG, et al.: Biliary infections: spectrum of imaging findings and management. *Radiographics* 29:2059–2080, 2009.

Hashimoto M, Itoh K, Takeda K, et al.: Evaluation of biliary abnormalities with 64-channel multidetector CT. *Radiographics* 28:119–134, 2008.

Kiewiet JJS, Leeuwenburgh MMN, Bipat S, et al.: A systematic review and meta-analysis of diagnostic performance of imaging in acute cholecystitis. *Radiology* 264:708–720, 2012.

Lee HK, Park SJ, Yi BH, et al.: Imaging features of adult choledochal cysts: A pictorial review. *Korean J Radiol* 10:71–80, 2009.

Menias CO, Surabhi VR, Prasad SR, et al.: Mimics of cholangiocarcinoma: Spectrum of disease. *Radiographics* 28: 1115–1129, 2008.

O'Conner OJ, Maher MM: Imaging of cholecystitis. *AJR Am J Roentgenol* 196:W367–W374, 2011.

O'Connor OJ, O'Neill SO, Maher MM: Imaging of biliary tract disease. *AJR Am J Roentgenol* 197:W551–W558, 2011.

Santiago I, Loureiro R, Curvo-Semedo L, et al.: Congenital cystic lesions of the biliary tree. *AJR Am J Roentgenol* 198:825–835, 2012.

Shanbhogue AKP, Tirumani SH, Prasad SR, et al.: Benign biliary strictures: A current comprehensive clinical and imaging review. *AJR Am J Roentgenol* 197:W295–W306, 2011.

Yeh BM, Liu PS, Soto JA, et al.: MR imaging and CT of the biliary tract. *Radiographics* 29:1669–1688, 2009.

CHAPTER 13

PANCREAS

William E. Brant

Multidetector computed tomography (MDCT) is the imaging method of choice for evaluation of pancreatitis and is comparable to magnetic resonance imaging (MRI) for detection and staging of pancreatic tumors. Rapid acquisition times allow for high-resolution scanning of the entire pancreas within a single breath hold in most instances.

COMPUTED TOMOGRAPHY TECHNIQUE

Computed tomography (CT) evaluation of pancreatitis is usually performed as a routine abdomen assessment with extension of CT scanning to the pelvis if large fluid collections are present. Water may be substituted for oral contrast agents if stones in the distal common bile duct (CBD) are suspected. CT evaluation for a pancreatic mass is performed as a multiphase dynamic scan of the entire pancreas. Optimally, each phase is performed during a single breath hold. Oral contrast agents are routinely given. CT without intravenous contrast is performed from the liver dome through the iliac crest using 2.5-mm collimation and image reconstruction with 5-mm-thick slices. A power injector is used to administer 120 to 150 mL of intravenous contrast at 4 to 5 mL/second. The arterial-phase scan is obtained 30 to 35 seconds following the onset of injection using 1.25-mm collimation and image reconstruction with 2.5-mm slices. Both the liver and pancreas show arterial opacification with minimal contrast in the portal vein. The venous-phase scan of the entire abdomen is obtained 70 to 80 seconds following the initiation of contrast injection using 2.5-mm collimation and image reconstruction with 5-mm-thick slices. Delayed scans may be obtained 3 minutes after contrast injection through the liver and kidneys. Three-dimensional reconstructions may be performed as CT angiograms.

NORMAL ANATOMY OF THE PANCREAS

The pancreas lies within the anterior pararenal compartment of the retroperitoneal space, behind the left lobe of the liver and the stomach in front of the spine and great vessels (Fig. 13-1). The peritoneum-lined lesser sac forms a potential space between the stomach and pancreas. The pancreas is divided anatomically into four parts: the head, including the uncinate process, the neck, the body, and the tail. The pancreas somewhat resembles a question mark turned on its left side with the hook portion formed by the pancreatic head and uncinate process as they lie cradled in the duodenal loop. The portal vein fills the center of the hook. The uncinate process cradles the superior mesenteric vein (SMV) and tapers to a sharpened point directed leftward beneath the SMV. The neck is the slightly constricted portion of the pancreas just ventral to the portal vein confluence. The body and tail taper as they extend toward the splenic hilum. The pancreas is usually directed upward and to the left, although it may form an inverted U shape with the tail directed caudad. Sequential CT slices must be mentally summated to assess the shape and size of the pancreas. The gland is 15 to 20 cm long. The maximum dimensions for width are 3.0 cm for the head, 2.5 cm for the body, and 2.0 cm for the tail. The gland is larger in young patients and progressively decreases in size with age. The CT attenuation is uniform and approximately equal to that of muscle. In young patients the pancreas resembles a slab of meat. Progressive infiltration of fat between the lobules of the pancreas gives it a feathery appearance with advancing age. The pancreatic duct is best visualized with thin slices (1.5 to 2.5 mm). It tapers smoothly to the tail, measuring a maximum of 3.5 mm in diameter in the head, 2.5 mm in the body, and 1.5 mm in the tail. The main duct (of Wirsung) joins the CBD at the sphincter of Oddi to enter the duodenum. The accessory duct (of Santorini) draining the anterior and superior portions of the pancreatic head drains into the duodenum via the minor papilla.

The complex vascular anatomy around the pancreas must be understood to correctly interpret pancreatic CT. The splenic vein runs a relatively straight course in the dorsum of the

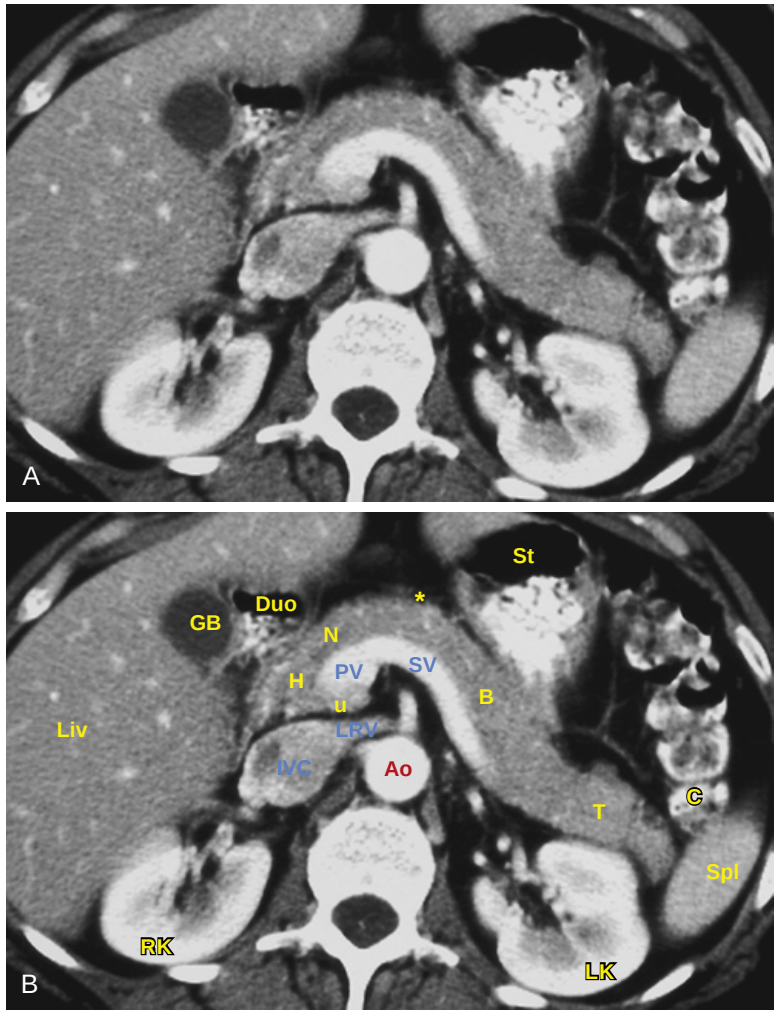

FIGURE 13-1 ■ Normal pancreas anatomy. *A,* Computed tomography (CT) image of a normal pancreas. *B,* Same image as in *A* with the anatomic structures labeled.

pancreas from the splenic hilum to its junction with the SMV just posterior to the neck of the pancreas. The plane of fat between the splenic vein and pancreas must not be mistaken for the pancreatic duct. The splenic artery runs an undulating course through the pancreas from the celiac axis to the spleen. Atherosclerotic calcifications are common in the splenic artery and may be easily mistaken for pancreatic calcifications. The superior mesenteric artery (SMA) arises from the aorta dorsal to the pancreas and courses caudally, surrounded by a collar of fat. The SMV courses cranially, just to the right of the superior mesenteric artery, until it joins the splenic vein to form the portal vein. The pancreatic head entirely surrounds this junction, with the uncinate process extending beneath the SMV. The portal vein courses upward and rightward with the hepatic artery and the CBD to the porta hepatis.

PANCREAS DIVISUM

The most common anomaly of the pancreatic ductal system is pancreas divisum, which is present in 4% to 10% of the population. In this anomaly, as a result of failure of fusion of the dorsal and ventral pancreas during embryologic development, the dorsal duct draining the majority of the pancreas empties into the minor papilla via the duct of Santorini rather than into the major papilla via the duct of Wirsung. Thin-section MDCT shows the dorsal pancreatic duct coursing posterior to the descending portion of the CBD cephalad to the sphincter of Oddi (Fig. 13-2). The distal dorsal pancreatic duct may be dilated at the junction with the duodenum, an anomaly known as a *santorinicele*. In most patients, pancreas divisum is an incidental finding of no significance. However, constriction of

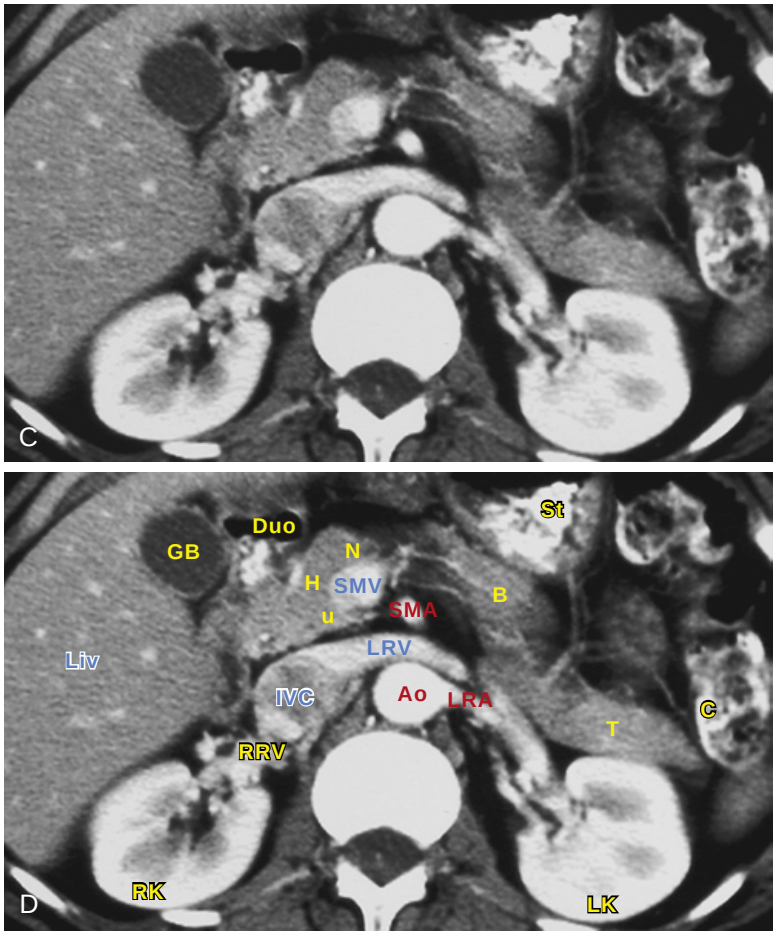

FIGURE 13-1, cont'd ■ *C*, CT image of a normal head and uncinate process of the pancreas. *D*, Same image as in *C* with the anatomic structures labeled. Ao, aorta; B, body; C, colon; Duo, duodenum; GB, gallbladder; H, head; IVC, inferior vena cava; Liv, liver; LK, left kidney; LRV, left renal vein; N, neck; PV, commencement of the portal vein; RK, right kidney; RRV, right renal vein; SMA, superior mesenteric artery; SMV, superior mesenteric vein; Spl, spleen; St, stomach; SV, splenic vein; T, tail; u, uncinate process of the pancreatic head. The asterisk (*) indicates the location of the lesser sac.

the dorsal duct at the minor papilla predisposes 25% to 38% of patients with pancreas divisum to recurrent pancreatitis.

ANNULAR PANCREAS

Incomplete rotation of the embryologic ventral pancreas results in a condition in which a segment of the pancreas encircles and often constricts the descending duodenum. Annular pancreas is rare, occurring as an isolated anomaly or in association with other congenital anomalies. It may present in the neonatal period with duodenal or biliary obstruction. In adults it may present with ulcer disease, duodenal obstruction, or pancreatitis. CT shows pancreatic tissue encircling the second portion of the duodenum (Fig. 13-3). Symptomatic cases warrant surgical resection.

FATTY INFILTRATION OF THE PANCREAS

Fatty infiltration of the pancreas occurs commonly with aging and obesity without affecting the function of the pancreas.

- Because the gland is not encapsulated, fatty infiltration between the lobules in older patients gives the pancreas a delicate, feathery appearance resembling a dust mop (Fig. 13-4).
- Fatty replacement may be diffuse or distributed unevenly through the pancreas. Common areas of focal sparing of fat infiltration are the head and uncinate process. In some cases the head and uncinate process are involved, and the remainder of the pancreas is spared.

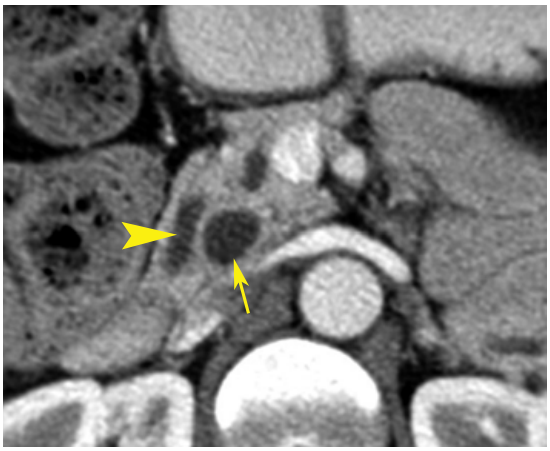

FIGURE 13-2 ■ Pancreas divisum. Magnified view of a contrast-enhanced computed tomography image of the pancreatic head shows a dilated pancreatic duct (*arrowhead*) bypassing the common bile duct (CBD, *arrow*). The main (dorsal) pancreatic duct inserts into the more proximal minor papilla rather than joining the CBD to insert into the larger major papilla. This patient had a history of recurrent pancreatitis, likely related to a low-grade obstruction at the minor papilla.

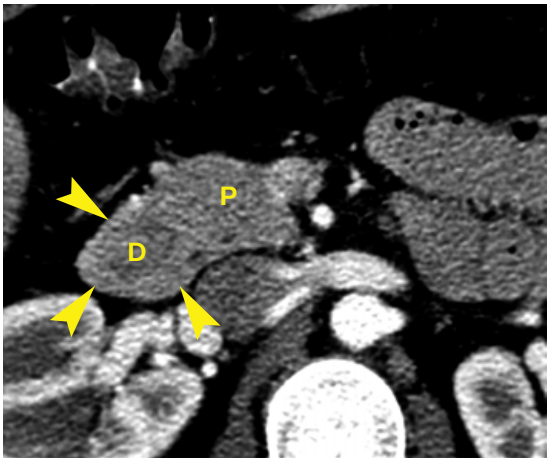

FIGURE 13-3 ■ Annular pancreas. Magnified view of a contrast-enhanced computed tomography image of the head of the pancreas (P) shows pancreatic tissue (*arrowheads*) completely encircling the slightly lower-attenuation second portion of the duodenum (D). The duodenum is compressed and partially obstructed by the encircling pancreas.

- In advanced cystic fibrosis the pancreatic parenchyma is atrophic and is diffusely replaced by fat (Fig. 13-5), and the exocrine function of the pancreas is severely impaired.

ACUTE PANCREATITIS

Inflammation of the pancreas damages acinar tissue and leads to focal disruption of small ducts,

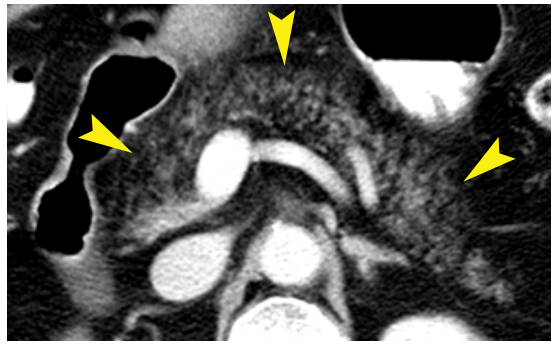

FIGURE 13-4 ■ Fatty infiltration of the pancreas. The pancreas (*arrowheads*) shows fat infiltrating between the atrophic lobules of parenchyma. Despite diffuse atrophy and fatty infiltration, the exocrine and endocrine functions of the pancreas were normal in this elderly patient.

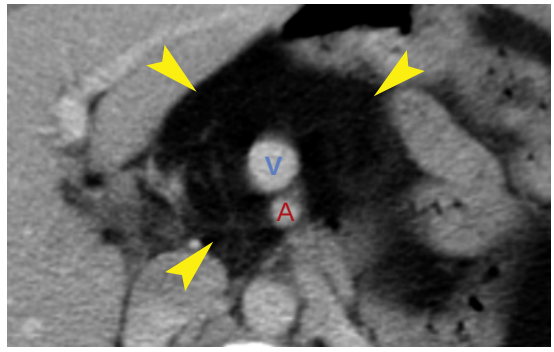

FIGURE 13-5 ■ Cystic fibrosis. Image of the pancreatic head in a patient with cystic fibrosis shows near-complete atrophy of the pancreatic parenchyma (*arrowheads*) with replacement by fat. This is a common computed tomography finding in patients with cystic fibrosis. V, superior mesenteric vein; A, superior mesenteric artery.

resulting in leakage of pancreatic juice. The absence of a capsule around the pancreas allows easy access of pancreatic secretions to surrounding tissues. Pancreatic enzymes digest through fascial layers to spread to multiple anatomic compartments. Acute pancreatitis in adults is most often caused by passage of a gallstone or by alcohol abuse (Table 13-1). The diagnosis of pancreatitis is made clinically by the presence of acute abdominal pain and elevated serum amylase and lipase levels. The role of CT is to document the presence and severity of disease and complications. The severity of CT findings correlates with prognosis. Demonstration of necrotic pancreatic tissue indicative of necrotizing pancreatitis is associated with increased morbidity and mortality. Other prognostic factors associated with increased risk of complications include age, gallstone disease, and organ failure on admission.

TABLE 13-1 Causes of Acute Pancreatitis

Alcohol abuse
Gallstone passage or impaction (most common cause)
Metabolic disorders
Hereditary pancreatitis, autosomal dominant
Hypercalcemia
Hyperlipidemia, types I and V
Malnutrition
Trauma
Blunt abdominal trauma
Surgery
Endoscopic retrograde cholangiopancreatography
Penetrating ulcer
Malignancy
Pancreatic adenocarcinoma
Lymphoma
Drugs (corticosteroids, tetracycline, furosemide, and many others)
Infection
Viral (mumps, hepatitis, infectious mononucleosis, AIDS)
Parasitic (ascariasis, clonorchiasis)
Structural
Choledochocele
Pancreas divisum
Idiopathic (20% of cases of acute pancreatitis)

- *Pancreatic changes* include focal or diffuse enlargement of the pancreas, a decrease in the density of pancreatic parenchyma due to edema, and blurring of the margins of the gland by inflammation. The presence of these findings constitutes interstitial edematous pancreatitis.
- *Peripancreatic changes* include stranding densities in fat and blurring of fat planes with thickening of involved retroperitoneal fascia.

Complications of pancreatitis include the following:

- *Necrosis* is liquefaction of portions of the gland that can be identified by lack of contrast enhancement after bolus contrast administration (Fig. 13-6). Necrotic tissue is highly susceptible to infection, which develops in 30% of patients. Accurate diagnosis requires bolus contrast administration and scanning during the arterial phase of enhancement. The presence of necrosis establishes the diagnosis of necrotizing pancreatitis, which is associated with increased severity of disease and increased risk of death. Long-segment necrosis (>2 cm) is associated with discontinuity of the pancreatic duct and continuing leakage of pancreatic secretions.

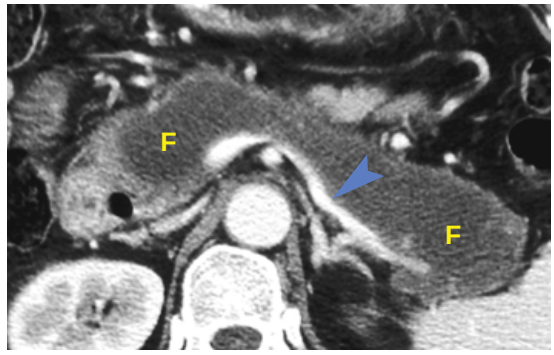

FIGURE 13-6 ■ Necrotizing pancreatitis. Liquefaction necrosis has completely destroyed the pancreas, replacing it with a loculated collection of fluid (F) in the pancreatic bed anterior to the splenic vein (*arrowhead*).

- *Acute peripancreatic fluid collections* are nonencapsulated homogeneous aggregations of fluid in the pancreatic bed and retroperitoneum and often throughout the abdomen (Figs. 13-7 and 13-8). Most acute peripancreatic fluid collections spontaneously resolve within a few weeks.
- *Acute necrotizing collections* contain both fluid and variable amounts of necrotic, nonliquefied material. These collections are highly susceptible to infection. Most necrotic material will liquefy within 6 weeks.
- *Walled-off necrosis* (WON) refers to a fluid collection persisting longer than 4 weeks that contains necrotic pancreatic or peripancreatic tissue. A WON is encapsulated by a thick, nonepithelialized wall. Drainage of the nonliquefied necrotic material may require surgery.
- *Pseudocysts* are well-defined round or oval collections of fluid with a clearly identifiable enhancing fibrous capsule. The fluid collection must remain present for 4 to 6 weeks for the fibrous capsule to form and for the fluid collection to qualify as a pancreatic pseudocyst (Fig. 13-9). By definition, a pseudocyst contains only fluid and can be effectively treated in most cases via catheter drainage.
- *Infection* occurs in 30% to 70% of patients with bacterial growth within necrotic tissues and fluid collections. Infection greatly worsens the prognosis, with mortality rates of 20% to 30% for infected necrosis versus 5% to 10% for sterile necrosis. Fluid collections containing gas (Fig. 13-10) are suspicious for infection, but infected fluid

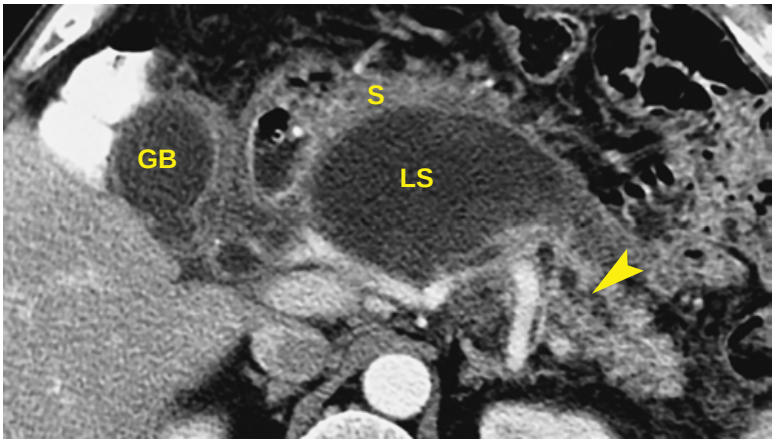

FIGURE 13-7 ■ Acute pancreatitis: fluid collections. Fluid collections resulting from acute pancreatitis extend from the necrotic pancreas into the lesser sac (LS), compressing the stomach (S) and extending around the gallbladder (GB). The distal pancreatic duct *(arrowhead)* is dilated.

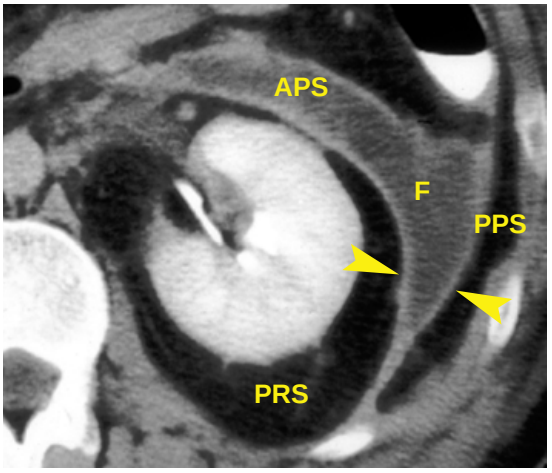

FIGURE 13-8 ■ Acute pancreatitis: fluid collection. Pancreatic fluid (F) and inflammation extend from the pancreas in the anterior pararenal space (APS) partially around the left kidney between the leaves of the posterior renal fascia (*arrowheads*). Note that the perirenal space (PRS) and the posterior pararenal space (PPS) are spared.

collections may be indistinguishable from sterile fluid collections. CT, ultrasonography, or endoscopic ultrasound-guided aspiration is needed to confirm the diagnosis.

- *Hemorrhage* is caused by erosion of blood vessels or bowel tissue. It is seen as high-attenuation fluid in the retroperitoneum or peritoneal cavity. Hemorrhage commonly accompanies necrosis, resulting in the interchangeable terms *hemorrhagic pancreatitis* and *necrotizing pancreatitis.*
- *Pseudoaneurysms* are encapsulations of arterial hemorrhage that have continued communication with the eroded artery. Swirling and back-and-forth blood flow continues within the pseudoaneurysm. The risk of a massive hemorrhage is high. A pseudoaneurysm must be excluded on the basis of contrast-enhanced CT or Doppler ultrasonography findings prior to percutaneous puncture of pancreatic fluid collections (Fig. 13-11). Pseudoaneurysms occur in 3% to 10% of patients with acute pancreatitis.
- *Thrombosis* of the splenic vein and other peripancreatic vessels occurs as a result of the inflammatory process. The thrombosed veins are distended with a low-attenuation thrombus and fail to enhance on venous-phase scans.
- *Pancreatic ascites* is caused by leakage of pancreatic juice into the peritoneal cavity, which induces secretion of fluid from peritoneal membranes. Pancreatic ascites contains a high level of amylase.
- *Recurrence* of acute pancreatitis occurs in half of patients in whom the cause is alcohol abuse.

CHRONIC PANCREATITIS

Chronic pancreatitis is a chronic inflammatory disease of the pancreas characterized by progressive pancreatic damage with irreversible fibrosis. Affected patients have chronic abdominal pain and may develop impairment of the endocrine and exocrine functions of the pancreas. This process results in major structural abnormalities in varying combinations, including parenchymal atrophy, calcifications, stricture and dilatation of the pancreatic duct, fluid collections, pseudomass formation, and alterations in peripancreatic fat. Although many patients with chronic pancreatitis have recurrent episodes of acute pancreatitis, chronic pancreatitis appears to be a separate entity. Patients with chronic pancreatitis are 13 years younger on average than those with acute pancreatitis. Acute pancreatitis seldom results in the development of chronic pancreatitis. Causes of chronic pancreatitis include alcoholism (60%),

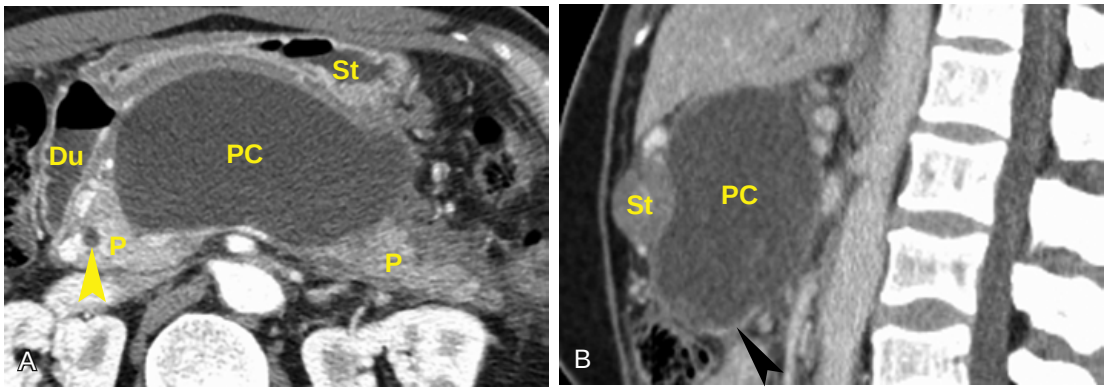

FIGURE 13-9 ■ Pancreatic pseudocyst. *A,* Axial postcontrast computed tomography (CT) image shows a persisting fluid collection (PC) anterior to and compressing the pancreas (P). The stomach (St) is compressed and displaced anteriorly, while the duodenum (Du) is displaced laterally. The common bile duct (*arrowhead*) is seen in the pancreatic head. *B,* A sagittal reconstructed image from the same CT study provides better demonstration of the capsule (*arrowhead*) of the pseudocyst (PC).

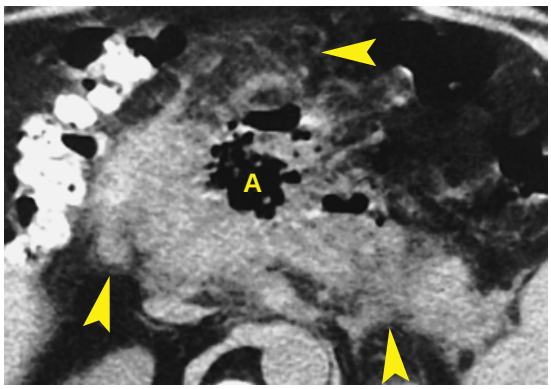

FIGURE 13-10 ■ Pancreatic abscess. A penetrating duodenal ulcer resulted in pancreatitis, a pancreatic abscess, and a pancreaticoduodenal fistula. An extensive gas collection (A) occupies the pancreatic bed. Peripancreatic inflammation (*arrowheads*) blurs the margins of the pancreas and extends into the small-bowel mesentery.

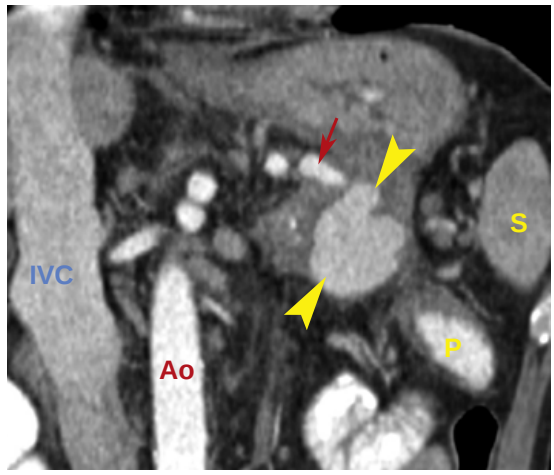

FIGURE 13-11 ■ Pseudoaneurysm. In a patient with acute pancreatitis, postcontrast coronal reconstruction computed tomography shows a lobulated, enhancing pseudoaneurysm (*arrowheads*) arising from the splenic artery (*arrow*). Anatomic landmarks include the aorta (Ao), the inferior vena cava (IVC), the tail of the pancreas (P), and the spleen (S).

hereditary autosomal dominant disorder, autoimmune diseases, tropical pancreatitis, nonalcoholic duct-destructive pancreatitis, and idiopathic causes (30%).

- Calcifications are commonly present (30% to 50% of cases) in focal areas or spread diffusely throughout the pancreas (Fig. 13-12). Calcifications occur within the ductal system and vary in appearance from finely stippled to coarse. Pancreatic calcifications occur most frequently in chronic pancreatitis due to alcoholism and in hereditary pancreatitis.
- The gland is focally or diffusely atrophic in 54% of cases (Fig. 13-13). Atrophy may result in exocrine insufficiency and diabetes mellitus.
- The pancreatic duct has focal strictures and dilated segments in 68% of cases. This "beaded" dilatation is characteristic (Fig. 13-13).
- Focal areas of pancreatic enlargement caused by focal inflammation are common (30% of cases) and must be distinguished from tumors (Fig. 13-14). The presence of calcifications within the mass strongly indicates pancreatitis over a tumor. Percutaneous biopsy guided by ultrasonography or CT, or endoscopic ultrasound-guided biopsy, is commonly needed to make an accurate diagnosis.
- The bile ducts may be dilated because of an inflammatory stricture of the CBD as it passes through the pancreas (Fig. 13-12).

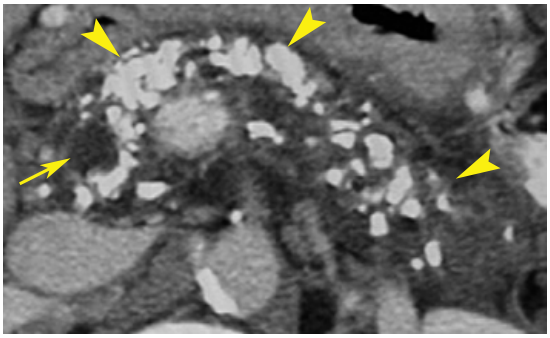

FIGURE 13-12 ■ Chronic pancreatitis: calcifications. Numerous coarse calcifications are seen throughout the pancreas (*arrowheads*) in this patient with recurrent alcoholic pancreatitis. The common bile duct (*arrow*) is mildly dilated because of a benign stricture in the pancreatic head.

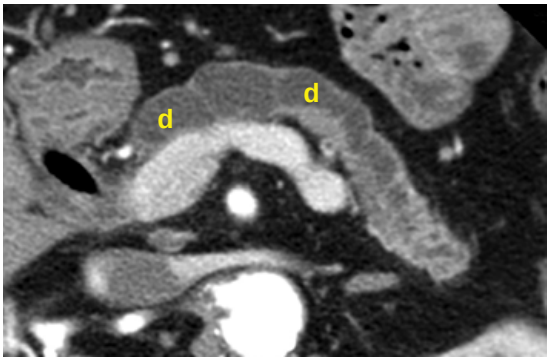

FIGURE 13-13 ■ Chronic pancreatitis: dilated pancreatic duct. The pancreatic duct (d) shows marked beaded dilatation. The pancreatic parenchyma is severely atrophied.

- Fluid collections are caused by superimposed acute pancreatitis (30% of cases).
- Pancreatic pseudocysts are found in 25% to 40% of patients.
- Peripancreatic tissues show inflammatory changes with fascial thickening and stranding densities in peripancreatic fat. These changes result in poor definition of the pancreatic margins.

AUTOIMMUNE PANCREATITIS

Autoimmune pancreatitis is a variant of chronic pancreatitis characterized by periductal lymphoplasmacytic inflammation. Older men aged 60 to 70 years are primarily affected. Patients present with abdominal pain, anorexia, weight loss, and obstructive jaundice. Immunoglobulin G4 levels are elevated, which serves as a marker that distinguishes this condition from neoplastic disease. Other associated conditions include panniculitis, sclerosing cholangitis, ulcerative colitis, fibrosing mediastinitis, and retroperitoneal fibrosis.

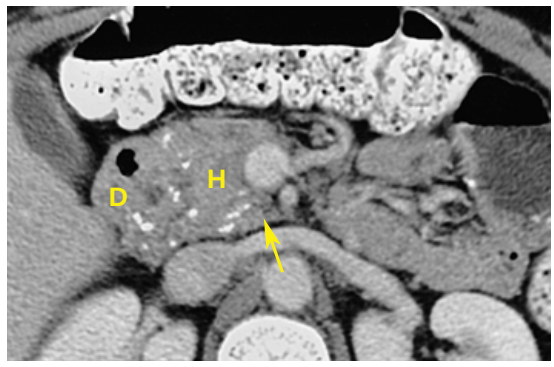

FIGURE 13-14 ■ Chronic pancreatitis: mass. Chronic pancreatitis causes enlargement of the pancreatic head (H) and blunting of the tip of the uncinate process (*arrow*). The mass partially encases the duodenum (D). A benign etiology is suggested by the presence of calcifications, which are common with chronic pancreatitis and rare with pancreatic carcinoma. Compare with Figures 13-16 and 13-17.

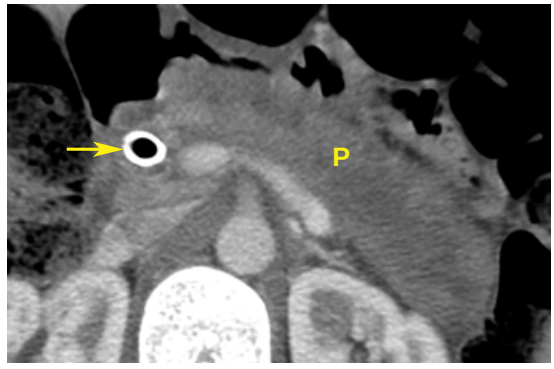

FIGURE 13-15 ■ Autoimmune pancreatitis. Postcontrast computed tomography shows that the pancreas (P) is diffusely enlarged and amorphous with well-defined margins. A wall stent (*arrow*) has been placed in the common bile duct because of a distal stricture associated with autoimmune pancreatitis.

- The pancreas is diffusely enlarged with a characteristic smooth, capsule-like rim, an appearance termed *sausage pancreas* (Fig. 13-15).
- Postcontrast images show weak and delayed enhancement of the parenchyma.
- The pancreatic duct appears diffusely and irregularly narrowed.
- The CBD is often narrowed with a thickened enhancing wall.
- Focal enlargement may occur and mimic neoplasia. Focal autoimmune pancreatitis shows slow progressive enhancement, whereas adenocarcinoma shows persistent low attenuation without notable enhancement. Pancreatic and peripancreatic blood vessels may be narrowed by either condition. Positron emission

tomography combined with CT (PET-CT) reveals characteristic multifocal pancreatic and peripancreatic uptake in autoimmune pancreatitis that is lacking in adenocarinoma.
- Autoimmune pancreatitis characteristically exhibits partial or complete resolution with corticosteroid treatment, a response not observed for other forms of chronic pancreatitis.

GROOVE PANCREATITIS

Groove pancreatitis characteristically involves the groove at the junction of the pancreatic head and the descending duodenum. The wall of the duodenum is thickened and fibrotic and contains cystic lesions. Most affected patients are men aged 30 to 50 years with a history of alcohol abuse. Duodenal obstruction results in severe abdominal pain, nausea, vomiting, and weight loss. The cause of groove pancreatitis is unknown.
- CT shows focal low-attenuation inflammation of the pancreatic head with inflammatory thickening and small cysts in the wall of the duodenum.
- The CBD is smoothly narrowed.
- In a variant form, fibrosis and inflammation occur only in the groove, sparing the pancreatic head.
- Differentiation from adenocarcinoma is difficult. Vascular invasion is strong evidence of tumor tissue. Smooth tapering of the CBD on magnetic resonance cholangiopancreatography indicates groove pancreatitis, whereas an abrupt stricture indicates carcinoma. Table 13-2 lists diagnostic considerations for solid lesions of the pancreas.

ADENOCARCINOMA OF THE PANCREAS

Pancreatic carcinoma is an aggressive and usually fatal tumor. Only 3% of afflicted patients survive for 5 years. The only realistic hope for a cure is early detection and aggressive surgery (Whipple procedure). Most patients are 60 to 80 years of age. Ductal adenocarcinoma accounts for 90% of pancreatic malignancies. CT plays a pivotal role in preoperative staging, separating those patients with an obviously *unresectable* tumor from the 10% to 15% who have *potentially resectable* pancreatic carcinoma. Of the latter patients, 70% to 85% can undergo resection. CT angiography is very helpful in determining vascular involvement by tumor. Unfortunately, most of those who undergo aggressive resection still eventually die of their disease.

TABLE 13-2 Solid Lesions of the Pancreas: Differential Diagnosis

Neoplastic solid tumors
Ductal adenocarcinoma
Pancreatic neuroendocrine tumor
Pancreatic lymphoma
Metastases to the pancreas
Solid pseudopapillary tumor
Pancreaticoblastoma
Acinar cell carcinoma
Mesenchymal tumors (sarcoma, fibrous histiocytoma, etc.)
Nonneoplastic solid lesions
Focal chronic pancreatitis
Autoimmune pancreatitis
Groove pancreatitis
Focal sparing of diffuse pancreatic fatty infiltration
Intrapancreatic accessory spleen
Developmental pancreas lobulation
Sarcoidosis of the pancreas

- The tumor appears as a hypodense mass (96% of cases) that enhances minimally compared with normal pancreatic parenchyma. Because focal chronic pancreatitis may closely simulate malignancy in the pancreas, biopsy is frequently needed to confirm the diagnosis. Calcifications are rarely associated with adenocarcinoma. Tumors are localized in the head (60%), body (15%), and tail (5%), and are diffuse throughout the pancreas in 20% of cases. Table 13-2 outlines the differential diagnosis for solid lesions of the pancreas.
- The tumor may be subtle, appearing as focal enlargement of the pancreas with loss of surface lobulation.
- The pancreatic duct the pancreatic duct or CBD or both are commonly dilated proximal to the tumor.
- Atrophy of pancreatic tissue may occur proximal to the tumor.
- Signs of acute or chronic pancreatitis may be simultaneously present.

Signs of potential resectability include the following:
- Isolated pancreatic mass with or without dilatation of the bile and pancreatic ducts (Fig. 13-16).
- Combined bile/pancreatic duct dilatation without an identifiable pancreatic mass (pancreatic duct >5 mm in head or >3 mm in tail; CBD >9 mm). In 10% of cases the tumor is isoattenuating to pancreatic parenchyma. These patients may

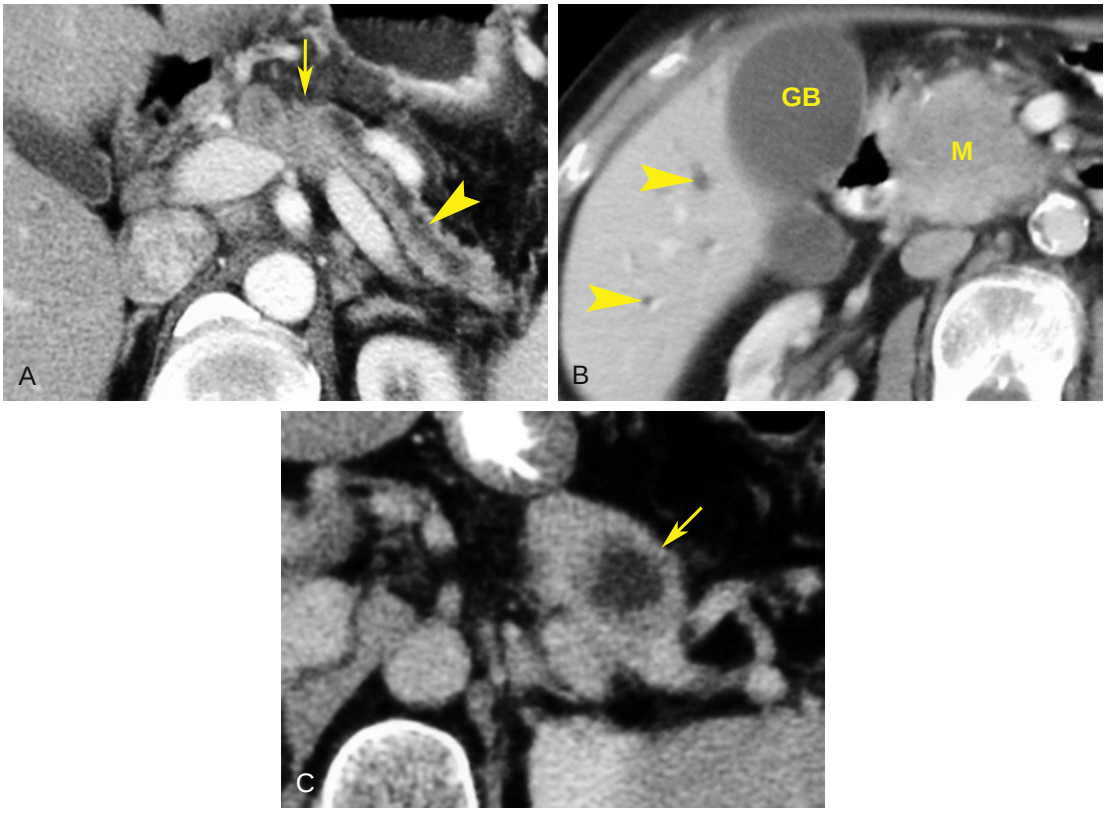

FIGURE 13-16 ■ Potentially resectable pancreatic carcinomas in three patients. *A,* A subtle tumor (*arrow*) in the pancreatic body is detected because it obstructs and dilates the pancreatic duct (*arrowhead*), resulting in atrophy of the pancreatic tail. *B,* A mass (M) in the pancreatic head obstructs the common bile duct, resulting in dilatation of the intrahepatic bile ducts (*arrowheads*) and distention of the gallbladder (GB). *C,* An isolated mass (*arrow*) in the pancreatic tail was discovered incidentally and showed no additional findings. All three lesions were completely resected during surgery.

require MRI or endoscopic ultrasound (US) to define the mass.

- Detectable regional lymph nodes may or may not be involved with tumor. Size of nodes is not a reliable criterion for tumor involvement. The presence of enlarged lymph nodes (>10 mm) does not preclude resectability.
- Fat planes around the celiac axis, SMA, and hepatic artery show no signs of tumor involvement.
- Venous involvement of the SMV or portal vein with tumor abutment but without narrowing of the vessel lumen may allow surgical resection of the tumor with vein reconstruction.

Signs of unresectability include the following:

- Involvement of the major arteries or long-segment involvement or occlusion of the major veins makes the tumor unresectable (Fig. 13-17)
- Extension of the tumor beyond the margins of the pancreas, the presence of liver or distant metastases, and metastases to lymph nodes outside the field of resection
- Tumor tissue invasion of adjacent organs (spleen, stomach, duodenum)
- Tumor encasement (>180°) of the celiac axis, SMA, or aorta, with signs including thickening of the vessels walls; soft tissue involvement of perivascular fat abutting the vessels walls; narrowing, encasement, or distortion of the vessel lumen; and the absence of vessel enhancement, implying occlusion or dilatation of collateral vessels
- Long-segment occlusion of the SMV or portal vein precluding surgical reconstruction
- Ascites, presumptive evidence of peritoneal carcinomatosis, possibly confirmed by paracentesis

NEUROENDOCRINE TUMORS

Neuroendocrine tumors (NETS; previously referred to as islet cell tumors) account for 10%

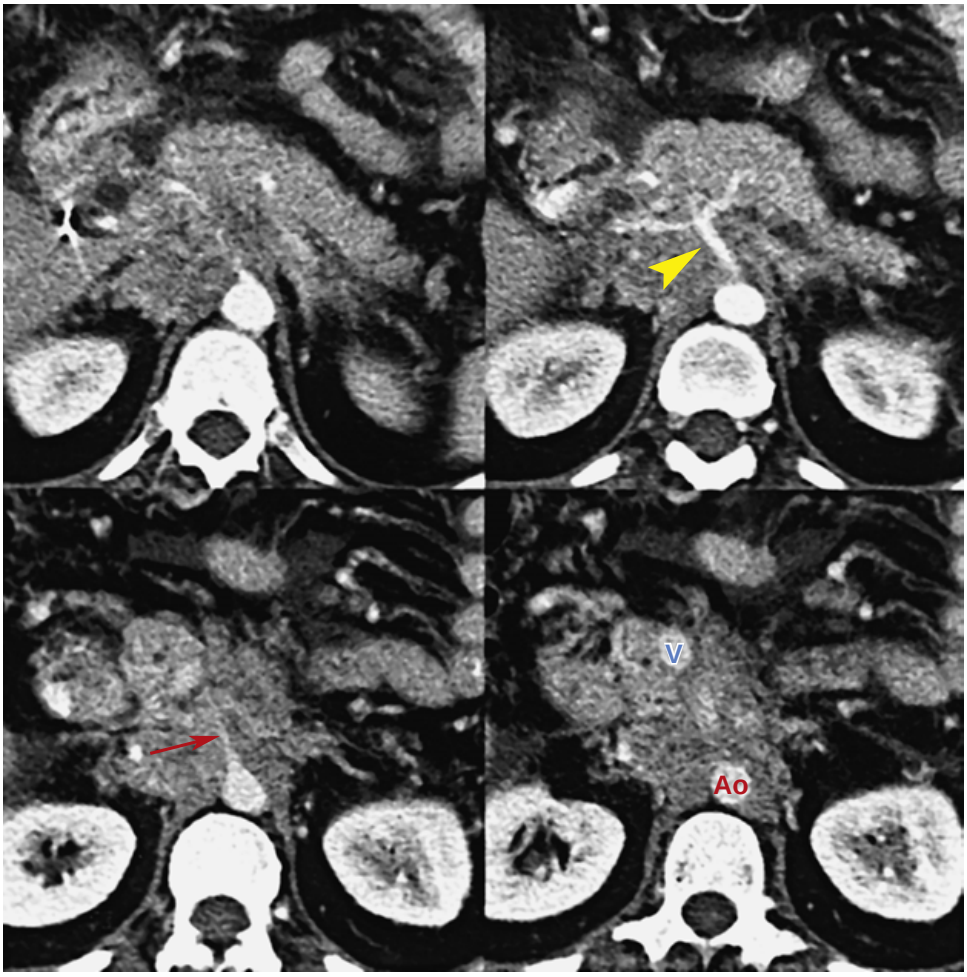

FIGURE 13-17 ■ Unresectable pancreatic carcinoma. Four images from a postcontrast multidetector computed tomography examination demonstrate tumor encasement of the celiac axis (*arrowhead*), the common hepatic artery and splenic artery, the superior mesenteric artery (*arrow*), and the superior mesenteric vein (V). The tumor extensively infiltrates the retroperitoneal fat and partially encases the aorta (Ao).

of all pancreatic neoplasms. Tumors may be functioning and producing metabolically active hormones, with hypersecretion causing clinical symptoms, or may be nonfunctioning, presenting as locally advanced disease with a mass effect, bowel obstruction, or metastases. Up to 25% of NETS are associated with multiple endocrine neoplasia type 1, neurofibromatosis type 1, von Hippel–Lindau syndrome, or tuberous sclerosis. Functioning NETS produce distinct clinical syndromes and usually present while the tumors are small. Nonfunctioning tumors (60% to 80% of pancreatic NETS) are clinically silent until they present with symptoms of a large growing mass. Functioning tumors vary in malignant potential from 10% for insulinoma to 60% for gastrinoma, 70% for glucagonoma, and 75% for vipoma. Up to 90% of nonfunctioning tumors are malignant.

- Small tumors (1to 2 cm) are homogeneous and are usually isodense with the unenhanced pancreas. They enhance brightly and usually uniformly during the arterial phase of contrast administration (Fig. 13-18). Hormone-producing tumors are usually small.
- Large tumors (4 to 20 cm) are usually heterogeneous with calcification, cystic degeneration, necrosis, vascular invasion, and direct tumor extension into adjacent structures (Fig. 13-19). Nonfunctioning tumors are commonly large.
- Metastases (20% of 40% of cases at diagnosis) occur to lymph nodes and the liver and to distant organs (lungs, bones, peritoneal cavity, brain, and breast). Metastases are usually hypervascular and exhibit avid enhancement.

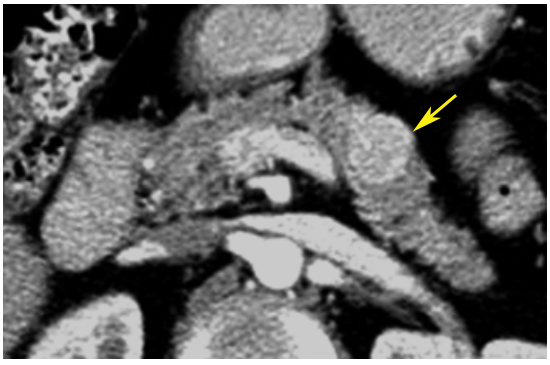

FIGURE 13-18 ■ Small neuroendocrine tumor: insulinoma. A small, insulin-producing neuroendocrine tumor (*arrow*) shows early enhancement on an arterial-phase computed tomography image. The patient presented with episodes of hypoglycemia. Hormone-producing neuroendocrine tumors usually present clinically while they are still small.

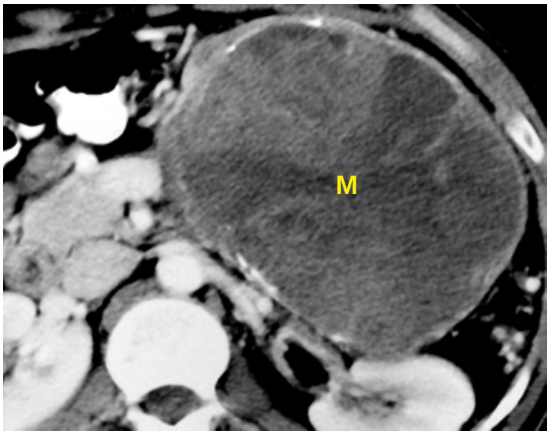

FIGURE 13-19 ■ Malignant nonfunctioning neuroendocrine tumor. A huge, heterogeneous, solid mass (M) arising from the body and tail of the pancreas displaces the bowel and compresses the left kidney. Non-hormone-secreting tumors may grow to a large size before presenting clinically.

PANCREATIC LYMPHOMA

Lymphoma must be differentiated from adenocarcinoma because the diagnosis and treatment are radically different. Lymphoma involves the pancreas most commonly by direct extension from peripancreatic lymphadenopathy. Most are non-Hodgkin's B-cell lymphomas with pancreatic involvement in 30% of patients, especially those with AIDS-related lymphoma. Primary pancreatic lymphoma is rare (less than 0.5% of pancreatic tumors).

- A focal tumor that is well circumscribed with homogeneous attenuation less than that of muscle and weak but uniform enhancement is characteristic. A feature that distinguishes pancreatic lymphoma from adenocarcinoma is that the main pancreatic duct is typically not dilated or is minimally dilated.
- Diffuse infiltration of the pancreas resembles pancreatitis, but without clinical evidence of its occurrence.
- Peripancreatic lymphadenopathy that extends into and displaces the pancreas is characteristic of secondary pancreatic lymphoma (Fig 13-20).
- A bulky mass with no or minimal dilatation of the pancreatic duct strongly indicates lymphoma over adenocarcinoma.
- Lymphadenopathy below the level of the renal veins is seen with lymphoma but not with pancreatic adenocarcinoma.
- Vascular invasion, tumor necrosis, and calcification are rare.

METASTASES TO THE PANCREAS

Metastases to the pancreas are unusual, being present in only 3% to 12% of patients with advanced malignancy. The most common primary tumors are melanoma and carcinomas of the kidney, lung, or breast. Metastases account for 2% to 4% of pancreatic masses.

- Most tumors are round or ovoid with smooth, discrete margins.
- Metastases are found with equal frequency in all portions of the pancreas.
- Most metastases (75%) exhibit heterogeneous contrast enhancement.
- Renal cell carcinoma metastases are often uniformly hypervascular (Fig. 13-21) and resemble NETS.
- Tumors are commonly solitary (50% to 79% of cases) and simulate primary pancreatic adenocarcinoma.
- Diffuse involvement (5% to 44% of cases) causes generalized pancreatic enlargement.
- Multiple nodules are found in 5% to 17% of cases.
- Involvement of pancreatic blood vessels is rare.
- Lesions in the head and neck may obstruct the main pancreatic duct (37% of cases) or CBD.
- Metastases in other organs and at other sites are usually present.

CYSTIC LESIONS

Cystic lesions of the pancreas are being discovered with increasing frequency. While most are benign, many are malignant or potentially malignant and require accurate diagnosis to direct treatment (Table 13-3).

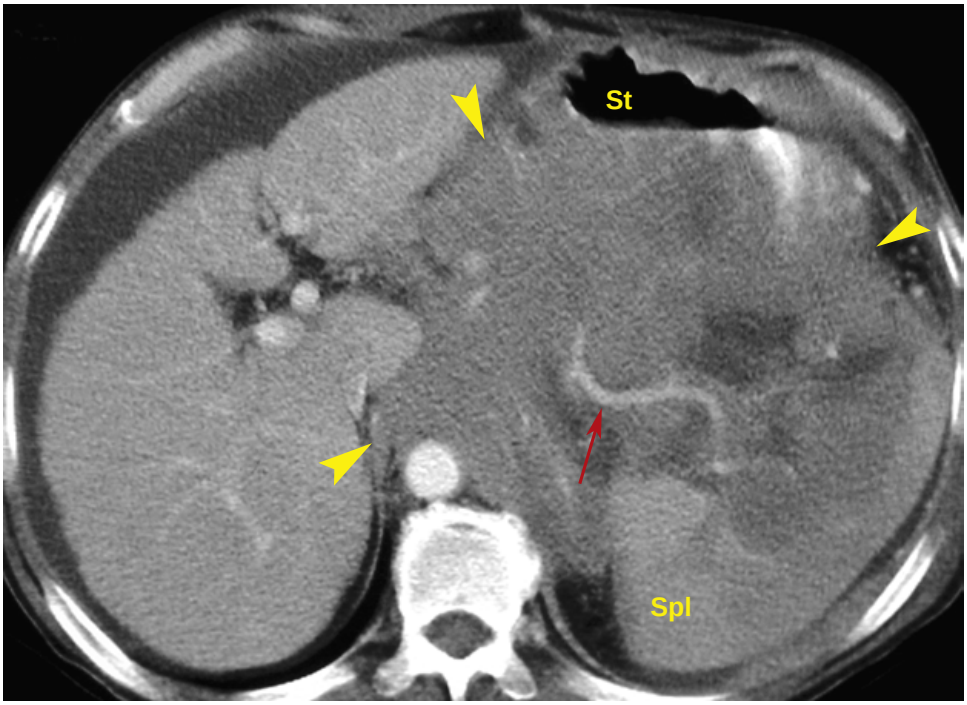

FIGURE 13-20 ■ Lymphoma. Massive confluent adenopathy (*arrowheads*) envelops the pancreas, invades the spleen (Spl), and displays the stomach (St). Only the splenic artery (*arrow*) is clearly visible within the tumor mass.

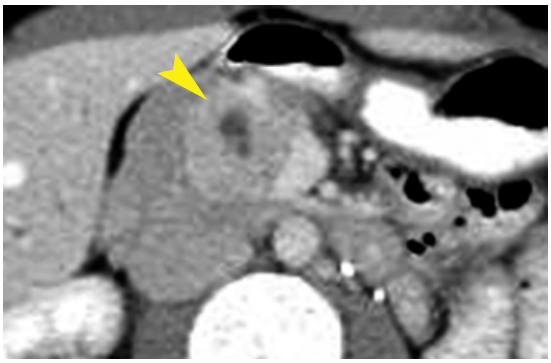

FIGURE 13-21 ■ Metastasis from renal cell carcinoma to the pancreas. The brightly enhancing tumor (*arrowhead*) in the head of the pancreas proved to be a metastasis from renal carcinoma after a nephrectomy carried out years earlier. The tumor shows low-attenuation central necrosis.

TABLE 13-3 **Cystic Lesions of the Pancreas: Differential Diagnosis**

Pseudocyst
Serous cystadenoma
Mucinous cystic neoplasm
Intraductal papillary mucinous neoplasm
Solid and papillary epithelial neoplasm
True epithelial cyst
Duodenal diverticulum
Cystic neuroendocrine tumors
Ductal adenocarcinoma with cystic degeneration
Cystic metastases
Cystic degeneration in sarcoma, hemangioma, and paraganglioma

Pseudocysts

By far the most common cystic lesions in and around the pancreas, pseudocysts are collections of pancreatic fluid that have become encapsulated within fibrous walls. They result from episodes of acute pancreatitis. Although most patients with pancreatitis have abdominal pain, some do not. Pseudocysts must always be included in the differential diagnosis of cystic pancreatic lesions. Fluid aspirated from pseudocysts has high levels of amylase.

- Pseudocysts appear as low-attenuation collections of fluid (Fig. 13-9). Collections are unilocular or multilocular. The fluid attenuation may be higher than that of simple fluid because of the presence of hemorrhage or liquefied cellular debris.
- Distinct walls are well defined and of variable thickness. There is no solid tissue or enhancing components. Calcifications are occasionally present in the cyst wall.
- Most are unilocular. Some contain a few septa.
- Signs of pancreatitis are usually present.

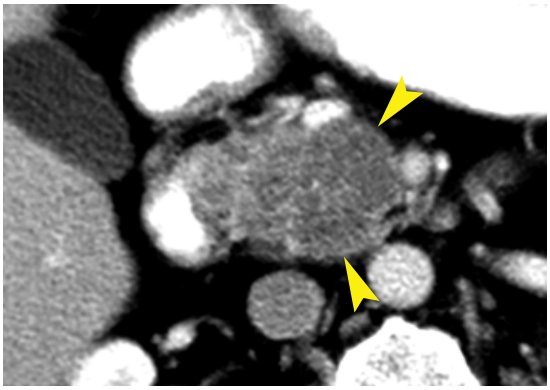

FIGURE 13-22 ■ Serous cystadenoma: honeycomb appearance. This cystic lesion (*arrowheads*) arising in the pancreatic head has somewhat larger cysts that create a honeycomb appearance. The location and appearance are characteristic of serous cystadenoma.

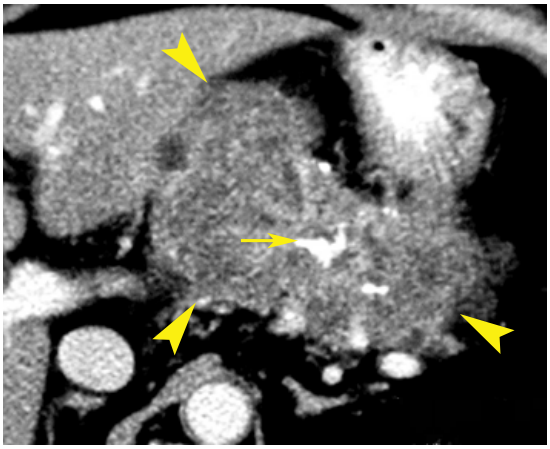

FIGURE 13-23 ■ Serous cystadenoma. Although it consists of innumerable tiny cysts, this tumor (between *arrowheads*) resembles a solid mass. The central calcification (*arrow*) within a stellate scar is characteristic. This is a benign tumor arising from the neck of the pancreas.

Serous Cystadenoma

Serous cystadenomas are benign cystic pancreatic tumors with no malignant potential. Most lesions are discovered incidentally. These tumors are common in patients with von Hippel–Lindau disease. Serous cysts contain clear fluid. Endoscopic ultrasound-guided aspiration that yields clear rather than mucinous fluid helps in confirming the diagnosis. These lesions occur in two morphologic forms.

- The characteristic appearance (present in only 20% of cases) is a well-circumscribed mass of innumerable tiny cysts with a spongy, honeycomb appearance (Fig. 13-22). A central stellate scar, often with calcification (Fig. 13-23), may be present. The innumerable tiny cysts may appear as a solid mass of low attenuation.

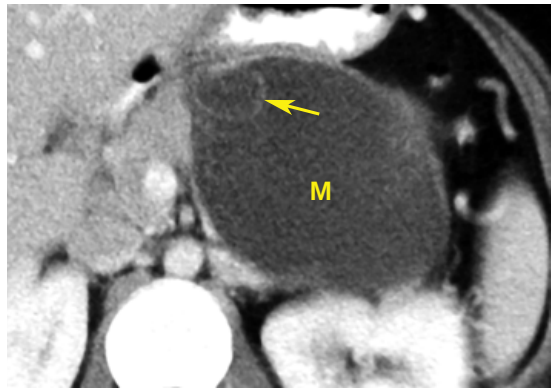

FIGURE 13-24 ■ Mucinous cystic neoplasm. A large cystic mass (M) arises from the body of the pancreas. A thin enhancing septation (*arrow*) is present. The differential diagnosis would include pseudocyst and the macrocystic form of serous cystadenoma.

- The more common unilocular form is 2 to 6 cm in size and may be indistinguishable from mucinous cystic neoplasms. A lobulated contour, the absence of wall enhancement, and a location in the pancreatic head are indicative of serous cystadenoma.
- Serous cystadenomas are most common in the pancreatic head.

Mucinous Cystic Neoplasm

Mucinous cystic neoplasms (MCNs) are rare primary tumors of the pancreas found most commonly in middle-aged women (95% of cases). All are cystadenocarcinomas, although most are of low grade. Low-grade MCNs have an excellent prognosis on surgical resection. High-grade invasive mucinous cystadenocarcinomas (6% to 36% of cases) have a poor prognosis. Histologic identification of ovarian stroma distinguishes MCNs from other pancreatic tumors. Surgical resection is recommended for all MCNs.

- Tumors appear as multiloculated cysts with thin (<2 mm) septa (Fig. 13-24). Six or fewer cysts larger than 2 cm are considered typical of the lesion. CT may not demonstrate the thin septa on unenhanced images, but the septa usually enhance and are well seen following contrast administration.
- Attenuation of fluid within the cyst varies with content (water to mucoid to hemorrhagic density).
- Calcifications are seen in the capsule or septa in 10% of lesions. Peripheral calcifications are characteristic of MCN, while serous cystadenomas have only central calcifications.
- Lesions range in size from 2 to 36 cm, with an average size of 6 to 10 cm.

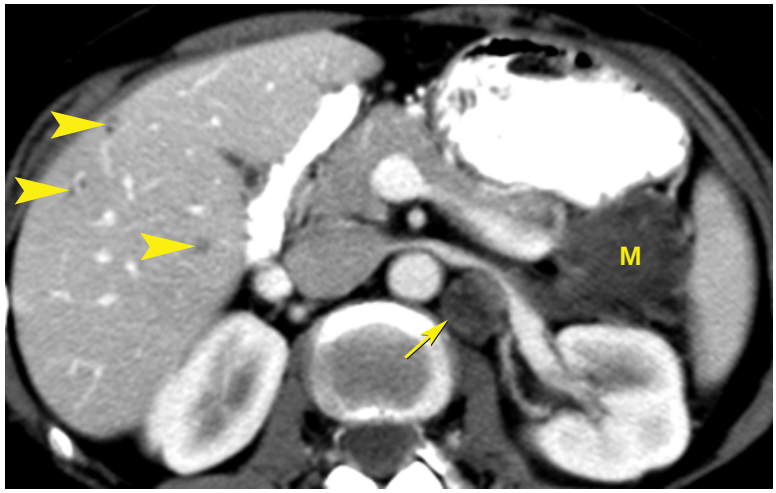

FIGURE 13-25 ■ Mucinous cystic neoplasm: metastases. A low-attenuation cystic mass (M) is evident at the tail of the pancreas. Small low-attentuation lesions (*arrowheads*) in the liver and an enlarged lymph node (*arrow*) behind the left renal vein represent metastatic spread of the malignant tumor.

- Tumors are most common in the distal body and tail of the pancreas.
- These tumors do not communicate with the ductal system of the pancreas.
- Metastases may be evident (Fig. 13-25).

Intraductal Papillary Mucinous Neoplasm

As their name implies, intraductal papillary mucinous neoplasms (IPMNs) secrete mucin into the pancreatic ducts, leading to progressive dilatation of the ducts. IPMNs are divided into main-duct and branch-duct types. Branch-duct tumors have a better prognosis. The prevalence of cancer in branch-duct IPMNs is 15% to 20%, compared to 60% to 92% for main-duct IPMNs. IPMNs arise from the epithelium lining the pancreatic ducts. Histology ranges from hyperplasia to adenocarcinoma. IPMNs are differentiated histologically by the absence of ovarian stroma that characterize MCNs.

- IPMNs arising in the main pancreatic duct lead to marked diffuse or segmental enlargement of the pancreatic duct associated with atrophy of the pancreatic parenchyma (Fig. 13-26). Amorphous calcification may be evident within the dilated duct.
- IPMNs of branch ducts yields a bunch-of-grapes appearance that bulges the contour of the pancreas. Branch-duct IPMNs are most common in the uncinate process (Fig. 13-27).
- Intraductal papillary solid masses may be seen within the dilated pancreatic ducts and serve as strong evidence of malignancy. Dilatation of the main pancreatic duct to greater than 15 mm is also predictive of malignancy.

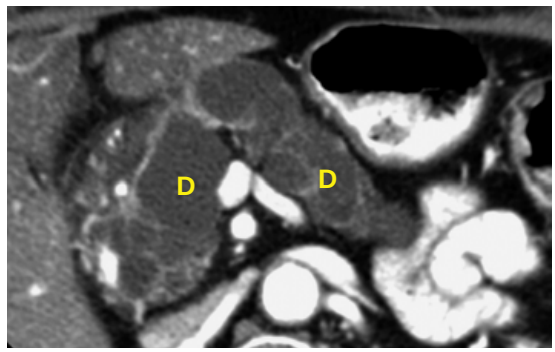

FIGURE 13-26 ■ Intraductal papillary mucinous neoplasm: main-duct type. The main pancreatic duct (D) is massively and diffusely dilated in a beaded pattern. Very little pancreatic parenchyma is visible.

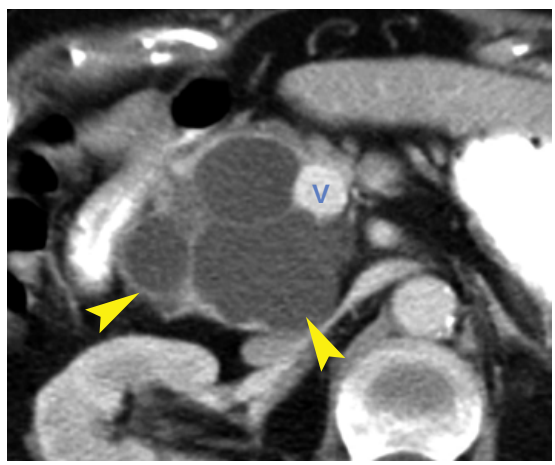

FIGURE 13-27 ■ Intraductal papillary mucinous neoplasm: branch-duct type. A multicystic mass (*arrowheads*) arises from the uncinate process of the pancreas and envelops the superior mesenteric vein (V). Magnetic resonance cholangiopancreatography confirmed communication of the lesion with the pancreatic duct.

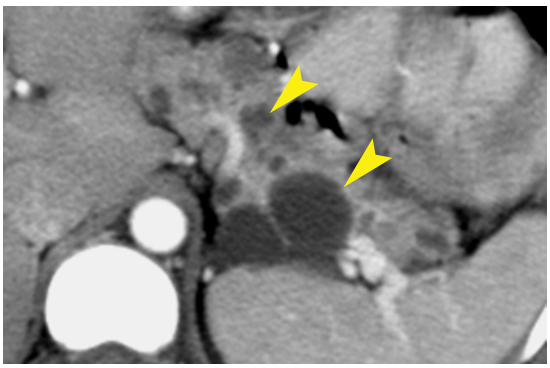

FIGURE 13-28 ■ von Hippel–Lindau syndrome. Multilocular and unilocular cysts (*arrowheads*) are seen throughout the pancreas in this patient with von Hippel–Lindau syndrome.

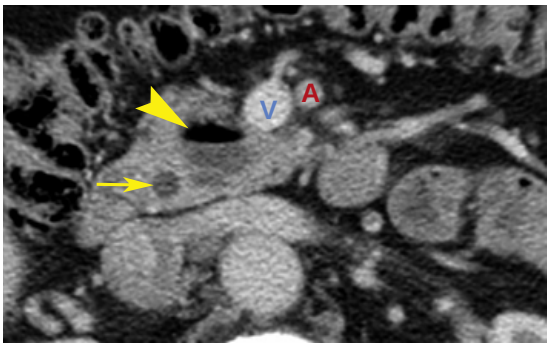

FIGURE 13-29 ■ Duodenal diverticulum. A diverticulum (*arrowhead*) arising from the second portion of the duodenum creates a mass with an air–fluid level in the uncinate process of the pancreas. Duodenal diverticuli may mimic a cystic pancreatic neoplasm or, in the right clinical setting, an abscess. The common bile duct (CBD, *arrow*) courses adjacent to the diverticulum. Occasionally, the CBD may insert into the diverticulum instead of the duodenum. This may result in CBD obstruction. V, superior mesenteric vein; A, superior mesenteric artery.

- Magnetic resonance cholangiopancreatography and endoscopic retrograde cholangiopancreatography reveal the characteristic communication between the IPMN and the pancreatic duct.

True Epithelial Cysts

True pancreatic cysts are rare and are seen far less frequently than pancreatic pseudocysts. Congenital epithelial lined cysts are usually solitary. Multiple pancreatic cysts are seen with von Hippel–Lindau disease (50% of patients) and autosomal dominant polycystic disease (5% of patients). On rare occasions, epithelial-lined cysts are seen in patients with cystic fibrosis.

- Cysts appear as well-defined, fluid-filled masses of various sizes with walls of variable thickness (Fig. 13-28). Internal septa and contrast enhancement are not present.
- In von Hippel–Lindau disease, the pancreas is also involved with serous cystadenomas (12%) and neuroendocrine tumors (7% to 12%). A small number of the neuroendocrine tumors are malignant. The cystic lesions in the pancreas are benign.

Duodenal Diverticulum

Duodenal diverticula are common lesions that may be entirely fluid-filled and mimic a cystic neoplasm of the pancreas (Fig. 13-29).

SUGGESTED READING

Borghei P, Sokhandon F, Shirkhoda A, Morgan DE: Anomalies, anatomic variants, and sources of diagnostic pitfalls in pancreatic imaging. *Radiology* 266:28–36, 2013.

Coakley FV, Hanley-Knutson K, Mongan J, et al.: Pancreatic imaging mimics: Part 1, imaging mimics of pancreatic adenocarcinoma. *AJR Am J Roentgenol* 199:301–308, 2012.

Horger M, Lamprecht H-G, Bares R, et al.: Systemic IgG-4-related sclerosing disease: Spectrum of imaging findings and differential diagnosis. *AJR Am J Roentgenol* 199: W276–W282, 2012.

Khan A, Khosa F, Eisenberg RL: Cystic lesions of the pancreas. *AJR Am J Roentgenol* 196:W668–W677, 2011.

Low G, Panu A, Millo N, Leen E: Multimodality imaging of neoplastic and noneneoplastic solid lesions of the pancreas. *Radiographics* 31:993–1015, 2011.

Mortele KJ, Rocha TC, Streeter JL, Taylor AJ: Multimodality imaging of pancreatic and biliary congenital anomalies. *Radiographics* 26:715–731, 2006.

O'Connor OJ, Buckley JM, Maher MM: Imaging of the complications of acute pancreatitis. *AJR Am J Roentgenol* 197:W375–W381, 2011.

Perez-Johnston R, Sainani NI, Sahani DV: Imaging of chronic pancreatitis (including groove and autoimmune pancreatitis). *Radiol Clin North Am* 50:447–466, 2012.

Raman SP, Salaria SN, Hruban RH, Fishman EK: Groove pancreatitis: Spectrum of imaging findings and radiology-pathology correlation. *AJR Am J Roentgenol* 201:W29–W39, 2013.

Raman SP, Hruban RH, Cameron JL, et al.: Pancreatic imaging mimics: Part 2, pancreatic neuroendocrine tumors and their mimics. *AJR Am J Roentgenol* 199:309–318, 2012.

Sahani DV, Bonaffini PA, Fernandez-Del Castillo C, Blake MA: Gastroenteropancreatic neuroendocrine tumors: Role of imaging in diagnosis and management. *Radiology* 266: 38–61, 2013.

Shanbhogue AKP, Fasih N, Surabhi VR, et al.: A clinical and radiologic review of uncommon types and causes of pancreatitis. *Radiographics* 29:1003–1026, 2009.

Sunnapwar A, Prasad SR, Menias CO, et al.: Nonalcholic, nonbiliary pancreatitis: Cross-sectional imaging spectrum. *AJR Am J Roentgenol* 195:67–75, 2012.

Tanaka M, Chari S, Adsay V, et al.: International consensus guidelines for management of intraductal papillary mucinous neoplasms and mucinous cystic neoplasms of the pancreas. *Pancreatology* 6:17–32, 2006.

Tempero MA, Amoletti JP, Behrman S, et al.: Pancreatic adenocarcinoma. *J Natl Compr Canc Netw* 8:972–1017, 2010.

Thoeni RF: The revised Atlanta classification of acute pancreatitis: Its importance for the radiologist and its effect on treatment. *Radiology* 262:751–764, 2012.

Yu J, Turner MA, Fulcher AS, Halvorsen RA: Congenital anomalies and normal variants of the pancreaticobiliary tract and pancreas in adults: Part 2, pancreatic duct and pancreas. *AJR Am J Roentgenol* 187:1544–1553, 2006.

CHAPTER 14

SPLEEN

William E. Brant

With high-resolution multidetector computed tomography (MDCT) and dynamic multiphase postcontrast protocols, an increasing number of splenic lesions are being detected. These require characterization by combining imaging findings with clinical data. At a minimum, splenic lesions should be characterized as benign or potentially malignant.

ANATOMY

The spleen occupies a relatively constant position in the left upper quadrant of the abdomen. It is a soft and pliable organ that conforms to the shape of adjacent structures (Fig. 14-1). The diaphragmatic surface is smooth and convex, conforming to the dome of the diaphragm, whereas the visceral surface has concavities for the stomach, kidney, and colon. The splenic artery and vein course in close relationship with the pancreas to the splenic hilum, where each vessel divides into multiple branches. The normal spleen has lobulations, notches, and clefts that may be mistaken for abnormalities (Fig. 14-2). Lobulations in the splenic contour can generally be identified on serial slices as part of the spleen. They have sharply defined margins and no perisplenic abnormalities, and they enhance with the remainder of the spleen.

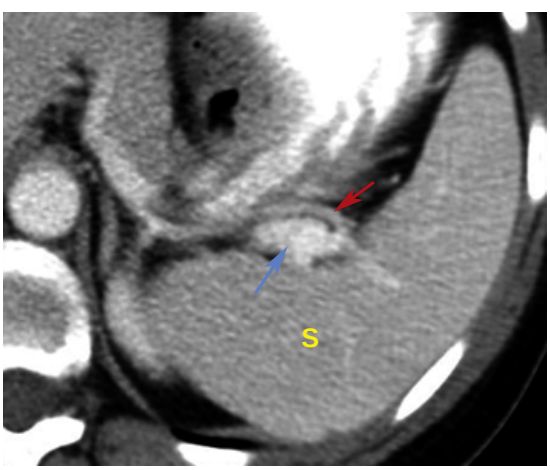

FIGURE 14-1 ■ Normal spleen. Postcontrast computed tomography shows the smooth contours and homogeneously enhanced parenchyma of a normal spleen (S). The splenic artery (*red arrow*) and splenic vein (*blue arrow*) are seen at the hilum of the spleen.

The computed tomography (CT) density of the normal spleen is less than or equal to the CT density of the normal liver. The normal unenhanced attenuation of the spleen is 40 to 60 Hounsfield units (HU), which is 5 to 10 HU less than for the normal unenhanced liver. Most splenic lesions are seen best on contrast-enhanced CT scans.

A heterogeneous, serpentine, cord-like enhancement pattern is expected for the spleen during arterial-phase imaging (Fig. 14-3). This pattern is caused by variable blood flow through the red pulp and white pulp of the normal spleen. Delayed images show uniform enhancement of the splenic parenchyma. Fast contrast injection rates, congestive heart failure, portal hypertension, and splenic vein thrombosis are associated with exaggeration and prolongation of the serpentine enhancement pattern.

TECHNICAL CONSIDERATIONS

The spleen is included on every CT scan of the abdomen. Typically, images are viewed at a slice thickness of 2.5 to 5 mm. Contrast is administered at 2 to 3 mL/second for a total dose of 120 to 150 mL. Routine scans are obtained at 50 to 60 seconds after contrast injection (essentially the portal venous phase). To characterize a splenic mass, after noncontrast imaging, dual-phase postcontrast images are obtained at 30 and 60 seconds.

ANOMALIES

Accessory Spleen

Accessory spleens, or splenules, are nodules of normal splenic tissue that are formed separately from the main spleen. They are present in 10% to 30% of individuals and may be solitary or multiple.

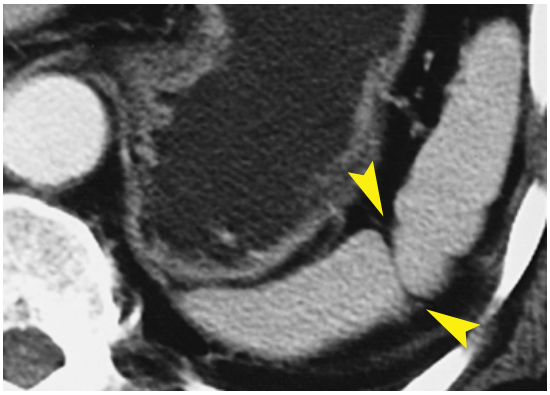

FIGURE 14-2 ■ Normal cleft. A prominent but normal cleft (*arrowheads*) is evident in the spleen.

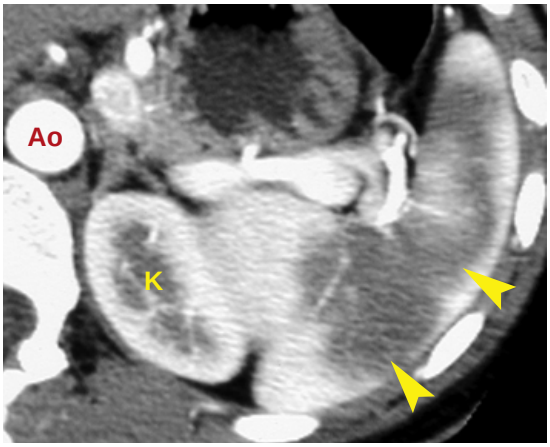

FIGURE 14-3 ■ Normal splenic flow defects. Inhomogeneous enhancement of the spleen produces a pseudomass effect (*arrowheads*) during the early stage of intravenous contrast medium administration using a power injector. The bright enhancement of the aorta (Ao) and enhancement of only the cortex of the kidney (K) indicate the early arterial stage of contrast enhancement. Images obtained a few minutes later (not shown) demonstrated uniform density of the spleen.

- Splenules appear as round or oval masses of up to 2 to 3 cm in diameter, most commonly located in the hilum of the spleen (Fig. 14-4).
- They have the same CT density, tissue texture, and enhancement pattern as the main spleen.
- Accessory spleens may hypertrophy after splenic resection.

Wandering Spleen

Wandering spleen refers to a normal spleen that is found outside the left upper quadrant of the abdomen. Congenital laxity of the ligaments, often associated with anomalies of intestinal fixation, allows the spleen to be freely mobile and to

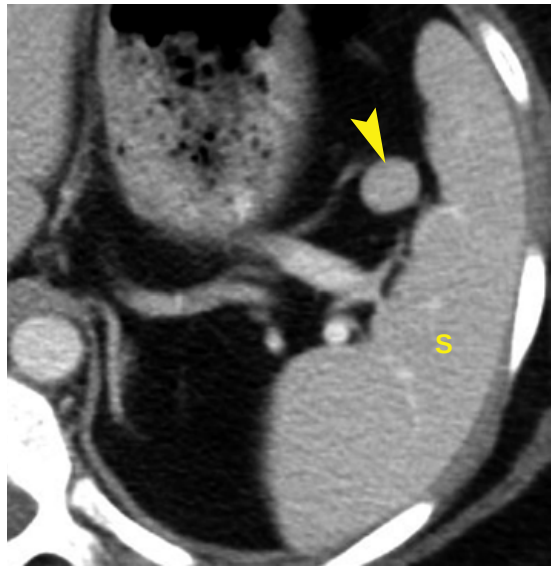

FIGURE 14-4 ■ Accessory spleen. An accessory spleen (*arrowhead*) is evident near the hilum of the spleen (S).

be located anywhere in the abdomen. Wandering spleens are usually asymptomatic but may be a cause of a palpable abdominal mass and are more susceptible to traumatic injury and torsion.

- The diagnosis is made by noting the absence of a normal spleen in its typical location and recognizing that the ectopic mass is supplied by splenic vessels.

Splenic Regeneration/Splenosis

Remnants of splenic tissue after splenic injury and remnant accessory spleens may hypertrophy after splenectomy, resulting in single or multiple left upper-abdominal masses. The diagnosis is suggested clinically when a patient with a history of splenectomy has no Howell–Jolly bodies on a peripheral blood smear. Howell–Jolly bodies are remnants of nuclear material in red blood cells that are usually removed from the circulating blood by splenic tissue.

- Regenerative splenic remnants have the CT appearance of abnormally shaped splenic tissue with an otherwise normal appearance (Fig. 14-5). The presence of splenic tissue may be confirmed by technetium-99m sulfur colloid radionuclide imaging.

Splenomegaly

Spleen size varies with age, body habitus, state of hydration, and nutrition. The spleen normally decreases in size with age. The causes of splenomegaly are exhaustive but can be classified into myeloproliferative, infectious, congestive, and

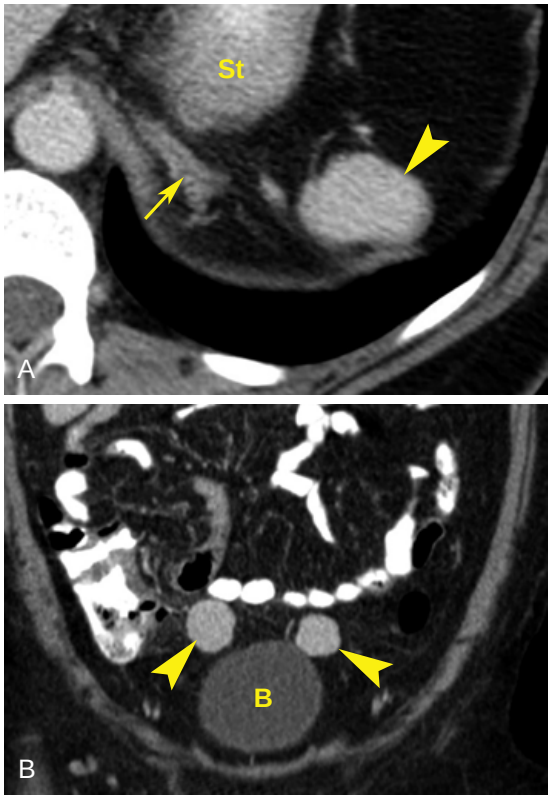

FIGURE 14-5 ■ Splenic regeneration. *A,* In a patient who underwent splenectomy for a severely shattered spleen, contrast-enhanced computed tomography shows a uniformly enhancing rounded mass (*arrowhead*) in the splenic bed. Anatomic landmarks include the stomach (St) and left adrenal gland (*arrow*). *B,* A coronal image of the same patient shows similar enhancing rounded masses (*arrowheads*) near the bladder (B). A technetium sulfur colloid radionuclide scan confirmed that functioning splenic tissue regenerated from remnants of the shattered spleen.

infiltrative categories. Most conditions do not affect the CT density of the spleen, so differentiation is based on other CT findings or clinical evaluation.

- Size greater than 12 to 14 cm in any dimension is a primary sign of splenomegaly in adults.
- Extension of the spleen tip inferior to the lower pole of the left kidney is an imaging sign of splenomegaly.

FOCAL LESIONS

Cysts

Cystic lesions of the spleen have a variety of etiologies. An accurate diagnosis can usually be made by correlating CT findings with the medical history and clinical findings.

FIGURE 14-6 ■ Post-traumatic cyst. Liquefaction of an old hematoma resulted in the formation of this cystic mass (*arrow*) with a densely calcified thickened wall.

- *Post-traumatic cyst* is the most common splenic cyst, accounting for 80% of all splenic cystic lesions. This cyst results from previous hemorrhage, infarction, or infection, and basically represents the end stage of an intrasplenic hematoma. It is a false cyst without an epithelial lining. The wall is fibrous tissue of variable thickness. Internal debris, fluid levels, and milk of calcium are common features. Calcification is found in the wall in 30% to 40% of cases (Fig. 14-6).
- *Congenital epithelial-lined cysts* are true cysts with epithelium lining the cyst wall. Other terms for this entity include epidermoid cyst and mesothelial cyst. The cysts are usually solitary and account for up to 20% of splenic cysts. CT reveals a well-defined, spherical, and usually unilocular cyst with thin walls (Fig. 14-7). The cyst contents are of water density without contrast enhancement. Internal debris is sometimes present. Calcification is found in the walls in about 5% of cases.
- *Echinococcal cysts* may be indistinguishable from traumatic and epithelial cysts but are rare in the United States. Patients have abdominal pain, fever, and splenomegaly. The lesion consists of a larger mother cyst containing smaller daughter cysts near the periphery. Ring-like calcification of the walls of the mother cyst and the internal daughter cysts is common. Hydatid sand appears as layering internal debris of higher density than that of the cyst fluid. Less than 2% of patients with hydatid disease have splenic involvement. Because of the risk of spontaneous or

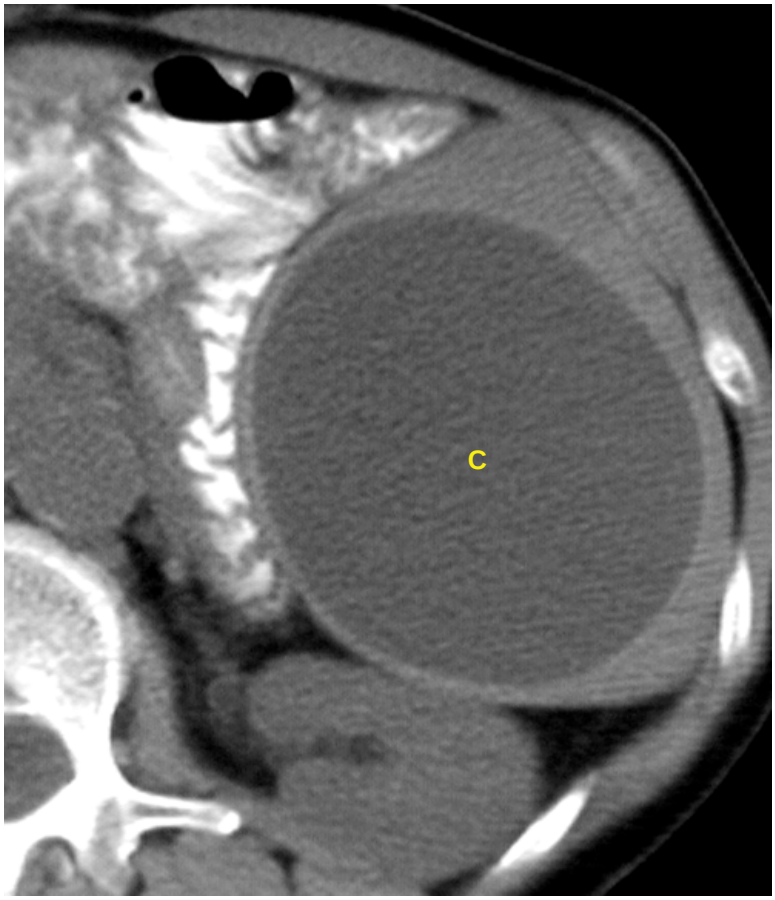

FIGURE 14-7 ■ Epidermoid cyst. A large cyst (C) expands the spleen, compressing the left kidney and displacing the bowel, on this noncontrast computed tomography image.

FIGURE 14-8 ■ Pancreatic pseudocysts. Subcapsular fluid collections associated with acute pancreatitis are present in the spleen (S) and liver (L). Loculated fluid is also seen in a recess of the lesser sac (LS). High amylase content of the fluid was confirmed by computed tomography-guided aspiration and drainage.

post-trauma rupture, splenic echinococcal cysts are usually treated surgically.

- *Pancreatic pseudocysts* result from pancreatitis in which fluid gains access to the splenic parenchyma from the pancreas via dissection through the splenic hilum (Fig. 14-8). CT demonstrates a characteristically subcapsular fluid collection of water attenuation. Findings for pancreatitis are usually present.

Infarction

Splenic infarctions may be asymptomatic or present with left upper-quadrant pain. Causes

FIGURE 14-9 ■ Infarction. The spleen shows multiple low-attenuation lesions extending to the splenic capsule in this patient with splenomegaly related to chronic lymphocytic leukemia. While some lesions are wedge-shaped, others are not. Extension to the splenic capsule is the most characteristic finding of splenic infarction.

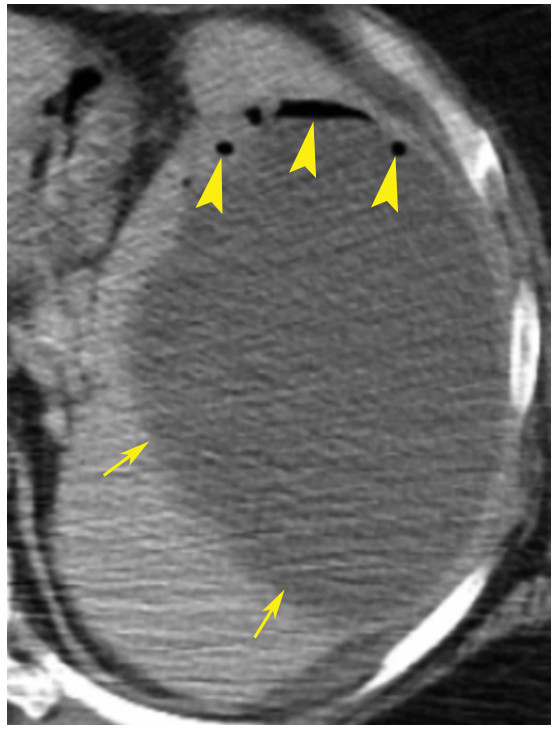

FIGURE 14-10 ■ Abscess. Computed tomography image of a leukemia patient shows a large fluid collection (*arrows*) within the enlarged spleen. Gas bubbles (*arrowheads*), which rise nondependently within the fluid, are strong evidence of abscess.

include involvement of splenic vessels by atherosclerosis, arteritis, tumor, or pancreatitis. Additional causes include systemic emboli and sickle disease. Splenomegaly is a predisposing factor for infarction. Infarcts easily become infected if the patient develops bacteremia.

- The classic appearance of an acute infarction is a wedge-shaped, low-attenuation defect that extends to the splenic capsule. Extension to the splenic capsule is the characteristic finding, as many splenic infarcts are not wedge-shaped (Fig. 14-9).
- Infarctions will atrophy over time, resulting in depressed areas and notching of the splenic contour. Calcifications may occur in the infarcted area.

Bacterial Abscesses

Bacterial abscesses occur uncommonly but are associated with high mortality when untreated. Signs and symptoms may be vague. Diseased spleens are particularly susceptible to abscess formation when organisms are delivered hematogenously from distant foci of infection. Abscesses may also result from spread of infection from adjacent organs or from suppuration in a traumatic hematoma. Patients are often debilitated by diabetes, immune system compromise, or intravenous drug abuse.

- Abscesses appear on CT as single or multiple low-density areas with ill-defined walls, which may be thickened and enhance with contrast medium. Internal attenuation is 20 to 40 HU. Abscesses may contain gas (20%) or demonstrate fluid levels. Gas within the splenic fluid collection is considered to be diagnostic of abscess (Fig. 14-10). Percutaneous aspiration of infected fluid confirms the diagnosis. The treatment recommended is catheter drainage or splenectomy.

Microabscesses

Patients who are immunocompromised due to AIDS, chemotherapy, lymphoma, leukemia, or organ transplantation may develop microabscesses caused by opportunistic infections. Causes include fungi (*Candida*, *Aspergillus*, *Cryptococcus*, *Histoplasma*), tuberculosis, *Pneumocystis jiroveci* (*carinii*), and cytomegalovirus.

- Multiple low-density defects in the spleen are 2 to 3 mm (up to 10 mm) in size (Fig. 14-11).

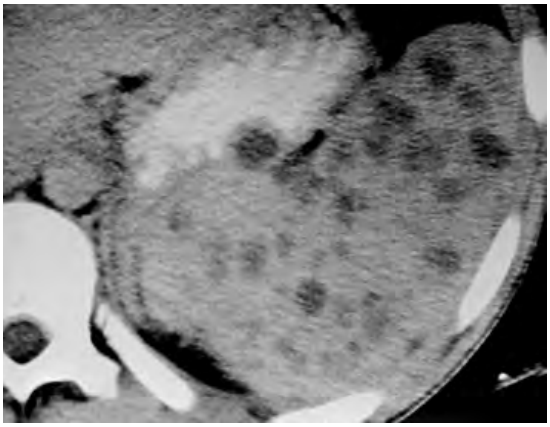

FIGURE 14-11 ■ Microabscesses. Many ill-defined, low-attenuation lesions are seen in the spleen in this patient with acute myelogenous leukemia. The lesions resulted from *Candida albicans* sepsis.

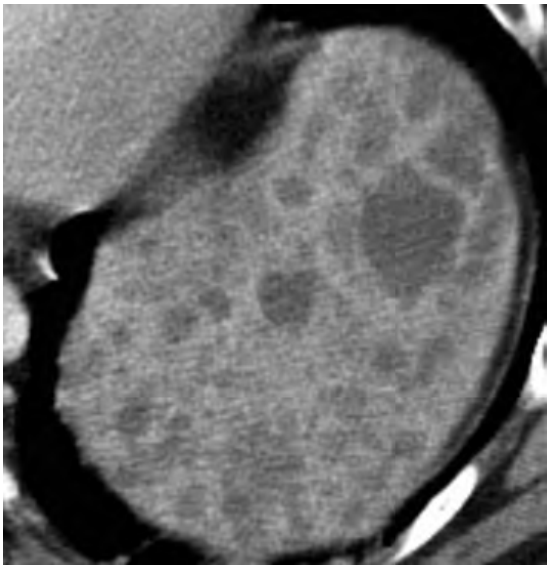

FIGURE 14-12 ■ Kaposi's sarcoma. Computed tomography of the spleen in a patient with AIDS and cutaneous lesions of Kaposi's sarcoma shows innumerable low-attenuation lesions throughout the spleen that are indistinguishable from the microabscesses of opportunistic infection.

- The differential diagnosis of multiple small, low-density splenic defects includes lymphoma, Kaposi's sarcoma (Fig. 14-12), sarcoidosis, and metastases.

Lymphoma

The spleen is the largest lymphoid organ in the body, so it is hardly surprising that involvement by lymphoma is common. Primary splenic lymphoma is rare, but secondary involvement of the spleen by systemic lymphoma is common. Approximately one-third of all patients with lymphoma have involvement of the spleen. CT is not reliable in the detection of lymphomatous involvement. The spleen may be normal yet involved, or may be enlarged and not involved. Focal lesions are a reliable sign of disease.

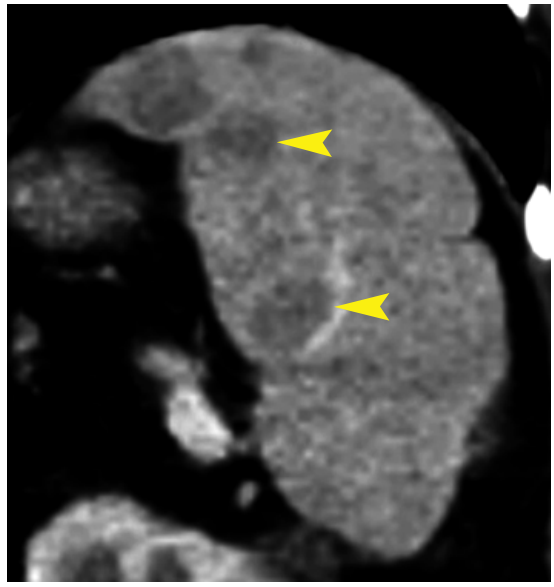

FIGURE 14-13 ■ Lymphoma. A coronal computed tomography image of the spleen shows multiple ill-defined, low-attenuation lesions (*arrowheads*) that proved to be non-Hodgkin's lymphoma.

- Diffuse infiltration may result in homogeneous enlargement without masses.
- Multiple lesions are the most characteristic. They vary from a miliary pattern of tiny lesions up to lesions of 2 to 10 cm in size. Lesions do not enhance on intravenous contrast administration (Fig. 14-13).
- A solitary large mass may represent a confluent deposit of lymphomatous tissue.
- Enlarged nodes are usually seen in the splenic hilum, along the splenic vessels, and elsewhere in the abdomen.

Metastases

Melanoma and lung, breast, and ovarian carcinomas are the most common sources of splenic metastases. Metastases are surprisingly uncommon and are seen in only 7% of patients with widespread malignancy. Melanoma is the source of 50% of the splenic metastases detected on imaging studies. Lesions appear late in the course of the disease.

- Most metastases appear as ill-defined, low-density, but not water-density, nodules with some degree of peripheral enhancement (Fig. 14-14).

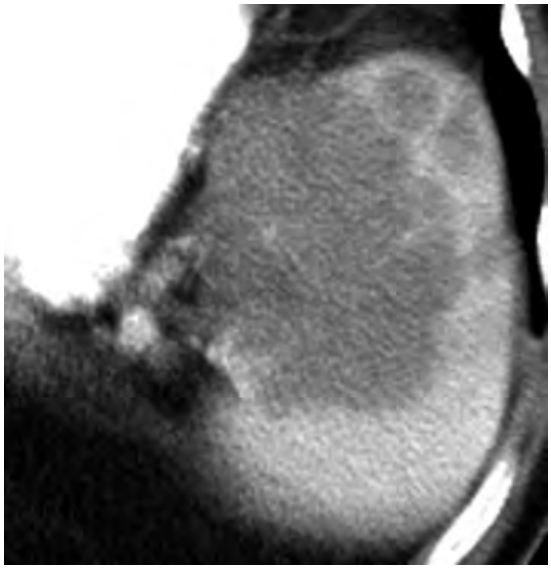

FIGURE 14-14 ■ Metastases. Metastases from malignant melanoma cause multiple homogeneous, low-attenuation lesions in the spleen.

FIGURE 14-15 ■ Sarcoidosis. Multiple ill-defined, low-attenuation lesions (*arrowheads*) of the spleen represent the noncaseous granulomas of sarcoidosis. The appearance overlaps that of microabscesses, metastases, lymphoma, and Kaposi's sarcoma.

- Melanoma commonly causes well-defined cystic metastases.
- Isolated splenic lesions seen in patients with known malignancy are usually not metastases unless widespread metastatic disease is present.

Sarcoidosis

Sarcoidosis is a systemic granulomatous disease that may involve many abdominal organs, particularly the liver and spleen. About 60% of patients with sarcoidosis have involvement of the spleen. Liver involvement is even more common but is often not detectable with CT.

- Sarcoidosis of the spleen may cause splenomegaly or be evident as single or multiple low-attenuation nodules with indistinct margins (Fig. 14-15).

Hemangioma

Although unusual, hemangiomas are the most common neoplasm of the spleen. As in the liver, the lesions consist of endothelial-lined, blood-filled spaces of varying size. Most are asymptomatic, but very large hemangiomas may cause pain and splenomegaly. Confident diagnosis may be difficult because of wide variations in appearance.

- The lesions may appear cystic or solid on unenhanced CT. They may be solitary or multiple. Size varies from 1 to 15 cm. Klippel–Trenaunay–Weber syndrome is associated with multiple splenic hemangiomas that appear strikingly cystic.
- Following contrast administration, splenic hemangiomas may exhibit characteristic nodular enhancement from the periphery that is very similar to the enhancement pattern of liver hemangiomas (Fig. 14-16). However, atypical patterns of enhancement are common.
- Some lesions remain hypodense, whereas others enhance uniformly during arterial-phase contrast.
- Central punctate or peripheral curvilinear calcifications may be present.

Lymphangioma

Lymphangioma is an uncommon splenic tumor that is usually small and asymptomatic.

- On CT lymphangiomas are usually small, multiple, homogeneous, and cystic in appearance with an internal attenuation of 15 to 35 HU. They exhibit no contrast enhancement and are typically subcapsular in location.

Hamartoma

Hamartomas are rare lesions consisting of a mixture of normal elements of splenic tissue. They may be single or multiple and are associated with tuberous sclerosis.

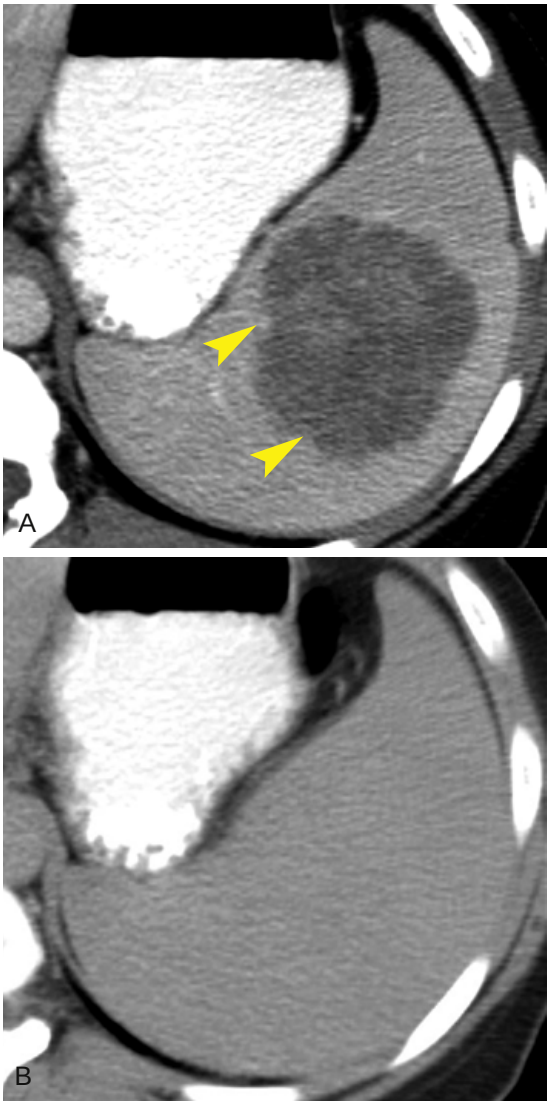

FIGURE 14-16 ■ Hemangioma. *A,* A relatively early postcontrast image shows small nodules of peripheral enhancement (*arrowheads*). *B,* A delayed postcontrast scan shows that the lesion has become isodense with the splenic parenchyma and is no longer evident.

- The CT appearance may be similar to that of splenic hemangioma. However, differentiation is usually not important, as both are benign lesions.
- Lesions are of low attenuation or isointense to spleen on noncontrast CT (Fig. 14-17) and show slow enhancement after contrast administration, usually becoming isointense on delayed postcontrast images. The lesion typically bulges the contour of the spleen. Central punctate or peripheral curvilinear calcifications may be present.

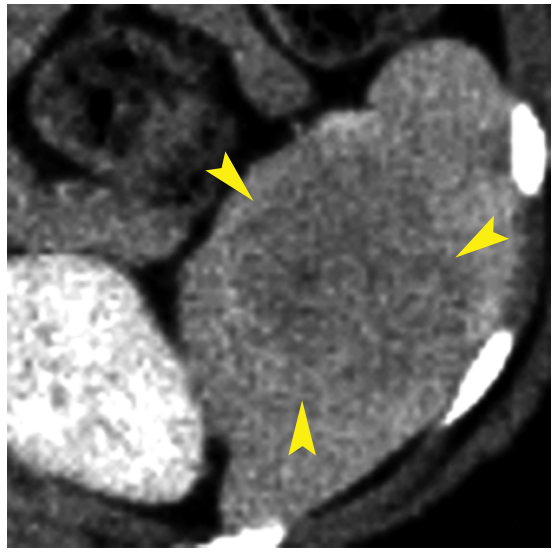

FIGURE 14-17 ■ Hamartoma. A large but subtle, poorly defined lesion (*arrowheads*) in the spleen proved to be a splenic hamartoma on biopsy.

Angiosarcoma

Angiosarcoma is a very rare primary malignancy of the spleen. The tumor is aggressive, usually presenting with widespread metastases, especially to the liver. Most patients die of their disease within 12 months. The tumor may spontaneously rupture and hemorrhage into the peritoneal cavity.

- Multiple discrete, but poorly defined, enhancing nodules are the most common CT appearance.
- Angiosarcoma may also appear as a complex mass of cystic and solid components that enhance irregularly (Fig. 14-18).
- The spleen is usually enlarged.

Splenic Calcifications

Splenic calcifications are a frequent CT finding.

- Multiple small focal calcifications (Fig. 14-19) in a spleen with an otherwise normal appearance are the result of previous infection with histoplasmosis or tuberculosis.
- Larger, coarser calcifications result from previous infarction, infection, or trauma.
- Sickle hemoglobinopathy alone or in combination with thalessemia or hemoglobin C disease can result in infarction and calcification of the entire spleen, which atrophies and becomes functionless.

FIGURE 14-18 ■ Angiosarcoma. A complex mass of low- and high-density components with tangled enhancing vessels replaces most of the splenic parenchyma. Metastatic tumor is the cause of enlargement of a lymph node (N) in the splenic hilum.

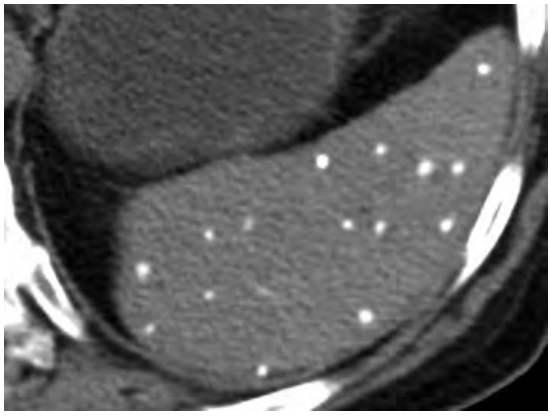

FIGURE 14-19 ■ Calcified granulomas. Calcified granulomas without an associated mass are seen in the spleen on this noncontrast computed tomography image. These were most likely caused by histoplasmosis.

SUGGESTED READING

Abbott RM, Levy AD, Aguilera NS, et al.: Primary vascular neoplasms of the spleen: Radiologic–pathologic correlation. *Radiographics* 24:1137–1163, 2004.

Ahmed S, Horton KM, Fishman EK: Splenic incidentalomas. *Radiol Clin North Am* 49:323–347, 2011.

Kaza RK, Azar S, Al-Hawary MM, Francis IR: Primary and secondary neoplasms of the spleen. *Cancer Imaging* 10:173–182, 2010.

Lake ST, Johnson PT, Kawamoto S, et al.: CT of splenosis: Patterns and pitfalls. *AJR Am J Roentgenol* 199:W686–W693, 2012.

Mortele KJ, Mortele B, Silverman SG: CT features of the accessory spleen. *AJR Am J Roentgenol* 183:1653–1657, 2004.

Saboo SS, Krajewski KM, O'Regan KN, et al.: Spleen in haematological malignancies: Spectrum of imaging findings. *Br J Radiol* 85:81–92, 2012.

Singh AK, Shankar S, Gervais DA, et al.: Image-guided percutaneous splenic interventions. *Radiographics* 32:523–534, 2012.

Urritia M, Mergo PJ, Ros LH, et al.: Cystic lesions of the spleen: Radiologic-pathologic correlation. *Radiographics* 16:107–129, 1996.

CHAPTER 15

KIDNEYS AND URETERS

William E. Brant

KIDNEYS

Anatomy of the Retroperitoneal Space

A detailed understanding of the retroperitoneal fascial planes and compartments is a prerequisite for accurate interpretation of abdominal computed tomography (CT). The retroperitoneal space between the diaphragm and the pelvic brim is divided into three main compartments—the anterior pararenal, perirenal, and posterior pararenal spaces—by the anterior and posterior renal fascia (Fig. 15-1).

The *anterior pararenal space* extends between the posterior parietal peritoneum and the anterior renal fascia. It is bounded laterally by the lateroconal fascia, which is the continuation of the posterior layer of the posterior renal fascia. The pancreas, duodenal loop, and ascending and descending portions of the colon are within the anterior pararenal space.

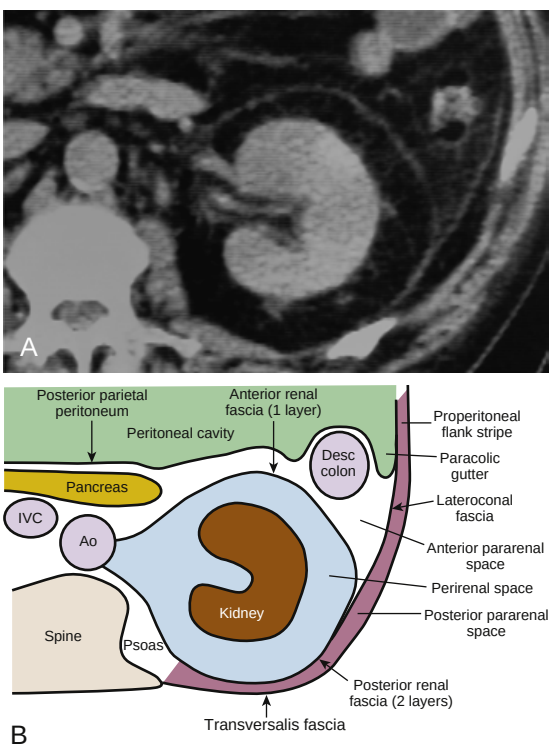

FIGURE 15-1 ■ Retroperitoneal anatomy. *A*, Computed tomography image of the left kidney. *B*, Diagram demonstrating the fascial planes and compartments of the retroperitoneum. Desc, descending; IVC, inferior vena cava; Ao, aorta.

The anterior and posterior renal fasciae encompass the kidney, renal pelvis, proximal ureter, adrenal gland, and perirenal fat within the *perirenal space*. The perirenal space is an inverted cone shape extending from the diaphragmatic fascia to the iliac fossa. The anterior renal fascia (Gerota fascia) is thin and consists of one layer of connective tissue. The posterior renal fascia (Zuckerkandl fascia) is thicker and consists of two layers of connective tissue. The anterior layer of the posterior renal fascia is continuous with the anterior renal fascia. The posterior layer of the posterior renal fascia is continuous with the lateroconal fascia and forms the lateral boundary of the anterior pararenal space. The anterior and posterior layers of the posterior renal fascia may be separated by inflammatory processes, such as pancreatitis, extending from the anterior pararenal space. The perirenal space is discontinuous across the midline due to fusion of the renal fascial layers with connective tissues surrounding the aorta and inferior vena cava (IVC). The perirenal space on the right abuts the bare area of the liver, allowing spread of inflammatory and neoplastic processes from the right kidney to the liver. On the left the perirenal space abuts the left subphrenic space. The ureter passes through the apex of the cone of the perirenal space as it courses to the pelvis.

The *posterior pararenal space* is a potential space, usually occupied only by fat, extending from the posterior renal fascia to the transversalis fascia. The posterior pararenal fat continues into the flank as the properitoneal fat stripe seen on conventional radiographs of the abdomen. This compartment is limited medially by the lateral edge of the psoas and quadratus lumborum muscles.

The kidneys are covered by a tight, fibrous capsule that produces a sharp margin defined by perirenal fat on CT. Subcapsular collections of

fluid or blood compress and distort the renal parenchyma, often without affecting the perirenal fat. The perirenal fat extends into the renal sinus, outlining blood vessels and the renal collecting system. Connective tissue septa extend between the kidney and the renal fascia. These septa divide the perirenal space into multiple compartments and may be seen as prominent stranding densities in the perirenal fat when they are thickened by inflammation, hemorrhage, or ischemia. The renal arteries and veins can be identified from the great vessels to the kidneys. The right renal artery courses behind the vena cava. The left renal vein crosses between the aorta and the superior mesenteric artery. The aorta and IVC and their branches are invested by fascial layers that usually, but not always, prevent communication with the para- and perirenal spaces.

Technical Considerations

Because the kidneys actively concentrate contrast medium within the parenchyma, most renal abnormalities are best seen on CT after intravenous (IV) contrast medium administration. Unenhanced CT is performed to demonstrate calcifications and calculi that may be obscured by contrast agent. Multidetector helical CT (MDCT) is optimal for renal evaluation and is the current technique of choice. The sensitivity for detection of renal masses varies considerably with imaging modality: 67% for traditional excretory urography, 79% for sonography, and at least 95% for MDCT.

CT for Renal Masses

To evaluate renal masses, MDCT is used with contiguous thin slices for a single breath hold at identical locations before and after bolus contrast administration.

- MDCT protocols use collimation as thin as 0.625 mm for a single breath hold of 15 to 20 seconds. Axial images are usually viewed at a slice thickness of 2.5 to 5 mm. Highly detailed reconstructions are routinely made in coronal and sagittal planes.
- A *precontrast scan* is performed through both kidneys (Fig. 15-2*A*) to document the presence of calculi and calcifications and to serve as a baseline to assess lesion enhancement.
- IV administration of 100 to 150 mL of 60% iodine nonionic contrast is delivered by a power injector at 2.5 to 3.0 mL/second.
- A *corticomedullary-phase scan* is obtained using a 30-second scan delay (Fig. 15-2*B* and *C*). This scan extends from the dome of the diaphragm through the bottom of the kidneys. Scanning is performed during this phase to evaluate other abdominal organs for metastatic disease and to evaluate the renal arteries and veins.
- A *nephrogram-phase scan* is obtained at 80 to 90 seconds after contrast injection (Fig. 15-2*D*). The scan extent includes only the kidneys from top to bottom.
- A *pyelogram-phase scan* is obtained at 3 to 5 minutes after injection.
- The scan may be continued through the pelvis to evaluate the retroperitoneum, ureters, and bladder.

Corticomedullary-Phase Scans

When scanning the abdomen for reasons other than renal mass characterization, renal images are commonly obtained with contrast enhancement

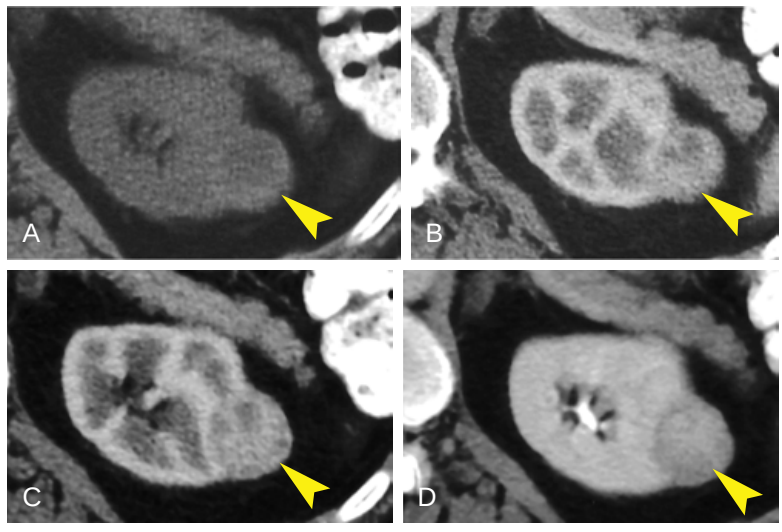

FIGURE 15-2 ■ Computed tomography (CT) of a renal mass. *A*, Noncontrast, *B* and *C*, corticomedullary-phase, and *D*, nephrogram-phase images from a MDCT study demonstrate a small renal carcinoma (*arrowheads*) arising from the left kidney. The tumor is nearly isointense with the renal parenchyma in the noncontrast image. Early arterial enhancement of the tumor coincides with enhancement of the renal cortex in the corticomedullary phase images. The tumor is mildly hypointense compared with the renal parenchyma during the nephrogram phase.

limited to the renal cortex (Fig. 15-2*B* and *C*). The corticomedullary phase is usually seen at about 30 to 50 seconds after contrast injection into an arm vein. This phase is of limited use for detection of renal masses, because only the renal cortex is enhanced and the medullary portions of the kidney remain unenhanced. The corticomedullary phase defines the renal artery and vein better than the nephrogram phase does.

CT Urogram

The CT urogram (CT-IVP, CT intravenous pyelogram) has evolved as the imaging method of choice to provide the most comprehensive evaluation of the urinary tract, often used in the setting of hematuria. A noncontrast CT scan is obtained from the kidneys through the bladder to document the presence of calculi or parenchymal calcifications. The renal parenchyma is evaluated in the nephrogram phase. The collecting system and ureters are documented by MDCT with thin collimation and coronal reformation of the ureters. The bladder is best evaluated when distended with urine. The patient is instructed to avoid urination before the examination, or if present the Foley catheter is clamped.

- No bowel preparation or oral contrast is needed.
- A precontrast (stone protocol) CT from the top of the kidneys through the base of the bladder is obtained.
- A volume of 125 to 150 mL of 60% iodine nonionic contrast is injected intravenously at 3 to 4 mL/second.
- A nephrogram-phase scan is obtained at a delay of 80 seconds using 2.5-mm or thinner collimation and a single breath hold.
- A pyelogram-phase scan is obtained at 5 to 8 minutes after contrast injection using thin slices (1.25 mm) through the full length of the kidneys, ureters, and bladder. Images are reconstructed in axial, coronal, and sagittal planes (Fig. 15-3).

Stone Protocol CT

Renal stone CT (sometimes called CT-KUB, denoting CT of the kidneys, ureters, and bladder) is noncontrast MDCT of the urinary tract used to diagnose the presence of urinary tract calculi and to detect acute urinary obstruction caused by stones.

- No oral or IV contrast is administered.
- Data acquisition is continuous from the top of the kidneys through the base of the bladder (mid-T-12 level through the symphysis pubis) using collimation of 0.625 to 2.5 mm. Images may be viewed at a slice thickness of 1.25 to 2.5 mm. Thin slices allow identification of very small stones that may be overlooked with thicker slices.
- Turning the patient to the prone position will allow differentiation of stones impacted at the ureterovesical junction (UVJ) from stones that have already passed into the bladder.
- When noncontrast renal stone CT is equivocal, IV contrast may be given to clarify the diagnosis.

Horseshoe Kidney

Congenital fusion of the lower poles of the kidneys is a relatively common (1 to 4 cases per 1000 individuals) congenital anomaly.

- The isthmus extends across the aorta just below the origin of the inferior mesenteric artery, which prevents normal ascent of the kidneys to the renal beds (Fig. 15-4). The tissue connecting the lower poles of the kidneys may be functioning renal parenchyma or fibrous bands.
- The fused kidneys are low in position and malrotated, with the renal pelvis directed anteriorly and the lower poles converging instead of diverging. Malposition is associated with multiple renal arteries of anomalous origin and urinary stasis, often resulting in stone formation and recurrent infection.
- Transitional cell carcinoma (TCC) is three to four times more common in horseshoe kidneys than in the general population.

Renal Masses

Features that must be evaluated to characterize a renal mass are the presence and type of calcification, attenuation of the mass before and after contrast administration, the margin of the mass with the kidney and with surrounding tissues, and the presence and thickness of septa and the wall thickness of cystic masses. Artifactual pseudoenhancement, related to the beam hardening effect from iodinated contrast, may increase the attenuation of lesions by up to 10 Hounsfield units (HU). Attenuation must increase by a *minimum of 20 HU* following bolus IV contrast administration to be considered enhancement. An increase in attenuation of less than 10 HU is not considered enhancement. An increase in attenuation of 10 to 20 HU is equivocal enhancement.

Renal Cell Carcinoma

Renal cell carcinoma (RCC) accounts for 90% of solid tumors of the kidney. Most large lesions can

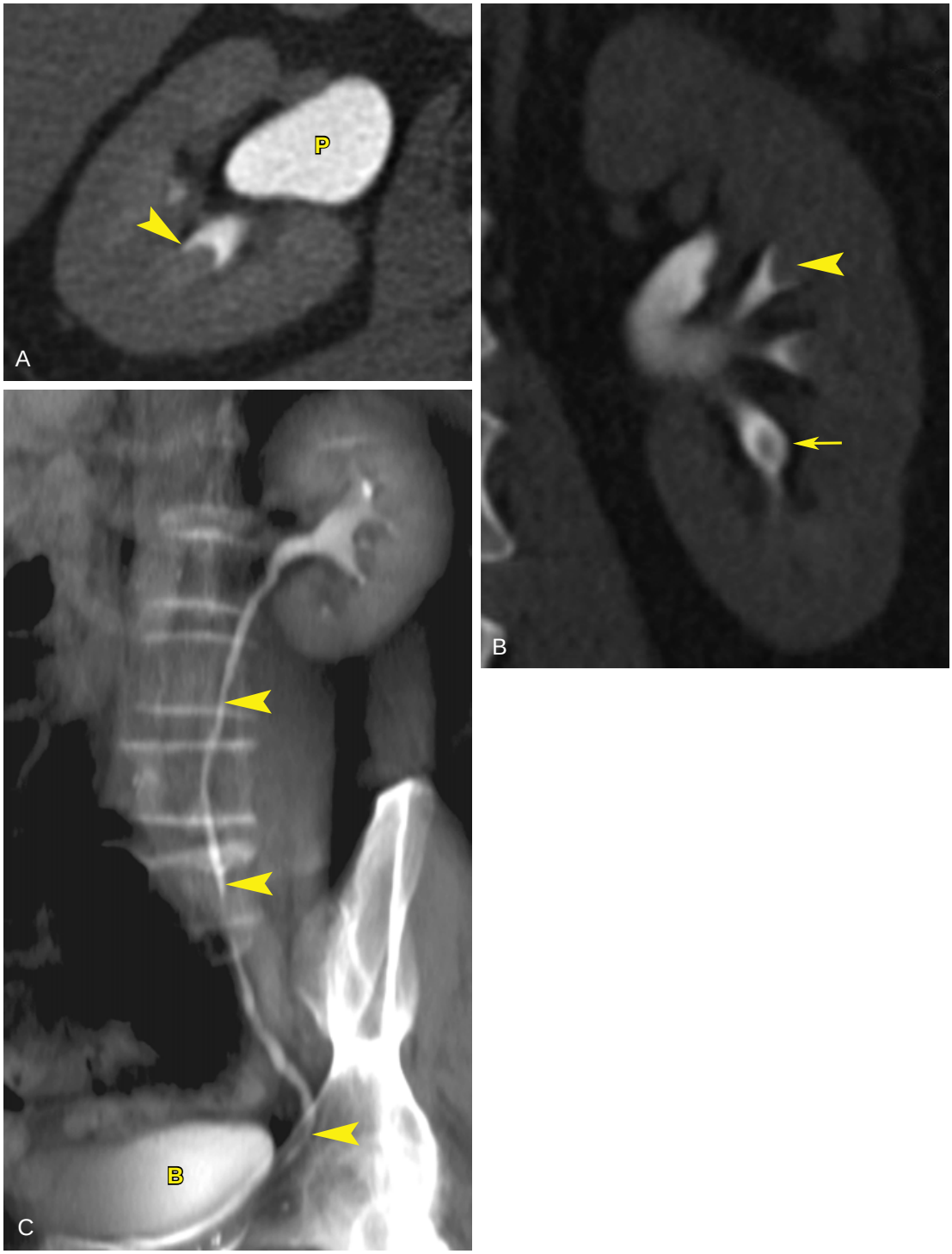

FIGURE 15-3 ■ Computed tomography (CT) intravenous pyelogram. *A*, Axial CT image of the right kidney during the pyelogram phase shows the contrast-opacified renal pelvis (P) and the normal cup shape of the renal calyx with sharp forices (*arrowhead*). The medullary pyramid of the renal lobe fits into the calyceal cup. *B*, Coronal view of the left kidney shows normal calyces appearing as cup-shaped (*arrowhead*) or circular (*arrow*) structures, depending on the plane of the CT section. *C*, An oblique view of the left ureter (*arrowheads*), collecting system, kidney, and bladder (B) was created from a series of thin-slice axial CT images. This nicely demonstrates the course and size of the ureter. Portions of the normal ureter may be nonopacified because of ureteral peristalsis.

be easily diagnosed by CT. Small lesions are commonly indeterminate. About 15% to 20% of small, solid renal tumors are benign. Histologic subtypes of RCC have distinctive imaging findings and vary in prognosis.

- Clear cell, also called conventional, RCC accounts for 70% of RCCs. Tumors are typically heterogeneous with mixtures of solid tissue, cysts, and foci of hemorrhage and necrosis (Fig. 15-5). Tumors arise from the renal cortex and show expansile growth with hypervascularity. Tumor enhancement exceeds 84 HU in the corticomedullary phase and 44 HU in the excretory phase. Multicentric and bilateral tumors are rare (<5%). Clear cell RCC has the least favorable prognosis.
- Multilocular cystic RCC is a variant of clear cell RCC. Clusters of cysts of variable size are bound by a thin, fibrous capsule and have septa of variable thickness that contain clear cell RCC (Fig. 15-6). About 20% have calcification in the wall or septa.
- Papillary (chromophil) RCC accounts for 10% to 15% of RCCs. It occurs most commonly in end-stage kidney failure. On CT it appears as hypovascular, homogeneous solid tumors. Enhancement is far less prominent than with clear cell RCC (Fig. 15-7). Bilateral and multicentric tumors are more common than with other cell types. As the tumors become large, they may develop hemorrhage, necrosis, and calcification. Very rarely tumors may contain macroscopic fat due to the presence of cholesterol-filled macrophages. Cystic papillary RCCs have enhancing nodules or papillary projections that project from the cyst wall (see Fig. 15-24). On discovery, 70% of papillary RCCs are confined to the kidney, resulting in a good prognosis after surgical removal.
- Chromophobe RCCs account for 5% of RCCs. On ultrasound, small chromophobe RCCs appear homogeneously hyperechoic, mimicking the appearance of small angiomyolipoma (AML). This finding necessitates the performance of CT or magnetic resonance (MR) imaging to differentiate the two lesions. Characteristically, chromophobe RCCs show homogeneous enhancement, even when large. A spoke-wheel pattern of enhancement for some tumors mimics oncocytoma. Most tumors (86%) are stage 1 or 2 on discovery, resulting in a relatively good prognosis.
- Hereditary cancer syndromes are associated with early development of multicentric and bilateral RCCs accounting for 5% of RCCs. von Hippel–Lindau syndrome is associated with clear cell RCC, whereas Birt–Hoff–Dube

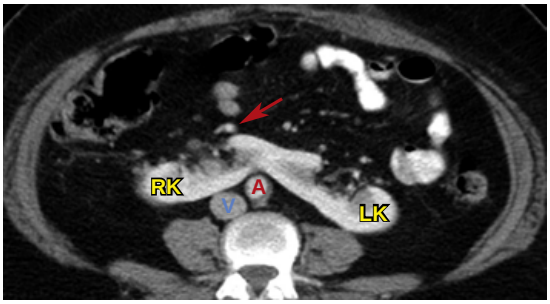

FIGURE 15-4 ■ Horseshoe kidney. The lower poles of the right kidney (RK) and left kidney (LK) are fused across the midline anterior to the aorta (A) and inferior vena cava (V). The fused kidney is held low in position within the abdomen because its ascent to a normal location is impaired by the origin of the inferior mesenteric artery (*arrow*).

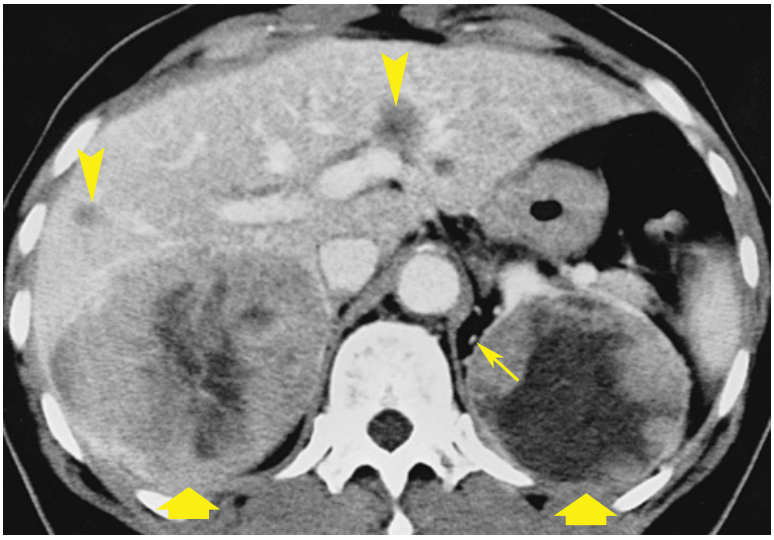

FIGURE 15-5 ■ Bilateral clear cell renal cell carcinomas. Renal cell carcinomas (*short fat arrows*) arise from the upper poles of both kidneys. The low-attenuation regions within the tumors are foci of necrosis and hemorrhage. Enhancing tumor vessels (*thin arrow*) are seen in the perirenal fat. Metastases are present in the liver (*arrowheads*).

syndrome is associated with chromophobe RCC.
- Other rare cell types each account for less than 1% of RCCs. Renal medullary carcinoma is associated with sickle cell trait. Collecting-duct RCC is highly aggressive. Mucinous tubular and spindle cell RCCs are found predominantly in women. Translocation (juvenile) RCCs occur in children and young adults.
- On unenhanced CT, RCCs contain noncalcified solid areas measuring 20 to 70 HU. Homogeneous lesions with attenuation outside this range tend to be benign. This finding is of increasing importance because current practice favors the performance of increasing numbers of unenhanced abdominal CTs.
- Small, solid renal lesions (<3 cm) are being discovered with increasing frequency by CT, MR imaging, or ultrasound. Benign and malignant lesions overlap in appearance, with 15% to 20% of these small lesions being benign. The differential diagnosis includes RCC, oncocytoma, angiomyolipoma without visible fat, papillary adenoma, and metanephric adenoma. Percutaneous biopsy is used to diagnose these lesions prior to percutaneous ablation procedures or surgery.

CT Staging of RCC

RCC responds poorly to all types of radiation therapy and chemotherapy despite many innovative new therapy attempts. The only completely effective therapy remains surgical excision or percutaneous ablation of all of the tumor. CT is highly accurate in assisting the urologist in planning surgery or ablation procedures. Nephron-sparing surgery with partial nephrectomy performed laparoscopically or with robotics or procedures such as radiofrequency ablation and cryoablation decrease the morbidity for treatment of small tumors. Immunotherapy shows promise in the treatment of advanced disease.

- Extension of tumor tissue through the renal capsule into the perinephric fat is not accurately demonstrated by CT. However, this differentiation does not affect the surgical approach to the lesion.
- Tumor tissue may grow into the main renal vein (20% to 35% of cases) and IVC (4% to 10% of cases). Venous invasion consists of tumor tissue growing within the vein, often associated with variable amounts of

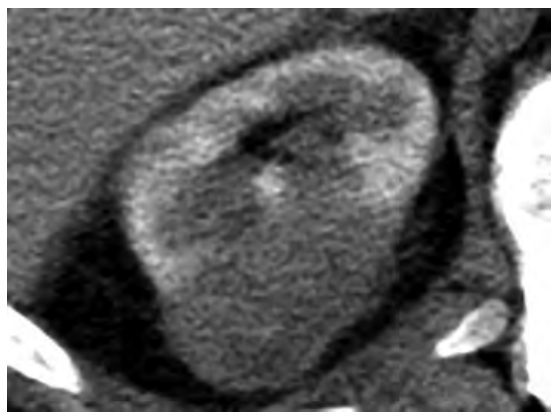

FIGURE 15-7 ■ Papillary renal cell carcinoma. Computed tomography image during the corticomedullary phase of contrast enhancement shows low-grade enhancement within a poorly defined mass arising from the right kidney.

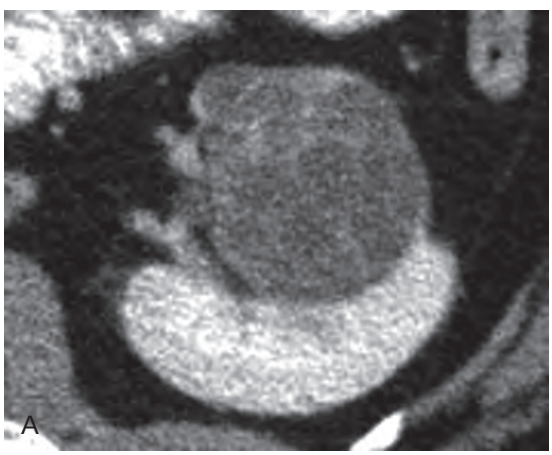

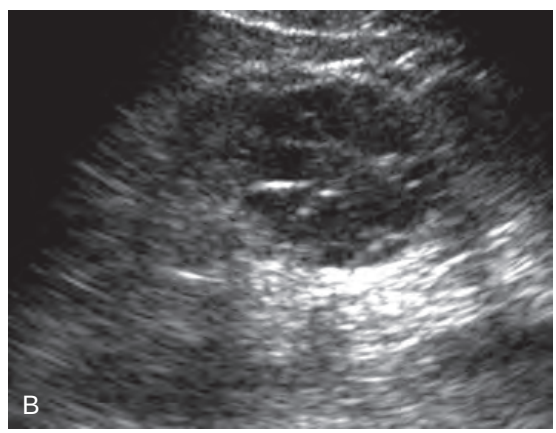

FIGURE 15-6 ■ Multilocular cystic renal cell carcinoma. *A,* Pyelogram-phase computed tomography image shows a low-attenuation, heterogeneous mass projecting from the left kidney. Enhancing septa are faintly demonstrated. *B,* Ultrasound provides better demonstration of the multicystic nature of the mass. Pathologic examination after surgical removal confirmed a multicystic mass lined by clear cell carcinoma.

bland thrombus. Involved veins are usually enlarged. A tumor thrombus is seen as nodular low density within the vein (Figs. 15-8 and 15-9). Enhancement of the thrombus within the vein is evidence that the thrombus consists of a growing tumor. Determining the presence or absence of venous involvement is essential to surgical planning (Fig. 15-9). CT is 95% accurate in the determination of venous involvement.

- Regional lymph nodes >2 cm in short axis nearly always contain metastatic tumor. Involved lymph nodes are most common in renal hilum, pericaval, and periaortic regions.
- Lymph nodes of 1 to 2 cm in short axis are indeterminate and may be either hyperplastic or metastatic. They should always be removed at surgery to determine prognosis. Lymphadenectomy does not improve prognosis.
- Lymph nodes of <1 cm in short axis are usually benign.
- Hematogenous metastases are most common in lung, liver, and bone.
- Adrenalectomy is optional if the adrenal gland appears normal on CT.

FIGURE 15-8 ■ Tumor invasion of right renal vein and inferior vena cava (IVC). An infiltrative renal cell carcinoma (T) replaces parenchyma in the right kidney, and a tumor thrombus extends into the right renal vein (*arrowhead*) and IVC (*arrow*).

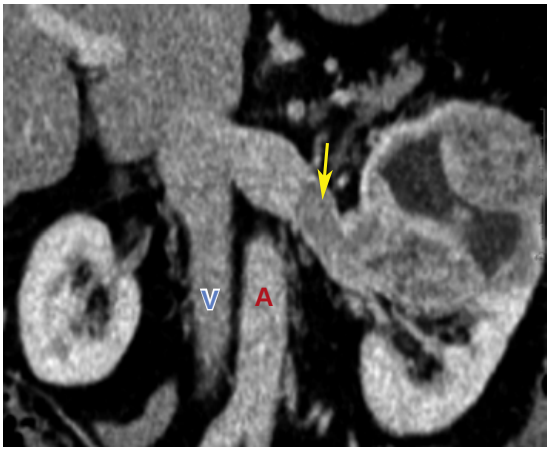

FIGURE 15-9 ■ Tumor invasion of the left renal vein. A coronal-plane image nicely shows a tumor (*arrow*) extending from the left upper pole renal mass into the left renal vein. A segment of the left renal vein near the inferior vena cava (V) is spared, allowing the urologist space to clamp the left renal vein and avoid venous spread of the tumor during surgery. A, aorta.

RCC Recurrence

CT is highly accurate for surveillance for recurrent disease after surgery. RCC recurrence usually occurs in the first 6 years after surgery. The median time for appearance of detectable recurrent disease is 15 to 18 months after nephrectomy. The risk of recurrence increases with tumor stage at the time of the initial surgery. RCC occasionally recurs after a patient has been apparently disease-free for 10 or more years.

- Local recurrence in the renal fossa occurs in 5% of patients (Fig. 15-10). Recurrent tumor appears as an irregularly enhancing mass that commonly involves the psoas or quadratus lumborum muscle. Adjacent structures, including the bowel, which usually occupies the renal fossa after nephrectomy, are displaced.
- Lymphatic recurrence usually occurs in lymph nodes close to the renal vascular pedicle.
- Distant metastases develop in 20% to 30% of patients. The most common sites are the lungs (50% to 60%), mediastinum, bone,

FIGURE 15-10 ■ Renal cell carcinoma recurrence. Computed tomography image obtained 1 year after left nephrectomy for renal cell carcinoma reveals a recurrent mass (*arrow*) in the left renal bed involving the left adrenal gland (*arrowhead*) and the spleen (S).

liver, contralateral kidney or adrenal gland, and brain.
- Late metastases (>10 years after surgery) are most common in lung, pancreas, bone, skeletal muscle, and bowel. Surgical resection of isolated late metastases may be curative.

Oncocytoma

Oncocytoma is a benign solid tumor that arises from the proximal renal tubule. Most cases are seen in men in their 60s. Oncocytomas account for about 5% of renal neoplasms. Unfortunately, no imaging test can reliably differentiate these benign tumors from RCC. Treatment is surgical. Exploration with limited tumor excision may be attempted if CT findings suggest the possibility of oncocytoma.
- Classic CT features of oncocytoma, which unfortunately can also be seen with RCC, are homogeneous attenuation after contrast injection and a central, sharply marginated, stellate, low-attenuation scar (~33% of tumors). Most are solitary, well-defined, homogeneous tumors arising in the renal cortex. Features more characteristic of RCC, such as heterogeneous attenuation, necrosis, and hemorrhage, may also be seen with oncocytoma (Fig. 15-11).

Angiomyolipoma

AML is a benign tumor composed of blood vessels (angio), smooth muscle (myo), and fat (lipoma). Tumor arteries have thicker than normal, but abnormally weak, vessel walls and are predisposed to aneurysm formation. Larger tumors and larger aneurysms have a higher rate of rupture, making hemorrhage the most common complication. AML occurs in two distinct clinical settings. Sporadic and usually solitary tumors (80% to 90%) are most common in middle-aged women (female to male ratio of 4:1; average age 43 years). Multifocal and bilateral tumors occur in association with tuberous sclerosis (TS). Many tumors are discovered incidentally during CT, MR, or ultrasound imaging for other reasons. The presence of distinct pockets of fat allows a specific CT diagnosis of AML.
- The proportion of each tissue element present within the tumor determines the imaging appearance.
- CT typically shows a well-marginated, predominantly fat-containing lesion arising from the cortex (Fig. 15-12). Most tumors are less than 5 cm in size. Vascular and smooth muscle portions of the tumor enhance with contrast administration.
- The diagnostic feature of AML on CT is the presence of fat (CT density <–20 HU) (Fig. 15-12). Elements of soft-tissue density are often dispersed throughout a background of distinctly fatty tissue. At other times, soft-tissue density predominates, and diagnosis is made by the presence of small, discrete pockets of fat. Thin-section CT (collimation 1 to 3 mm) is recommended for confident diagnosis. Use of IV contrast is not necessary to confirm the presence of fat within the lesion.
- Sonography characteristically demonstrates AML as small (<3 cm), well-defined echogenic tumors. Unfortunately, up to 32% of small (<3 cm) RCCs also appear as echogenic masses. Therefore CT characterization of all small, echogenic renal mass lesions is recommended.
- Hemorrhage is common with AML because of the characteristically weak wall of the tumor blood vessels. Hemorrhage commonly extends into the perirenal space, may obscure fat density within the tumor, and often makes tumor margins indistinct.

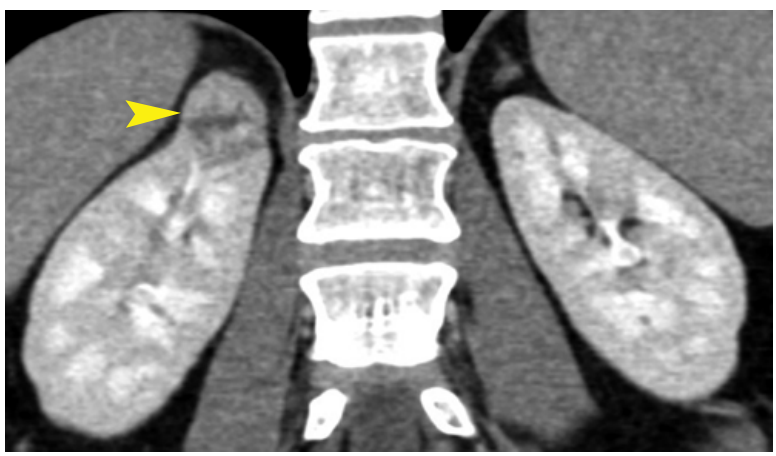

FIGURE 15-11 ■ Oncocytoma. Coronal-plane computed tomography during the nephrogram phase shows a small heterogeneous mass (*arrowhead*) arising from the upper pole of the right kidney. Although pathology revealed a benign oncocytoma, on CT the mass is indistinguishable from a renal carcinoma.

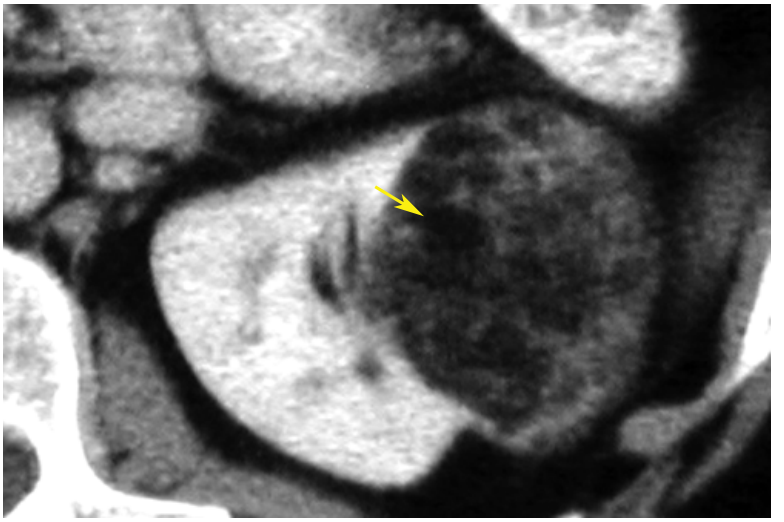

FIGURE 15-12 ■ Solitary angiomyolipoma. Foci of distinct fat density (*arrow*) define this renal mass as an angiomyolipoma. Compare the fat density within the lesion to the fat surrounding the kidney. Areas of soft-tissue density, representing smooth muscle, are also evident within the mass.

FIGURE 15-13 ■ Tuberous sclerosis: bilateral angiomyolipomas. Both kidneys in this patient with tuberous sclerosis are extensively replaced by angiomyolipomas. The tumor (*arrows*) arising from the right kidney extends all the way to the anterior abdominal wall. Low-attenuation areas within the tumor are nearly identical in density to subcutaneous and intra-abdominal fat, confirming the diagnosis of angiomyolipoma. Nodules and strands of soft-tissue density correspond to smooth muscle components of the tumor. Bright dots (*arrowhead*) represent blood vessels within the highly vascular tumor. Functioning renal parenchyma enhances brightly with contrast medium. Despite extensive renal involvement by tumor, the patient had normal renal function.

The risk of hemorrhage is increased when tumors exceed 4 cm in size.

- Approximately 5% of AMLs show no areas of distinct fat attenuation on CT. These tumors are indistinguishable from RCC. However, AML is suggested if the lesions show homogeneous high attenuation on unenhanced CT and homogeneous increased attenuation on enhanced CT.
- In patients with TS, multiple cysts and AMLs are usually found in both kidneys (80% of patients). Lesions are often large, and the risk of hemorrhage is increased (Fig. 15-13).
- Tumors may grow extensively into the perirenal space. Tumor margins are commonly indistinguishable from perirenal fat. These lesions resemble retroperitoneal liposarcomas. A distinguishing feature is a distinct defect in the kidney from which AMLs arise. AMLs characteristically expand in size when they spread outside the renal capsule. Liposarcomas may displace or compress the kidney but usually do not invade the kidney.
- A few cases of fat-containing RCCs have been reported. In each case the presence of fat has been attributed to osseous metaplasia

of stromal portions of the tumor with fatty marrow growth or the presence of fat-laden macrophages in chromophobe RCCs. Calcifications are usually present in association with fat deposits arising from bone marrow. Intratumoral calcifications are virtually never present with AML. Fat-containing RCCs show other signs of malignancy.

Transitional Cell Carcinoma

TCC may arise anywhere along the uroepithelium lining the collecting system, renal pelvis, ureter, or bladder. Most tumors (90%) arise in the bladder, with only 5% to 10% arising within the renal pelvis or ureter. A characteristic of TCC is that additional TCCs may be present synchronously or may arise subsequently elsewhere in the uroepithelium. CT is increasingly used for detection and staging. Four patterns of disease have been described.

- On unenhanced CT, TCC is isodense to renal parenchyma. With contrast, TCC shows variable, but usually poor, enhancement.
- *Single or multiple filling defects* (35%) *in the renal pelvis* have a smooth surface or a stippled papillary pattern (Fig. 15-14) with tracking of contrast into the interstices of the tumor. Renal sinus fat may be compressed by the tumor.
- *Filling defects* are seen *within dilated calyces* obstructed at the infundibulum (26%). A "phantom" calyx fails to opacify and may be associated with either a focal delayed or an increasingly dense lobar nephrogram.
- *Thickening of the wall of the renal pelvis* (Fig. 15-15) may be relatively subtle.
- *Absent or decreased contrast excretion* (13%) is caused by long-standing obstruction at the ureteropelvic junction (UPJ).
- *Diffuse hydronephrosis with renal enlargement* (6%) is seen with tumor obstruction at the UPJ.
- Most (>70%) ureteral uroepithelial tumors occur in the distal ureter. Tumors appear as small filling defects in the contrast-filled ureter or as circumferential thickening of the wall of the ureter on CT urography. The ureter proximal to the tumor may be dilated. Calcified ureteral TCC may be mistaken for calculi. A calcified tumor located at a position atypical for impacted calculi may be a clue to diagnosis. Calculi typically impact at the UPJ, pelvic brim, or UVJ.
- Large tumors invade the renal sinus fat and infiltrate the parenchyma. Differentiation from RCC may be difficult. TCC tumors center on the renal pelvis. RCC tumors center on the renal parenchyma.
- Advanced disease shows extrarenal extension, regional lymph node involvement, and distant metastases to lung and bone. TCC may rarely invade the renal vein and IVC.
- Calcification occurs in up to 5% of tumors. It may appear coarse, punctate, linear, granular, or stippled and indistinct.

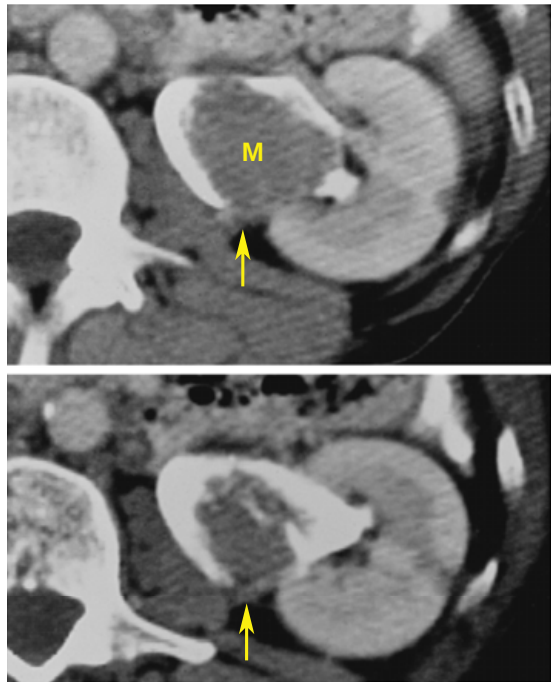

FIGURE 15-14 ■ Transitional cell carcinoma: renal pelvis. Two sequential images of the left kidney demonstrate a transitional cell carcinoma appearing as a mass (M) of soft-tissue attenuation surrounded by high-attenuation contrast agent within the renal pelvis. The tumor extends through the wall of the renal pelvis into the perirenal fat (*arrows*).

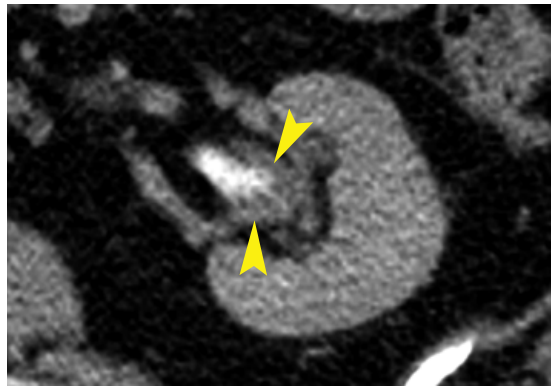

FIGURE 15-15 ■ Transitional cell carcinoma: renal pelvis. Pyelogram-phase computed tomography in a patient with hematuria reveals irregular thickening (*arrowheads*) of the walls of the renal pelvis.

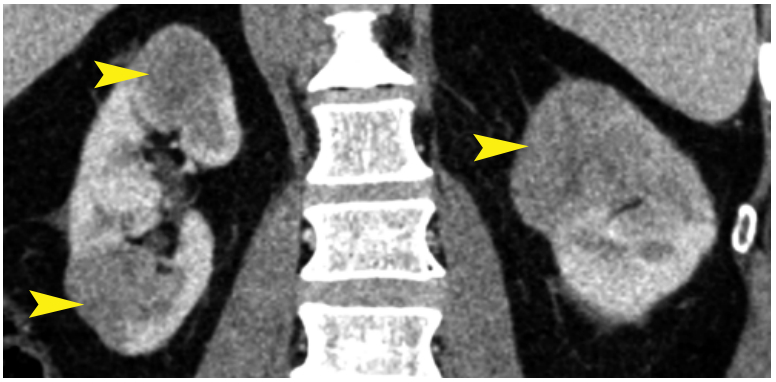

FIGURE 15-16 ■ Renal lymphoma: multiple masses. Coronal-plane computed tomography shows multiple low-attenuation, ill-defined masses in both kidneys (*arrowheads*), proven by percutaneous biopsy to be lymphoma.

Renal Lymphoma

Renal involvement with lymphoma almost always occurs in the setting of systemic disease. Whereas autopsy studies show that the kidneys are involved in 34% of 68% of patients with lymphoma, CT shows renal involvement in only 3% to 8% of cases. B-cell non-Hodgkin's and Burkitt's lymphomas are the most common lymphoma types that involve the kidney. Five characteristic patterns of involvement have been described. Atypical patterns of involvement present a diagnostic challenge.

- On unenhanced CT, lymphoma is homogeneous and typically of lower attenuation than the renal cortex. Margins with the renal parenchyma are usually indistinct.
- Following contrast enhancement, lymphoma remains homogeneous and is always hypodense compared to enhanced renal parenchyma.
- *Multiple bilateral renal masses* are the most common (60%) CT appearance of lymphoma (Fig. 15-16). Occasionally, the multiple masses may affect only one kidney. The size of the lesions is typically 1 to 3 cm. Necrosis and calcification are rare. Retroperitoneal adenopathy is often not present.
- *Contiguous invasion from the retroperitoneum* is seen in 35% to 60% of cases. Bulky retroperitoneal adenopathy extends along the renal vessels into the renal sinus and then into the renal parenchyma (Fig. 15-17). Tumor encasement of the renal artery and vein hardly ever results in thrombosis, a finding highly characteristic of lymphoma.
- A *solitary mass* (10% to 20% of cases) may highly resemble RCC. However, the mass is routinely very homogeneous and shows minimal enhancement (Fig. 15-18). Tumor invasion of the renal vein is exceedingly rare.

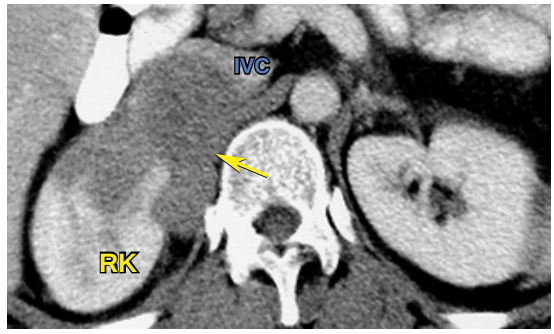

FIGURE 15-17 ■ Renal lymphoma: contiguous invasion. A homogeneous, minimally enhancing mass (*arrow*) invades the right kidney (RK) and distorts the inferior vena cava (IVC) and displaces it anteriorly.

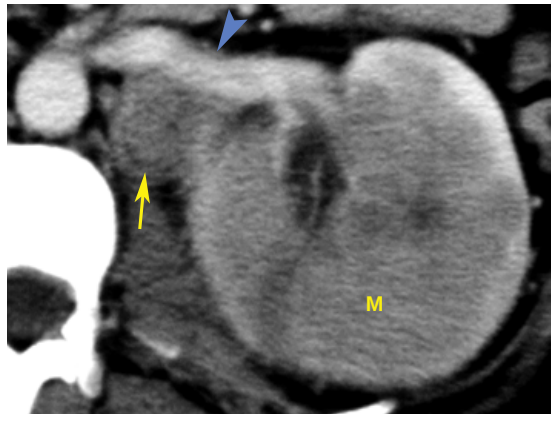

FIGURE 15-18 ■ Renal lymphoma: solitary mass. Lymphoma replaces parenchyma in the midportion of the left kidney, appearing as a large mass (M) with ill-defined borders. An enlarged lymph node (*arrow*) is seen posterior to the left renal vein (*arrowhead*). Note that the renal vein is uninvolved. Renal cell carcinoma commonly invades the renal vein, whereas renal lymphoma rarely does. Compare this to Figure 15-9.

- *Perirenal lymphoma* most often accompanies contiguous invasion from the retroperitoneum. Bulky disease surrounds the kidney but usually does not compress the parenchyma or interfere with its function.

Disease patterns include multiple perirenal masses, soft-tissue nodules and plaques, a curvilinear, soft-tissue mass separate from the kidney (Fig. 15-19), and thickened renal fascia.

- *Diffuse infiltration* (~20%) enlarges the kidney without altering its reniform shape. Nearly all cases involve both kidneys. Contrast enhancement is typically limited, patchy, and associated with poor contrast excretion.
- The absence of involvement of retroperitoneal nodes is relatively common (up to 43% of all cases) and does not exclude lymphoma as the cause of a renal mass.
- Atypical manifestations include spontaneous hemorrhage, necrosis, heterogeneous attenuation, cystic changes, and calcification. Atypical findings are most common after treatment. After successful therapy, the CT appearance of the kidney usually returns to normal eventually.
- When imaging findings suggest renal lymphoma, image-guided biopsy of the lesions should be recommended so that unnecessary surgery can be avoided and proper treatment instituted.

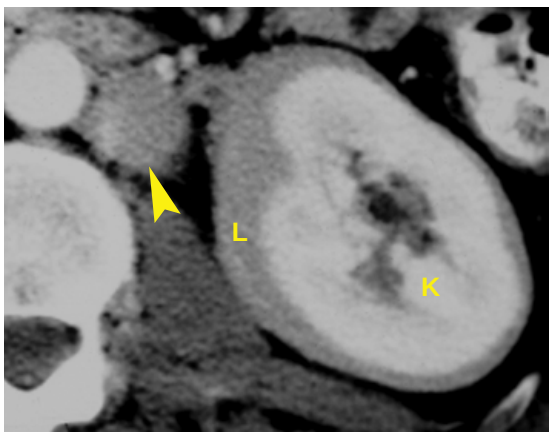

FIGURE 15-19 ■ Renal lymphoma: perirenal. The enhancing parenchyma of the left kidney (K) is completely encased by nonenhancing, homogeneous soft-tissue representing lymphomatous tissue (L). An enlarged lymph node (*arrowhead*) is seen between the kidney and the aorta.

Metastases to the Kidneys

Metastases to the kidneys are present in 7% to 13% of patients with extrarenal cancers on autopsy series. The most common primary cancers to metastasize to the kidneys are lung, breast, and gastrointestinal adenocarcinomas. Lesions are identified on CT usually only in patients with advanced widespread metastatic disease.

- Multiple, bilateral, low-attenuation renal nodules are the most common CT pattern (Fig. 15-20).
- Solitary exophytic masses may be seen with colon cancer and melanoma.
- Diffusely infiltrative metastases are uncommon.

Papillary Adenoma

Papillary adenomas by pathologic definition are small (<5 mm), solid renal masses that arise from the epithelium of the renal tubules. They are solitary and subcapsular in location. Most are discovered incidentally in surgical specimens (7% of nephrectomies, 10% of autopsies). They are also found in association with long-term hemodialysis and acquired renal cystic disease. Lesions larger than 5 mm are considered carcinomas.

- CT shows a tiny, solid renal mass smaller than 5 mm that is indistinguishable from papillary RCC.

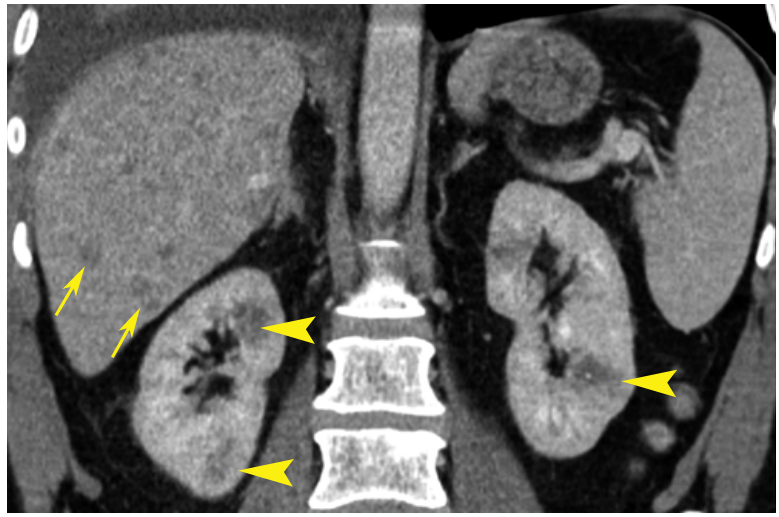

FIGURE 15-20 ■ Metastases to the kidney. Coronal-plane computed tomography image of a patient with colon cancer shows numerous ill-defined, low-attenuation lesions in both kidneys (*arrowheads*) and in the liver (*arrows*).

Metanephric Adenoma

Metanephric adenomas are very rare benign tumors of the kidneys histogenetically related to Wilms' tumor and nephroblastomatosis. The tumor do not have malignant potential. No treatment is needed.

- The typical appearance is a solitary, well-defined, solid mass with attenuation higher than that of renal parenchyma on noncontrast CT. The tumor is hypovascular and enhances minimally. The mean size is 5 cm. Larger masses are heterogeneous, with areas of hemorrhage, necrosis, and calcification (20%).

Cystic Renal Masses

Cystic renal masses are an extremely common finding on abdominal CT. The challenge is to separate the ubiquitous simple cyst and other benign cysts from a host of potentially malignant cystic lesions.

Bosniak Classification of Cystic Renal Masses

In 1986 Morton Bosniak described a classification system for cystic renal masses that is still widely utilized. The classification scheme was modified in 1993. Cystic lesion classification is based on CT findings.

- **Bosniak category I: benign simple cyst.** CT shows homogeneous internal attenuation of water density, a hairline-thin wall, no enhancement with IV contrast, and no septa, calcifications, or solid components (Fig. 15-21).
- **Bosniak category II: benign complicated cyst.** Cysts become complicated by developing internal hemorrhage or becoming infected. CT shows a minimally complicated benign cyst (Fig. 15-22) that may contain fine septa, thin calcification in the cyst wall, a short segment of minimally thickened and smooth calcification in the cyst wall, or uniform high internal attenuation in a sharply marginated cyst smaller than 3 cm. No lesions show enhancement. High-attenuation fluid within cysts represents an old hemorrhage.
- **Bosniak category IIF: follow-up.** This category was added in 1993 for lesions that are almost certainly benign but for which follow-up is recommended because findings are more pronounced than for category II lesions (Fig. 15-23). CT shows a large number of septa, minimal enhancement of the cyst wall or septa, thick or nodular calcification without enhancement, or totally intrarenal, nonenhancing, high-attenuation renal lesions of 3 cm or larger. No enhancing solid-tissue components are seen in these lesions. Follow-up CT is generally recommended at 6 months and 1 year and then annually for 5 years. The absence of change supports benignity, whereas an increase in septal thickness or solid components indicates that neoplasm is likely.
- **Bosniak category III: indeterminate cystic lesions.** These lesions have thickened walls, nodularity (Fig. 15-24), and septa which demonstrate contrast enhancement (Fig. 15-25). Lesions may be benign or malignant and include such entities as multilocular cystic nephroma, localized cystic renal disease, and multicystic RCC. Category III lesions may require surgical exploration.
- **Bosniak category IV: malignant cystic tumors.** CT shows findings seen in category III, but with enhancing soft-tissue components adjacent to or within the wall of the cystic lesion (Fig. 15-26). These lesions are clearly malignant.

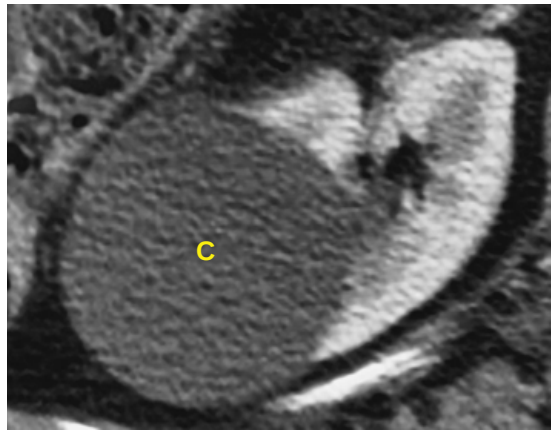

FIGURE 15-21 ■ Simple renal cyst: Bosniak category I. A large cyst (C) arising from the left kidney demonstrates the classic computed tomography features of a simple renal cyst with sharp definition, no discernible wall, homogeneous internal attenuation close to that of water, and no enhancement. No further evaluation or follow-up is necessary.

Simple Cysts

Simple renal cysts are benign, non-neoplastic, fluid-filled masses that are present in half the population older than 55 years. Small cysts are asymptomatic incidental findings. Large cysts (>4 cm) occasionally cause hypertension, hematuria, pain, or ureteral obstruction. Multiple and

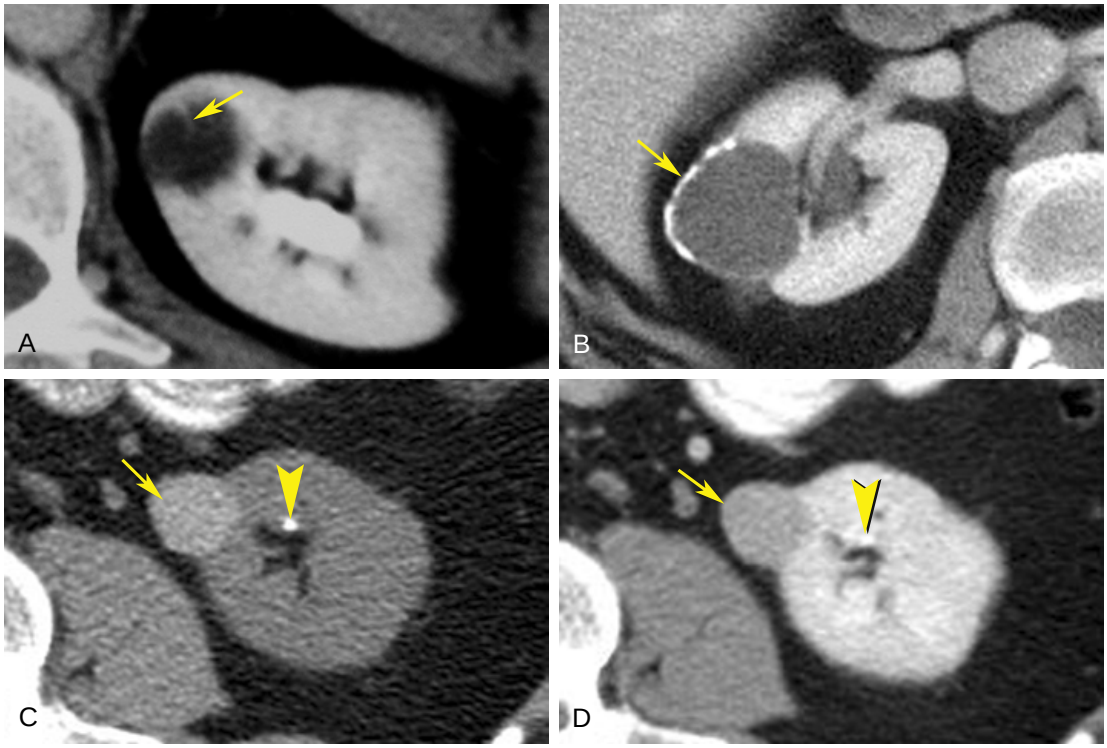

FIGURE 15-22 ■ Complicated renal cysts: Bosniak category II. *A*, A single thin septation (*arrow*) is present in this left renal cyst. B, The wall of this cyst extending from the right kidney has foci of thin, smooth calcification (*arrow*) in its wall. *C*, Noncontrast computed tomography (CT) demonstrates a uniformly high-attenuation (64 Hounsfield units) mass (*arrow*) arising from the left kidney. A renal calculus (*arrowhead*) is also demonstrated. *D*, Contrast-enhanced CT at the same location as *C* shows no enhancement of the renal mass. Findings are indicative of a Bosniak II high-density renal cyst. Note how contrast enhancement of the renal parenchyma obscures visualization of the renal calculus (*arrowhead*). High attenuation of fluid within a simple cyst represents an old hemorrhage.

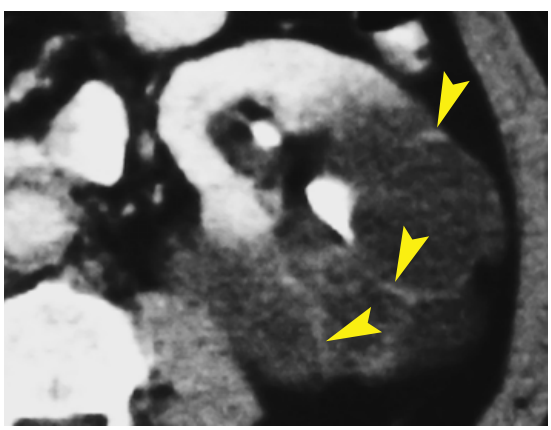

FIGURE 15-23 ■ Cystic mass with enhancing septa: Bosniak category IIF. A complex cystic mass arising from the left kidney has enhancing septations (*arrowheads*). Serial computed tomography scans over 3 years showed no change in this mass.

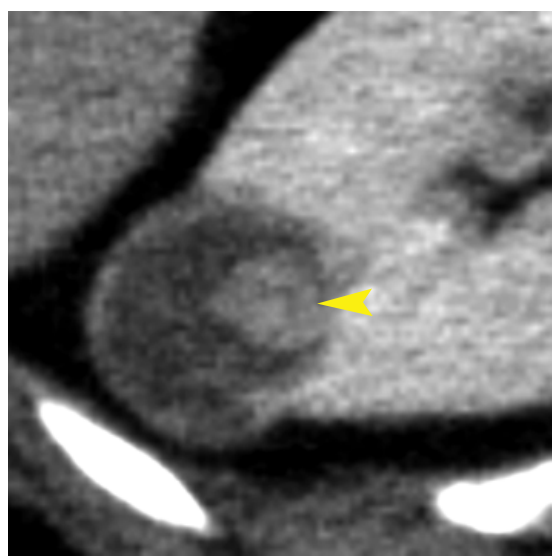

FIGURE 15-24 ■ Cystic mass with enhancing nodule: Bosniak category III. A cystic mass arising from the right kidney has a mildly enhancing nodule (*arrowhead*) that makes the mass indeterminate and possibly malignant. Surgical exploration was recommended. This lesion proved to be a papillary renal carcinoma.

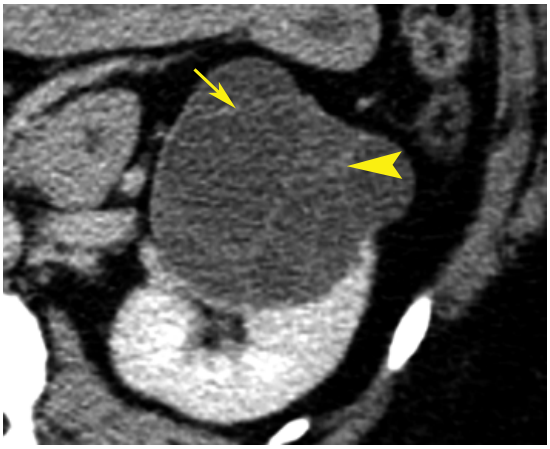

FIGURE 15-25 ■ Multilocular cystic renal tumor: Bosniak category III. Nephrogram-phase computed tomography of the left kidney in a 48-year-old woman shows a cystic mass with enhancing septations (*arrow*) and enhancing nodular components (*arrowhead*). These findings led to surgical removal. Pathology confirmed benign multilocular cystic nephroma.

bilateral cysts are common. Strict criteria that allow confident CT diagnosis of a renal mass as a simple cyst (Bosniak category I; Fig. 15-21) are as follows:

- Sharp margination with the renal parenchyma
- No perceptible wall
- Homogeneous attenuation close to the density of water (–10 to +20 HU)
- No enhancement after IV administration of contrast medium
- On follow-up, simple cysts commonly increase slowly in size

Renal Abscess

Pyelonephritis complicated by suppuration and liquefaction may result in the formation of an abscess. Alternatively, preexisting cysts may become infected. On CT, abscesses appear as thick-walled, low-attenuation fluid collections within the renal parenchyma (Fig. 15-27). Gas is sometimes seen within the pus collection. The wall commonly enhances with contrast medium administration. Extension of infection into the perirenal space is common.

Cystic or Multicystic RCC

Some clear cell renal carcinomas are composed of multiple fluid-filled, noncommunicating cystic spaces (Fig. 15-6). Malignant tumor cells line the loculations. Rarely, renal carcinoma may arise within or adjacent to a simple renal cyst. Cystic forms of papillary RCC appear as a cystic mass

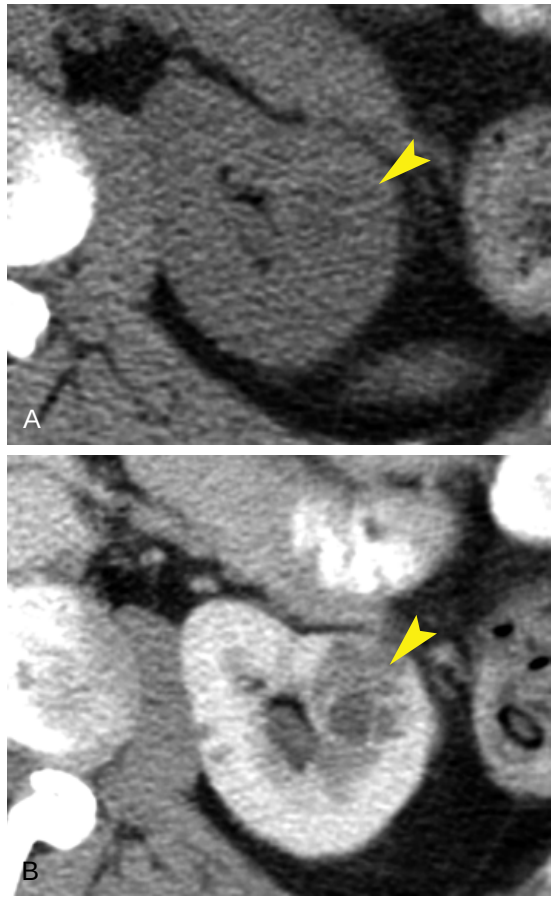

FIGURE 15-26 ■ Cystic mass with marked enhancement: Bosniak category IV. Computed tomography (CT) reveals a poorly marginated cystic mass (*arrowheads*) in the left kidney that showed enhancement from 18 Hounsfield units (HU) on noncontrast CT (A) to 48 HU on nephrogram-phase CT (B). Nephrectomy confirmed a clear cell renal cell carcinoma.

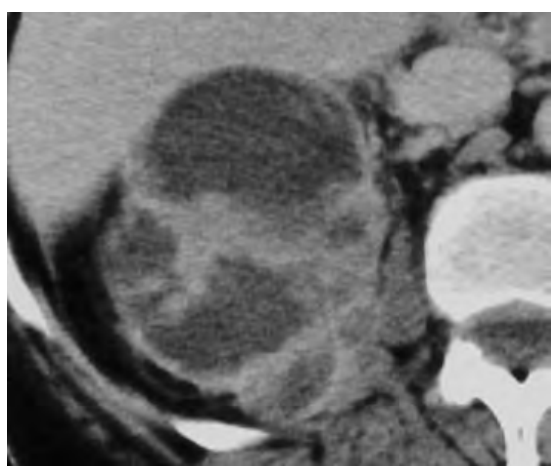

FIGURE 15-27 ■ Renal abscess. Computed tomography of a patient with flank pain and fever shows a large fluid collection extending from the upper pole of the right kidney. Irregular thick septations are present. The abscess resolved with catheter drainage and antibiotics.

with enhancing papillary projections or enhancing solid components (Fig. 15-24).

Multilocular Cystic Renal Tumor

Multilocular cystic renal tumor, also called multiloculare cystic nephroma or simply cystic nephroma, is an uncommon benign renal neoplasm composed of cysts of varying size separated by connective tissue septa. Two-thirds of these tumors occur in male infants between 2 months and 3 years of age. The remainder occur in women aged 40 to 60 years. Treatment is surgical excision.

- The mass is solitary and unilateral, and most commonly arises from the upper pole.
- The multiple fluid-filled locules range from a few millimeters to 2.5 cm in size.
- The septa enhance moderately but less than for RCC (Fig. 15-25).
- Small locules and high-density fluid within the locules may make portions of the mass appear solid.
- Calcification, hemorrhage, and necrosis are rare.

Localized Renal Cystic Disease

Localized renal cystic disease is a benign condition that resembles multilocular cystic nephroma. The lesion consists of multiple cysts of varying size separated by normal or atrophic renal parenchyma (Fig. 15-23). The disease is not hereditary and is not associated with renal insufficiency. Most patients are asymptomatic.

- Multiple simple cysts of varying size are separated by normally enhancing renal parenchyma.
- No discrete encapsulation is present.
- Other, clearly separate, benign cysts are often found nearby.
- The lesion most commonly affects a portion of one kidney.
- Occasionally one entire kidney is affected and resembles autosomal dominant polycystic kidney disease.
- Localized renal cystic disease is not associated with the presence of cysts in other organs.

Small Indeterminate Renal Masses

High-quality cross-sectional imaging has resulted in increased detection of small renal masses. The prognosis for cure of RCC is best when the lesions are small and are completely removed surgically before metastatic spread occurs. Currently some 25% to 40% of RCCs are discovered on imaging studies as an incidental renal mass. Before the age of widespread cross-sectional imaging, only 10% of RCCs were discovered incidentally. Improved detection of small tumors has resulted in improved overall prognosis. Unfortunately, improved techniques have also resulted in the detection of a large number of small renal lesions that are benign. The challenge to radiologists is to accurately differentiate benign from malignant lesions. Accurate characterization requires high-quality CT. Despite optimal imaging evaluation, a considerable number of renal masses, especially small ones, remain indeterminate. A number of strategies have been recommended.

- Most small renal masses are simple cysts (Fig. 15-28). Volume averaging of small cysts complicates assessment of lesion attenuation and contrast enhancement. Bright enhancement of surrounding renal parenchyma

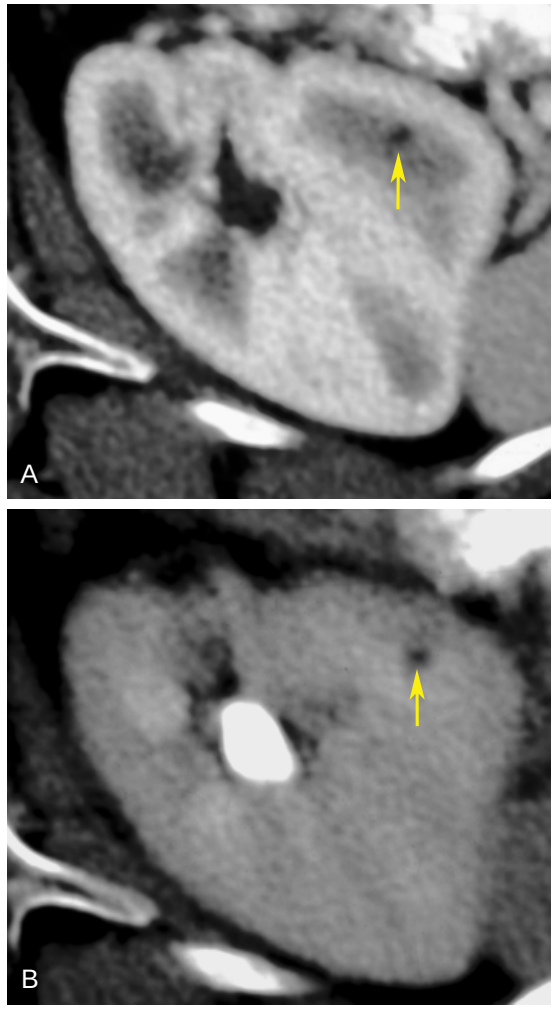

FIGURE 15-28 ■ Small indeterminate renal mass. Postcontrast corticomedullary phase, **A,** and pyelogram phase, **B,** images show a tiny, nonenhancing, low-attenuation renal mass (*arrows*). This most likely represents a tiny renal cyst.

during corticomedullary and nephrogram phases may increase the apparent attenuation of a simple cyst by 5 to 10 HU. Ultrasound is useful in characterizing small simple cysts that show this pseudoenhancement.

- In asymptomatic low-risk patients, lesions of <10 mm are assumed to be benign cysts.
- In high-risk patients (von Hippel–Lindau disease, strong family history of RCC, acquired renal cystic disease due to dialysis), the urologist may choose surgical excision.
- CT follow-up at 3- or 6-month intervals for at least 1 year is an option. Small RCCs tend to grow slowly (mean 0.36 cm/year) and are not an immediate threat to the patient's life (Fig. 15-29). Evidence of lesion growth or the appearance of more aggressive features is indicative of RCC.
- Historically, image-guided biopsy of a renal mass was rarely utilized. More recently, advances in biopsy and cytology techniques have confirmed the utility of percutaneous image-guided renal mass biopsy, especially for small lesions with an uncertain imaging diagnosis. Confirmation of a benign renal lesion obviously contributes significantly to limiting patient morbidity.

Multiple Renal Cysts

When *multiple renal cysts* are encountered, the following conditions should be considered.

Multiple Simple Cysts

Simple cysts increase in frequency with age and are commonly multiple and bilateral (Fig. 15-30). Patients older than 50 years with no cysts in other organs and who have no family history of renal cystic disease and have normal renal function are most likely to have multiple simple cysts.

Autosomal Dominant Polycystic Disease

The cortex and medulla of both kidneys are progressively replaced by multiple noncommunicating cysts of varying size in this common hereditary disorder. Although this disease may be detected in childhood and may even be evident in the fetus, most cases present clinically with hypertension and renal failure at age 30 to 50 years. The renal cysts are commonly complicated by bleeding or infection, which causes thickening of the cyst walls and an increase in attenuation of cyst fluid (Fig. 15-31).

FIGURE 15-29 ■ Tiny renal cell carcinoma. Serial nephrogram-phase computed tomography (CT) scans of the right kidney show three renal lesions: *A*, initial scan; *B*, scan at 1 year; and *C*, scan at 2 years. The posterior lesion (*arrowheads*) is of most concern because it is only slightly lower in attenuation than the enhanced renal parenchyma. Over time the lesion shows slow but progressive growth. Percutaneous biopsy prior to radiofrequency ablation confirmed renal cell carcinoma. The larger lesion (*curved arrows*) shows low attenuation, but its interface with the renal parenchyma is not well defined. However, serial CT shows no change in the lesion and no enhancement. The small lesion seen laterally (*long straight arrows*) is indeterminate because of its small size but also shows no change on follow-up and likely represents a tiny benign renal cyst.

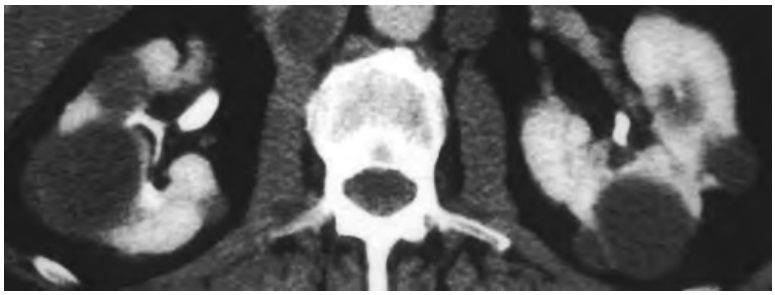

FIGURE 15-30 ■ Multiple simple cysts. Computed tomography demonstrates multiple simple cysts of various sizes throughout both kidneys. These are incidental findings.

Berry aneurysms are present in the circle of Willis in 10% to 15% of patients. CT findings become more pronounced as the disease progresses. Autosomal dominant ("adult") polycystic disease is differentiated from other conditions by the presence of cysts in other organs, most commonly the liver, a positive family history, and the presence of renal failure and hypertension. Diagnostic CT findings include the following:

- Progressive replacement of the renal parenchyma with cysts of varying size is associated with a progressive bilateral increase in renal volume (Fig. 15-31).
- Cysts are often present in other organs, most commonly the liver (30% to 50%) and pancreas (10%).
- Cysts in the kidneys may have calcified walls and high internal attenuation due to previous hemorrhage, infection, inflammation, or ischemia.
- Renal stones are common (20% to 40% of patients).

Multicystic Dysplastic Kidney

Multicystic dysplastic kidney is nonhereditary renal dysplasia in which the kidney consists of multiple thin-walled cysts held together by connective tissue. Renal dysplasia results from high-grade urinary tract obstruction during embryogenesis. The involved kidney is functionless. The imaging appearance depends on the age of the patient. At birth the involved kidney is greatly enlarged. In childhood and through early adulthood the affected kidney appears as a nonfunctioning multiloculated cystic mass that may be confused with a cystic renal neoplasm. With advancing age the kidney progressively shrinks and often becomes calcified. Rarely, only a portion of one kidney may be involved. Bilateral multicystic dysplastic kidneys occur but are fatal at birth. The opposite kidney is affected by UPJ obstruction, vesicoureteral reflux, or another anomaly in 30% of cases.

von Hippel–Lindau Disease

von Hippel–Lindau disease is a rare autosomal dominant disorder characterized by cerebellar, spinal cord, and retinal hemangioblastomas, renal and pancreatic cysts, RCC, and pheochromocytoma (Fig. 15-32).

- Multiple bilateral renal cysts are present in 50% to 75% of patients. Over time, cysts may gradually enlarge or involute.
- RCC occurs in 28% to 45% of patients. Tumors are most often solid, multicentric, and bilateral. Some appear as complex cysts with enhancing septa. Most are clear cell RCC.
- Pheochromocytoma is present in 30% of cases. The tumors are bilateral in 50% and malignant in 10% to 15% of these cases.

Tuberous Sclerosis

TS is an autosomal dominant syndrome characterized by multiple renal cysts and multiple and bilateral renal AMLs (Fig. 15-13) with seizures, mental retardation, adenoma sebaceum, and

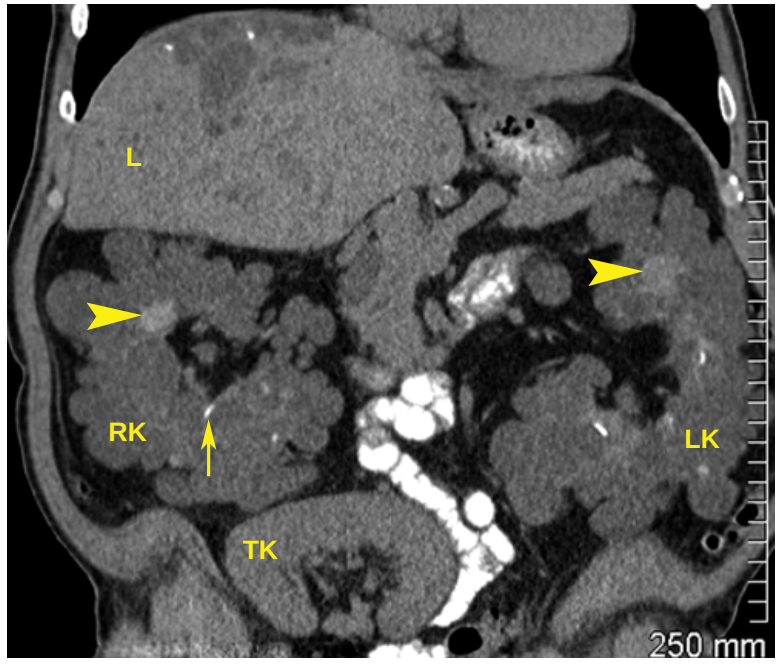

FIGURE 15-31 ■ Autosomal dominant polycystic kidney disease. A computed tomography image in the coronal-plane from a noncontrast scan shows that the native right kidney (RK) and left kidney (LK) are markedly enlarged and the parenchyma is replaced by innumerable cysts of variable size. Some of the renal cysts are high in attenuation (*arrowheads*), indicating previous hemorrhage. Some of the cysts contain calcification in the cyst wall (*arrow*). The liver (L) also shows the presence of multiple cysts. The findings are characteristic of autosomal dominant polycystic disease. Because of advanced renal failure, the patient received a transplant kidney (TK).

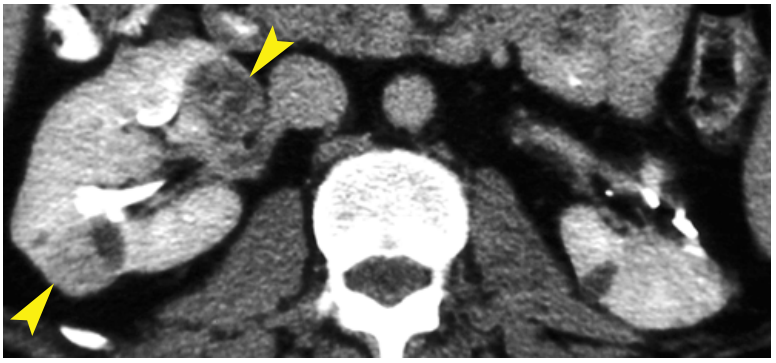

FIGURE 15-32 ■ von Hippel–Lindau disease. Two partially cystic renal cell carcinomas (*arrowheads*) are seen in the right kidney. A partial nephrectomy has been performed on the left to remove a renal cell carcinoma. The complete computed tomography scan showed numerous cysts in both kidneys.

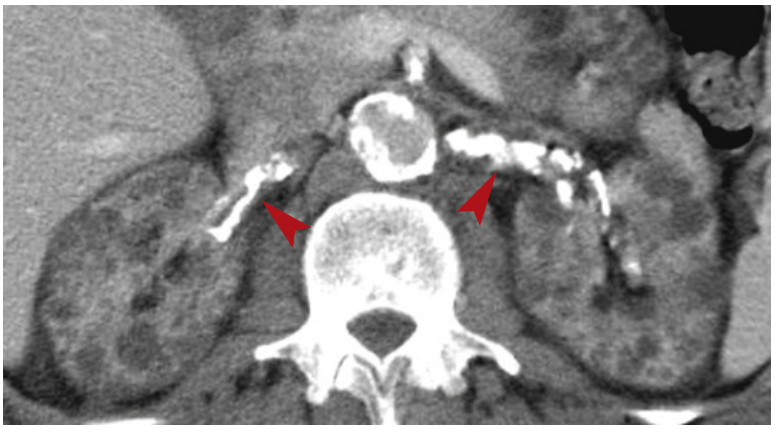

FIGURE 15-33 ■ Acquired renal cystic disease. Computed tomography scan of a patient with a 15-year history of hemodialysis revealed numerous small cysts in both kidneys. The kidneys are of low normal size. No solid masses were detected. Note the severe atherosclerosis involving both renal arteries (*arrowheads*) and the aorta in this patient with renal failure related to diabetes mellitus.

cutaneous, retinal, and cerebral hamartomas. In up to 60% of patients the condition occurs sporadically without a family history. Up to 40% of patients die by age 35 years of brain tumors, renal failure, or lung disease. Up to 75% of patients with TS have renal AMLs. About 20% of patients with renal AMLs have TS. Up to 50% of patients with TS have renal cysts. Compared to sporadic AMLs, the AMLs seen in association with TS are multiple, bilateral, and larger, and they grow. Rupture of AMLs is a significant risk, especially when female patients become pregnant. The renal cysts in TS are multiple and bilateral and occur in younger patients. RCC occurs with the same incidence as in the general population but occurs at an earlier age in patients with TS (average age 28 years). Retroperitoneal lymphangioleiomyomatosis may also occur, appearing as multiple retroperitoneal thin- or thick-walled cysts representing dilated lymphatic channels.

Acquired Renal Cystic Disease

Patients on chronic hemodialysis commonly develop innumerable cysts in their native kidneys. More than 90% of patients who are on dialysis for 5 to 10 years are affected. Many of the cysts are lined by a hyperplastic and dysplastic epithelium. The condition is complicated by hemorrhage from the cysts and the development of RCC (in 3% to 7% of patients).

- Affected kidneys are end-stage failed kidneys affected by conditions other than hereditary renal cystic disease. Thus, the kidneys are smaller than normal.
- The renal parenchyma is progressively replaced by myriad tiny cysts (<6 mm in size) (Fig. 15-33). Some cysts are up to 2 cm in size. The kidneys slowly enlarge over time as cysts develop. Fluid within the cysts is often of high attenuation because of the presence of blood products and calcium oxalates. Calcification of the cyst walls is common.
- The cysts usually regress within months of renal transplantation.

Infection

CT is indicated when complications of renal infection are suspected. Predisposing conditions, including urinary calculi, a neurogenic bladder, immune system compromise, diabetes, IV drug abuse, or chronic debilitating disease, increase the risk of complications that require intervention.

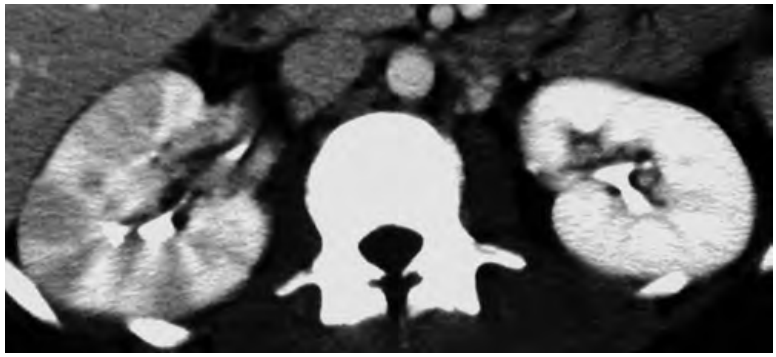

FIGURE 15-34 ■ Acute pyelonephritis. The right kidney shows the wedge-shaped areas of decreased parenchymal enhancement characteristic of acute pyelonephritis. Severe edema in affected regions of the kidney results in diminished blood flow, producing the enhancement defects. The left kidney is normal.

Most urinary tract infections are caused by gram-negative bacilli, but the incidence of fungal and tuberculous infections is increasing.

Acute Bacterial Pyelonephritis

Acute pyelonephritis is a multifocal infection of one or both kidneys. Patients with uncomplicated pyelonephritis usually exhibit resolution of all symptoms within 72 hours of the institution of appropriate antibiotic therapy. Patients who fail to improve should be imaged to detect complications. CT signs of acute bacterial infection of the kidneys include the following:

- Wedge-shaped areas of mottled decreased parenchymal enhancement are seen (Fig. 15-34). The CT appearance is very similar to that of renal infarction. Decreased enhancement is the result of decreased blood flow caused by edema and inflammation within the parenchyma confined by the renal capsule.
- A striated pattern of linear alternating increased and decreased attenuation on enhanced scans is particularly characteristic.
- High-attenuation areas of parenchyma on unenhanced scans indicate parenchyma hemorrhage caused by inflammation and ischemia.
- Stranding densities in the perirenal fat and thickening of the renal fascia occur as a result of inflammation and edema in the perirenal space.
- Severe localized infection (variously called focal pyelonephritis, acute focal bacterial nephritis, and lobar nephronia) produces a poorly defined, mottled, low-attenuation mass without distinct liquefaction. These phlegmons may resolve completely, result in a scar, or evolve into an abscess.
- *Emphysematous pyelonephritis* is a severe life-threatening necrotizing type of diffuse pyelonephritis that occurs in diabetics (90%), immune-compromised patients, and patients with urinary obstruction. Gas is produced from metabolism of glucose by gram-negative bacteria. CT shows gas in the renal parenchyma in addition to signs of renal inflammation (Fig. 15-35). Emergency nephrectomy may be required.
- *Emphysematous pyelitis* refers to gas confined to the renal pelvis and calyces. This finding may be found with infection, trauma, instrumentation, or a fistula and lacks the dire implications of gas within the renal parenchyma. CT reveals dilatation of the collecting system, which contains bubbles of gas or gas–fluid levels without gas present in the renal parenchyma.
- *Abscess* refers to a collection of pus and liquefied tissue within the kidney (Fig. 15-27) that may spread into the perirenal space (Fig. 15-36). CT demonstrates a fluid collection (10 to 30 HU) with an enhancing rim. Gas may be present within the collection, especially in patients who are diabetic. Large abscesses usually require catheter or surgical drainage.

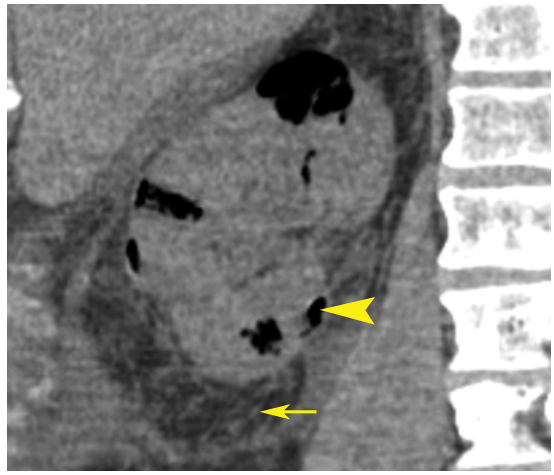

FIGURE 15-35 ■ Emphysematous pyelonephritis. Coronal-plane image from noncontrast computed tomography in a septic patient with right flank pain shows multiple gas collections (*arrowhead*) within the renal parenchyma. Stranding (*arrow*) within the perirenal fat is further evidence of inflammation.

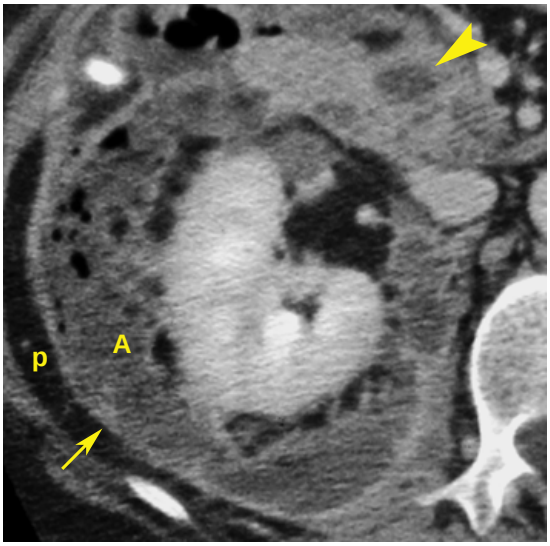

FIGURE 15-36 ■ Perirenal abscess. A bacterial abscess (A) complicating acute pyelonephritis in a diabetic patient has spread through the renal capsule into the perirenal space, appearing as a loculated collection of fluid and gas. The renal fascia (*arrow*) is thickened by inflammation but serves as a barrier preventing spread of infection to the posterior perirenal space (p). The purulent process has spread anteriorly to involve the head of the pancreas (*arrowhead*) in the anterior perirenal space.

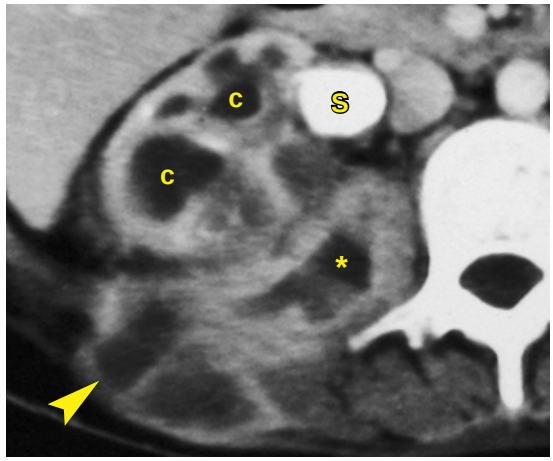

FIGURE 15-37 ■ Xanthogranulomatous pyelonephritis. A large stone (S) fills the renal pelvis and causes obstruction, resulting in dilatation of the collecting system (c). The chronic infective process extends from the kidney through the perirenal space (*) and into the subcutaneous soft-tissues (*arrowhead*). A nephrectomy was performed and yielded *Proteus* organisms on bacterial culture.

Pyonephrosis

Pyonephrosis is an acute infection with pus within an obstructed collecting system. Renal destruction is rapid, and urgent drainage of the collecting system is required.

- The collecting system is dilated and the contained fluid is of high attenuation, with layering sometimes evident.
- The wall of the collecting system is thickened (>2 mm).
- The renal parenchyma is often thinned. Intraparenchymal abscesses may be present.

Renal Tuberculosis

Tuberculosis (TB) remains the leading global cause of death from infectious disease. The urinary tract is the most common extrapulmonary site of infection and is involved in 15% to 20% of cases. The urinary tract may be involved even though chest radiographs do not show evidence of TB. Multiple caseous granulomas form in the cortex because of its favorable blood supply. These may remain dormant or reactivate, spreading organisms to the tubules, resulting in papillary necrosis. Progressive infection will eventually destroy the kidney.

- Disease is often unilateral, with a predilection for the poles of the kidney.
- Calcifications are a hallmark of the disease, shown by CT in 40% to 70% of cases. Calcifications are typically within the renal parenchyma and may be coarse, globular, curvilinear, or granular. Extensive calcification of a nonfunctioning kidney (putty kidney) is characteristic of end-stage renal TB.
- Fibrotic strictures of the infundibula, pelvis, and ureter are characteristic.
- Calyces are often dilated because of strictures of the collecting system. The dilated calyces are filled with clear fluid, debris, or calculi.
- Cortical thinning, caused by focal or diffuse parenchymal scarring, is usually present.

Xanthogranulomatous Pyelonephritis

Xanthogranulomatous pyelonephritis results from a combination of chronic renal obstruction and chronic infection. The renal parenchyma is progressively destroyed and replaced by lipid-filled macrophages. A staghorn calculus results in involvement of the entire kidney. A solitary calculus or infundibular stricture may result in focal involvement.

- CT reveals low-attenuation enlargement of the entire kidney or the affected area, with multiple low-attenuation masses representing dilated calyces. The kidney may enhance but fails to excrete contrast (Fig. 15-37).
- The obstructing calculus is seen within the renal pelvis or calyces.
- Extension of the infective process into the perirenal tissues is common.

URETERS

Anatomy

The ureter is a muscular tube approximately 30 cm long that lies on the psoas muscle. At the pelvic brim it courses medially to the sacroiliac joint then laterally near the ischial spine before it turns medially to enter the bladder through a submucosal tunnel (the UVJ). The ureter is lined by transitional epithelium and has a muscular wall consisting of circular and longitudinal muscle bundles and an outer adventitia that is continuous with the renal capsule and adventitia of the bladder. On unenhanced CT, 3 mm is the upper limit of the normal diameter. Peristalsis of the ureter occurs approximately six times per minute in well-hydrated patients. Peristalsis may result in short segments of dilated ureter without other evidence of obstruction.

Ureteral Duplication

Duplication of the ureters is the most common anomaly of the urinary tract. Complete duplication of the ureter may be an incidental normal variant or may be associated with ectopic insertion of the ureter, ectopic ureteroceles, and vesicoureteral obstructed ureteral duplication is more common in females.

- The ureter draining the upper pole of the kidney typically has fewer calyces, inserts into the bladder medially and inferiorly to the lower pole ureter (Weigert–Meyer rule), and is more likely to be ectopic and obstructed and end in a ureterocele. With high-grade obstruction the upper pole of the kidney is atrophic and is replaced by a cyst representing the dilated upper-pole pelvis (Fig. 15-38).
- The ureter draining the lower pole of the kidney typically inserts into the bladder at the normal location. The lower-pole system is prone to reflux if an ectopic ureterocele from the upper-pole system distorts the lower-pole UVJ.
- A higher frequency of UPJ obstruction is seen in the lower-pole system.
- When duplication is incomplete, the ureters typically fuse at a variable distance from the kidney, resulting in a single ureteral insertion into the bladder. Yo-yo reflux of urine occurs between the two ureters, induced by peristalsis of one ureter and then the other.

TCC of the Ureter

TCC accounts for 90% of ureteral tumors. About 75% occur in the distal ureter. More than 50% are associated with the presence or development of bladder TCC.

- Tumors appear as a soft-tissue mass of higher attenuation than unopacified urine that expands and obstructs the ureter (Fig. 15-39). When contrast is present the lesion appears as an irregular filling defect within high-attenuation urine. Irregular thickening of the ureteral wall is seen with stricturing lesions (Fig. 15-40). Enhancement of the tumor on IV contrast is minimal.

RENAL STONE DISEASE

MDCT has forever changed the imaging of renal stone disease. CT is now the imaging method of choice for detection of renal stones and diagnosis of the complications of renal stone disease. Conventional radiographs have a specificity of only 77% for stone detection. Conventional radiographs and intravenous pyelograms (IVPs) have been replaced by helical MDCT. CT for stones requires no contrast and no patient preparation. With MDCT the study is routinely completed in seconds. CT may also provide an alternate diagnosis for the patient's symptoms including other urinary pathology, acute appendicitis, diverticulitis, pancreatitis, adnexal masses, and leaking aneurysms.

CT Appearance of Urinary Stones

Whereas only about 85% of urinary stones are seen as calcificied densities on conventional radiographs, CT detects nearly all calculi. Calcium oxalate and calcium phosphate stones are most common (73%) and typically have a CT attenuation of 1200 to 2800 HU. Struvite stones (magnesium aluminum phosphate; 15% of renal stones) are seen with chronic infection. Struvite attenuation ranges from 600 to 900 HU. Uric acid stones (8%), which are radiolucent on conventional radiographs, have an attenuation of 200 to 450 HU. Cystine stones (1% to 4% of cases) are moderately radiopaque because of their sulfur content. Calcium may be present in some cystine stones. Cystine stones have attenuation values of 200 to 1100 HU, depending on their calcium content. High CT attenuation makes stones easy to differentiate from other urinary tract lesions such as tumors, hematoma, fungus balls, and sloughed papilla.

- Virtually all stones, even those that are radiolucent on conventional radiographs, are identified as high-attenuation foci on CT images viewed with soft-tissue windows (Figs. 15-37 and 15-41). The threshold size for stone detection by CT is approximately 1 mm.

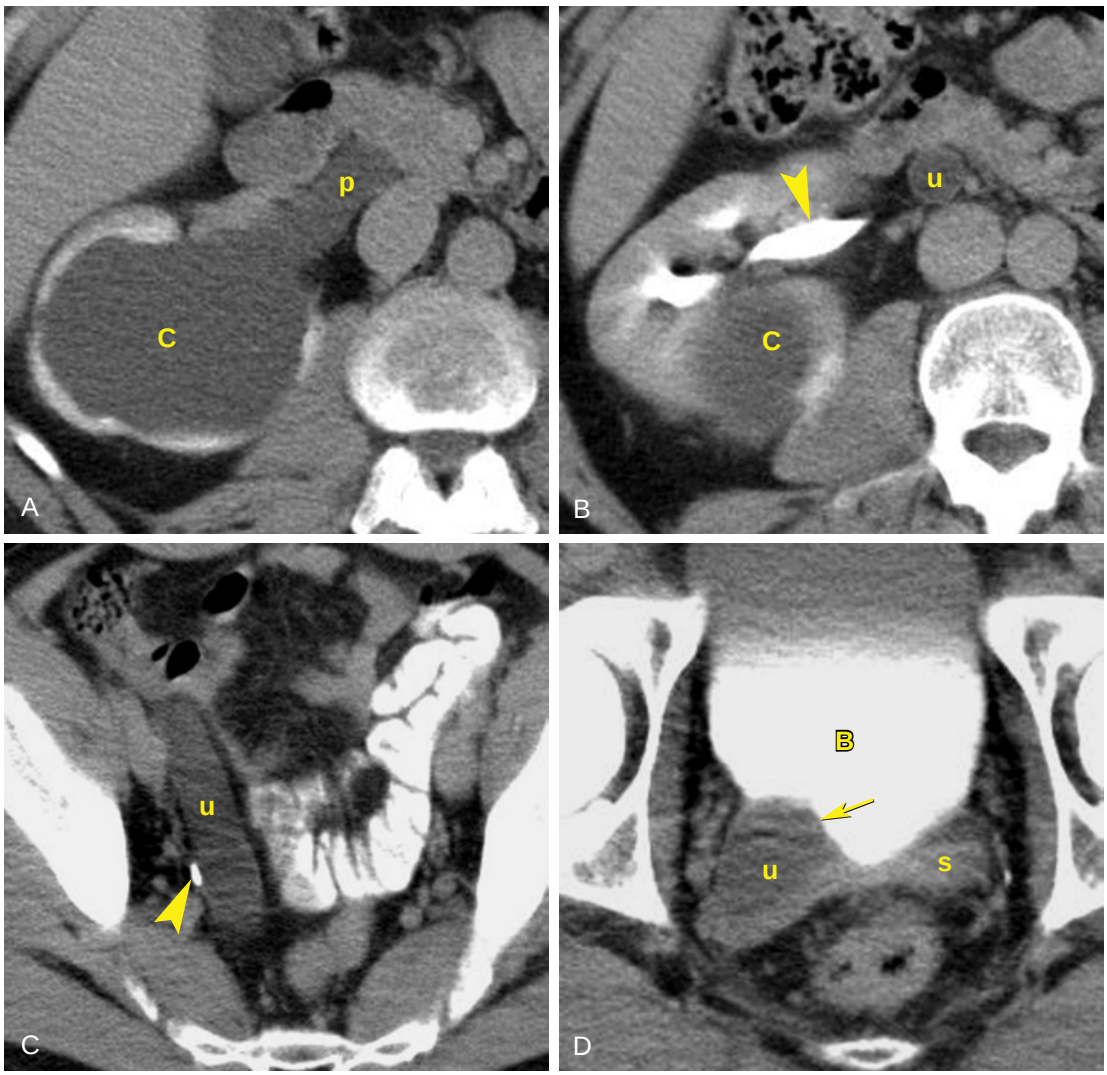

FIGURE 15-38 ■ Obstructed ureteral duplication. *A*, A cystic structure (C) at the upper pole of the right kidney communicates with a dilated pelvis (p). The cystic structure represents the obstructed collecting system of the upper pole of the kidney. The absence of contrast excretion into the obstructed collecting system is evidence of absent renal function of the upper pole. The parenchyma of the chronically obstructed upper pole system is markedly atrophic. *B*, Computed tomography image obtained inferior to *A* shows the caudal portion of the obstructed upper pole system (C) and the functioning lower pole system excreting contrast into a separate renal pelvis (*arrowhead*). The dilated ureter (u) continuing from the upper pole system is also evident. *C*, Lower in the pelvis, the greatly dilated upper pole ureter (u) resembles a fluid-filled sausage. The normal lower pole ureter (*arrowhead*) is normal in size and is filled with contrast. *D*, The dilated ureter (u) of the upper pole terminates in the bladder (B) as a bulging ectopic ureterocele (*arrow*). The bladder shows a contrast–urine fluid level, with the contrast agent excreted from the normally functioning lower pole system layering dependently. The normal lower pole ureter inserts into the bladder at a higher level. The seminal vesicles (s) are distorted and displaced by the dilated upper pole ureter.

- Ureteral calculi are usually geometric or oval in shape (Figs. 15-41 and 15-42). They are seldom completely round. This feature is useful in differentiating stones from phleboliths. It has been reported that the positive predictive value of geometric shape in identifying a calculus is as high as 100%.
- The single exception to stones being of high attenuation on CT is crystalline stones in urine related to the use of protease inhibitors (indinavir, Crixivan®) in the treatment of human immunodeficiency virus disease. These stones are of soft-tissue attenuation on CT scans but may cause acute ureteral obstruction. Contrast-enhanced CT demonstrates these stones as tiny filling defects in the collecting system or ureter.
- The burden of stones in the kidneys is easily determined by CT. Stones are seen in the region of the minor calyces or medullary

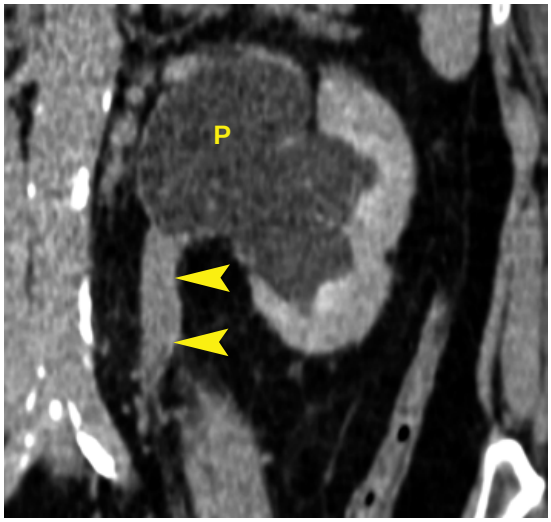

FIGURE 15-39 ■ Transitional cell carcinoma of the ureter obstructing the left kidney. Coronal-plane postcontrast computed tomography image shows marked dilatation of the left renal pelvis (P) and collecting system associated with delayed contrast excretion from the left kidney. The left proximal ureter (*arrowheads*) is dilated and of uniform soft-tissue attenuation replacing internal fluid attenuation. Transitional cell carcinoma was confirmed by ureteroscopic biopsy.

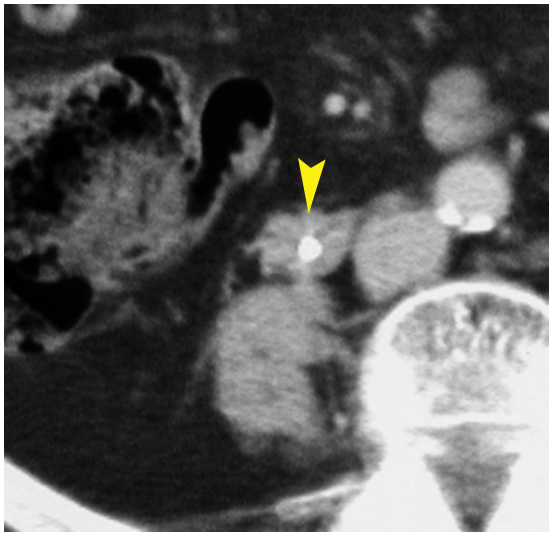

FIGURE 15-40 ■ Transitional cell carcinoma of the ureter. The wall of the ureter (*arrowhead*) is markedly and irregularly thickened, with soft-tissue strands extending into the adjacent fat. Computed tomography-guided percutaneous biopsy confirmed transitional cell carcinoma. A stent, seen as a high-density structure within the ureter, was placed because the ureter was severely strictured.

pyramids. The stone burden is defined as the number and size of stones present. Stone burden is used to determine therapy such as lithotripsy.

- The tips of the renal pyramids are of high attenuation when the patient is dehydrated

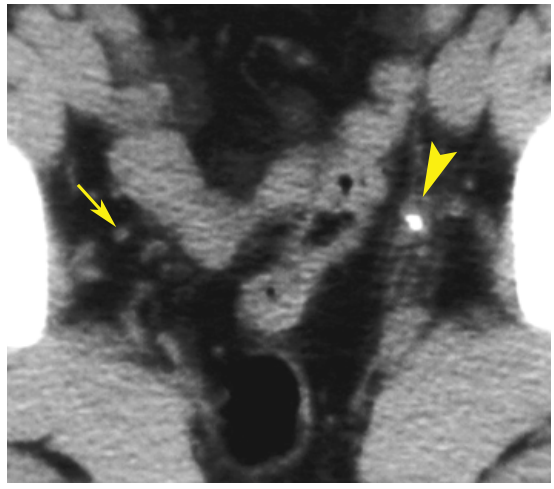

FIGURE 15-41 ■ Stone in the ureter: tissue rim sign. Noncontrast computed tomography (CT) of the pelvis shows a stone impacted in the distal left ureter (*arrowhead*), seen as an irregularly shaped, high-attenuation focus. The wall of the ureter produces a rim of soft-tissue density around the stone (the tissue rim sign). The normal right ureter (*arrow*) is identified by scrolling through sequential CT images, keeping track of the course of the ureter.

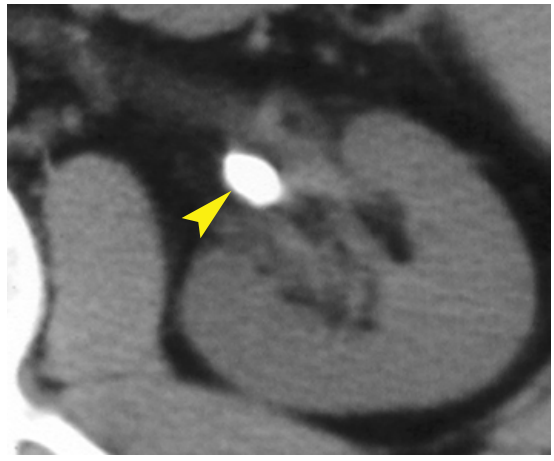

FIGURE 15-42 ■ Stone at the ureteropelvic junction (UPJ). A large stone is impacted at the left UPJ (*arrowhead*). A bloom artifact from the high-attenuation stone obscures the tissue rim sign. Careful inspection of serial computed tomography images confirms that the stone is located at the UPJ. Even though the obstruction is of high grade, the degree of hydronephrosis is slight because the obstruction is acute.

(Fig. 15-34). This normal finding of *white pyramids* should not be interpreted as representing renal stones.

Acute Ureteral Obstruction

Noncontrast MDCT has a sensitivity of 94% to 98% and specificity of 96% to 98% for acute ureteral obstruction caused by an impacted stone.

CT evidence of acute ureteral obstruction caused by stones includes the following.

- A stone is demonstrated in the ureter (Figs. 15-41, 15-42, and see 15-45*B*). The most common locations for stone impaction are at the UPJ, where the ureter crosses the pelvic brim, and at the UVJ. The ureter is followed on consecutive slices until a stone is identified. Scrolling on the CT monitor is the easiest way to follow the course of the ureter. Knowledge of the anatomy of the course of the ureter and of adjacent vessels is crucial for accurate interpretation.
- The size of the stone is measured and its location is precisely reported. The probability of spontaneous passage is related to size and location of the ureteral stone. Stones smaller than 4 mm nearly always pass spontaneously. Stones of 6 mm pass about half of the time. Stones larger than 8 mm rarely pass spontaneously. Stone size and location are important factors used to determine the treatment for stones that do not pass spontaneously. Stones >5 mm and located in the proximal two-thirds of the ureter are more likely to require lithotripsy or endoscopic removal.
- To confirm a stone in the ureter, the radiologist should look for a tissue rim sign (present in ~76% of cases). The *tissue rim sign* (Fig. 15-41) describes a halo of soft-tissue that surrounds stones in the ureter. The soft-tissue rim is the wall of the ureter. The tissue rim sign may be absent because of bloom effect artifacts or a very thin ureteral wall.
- The CT scout scan is useful for detection of stones and other abnormalities. Examination of the scout scan should be included in every CT interpretation. If the stone is visible on the scout scan, conventional radiographs can be used to monitor its passage. Calculi not visible on conventional radiographs can be followed, when necessary, with unenhanced CT.
- Secondary findings of urinary obstruction are common but often subtle (Fig. 15-43). Comparison to the opposite side is highly useful in differentiating preexisting findings from acute obstruction. The presence of multiple secondary findings improves the confidence and accuracy of diagnosing acute obstruction. The frequency of visualization of secondary signs increases with the duration of symptoms.
- The obstructed kidney may be enlarged and slightly decreased in CT density because of edema. A 5-HU attenuation decrease as compared to the opposite kidney is significant as evidence of edema in an obstructed kidney.
- Periureteral and perinephric fat stranding occurs secondary to edema produced by acute obstruction. The amount of edema present correlates with the severity of the obstruction. Many patients, particularly older ones, may have preexisting stranding in the perinephric fat. The radiologist should look for asymmetry of stranding on the involved side.
- The pelvicalyceal system is at most mildly dilated with acute stone obstruction. Dilated calyces are best seen at the poles of the kidney as rounded, fluid-filled structures that displace renal sinus fat. Comparison with the opposite kidney is always helpful. Profound dilatation of the collecting system is evidence of chronic rather than acute obstruction.
- The unilateral absence of white pyramids on the affected side has been described as

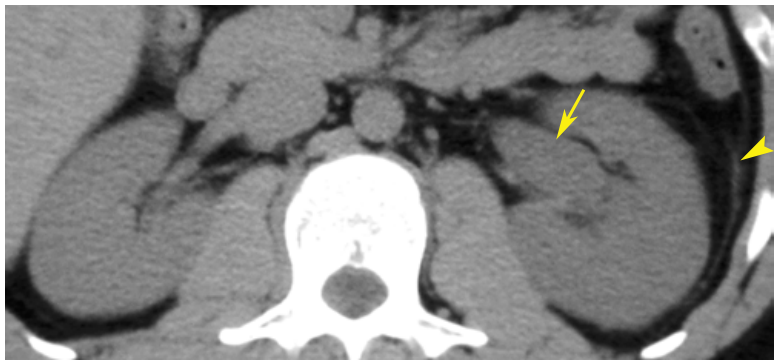

FIGURE 15-43 ■ Acutely obstructed kidney. Computed tomography (CT) image of a patient with left flank pain demonstrates subtle swelling and decreased density of the left kidney, with mild dilatation of the left renal pelvis (*arrow*) and calyces. The margin of the left kidney with perirenal fat is indistinct. The left renal fascia (*arrowhead*) is mildly thickened. This constellation of subtle findings is suggestive of left ureteral obstruction. A stone impacted at the left ureterovesical junction was seen on CT images through the pelvis.

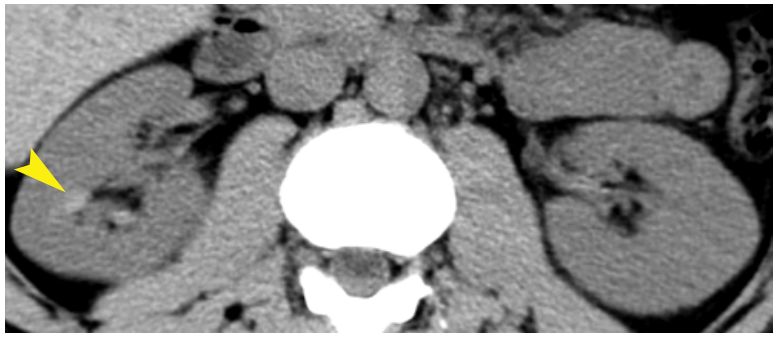

FIGURE 15-44 ■ Unilateral white pyramids. The tips of the medullary pyramids in the right kidney show high attenuation (*arrowhead*), indicating that this patient with left flank pain is dehydrated. On the symptomatic left side, no white pyramids are seen. The unilateral absence of white pyramids is a subtle sign of acute obstruction. A stone was demonstrated at the left ureterovesical junction.

a subtle sign of obstruction (Fig. 15-44). Edema and swelling counteract the urine concentration effect of systemic dehydration.

- The ureter is mildly dilated to the level of the stone. Normal ureteral peristalsis produces transient focal areas of dilatation and narrowing that must be differentiated from diffuse dilatation to the level of obstruction. The ureter below the obstructing calculus is not dilated.
- Focal perinephric fluid collections (Fig. 15-45) may occur secondary to rupture of the collecting system at the fornix of a calyx caused by obstruction and high urine output.
- Axial-plane CT images may be reformatted into coronal- and sagittal-plane images in problematic cases.

Pitfalls in Diagnosis of Stones in the Ureter

No imaging test is perfect. A wide variety of pitfalls complicate interpretation of renal stone CT.

- An extrarenal pelvis may mimic pelviectasis.
- Peripelvic cysts may simulate hydronephrosis (Fig. 15-46).
- Many patients, especially older ones, have preexisting stranding in the peripelvic fat. Comparison with the opposite side is critical for detection of asymmetric stranding.
- Preexisting postobstructive changes are difficult to differentiate from acute obstruction.
- Phleboliths commonly mimic stones (Fig. 15-47). Phleboliths are calcifications that originate in thrombi within pelvic veins. Most phleboliths are found in perivesical veins, in periprostatic veins in men, and in periuterine and perivaginal veins in women. Occasionally phleboliths are seen in the gonadal veins that parallel the course of the ureters. Most phleboliths are round. They are seldom oval and are never geometric in shape. Visualization of a central lucency is highly characteristic of phleboliths but is

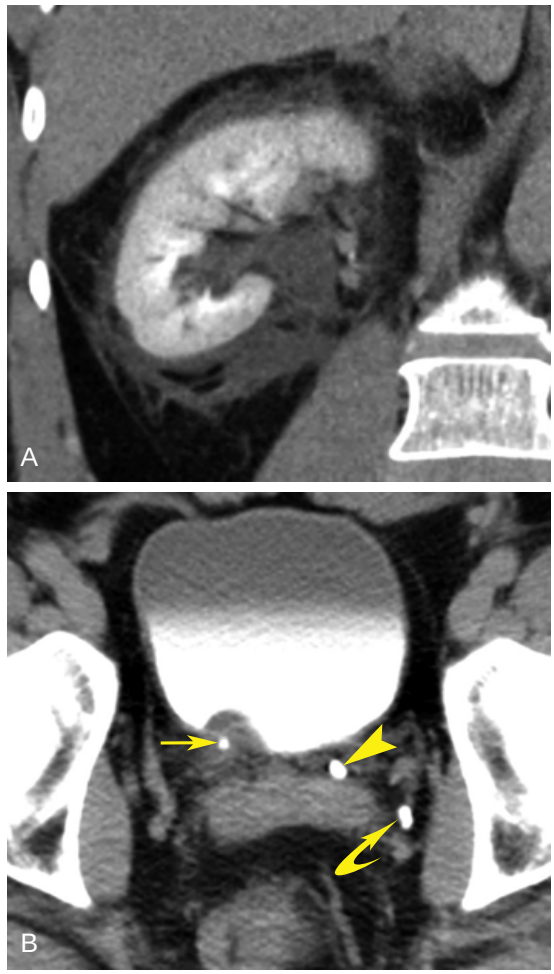

FIGURE 15-45 ■ Obstruction: ruptured calyx. *A,* Postcontrast computed tomography (CT) reconstructed in coronal-plane reveals delayed contrast excretion from the right kidney and fluid representing unopacified urine infiltrating the perirenal space. Acute high-grade obstruction of the kidney in a well-hydrated patient with good kidney function may result in rupture of the collecting system at the calyceal fornix. The diuretic effect of intravenous contrast administration may even precipitate the rupture. *B,* Axial CT image in the same patient reveals the obstructing stone (*long straight arrow*) impacted at the swollen ureterovesical junction. The normal contrast-filled left ureter (*arrowhead*) is also demonstrated. A phlebolith (*curved arrow*) is present posteriorly on the left.

FIGURE 15-46 ■ Peripelvic cysts. *A,* Noncontrast computed tomography (CT) reveals bilateral cystic structures (*arrows*) in the renal sinuses that resemble hydronephrosis. *B,* Postcontrast CT in the pyelogram phase shows no contrast filling of the cystic structures (*arrows*), indicating that they are peripelvic cysts. Contrast does opacify the collecting systems (*arrowheads*), which are compressed by the cysts within the renal sinuses of both kidneys. The clue to diagnosis is inspection of serial images that reveal no connection of the peripelvic cysts with a dilated renal pelvis.

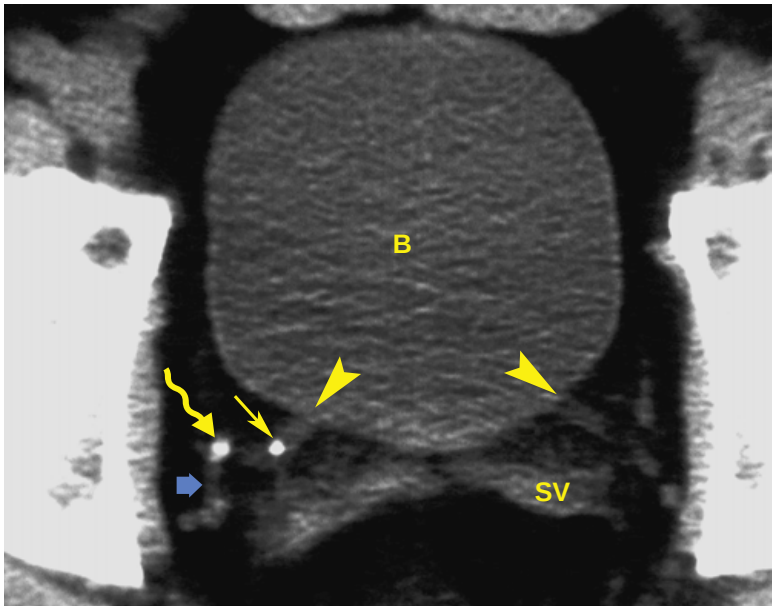

FIGURE 15-47 ■ Phlebolith and stone. The seminal vesicles (SV) serve as an anatomic landmark for the level of the ureterovesical junctions (UVJs, *arrowheads*). The right and left UVJs are located at the same axial level on computed tomography. A stone (*straight arrow*) is impacted in the distal right ureter. An adjacent phlebolith (*squiggly arrow*) is identified by the tail sign, representing the thrombosed vein (*short blue arrow*). The bladder (B) is filled with urine, making identification of the UVJs easier.

less often evident on CT than on conventional radiographs. The *tail sign* describes a tail of noncalcified vein extending from the phlebolith. A tail sign is reported as present in association with phleboliths in 21% to 65% of cases. Phleboliths are lower in attenuation than most stones, with a mean attenuation of 160 HU and a range of 80 to 278 HU. The probability that a calcification represents a phlebolith is 0.03% when mean attenuation is 311 HU or more.

- Atherosclerotic calcifications may be mistaken for ureteral stones. Differentiation is made by carefully examining serial slices and determining if the calcification is vascular or ureteral.
- When signs of ureteral obstruction are present yet no stone is evident, the radiologist should consider a recently passed stone, pyelonephritis, a stricture or tumor, or a stone related to protease inhibitor treatment.

- Stones passed from the ureter may be identified in the bladder or urethra or may not be seen.
- The radiologist should always look for evidence of nonurinary causes of flank pain. It has been reported that unenhanced CT is 94% accurate in the diagnosis of appendicitis. Adnexal masses are usually easily detected.
- Subsequent contrast-enhanced CT may be needed in up to 20% of cases to provide an unequivocal diagnosis.

SUGGESTED READING

Bosniak MA: The current radiological approach to renal cysts. *Radiology* 158:1–10, 1986.

Bosniak MA: Problems in the radiologic diagnosis of renal parenchymal tumors. *Urol Clin North Am* 20:217–230, 1993.

Bosniak MA: The Bosniak renal cyst classification: 25 year later. *Radiology* 262:781–785, 2011.

Brant WE: Spiral CT replaces IVP and KUB for renal stone disease. *Diag Imag* 2306:51–57, 2001.

Cheng PM, Moin P, Dunn MD, et al.: What the radiologist needs to know about urolithiasis: Part 1—pathogenesis, types, assessment, and variant anatomy. *AJR Am J Roentgenol* 198:W540–W547, 2012.

Cheng PM, Moin P, Dunn MD, et al.: What the radiologist needs to know about urolithiasis: Part 2—CT findings, reporting, and treatment. *AJR Am J Roentgenol* 198:W548–W554, 2012.

Craig WD, Wagner BJ, Travis MD: Pyelonephritis: Radiologic–pathologic review. *Radiographics* 28:255–276, 2008.

Freire M, Remer EM: Clinical and radiologic features of cystic renal masses. *AJR Am J Roentgenol* 192:1367–1372, 2009.

Hartman DS, Choyke PL, Hartman MS: A practical approach to the cystic renal mass. *Radiographics* 24:S101–S115, 2004.

Israel GM, Bosniak MA: Pitfalls in renal mass evaluation and how to avoid them. *Radiographics* 28:1325–1338, 2008.

Jung YY, Kim JK, Cho K-S: Genitourinary tuberculosis: Comprehensive cross-sectional imaging. *AJR Am J Roentgenol* 184:143–150, 2005.

Kambadakone AR, Eisner BH, Catalano OA, Sahani DV: New and evolving concepts in the imaging and management of urolithiasis: Urologists' perspective. *Radiographics* 30:603–623, 2010.

Katabathina VS, Kota G, Dasyam AK, et al.: Adult renal cystic disease: A genetic, biological, and developmental primer. *Radiographics* 30:1509–1523, 2010.

Leung RS, Biswas SV, Duncan M, Rankin S: Imaging features of von Hippel–Lindau disease. *Radiographics* 28:65–79, 2008.

Ng CS, Wood CG, Silverman PM, et al.: Renal cell carcinoma: Diagnosis, staging, surveillance. *AJR Am J Roentgenol* 191:1220–1232, 2008.

Pooler BD, Pickhardt PJ, O'Connor SD, et al.: Renal cell carcinoma: Attenuation values on unenhanced CT. *AJR Am J Roentgenol* 198:1115–1120, 2012.

Prando A, Prando P, Prando D: Urothelial cancer of the renal pelvicaliceal system: Unusual imaging manifestations. *Radiographics* 30:1553–1566, 2010.

Prasad SR, Humphrey PA, Catena AD, et al.: Common and uncommon histologic subtypes of renal cell carcinoma: Imaging spectrum with pathologic correlation. *Radiographics* 26:1795–1810, 2006.

Prasad SR, Surabhi VR, Menias CO, et al.: Benign renal neoplasms in adults: Cross-sectional imaging findings. *AJR Am J Roentgenol* 190:158–164, 2008.

Rowell AC, Sangster GP, Caraway JD, et al.: Genitourinary imaging: Part 1, congenital urinary anomalies and their management. *AJR Am J Roentgenol* 199:W545–W553, 2012.

Sheth S, Ali S, Fishman E: Imaging of renal lymphoma: Patterns of disease with pathologic correlation. *Radiographics* 26:1151–1168, 2006.

Silverman SG, Gan YU, Mortele KJ, et al.: Renal masses in the adult patient: The role of percutaneous biopsy. *Radiology* 240:6–22, 2006.

Stakhovsky O, Yap SA, Leveridge M, et al.: Small renal mass: What the urologist needs to know for treatment planning and assessment of treatment results. *AJR Am J Roentgenol* 196:1267–1273, 2011.

Tirkes T, Sandrasegaran K, Patel AA, et al.: Peritoneal and retroperitoneal anatomy and its relevance for cross-sectional imaging. *Radiographics* 32:437–451, 2012.

Umeoka S, Koyama T, Miki Y, et al.: Pictorial review of tuberous sclerosis in various organs. *Radiographics* 28:e32, 2008.

Vikram R, Sandler CM, Ng CS: Imaging and staging of transitional cell carcinoma: Part 2, upper urinary tract. *AJR Am J Roentgenol* 192:1488–1493, 2009.

Wasnik AP, Elsayes KM, Kaza RK, et al.: Multimodality imaging in ureteric and periureteric abnormalities. *AJR Am J Roentgenol* 197:W1083–W1092, 2011.

Wolin EA, Hartman DS, Olson JR: Nephrographic and pyelographic analysis of CT urography: Differential diagnosis. *AJR Am J Roentgenol* 200:1197–1203, 2013.

Wolin EA, Hartman DS, Olson JR: Nephrographic and pyelographic analysis of CT urography: Principles, patterns, and pathophysiology. *AJR Am J Roentgenol* 200:1210–1214, 2013.

CHAPTER 16

ADRENAL GLANDS

William E. Brant

The adrenal glands are the primary focus of attention in three clinical circumstances. A patient may be referred for imaging because a clinical diagnosis of adrenal hormone hyperfunction has been made. Computed tomography (CT) is then used to identify and characterize the lesion. The adrenal glands are commonly imaged to detect suspected metastatic disease, especially when the primary tumor, such as lung carcinoma, commonly metastasizes to the adrenals. Adrenal lesions are frequently detected incidentally on imaging studies performed for other indications (about 5% of all abdominal CT scans). The significance of the finding must be assessed radiographically and clinically. CT remains the imaging method of choice for evaluation of the adrenal glands.

NORMAL ADRENAL GLANDS

The adrenal glands have an outer cortex and an inner medulla that are functionally independent and anatomically distinct. The cortex secretes steroid hormones including cortisol, aldosterone, androgens, and estrogens. The medulla produces the catecholamines epinephrine and norepinephrine. The adrenal glands lie in the perirenal space, surrounded by fat. The glands are usually triangular, or an inverted V or Y shape (Fig. 16-1). The right adrenal gland lies above the right kidney, posterior to the inferior vena cava and between the right crus of the diaphragm and the right lobe of the liver. The left adrenal gland lies adjacent to the upper pole of the left kidney, posterior to the pancreas and splenic vessels and lateral to the left crus of the diaphragm. The limbs of the adrenal gland are 4 to 5 cm in length and normally do not exceed 10 mm in thickness. Limb thickness is uniform and the margins are straight or concave. Normal adrenal glands are approximately equal to muscle in CT attenuation on precontrast scans. Moderate enhancement is evident after contrast administration.

CT TECHNIQUE FOR AN ADRENAL MASS

Noncontrast scans are obtained to document adrenal anatomy, to measure the noncontrast attenuation of any lesions, and to serve as a baseline for contrast enhancement. A slice thickness of 0.625 to 2.5 mm is utilized. The attenuation of any adrenal nodule or mass lesion is measured using a range of interest (ROI) that encompasses most of the lesion. If the average attenuation of the lesion is below 10 Hounsfield units (HU), the lesion is highly likely to be a benign adrenal adenoma. If the average attenuation of the lesion is greater than 10 HU, a contrast-enhanced study should be performed. Routinely, 100 to 120 mL of nonionic contrast agent with an iodine concentration of 350 mg/mL is administered intravenously at 3.0 mL/second. Thin-section scans (optimally 0.625 mm) should be repeated through both adrenal glands, obtained at 60 seconds after contrast injection for the adrenal cortical phase and again at 15 minutes after injection for the delayed phase.

ADRENAL MASSES WITH A SPECIFIC IMAGING APPEARANCE

Myelolipoma

Myelolipoma is an uncommon benign adrenal tumor consisting of mature fat with interspersed hematopoetic bone-marrow elements. The lesion is not associated with endocrine abnormalities and has no malignant potential. The tumor is most often discovered as an incidental finding. Occasionally, tumors present with acute spontaneous painful hemorrhage. Tumors may also arise outside the adrenal gland.

- The presence of fat is characteristic. CT demonstrates large deposits of fat interspersed with higher-density soft tissue (Fig. 16-2). The fat is nearly equal to subcutaneous fat in CT attenuation, typically –80 to –100 HU. The soft-tissue components are relatively low in CT attenuation (20 to 30 HU), reflecting a mixture of fat and myeloid tissue.
- Small calcifications may be present.
- Hemorrhage alters the imaging appearance. CT shows acute hemorrhage as foci of high attenuation within the fatty mass.

- Tumors vary in size from 1 to 2 cm up to 17 cm. Growth of the lesion is reported in 50% of cases.
- Extra-adrenal myelipomas are most common in the presacral space and retroperitoneum, occurring less commonly in the mediastinum, abdomen, and muscle fascia.

Cysts

True cysts of the adrenal gland are lined with endothelium or epithelium. Most lesions are asymptomatic and are discovered incidentally. They may produce symptoms because of hemorrhage.

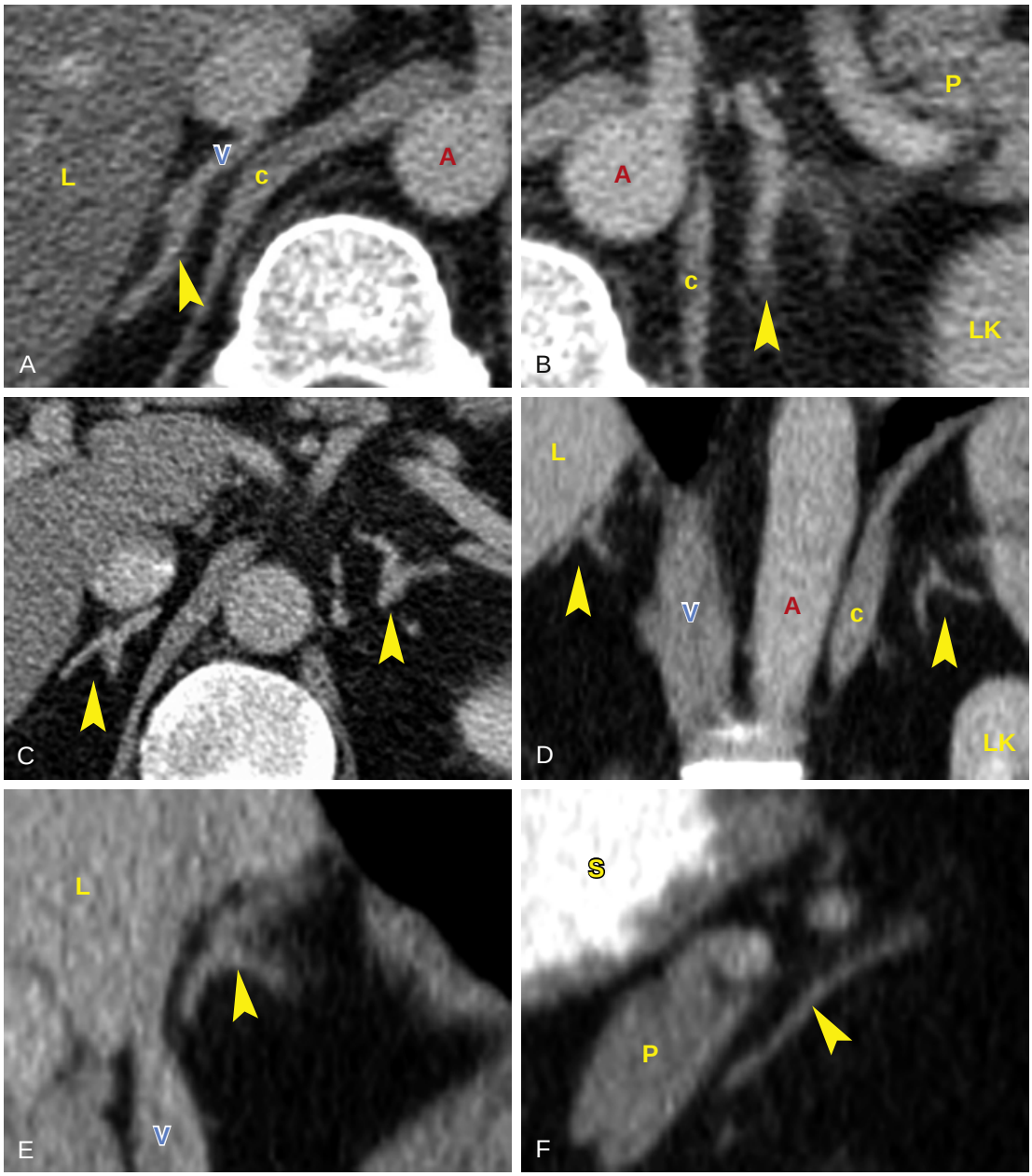

FIGURE 16-1 ■ Normal adrenal glands. *A*, Axial computed tomography (CT) image shows a linear appearance of the right adrenal gland (*arrowhead*). Note the anatomic landmarks used to identify the right adrenal gland: L, liver; V, inferior vena cava; A, aorta; c, right crus of the diaphragm. *B*, Axial CT image shows an inverted-Y appearance of the left adrenal gland (*arrowhead*). Note the anatomic landmarks used to identify the left adrenal gland: A, aorta; c, left crus of the diaphragm; P, pancreas; LK, left kidney. *C*, Axial CT image shows bilateral normal adrenal glands (*arrowheads*). Note the anatomic landmarks and the variable shape of the normal glands. *D*, Coronal CT image shows bilateral normal adrenal glands (*arrowheads*). A, aorta; L, liver; V, inferior vena cava; c, crus of the diaphragm; LK, left kidney. *E*, Sagittal CT image shows a normal right adrenal gland (*arrowhead*). L, liver; V, inferior vena cava. *F*, Sagittal CT image shows a normal left adrenal gland (*arrowhead*). S, stomach; P, pancreas.

- Cysts are well-marginated, thin-walled (<3 mm), non-enhancing, homogeneous, fluid-containing masses (Fig. 16-3). Thin internal septations are sometimes present.
- The wall may have thin peripheral calcification if previous hemorrhage has occurred.
- Cyst contents have characteristics of simple fluid (<20 HU) unless hemorrhage has occurred.

Pseudocysts

Pseudocysts account for about 40% of adrenal cysts. They occur as a sequela of previous adrenal hemorrhage. Pseudocysts have fibrous walls without a cellular lining.

- Pseudocyst appears as a hypodense mass with a thin or thick wall and, commonly, internal septations.
- Cyst contents are commonly of higher attenuation than simple fluid but do not enhance. Fluid–fluid levels may be present.
- Calcification in the wall is commonly present (56% of cases) (Fig. 16-4).

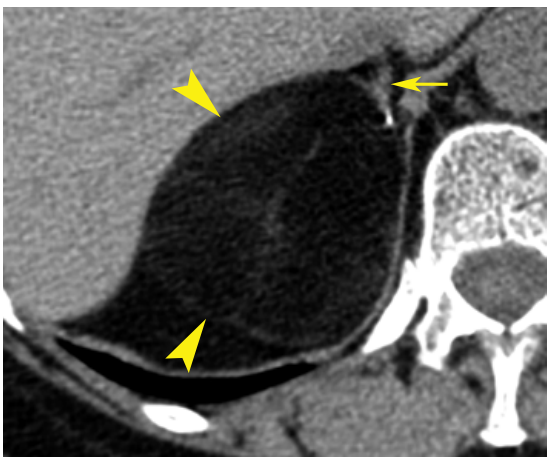

FIGURE 16-2 ■ Myelolipoma. A fat-density tumor (between *arrowheads*) arises from the right adrenal gland. The streaks of soft-tissue density within the tumor represent hematopoetic bone-marrow elements. A remnant of normal-appearing right adrenal gland (*arrow*) is evident.

Adrenal Hemorrhage

In the newborn, adrenal hemorrhage is commonly caused by hypoxia, birth trauma, or septicemia. In adults and older children, hemorrhage is induced by trauma, coagulopathy, or an underlying tumor.

- On unenhanced CT, an adrenal hemorrhage appears round or oval and hyperdense (50 to 90 HU) (Fig. 16-5). Stranding is commonly present in the periadrenal fat.
- Post-traumatic adrenal hemorrhage has a marked predisposition to be unilateral on the right side.
- With evolution and liquefaction of the blood clot, the adrenal mass shrinks and decreases in attenuation.
- Over time the hemorrhage may result in calcification of the adrenal gland.
- Chronic hemorrhage may be difficult to differentiate from other adrenal masses.

Pseudolesions

A variety of non-adrenal structures may simulate adrenal masses. Differentiation is made by having

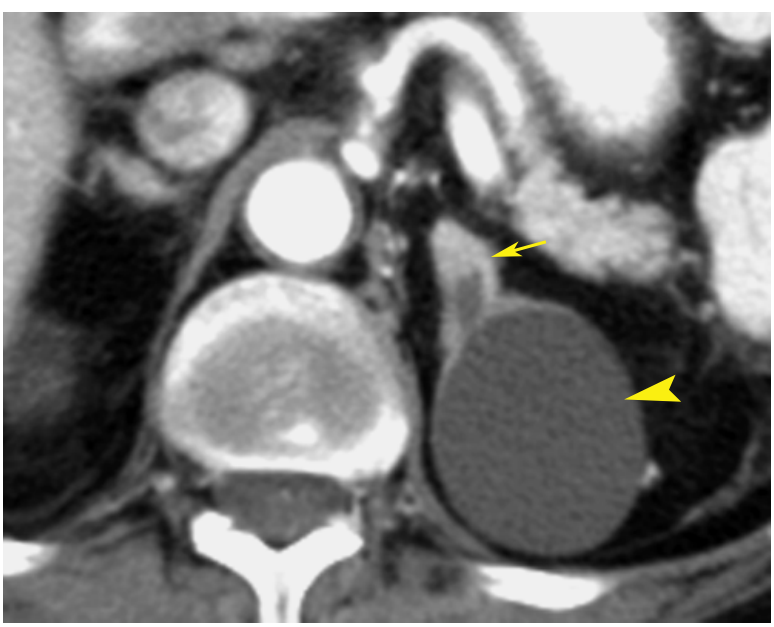

FIGURE 16-3 ■ Developmental adrenal cyst. A purely cystic mass (*arrowhead*) arises from the left adrenal gland (*arrow*). No discernible cyst wall is evident. The internal density is homogeneously low and near to water in attenuation.

a high index of suspicion and by performing appropriate correlative imaging tests. Accurate imaging diagnosis should obviously be made prior to performing an adrenal biopsy. Pseudolesions are much more common on the left side because of the larger number of structures in the region of the left adrenal gland. An optimal CT technique with oral and intravenous contrast agents and multiplanar reconstructions makes confusion of pseudolesions with real adrenal lesions less likely.

- Unopacified portions of the stomach or small bowel are differentiated from an adrenal mass by administering oral contrast and repeating the CT scan (Fig. 16-6).

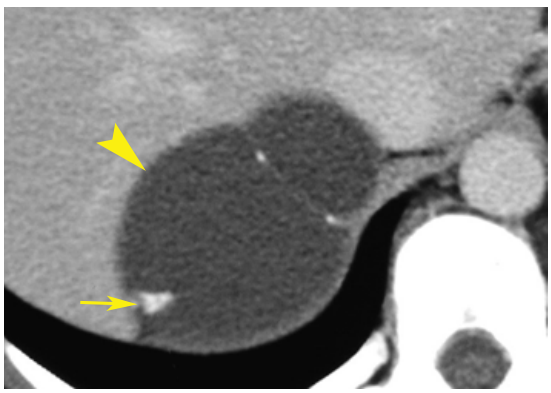

FIGURE 16-4 ■ Adrenal pseudocyst. This cystic right adrenal mass (*arrowhead*) has calcification in a thin septation and contains a coarse dense calcium deposit (*arrow).* This appearance is characteristic of a posthemorrhage adrenal pseudocyst.

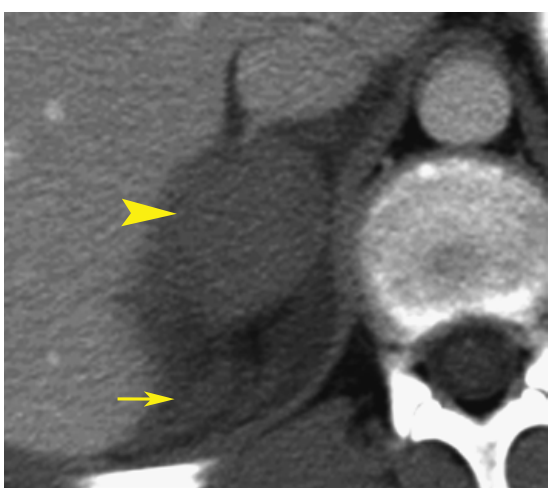

FIGURE 16-5 ■ Adrenal hemorrhage. Postcontrast computed tomography (CT) in a patient injured in a motor-vehicle accident shows hemorrhage expanding the right adrenal gland (*arrowhead*) and producing a homogeneous mass. Additional hemorrhage (*arrow*) is seen in the perirenal space. Follow-up CT 4 months later confirmed complete resolution of the adrenal hemorrhage.

- Tortuous blood vessels are identified by contrast-enhanced CT or Doppler ultrasound. Splenic artery aneurysms often have a calcified wall and mimic a pseudocyst.
- An accessory spleen or a splenic lobulation is recognized by its smooth margin and by CT attenuation and enhancement identical to splenic tissue.

Adrenocortical Carcinoma

Carcinoma of the adrenal gland is associated with adrenal hyperfunction in 50% of cases. Cushing syndrome is most common. Most primary carcinomas are easily differentiated from adenomas by their imaging findings. The tumor is aggressive and highly lethal, with a strong propensity to invade blood vessels.

- The adrenal mass is usually large (>5 to 6 cm) and markedly heterogeneous (Fig. 16-7). An adrenal mass that is larger than 6 cm and does not contain fat has 85% probability of being malignant.

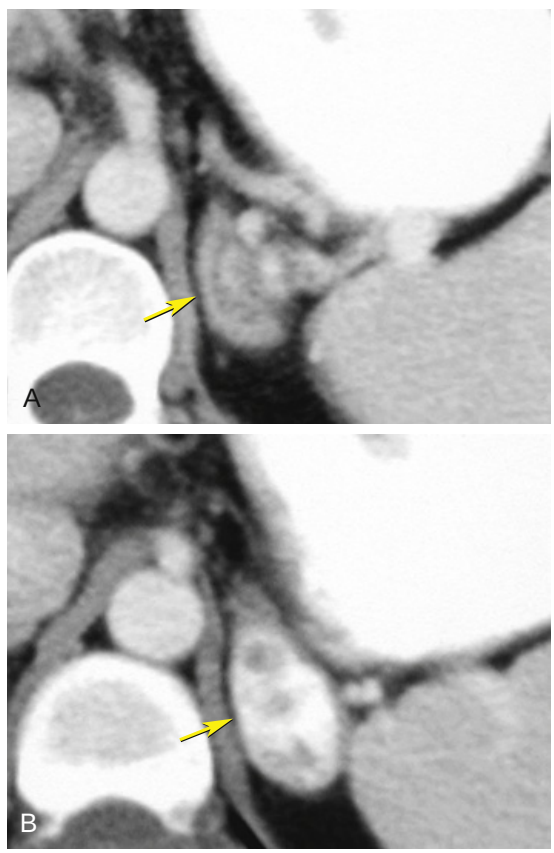

FIGURE 16-6 ■ Adrenal pseudotumor. *A*, An initial computed tomography (CT) scan reveals an apparent mass (*arrow*) in the region of the left adrenal gland. *B*, A subsequent CT scan after administration of additional oral contrast shows contrast filling a gastric diverticulum (*arrow*).

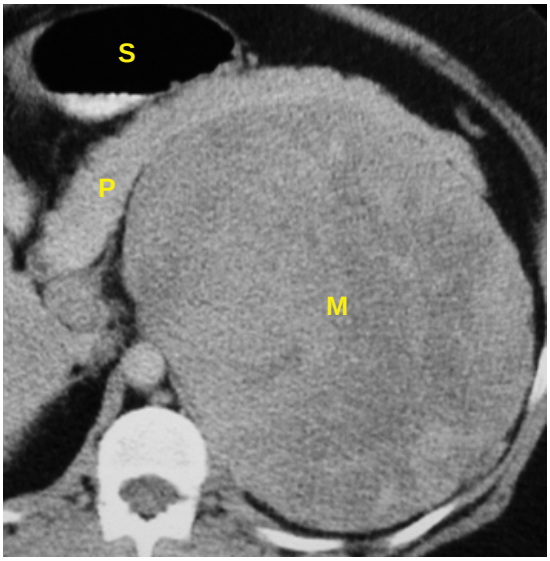

FIGURE 16-7 ■ Adrenal carcinoma. A huge, solid, heterogeneous mass (M) replaces the left adrenal gland. The pancreas (P) and stomach (S) are anteriorly displaced by the mass, confirming that the origin of the tumor is in the retroperitoneum.

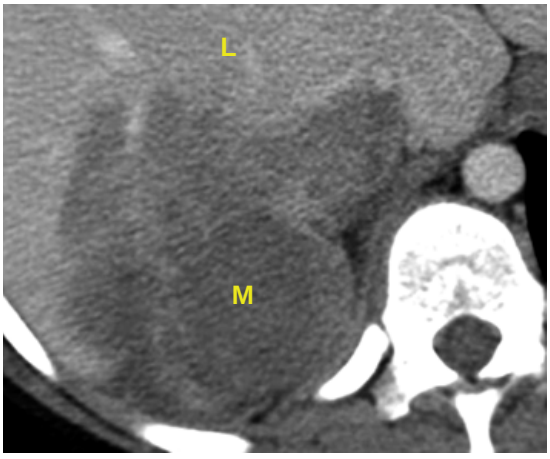

FIGURE 16-8 ■ Adrenal carcinoma with necrosis. Postcontrast computed tomography reveals a solid mass (M) arising from the right adrenal gland and invading the liver (L). Extensive low attenuation within the mass is evidence of necrosis.

- Central necrosis is common and irregular calcification (Fig. 16-8) is present in 30% of cases.
- Tumors enhance heterogeneously and have washout features characteristic for malignant lesions (Fig. 16-9).
- A tumor thrombus in the renal vein or inferior vena cava is a frequent complication that carries a significant risk of pulmonary embolus.

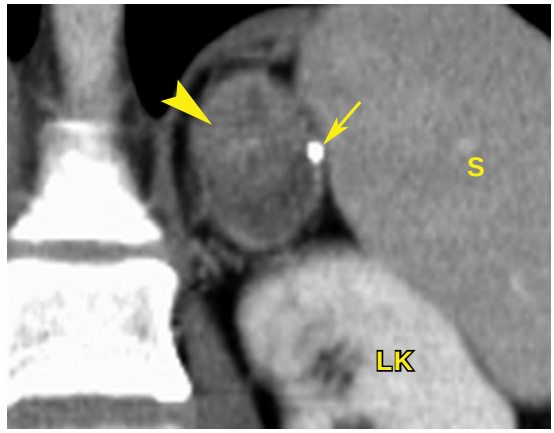

FIGURE 16-9 ■ Adrenal carcinoma. A coronal computed tomography image shows a heterogeneous mass (*arrowhead*) arising from the left adrenal gland. Coarse calcification is present (*arrow*). Contrast enhancement and washout were characteristic of malignancy. S, spleen; LK, left kidney.

- Direct invasion of adjacent structures and metastases to regional lymph nodes, liver, bone, and lung are common findings at presentation.
- Focal fat deposits are sometimes present in adrenal carcinomas. However, all fat-containing tumors reported have had other evidence of malignancy.
- Rarely, large, degenerated, benign adrenal adenomas have an appearance similar to adrenal carcinoma.

Lymphoma

The adrenal gland is involved in approximately 4% of patients with non-Hodgkin's lymphoma. Primary lymphoma arising in the adrenal gland is extremely rare.

- Most common is total encasement of the adrenal gland by retroperitoneal adenopathy (Fig. 16-10). The adrenal gland is often not visible.
- Other imaging appearances include small, discrete adrenal masses and diffuse adrenal enlargement. Both glands are involved in 50% of cases.
- Postcontrast washout is characteristic of malignant diseases.

Adrenal Calcifications

Most adrenal calcifications in both children and adults are sequelae of adrenal hemorrhage. Tuberculosis and histoplasmosis cause adrenal calcifications and may be associated with Addison disease.

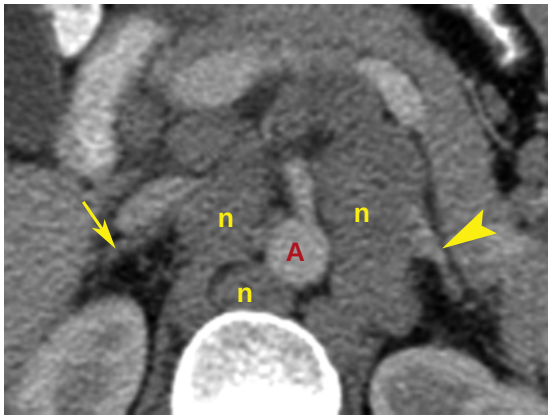

FIGURE 16-10 ■ Lymphoma. Enlarged lymphomatous nodes (n) surround the aorta (A) and partially engulf the left adrenal gland (*arrowhead*). The right adrenal gland (*arrow*) is spared.

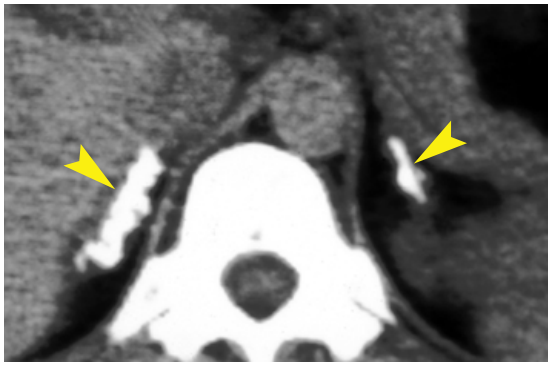

FIGURE 16-11 ■ Adrenal calcifications. Both adrenal glands (*arrowheads*) are densely calcified, probably as a result of remote hemorrhage.

- Coarse, punctate calcification in one or both glands without a mass being evident is characteristic of remote adrenal hemorrhage (Fig. 16-11).
- In children, adrenal tumors that calcify are neuroblastoma and gangioneuroma.
- In adults, adrenal tumors that calcify include adrenal carcinoma, pheochromocytoma, ganglioneuroma, and metastases.
- Wolman disease is a rare autosomal recessive condition associated with enlarged calcified adrenal glands, hepatomegaly, and splenomegaly.

HYPERFUNCTIONING ADRENAL LESIONS

Adrenal Hyperplasia

Adrenal hyperplasia is usually associated with adrenal endocrine hyperfunction, especially Cushing syndrome.

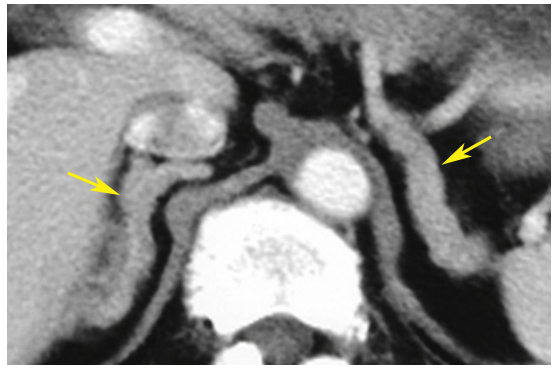

FIGURE 16-12 ■ Adrenal hyperplasia. Both adrenal glands (*arrows*) show diffuse thickening of the limbs.

- The adrenal glands most commonly are uniformly enlarged but maintain their normal adrenal shape (Fig. 16-12). The thickness of the limbs of the gland exceeds 10 mm.
- A multinodular pattern of adrenal hyperplasia may also occur. The appearance may be indistinguishable from multiple small adrenal metastases.
- Biochemical hyperplasia may be associated with a normal size and imaging appearance of the adrenal glands.

Cushing Syndrome

Excess secretion of glucocorticoids leads to *Cushing syndrome*. About 70% of patients have bilateral adrenal hyperplasia, 20% have a benign hyperfunctioning adrenal adenoma, and 10% have adrenocortical carcinoma. *Cushing disease* is caused by a pituitary adenoma that secretes adrenocorticotropic hormone, which stimulates the adrenal gland.

- Adenomas are round or oval and are usually <2 cm in diameter.
- Hyperfunctioning adenomas are indistinguishable from nonhyperfunctioning adenomas.
- Adrenal hyperplasia is usually diffuse, smooth, and bilateral. About 3% of patients with Cushing syndrome have nodular adrenal hyperplasia.

Conn Syndrome

Primary hyperaldosteronism is caused by a benign hyperfunctioning adenoma (80%) or by bilateral adrenal hyperplasia (20%) and is characterized clinically by hypokalemia and hypertension. Adrenal carcinoma is rarely a cause of hyperaldosteronism.

Adrenogenital Syndrome

Excess secretion of androgens may be a congenital or acquired condition. Congenital adrenogenital

FIGURE 16-13 ■ Aldosterone-secreting adenoma. A tiny left adrenal nodule (*arrow*) was identified as a benign aldosterone-secreting adenoma by adrenal vein sampling and surgical resection.

syndrome results from a congenital (autosomal recessive) enzyme deficiency and is associated with bilateral adrenal hyperplasia. Acquired adrenogenital syndrome is usually caused by a hyperfunctioning benign adrenal adenoma (80%) (Fig. 16-13), but 20% of cases are associated with adrenal cortical carcinoma.

Pheochromocytoma

Pheochromocytoma is a catecholamine-secreting tumor that arises from chromaffin cells of the sympathetic nervous system. Most tumors (90%) arise in the adrenal medulla and are benign and unilateral. About 10% ("rule of 10s") are extra-adrenal, with the most common location being the organ of Zuckerkandl near the origin of the inferior mesenteric artery. About 10% are bilateral and 10% are associated with syndromes including multiple endocrine neoplasia type 2, von Hippel–Lindau syndrome, tuberous sclerosis, Sturge–Weber syndrome, and neurofibromatosis.

- CT most often shows a round homogeneous mass with precontrast attenuation approximately equal to that of normal liver (Fig. 16-14).
- Cystic changes, central necrosis, and calcifications may be present, especially in larger lesions (Fig. 16-15).
- It has been reported that contrast enhancement with the old ionic contrast agents can precipitate a hypertensive crisis in some patients. Nonionic contrast appears to be safe to administer. Most lesions show avid enhancement. Washout characteristics following contrast administration are similar to those of malignant adrenal lesions for most pheochromocytomas, whether they are benign or malignant. Uncommonly, pheochromocytomas enhance poorly or show washout characteristic of benign lesions.
- Some pheochromocytomas present with spontaneous hemorrhage (Fig. 16-16).
- A minority of pheochromocytomas have contrast washout characteristics that mimic lipid-poor adrenal adenomas.
- Metaiodobenzylquanidine or indium-111 pentetreotide scintigraphy may be used to locate extra-adrenal pheochromocytoma not identified by CT.

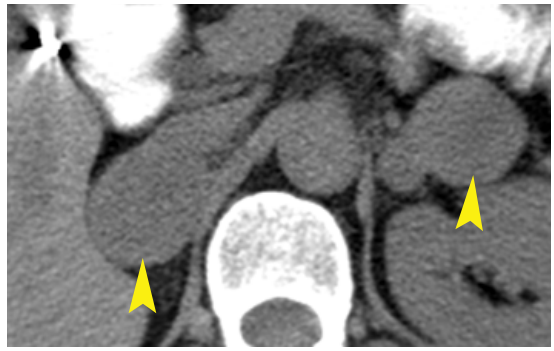

FIGURE 16-14 ■ Bilateral pheochromocytomas. Noncontrast computed tomography shows homogeneous, well-defined adrenal masses (*arrowheads*) of slightly lower attenuation than the normal liver.

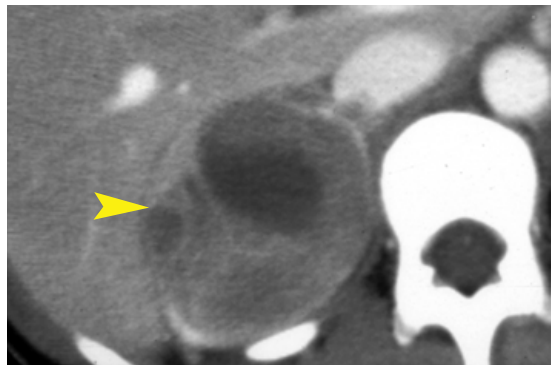

FIGURE 16-15 ■ Pheochromocytoma: necrotic. An unsuspected pheochromocytoma is seen as a heterogeneous mass (*arrowhead*) arising from the right adrenal. Necrosis and cystic changes are present. Nonionic contrast media was administered by intravenous bolus without any adverse effect. Hypertensive crises have been precipitated by intravenous injection of ionic contrast agents in patients with pheochromocytoma, but the incidence of serious adverse reaction is negligible for nonionic contrast agents.

PROBLEMATIC ADRENAL MASSES

Benign nonhyperfunctioning adrenal adenomas are common incidental findings on cross-sectional imaging examinations. Up to 5% of CT scans

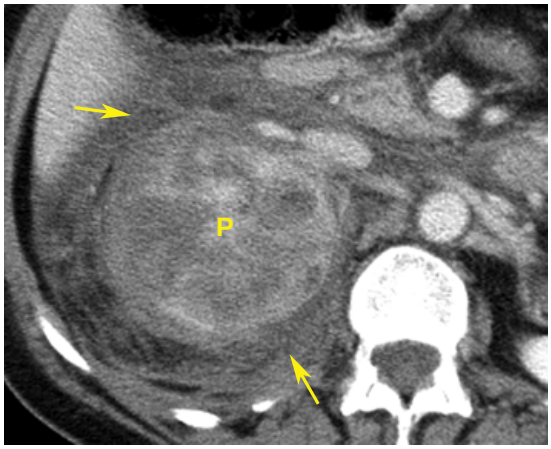

FIGURE 16-16 ■ Pheochromocytoma: spontaneous hemorrhage. Computed tomography revealed that a large right pheochromocytoma (P) in a patient who presented with sudden onset of right flank and abdominal pain was a hemorrhage (*arrows*) extending into the perirenal space.

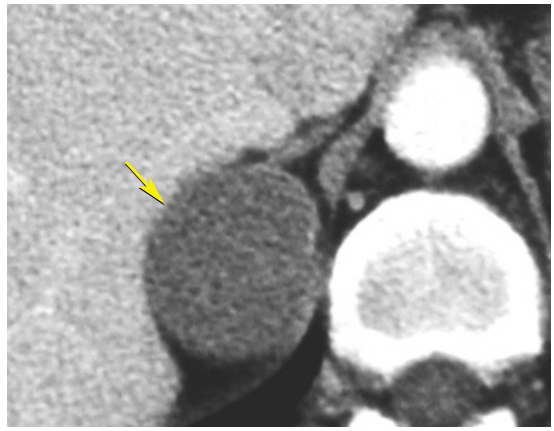

FIGURE 16-17 ■ Benign adrenal adenoma. Even though this CT scan was performed following intravenous contrast administration, the uniform low attenuation of a lipid-rich benign adrenal adenoma (*arrow*) is easily appreciated.

obtained for other reasons demonstrate an adrenal mass. Adrenal lesions discovered incidentally in patients without known malignant disease are almost never malignant. Even in patients with known malignancy, benign adrenal masses are more common than metastases to the adrenal glands. However, accurate tumor staging requires a definitive diagnosis of adrenal lesions.

Imaging differentiation of benign adenomas from metastases is based on the increased fat content found within most functioning adrenocortical adenomas. Cholesterol is a precursor of adrenocortical hormones, and cholesterol, fatty acids, and neutral fats are stored within functioning adrenal cells. CT and chemical shift magnetic resonance (MR) imaging accurately demonstrate the increased fat content of benign adenomas.

It should be noted that the lipid in benign adenomas is intracytoplasmic within adrenal cortical cells, whereas the lipid in myelolipomas is macroscopic and within fat cells. Thus, myelolipomas exhibit fat density on CT whereas adenomas exhibit low density but usually not as low as subcutaneous fat.

General Features of Benign Adrenal Adenomas

Patients with benign nonhyperfunctioning adenomas have no symptoms related to adrenal function and have normal adrenal hormone levels. Adenomas are found in 9% of patients at autopsy.

- Adrenal adenomas are typically sharply defined, homogeneous, round masses of <3 cm in size (Fig. 16-17). On noncontrast CT scans, adenomas are hypodense compared to normal liver. Lipid-rich adenomas (~70% of benign adenomas) have precontrast attenuation of –2 to 10 HU. Lipid-poor adenomas (~30% of benign adenomas) have precontrast attenuation of 20 to 25 HU.
- Contrast enhancement tends to be moderate in intensity and relatively uniform throughout the tumor. Washout of contrast is significantly more rapid for benign adenomas than for metastases. This important feature is used to characterize benign adenomas that are low in fat content (lipid-poor adenomas).
- Because of the variability in contrast administration and timing of routine CT imaging, adenomas cannot be definitively characterized as benign on a single postcontrast scan.
- A small adrenal mass with the characteristics described that remains stable in size and appearance on follow-up examination for 6 months or more is very likely to be benign.

General Features of Metastases to the Adrenal Glands

Metastases to the adrenal glands are found in 27% of patients with epithelial malignancies at autopsy. The most common primary tumors are lung, breast, and colon adenocarcinoma and melanoma.

- Larger metastases (>3 to 4 cm) tend to be heterogeneous and lobulated in contour with ill-defined margins. Hemorrhage and calcification are common. Enhancement is nonuniform (Fig. 16-18). These large, heterogeneous, irregular lesions should not be

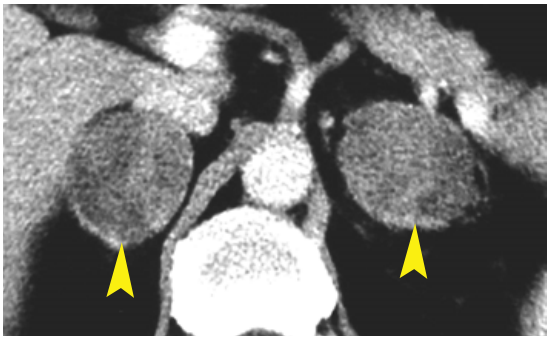

FIGURE 16-18 ■ Bilateral adrenal metastases. Adrenal metastases (*arrowheads*) from lung carcinoma are relatively well defined but heterogeneous in attenuation. Compare this to the uniform low attenuation of the benign adenoma in Figure 16-17.

confused with benign adrenal adenomas. Most adrenal masses of >5 cm are malignant (metastasis or adrenal carcinoma).

- Cystic changes may be present. Cystic metastases have thick, irregular walls that enhance with contrast.
- Smaller metastases (<3 cm) tend to be homogeneous, round, and relatively well defined. These lesions may be indistinguishable from benign adenomas on routine imaging. Size alone is not a useful criterion for distinguishing benign adenomas from metastases (Fig. 16-19).

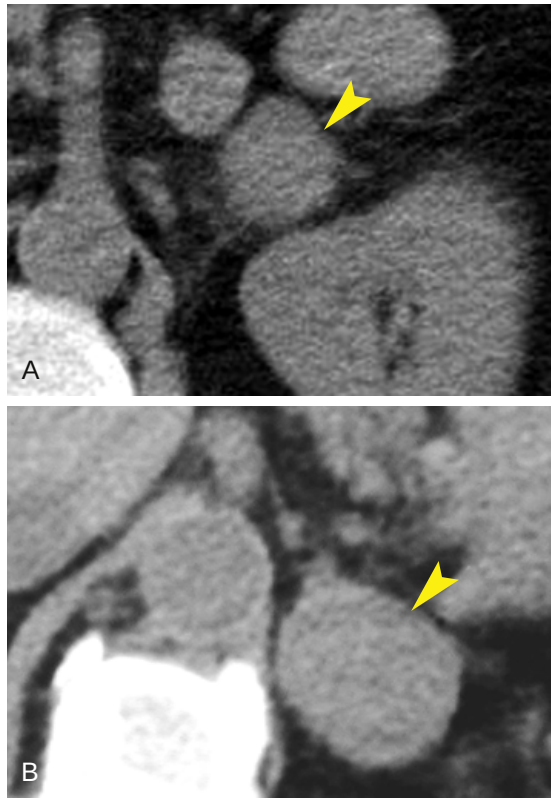

FIGURE 16-19 ■ Problematic adrenal lesions. *A,* This well-defined adrenal nodule (*arrowhead*) is a benign adenoma. *B,* This well-defined adrenal nodule (*arrowhead*) is a metastasis from lung carcinoma.

Features that Characterize Benign Adenomas and Adrenal Metastases

CT differentiation of benign adenomas from malignant lesions is based on high lipid content and/or rapid contrast washout that characterizes benign adrenal adenomas.

- **Unenhanced CT attenuation.** On unenhanced CT, mean attenuation of *<10 HU* is indicative of a benign adenoma (specificity 98%, sensitivity 71%). A threshold value of <2 HU yields specificity of 100% with sensitivity of 47%. This criterion defines "lipid-rich" benign adrenal adenomas (Fig. 16-20). Approximately 70% of benign adenomas are lipid-rich and can be characterized by unenhanced CT attenuation. The remaining 30% of benign adenomas are "lipid-poor" and will not be characterized as benign according to this criterion.
- To use threshold values for CT attenuation, the region-of-interest (ROI) cursor must be properly placed within the central half to two-thirds of the mass (Fig. 16-21). Any regions of calcification or necrosis should be excluded from the cursor measurement. Lesions with large areas of necrosis or cystic changes cannot be characterized according to contrast washout calculations.

FIGURE 16-20 ■ Benign lipid-rich adenoma. A well-defined 2.5-cm mass (*arrow*) arising from the right adrenal gland measures –2 HU in CT attenuation, characteristic of a benign lipid-rich adrenal adenoma.

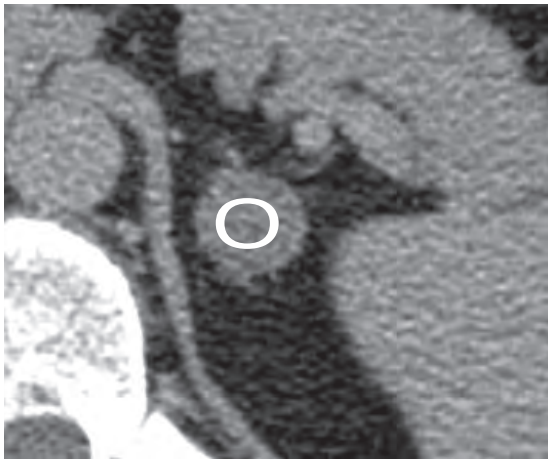

FIGURE 16-21 ■ Standardized range-of-interest measurement. Proper placement of a range-of-interest cursor on the central half to two-thirds of an adrenal lesion.

- **Enhanced CT attenuation.** Attenuation values for benign adenomas and metastases on routine contrast-enhanced CT scans show too much overlap to be clinically useful in differentiation. Unfortunately, many adrenal masses are discovered incidentally on postcontrast CT scans. These patients usually require reimaging to accurately characterize their lesions.
- **Contrast washout.** Although absolute postcontrast attenuation values have not been proven to be diagnostic, benign adenomas show characteristic brisk washout of contrast agents that can be used to characterize these lesions as benign. Metastases and other malignant lesions show a characteristically slow washout of contrast agent.
- **Percentage enhancement washout.** Two formulas are in use for determining the percentage enhancement washout, relative percentage washout (RPW) and absolute percentage washout (APW):

$$\text{RPW} = \frac{E - D}{E} \times 100,$$

where E is the enhanced attenuation and D is the delayed attenuation.

$$APW = \frac{E - D}{E - U} \times 100,$$

where U is the unenhanced attenuation.

The *unenhanced attenuation* is determined on a mid-lesion precontrast image using an ROI that encompasses half to two-thirds of the lesion. The *enhanced attenuation* is determined by ROI measurement in the same manner at the same location on the immediate postcontrast image of the lesion. The *delayed attenuation* is determined by ROI measurement in the same manner and at the same location on the 15-minute delayed image of the lesion.

RPW>40% is highly indicative of benign adenoma. RPW <40% indicates a likely malignant lesion.

APW>60% is highly indicative of a benign adenoma. APW <60% indicates a likely malignant lesion. RPW and APW criteria have sensitivity and specificity of nearly 100%.

- **Example:** CT of an adrenal lesion performed according to the adrenal mass protocol yielded the following data (Fig. 16-22).

Unenhanced attenuation: +26 H
Enhanced attenuation (immediate): +94 H
Delayed attenuation (15 minute): +30 H
RPW=64/94×100%=68%
APW=64/68×100%=94%
This lesion is characterized as a benign adrenal adenoma.

- **Chemical shift MR.** Chemical shift MR may be used to accurately characterize lipid-rich adenomas. Fat and water protons precess at different frequencies. Gradient echo image sequences can be performed so that fat and water proton signals can be separated within an imaged voxel. At 1.5 Tesla, fat and water protons are out of phase at an echo time (TE) of 2.3 milliseconds and in phase at TE of 4.6 milliseconds. Fat-containing adenomas show a distinct decrease in signal intensity on out-of-phase images (the signals from water and fat cancel out each other) compared to in-phase images (additive signal for water and fat) (Figs. 16-23 and 16-24). Subjective assessment of signal loss is equally as accurate as quantitative measurements of signal loss. Although MR is equally as accurate as noncontrast CT for characterization of lipid-rich adenomas, it offers no advantage over CT. Only lipid-rich adenomas that can be definitively characterized by noncontrast CT can be characterized by in-phase/out-of-phase MR. Attempts to assess gadolinium washout on MR have not been successful so far.
- Lesions that are not adequately characterized by CT or MR may require image-guided percutaneous biopsy. It has been shown that this procedure is safe and effective. CT is routinely used to guide the biopsy procedure.

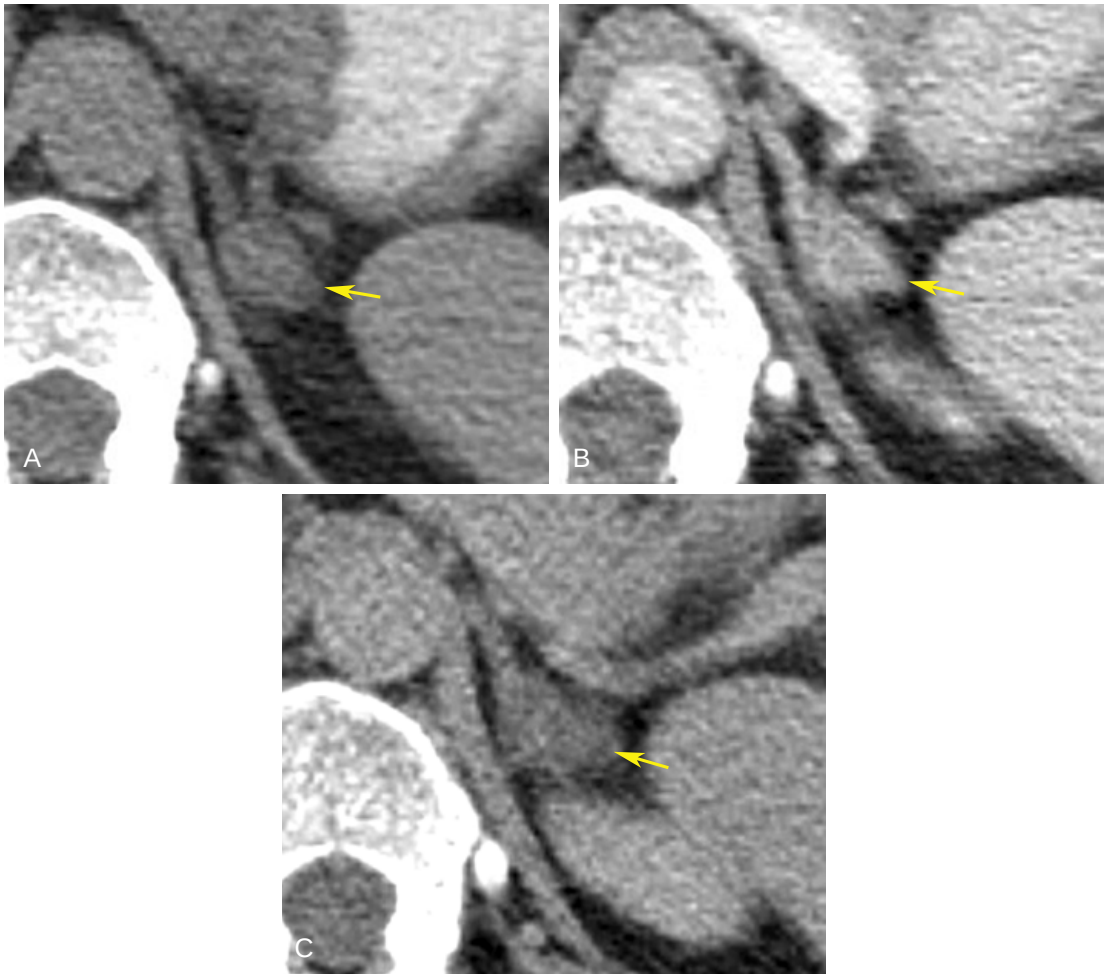

FIGURE 16-22 ■ Contrast enhancement washout: lipid-poor adenoma. *A*, A small left adrenal mass (*arrows*) measures +26 HU on unenhanced computed tomography (CT). This attenuation is not compatible with a lipid-rich adenoma. A decision was made to proceed with intravenous contrast using the CT adrenal mass protocol outlined at the beginning of this chapter. *B*, The immediate postcontrast scan demonstrates that the mass avidly enhances to +94 HU. *C*, The 15-minute delay postcontrast scan shows rapid washout of the contrast agent to an attenuation of +30 HU. The relative percentage washout is 68%, considered diagnostic of a lipid-poor adenoma.

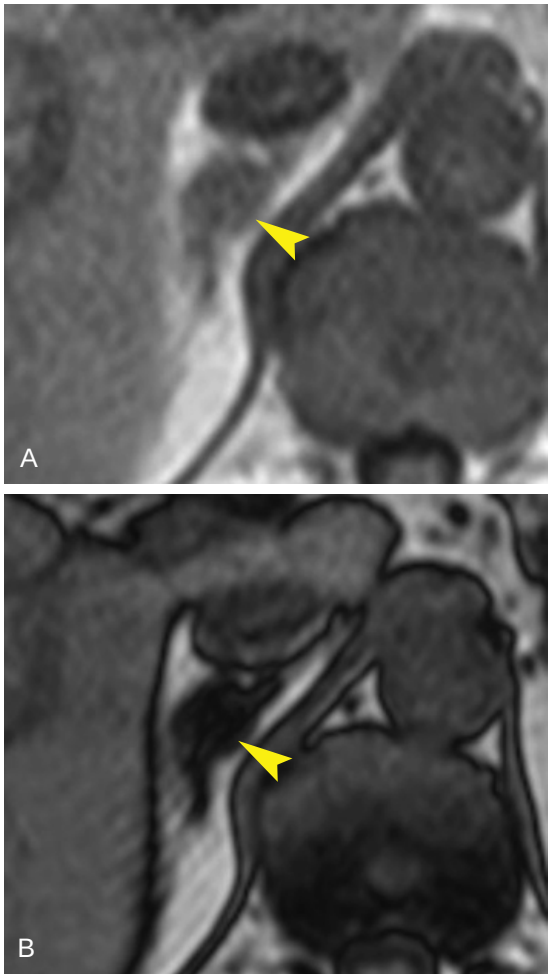

FIGURE 16-23 ■ Magnetic resonance (MR) of benign adrenal adenoma. *A,* In-phase MR image shows a right adrenal mass (*arrowhead*) with signal intensity close to that of the liver. *B,* Out-of-phase MR image shows a marked decrease in signal intensity for the mass (*arrowhead*), indicating the high intracellular lipid content of a benign lipid-rich adenoma.

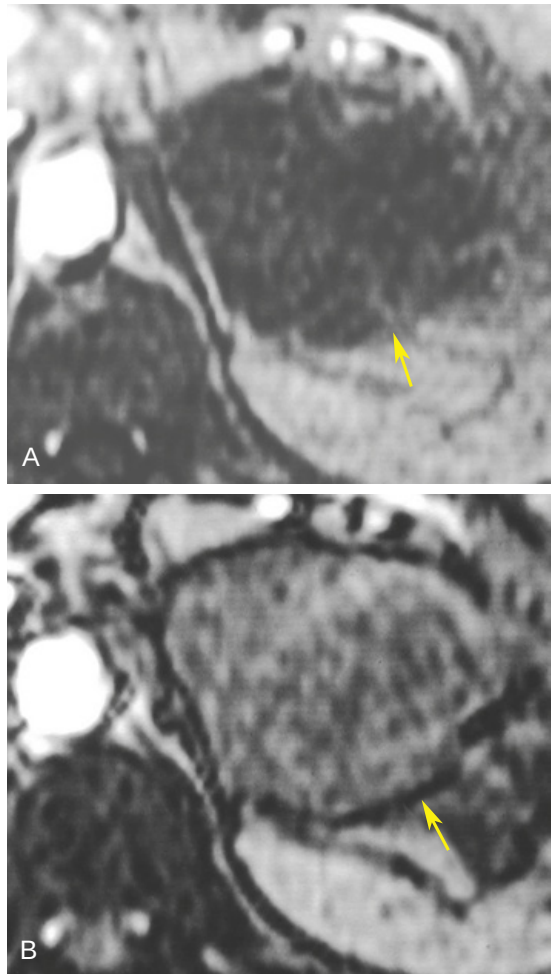

FIGURE 16-24 ■ Magnetic resonance (MR) of adrenal metastases. *A,* In-phase MR image shows an ill-defined left adrenal mass (*arrow*) of low signal intensity. *B,* Out-of-phase MR image shows an increase rather than a decrease in signal intensity. This patient has metastatic sarcoma.

SUGGESTED READING

Bharwani N, Rockall AG, Sahdev A, et al.: Adrenocortical carcinoma: The range of appearances on CT and MRI. *AJR Am J Roentgenol* 196:W706–W714, 2011.

Bittman ME, Lee EY, Restrepo R, Eisenberg RL: Focal adrenal lesions in pediatric patients. *AJR Am J Roentgenol* 200:W542–W556, 2013.

Blake MA, Cronin CG, Boland GW: Adrenal imaging. *AJR Am J Roentgenol* 194:1450–1460, 2010.

Boland GWL: Adrenal imaging: Why, when, what, and how? Part 1: Why and when to image. *AJR Am J Roentgenol* 195:W377–W381, 2010.

Boland GWL: Adrenal imaging: Why, when, what, and how? Part 2: What technique? *AJR Am J Roentgenol* 196:W1–W5, 2011.

Boland GWL: Adrenal imaging: Why, when, what, and how? Part 3: The algorithmic approach to definitive characterization of the adrenal incidentaloma. *AJR Am J Roentgenol* 196:W109–W111, 2011.

Boland GWL, Blake MA, Hahn PF, Mayo-Smith WW: Incidental adrenal lesions: Principles, techniques, and algorithms of imaging characterization. *Radiology* 249:756–776, 2008.

Ganeshan D, Bhosale P, Kundra V: Current update on cytogenetics, taxonomy, diagnosis, and management of adrenocortical carcinoma: What radiologists should know. *AJR Am J Roentgenol* 199:1283–1293, 2012.

Johnson PT, Horton KM, Fishman EK: Adrenal mass imaging with multidetector CT: Pathologic conditions, pearls, pitfalls. *Radiographics* 29:1333–1351, 2009.

Jordan E, Poder L, Courtier J, et al.: Imaging of nontraumatic adrenal hemorrhage. *AJR Am J Roentgenol* 199:W91–W99, 2012.

Leung K, Stamm M, Raja A, Low G: Pheochromocytoma: The range of appearances on ultrasound, CT, MRI, and functional imaging. *AJR Am J Roentgenol* 200:370–378, 2013.

Patel J, Davenport MS, Cohan RH, Caoili EM: Can established CT attenuation and washout criteria for adrenal adenoma accurately exclude pheochromocytoma? *AJR Am J Roentgenol* 201:122–127, 2013.

Uppot RN, Gervais DA: Imaging-guided adrenal tumor ablation. *AJR Am J Roentgenol* 200:1226–1233, 2013.

CHAPTER 17

GASTROINTESTINAL TRACT

William E. Brant

BASIC PRINCIPLES

Computed tomography (CT) complements endoscopy and barium examination of the gastrointestinal (GI) tract by demonstration of intramural and extraintestinal components of GI disease, including disease in the mesentery, peritoneal cavity, lymph nodes, and liver. CT is used to diagnose the presence of GI disease, evaluate its nature and extent, and demonstrate complications such as abscess, phlegmon, fistula, and perforation. CT is excellent for determining the extent of GI disease but is seldom specific for its nature.

The GI tract is shown on every CT of the abdomen. The intestinal lumen should be distended and opacified for routine abdominal CT by administration of 700 to 800 mL of 2% to 3% iodinated or barium contrast agent at least 1 hour before routine scanning. Water is an excellent contrast agent for the lumen of the stomach and upper intestinal tract and can be used whenever disease in the upper abdomen is suspected. Intravenous contrast medium is used to assess enhancement of the GI mucosa and of lesions, to demonstrate blood vessels, and to evaluate the solid organs of the abdomen. Thin-section scans improve lesion definition. The short scan times of multidetector CT (MDCT) improve image quality by limiting motion artifacts. Collapsed bowel loops without intraluminal contrast enhancement may mimic adenopathy and mass lesions. However, when scans are obtained during the arterial phase of bolus contrast enhancement, identification of enhanced bowel wall confirms the nature of nondistended bowel.

A CT hallmark of intestinal disease is thickening of the bowel wall. When fully distended, the bowel wall is 1 to 2 mm thick. When collapsed, the bowel wall should not exceed 3 to 4 mm, except in the stomach near the esophageal junction, where the normal stomach wall may be 2 cm thick when collapsed. The CT appearance of wall thickening is helpful in differentiating benign from malignant wall thickening (Table 17-1). Benign wall thickening usually does not exceed 1 cm, is homogeneous in attenuation, and is circumferential, symmetrical, and segmental in distribution. The "double halo" and "target" appearance of the intestine in cross-section is due to inflammation, edema, and hyperemia and is best demonstrated on contrast-enhanced scans. Neoplastic wall thickening is thicker (1 to 2 cm), asymmetrical, nodular, lobulated, or spiculated in contour and tends to narrow the intestinal lumen. Benign wall thickening is caused by inflammatory bowel disease, intestinal ischemia, and intramural hemorrhage. Neoplastic wall thickening occurs in adenocarcinoma, lymphoma, and GI stromal tumors.

CT ENTEROGRAPHY

CT enterography using MDCT is a first-line modality for examination of small bowel disease. CT enterography differs from routine CT of the abdomen and pelvis in the use of large volumes of low-attenuation intraluminal contrast agent to optimally distend the bowel lumen, matched with thin-slice collimation and routine high-detail coronal and sagittal reformations. Low-attenuation intraluminal contrast paired with intravenous contrast administration optimally displays both the lumen and wall of the small bowel (Fig. 17-1). Advantages of CT enterography over traditional barium-based small-bowel follow-through examination include demonstration of the entire thickness of the bowel wall and disease in the mesentery, as well as display of bowel loops without superimposition. Indications for CT enterography include Crohn disease and other suspected inflammatory bowel diseases, intermittent small-bowel obstruction, obscure GI bleeding, and suspected tumors of the small bowel. A typical protocol for CT enterography includes the following:

- A minimum 4-hour fast.
- Administration of low-attenuation (20 Hounsfield units, HU) oral contrast agent (typically VoLumen), a low-concentration barium sulfate suspension (0.1% weight/volume, Bracco E-Z-EM). A total volume of 1400 mL is given in divided doses: 450 mL 60 minutes before scanning, 450 mL

TABLE 17-1 Benign versus Malignant Bowel-Wall Thickening

Benign	Malignant
Homogeneous attenuation	Heterogeneous attenuation
Symmetrical	Asymmetrical
Circumferential	Eccentric
Thickening <1 cm	Thickening >1 to 2 cm
Segmental or diffuse involvement	Focal mass
Double halo sign	Abrupt transition
Dark inner ring	Lobulated contour
Bright outer ring	Spiculated contour
Target sign	Narrowed bowel lumen
Bright inner ring	Enlarged lymph nodes
Dark middle ring	Liver metastases
Bright outer ring	

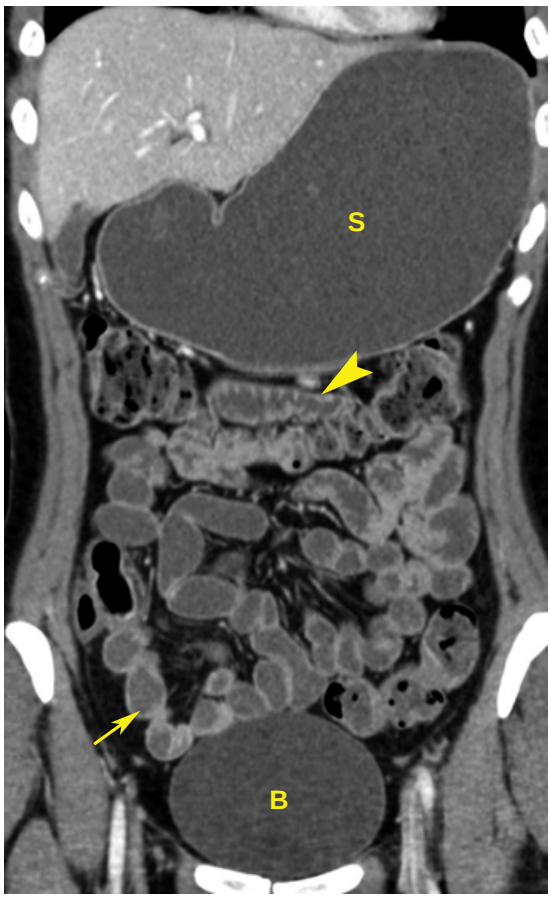

FIGURE 17-1 ■ Computed tomography (CT) enterography. Coronal image from a CT enterography examination using low-attenuation intraluminal contrast as well as intravenous contrast shows the normal fold pattern of the jejunum (*arrowhead*) and the normal absence of folds of the ileum (*arrow*). The stomach (S) is well distended with intraluminal contrast agent. The bladder (B) is also filled.

40 minutes before scanning, 250 mL 20 minutes before scanning, and 250 mL 10 minutes before scanning. Glucagon (0.5 mg) may be given intramuscularly to inhibit bowel motion.

- Administration of 125 mL of 60% iodine intravenous contrast agent at 3 to 4 mL/second provides enhancement of the bowel wall and of any lesions.
- MDCT scanning performed from the dome of the diaphragm through the ischial tuberosities utilizing 0.625-mm collimation with reconstructions at a slice thickness of 2.5 mm.
- For inflammatory bowel disease or other diffuse bowel pathology, images obtained after contrast administration only in the portal venous phase using an 80-second delay.
- For occult GI bleeding or suspected GI malignancy, scans obtained in the arterial phase (30-second scan delay), portal venous phase (80-second delay), and delayed phase (3-minute delay).
- Images reconstructed in axial, coronal, and sagittal planes.

CT ENTEROCLYSIS

CT enteroclysis is performed on patients with small-bowel obstruction to find the level and cause of the obstruction (Fig. 17-2). For CT enteroclysis, contrast medium for small-bowel distention is injected into the small bowel through a nasojejunal tube rather than given orally as for CT enterography. A nasojejunal tube is positioned at the duodenojejunal junction under fluoroscopic guidance. A total volume of 1200 to 1600 mL of low-attenuation oral contrast medium is injected into the small bowel at 60 to 120 mL/minute. Glucagon, or other antispasmodic medication, is administered. Intravenous contrast is utilized and MDCT scanning is performed using the same parameters as for CT enterography.

CT COLONOGRAPHY

CT colonography is used to investigate the colon for colorectal polyps and cancers. Numerous studies have shown that CT colonography is nearly equal to traditional optical colonoscopy in detecting cancer and precancerous lesions. Many patients prefer CT colonography over colonoscopy because of perceived safety and convenience. The obvious disadvantage of CT colonography is that lesions that require biopsy

will require the patient to undergo subsequent colonoscopy.

- Standard bowel preparation, similar to that used for colonoscopy, is begun the day prior to the examination.
- Barium sulfate and iodinated contrast solutions are given orally to tag remaining stool and colonic fluid.
- For the examination, a catheter is placed in the rectum, and the colon is insufflated using an automated carbon dioxide system that provides pressure and volume regulation.
- MDCT scanning is performed using 1.25-mm collimation and a low-radiation-dose protocol with the patient in both prone and supine positions.
- Images are reviewed on a workstation that provides three-dimensional volume rendering with endoluminal display and "fly-through" capability (Fig. 17-3).

FIGURE 17-2 ■ Computed tomography (CT) enteroclysis: distal small-bowel obstruction. Coronal image from a CT enteroclysis examination shows diffuse dilatation of the small bowel with low-attenuation intraluminal contrast agent and air. An adhesion was the cause of this obstruction.

ESOPHAGUS

Anatomy

The esophagus is a muscular tube that extends from the cricopharyngeus muscle at the level of the cricoid cartilage to the stomach. The major portion of its length is within the middle mediastinum. The cervical portion extends from the level of the C6 vertebral body to the thoracic inlet. A short abdominal segment extends below the diaphragm to the gastroesophageal junction. The esophagus is lined by squamous epithelium to the gastric junction, where the mucosa abruptly changes to columnar epithelium. The lack of serosal covering allows early invasion by esophageal tumors into periesophageal tissues. The musculature of the esophageal wall is striated in the upper third, striated and smooth muscle in

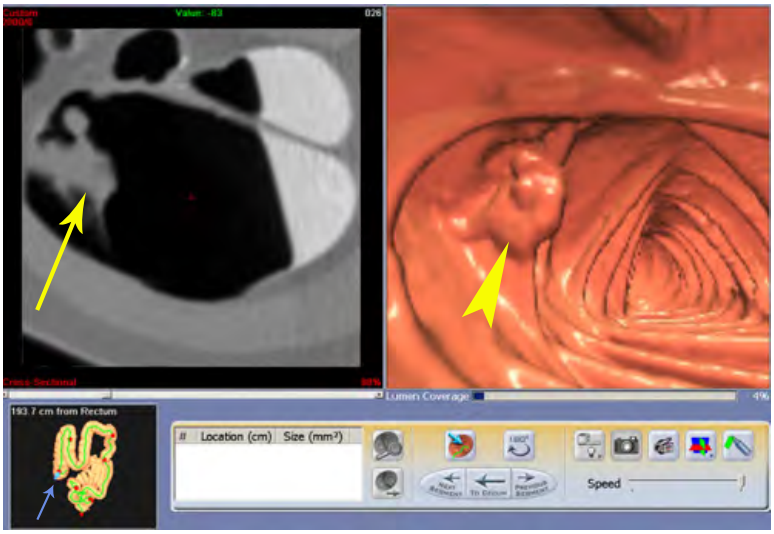

FIGURE 17-3 ■ CT colonography. Image display from a three-dimensional computer work station used for interpretation of CT colonography examinations displays a complex lobulated polyp (*arrowhead*) on a three-dimensional reconstruction. An axial image shows the polyp (*yellow arrow*) on a conventional CT slice. The lower left image shows the tortuous course of the colon and the location of the polyp in the cecum (*blue arrow*) 193.7 cm from the anal verge. Accurate landmarks allow for rapid localization of the polyp for removal by colonoscopy. Computer displays in full color with multiple image planes and three-dimensional reconstructions are routinely utilized.

the middle third, and solely smooth muscle in the distal third.

On CT the esophagus appears as an oval of soft-tissue density often containing air or contrast material within its lumen (Fig. 17-4). When distended, the wall of the esophagus should not exceed 3 mm in thickness. In the neck and upper thorax, the esophagus courses between the trachea and the spine. In the lower thorax, the esophagus courses to the right of the descending aorta between the left atrium and the spine. The esophagus enters the abdomen through the esophageal hiatus and courses to the left to join the stomach. The edges of the diaphragmatic crura forming the esophageal hiatus are seen as often prominent, teardrop-shaped structures partially surrounding the esophagus. Air columns in the esophagus longer than 10 to 15 cm may be evidence of stricture or impaired peristalsis. Air–fluid levels in the esophagus are always abnormal.

Esophageal Carcinoma

Because of the lack of serosal covering, carcinoma spreads beyond the esophagus early in its course, resulting in a poor prognosis. Some 90% of tumors are squamous cell carcinoma, and the remaining 10% are adenocarcinoma arising in Barrett esophagus in the distal esophagus. The CT findings in esophageal carcinoma may be duplicated by benign disease. Diagnosis depends on biopsy. CT is performed to assess the extent of disease and to identify those patients whose disease cannot be surgically resected. The CT findings in esophageal carcinoma include the following:

- Irregular thickening of the wall of the esophagus of more than 3 mm (Fig. 17-5)
- An intraluminal polypoid mass
- Eccentric narrowing of the lumen
- Dilatation of the esophagus above the area of narrowing with air or fluid
- Invasion of periesophageal tissues: fat, aorta, trachea
- Tumor invasion of the trachea or bronchi is suggested by a tumor that displaces or indents the posterior airway wall (90% accurate).
- Tumor invasion of the aorta is suggested by an arc of contact of greater than 90° between the tumor and the aorta. An arc of less than 45° indicates no invasion, and an arc between 45° and 90° is indeterminate. These findings are about 80% accurate.
- Metastases to lymph nodes, liver, and other organs
- Esophageal carcinoma spreads to paraesophageal, other mediastinal, gastrohepatic ligament, and left gastric nodal chains (Fig. 17-6). Microscopic disease in normal-sized nodes and lymph node enlargement due to benign conditions limit the CT accuracy of nodal involvement by esophageal carcinoma to 39% to 85%.
- Tumor recurrence after esophagectomy is well demonstrated by CT. Tumors may

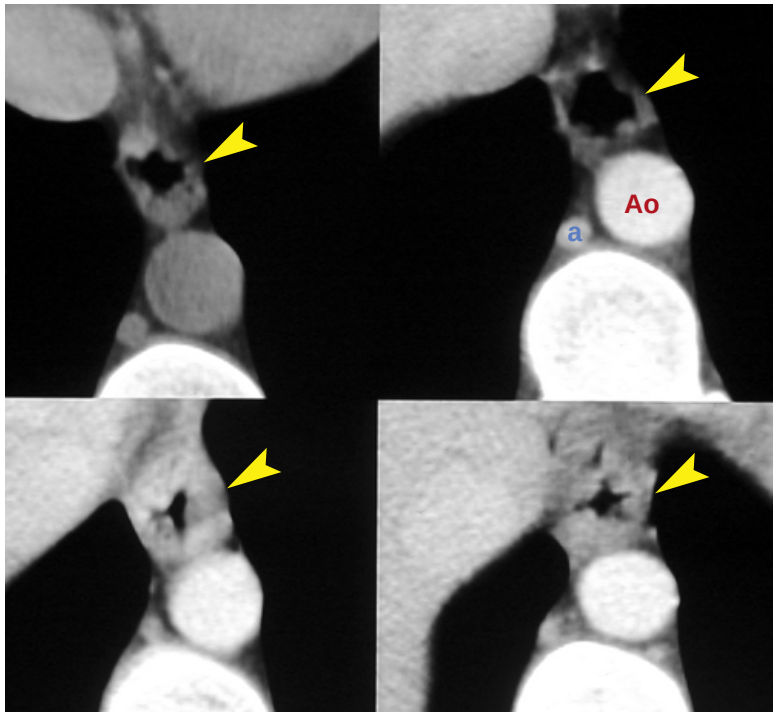

FIGURE 17-4 ■ Normal esophagus. Sequential axial computed tomography slices demonstrate the normal appearance of the esophagus (*arrowheads*). The descending thoracic aorta (Ao) and azygos vein (a) are evident.

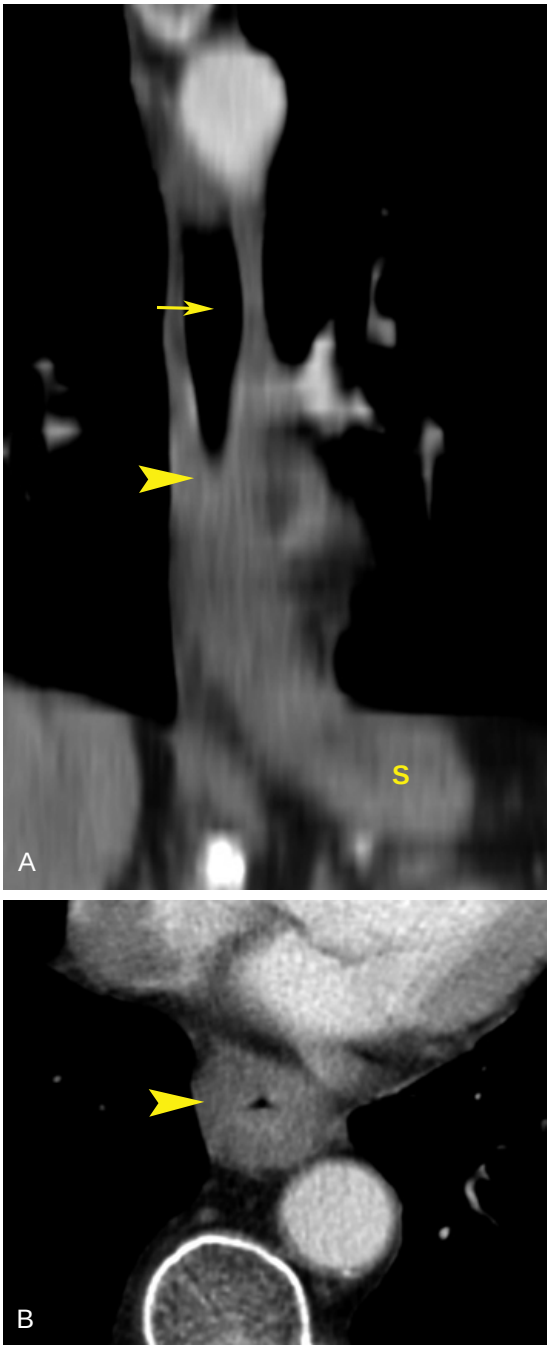

FIGURE 17-5 ■ Adenocarcinoma: esophagus. *A,* Coronal reconstruction computed tomography (CT) image shows distention of the normal upper esophagus (*arrow*) with air caused by abrupt narrowing of the lumen of the mid-esophagus (*arrowhead*). The stomach (S) is evident below the diaphragm. *B,* Axial CT image at the level of the stricture shows circumferential thickening of the wall of the esophagus (*arrowhead*) with narrowing of its lumen marked by a small pocket of air. Biopsy revealed adenocarcinoma in a long segment of Barrett esophagus.

recur anywhere within the mediastinum, in distant lymph nodes in the neck or abdomen, and in the liver, lung, pleural space, adrenal glands, or peritoneal cavity.

Esophageal Leiomyoma

Leiomyoma is the most common benign tumor of the esophagus. Smooth muscle tumors of the esophagus are true leiomyomas and are not classified as GI stromal tumors (GISTs). Most are asymptomatic until they become very large and cause dysphagia. Endoscopy demonstrates a submucosal mass that is usually easily differentiated from carcinoma.

- On CT, leiomyoma appears as a smooth, well-defined 2- to 8-cm mass of uniform soft-tissue attenuation. The esophageal wall is eccentrically thickened, and the lumen is deformed. A large, well-defined mass is much more likely to be a leiomyoma than a carcinoma.
- Leiomyomas are multiple in about 4% of cases.
- Leiomyomas are the only tumor of the esophagus that may have coarse calcifications (Fig. 17-7).
- Leiomyosarcomas tend to grow intraluminally, are usually large (>5 cm), have heterogeneous attenuation, and may ulcerate.

Esophageal Varices

Esophageal varices are most often caused by portal hypertension but may occur with superior vena cava obstruction. The major complication is hemorrhage.

- Varices are clearly recognized on postcontrast CT as well-defined, enhancing nodular and tubular densities adjacent to the esophagus and within its wall (Fig. 17-8).
- Varices cause scalloped thickening of the esophageal wall that may be indistinguishable from tumor or inflammation without the use of contrast medium enhancement.
- Signs of cirrhosis, portal hypertension, and other portosystemic collateral vessels are usually present.

Esophagitis

Causes of esophagitis include gastroesophageal reflux, radiation, and infection. Infectious esophagitis is most commonly seen in immunosuppressed patients. Causative organisms include *Candida*, herpes simplex virus, cytomegalovirus, and tuberculosis.

- The major CT finding of severe esophagitis is a relatively long segment of

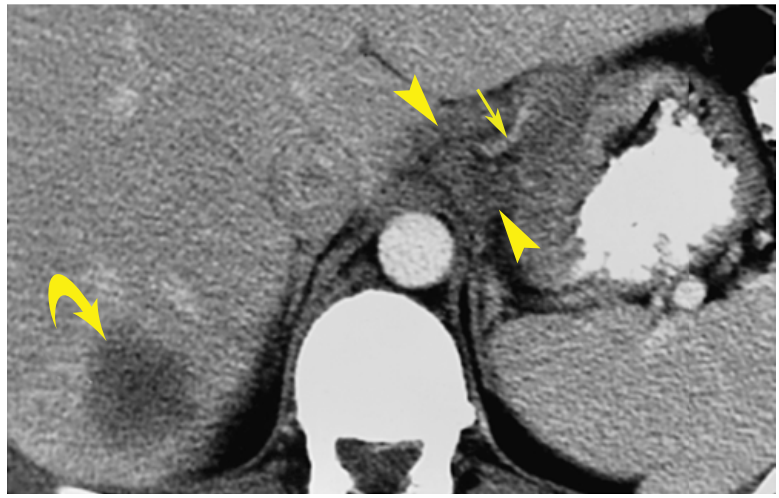

FIGURE 17-6 ■ Carcinoma of the gastroesophageal junction. Carcinoma arising near the gastroesophageal junction has spread to the liver (*curved arrow*) and to lymph nodes (*arrowheads*) surrounding the celiac axis (*straight arrow*).

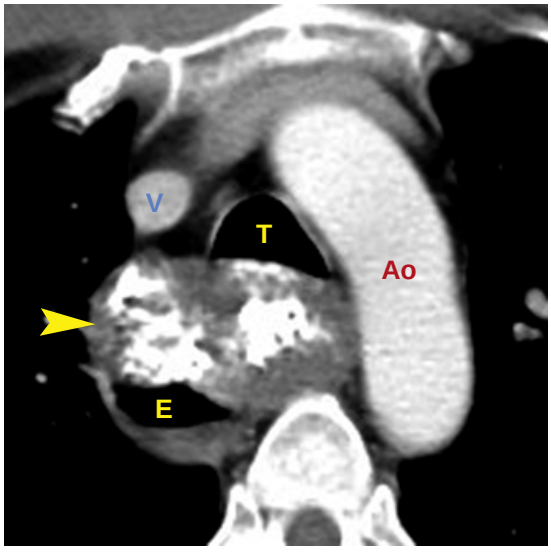

FIGURE 17-7 ■ Leiomyoma of the esophagus. Axial computed tomography in a patient with dysphagia reveals a large tumor (*arrowhead*) with coarse calcifications eccentrically narrowing and displacing the lumen of the esophagus (E). Surgical removal confirmed a benign leiomyoma. Ao, aortic arch; T, trachea; V, superior vena cava.

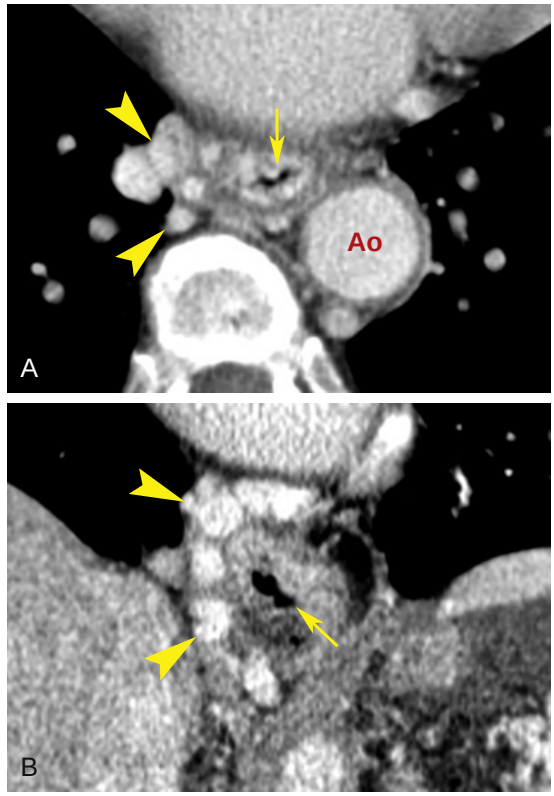

FIGURE 17-8 ■ Esophageal varices. Numerous large enhancing varices (*arrowheads*) resulting from cirrhosis and portal hypertension surround and indent the distal esophagus (*arrow*). *A,* Axial postcontrast computed tomography (CT). *B,* Coronal postcontrast CT in the same patient. Ao, descending thoracic aorta.

symmetrical circumferential wall thickening (>5 mm), often with mucosal enhancement (Fig. 17-9).

- Presence of a target sign indicating submucosal edema helps to differentiate esophagitis from other causes of wall thickening.
- Strictures are seen as areas of luminal narrowing with dilatation of the esophagus above the lesion.
- Severe esophagitis may lead to deep ulcers, perforation, mediastinitis, and abscess.

Esophageal Injury and Perforation

Esophageal perforation may be traumatic or iatrogenic after instrumentation, or may result from neoplasm or inflammation. Boerhaave syndrome is spontaneous rupture of the esophagus associated

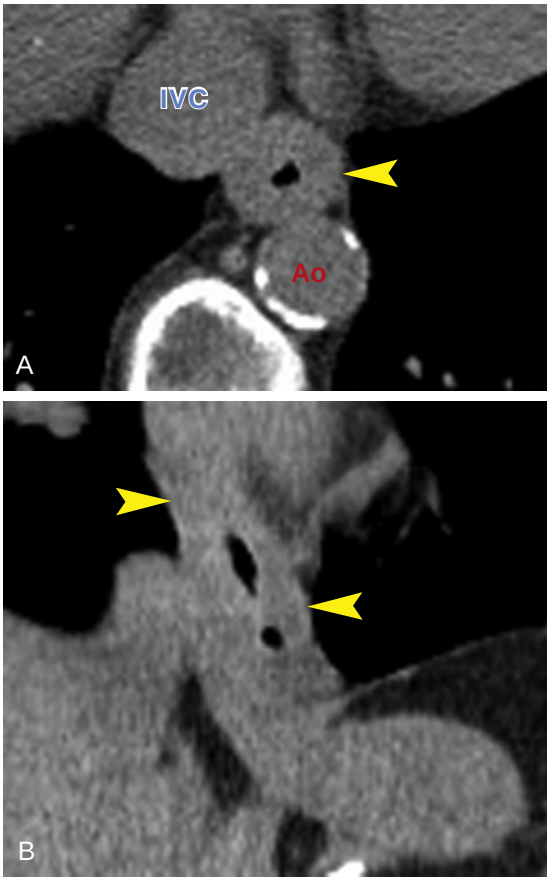

FIGURE 17-9 ■ Esophagitis. Reflux esophagitis causes circumferential thickening of the wall of the distal esophagus (*arrowheads*). *A,* Axial noncontrast computed tomography (CT). *B,* Coronal noncontrast CT in the same patient. Ao, descending thoracic aorta; IVC, inferior vena cava.

with violent vomiting. Because it may be lethal, prompt recognition of esophageal perforation is essential. Underlying esophageal disease is often present.

- Wall thickening, high-attenuation intramural hematoma, and mediastinal inflammation are signs of esophageal injury.
- Periesophageal fluid or contrast and extraluminal mediastinal air are the most specific findings of esophageal perforation. (Fig. 17-10).
- Pleural effusions are common.

STOMACH

Anatomy

The posteriorly located gastric fundus is seen on CT sections through the dome of the diaphragm. The esophagus joins the stomach a short distance below the fundus. A prominent pseudotumor, caused by thickening of the gastric wall due to incomplete distention, is often seen near the gastroesophageal junction. Additional distention with more air or contrast agent will eliminate this pseudotumor. The body of the stomach sweeps toward the right. The antrum crosses the midline of the abdomen between the left lobe of the liver and the pancreas to join the duodenal bulb in the region of the gallbladder.

The normal gastric wall should not exceed 5 mm in thickness when the stomach is well distended. Rugal folds are commonly visualized, even with good distention. Like the esophagus, benign and malignant conditions produce similar CT findings. CT is performed to document the extent of extraluminal disease.

Technical Considerations

The stomach must be filled with positive contrast medium or distended with air or water for optimal assessment by CT. An oral contrast agent or water (200 to 300 mL) is routinely given to fill the stomach just before the patient lies down on the CT couch. Alternatively, distention of the stomach with air may be achieved by giving gas-producing crystals (4 to 6 g of Citrocarbonate granules with 16 to 30 mL of water) instead of an opaque contrast agent. The patient can be repositioned in the prone or decubitus position to optimize distention of the different portions of the stomach with air or contrast agent.

Hiatus Hernia and Gastric Volvulus

Hiatus hernia is a protrusion of any portion of the stomach into the thorax. A major reason to recognize a hiatus hernia is to avoid mistaking it for a tumor. Large hiatus hernias are associated with gastric volvulus.

- On CT, a sliding hiatus hernia (95% of hiatus hernias) is identified by recognition of gastric folds appearing above the esophageal hiatus (Fig. 17-11). The herniated stomach may create an air- or contrast-filled mass contiguous with the esophagus above and the remainder of the stomach below.
- The edges of the esophageal hiatus are often widely separated, exceeding 15 mm in width.
- With a paraesophageal hernia, the gastric cardia and gastroesophageal junction are below the esophageal hiatus and the fundus of stomach is above the hiatus adjacent to the distal esophagus. A variant of paraesophageal hernia is the coexistence of a sliding hiatus hernia with the paraesophageal intrathoracic fundus.

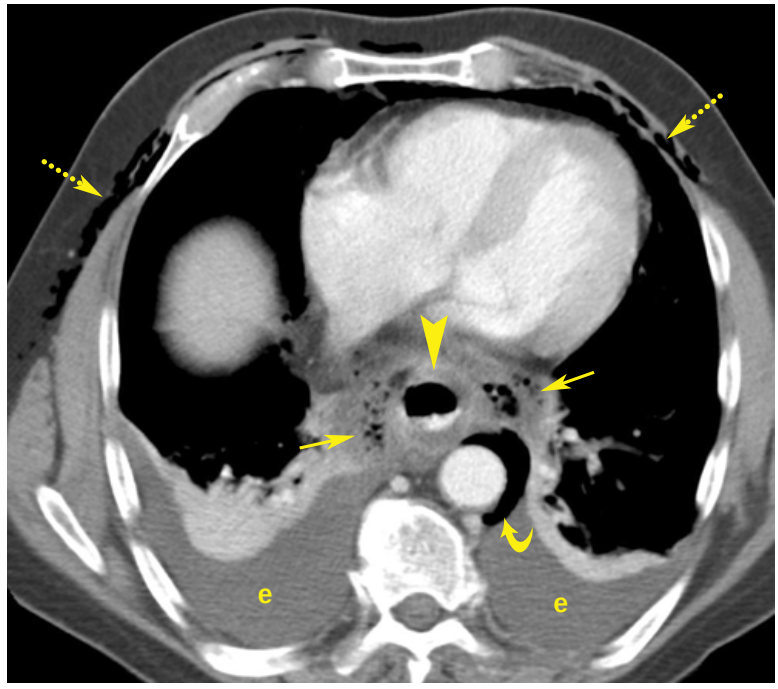

FIGURE 17-10 ■ Perforation of the esophagus. Perforation of the distal esophagus during a stenting procedure for esophageal stricture is evidenced by extensive air in the mediastinum (*straight arrows*), around the aorta (*curved arrow*), and in the subcutaneous tissues of the chest (*dotted arrows*). The esophagus (*arrowhead*) has a thickened wall. Bilateral pleural effusions (e) are evident.

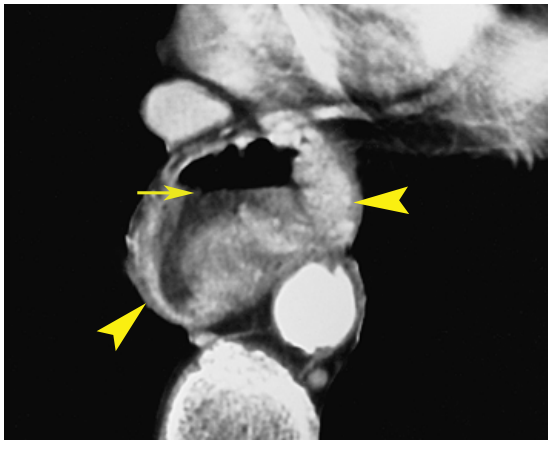

FIGURE 17-11 ■ Hiatus hernia. An axial computed tomography image shows a portion of the stomach extending through the esophageal hiatus to form a hiatus hernia (*arrowheads*). Gastric folds are evident. Fluid retained within the herniated stomach forms an air–fluid level (*arrow*).

- In *organoaxial rotation* the stomach rotates around its long axis, resulting in the convex greater curvature of the stomach being positioned in the chest anteriorly, superiorly, and to the right of the concave lesser curvature.
- In the much less common *mesenteroaxial rotation*, the stomach turns upside down. The antrum and pylorus are superior and in the chest, whereas the fundus is near the diaphragm.
- The term *gastric volvulus* refers to abnormal gastric rotation associated with strangulation and obstruction. Patients have acute abdominal pain, nausea, and vomiting. Complete gastric obstruction occurs for twisting greater than 180°. CT shows gastric distention with retained contrast, air, and food. Emergency surgical repair is needed to avoid ischemia.

Thickened Gastric Wall

Thickening of the gastric wall, either focal or diffuse, is an important but nonspecific sign of gastric disease. With good technique, which includes aggressive distention of the stomach with air or contrast agent, wall thickening of greater than 5 mm can be considered abnormal. Causes include carcinoma, lymphoma, gastric inflammation (peptic or Crohn disease), perigastric inflammation (pancreatitis), and radiation. CT may show gastric ulcers as collections of contrast agent within a thickened wall. Penetrating ulcers appear as a sinus tract, marked by contrast agent or air, extending to adjacent structures.

Gastritis

Gastritis is a very common disease with numerous causes, including alcohol, aspirin, nonsteroidal anti-inflammatory drugs, and viral, fungal, or *Helicobacter pylori* infection.

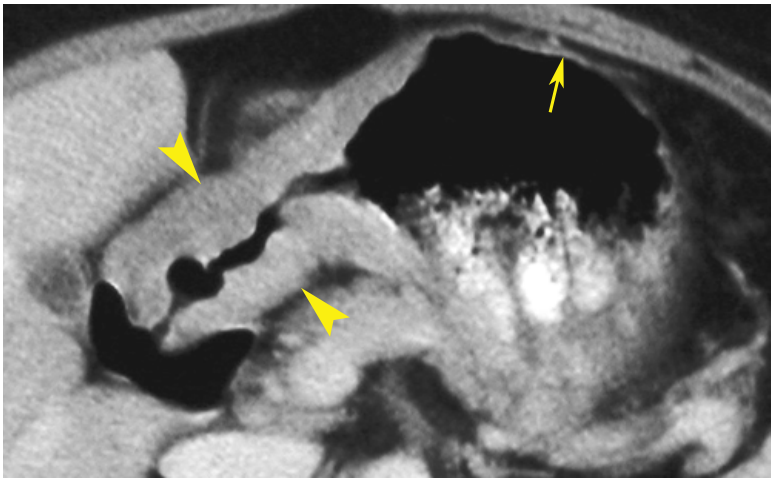

FIGURE 17-12 ■ Gastric carcinoma. Nodular thickening of the wall of the distal stomach and gastric antrum (*arrowheads*) is striking in comparison to the normal wall of the gastric body (*arrow*).

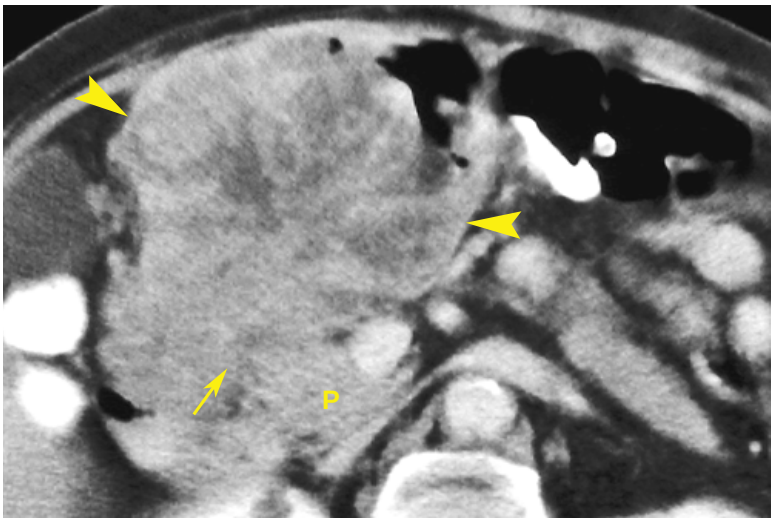

FIGURE 17-13 ■ Large gastric carcinoma. Adenocarcinoma of the distal stomach produces a large heterogeneous mass (*arrowheads*) containing low-attenuation areas of necrosis and hemorrhage. The tumor has extended through the stomach wall, obliterated the fat plane between the stomach and the pancreas, and invaded (*arrow*) the pancreas (P).

- Thickened gastric folds are the best CT sign of gastritis.
- Wall thickening is often focal and is most common in the antrum.
- The mucosa may enhance brightly during arterial-phase CT due to hyperemia, causing a three-layer wall appearance that differentiates this benign condition from malignant wall thickening.
- *Emphysematous gastritis* is a rare life-threatening condition characterized by air within the thickened gastric wall. It is caused by invasion of the gastric wall by gas-producing *Escherichia coli*.

Gastric Carcinoma

Adenocarcinoma is the cause of 95% of gastric malignancy. CT is used to stage the disease and identify patients whose disease is not surgically resectable.

- The primary tumor appears as focal, nodular, or irregular thickening of the gastric wall (Fig. 17-12), or as a polypoid intraluminal mass of soft-tissue attenuation.
- Diffuse wall thickening with irregular narrowing of the lumen is indicative of scirrhous carcinoma (linitis plastica).
- Extension of tumor into the perigastric fat is nearly always present when the wall thickness exceeds 2 cm (Fig. 17-13). The serosal surface is blurred, and strands and nodules of tumor are seen in the adjacent fat.
- Perigastric lymph nodes are considered to be involved when the short axis diameter is >6 mm. A round shape and heterogeneous or marked enhancement are additional signs of nodal involvement. Nodes near the celiac

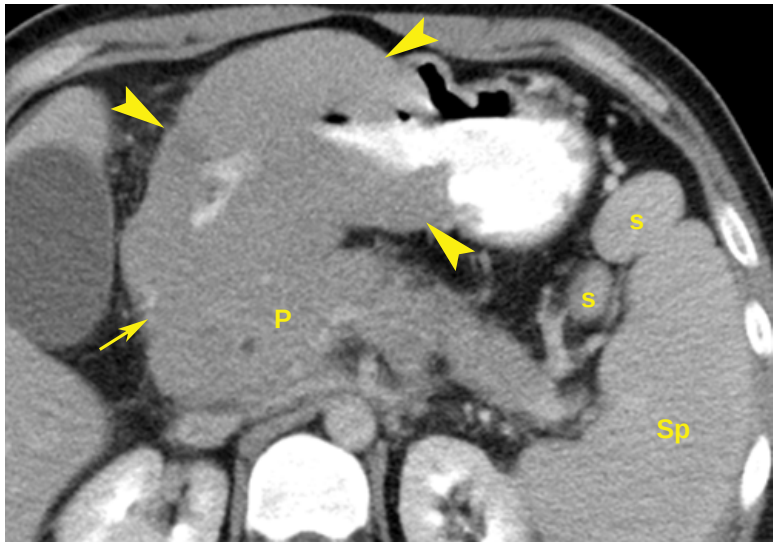

FIGURE 17-14 ■ Gastric lymphoma. Non-Hodgkin's lymphoma (*arrowheads*) causes a large mass that massively thickens the wall of the distal stomach. Compare to Figure 17-13. Note the homogeneous attenuation of lymphoma compared to the large adenocarcinoma. Lymphoma also obliterates the fat plane (*arrow*) between the stomach and the pancreas (P). The spleen (Sp) and two splenules (s) are enlarged.

axis and in the gastrohepatic ligaments are most likely to be involved.
- Hematogenous metastases go first to the liver and then to the lungs, adrenal glands, kidneys, bones, and brain.
- Peritoneal carcinomatosis may occur.
- Local recurrence of gastric carcinoma appears as focal wall thickening at the anastomosis or in the remaining stomach. Nodal recurrence is most common along the course of the hepatic artery or in the paraaortic region. Peritoneal recurrence is seen in the cul-de-sac, on parietal peritoneal surfaces, or on the surface of the bowel.

Gastric Lymphoma

The stomach is the most common site of involvement for primary gastrointestinal lymphoma. Most cases (90% to 95%) are non-Hodgkin's lymphoma of B-cell origin. Mucosa-associated lymphoid tissue (MALT) lymphoma is an indolent form of lymphoma with a significantly better prognosis.
- Gastric lymphoma may cause a polypoid mass, diffuse wall infiltration with featureless walls, or markedly thickened walls with nodular thickened folds.
- CT features that favor a diagnosis of lymphoma over carcinoma include more dramatic thickening of the stomach wall (exceeding 3 cm), involvement of more than one region of the GI tract, transpyloric spread of tumor (occurs in 30% of gastric lymphoma patients), and more widespread adenopathy above and below the level of the renal hilum (Fig. 17-14). Luminal narrowing is typical of carcinoma but rare with lymphoma.
- Low-grade MALT lymphomas are superficial spreading lesions that are seen as mucosal nodularity, shallow ulcers, and minimal fold thickening.
- High-grade lymphomas tend to be seen as bulky mass lesions or marked fold and wall thickening.

Gastrointestinal Stromal Tumors

The belief that GI mesenchymal tumors arise from a common precursor cell (the Cajal cell) has led to the term *GIST*. Most GISTs arise in the muscularis propria throughout the GI tract, with 60% to 70% of these arising in the stomach and 20% to 30% arising in the small bowel. Lesions are rare in the colon and rectum. Other primary sites of origin include the omentum, mesentery, and retroperitoneum. Gastric tumors previously identified as leiomyomas, leiomyosarcomas, and leiomyoblastomas are now mostly classified as GISTs. Approximately 10% to 30% of GISTs are malignant. GISTs are differentiated from true leiomyomas and leiomyosarcomas by the presence of KIT (CD117) protein, a tyrosine kinase growth factor receptor that is detected by immunohistochemical staining. Only in the esophagus are leiomyomas more common than GISTs. In other portions of the GI tract, GISTs are the most common mesenchymal tumors. Most tumors present with GI bleeding resulting from mucosal ulceration. GISTs are rarely seen in patients younger than 40 years.
- Tumors arise from the bowel wall and grow away from the gut lumen to project into

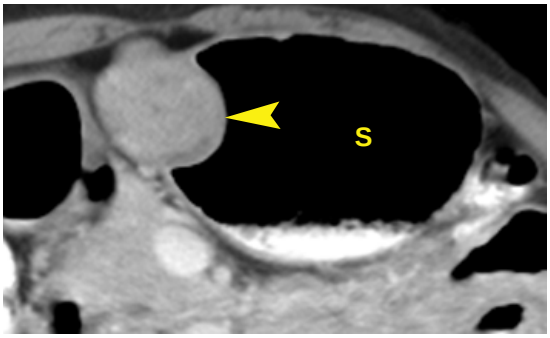

FIGURE 17-15 ■ Gastric gastrointestinal stromal tumor: benign. A wall mass (*arrowhead*) of uniform attenuation and enhancement projects into both the lumen of the stomach (S) and the abdominal cavity.

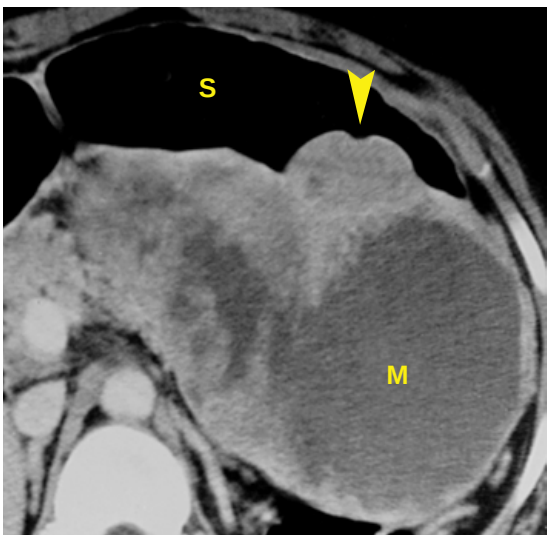

FIGURE 17-16 ■ Gastric gastrointestinal stromal tumor: malignant. A huge heterogeneous mass (M) arises from the posterior wall of the stomach (S). Large low-density areas within the mass correspond to hemorrhage and necrosis. An ulcer crater (*arrowhead*) is identified within a nodular tumor projection into the gastric lumen.

the abdominal cavity. The size varies from millimeters to 30 cm. Small lesions that are homogeneous in attenuation are usually benign (Fig. 17-15).

- Ulceration of the luminal surface is seen in 50% of lesions.
- Cystic degeneration, hemorrhage, and necrosis are common, especially in large lesions (Fig. 17-16). The tumor cavity may communicate with the gut lumen and contain air or oral contrast. Calcification in the tumor is rare.
- Contrast enhancement is seen in viable tumor, most commonly in the periphery of the mass.

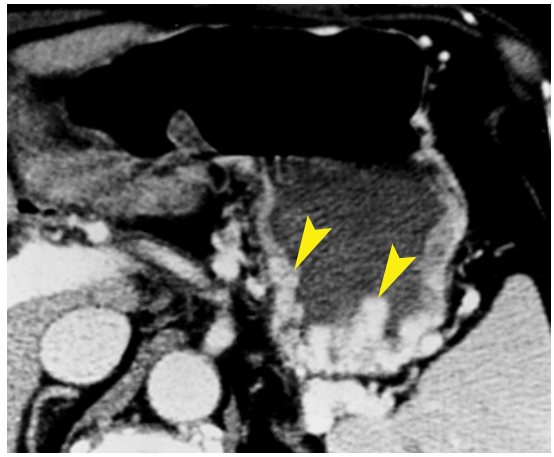

FIGURE 17-17 ■ Gastric varices. Bolus intravenous administration of contrast medium causes bright enhancement of varices (*arrowheads*) in the wall of the gastric fundus in this patient with alcoholic liver disease and portal hypertension.

- The risk of malignancy is increased in tumors that arise outside the stomach or are larger than 5 cm in size. Metastases are most common in the liver and the peritoneal cavity.

Gastric Varices

Gastric varices occur as a result of portal hypertension or splenic vein thrombosis.

- Varices appear as well-marginated clusters of rounded and tubular densities in, or adjacent to, the wall of the stomach, most commonly in the fundal region. Bright enhancement with intravenous contrast administration clinches the diagnosis (Fig. 17-17).
- CT signs of liver disease and other portosystemic collateral vessels are often present.
- Gastric varices without esophageal varices is a hallmark finding associated with splenic vein thrombosis.

SMALL BOWEL

Anatomy

The duodenum extends from the pylorus to the ligament of Treitz, forming the familiar C loop. The duodenum becomes retroperitoneal at the right free edge of the hepatoduodenal ligament, closely related to the neck of the gallbladder. The descending duodenum passes to the right of the pancreatic head to just below the uncinate process, where the duodenum turns to the left. The horizontal portion crosses anterior to the inferior

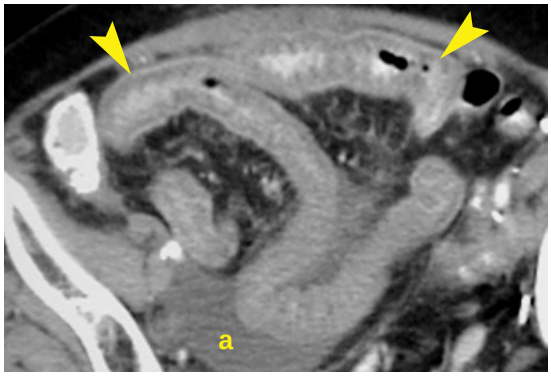

FIGURE 17-18 ■ Wall thickening caused by radiation enteritis. Loops of small bowel in the pelvis exhibit characteristic benign, diffuse, circumferential wall thickening (*arrowheads*). In this case the thickening is associated with radiation enteritis. Ascites (a) is present.

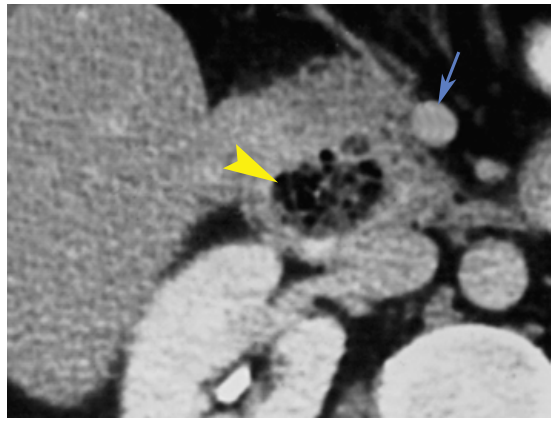

FIGURE 17-19 ■ Duodenal diverticulum. A diverticulum, arising from the second portion of the duodenum, is seen as a mass (*arrowhead*) containing air and fluid that displaces the superior mesenteric vein (*arrow*).

vena cava and aorta and posterior to the superior mesenteric vein and artery. The fourth portion ascends just left of the aorta to the ligament of Treitz, where the bowel becomes the intraperitoneal jejunum.

The jejunum occupies the left upper abdomen, whereas the ileum lies in the right lower abdomen and pelvis. Jejunal loops are feathery with distinct folds. Ileal loops are featureless with thin walls. Distention of the lumen with oral contrast medium is essential for adequate evaluation of the bowel. Unopacified small bowel may mimic adenopathy and abdominal masses. The small-bowel mesentery contains many vessels that are easily visualized when outlined by fat. The normal luminal diameter of the small bowel does not exceed 2.5 cm. The normal wall thickness is less than 3 mm.

Normal small bowel shows uniform mural enhancement with contrast administration. With full luminal distension the enhancing wall is thin, measuring 1 to 2 mm. Enhancement is best appreciated with the low-attenuation contrast agents routinely used for CT enterography. The absence of mural enhancement is indicative of ischemia. A target appearance of mural enhancement with high-attenuation mucosa and serosa separated by low-attenuation submucosa is indicative of a benign process such as Crohn disease, infection, angioedema, hemorrhage, or radiation enteritis. Heterogeneous enhancement is typical of small-bowel tumors. Mild wall thickening (3 to 4 mm) is most characteristic of hypoalbuminemia, infectious enteritis, or mild Crohn disease. Moderate wall thickening (5 to 9 mm) is seen with ischemia caused by mesenteric vein thrombosis, intramural hemorrhage, vasculitis, radiation (Fig. 17-18), and moderate Crohn disease. Marked wall thickening (>10 mm) is associated with lymphoma and other neoplasms, vasculitis, and intramural hemorrhage. Infectious enteritis seldom causes this degree of wall thickening. Mural thickening of >20 mm is almost always neoplastic. Benign conditions generally cause symmetrical thickening along the circumference of the wall. Asymmetrical wall thickening suggests neoplastic disease. Lymphoma is an exception, commonly causing symmetrical wall thickening.

Small-Bowel Diverticula

Small-bowel diverticula may cause unusual collections of fluid, air, contrast material, or soft-tissue nodules in the fat and tissues adjacent to the bowel. These must not be mistaken for abscesses, pancreatic pseudocysts, or tumors. Rescanning the patient will often demonstrate a significant change in the appearance of diverticula.

- Typically, diverticula appear as mucosal sacs without folds and containing air or contrast located adjacent to a loop of bowel (Fig. 17-19).

Small-Bowel Neoplasms

Both benign and malignant small-bowel tumors are uncommon. CT enterography is the optimal imaging technique for demonstrating small-bowel tumors, which appear as soft-tissue masses or wall thickening. CT excels in demonstrating extraluminal tumor growth, involvement of adjacent structures, adenopathy, and complications such as fistulas and necrosis.

- *Lymphomas* appear as single or multiple, often large (9 cm), soft-tissue masses, a discrete polyp that may be the lead point of intussusception, or as focal or diffuse

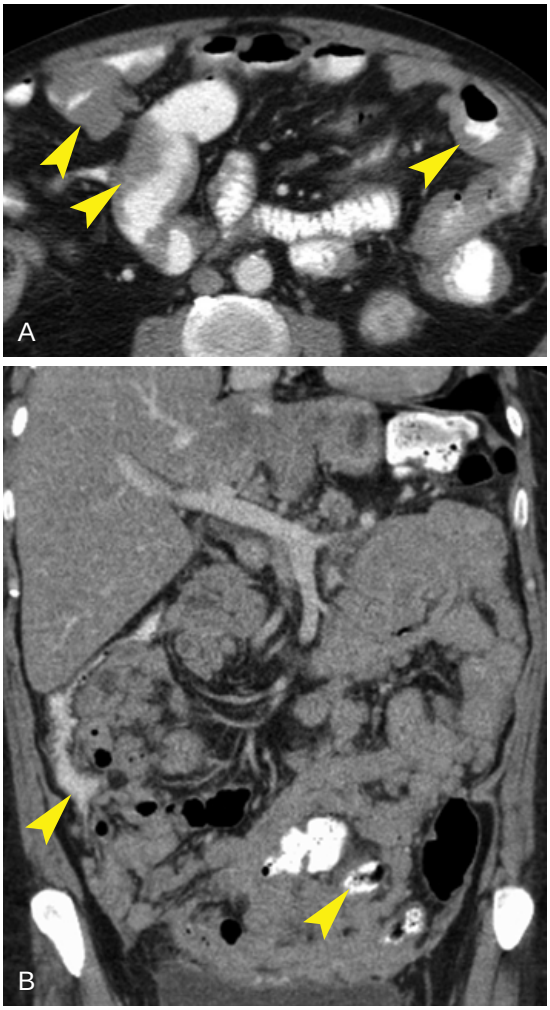

FIGURE 17-20 ■ Small-bowel lymphoma. *A,* Axial computed tomography (CT) shows loops of small bowel in the central abdomen with asymmetrical nodular wall thickening (*arrowheads*). *B,* Coronal CT in a different patient reveals diffuse involvement of the small bowel and mesentery with lesser involved loops of small bowel (*arrowheads*) showing a mass effect on the contrast-filled lumen.

nodular wall thickening with or without aneurismal distention of the bowel lumen (Fig. 17-20). Wall thickening is usually symmetrical around the lumen but may be asymmetrical, resembling adenocarcinoma. Ulceration is common. The ileum is the most common location. Mesenteric or bulky retroperitoneal adenopathy is seen in 50% of cases.

- *Carcinoid* (neuroendocrine) tumors occur most commonly in the appendix (50%) and mesenteric small bowel (20%). They are the second most common small-bowel malignancy. All tumors have the potential to metastasize and are considered malignant, although some may have an indolent course. The primary tumor tends to be small and difficult to detect on CT. It appears as a brightly enhancing wall mass. Aggressive tumors tend to be larger than 2 cm and have necrosis and ulceration. Tumor invasion of the bowel wall induces a dramatic fibrosing reaction in the mesentery that is a hallmark in CT diagnosis (Fig. 17-21). Linear strands of fibrosis radiate into the mesenteric fat from the soft-tissue mass or focal wall thickening of the primary tumor. *Carcinoid syndrome* (cutaneous flushing and diarrhea) is associated with release of vasoactive amines by the tumor. The syndrome occurs only in the presence of liver metastases, because the liver metabolizes amines released into the portal venous system. Metastases are hypervascular and are best seen on arterial-phase images.
- *Adenocarcinoma* of the small bowel is a rare lesion that is most common in the duodenum (50%), especially near the ampulla. Tumors appear as a constricting annular mass with abrupt irregular margins and overhanging edges, as a distinct polypoid nodule, or as an ulcerative mass. Only a short segment of bowel is involved. Partial or complete obstruction may be present (Fig. 17-22).
- *GISTs* are most commonly solitary benign tumors that occur anywhere in the small bowel. Malignant GISTs are most common in the distal small bowel. Small GISTs appear homogeneous, whereas large GISTs are heterogeneous, necrotic, and often ulcerated (Fig. 17-23).

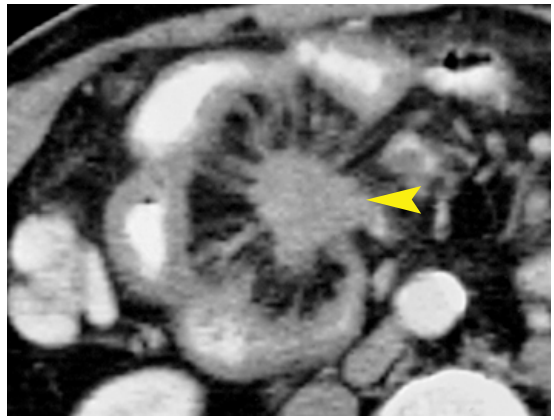

FIGURE 17-21 ■ Carcinoid tumor. A carcinoid (neuroendocrine) tumor arising in the ileum causes a mass (*arrowhead*) in the small-bowel mesentery. Characteristic thick fibrotic strands radiate from the mass to the adjacent bowel, which shows wall thickening.

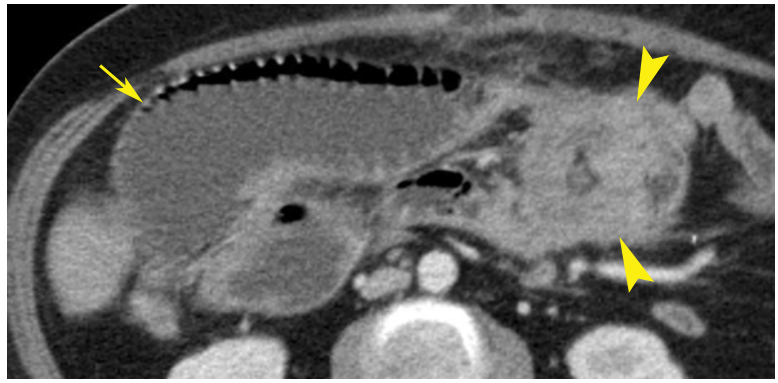

FIGURE 17-22 ■ Adenocarcinoma of the jejunum. An irregular solid mass (*arrowheads*) that caused obstruction of the proximal small bowel (*arrow*) proved to be an adenocarcinoma arising in the jejunum.

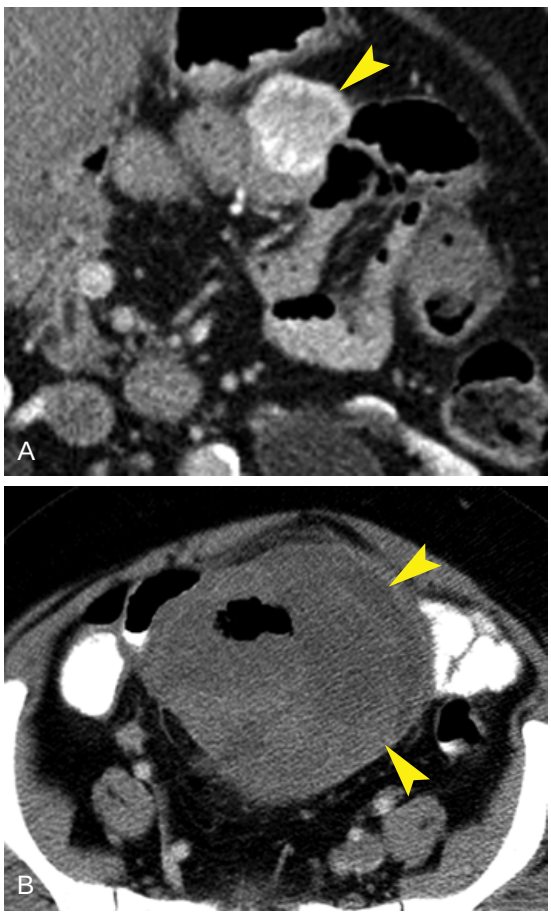

FIGURE 17-23 ■ Small-bowel gastrointestinal stromal tumor (GIST). *A,* A small GIST (*arrowhead*) arising in the jejunum shows marked enhancement on this axial postcontrast computed tomography (CT). *B,* Postcontrast CT shows a very large GIST (*arrowheads*) arising from the distal small bowel in the pelvis. The tumor shows weak enhancement, necrosis, and ulceration. It proved to be malignant.

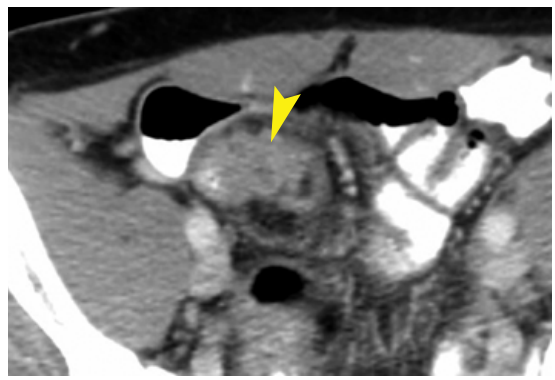

FIGURE 17-24 ■ Metastasis to the small bowel. An irregular nodular mass (*arrowhead*) extending from the wall of the ileum into the mesentery is a hematogenous metastasis from breast cancer. The patient had widespread metastatic disease.

- *Metastases* to the small bowel occur as serosal implants with peritoneal carcinomatosis or with hematogenous spread of tumor as intramural masses (Fig. 17-24). Metastases closely resemble the primary tumor in CT appearance. The most common primaries are malignant melanoma and breast, lung, and renal cell carcinoma. Lesions from melanoma are small and round and may cause intussusception. Metastases may be single or multiple, flat or polypoid, submucosal or ulcerative, producing a "target" appearance.
- *Multiple small bowel polyps* are found in Peutz–Jeghers syndrome and other polyposis syndromes. Polyps associated with Peutz–Jeghers syndrome are hamartomatous.

Crohn Disease

Crohn disease is characterized by inflammation of the bowel mucosa, bowel wall, and mesentery, with marked submucosal edema. These features

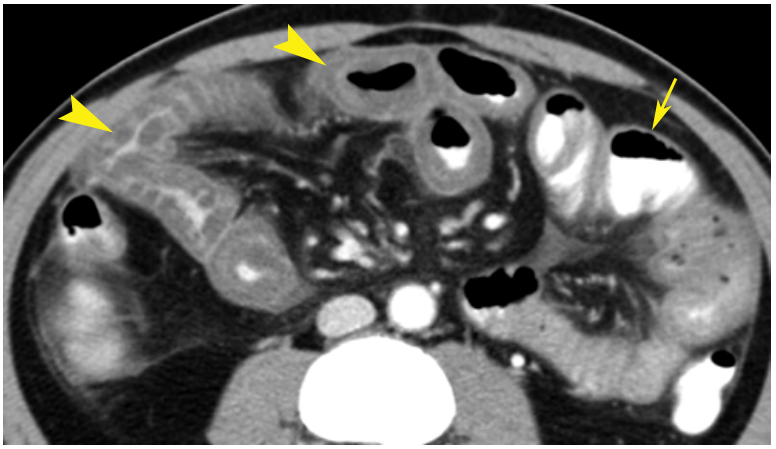

FIGURE 17-25 ■ Crohn disease: wall thickening. Many loops of small bowel show circumferential wall thickening (*arrowheads*), whereas others (*arrow*) are unaffected, representing skip lesions.

are nicely reflected in the CT appearance, especially on CT enterography.

- The small bowel, especially the terminal ileum, is affected in 80% of cases, and the colon is affected in 50%.
- Circumferential thickening of the bowel wall (>3 mm) is a hallmark of the disease (Fig. 17-25). Thickening can be up to 3 cm. Wall thickening may be homogeneous or have a stratified *target* or *double halo* appearance caused by bands of edema.
- Acutely inflamed bowel demonstrates marked wall enhancement after intravenous contrast administration. The degree of enhancement correlates with the inflammation intensity and is the best indicator of active disease.
- The *comb sign* produced by hyperemic thickening of the vasa recta is a sign of active disease. The swollen blood vessels produce a comb-like appearance extending from the thickened bowel wall into the mesenteric fat.
- Wall thickening results in strictures that narrow the bowel lumen in advanced disease.
- *Skip areas* of normal bowel intervening between diseased segments are characteristic of Crohn disease.
- Diffuse haziness and increased density of the mesenteric fat are evidence of mesenteric inflammation.
- Fistulas and sinus tracts between bowel loops (Fig. 17-26) or extending to the bladder, adjacent muscle, or skin surface are characteristic of Crohn disease. Fistulas appear as linear tracts, often containing fluid, that extend extraluminally between bowel loops, bladder, or skin. Fistulas usually show enhancement.
- Extramural abscesses appear as fluid collections in the mesentery. Mesenteric lymph nodes may be enlarged. Mesenteric abscesses contain fluid, air, or contrast material.

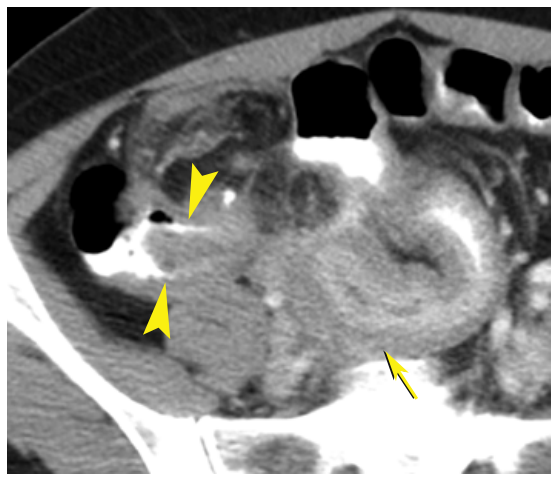

FIGURE 17-26 ■ Crohn disease: fistulas. The ileum (*arrow*) in the right lower quadrant exhibits marked wall thickening and matting of bowel loops caused by inflammation of the mesentery. A double-tract bowel lumen (*arrowheads*) is seen, indicating the formation of an ileo–ileal fistula.

Celiac Disease

Celiac disease is chronic inflammation of the small bowel caused by ingestion of gluten in patients who are susceptible to the irritative properties of gluten. Although some patients are asymptomatic, others have abdominal pain and malabsorption.

- The chronic inflammatory process results in dilated and fluid-filled small-bowel loops (Fig. 17-27). The duodenum, jejunum, and ileum are involved. Wall thickening is present early in the disease, followed by atrophy and wall thinning. Fat deposition in the wall is stimulated by chronic inflammation.

FIGURE 17-27 ■ Celiac disease. Coronal image from a computed tomography enterography examination shows findings of advanced celiac disease with diffuse dilatation of loops of the small bowel from the duodenum to the ileum, diffuse thinning of the wall of the small bowel, and ascites. Chronic malnutrition has resulted in weight loss and the presence of very little subcutaneous or mesenteric fat.

- Jejunization of the ileum is a characteristic finding seen as a decrease in folds in the jejunum and an increase in folds in the ileum. The jejunum appears atrophic.
- Flocculation occurs when barium is administered as oral contrast. The term refers to precipitation of small, high-attenuation flecks of barium distributed throughout the dilated small bowel as a result of progressive dilution of enteric barium.
- Patients are prone to transient small-bowel intussusception.
- Additional findings include increased vascularity of the mesentery, and mesenteric and retroperitoneal adenopathy.

Mesenteric Ischemia

Mesenteric ischemia may be classified as acute or chronic. Arterial causes of acute mesenteric ischemia are most common and include occlusion of the superior mesenteric artery caused by thrombosis or emboli (60% to 70% of cases) and low-flow states related to cardiac malfunction. Thrombosis of the superior mesenteric vein accounts for 5% to 15% of cases. *Intestinal angina* refers to chronic mesenteric ischemia usually related to atherosclerosis.

- Findings of bowel ischemia caused by venous occlusion include circumferential wall thickening due to edema or hemorrhage, mural hyperenhancement if the arterial supply is intact or mural hypoenhancement if the arterial supply is impaired, venous engorgement in the mesentery, and a visible thrombus in the superior mesenteric vein.
- With exclusive arterial occlusion the bowel wall becomes thinner, lacking in edema or hemorrhage. Mural enhancement is absent. Thrombi or emboli may be evident in the mesenteric arteries. Infarction may result in perforation.
- Acute ischemia may result in pneumatosis and portal venous gas (Fig. 17-28).

Small-Bowel Obstruction

CT has sensitivity of 90% to 95% in detecting small-bowel obstruction (SBO) and of 47% to 73% in identifying its cause. CT enteroclysis is useful in evaluating equivocal cases.

- If the bowel is significantly distended on a conventional radiograph, administration of oral contrast is not needed. Intravenous contrast is recommended because it provides enhancement of the bowel wall and better visualization of pathologic processes. Oral contrast may obscure assessment of small-bowel mural enhancement.
- *Complete mechanical SBO* appears as dilatation of the proximal small bowel (>2.5 cm) with a distinct transition zone to collapsed distal bowel (Fig. 17-29). No oral contrast passes the transition zone. The colon is collapsed and contains minimal fluid or gas.
- *Paralytic ileus* appears as dilatation of both the proximal and distal small bowel without a transition zone. The colon is distended with fluid and gas and may contain oral contrast. However, a totally collapsed descending colon is common in nonobstructive ileus and should not be mistaken for evidence of a transition zone.
- The appearance of *partial mechanical SBO* falls between that of complete SBO and ileus. The proximal bowel is less dilated and the transition zone is less distinct. The bowel distal to the obstruction is not completely collapsed. The colon is normal or slightly dilated and contains moderate amounts of fluid and gas. The *small-bowel feces sign* (Fig. 17-30) is uncommon but highly indicative of partial SBO. Intestinal

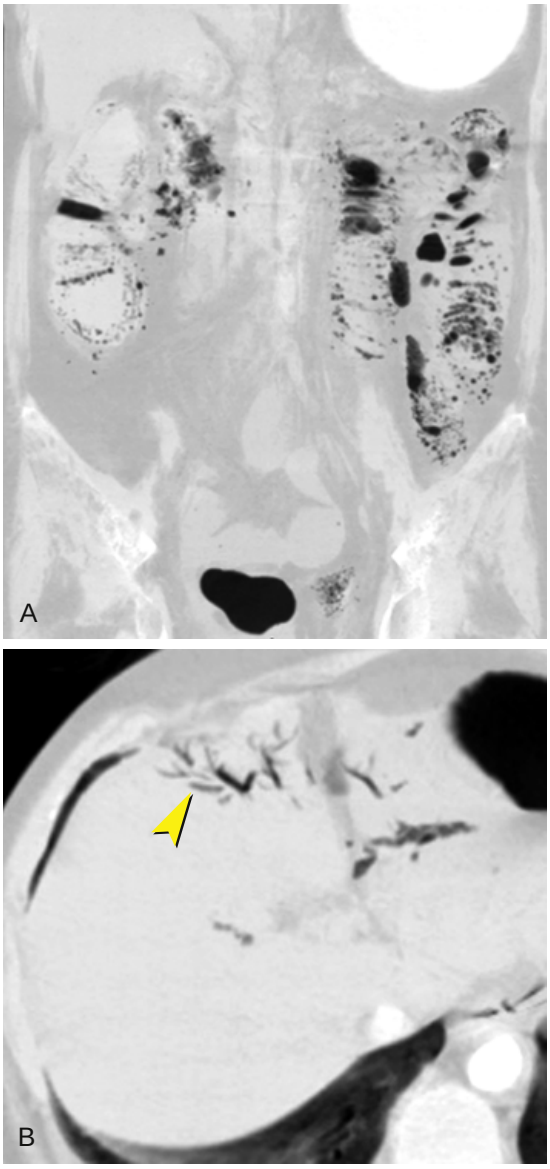

FIGURE 17-28 ■ Mesenteric ischemia: pneumatosis. *A,* Coronal computed tomography (CT) image shown using a lung window reveals diffuse pneumatosis (gas in the wall) of the small and large bowel. *B,* Axial CT image in the same patient shown with lung windows demonstrates gas (*arrowhead*) in the portal veins within the liver.

transit is slowed, resulting in increased water absorption causing the contents of the small bowel to resemble feces.

- Adhesions cause 50% to 75% of SBOs but are not directly visualized by CT. An abrupt transition from dilated to nondilated bowel without other findings suggests adhesions as the cause (Fig. 17-30). Beaklike narrowing at the transition zone is characteristic of adhesions but is not common.

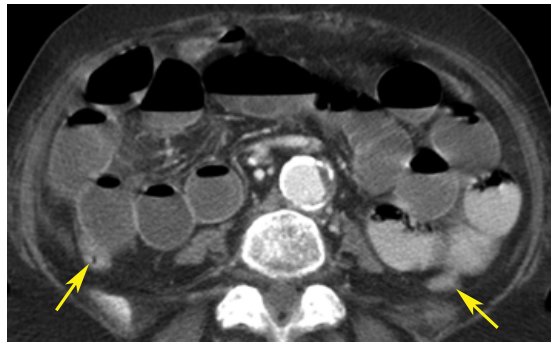

FIGURE 17-29 ■ Small-bowel obstruction. Computed tomography demonstrates diffuse dilatation of the small bowel without wall thickening. Most of the loops contain fluid. The colon (*arrows*) is collapsed. The findings indicate obstruction of the distal small bowel.

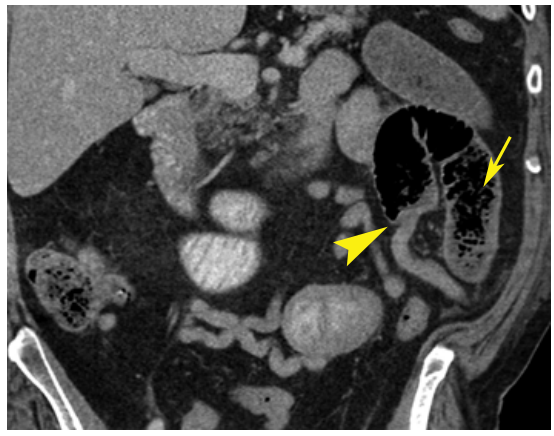

FIGURE 17-30 ■ Small-bowel obstruction: abrupt transition. Coronal computed tomography nicely demonstrates an abrupt transition (*arrowhead*) between dilated proximal small bowel and non-dilated small bowel. This finding is indicative of an adhesion causing an obstruction in the proximal small bowel. The obstructed and dilated part of the small bowel exhibits the small-bowel feces sign (*arrow*).

- Tumor, abscess, intussusception, inflammation, endometriosis, and hernia causing obstruction are identified by characteristic signs. Hernias are the second most common cause of SBO, accounting for 10% of cases.
- *Closed-loop obstruction* has higher morbidity and mortality than simple obstruction. Closed-loop obstruction refers to a loop of bowel occluded at two adjacent points along its course, usually due to adhesions or internal hernia. The obstructed loop may twist, resulting in volvulus. The *beak* or *whirl* sign may be seen at the obstruction and volvulus. Dilated bowel loops with stretched and prominent mesenteric vessels converging on a site of obstruction suggest closed-loop obstruction. *Strangulation* refers

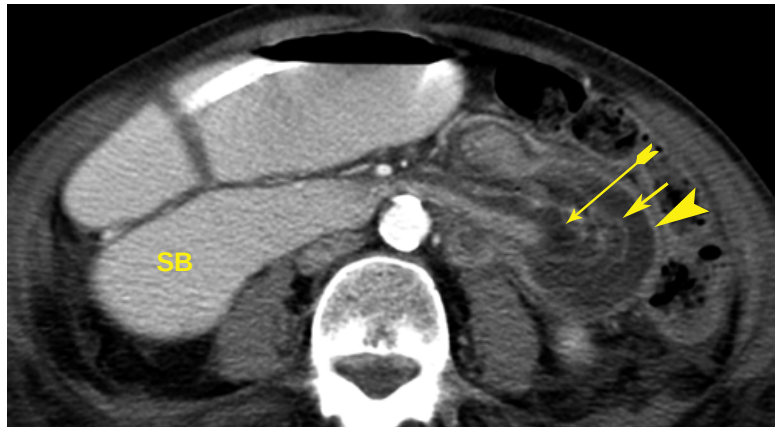

FIGURE 17-31 ■ Intussusception. A metastasis from melanoma to the ileum served as a lead mass for entero–entero intussusception. This image shows the target appearance characteristic of intussusception with the receiving loop (*arrowhead*), the invaginating loop (*arrow without tail*), and the eccentric mesentery (*arrow with tail*). The upstream small bowel (SB) is dilated and obstructed.

to closed-loop obstruction with intestinal ischemia. Strangulation is suggested by associated mild circumferential thickening of the bowel wall with the low-density concentric rings indicative of wall edema (target and halo signs). Poor or absent enhancement of the bowel wall is indicative of ischemia.

- *Midgut volvulus* is most common in children but may occur in adults. Most cases are associated with congenital malrotation of the small bowel with abnormal fixation of the small-bowel mesentery and a short mesenteric root. The small bowel twists around its mesentery, resulting in closed-loop obstruction. Intermittent volvulus causes intermittent abdominal pain that may be difficult to diagnose. CT shows swirling of the mesenteric vessels, reversed positions for the superior mesenteric artery and vein, ectopic location of small-bowel loops, and an abnormal position for the ligament of Treitz.
- *Intussusception* is an uncommon cause of SBO in adults (~5% of cases). Causes include lipoma and other benign submucosal tumors, carcinoma, metastatic disease, and lymphoma. CT demonstrates characteristic findings of bowel within bowel (Fig. 17-31). The distal receiving segment (intussuscipiens) is markedly dilated and has a thickened wall. Its lumen contains the entering loop (intussusceptum), which appears as an eccentric soft-tissue mass with an adjacent crescent of fat that represents the invaginated mesentery. The mass causing the intussusception can often be identified at the leading end of the intussusceptum.
- *Transient intussusception* is sometimes observed (Fig. 17-32). It is not associated with any symptoms and does not cause bowel obstruction. Most cases are of a jejuno–jejunal invagination. The appearance is similar to that of obstructing intussusception with an intraluminal soft-tissue mass with eccentric intraluminal mesentery. The segment of involved bowel is short (a few centimeters), the intussuscipiens is only slightly dilated, and no upstream bowel obstruction is present.

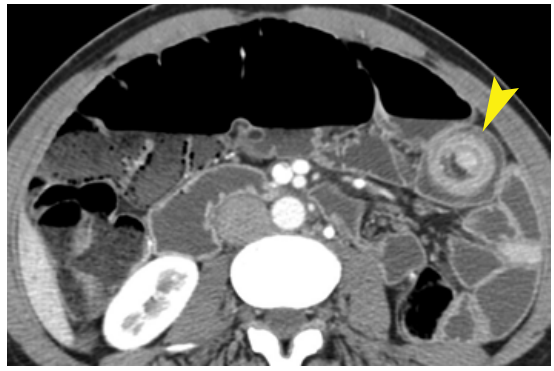

FIGURE 17-32 ■ Transient intussusception. An axial image from computed tomography (CT) enterography examination shows a transient intussusception (*arrowhead*). Serial images showed that the intussusception was a short segment. The patient remained asymptomatic. The intussuscipiens is only slightly dilated. Transient intussusception has been reported as a not uncommon finding during CT enterography.

MESENTERY

Misty Mesentery

The term *misty mesentery* refers to a vaguely defined area of increased attenuation in mesenteric fat. Misty mesentery may be caused by mesenteric edema (hypoproteinemia, portal hypertension, mesenteric vein thrombosis), hemorrhage (trauma, ischemia, blood clotting disorders), inflammation (pancreatitis, inflammatory bowel disease), early-stage lymphoma or primary mesenteric neoplasms, or sclerosing mesenteritis.

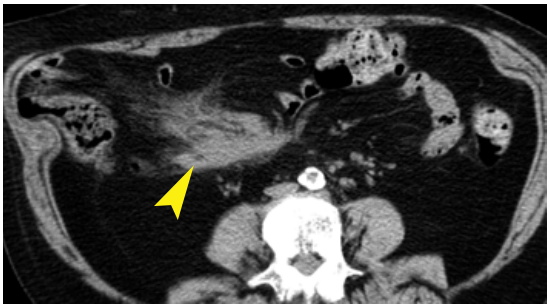

FIGURE 17-33 ■ Sclerosing mesenteritis. Noncontrast computed tomography reveals an ill-defined mass (*arrowhead*) with stranding densities extending into the mesentery. This elderly patient has had several abdominal surgeries and complained of continuing abdominal pain.

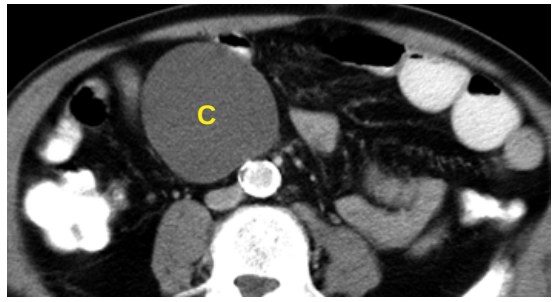

FIGURE 17-34 ■ Mesenteric cyst. A thin-walled, completely cystic, homogenous, nonenhancing mass (C) within the mesentery is characteristic of a mesenteric cystic lymphangioma (mesenteric cyst).

- An ill-defined focus of mesenteric fat shows increased attenuation. The radiologist should correlate this observation with clinical and other imaging findings to determine the likely cause.
- *Sclerosing mesenteritis* refers to an inflammatory disorder of unknown cause affecting the mesentery. It usually involves the small-bowel mesentery but may also affect the mesocolon. Early-stage disease is infiltration of fat with foamy macrophages (mesenteric lipodystrophy), followed by infiltration of fat with plasma cells, leukocytes, and foamy macrophages (mesenteric panniculitis). The final stage is fat necrosis with fibrosis and tissue retraction (retractile mesenteritis) (Fig. 17-33). Patients may present with abdominal pain. The cause is unknown, but sclerosing mesenteritis has been associated with abdominal surgery, trauma, autoimmune diseases, vasculitis, infection, and various malignancies.
- Continuing inflammation may coalesce into a soft-tissue mass that envelops the mesenteric vessels. Preservation of fat around enveloped vessels (the *fat halo sign*) is characteristic. Retractile mesenteritis is more fulminant, with the development of irregular, fibrotic soft-tissue masses within the mesentery. Calcification may develop in areas of fat necrosis. The appearance may be indistinguishable from carcinoid tumor in the mesentery.

Cystic Mesenteric Masses

Cystic lesions primary to the mesentery are more common than primary mesenteric neoplasms.

- Mesenteric and omental cysts are cystic lymphangiomas. They are generally unilocular and thin-walled and contain serous fluid (Fig. 17-34). Internal hemorrhage may occur, which increases the attenuation of contained fluid.
- Enteric duplication cysts are thick-walled unilocular cysts that duplicate the normal bowel wall. Contents are usually serous. They may be attached to normal bowel or free within the mesentery.
- Enteric cysts are similar, but with thinner walls because they are lined by GI mucosa and do not contain the muscle layers of the bowel wall.
- Cystic mesothelioma is a rare benign tumor that presents as a unilocular or multilocular cystic mesenteric mass.
- Cystic teratomas contain fat and calcifications.

Mesenteric Neoplasms

A wide variety of lesions may produce solid masses within the mesentery.

- *Lymphoma* is the most common malignancy seen in the mesentery. Lymphoma of the small bowel appears as a discrete solitary mass, multiple masses, or focal nodular or circumferential wall thickening. Mesenteric involvement may consist of enlarged individual mesenteric nodes or large confluent masses (Fig. 17-35). Lymphomatous masses characteristically sandwich mesenteric vessels between thin layers of spared mesenteric fat (the *sandwich* sign). Retroperitoneal adenopathy is commonly present.
- *Metastases* to the mesentery are far more common than primary tumors arising in the mesentery. Metastatic spread to the mesentery may occur by direct extension (carcinoid), lymphatic flow (bowel malignancies), hematogenous spread to the bowel wall (melanoma and breast cancer), and peritoneal seeding (ovarian and colon cancers).
- *Mesenteric fibromatosis* (*desmoid tumor*) arises most commonly in the mesentery of the

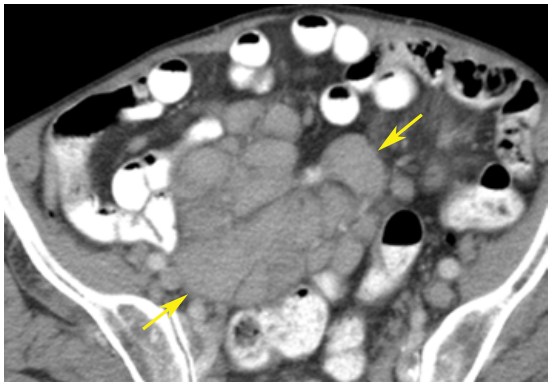

FIGURE 17-35 ■ Mesenteric lymphoma. Multiple bloated, lymphomatous lymph nodes coalesce into a bulky mesenteric mass (*arrows*).

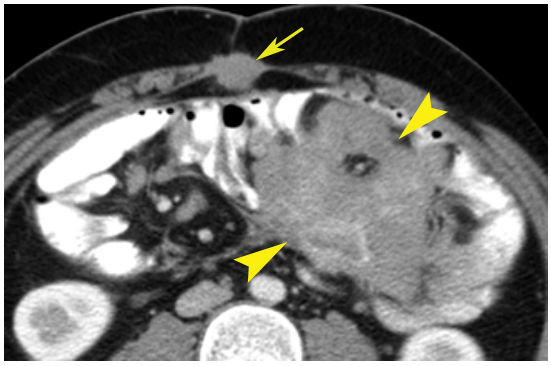

FIGURE 17-36 ■ Mesenteric fibromatosis. In a patient with Gardner syndrome after total colectomy, mesenteric fibromatosis (desmoid tumor) caused a homogeneous soft-tissue mass (*arrowheads*). A desmoid tumor is also seen in the anterior abdominal wall (*arrow*).

small bowel. In Gardner syndrome, tumors are also found in the abdominal wall. The lesion consists of bland fibroblastic cells suspended in collagenous stroma. This produces a well-defined, homogeneous solid mass without hemorrhage, necrosis, or cystic changes (Fig. 17-36).

- *GISTs* that arise in the mesentery or omentum tend to be large (>10 cm) and demonstrate prominent hemorrhage, necrosis, and cystic changes.
- *Sarcomas* that arise in the mesentery or omentum are indistinguishable from GISTs. Tissue types include leiomyosarcoma, fibrosarcoma, malignant fibrous histiocytoma, and liposarcoma.

APPENDIX

Anatomy

The normal appendix can be seen on CT as a thin-walled tubular structure surrounded by

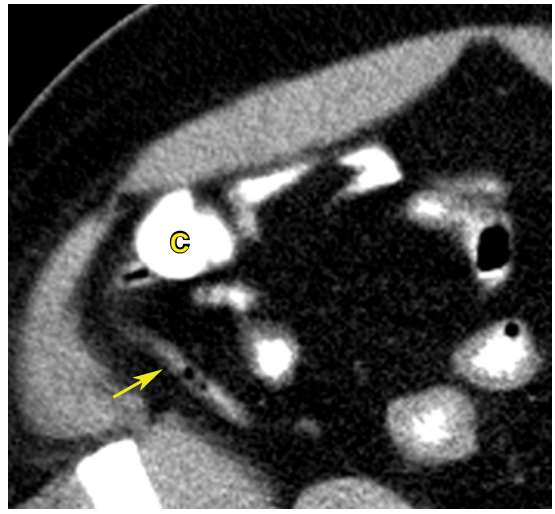

FIGURE 17-37 ■ Normal appendix. The worm-like normal appendix (*arrow*) extends from the cecum (C). The periappendiceal fat provides sharp definition of the wall, with no inflammatory infiltration.

mesenteric fat. It may be collapsed or filled with gas (60%), fluid, or contrast material. The normal appendix does not exceed 6 mm in diameter and has a sharp outer contour defined by homogeneous low-attenuation fat (Fig. 17-37). The origin of the appendix is between the ileocecal valve and the cecal apex, always on the same side of the cecum as the valve. Approximately one-third of appendixes course inferomedially from the cecum, whereas two-thirds are retrocecal.

Appendicitis

Acute appendicitis is the most common cause of acute abdominal pain, affecting 6% of the population. CT has sensitivity of 95% to 98% for the diagnosis.

- CT findings diagnostic of acute appendicitis are a distended appendix (>6 mm in diameter), thickened walls that enhance, and periappendiceal inflammatory changes with stranding in the fat (Fig. 17-38).
- The presence of an appendicolith, appearing as a ringlike or homogeneous calcification within or adjacent to a phlegmon or abscess, is diagnostic of appendicitis. Appendicoliths may be seen in 28% of adult patients with acute appendicitis. Examination of CT images with bone windows aids in the detection of appendicoliths.
- Appendicitis confined to the distal tip is more difficult to diagnose. The proximal appendix may be collapsed or filled with air or contrast material. The inflamed distal

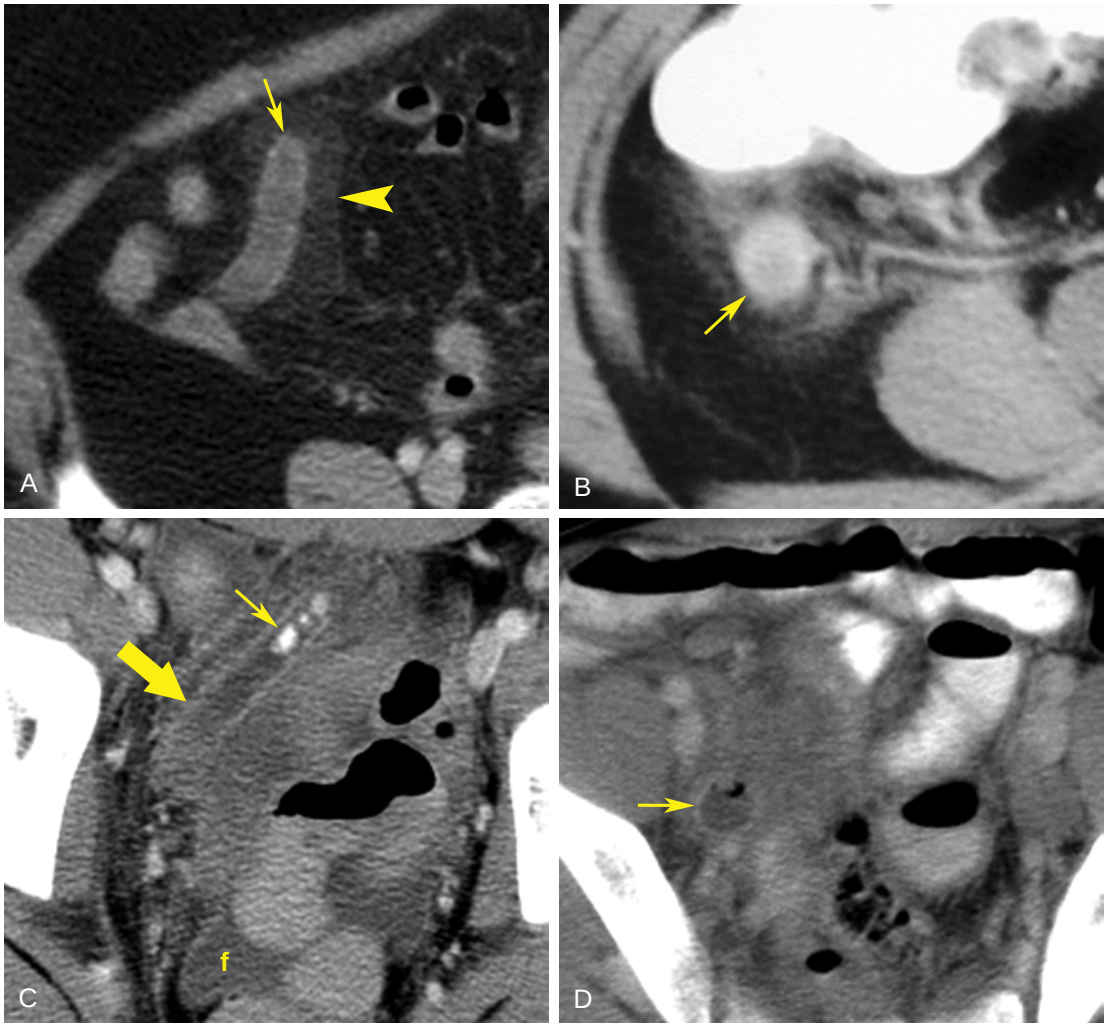

FIGURE 17-38 ■ Acute appendicitis. Four different examples of acute appendicitis. *A,* The swollen appendix, measuring 9 mm in diameter, is identified by its bulbous tip (*arrow*). The periappendiceal fat is infiltrated by edema (*arrowhead*). *B,* The inflamed appendix (*arrow*) in cross-section. The wall of the appendix is markedly enhanced and extensive inflammation is present in the surrounding fat. *C,* A row of high-attenuation appendicoliths (*thin arrow*) is seen occluding the proximal appendix (*thick arrow*), which is dilated with an enhancing wall. Fluid (f) in the cul-de-sac is indicative of perforation, which was confirmed at surgery. *D,* The appendix (*arrow*) is difficult to identify because of the surrounding fluid and inflammation. Examination of serial images is needed to identify its origin from the cecum and its bulbous tip.

appendix is distended (average 13 mm) with a thickened enhancing wall and periappendiceal fat stranding. A transition zone between the normal, thin appendiceal wall and the thickened wall with a narrowed lumen is seen.

- Complications associated with perforated appendicitis include phlegmon, seen as a periappendiceal soft-tissue mass (>20 HU), and abscess, seen as a fluid collection (<20 HU). Phlegmons and abscesses of less than 3 cm generally resolve with antibiotic treatment, whereas abscesses larger than 3 cm usually require surgical or catheter drainage.
- Additional complications that may be demonstrated by CT include SBO, hepatic abscess, and mesenteric vein thrombosis.
- Alternative diagnoses that may be demonstrated by CT in patients referred for suspected appendicitis include Crohn disease, cecal diverticulitis, perforated cecal carcinoma, a ureteral stone, mesenteric adenitis, a hemorrhagic ovarian cyst, and pelvic inflammatory disease.

Mucocele of the Appendix

Mucocele refers to a distended appendix filled with mucus. Causes include simple chronic

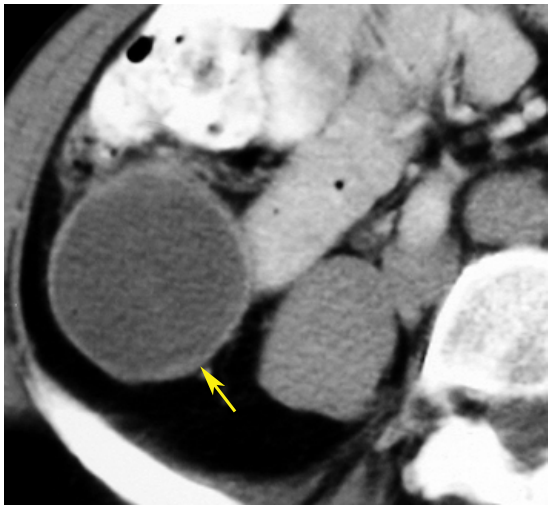

FIGURE 17-39 ■ Mucocele of the appendix. The appendix (*arrow*) is markedly dilated and filled with fluid. At surgery the appendix was filled with mucin and a small, benign, mucinous cystadenoma causing obstruction was discovered.

obstruction, hyperplasia of the appendiceal mucosa, or, most commonly, an obstructing benign or malignant neoplasm of the appendix.

- On CT, a mucocele appears as a well-encapsulated, cystic mass with thin walls that may be calcified (Fig. 17-39). Size is variable up to 15 cm. Mucoceles smaller than 2 cm in diameter are likely to be caused by a simple retention cyst near the appendix origin. Those larger than 2 cm are usually caused by a mucin-producing neoplasm.
- Curvilinear calcification is seen in the wall in 50% of patients.

Neoplasms of the Appendix

Neoplasms of the appendix may present with acute appendicitis, intussusception, GI bleeding, or mucocele.

- Carcinoid tumors are most common, accounting for 80% of appendiceal neoplasms. Most tumors are in the distal third of the appendix and cause no symptoms. Many are small and overlooked on CT. Tumors obstruct the appendix in 25% of cases. They appear as small, irregular nodules, sometimes calcified, mimicking an appendicolith. Some appear as diffuse wall thickening.
- Adenomas and adenocarcinomas are usually mucin-producing tumors often producing a mucocele. Findings include a soft-tissue mass, often with calcification, and irregular wall thickening (Fig. 17-40).

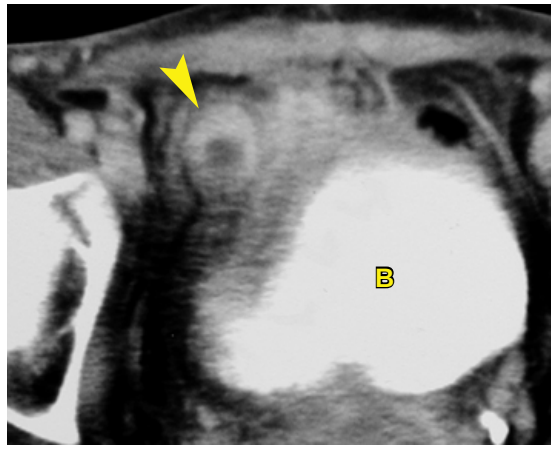

FIGURE 17-40 ■ Carcinoma of the appendix. The appendix (*arrowhead*) is dilated and has irregular wall thickening with associated infiltration of the periappendiceal fat. Surgical resection confirmed adenocarcinoma of the appendix. B, bladder.

COLON AND RECTUM

Anatomy

The colon is easily identified by its location and its haustral markings when it is distended by air or contrast agent. Mottled fecal material serves as a marker of the colon and rectum. The scout view of the abdominal CT should be inspected to determine the general outline and course of the colon. The cecum generally occupies the right iliac fossa, although, because of its variably long mesentery, it may be found almost anywhere in the abdomen or pelvis. Its identity is confirmed by recognizing the ileocecal valve or appendix. The ascending colon occupies a posterior and lateral position in the right flank. The hepatic flexure makes one or more sharp bends near the undersurface of the liver and gallbladder. The transverse colon sweeps across the abdomen on a long and mobile mesentery. Because of its anterior position the transverse colon is usually filled with air when patients are supine for CT. The splenic flexure makes one or more tight bends near the spleen. The descending colon extends caudad down the left flank. The radiologist should remember that the ascending and descending portions of the colon are retroperitoneal. The peritoneum sweeps over their anterior surfaces and extends laterally to form the paracolic gutters that distend with fluid when ascites is present. The sigmoid colon begins in the left iliac fossa and extends a variable distance craniad before it dives toward the rectum. The sigmoid becomes the rectum at the level of the third sacral segment. The rectum distends to form the rectal ampulla and then abruptly narrows to form the

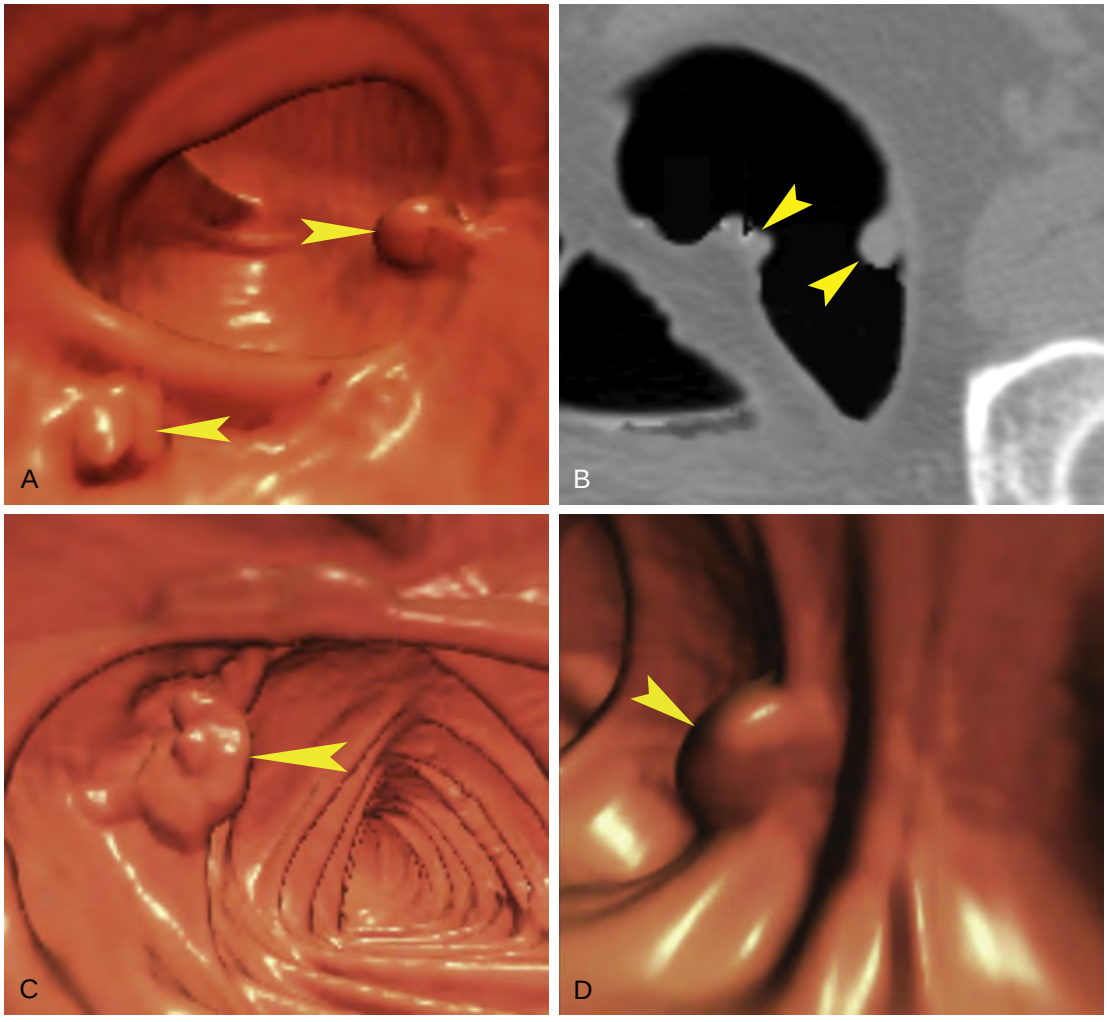

FIGURE 17-41 ■ Computed tomography (CT) colonography. A, Three-dimensional reconstruction virtual colonoscopy image showing two polyps (*arrowheads*) projecting into the colon lumen. Several colonic folds are visible. *B,* Source CT image showing the same two polyps (*arrowheads*) as in *A. C,* A villous polyp (*arrowhead*) with a lobulated contour is demonstrated. *D,* A well-defined polyp (*arrowheads*) projects from a fold.

anal canal. Fat around the colon is normally of uniform low attenuation. Soft-tissue stranding densities in the pericolonic fat are indicative of inflammatory changes or neoplastic invasion.

The peritoneum covering the anterior surface of the rectum extends to the level of the vagina, forming the rectovaginal pouch of Douglas. In males, the peritoneum extends to the seminal vesicles, 2.5 cm above the prostate, forming the rectovesical pouch. Three anatomic compartments are important to recognize when staging rectal carcinoma: (1) the peritoneal cavity above the peritoneal reflections, (2) the extraperitoneal compartment between the peritoneum and the levator ani muscle that forms the pelvic diaphragm, and (3) the perineum, identified by the triangular ischiorectal fossa below and lateral to the levator ani. The lower two-thirds of the rectum are extraperitoneal. On CT the thickness of the wall of the normal colon does not exceed 3 mm.

Technical Considerations

For routine scanning, the rectum and colon can usually be adequately opacified by giving contrast agents orally. Scanning is then carried out through the entire abdomen and pelvis. Demonstration of subtle findings is improved by thin slices (1.25 to 2.5 mm) through a defined area of abnormality. Enhancement with intravenous contrast medium is optional but usually helpful. CT colonography is generally used to screen for colorectal neoplasia (Fig. 17-41).

Colorectal Carcinoma

Colon cancer is the second leading cause of cancer death in the United States. Most (70%) colon cancers occur in the rectosigmoid region. The remainder are scattered fairly evenly throughout the rest of the colon. Colon cancer spreads by (1) direct extension with penetration of the colon wall, (2) lymphatic drainage to regional nodes, (3) hematogenous routes through portal veins to the liver, and (4) intraperitoneal seeding. CT has become routine for preoperative staging and surgical planning. However, the accuracy of CT staging ranges from 17% for early lesions to 81% for advanced lesions. Inaccuracies arise from nonspecific CT signs of tumor spread through the bowel wall and a high incidence of tumor-involved lymph nodes being smaller than 10 mm.

- The primary tumor may be a colon polyp. Polyps are seen as well-defined oval or round intraluminal projections usually seen best in profile (Fig. 17-41). Polyps ≤5 mm in size are nearly all hyperplastic and are considered by most to be clinically insignificant (99% hyperplastic, 1% adenomatous). Polyps in the range from 6 to 9 mm may contain dysplasia or very rarely cancer (<1%); however, 50% of lesions in this size range are adenomas. Polyps in the range of 10 to 15 mm have 80% probability of being an adenoma and 1% to 5% probability of being a cancer. Polyps >2 cm in size have a 40% probability of being cancerous.
- Cancers appear as a larger intraluminal mass with nodular contours and irregular mucosal surfaces, or as a soft-tissue mass that narrows the lumen of the colon (Fig. 17-42). Central low attenuation represents hemorrhage or necrosis. Air within the tumor indicates ulceration.
- Flat lesions appear as focal, lobulated thickening of the bowel wall (>3 mm). Flat adenomas and annular constricting lesions are the major sources of interpretation error on CT colonography
- *Apple core* lesions exhibit irregular bulky thickening of the circumferential wall with marked and irregular narrowing of the bowel lumen (Fig. 17-43).
- Linear soft-tissue strands extending from the colonic mass into pericolonic fat suggest, but are not diagnostic of, extension of tumor through the bowel wall. Edema may cause stranding in the pericolonic fat and thickening of the wall of the colon proximal to the tumor.
- Loss of fat planes between the tumor and adjacent structures suggests local invasion.

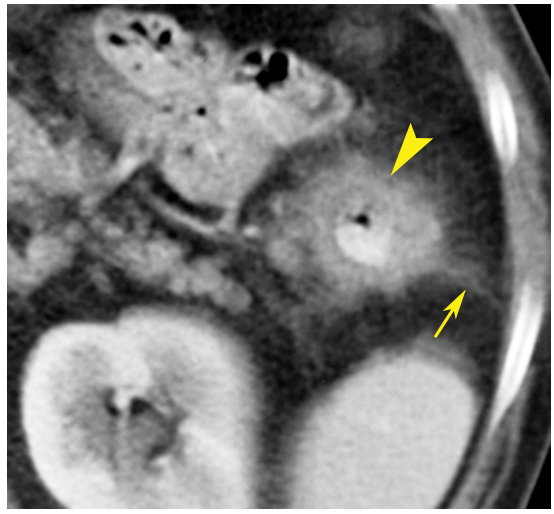

FIGURE 17-42 ■ Colon carcinoma: wall thickening. A carcinoma of the descending colon near the splenic flexure causes thickening of the colon wall (*arrowhead*) and narrowing of the lumen. Stranding densities (*arrow*) extending into the pericolonic fat suggest tumor extension through the bowel wall.

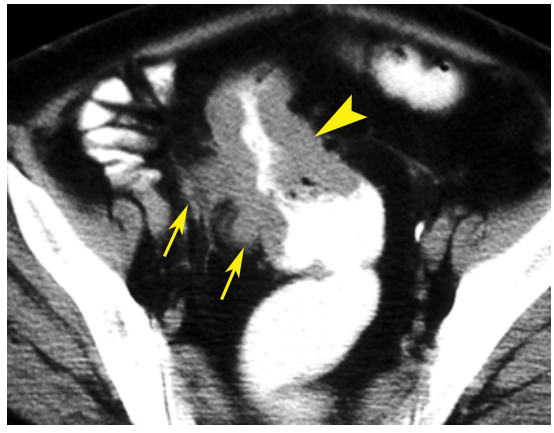

FIGURE 17-43 ■ Rectal carcinoma: apple core lesion. The rectum is involved with marked wall thickening (*arrowhead*) associated with severe and irregular narrowing of the lumen. Spread of tumor tissue into perirectal fat is evident (*arrows*).

- Regional lymph nodes >1 cm in size are considered positive for metastatic disease. However, some nodes smaller than 1 cm may contain tumor and some nodes larger than 1 cm may not contain tumor, limiting the value of CT.
- Distant metastases are seen in the liver (75%), lung (5% to 50%), adrenal glands (14%), and elsewhere.
- Complications of colon malignancy include bowel obstruction, perforation, and fistula formation (Fig. 17-44). Obstructing colon

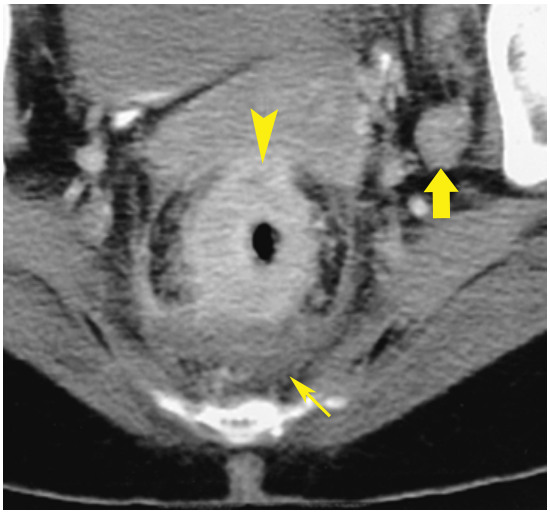

FIGURE 17-44 ■ Rectal carcinoma: perforation. The rectal wall (*arrowhead*) is markedly and circumferentially thickened, with an ill-defined outer margin. Low-attenuation fluid in the presacral area (*thin arrow*) suggests focal perforation. An enlarged metastatic internal iliac lymph node (*thick arrow*) is evident.

cancers may cause ischemic colitis proximal to the tumor.

- Calcifications in the primary tumor and metastases occur with mucinous adenocarcinoma.

Colorectal Cancer Recurrence

CT is more valuable in the detection of colorectal cancer recurrence than it is for initial staging. One-third of patients who have undergone colorectal cancer resection will develop recurrent disease, most (70% to 80%) within 2 years. About half of colon cancer recurrences occur at the site of the original tumor, whereas the remainder recur at distant sites, especially in the liver. Multiple sites of tumor recurrence are more common than a solitary site of recurrence.

- Recurrences appear as irregular masses, often with a low-density necrotic center and an enhancing periphery. The bowel anastomosis marking the location of the original tumor may be identified by high-attenuation metallic bowel clips.
- Presacral soft-tissue densities seen in patients with abdominoperineal resection may be recurrent tumor or fibrosis. Recurrent tumor tends to be nodular and convex anteriorly and enlarges over time. Fibrosis tends to be more uniform and concave anteriorly and remains stable or shrinks over time. Percutaneous biopsy is generally required for confirmation.

FIGURE 17-45 ■ Lymphoma rectum. In a patient with acquired immunodeficiency syndrome, non-Hodgkin's lymphoma caused a bulky rectal mass (*arrowhead*) that distorts the rectal lumen.

Colon Lymphoma

Colon lymphoma is less common than gastric or small-bowel lymphoma but has a striking and fairly characteristic CT appearance. It occurs more commonly in association with ulcerative colitis or Crohn disease. Patients with the acquired immunodeficiency syndrome (AIDS) or who have had an organ transplant have a much higher incidence of colon involvement with lymphoma than the general population.

- Marked thickening of the bowel wall often exceeds 4 cm. Wall thickening may involve a long segment and be associated with loss of haustral markings.
- Multiple intraluminal nodules or a focal intramural mass (Fig. 17-45) are additional appearances.
- The soft-tissue mass is homogeneous without calcification or necrosis.
- Minimal to no enhancement of the mass occurs with intravenous contrast medium.
- Regional and diffuse adenopathy is often massive.
- Lymphoma characteristically causes much larger soft-tissue masses than does carcinoma. The absence of a desmoplastic reaction is typical, and the colon lumen is commonly dilated or normal rather than constricted at the site of tumor involvement. Bowel obstruction is uncommon.

Lipoma

CT can be used to make a specific and noninvasive diagnosis of GI lipoma by demonstrating homogeneous fat density (–80 to –120 HU)

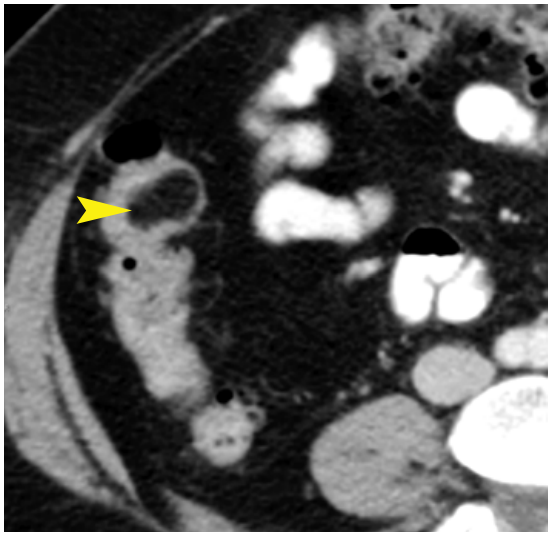

FIGURE 17-46 ■ Lipoma colon. Axial computed tomography reveals a fat-attenuation mass (*arrowhead*) within the colon lumen. Note that the density of the lesion is identical to that of intra-abdominal fat.

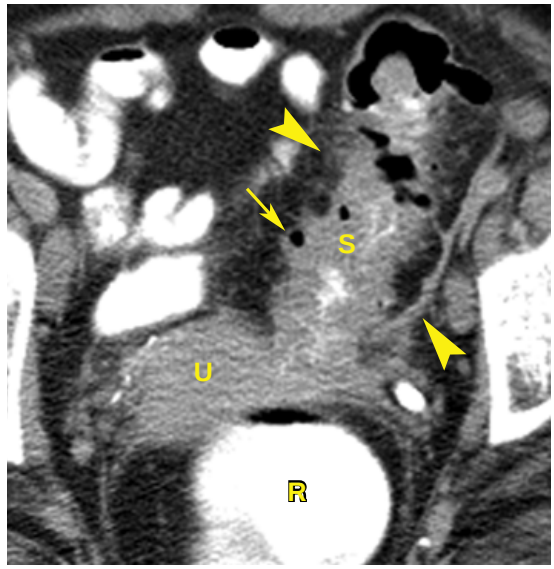

FIGURE 17-47 ■ Acute diverticulitis: uncomplicated. The sigmoid colon (S) shows wall thickening and luminal narrowing. Pericolonic inflammation is manifest in fascial thickening and stranding in the pericolonic fat (*arrowheads*). Several diverticula (*arrow*) are evident in the inflamed portion of the colon. U, uterus; R, rectum.

within a sharply defined tumor (Fig. 17-46). Most lipomas are 2 to 3 cm, are round or ovoid, and are clinically silent. Some may bleed or be a cause of intussusception. Lipomas occur most commonly in the colon (65% to 75%) and small bowel (20% to 25%) and uncommonly in the stomach (5%), esophagus, and pharynx. They are often pedunculated lesions.

Acute Diverticulitis

Diverticulosis refers to small sac-like outpouchings of mucosa and submucosa through the muscular layers of the wall of the colon. Diverticula are most common in the sigmoid colon but may occur throughout the colon. The incidence of diverticulosis increases with age, affecting over 80% of the population over the age of 85 years. Obstruction of the neck of a diverticulum by feces, undigested food particles, or inflammation results in *acute diverticulitis*. Microperforation of the diverticulum causes pericolic inflammation. The inflammatory process commonly spreads to adjacent diverticula to affect a short or long segment of the colon.

- Diverticula are easily visualized on CT as small, rounded collections of air, feces, or contrast material outside the lumen of the colon. Size ranges from 1 mm to 2 cm. Thickening of the muscular wall of the colon is commonly associated.
- Acute diverticulitis appears on CT as a long colon segment (often 5 cm or more) with wall thickening, hyperemic contrast enhancement, and inflammatory changes that extend into the pericolonic fat (Fig. 17-47). Identification of diverticula in the involved segment confirms the diagnosis of acute diverticulitis.
- Because most diverticula occur along the mesenteric surface of the colon, perforation due to diverticulitis is confined initially to between the leaves of the mesocolon. The inflammatory mass that forms is extraluminal and extraperitoneal. CT is more suitable for documentation of this extraluminal disease than is barium enema.
- Sinus tracts and fistulas may extend to adjacent organs or the skin and are represented by linear fluid or air collections. Air in the bladder suggests the possibility of a colovesical fistula.
- Abscess formation may be extensive (Fig. 17-48). Obstruction of the colon or urinary tract may result from the inflammatory process.
- Diverticulitis of the right colon may be confused with acute appendicitis or Crohn disease.
- The CT appearance of diverticulitis overlaps that of colon cancer. Fluid in the sigmoid mesentery with engorgement of mesenteric vessels favors a diagnosis of diverticulitis. Enlarged lymph nodes in the mesentery and the presence of an intraluminal mass are indicative of cancer. Equivocal cases require biopsy.

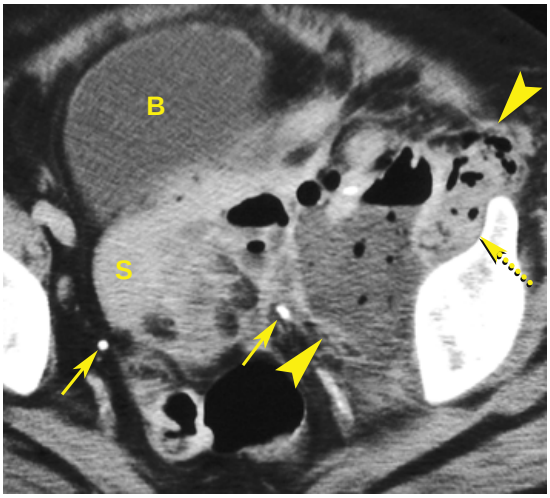

FIGURE 17-48 ■ Acute diverticulitis: perforation and abscess. Diverticulitis arising in the sigmoid colon (S) has ruptured and caused a large pelvic abscess (*arrowheads*) containing air bubbles and fluid. The left iliopsoas muscle (*dotted arrow*) is involved by the abscess. Note the proximity of the ureters (*solid arrows*) to the inflammatory process. They can easily become involved and obstructed. B, bladder.

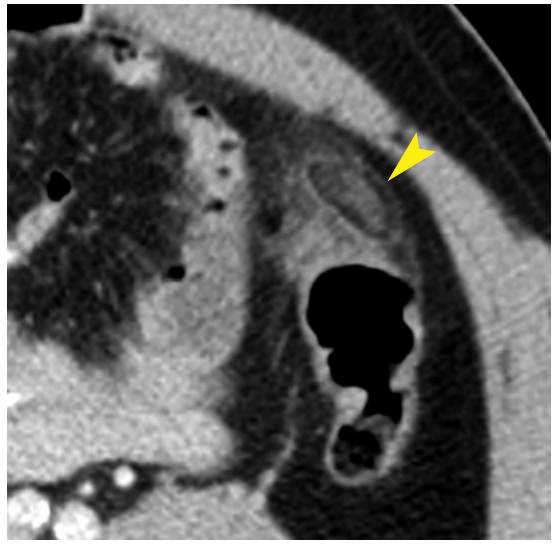

FIGURE 17-49 ■ Epiploic appendagitis. Axial computed tomography shows a pericolonic focus of inflammation enveloping a focus of fat (*arrowhead*). This finding is characteristic of epiploic appendagitis.

- *Epiploic appendagitis* commonly mimics acute diverticulitis or acute appendicitis. Epiploic appendages are fat-containing, peritoneum-bounded sacs containing blood vessels that extend from the serosa of the colon. They vary in size from 5 mm to 5 cm and occur throughout the colon but are most numerous in the sigmoid colon. Normal epiploic appendages are usually not evident on CT. The sacs may undergo torsion, causing acute ischemia and inflammation. Although the disease is self-limiting, acute pain may be severe. CT shows an oval fat-attenuation lesion 2 to 5 cm in size with surrounding inflammatory changes abutting the wall of the colon (Fig. 17-49). Symptoms generally resolve within 2 weeks, but CT findings may persist for 6 months.
- *Meckel diverticulitis* may also mimic acute colonic diverticulitis. Meckel diverticulum is the most common congenital anomaly of the GI tract, occurring as a failure of obliteration of the omphalomesenteric duct that connects the yolk sac to the GI tract during embryonic life. Meckel diverticulum extends from the ileum about 100 cm proximal to the ileocecal valve. The diverticulum may become obstructed and inflamed, similar to acute appendicitis. When inflamed, the diverticulum appears as a blind-ending pouch with a thickened wall, mural enhancement, and inflammation of surrounding fat, usually located in the central abdomen near the midline.

Colitis

Patients with colitis commonly present with vague abdominal symptoms. CT is often the first imaging study that is obtained. Thickening of the colon wall is the CT hallmark of colitis. Wall thickness of >3 mm when the colon is distended represents abnormal thickening. Bowel with mural thickening commonly exhibits homogeneous mural enhancement, or a target or halo appearance. The target or halo appearance is highly indicative of an inflammatory or infectious process rather than a neoplasm.

- *Ulcerative colitis* (UC) is characterized by inflammation and diffuse ulceration of the colon mucosa. The disease starts in the rectum and extends contiguously proximally to involve part or all of the colon. The CT hallmarks of UC are wall thickening and lumen narrowing (Fig. 17-50). The inflammatory pseudopolyps that result from extensive mucosal ulceration are sometimes seen on CT. Mural thickening is usually in the range of 7 to 8 mm and commonly exhibits the target or halo appearance. Narrowing of the rectal lumen with thickening of the rectal wall and widening of the presacral space is characteristic. Edematous stranding and mildly enlarged lymph nodes may be seen in the pericolonic fat and mesocolon. UC predominantly involves the

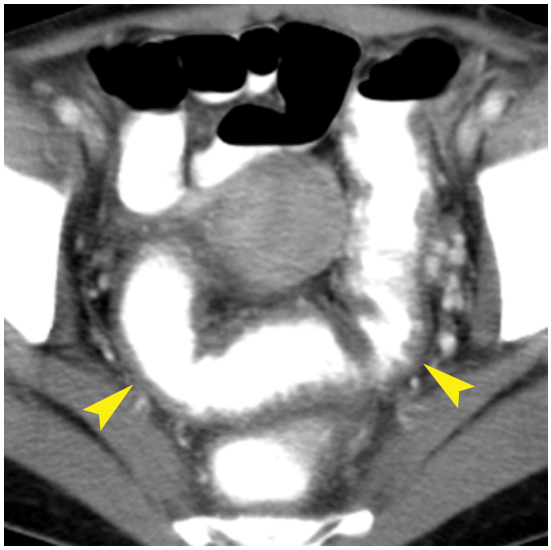

FIGURE 17-50 ■ Ulcerative colitis. The findings of ulcerative colitis on computed tomography are often not dramatic. This scan demonstrates wall thickening (*arrowheads*) and pericolonic inflammatory changes involving the sigmoid colon and rectum. These findings are indicative of colitis but are not specific for the cause.

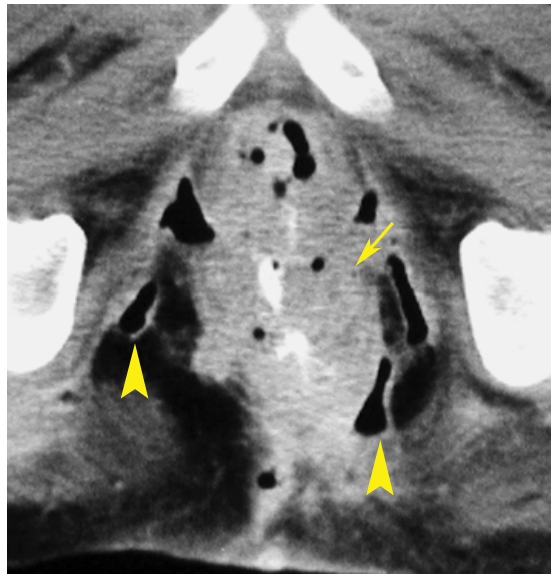

FIGURE 17-51 ■ Crohn colitis: perianal fistulas. Computed tomography shows marked irregular thickening of the wall of the rectum (*arrow*), infiltration of the perirectal fat, and perianal fistulas extending into the ischiorectal fossa (*arrowheads*). The presence of fistulas is typical of Crohn colitis.

colon but may extend to the terminal ileum as *backwash ileitis*.

- *Crohn colitis* is characterized by transmural inflammation that usually affects the terminal ileum and proximal colon and then extends distally. Bowel wall thickening in Crohn colitis is typically 10 to 20 mm, compared to 7 to 8 mm for UC. In Crohn colitis the outer wall is irregular, whereas in UC the outer wall is smooth. Acute active disease shows layering of the colon wall (target and halo signs), whereas chronic disease with fibrosis show homogeneous enhancement of the colon wall. Fibrous and fat proliferation in the mesentery (*creeping fat*) separates bowel loops with extensive fat containing fibrous strands. Lymph nodes of up to 1 cm in size are seen in the mesentery and mesocolon. Fistulas and sinus tracts are additional characteristics of Crohn disease (Fig. 17-51). These may lead to intra-abdominal abscesses, which occur in 15% to 20% of patients. Phlegmons are poorly defined inflammatory masses that occur in the mesentery or omentum.
- *Pseudomembranous colitis* results from overgrowth of *Clostridium difficile* in the colon as a complication of antibiotic therapy. A cytotoxic enterotoxin produced by the bacillus ulcerates the mucosa and creates pseudomembranes of mucin, fibrin, inflammatory cells, and sloughed mucosal cells. Pancolitis or segmental colitis with irregular wall thickening (up to 30 mm) and a shaggy endoluminal contour is characteristic. Submucosal edema is marked, resulting in the *accordion pattern* that is characteristic of pseudomembranous colitis on CT (Fig. 17-52).
- *Typhlitis* or neutropenic colitis refers to a potentially fatal infection of the cecum and ascending colon in patients who are neutropenic and severely immunocompromised. It is classically seen in patients with leukemia who are undergoing chemotherapy. CT demonstrates marked circumferential, symmetrical wall thickening (10 to 30 mm), low-attenuation edema within the cecal wall, and pericecal fluid and inflammation (Fig. 17-53). Colon-wall ischemia leads to pneumatosis, necrosis, and perforation.
- *Ischemic colitis* occurs most commonly in the setting of low cardiac output in a patient with extensive but nonocclusive vascular disease. Most patients are older than 70 years. CT features are mild to moderate circumferential thickening of the wall in a segment of colon corresponding to an anatomic vascular distribution. Watershed areas at the splenic flexure and rectosigmoid are most commonly affected. Submucosal edema produces the target or halo sign on postcontrast scans. Stranding and inflammation are seen in the pericolonic fat. Hemorrhage and pneumatosis may occur in the bowel wall.

- *Radiation colitis* occurs only within areas treated by radiation. CT in the acute phase demonstrates mild wall thickening and pericolonic stranding confined to the radiation port. Chronic radiation injury is seen 6 to 24 months after treatment and appears as mural thickening with prominent stranding in expanded pericolonic fat. These findings are seen most often in the rectum and sigmoid in patients who have undergone pelvic radiation.
- *Infectious colitis* may be caused by bacteria (*Shigella*, *Salmonella*, *Campylobacter*, *Yersinia*, *Staphylococcus*), fungi (histoplasmosis, mucormycosis, actinomycosis), viruses (herpes, cytomegalovirus), parasites (amebiasis), or tuberculosis. Differentiation is based on clinical findings because the CT findings are nonspecific. Circumferential wall thickening with homogeneous enhancement or wall edema affects all or portions of the colon. Inflammatory changes are seen in pericolic fat. Air–fluid levels are seen in the colon because of increased volumes of fluid mixed with feces.
- *Enterohemorrhagic colitis* is caused by a specific strain of *E. coli* most commonly acquired from undercooked ground beef. Patients present with cramps and watery diarrhea that progresses to bloody diarrhea. CT demonstrates wall thickening of up to 20 mm in segments of the colon, with submucosal edema (target sign) and stranding of the pericolonic fat.
- *Toxic megacolon* is a potentially fatal complication of many types of colitis. The CT hallmarks are dilatation of the colon (>5 cm) with thinning of the colon wall, pneumatosis, and perforation (Fig. 17-54).

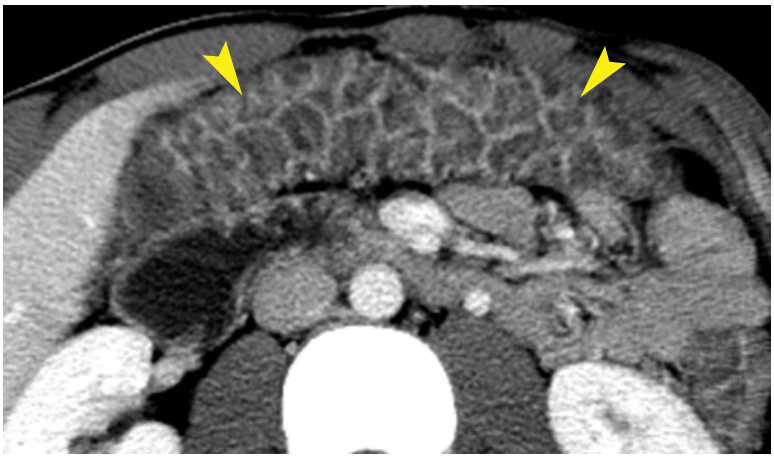

FIGURE 17-52 ■ Pseudomembranous colitis. The transverse colon (*arrowheads*) demonstrates the "accordion pattern" of irregular wall thickening characteristic of *Clostridium difficile* colitis.

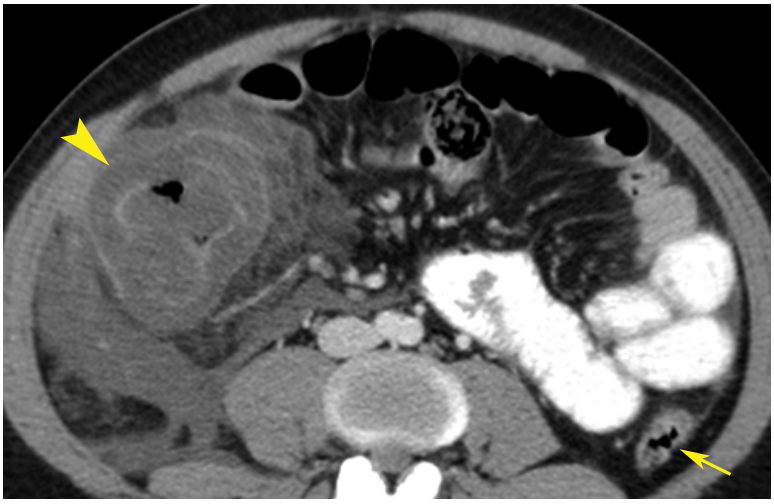

FIGURE 17-53 ■ Typhlitis. The ascending colon (*arrowhead*) and cecum demonstrate dramatic wall thickening, poor enhancement, and pericolonic fluid collections and edema. The descending colon (*arrow*) is unaffected. This patient was neutropenic as a result of chemotherapy.

Pneumatosis Intestinalis and Ischemic Bowel

Pneumatosis intestinalis is the term applied to all cases of intramural intestinal gas. This is an imaging sign and not a diagnosis. At least 58 causative factors ranging from life-threatening to insignificant have been reported. The major causes can be grouped into four categories. *Bowel necrosis* is the most important because it is life-threatening. Bowel necrosis may occur with any cause of bowel ischemia, volvulus, necrotizing enterocolitis, typhlitis, or sepsis. *Mucosal disruption* related to peptic ulcers, endoscopy, enteric tubes, trauma, child abuse, ulcerative colitis, or Crohn disease may cause pneumatosis. *Increased mucosal permeability* is associated with immunosuppression in AIDS, organ transplantation, chemotherapy, steroid therapy, or graft versus host disease. In *pulmonary conditions* such as chronic obstructive pulmonary disease, asthma, cystic fibrosis, chest trauma, and mechanical ventilation, air from disrupted alveoli may dissect along the bronchopulmonary interstitium to the mediastinum and retroperitoneum to extend along the visceral vessels to the bowel wall. The key is to differentiate patients with pneumatosis indicative of significant disease from those in whom pneumatosis is an incidental finding. The clinical condition of the patient is key. Patients who are asymptomatic can be safely observed. Those who are critically ill with evidence of bowel ischemia require urgent surgery. Patients with bowel ischemia usually have predisposing conditions such as hypotension, congestive heart failure, cardiac arrhythmias, sepsis, or dehydration.

- Cystic pneumatosis appears as well-defined blebs or grapelike clusters of spherical air collections in the subserosal region of the bowel wall. The surrounding tissue is usually normal and the cause is usually benign (Fig. 17-55). These air cysts may rupture, resulting in *benign pneumoperitoneum.*
- Linear pneumatosis appears as streaks of gas within and parallel to the bowel wall. This may be associated with either benign or ischemic causes. The patient may need to be turned from the supine to prone or lateral decubitus position to confirm that gas is in the bowel wall rather than in the bowel lumen.
- Findings of bowel ischemia that may be seen in addition to pneumatosis include intestinal dilatation, thickening of the bowel wall with submucosal edema or hemorrhage that may appear as thumbprinting or the target sign, engorgement of mesenteric vessels, thrombosis of mesenteric vessels, and gas in mesenteric or portal veins (Fig. 17-56).

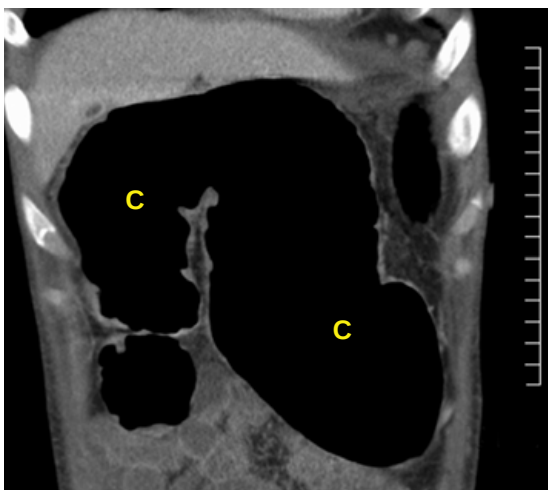

FIGURE 17-54 ■ Toxic megacolon. In a young patient with severe ulcerative colitis, coronal computed tomography demonstrates marked dilatation of the colon (C) with thinning of its walls. The diameter of the lumen of the colon exceeds 7 cm. This finding places the patient at high risk of colon perforation.

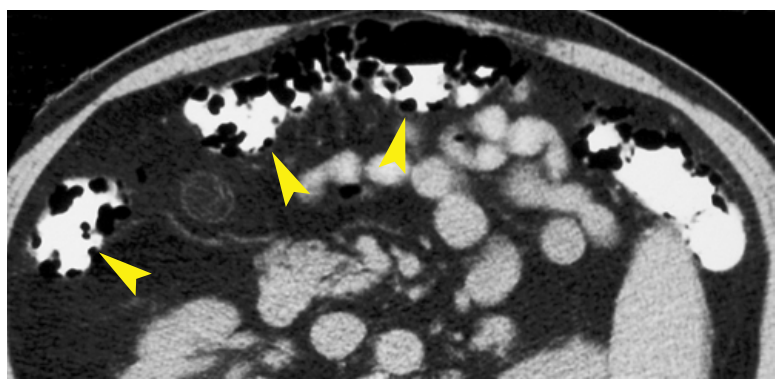

FIGURE 17-55 ■ Pneumatosis coli: benign. Computed tomography reveals well-defined bubbles of air (*arrowheads*) in the dependent and nondependent wall of the transverse colon. The colon wall is not thickened. No pericolonic inflammation is present. The patient was not acutely ill. These findings are indicative of benign pneumatosis.

FIGURE 17-56 ■ Pneumatosis: bowel ischemia. In an acutely ill patient, computed tomography reveals gas in the wall and folds of the small bowel and large bowel. Wall thickening and pericolonic edema are present. This patient died of acute bowel infarction.

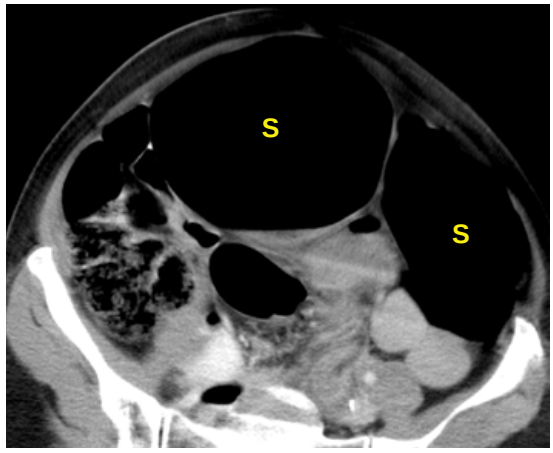

FIGURE 17-57 ■ Sigmoid volvulus. Axial computed tomography of the lower abdomen shows that two portions of the sigmoid colon (S) are markedly dilated and adjadent to each other. Serial images showed convergence of the dilated loops toward the left lower quadrant. Sigmoid volvulus was confirmed by sigmoidoscopy.

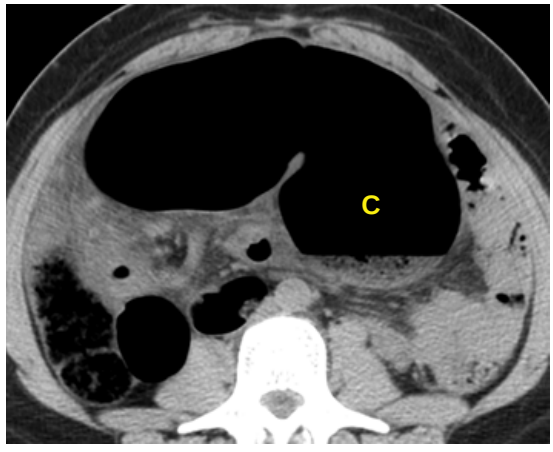

FIGURE 17-58 ■ Cecal volvulus. Computed tomography demonstrates a markedly dilated cecum (C) transposed to the left upper quadrant of the abdomen. The distal small bowel was also dilated.

Colonic Volvulus

Volvulus of the large bowel involves twisting or folding of an intraperitoneal segment of the colon. Diagnosis is usually made by conventional radiographs of the abdomen, but CT is used to detect evidence of ischemia.

- *Sigmoid volvulus* involves twisting of the sigmoid colon on its mesocolon approximately 15 cm above the anal verge. A CT scout scan or conventional radiography demonstrates the distended sigmoid colon, which appears like a bent inner tube with the apex pointing toward the left lower quadrant (Fig. 17-57). Axial CT shows the distended colon with the mesenteric twist, appearing as a *whirl*. Signs of bowel ischemia include wall thickening, infiltration of pericolonic fat, and pneumatosis. Sigmoid volvulus accounts for 60% to 75% of colonic volvulus.
- *Cecal volvulus* characteristically has the dilated gas-filled cecum twisted into the left upper quadrant or central abdomen with the apex of the distended colon pointed toward the right lower quadrant and the whirl of cecal mesentery in the right abdomen. The axis of torsion is in the ascending colon above the ileocecal valve. The small bowel is more commonly dilated in association with cecal volvulus (Fig. 17-58). The distal colon is decompressed. Ischemic changes are also more common. Cecal volvulus accounts for 25% to 40% of colonic volvulus.
- *Cecal bascule* refers to a folding rather than a twisting of a mobile cecum. The cecum folds over on itself, like folding the toe of a sock. The cecum is markedly distended and is displaced into the central abdomen (Fig. 17-59). The small bowel is often not obstructed.

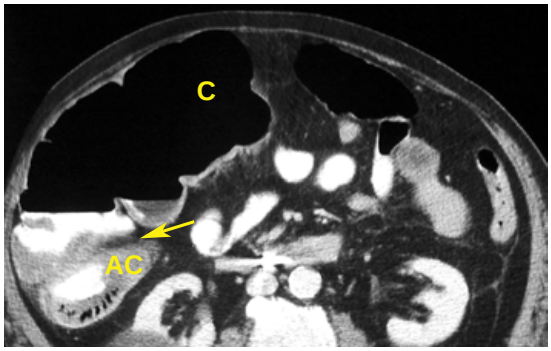

FIGURE 17-59 ■ Cecal bascule. The cecum (C) is dilated and displaced into the central abdomen. A fold (*arrow*) separates the dilated cecum and proximal ascending colon from the nondilated distal ascending colon (AC).

Acute GI Bleeding

Acute GI bleeding is typically initially evaluated with upper-GI-tract endoscopy and colonoscopy. If these fail to identify a cause of bleeding, multiphase contrast-enhanced CT enterography with arterial, portal venous, and delayed phases may be helpful.

- Active bleeding appears as a gradual accumulation of intravenous contrast material within the bowel lumen.
- Angiodysplasia, the most common cause of occult GI bleeding, appears as a markedly enhancing nodule or plaque that fades in enhancement on delayed-phase images.
- Other causes of GI bleeding include neoplasms, Meckel diverticulum, and vascular malformations.

SUGGESTED READING

Duran R, Denys AL, Letovanec I, et al.: Multidetector CT features of mesenteric vein thrombosis. *Radiographics* 32:1503–1522, 2012.

Elsayes KM, Al-Hawary MM, Jagdish J, et al.: CT enterography: Principles, trends, and interpretation of findings. *Radiographics* 30:1955–1974, 2010.

Furukawa A, Kanasaki S, Kono N, et al.: CT diagnosis of acute mesenteric ischemia from various causes. *AJR Am J Roentgenol* 192:408–416, 2009.

Iyer RB, Silverman PM, Tamm EP, et al.: Diagnosis, staging, and follow-up of esophageal cancer. *AJR Am J Roentgenol* 181:785–793, 2003.

Johnson CD: CT colonography: Coming of age. *AJR Am J Roentgenol* 193:1239–1242, 2009.

Johnson CD, Herman BA, Chen MH, et al.: The national CT colonography trial: Assessment of accuracy in participants 65 years of age and older. *Radiology* 263:401–408, 2012.

Kim DH, Pickhardt PJ, Taylor AJ, et al.: CT colonography versus colonoscopy for the detection of advanced neoplasia. *N Engl J Med* 357:1403–1412, 2007.

Kim JH, Eun HW, Goo DE, et al.: Imaging of various gastric lesions with 2D MPR and CT gastrography performed with multidetector CT. *Radiographics* 26:1101–1116, 2006.

Kim TJ, Lee KH, Kim JH, et al.: Postoperative imaging of esophageal cancer: What chest radiologists need to know. *Radiographics* 27:409–429, 2007.

Kiyosue H, Ibukuro K, Maruno M, et al.: Multidetector CT anatomy of drainage routes of gastric varices: A pictorial review. *Radiographics* 33:87–100, 2013.

Laing CJ, Tobias T, Rosenblum DI, et al.: Acute gastrointestinal bleeding: Emerging role of multidetector CT angiography and review of current imaging techniques. *Radiographics* 27:1055–1070, 2007.

Lee NK, Kim S, Kim GH, et al.: Hypervascular subepithelial gastrointestinal masses: CT–pathologic correlation. *Radiographics* 30:1915–1934, 2010.

Levy AD, Remotti HE, Thompson WM, et al.: Gastrointestinal stromal tumors: Radiologic features with pathologic correlation. *Radiographics* 23:283–304, 2003.

Levy AD, Sobin LH: Gastrointestinal carcinoids: Imaging features with clinicopathologic correlation. *Radiographics* 27:237–257, 2007.

Lewis RB, Mehrotra AK, Rodriquez P, Levine MS: Esophageal neoplasms: Radiologic–pathologic correlation. *Radiographics* 33:1083–1108, 2013.

Macari M, Megibow AJ, Balthazar EJ: A pattern approach to abnormal small bowel: Observations at MDCT and CT enterography. *AJR Am J Roentgenol* 188:1344–1355, 2007.

Mang T, Maier A, Plank C, et al.: Pitfalls in multidector row CT colonography: A systematic approach. *Radiographics* 27:431–454, 2007.

McLaughlin PD, Filippone A, Maher MM: The "misty mesentery": Mesenteric panniculitis and its mimics. *AJR Am J Roentgenol* 200:W116–W123, 2013.

McLaughlin PD, Filippone A, Maher MM: Neoplastic diseases of the peritoneum and mesentery. *AJR Am J Roentgenol* 200:W420–W430, 2013.

McLaughlin PD, Maher MM: Primary malignant diseases of the small intestine. *AJR Am J Roentgenol* 201:W9–W14, 2013.

Moawad FJ, Maydonovitch CL, Cullen PA, et al.: CT colonography may improve colorectal cancer screening compliance. *AJR Am J Roentgenol* 195:1118–1123, 2010.

Paulsen SR, Huprich JE, Fletcher JG, et al.: CT enterography as a diagnostic tool in evaluating small bowel disorders: Review of clinical experience with over 700 cases. *Radiographics* 26:641–657, 2006.

Peterson CM, Anderson JS, Hara AK, et al.: Volvulus of the gastrointestinal tract: Appearance at multimodality imaging. *Radiographics* 29:1281–1293, 2009.

Pickhardt PJ: Screening CT colonography: How I do it. *AJR Am J Roentgenol* 189:290–298, 2007.

Pickhardt PJ, Levy AD, Rohrmann CA Jr, Kende AI: Primary neoplasms of the appendix: Radiologic spectrum of disease with pathologic correlation. *Radiographics* 23:645–662, 2003.

Pickhardt PJ, Kim DH, Menias CO, et al.: Evaluation of submucosal lesions of the large intestine. Part 1, neoplasms. *Radiographics* 27:1681–1692, 2007.

Pickhardt PJ, Kim DH, Menias CO, et al.: Evaluation of submucosal lesions of the large intestine. Part 2, nonneoplastic causes. *Radiographics* 27:1693–1703, 2007.

Purysko AS, Remer EM, Leao Filho HM, et al.: Beyond appendicitis: Common and uncommon gastrointestinal causes of right lower quadrant abdominal pain at multidetector CT. *Radiographics* 31:927–947, 2011.

Sandrasegaran K, Rajesh A, Rydberg J, et al.: Gastrointestinal stromal tumors: Clinical, radiologic, and pathologic features. *AJR Am J Roentgenol* 184:803–811, 2005.

Scholz FJ, Afnan J, Beht SC: CT findings in adult celiac disease. *Radiographics* 31:977–992, 2011.

Sheth S, Horton KM, Garland MR, Fishman EK: Mesenteric neoplasms: CT appearances of primary and secondary tumors and differential diagnosis. *Radiographics* 23:457–473, 2003.

Silva AC, Vens EA, Hara AK, et al.: Evaluation of benign and malignant rectal lesions with CT colonography and endoscopic correlation. *Radiographics* 26:1085–1099, 2006.
Silva AC, Pimenta M, Guimaraes LS: Small bowel obstruction: What to look for. *Radiographics* 29:423–439, 2009.
Singh AK, Gervais DA, Hahn PF, et al.: Acute epiploic appendagitis and its mimics. *Radiographics* 25:1521–1534, 2005.
Thomas AG, Vaidhyanath R, Kirke R, Rajesh A: Extranodal lymphoma from head to toe: Part 2, the trunk and extremities. *AJR Am J Roentgenol* 197:357–364, 2011.
Wiesner W, Khurana B, Ji H, Ros PR: CT of acute bowel ischemia. *Radiology* 226:635–650, 2003.
Young CA, Menias CO, Bhalla S, Prasad SR: CT features of esophageal emergencies. *Radiographics* 28:1541–1553, 2008.

CHAPTER 18

PELVIS

William E. Brant

ANATOMY

The true (lesser) pelvis is divided from the false (greater) pelvis by an oblique plane extending across the pelvic brim from the sacral promontory to the symphysis pubis. The true pelvis contains the rectum, bladder, pelvic ureters, and prostate and seminal vesicles in the male, or vagina, uterus, and ovaries in the female. The false pelvis is open anteriorly and is bounded laterally by the iliac fossae. It contains small-bowel loops and portions of the ascending, descending, and sigmoid colon.

Muscle groups form prominent anatomic landmarks on computed tomography (CT). The psoas muscles extend from the lumbar vertebra through the greater pelvis to join with the iliacus muscles arising from the iliac fossa. The iliopsoas muscles exit the pelvis anteriorly to insert on the lesser trochanters of the femurs. The obturator internus muscles line the interior surface of the lateral walls of the true pelvis. Involvement of these muscles by pelvic tumors precludes surgical resection of such tumors. The piriformis muscles arise from the anterior sacrum and exit the pelvis through the greater sciatic foramen to insert on the greater trochanter of the femur. The piriformis forms a portion of the lateral wall of the true pelvis. The pelvic diaphragm, composed of the levator ani anteriorly and the coccygeus posteriorly, stretches across the pelvis to separate the pelvic cavity from the perineum. The pelvic diaphragm is penetrated by the rectum, urethra, and vagina.

The pelvis is divided into three major anatomic compartments (Figs. 18-1 and 18-2). These are important to understand because anatomic compartments allow determination of the origin and spread of disease. The peritoneal cavity extends to the level of the vagina, forming the pouch of Douglas in females, or to the level of the seminal vesicles, forming the rectovesical pouch in males. The extraperitoneal space of the pelvis is continuous with the retroperitoneal space of the abdomen. Pathologic processes from the pelvis may spread preferentially into the retroperitoneal compartments of the abdomen. The retropubic space (of Retzius) is continuous with the posterior pararenal space and the extraperitoneal fat of the abdominal wall. Fascial planes also allow communication with the scrotum and labia. The presacral space between the sacrum and the rectum normally contains only fat. Any soft-tissue density in this space is abnormal and must be explained. The perineum lies below the pelvic diaphragm. On CT the most obvious portion of the perineum is the ischiorectal fossa. This fossa is seen as a triangular area of fat density extending between the obturator internus laterally, the gluteus maximus posteriorly, and the anus and urogenital region medially.

The arteries and veins define the locations of the major lymphatic node chains in the pelvis (Fig. 18-3). The aorta and vena cava divide to form the common iliac vessels at the level of the top of the iliac crest. The common iliac vessels divide at the pelvic brim, marked on CT by the transition between the convex sacral promontory and the concave sacral cavity. The internal iliac (hypogastric) vessels course posteriorly across the sciatic foramen, dividing rapidly into smaller branches. The external iliac vessels course anteriorly adjacent to the iliopsoas to exit the pelvis at the inguinal ligament. Pelvic lymph nodes are classified with their accompanying vessels and are correspondingly named the common iliac, internal iliac, and external iliac nodal chains. The obturator nodes are satellites of the external iliac chain and course along the midportion of the obturator internus. Inguinal nodes in the subcutaneous tissue near the common femoral vessels drain the perineum but not the true pelvis. Pelvic lymph nodes are considered pathologically enlarged when they exceed 10 mm in short axis.

The bladder is best appreciated on CT when filled with urine or contrast agent. The normal bladder wall does not exceed 5 mm in thickness when the bladder is distended. The dome of the bladder is covered by peritoneum, whereas its base and anterior surface are extraperitoneal. The ureters course anterior to the psoas, cross over the common iliac vessels at the pelvic brim, pass on either side of the cervix, and insert into the bladder trigone. In males, the ureters insert into the bladder just above the prostate at the level of the seminal vesicles.

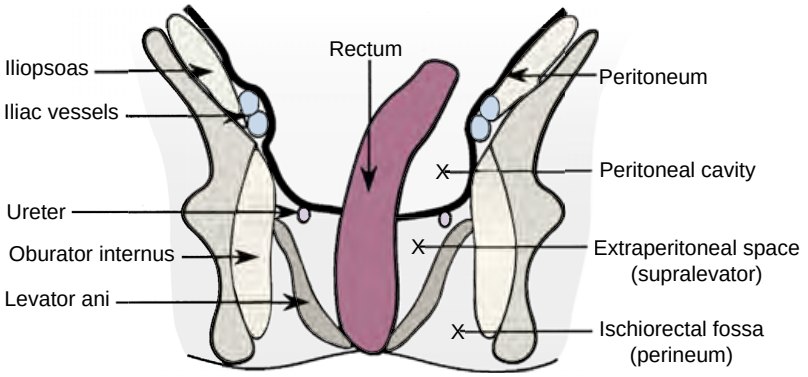

FIGURE 18-1 ■ Anatomic compartments of the pelvis. Diagram of a posterior coronal section at the level of the rectum demonstrates the major anatomic compartments of the pelvis.

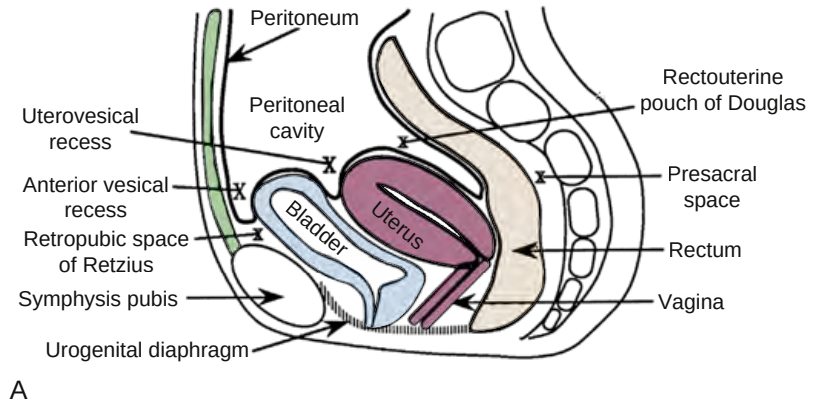

A

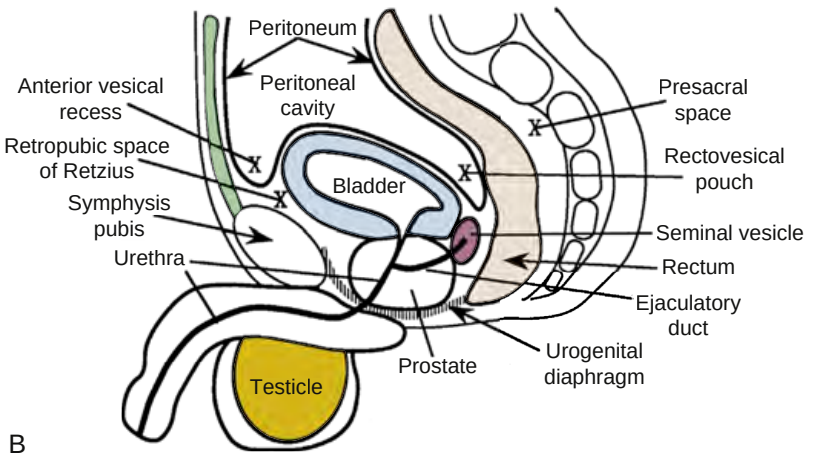

B

FIGURE 18-2 ■ Anatomic compartments of the pelvis. Diagrams of the midline sagittal planes through *A*, a female and *B*, a male pelvis demonstrating the pelvic compartments and peritoneal recesses and their relationships to pelvic organs.

The vagina is seen in cross-section as a flattened ellipse of soft tissue between the bladder and rectum. An inserted tampon will outline the cavity of the vagina with air density and is useful in marking the vagina for pelvic CT. The level of the cervix is recognized by the transition from the elliptical shape of the vagina to the rounded shape of the cervix. Contrast-filled ureters are frequently identified in close proximity to the cervix. The uterus is seen as a homogeneous, smooth-outlined oval of soft-tissue density. The myometrium is highly vascular, causing the uterus to enhance more than most pelvic organs. Assessment of the uterus on CT is made difficult by variations in position and flexion of the uterus and the amount of bladder filling. The broad ligament is a sheet-like fold of peritoneum that drapes over the uterus and extends laterally to the pelvic sidewalls. Between the leaves of the broad ligament is the parametrium, which is loose connective tissue and

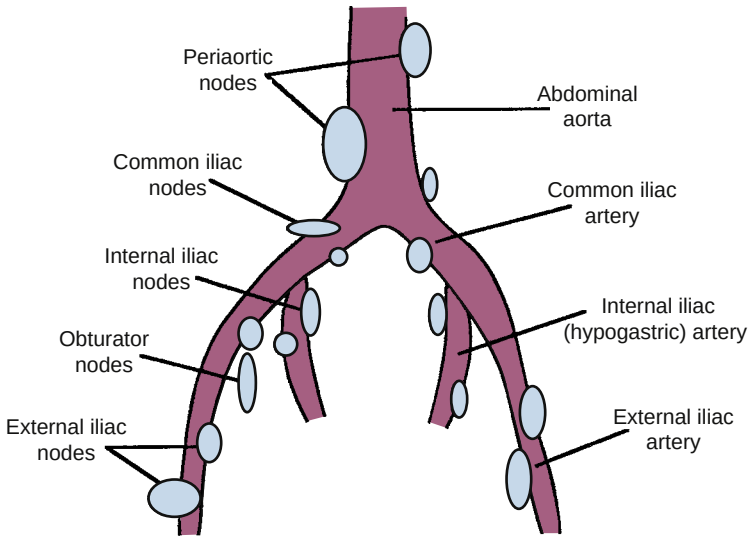

FIGURE 18-3 ■ Pelvic lymph node chains. Diagram of the aortic bifurcation and the iliac arteries illustrating the classification and naming of pelvic lymph nodes.

fat through which pass the fallopian tubes, uterine and ovarian blood vessels and lymphatics, the pelvic ureters, and the round ligament. Determination of tumor extension into the parametrium is an important part of gynecologic tumor staging. The fallopian tube forms the superior free edge of the broad ligament, best seen when outlined by ascites. The fallopian tube with its covering broad ligament is rather like a sheet folded over a clothesline, with the parametrium between the folds of the sheet. The cardinal ligaments extend laterally from the cervix to the obturator internus muscles, forming the base of the broad ligament. The cardinal ligaments appear on CT as triangular densities extending laterally from the cervix. The round ligaments extend from the uterine fundus through the internal inguinal ring to terminate in the labia majora. Uterosacral ligaments extend in an arc from the cervix to the anterior sacrum. Uterine arteries branch from the hypogastric trunk and course in the parametrium just superior to the cardinal ligaments. Enhanced parametrial blood vessels are commonly prominent on bolus-contrast-enhanced CT scans. Normal ovaries are sometimes difficult to identify on CT. Because they are mobile, they may be anywhere in the pelvis, but they are most commonly seen adjacent to the uterine fundus. They appear as oval soft-tissue densities, approximately 2 cm × 3 cm × 4 cm. The presence of cystic follicles allows positive identification of the ovaries.

The normal prostate gland is seen at the base of the bladder as a homogeneous, rounded soft-tissue organ up to 4 cm in maximal diameter. Prostate zonal anatomy is not demonstrated by CT. A well-defined plane of fat separates the prostate from the obturator internus. This fat plane may be invaded by carcinoma. Denonvilliers fascia provides a particularly tough barrier between the prostate and rectum, usually preventing spread of tumors from one organ to the other. The paired seminal vesicles produce a characteristic bow-tie-shaped soft-tissue structure in the groove between the bladder base and the prostate. Normal testes are easily identified in the scrotum as homogeneous oval structures 3 to 4 cm in diameter. The spermatic cord can be recognized in the inguinal canal as a thin-walled oval structure of fat density containing small dots representing the vas deferens and spermatic vessels.

TECHNICAL CONSIDERATIONS

The ideal technique for CT imaging of the pelvis requires optimal bowel opacification. A typical procedure involves giving 500 mL of dilute contrast agent orally the evening preceding the examination and repeating the dose 45 to 60 minutes before the examination. The colon and rectum can be distended by placing a tube in the rectum and insufflating with 20 puffs of air, or to the limit of patient comfort. All patients are asked to avoid urination for 30 to 40 minutes before the examination to allow bladder filling. Intravenous contrast medium is routinely given via a mechanical injector at 2 to 3 mL/second for a total dose of 150 mL of 60% contrast agent. CT images through the pelvis are viewed as contiguous 2.5- to 5-mm-thick slices. The abdomen should be scanned as well in patients with known or suspected pelvic malignancy. To optimize contrast medium enhancement of pelvic organs, the pelvis can be scanned first, and then the abdomen. Coronal and sagittal plane reconstructions are often helpful.

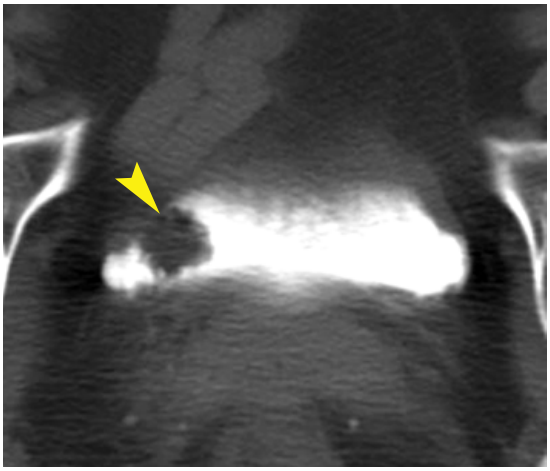

FIGURE 18-4 ■ Transitional cell carcinoma of the bladder: polypoid. Bone windows provide the best visualization of a polypoid frond-like mass (*arrowhead*) projecting into the bladder lumen and seen as a filling defect within the intraluminal contrast material.

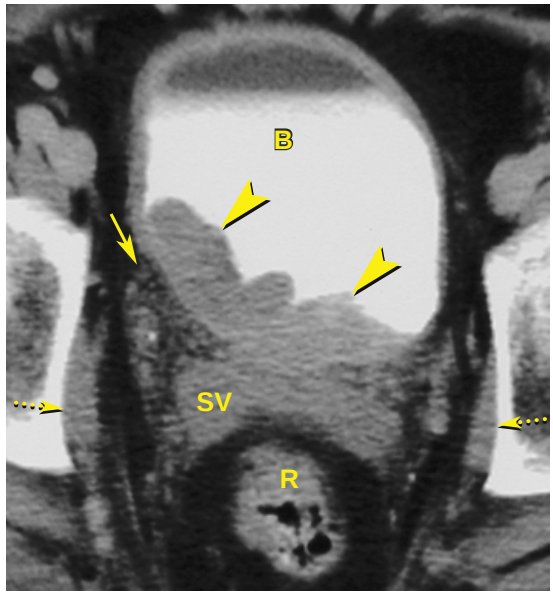

FIGURE 18-5 ■ Transitional cell carcinoma of the bladder: wall thickening. Spreading tumor (*arrowheads*) thickens the bladder wall and projects into the bladder lumen (B) near the trigone. Tiny nodules and strand-like densities (*solid arrow*) infiltrate the normally clear fat triangle between the bladder and the seminal vesicles (SV). In this case the tumor did penetrate the bladder wall and infiltrate the perivesical fat. However, this finding is not a reliable indication of tumor spread. The obturator internus muscles (*dotted arrows*) are clearly not involved, indicating that this tumor is potentially resectable. Clear fat separates these muscles from the perivesical tumor nodules. R, rectum.

BLADDER

Bladder Carcinoma

Bladder cancer may be superficial and confined to the mucosa. However, with invasion of the bladder wall musculature, risk of spread to regional and distant nodes increases. As the number and size of nodal metastases increase, so does the risk of hematogenous spread to bone and lung. CT is useful for the staging of advanced disease but is not accurate in defining early-stage disease. Patients are generally referred for CT staging after muscle invasive disease is suspected on cystoscopy. The key elements of staging are the depth of tumor invasion into the bladder wall and the involvement of adjacent and distant sites by tumor. Most (95%) malignant bladder tumors are uroepithelial (transitional cell) carcinomas that carry a risk of multiple synchronous tumors in the ipsilateral ureter and renal collecting system. Squamous cell carcinomas (5%) are usually associated with chronic inflammation. Adenocarcinomas account for less than 2% of bladder tumors. CT findings are as follows:

- The primary tumor appears as a focal thickening of the bladder wall or as a soft-tissue mass projecting into the bladder lumen (Fig. 18-4). Early postcontrast scans may demonstrate a weakly enhancing mural nodule on a background of low-attenuation urine. Delayed scans show a soft-tissue filling defect on a background of high-attenuation, contrast-opacified urine. Masses may be plaque-like, polypoid, or papillary.
- Multicentric tumors occur in 30% to 40% of cases, with tumors in the upper tracts in 2% to 5% of cases. The radiologist should always look for additional tumors.
- The bladder must be well distended or else subtle tumors, especially small, flat lesions, can easily be overlooked. Bladder tumors enhance maximally at 60 seconds after contrast injection, stressing the need to scan the pelvis during this time frame.
- Calcifications are seen in 5% of transitional cell carcinomas.
- Perivesical spread is seen as soft-tissue density in the perivesical fat (Fig. 18-5). Extension to the pelvic sidewall musculature precludes complete surgical resection.
- Pelvic lymph nodes larger than 10 mm in short axis are considered positive for metastatic disease. Smaller nodes are unlikely to be involved.
- Hematogenous metastases are most common in liver, lungs, bones, and adrenal glands.
- Rare bladder tumors to be considered in the differential diagnosis include pheochromocytoma, leiomyoma, lymphoma (Fig. 18-6), sarcoma, and metastases.

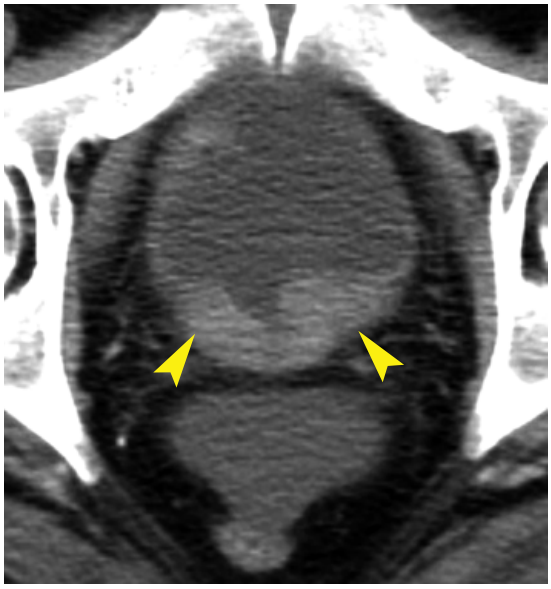

FIGURE 18-6 ■ Lymphoma of the bladder. Lymphoma (*arrowheads*) causes nodular thickening that extends into the bladder lumen, mimicking transitional cell carcinoma.

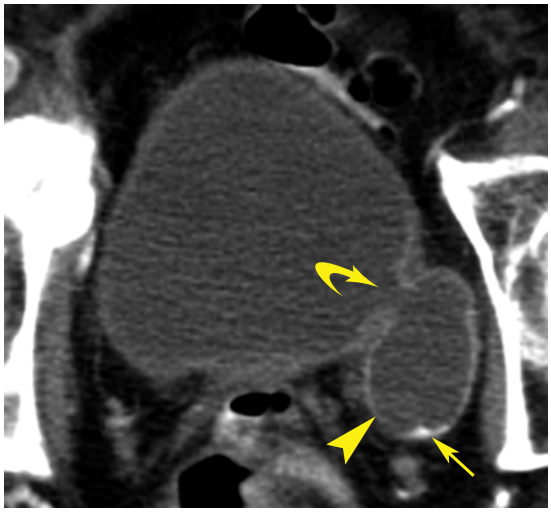

FIGURE 18-7 ■ Bladder diverticulum. A bladder diverticulum (*arrowhead*) extends from the lateral wall of the bladder and maintains communication with the bladder lumen through a large ostium (*curved arrow*). Small stones (*straight arrow*) layer dependently in the diverticulum. Bladder diverticula serve as a site for urinary stasis, which is a predisposing factor for urinary infection and stone formation.

Bladder Diverticulum

A bladder diverticulum is seen as a cystic pelvic mass. Identification of communication with the bladder lumen is the key to correct diagnosis (Fig. 18-7). Bladder diverticula provide a site for urine stasis, which commonly results in stone formation and recurrent infection.

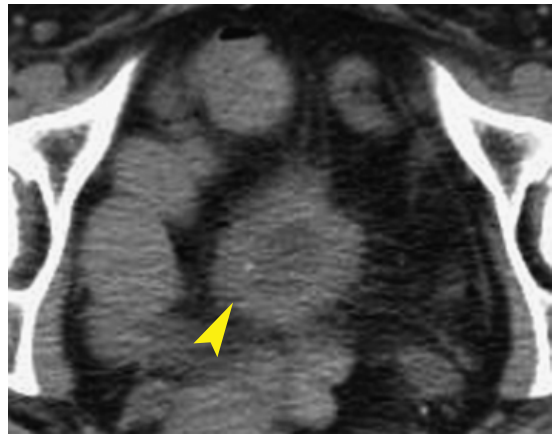

FIGURE 18-8 ■ Chronic cystitis. The bladder (*arrowhead*) is contracted and thick-walled in a paraplegic patient with neurogenic bladder and chronic cystitis. Inflammatory stranding extends into the pericystic fat.

Cystitis

Cystitis refers to inflammation of the bladder wall. It is a common condition affecting patients of all ages. It is most common in women.

- *Acute bacterial cystitis* is most common and is usually caused by *Escherichia coli* infection. The diagnosis is made clinically, and imaging is usually not required. Bullous mucosal edema may thicken the bladder wall and give it a cobblestone appearance. Chronic cystitis is usually related to poor bladder emptying caused by neurogenic bladder or chronic bladder outlet obstruction and may result in a fibrotic contracted bladder with a thick wall (Fig. 18-8).
- *Cystitis cystica* and *cystitis glandularis* are inflammatory disorders that result from chronic irritation of the bladder wall caused by recurrent bacterial cystitis or bladder stones. CT shows multiple hypervascular, enhancing, polypoid masses of varying size.
- *Interstitial cystitis* is an uncommon idiopathic disease characterized by fibrosis of the bladder wall. Bladder volume is restricted, and the bladder wall ultimately becomes thinned.
- *Emphysematous cystitis* refers to the presence of gas in the bladder wall and lumen caused by bacterial infection in glucose-laden urine. The disease occurs in patients with diabetes mellitus who have bladder dysfunction related to neurogenic bladder, bladder diverticula, or chronic bladder outlet obstruction. CT shows thickening and streaks and bubbles of gas in the bladder wall (Fig. 18-9). Gas in the bladder lumen forms air–fluid levels.

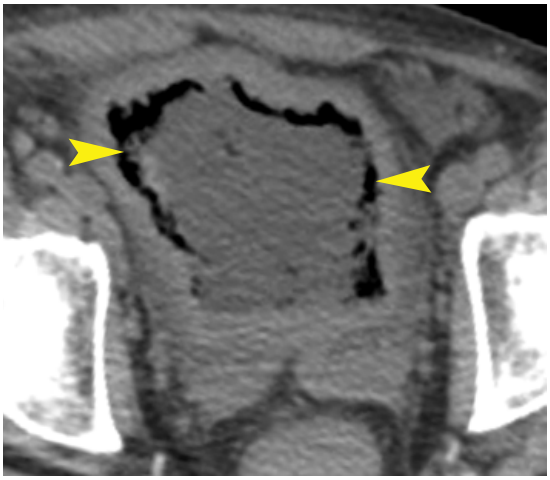

FIGURE 18-9 ■ Emphysematous cystitis. Gas (*arrowheads*) is present in the wall of the bladder in this diabetic patient with urinary sepsis.

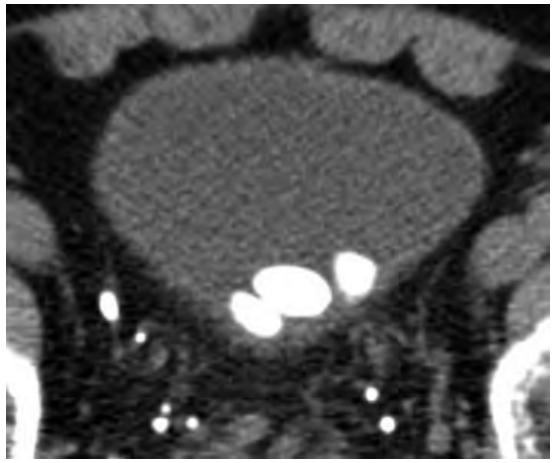

FIGURE 18-10 ■ Bladder stones. Three calculi are seen as oval high-attenuation objects within the bladder lumen.

- *Tuberculosis* of the bladder is an extension of renal tuberculosis. Acute CT findings include bladder wall thickening, trabeculation, and irregular mucosal masses representing tubercles. In the chronic stage the bladder becomes contracted and the wall is commonly calcified.
- *Schistosomiasis* is caused by infestation with the *Schistosoma haematobium* parasite, most commonly found in Africa. Eggs laid in the bladder wall produce nodular wall thickening in the acute phase and result in a fibrotic contracted bladder with wall and distal ureteral calcification in the chronic phase.

Bladder Stones

Bladder stones are much less common than kidney stones. Bladder stones may form primarily within the bladder from foreign bodies within the bladder or from kidney stones that are retained within the bladder. Most occur in the setting of urinary stasis within the bladder caused by neurogenic bladder, enlarged prostate, recurrent urinary infections, or a bladder diverticulum.

- CT is sensitive for detection of even very small stones in the bladder. Stones appear as foci of high attenuation (Fig. 18-10).

UTERUS

Leiomyoma

Leiomyomas (fibroids) are found in up to 40% of women older than 30 years. As frequent findings, their CT features should be recognized.

- Leiomyomas appear as homogeneous or heterogeneous masses that may be hypodense, isodense, or hyperdense relative to enhanced myometrium (Fig. 18-11). Diffuse enlargement of the uterus and lobulation of its contour are common.
- Coarse, dystrophic mottled calcifications within the mass are common and characteristic.
- Cystic degeneration produces interior low density and may convert the mass into a large cavity.
- Pedunculated leiomyomas may appear as adnexal rather than uterine masses. Parasitic leiomyomas are separate from the uterus, having twisted and detached from the uterine pedicle and implanted on the peritoneum.
- Lipoleiomyomas are variant tumors consisting of smooth muscle, fibrous tissue, and mature fat. CT shows foci of fat attenuation (below –30 Hounsfield units, HU) within the tumor.
- Rare leiomyosarcomas cannot be accurately differentiated from leiomyomas by CT appearance alone. Rapid growth of a uterine mass in a postmenopausal woman suggests malignancy. Leiomyosarcomas appear as large masses with prominent irregular low-attenuation areas of necrosis and hemorrhage. The appearance of leiomyosarcoma overlaps that of benign leiomyoma with extensive degeneration.

Carcinoma of the Cervix

Although CT has been used to stage cervical carcinoma, magnetic resonance (MR) is preferable

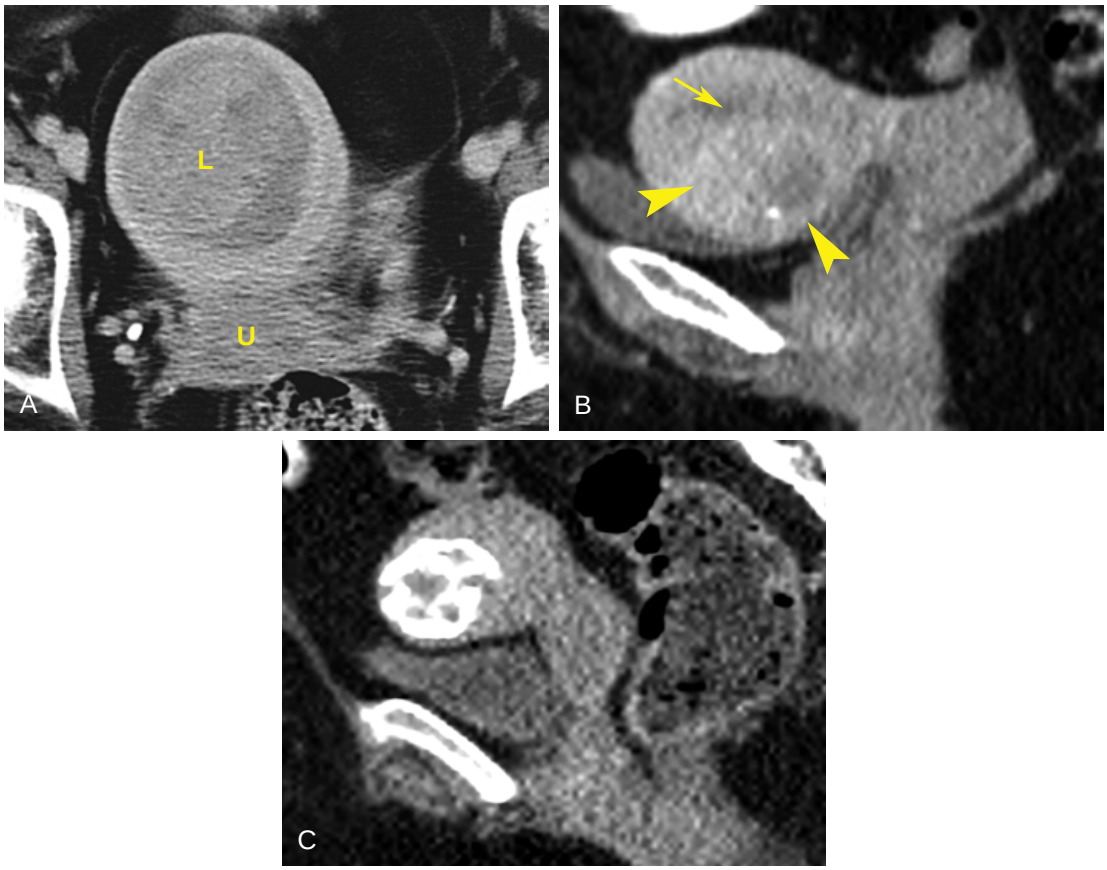

FIGURE 18-11 ■ Leiomyoma uteri. *A,* Axial computed tomography (CT) shows a large leiomyoma (L) extending anteriorly from the uterus (U). *B,* Sagittal postcontrast CT image of another patient shows a more subtle leiomyoma of the posterior wall (*arrowheads*) with inhomogeneous enhancement and a single punctate calcification. The endometrium (*arrow*) is slightly lower in attenuation than the enhanced myometrium. *C,* Sagittal CT image demonstrates the coarse "popcorn" calcification characteristic of degenerated leiomyomas.

in most instances. CT is useful in staging advanced disease and detecting recurrence. Cervical malignancies are squamous cell carcinomas (85%) and adenocarcinomas (15%) that spread primarily by direct extension to adjacent organs and tissues. Lymphatic spread to regional nodes is common. Hematogenous spread to lung, bone, and brain is uncommon and occurs late in the course of the disease. The accuracy of CT staging is approximately 65%, compared with 90% reported for MR. CT findings are as follows:

- The normal cervix enhances variably on early postcontrast scans but is uniformly enhanced on scans obtained with a delay of several minutes. The primary tumor may be of low attenuation (50%) or isoattenuating (50%) compared to normal cervix (Fig. 18-12). Low attenuation is caused by reduced vascularity, necrosis, or ulceration. The primary tumor may enlarge the cervix (>3.5 cm in diameter).

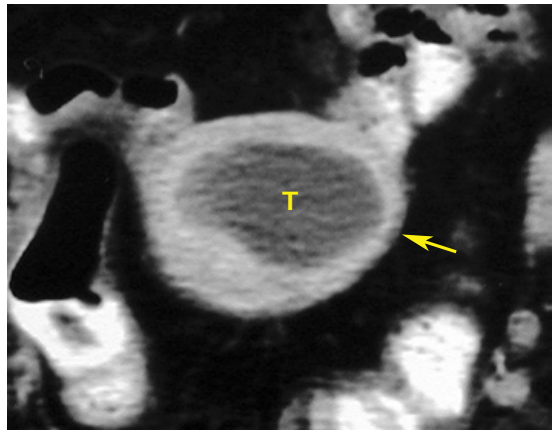

FIGURE 18-12 ■ Cervical carcinoma confined to the cervix. Postcontrast axial computed tomography through the cervix demonstrates a squamous cell carcinoma of the cervix as a low-attenuation tumor (T) confined within the enhancing cervix. The cervical tissue is asymmetrically thinned on the left (*arrow*), but the paracervical tissues are not invaded.

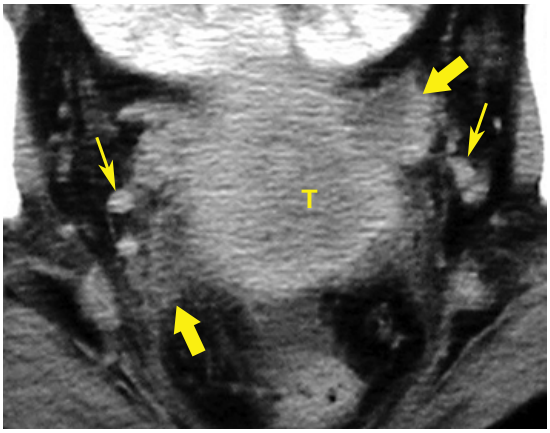

FIGURE 18-13 ■ Cervical carcinoma with invasion of the parametrium. Axial computed tomography through the cervix shows that the cervical tumor (T) is slightly lower in attenuation than the enhancing cervix. However, tumor extension into the parametrium (*thick arrows*) is apparent. The soft-tissue density of the tumor approaches the ureters (*thin arrows*) but does not involve them.

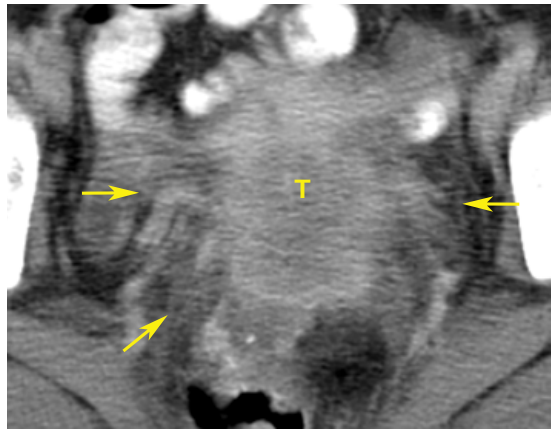

FIGURE 18-14 ■ Cervical carcinoma with invasion of the parametrium and ureter obstruction. An ill-defined tumor mass (T) of squamous cell carcinoma of the cervix shows extensive nodular stranding (*arrows*) in the parametrium, indicating tumor invasion. The left ureter was obstructed at this level.

- Fluid collections in the uterine cavity, representing serous fluid, blood, or pus, are common due to tumor obstruction of the cervix.
- Spread of tumor by direct extension (Figs. 18-13 and 18-14) is seen as thick, irregular tissue strands or masses fanning out from the cervix into the parametrium, often encasing the ureters, extending into the vagina or to the pelvic sidewalls. Normal broad, round, cardinal, and uterosacral ligaments should not be mistaken for tumor extension. Encasement of the ureter is a specific sign of parametrial invasion.
- Extension to the pelvic sidewall is indicated when tumor nodules are seen within 3 mm of the obturator internus or piriformis muscles. Tumor invasion is seen as an enhancing mass within enlarged muscles.
- Invasion of the bladder or rectum is indicated by loss of the perivesical or perirectal fat plane, nodular thickening of the wall of the bladder or rectum, or a mass within the bladder or rectum. Air within the bladder suggests fistula formation.
- Enlarged lymph nodes (>10 mm in short axis) are strong evidence of metastatic involvement, but cervical carcinoma will commonly involve nodes without enlarging them. These small but involved nodes cannot be differentiated from benign nodes by CT. Necrotic lymph nodes are likely involved by tumor.
- Recurrences appear as soft-tissue masses anywhere in the pelvis but most commonly at the top of the vaginal cuff in patients who have undergone hysterectomy. Enlarged nodes are also suggestive of recurrence. Biopsy is usually needed to confirm the diagnosis.

Endometrial Malignancy

Carcinoma of the endometrium is the most common invasive gynecologic malignancy. Peak incidence occurs at age 55 to 65 years. Most tumors (90%) are endometrioid adenocarcinomas. Clear-cell and papillary serous subtypes are more aggressive. Müllerian mixed tumor is a sarcoma of the endometrium. Tumors spreads first by invasion of the myometrium and then by lymphatic channels to regional nodes, or by direct extension through the uterine wall to parametrial tissues. When the uterine serosa is penetrated, diffuse peritoneal spread may occur. Hematogenous spread to lung, bone, liver, and brain is much more common with endometrial than cervical cancer. As with cervical carcinoma, MR is preferred for preoperative imaging staging of known tumors. CT is generally not used for initial diagnosis or local staging, although unsuspected tumors may be encountered on CT. Staging accuracy is reported as approximately 60% for CT, compared to 90% for MR. Surgical staging is the method of choice. Imaging staging is useful in patients with advanced disease or those who are difficult to examine.

- Endometrial cancers are isoattenuating with uterine tissue on unenhanced CT, and therefore cannot be reliably differentiated.

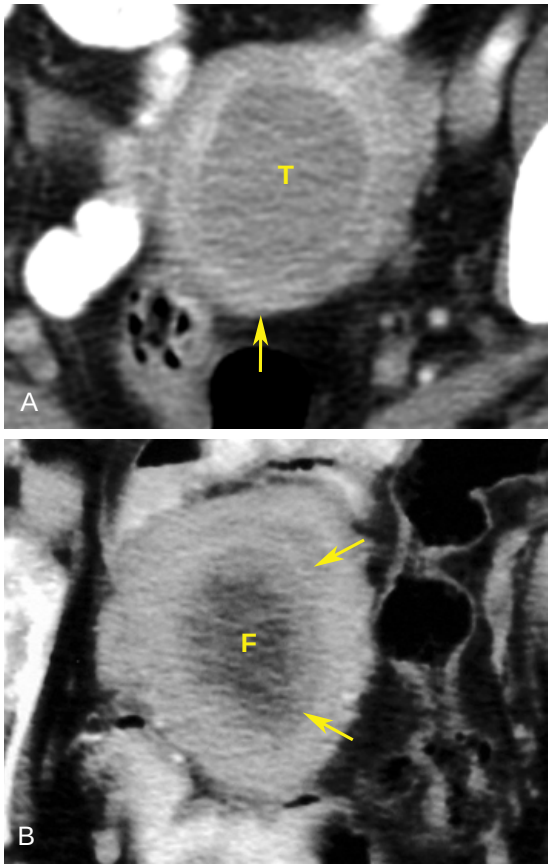

FIGURE 18-15 ■ Endometrial carcinoma. *A,* A low-density tumor mass (T) of endometrial carcinoma fills the uterine cavity of this postmenopausal woman. A few millimeters of posterior myometrium (*arrow*) were invaded by this neoplasm. *B,* In another postmenopausal patient, bloody fluid (F) distends the uterine cavity. An endometrial tumor (*arrows*) is intermediate in attenuation between the dark fluid and the enhancing myometrium. This tumor also invades less than 50% of the thickness of the myometrium.

- On postcontrast CT the primary tumor appears as diffuse thickening of the endometrium or as a hypodense polypoid mass within the endometrial cavity (Fig. 18-15). The uterine cavity is frequently fluid-filled because of obstruction by the tumor. Fluid may assist in outlining mural implants of tumor in the expanded uterine cavity. The uterus may be greatly enlarged. The tumor typically enhances heterogeneously and to a lesser extent than the surrounding myometrium.
- Myometrial invasion may be recognized as hypodense infiltrating tumor tissue within the more enhanced normal myometrium. CT is less than 60% accurate in evaluating the depth of myometrial invasion.
- Cervical invasion is indicated by heterogeneous enlargement of the cervix.
- Irregular uterine margins and strands and nodules of soft tissue extending into adjacent fat are evidence of parametrial invasion.
- Enlarged pelvic lymph nodes (>1 cm) indicate tumor involvement. However, as with other pelvic tumors, CT will miss microscopic nodal metastases that do not enlarge the nodes. CT can be used to guide percutaneous biopsy of suspicious lymph nodes.
- *Müllerian mixed tumor* is suggested by massive enlargement of the uterus, large areas of necrosis and hemorrhage within the tumor, and rapid growth of metastases.
- Tumor recurrences appear as pelvic soft-tissue masses or nodal enlargement. Most recurrences occur within 2 years.

OVARY

Ovarian Cancer

Ovarian malignancy encompasses a wide range of histologic tumor types, but most share a common pattern of spread and a similar range of CT appearances. Two-thirds of ovarian cancers are cystic, 25% are bilateral, and 15% are endocrinologically functional. The primary route of tumor spread is diffusion throughout the peritoneal cavity, present in 70% of cases at the time of diagnosis. Direct extension to pelvic organs, lymphatic spread to nodes, and hematogenous spread to lung, liver, and bone also occur. Most patients are directly referred for surgery for initial staging, hysterectomy, salpingo-oophorectomy, omentectomy, and tumor debulking without preoperative imaging. CT is, however, the imaging method of choice for documenting residual tumor and response to therapy and for detection of postoperative recurrence. MR remains inferior to CT, primarily because of difficulty in differentiating intraperitoneal tumor from bowel. The staging accuracy of CT is about 80%. CT findings of ovarian malignancy include the following:

- The primary tumor is usually cystic with thick, irregular walls, internal septations, and prominent soft-tissue components (Fig. 18-16). Uniformly solid tumors and mixed cystic–solid tumors also occur. Calcifications may be evident in both the primary tumor and metastases.
- Tumor extension to adjacent pelvic organs is suggested by distortion or an irregular interface between the tumor and myometrium, obliteration of tissue planes between the tumor and bladder or colon, separation of less than 3 mm between the tumor and

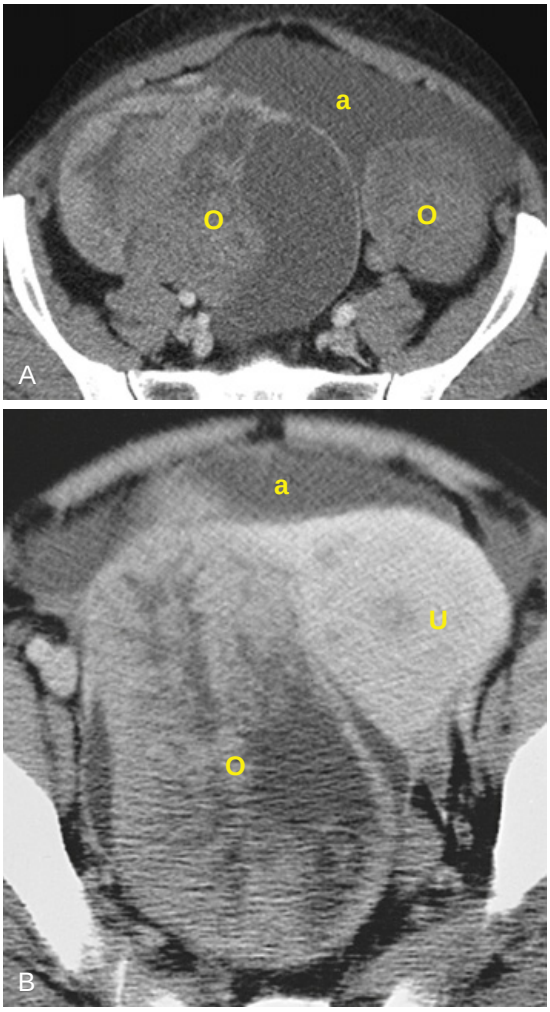

FIGURE 18-16 ■ Ovarian carcinoma. *A,* Both ovaries (O) are replaced and enlarged by tumors with predominant solid components. Ascites (a) is present providing strong evidence of tumor spread to the peritoneal cavity. *B,* A large mass (O) with predominant solid components arises from the right ovary and displaces the uterus (U) anteriorly and leftward. Ascites (a) is present.

intrapelvic muscles, and displacement or encasement of pelvic blood vessels.

- Direct tumor extension commonly involves the uterus, colon, small bowel, and bladder.
- Peritoneal implants are often seen as subtle, thickening, soft-tissue nodules, or enhancement of peritoneal surfaces (Figs. 9-4, 9-5, and 9-6). Key areas to carefully examine include the undersurfaces of the diaphragm, the paracolic gutters, the cul-de-sac, and the surface of the bowel. The presence of ascites makes peritoneal implants more evident on CT. *Omental cake* refers to irregular, often marked thickening of the greater omentum separating the bowel from the anterior abdominal wall. The greater omentum, normally of fat density, becomes of soft-tissue density when involved by tumor. CT will commonly miss even extensive peritoneal seeding when the tumor nodules are small (<5 mm).
- Bowel involvement is evidenced by thickening of the bowel wall, matting together of bowel loops, and findings of bowel obstruction.
- The presence of ascites usually indicates peritoneal spread even if peritoneal tumor nodules are not visualized.
- Lymphatic metastases usually follow gonadal lymphatics, skipping pelvic nodes, to involve nodes at the renal hilum, a pattern similar to that for testicular cancers.
- Hematogenous spread of tumor occurs late in the course of disease. Advanced disease or tumor recurrence may be seen as solid organ metastases in the liver and spleen.

Benign Adnexal Masses

Although ultrasonography is the primary imaging modality for female pelvic masses, adnexal masses may be discovered incidentally on CT. CT may also be used to further characterize unclear ultrasound diagnoses. The following are some conditions to consider:

- *Normal ovaries* are seen as oval soft-tissue masses of approximately 4 cm × 3 cm × 2 cm in size. Follicles are best seen on postcontrast scans (Fig. 18-17). Visualization of follicles provides definitive identification of the ovary. Normal follicles are thin-walled, low-attenuation cysts smaller than 3 cm in size. Postmenopausal ovaries are smaller and lack follicles, making them more difficult to identify. Ovaries may be confused with bowel, blood vessels, and lymph nodes.
- *Normal corpus luteum.* Following ovulation the corpus luteum is the highly vascular structure that identifies the location on the ovary of the ruptured dominant follicle. The normal corpus luteum is highly variable in appearance and may be seen as a collapsed cyst, a thick- or thin-walled cyst, or a solid mass. A key feature is intense enhancement of the cyst wall or solid tissue (Fig. 18-18). Patients presenting with pelvic pain related to ovulation may undergo CT examination, so this normal physiologic structure must be recognized. Recent ovulation may be further evidenced by a small volume of hemorrhagic fluid in dependent pelvic recesses. The normal corpus luteum resolves with menstruation.

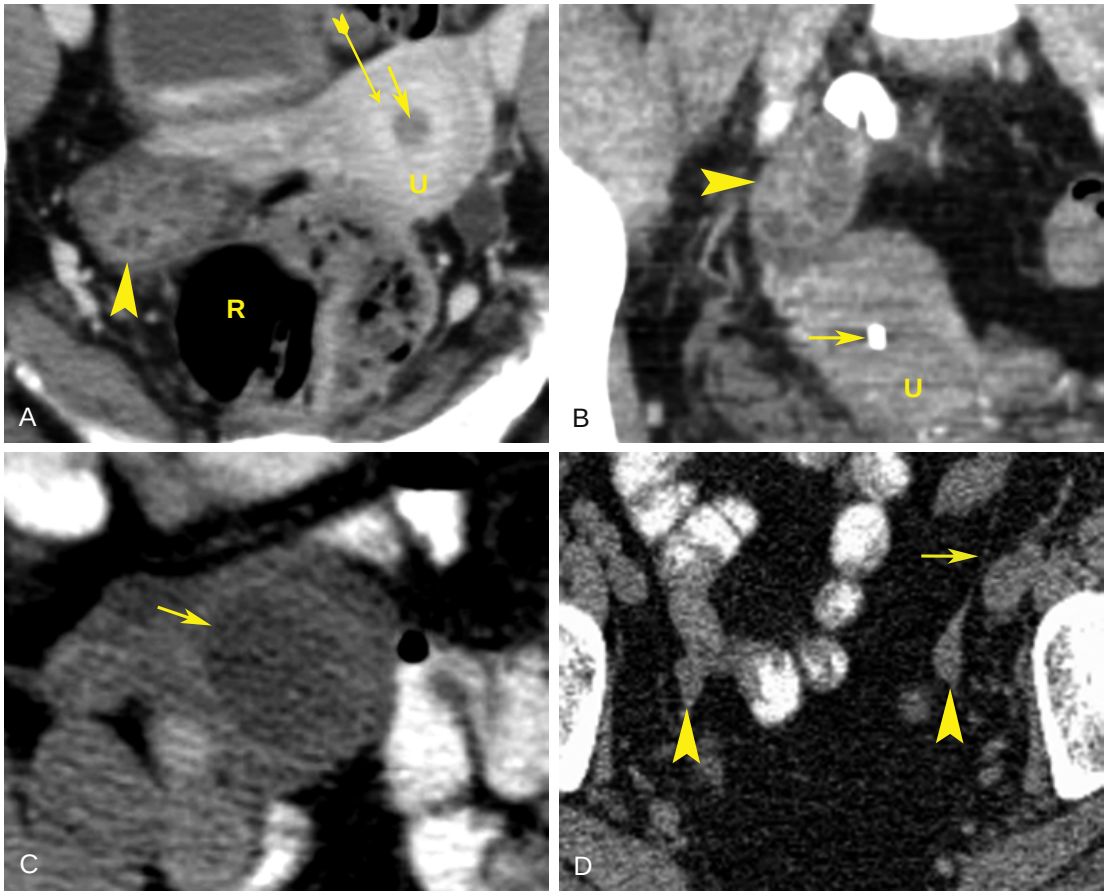

FIGURE 18-17 ■ Normal ovaries. *A,* A normal right ovary (*arrowhead*) containing numerous follicles is seen adjacent to the uterus (U) in a 32-year-old woman. Administration of intravenous contrast has enhanced the walls of the follicles, making them more visible than on noncontrast scans. The uterine cavity contains fluid (*arrow without tail*), and the endometrium (*arrow with tail*) is enhanced. R, rectum. *B,* In another patient, aged 25 years, coronal computed tomography demonstrates the variable position of the normal ovary (*arrowhead*) cranial to the uterus (U). An intrauterine device (*arrow*) is partially visualized within the uterine cavity. *C,* A thin-walled 2.5-cm cyst (*arrow*) on the right ovary is a dominant follicle in this 34-year-old woman. This physiologic structure is normal. No further evaluation or follow-up is necessary. *D,* Normal postmenopausal ovaries (*arrowheads*) are identified bilaterally in this 68-year-old woman. A landmark confirming the identity of the small postmenopausal ovary is the suspensory ligament (*arrow*) of the ovary, which extends in the broad ligament to the pelvic side wall.

- *Functional ovarian cysts.* Benign ovarian cysts, including follicular and corpus luteum cysts, are common incidental findings. On CT they are well defined and thin-walled (<3 mm), have homogeneous internal density close to that of water, and are greater than 3 cm in size (Fig. 18-19).
- *Hemorrhagic functional cysts* appear more complex, with internal attenuation greater than that of water. Fluid–fluid levels and clots outlined by lower-attenuation fluid may be present. The key features are that the walls of the cyst are uniform in thickness and enhancement and that no enhancement is present internally within the cyst. Functional and hemorrhagic ovarian cysts can be re-examined with ultrasound to determine if they resolve after one or two menstrual cycles.
- *Benign cystic teratoma.* The presence of fat-density fluid, teeth, bone, hair, or fat–fluid levels allows definitive CT diagnosis in most cases (Fig. 18-20). Dermoid plugs are conglomerations of tissue and hair that are seen as soft-tissue nodules inside the cysts.
- *Ovarian cystadenoma.* Benign ovarian tumors tend to have regular thin walls, fine septations, no solid components, and no associated ascites (Fig. 18-21). Definitive differentiation of benign from malignant cystic ovarian tumors is not possible with CT. If the lesion persists on follow-up ultrasound performed after two menstrual cycles, a cystic tumor may be suspected and further evaluation is warranted.
- *Paraovarian cysts* arise from the broad ligament, are uniformly benign, and account for

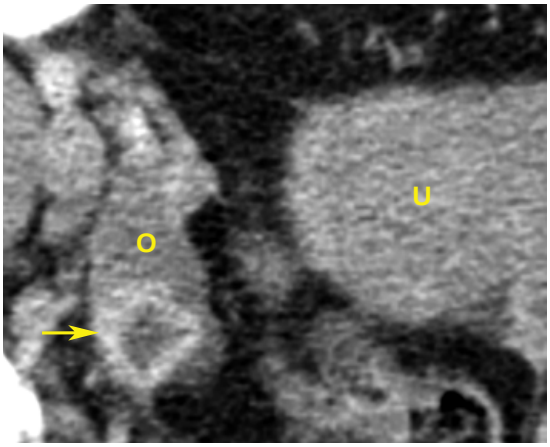

FIGURE 18-18 ■ Normal corpus luteum. A rim-enhancing mass (*arrow*) on the right ovary (O) of a 28-year-old woman is characteristic of a normal corpus luteum, marking the site of ovulation. A small volume of fluid is often seen in the cul-de-sac in association with this normal finding. U, uterus.

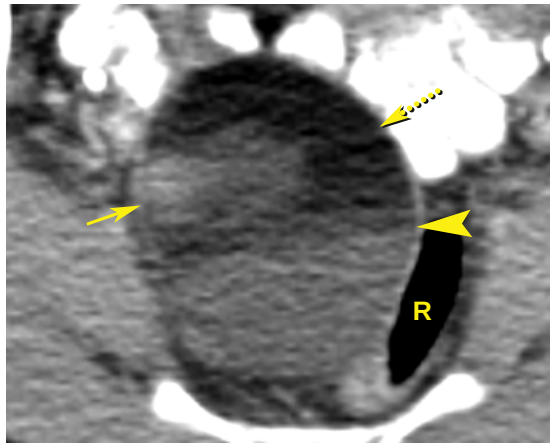

FIGURE 18-20 ■ Benign cystic teratoma. A mass impinging on the rectum (R) is definitively characterized by computed tomography as a benign cystic teratoma. Fat-attenuation fluid (*dotted arrow*) representing sebum is characteristic. Compare the attenuation of the fluid to intrapelvic and subcutaneous fat. Suspended hair within the sebum produces a fluid level (*arrowhead*), and a dermoid plug (*solid arrow*) produces a soft-tissue nodule.

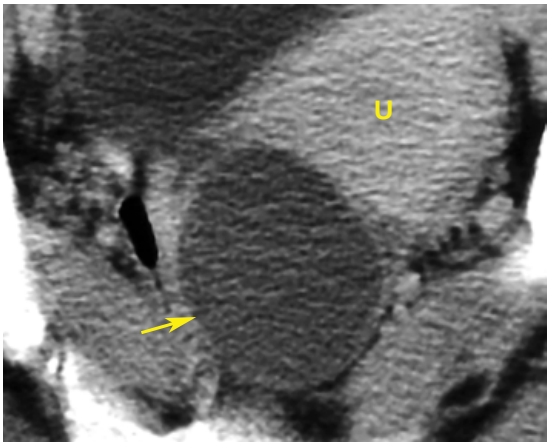

FIGURE 18-19 ■ Functional ovarian cyst. Computed tomography reveals a thin-walled, uniformly low-attenuation 4.5-cm cyst (*arrow*) in the right adnexa adjacent to the uterus (U). These characteristics are most indicative of a functional ovarian cyst. Follow-up with ultrasound 10 weeks later confirmed complete resolution.

FIGURE 18-21 ■ Benign mucinous ovarian cystadenoma. A large cystic mass containing homogeneous low-attenuation fluid extends out of the pelvis. The outer walls and the internal septations are thin (<3 mm). Surgical removal and pathologic examination are needed to confirm a benign diagnosis.

10% to 20% of all adnexal masses. Most are thin-walled simple cysts that may be large (≥ 8 cm) or small. Uncommonly they are multiple or bilateral. CT is diagnostic if the cyst can be assessed as being as separate from the ovary.

- *Endometriomas* arise from deposits of endometrial glands and stroma on peritoneal surfaces. Most (80%) arise on the ovary. The wall is initially thin but may thicken and become irregular with time. Internal contents are of high attenuation, reflecting blood. Coexisting endometrial deposits on adjacent tissues may cause scarring and retraction, simulating malignant disease. Endometrial deposits often result in enhancement of the peritoneal surface.
- *Peritoneal inclusion cysts* result from inflammation of the peritoneal lining that entraps a functioning ovary. The adhesions and inflammation impair absorption of peritoneal fluid and ovarian secretions. Patients

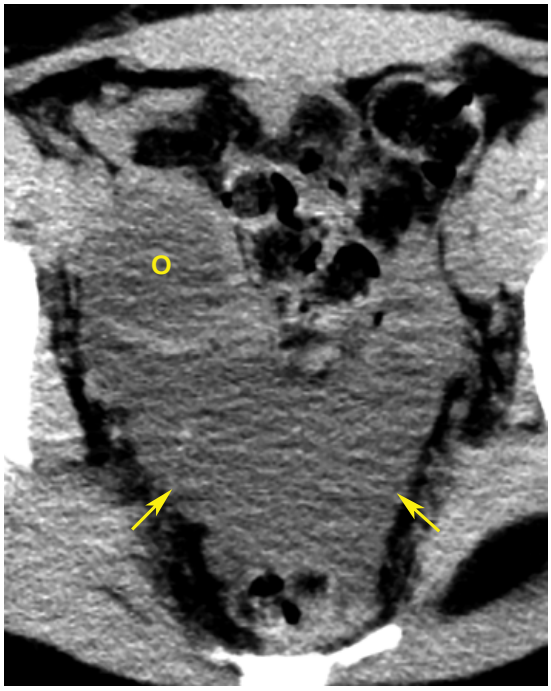

FIGURE 18-22 ■ Peritoneal inclusion cyst. Computed tomography image of the pelvis of a 41-year-old woman with chronic pelvic pain showing loculated fluid (*arrows*) distending the peritoneal recesses of the pelvis and incorporating the right ovary (O).

present with periodic pelvic pain and swelling and frequently have a history of endometriosis or pelvic inflammatory disease. CT shows a unilocular or multilocular cystic mass expanding the contours of pelvic peritoneal recesses and entrapping an ovary (Fig. 18-22). Fluid extension into peritoneal recesses, rather than forming a rounded mass, is characteristic.

- *Hydrosalpinx* refers to a dilated fallopian tube filled with fluid caused by blockage of the tube at the fimbriated end. Causes include endometriosis, pelvic inflammatory disease, and scarring resulting from other infectious or inflammatory diseases of the pelvis. As the tube dilates, it becomes tortuous, folding back on itself and simulating a septated mass. Sagittal and coronal reformations are often helpful in recognizing the complex mass as a dilated tube (Fig. 18-23).
- *Spinal meningeal cyst*, also called a perineural, arachnoid, or nerve-root-sheath cyst, may mimic an ovarian or adnexal lesion. The cyst arises from and is intimately associated with the sacrum. It may be unilocular or multilocular, has thin walls, and contains fluid (cerebrospinal fluid) of water attenuation.

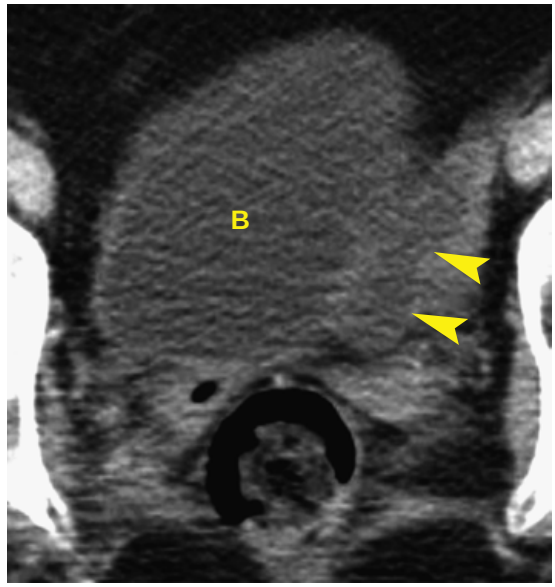

FIGURE 18-23 ■ Hydrosalpinx. Axial computed tomography of the pelvis reveals an elongated, fluid-filled, tubular structure (*arrowheads*) with thick walls abutting the bladder (B).

Pelvic Inflammatory Disease

Pelvic inflammatory disease (PID) refers to infection and inflammation of the endometrium, fallopian tubes, and ovaries. Infection is caused by *Neisseria gonorrhoeae* or *Chlamydia trachomatis*, or is polymicrobial. CT is commonly the initial imaging study.

- Early findings include thickening of the fallopian tubes and enlargement (edema) and abnormal enhancement of the ovaries. Thickening of the wall of the fallopian tube is a highly specific CT finding of acute PID.
- More advanced PID presents with dilated fallopian tubes filled with high-attenuation fluid (pyosalpinx) and complex fluid collections with septa, debris, fluid–fluid levels, or gas in the adnexa. This inflammatory mass is called a *tubo-ovarian abscess* (Fig. 18-24).
- The inflammatory process may incorporate adjacent small or large bowel, obstruct the ureters, and inflame and thicken the bladder wall.

Adnexal Torsion

In adnexal torsion the ovary, fallopian tube, or both structures twist on the vascular pedicle, causing vascular compromise. Torsion may be partial, impairing only venous drainage, complete, occluding the arterial supply, or intermittent. Unrelieved torsion may result in hemorrhagic infarction of the ovary. Because

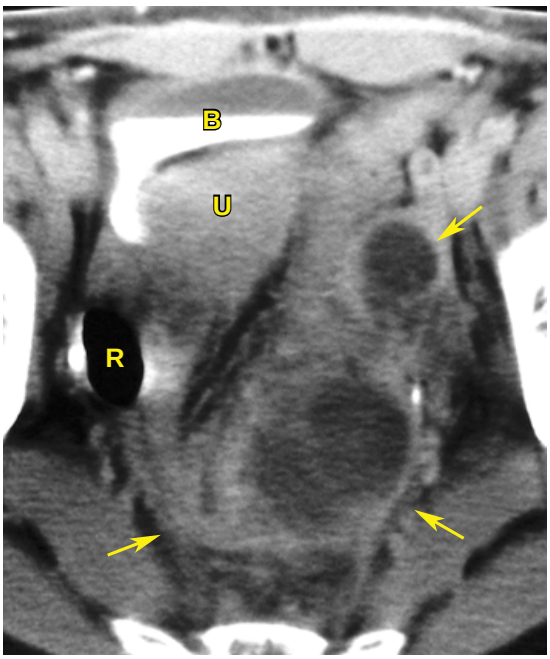

FIGURE 18-24 ■ Tubo-ovarian abscess. A poorly marginated cystic and solid inflammatory mass (between *arrows*) displaces the rectum (R), uterus (U), and bladder (B) anteriorly and rightward. The left ovary and dilated left fallopian tube are incorporated within the mass but are not definitively identified. The patient was suffering from sepsis and had acute pelvic pain.

patients often present with severe pain, CT may provide the initial images.

- Most cases of torsion involve a pre-existing adnexal mass, most commonly a benign cystic teratoma, hydrosalpinx, or functional cyst. The wall of the mass thickens, and its contents may become hemorrhagic with torsion.
- Major findings are thickening of the wall of the fallopian tube (>3 mm), tubal distention, smooth thickening of the wall of the mass, pelvic ascites, and deviation of the uterus to the affected side (Fig. 18-25).
- The twisted vascular pedicle may be visualized.

PROSTATE

Benign Prostatic Hypertrophy

Benign prostatic hypertrophy results in nodular enlargement of the prostate with constriction of the urethra and obstruction to bladder emptying. It is indistinguishable from prostate carcinoma on CT.

- The prostate is enlarged and commonly has a lobulated contour (Fig. 18-26). Nodules may cause high- and low-density regions within the prostate with variable enhancement.

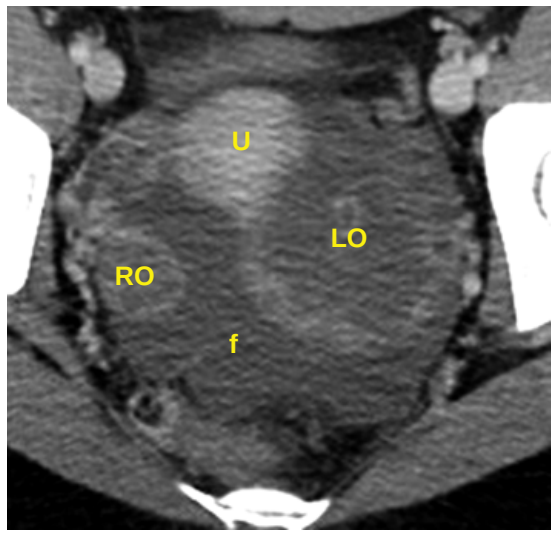

FIGURE 18-25 ■ Left adnexal torsion. Computed tomography of a 20-year-old woman with severe left pelvic pain shows complex enlargement of the left ovary (LO) with wall thickening, fluid (f) in the cul-de-sac, and a normal right ovary (RO). Acute left adnexal torsion was confirmed at surgery. U, uterus.

- Cystic degeneration and coarse calcifications are common.
- The bladder base is elevated, and the prostate projects upward into the bladder lumen.
- Thickening and trabeculation of the bladder wall result from bladder outlet obstruction. Diverticula may project through the bladder wall.

Prostate Cancer

Prostate cancer is the second most common malignancy in males. Prostate carcinoma spreads by direct extension to periprostatic tissues and the seminal vesicles. Lymphatic spread is similar to that for bladder cancer, with early involvement of internal iliac and obturator nodes and later involvement of para-aortic nodes. Hematogenous spread to the axial skeleton via vertebral veins is particularly characteristic. CT does not demonstrate the intraprostatic architecture and is poor at demonstrating intraprostatic tumors (Fig. 18-27). CT for regional staging of prostate cancer is neither sensitive nor specific enough to be clinically useful. CT may be used to detect distant metastases.

- Enlargement of the prostate is common and may be due to benign prostatic hypertrophy and/or tumor growth. Nodules or stranding densities in the periprostatic fat are signs of tumor extension outside the prostate gland.
- Asymmetric size of the seminal vesicles and infiltration of fat between the bladder base,

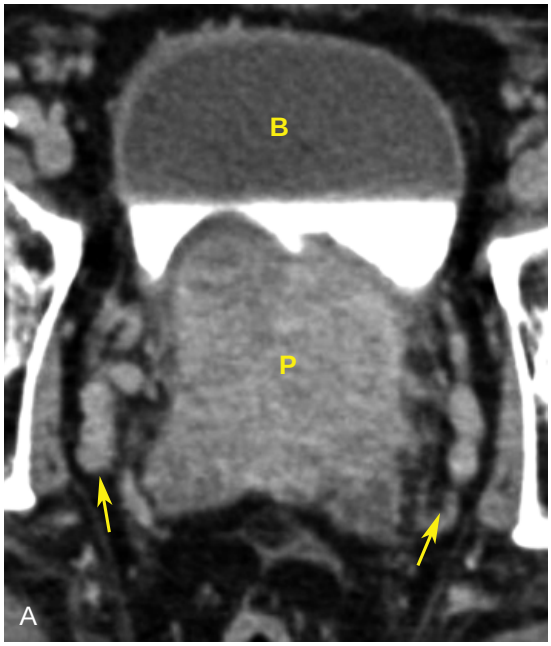

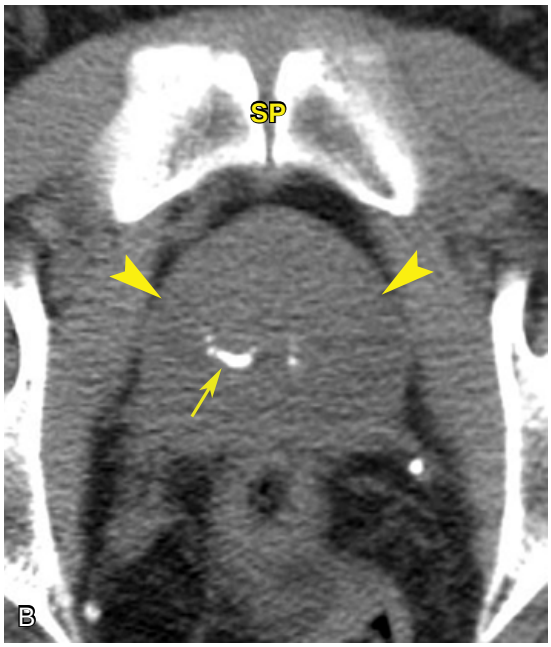

FIGURE 18-26 ■ Benign prostatic hypertrophy. *A,* Delayed postcontrast computed tomography (CT) reveals a large heterogeneous prostate (P) bulging into the base of the bladder (B). The wall of the bladder shows mild hypertrophy reflecting outflow obstruction caused by prostatic enlargement. Prominent periprostatic vessels (*arrows*) are evident. Prominent pelvic vessels are a common and benign finding confirmed by documenting contrast enhancement of the venous structures. *B,* Noncontrast CT in another patient shows the characteristic coarse and linear calcifications (*arrow*) associated with benign prostatic hypertrophy and chronic prostatitis. The prostate (*arrowheads*) is mildly enlarged. The symphysis pubis (SP) is the anatomic landmark for the normal location of the prostate.

FIGURE 18-27 ■ Prostate cancer. Coronal computed tomography (CT) image shows massive nodular enlargement of the prostate (P) with elevation of the base of the bladder (B) and projection into the bladder lumen of prominent nodules. Transrectal prostate biopsy revealed predominantly benign prostatic hypertrophy with cancer in the right prostate lobe. The cancer is indistinguishable from benign hypertrophy on CT. Cystoscopy is indicated to exclude a uroepithelial tumor arising from the bladder mucosa.

prostate, and seminal vesicles are evidence of tumor involvement. Bladder involvement is very difficult to detect accurately. Rectal invasion is rare.

- Nodes larger than 10 mm are usually involved with metastatic tumor.

TESTES

Testicular Cancer

Testicular germ-cell tumors can be separated into seminomas (40%) and nonseminomas (60%). Seminomas are treated with orchiectomy and radiation and generally do not require retroperitoneal node dissection for staging. Nonseminomas are radioresistant, are treated with orchiectomy and chemotherapy, and generally do require retroperitoneal node dissection for staging. Lymphatic spread of tumor is most common, with nodal involvement following an orderly ascending pattern. Initial spread is along the gonadal lymphatics, following the testicular veins to the renal hilar nodes. Alternatively, lymphatic metastases may follow the external iliac chain to

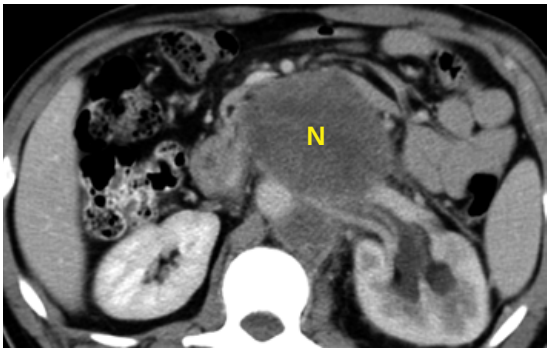

FIGURE 18-28 ■ Metastatic testicular cancer. In a patient with carcinoma of the left testis, computed tomography at the level of the left renal hilum shows massive confluent adenopathy (N) enveloping the left renal vessels and the aorta. This location is typical for metastatic spread of cancer from the left testis along the gonadal lymphatics, which parallel the course of the left testicular vein.

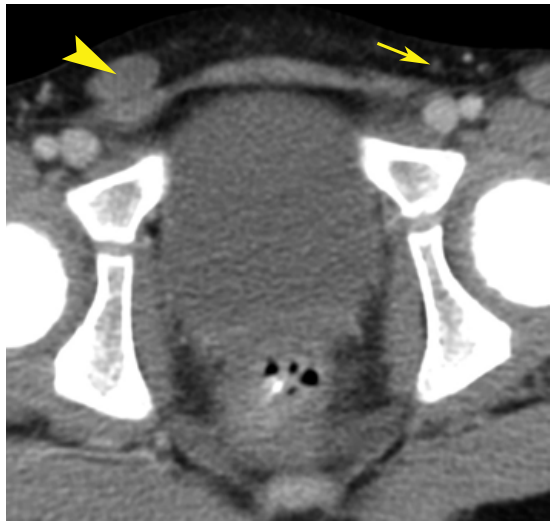

FIGURE 18-29 ■ Undescended testis. An undescended testis (*arrowhead*) is seen in the right inguinal canal near the external inguinal ring in this 5-year-old boy. A normal spermatic cord (*arrow*) in the inguinal canal is seen on the left.

the para-aortic nodes. Internal iliac and inguinal nodes are generally not involved. Lymphatic spread to the mediastinum and hematogenous spread to the lungs rarely occur without para-aortic disease, except for choriocarcinoma, which exhibits early hematogenous spreading. CT remains the imaging method of choice for initial tumor staging.

- Pelvic and retroperitoneal adenopathy is most pronounced on the side of involvement. Nodal enlargement near the ipsilateral renal hilum is particularly characteristic (Fig. 18-28). Inguinal nodes are involved only when the scrotum is invaded by tumor. Bulky nodal metastases may have low attenuation internally as a result of tumor necrosis. Cystic changes and heterogeneity of any lymph node attenuation are signs of tumor involvement. Using a short-axis dimension of ≥ 8 mm as the criterion for nodal involvement is highly specific but has low sensitivity. Up to 30% of patients may have metastatic nodal spread not detectable by CT.
- Absence of the spermatic cord identifies the side of orchiectomy.

Undescended Testes

Undescended testes may be located anywhere along the course of testicular descent from the lower pole of the kidney to the superficial inguinal ring. Undescended testes carry a high risk of malignancy (48-fold risk) and torsion (10-fold risk). CT has a sensitivity of 95% for detection of ectopic testes.

- An undescended testis appears as an oval soft-tissue density of up to 4 cm. Undescended testes are usually atrophic. CT detection of intra-abdominal testes requires optimal bowel opacification and intravenous contrast medium enhancement to opacify normal structures.
- Testes in the inguinal canal can be easily identified on CT as long as one knows where to look (Fig. 18-29). The inguinal canal runs an oblique, medially directed course through the flat muscles of the abdominal wall between the deep and superficial inguinal rings. The deep (internal) inguinal ring is located midway between the anterior–superior iliac spine and the symphysis pubica. The superficial (external) inguinal ring is located just above the pubic crest.

SUGGESTED READING

Avery LL, Scheinfeld MH: Imaging of penile and scrotal emergencies. *Radiographics* 33:721–740, 2013.

Bharwani N, Stephens NJ, Heenan SD: Imaging of bladder cancer. *Imaging* 20:97–111, 2008.

Chu LC, Ross HM, Lotan TL, Macura KJ: Prostate stromal neoplasms: Differential diagnosis of cystic and solid prostatic and periprostatic masses. *AJR Am J Roentgenol* 200:W571–W580, 2013.

Cohen DT, Oliva E, Hahn PF, et al.: Uterine smooth-muscle tumors with unusual growth patterns: Imaging with pathologic correlation. *AJR Am J Roentgenol* 188:246–255, 2007.

Hardesty LA, Sumkin JH, Hakim C, et al.: The ability of helical CT to preoperatively stage endometrial carcinoma. *AJR Am J Roentgenol* 176:603–606, 2001.

Hiller N, Appelbaum L, Simanovsky N, et al.: CT features of adnexal torsion. *AJR Am J Roentgenol* 189:124–129, 2007.

Jeong YY, Kang HK, Chung TW, et al.: Uterine cervical carcinoma after therapy: CT and MR imaging findings. *Radiographics* 23:969–981, 2003.

Kaur H, Silverman PM, Iyer RB, et al.: Diagnosis, staging, and surveillance of cervical carcinoma. *AJR Am J Roentgenol* 180:1621–1632, 2003.

Kreydin EI, Barrisford GW, Feldman AS, Preston MA: Testicular cancer: What the radiologist needs to know. *AJR Am J Roentgenol* 200:1215–1225, 2013.

Kwek JW, Iyer RB: Recurrent ovarian cancer: Spectrum of imaging findings. *AJR Am J Roentgenol* 187:99–104, 2006.

Lalwani N, Prasad SR, Vikram R, et al.: Histologic, molecular, and cytogenetic features of ovarian cancers: Implications for diagnosis and treatment. *Radiographics* 31:625–646, 2011.

Lubner MG, Simard ML, Peterson CM, et al.: Emergent and nonemergent nonbowel torsion: Spectrum of imaging and clinical findings. *Radiographics* 33:155–173, 2013.

Moyle PL, Kataoka MY, Nakai A, et al.: Nonovarian cystic lesions of the pelvis. *Radiographics* 30:921–938, 2010.

Saksouk FA, Johnson SC: Recognition of the ovaries and ovarian origin of pelvic masses with CT. *Radiographics* 24:S133–S146, 2004.

Sam JW, Jacobs JE, Birnbaum BA: Spectrum of CT findings in acute pyogenic pelvic inflammatory disease. *Radiographics* 22:1327–1334, 2002.

Shah SH, Jagannathan JP, Krajewski K, et al.: Uterine sarcomas: Then and now. *AJR Am J Roentgenol* 199:213–223, 2012.

Sohaib SA, Koh D-M, Husband JE: The role of imaging in the diagnosis, staging, and management of testicular cancer. *AJR Am J Roentgenol* 191:387–395, 2008.

Tabatabaei S, Saylor PJ, Coen J, Dahl DM: Prostate cancer imaging: What surgeons, radiation oncologists, and medical oncologists want to know. *AJR Am J Roentgenol* 196:1263–1266, 2011.

Wong-You-Cheong JJ, Woodward PJ, Manning MA, Sesterhenn IA: Neoplasms of the urinary bladder: Radiologic–pathologic correlation. *Radiographics* 26:553–580, 2006.

Wong-You-Cheong JJ, Woodward PJ, Manning MA, Davis CJ: Inflammatory and nonneoplastic bladder masses: Radiologic–pathologic correlation. *Radiographics* 26:1847–1868, 2006.

Woodward PJ, Hosseinzadeh K, Saenger JS: Radiologic staging of ovarian carcinoma with pathologic correlation. *Radiographics* 24:225–246, 2004.

Yitta S, Hecht EM, Mausner EV, Bennett GL: Demystifying uterine and cervical contrast enhancement at multidetector CT. *Radiographics* 31:647–661, 2011.

CHAPTER 19

CT IN MUSCULOSKELETAL TRAUMA

Nancy M. Major

INTRODUCTION

The advent of increasing numbers of rows of detectors has increased the uses for computed tomography (CT) technology. Multidetector CT (MDCT) has the ability to produce near-isotropic voxel images that allow for multiplanar reformations and faster data acquisition. This technique is particularly valuable in the setting of trauma, for which conventional radiographs can be difficult to obtain because patients may be unable to comply with positioning requirements. Volume-rendered spiral CT can result in significant savings in terms of patient time spent in the radiology department. This technique also provides useful information for appropriate treatment and surgical planning by displaying three-dimensional spatial relationships in a two-dimensional image.

CT has two major roles in the evaluation of musculoskeletal trauma: (1) to define or exclude a fracture that was equivocal on conventional radiographs and (2) to determine the extent of a previously diagnosed fracture to assist in guiding therapy. In both trauma and nontrauma settings, spiral CT can provide information regarding soft-tissue abnormalities and demonstrate the osseous anatomy, particularly in anatomically complex areas such as the spine, pelvis, and scapula, for which conventional radiography may be limited.

Optimization of scanning techniques depends on the clinical question being addressed and the anatomic location. Small areas of interest combine narrow collimation (1 to 2 mm) and a pitch of 1 to 1.5 with small reconstructed increments (1 mm). Large areas of interest can be examined with wider collimation (3 mm) and a pitch of 1 to 2 with reconstruction every 2 to 3 mm.

There is considerable interest in CT dose reduction. In some circumstances, such as imaging of metallic prostheses, the exposure factors (peak kilovoltage, kVp, and mA) cannot be reduced without affecting image quality. Patient dose can be limited by careful positioning of the anatomic structure and limiting the area to be scanned. Low-kilovoltage techniques have been described for extremity and pelvis imaging without significant degradation of images. The polytrauma patient dose can be decreased by making a single pass of the chest, abdomen, and pelvis rather than scouting and scanning each region separately.

For evaluation of soft-tissue neoplasms and assessment of abscess formation, intravenous contrast is often administered. Rapid acquisition and a spiral technique allow collection of a data set at peak contrast enhancement. If vascular imaging is necessary, three-dimensional or volume-rendering techniques require optimal administration of contrast. Injection rates are typically 3 mL/second with a scanning delay that depends on the region being scanned. Typical scan delays are 40 seconds for abdominal examinations and 70 seconds for assessment of the lower extremities.

Postoperative studies in patients with orthopedic hardware also benefit from volume-rendered imaging. The presence of metal on cross-sectional imaging can be a source of frustration for the radiologist and orthopedist because of streak artifacts produced by the metal. Spiral CT with volume rendering eliminates most streak artifacts and produces high-quality images.

Infection or neoplastic diseases can also be evaluated successfully with volume-rendered imaging. Therapeutic planning can be aided by the information available from three-dimensional images detailing bone or vascular involvement.

In the trauma setting, MDCT is used to assess other body regions, and studies have shown that the spine can be included as part of the scan. Because of the high-quality two- and three-dimensional images, adequate images of the thoracic and lumbar spine can be obtained from chest and abdominal CT data.

Three-dimensional reconstructions are often performed for fractures of the acetabulum, scapula, and calcaneus and for complicated fractures of the pelvis to assist with surgical planning (Fig. 19-1).

According to the current American College of Radiology appropriateness criteria, the use of radiography in patients suspected of having a cervical spine injury should be reserved for adult patients when MDCT is not readily available, indicating that radiography should not be considered a substitute for CT. However, radiation exposure should always be minimized. Exposure during CT evaluations can be reduced by the use of automated exposure-control options according to the patient's body habitus. Many CT manufacturers have developed dose-reduction solutions.

TRAUMA

Spine

Cervical Spine

MDCT is frequently used to assess acute injuries to the cervical spine, particularly the lower cervical region, which is often difficult to assess with conventional radiographs. Before helical scanning became available, conventional radiographs were the only radiological means of imaging the cervical spine to exclude or diagnose injury following blunt trauma. Limitations of conventional radiography include poor visualization of areas with overlapping structures and the presence of other pathology such as osteoarthrosis or rheumatoid arthritis or superimposed artifacts such as an endotracheal tube. In addition, the upper thoracic spine can be difficult to image on conventional radiographs for similar reasons and is well visualized on MDCT.

MDCT can detect 97% to 100% of cervical spine fractures, compared to 60% to 70% on conventional radiographs. MDCT is widely used to complement conventional radiography for examination of the cervical spine following blunt trauma (Fig. 19-2). The detection accuracy for ligamentous injury on MDCT is not clearly documented, and magnetic resonance imaging (MRI) is highly sensitive in detecting these injuries (Fig. 19-3).

Lumbar Spine

Compression deformities of the lumbar spine are regularly seen on routine spine evaluation via conventional radiographs. When such an observation is made in the setting of trauma, an acute fracture is difficult to exclude as a cause, particularly if the patient is experiencing pain referable to this area. Cross-sectional imaging can aid in diagnosing fractures of the vertebral body (Fig. 19-4). Extension into the posterior elements, representing an unstable fracture, can be recognized on conventional anteroposterior radiography as widening of the interpedicular distance. If the patient has neurologic symptoms, MRI can be performed. If a fracture is suspected on screening of the thoracolumbar spine during a CT assessment of the chest and abdomen/pelvis for internal organ injury, a

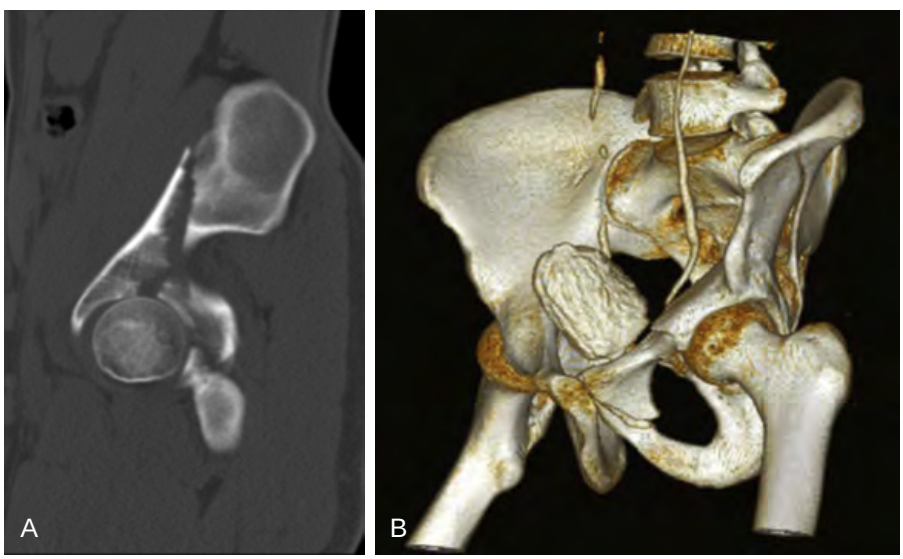

FIGURE 19-1 ■ Comminuted supra-acetabular fracture. *A,* Sagittal reformatted computed tomography (CT) of the hip demonstrates a comminuted supra-acetabular fracture extending into the iliac wing. *B,* A three-dimensional image of a complex acetabular fracture. The diagnosis was readily made with conventional radiography, axial CT, and reformatting. Three-dimensional imaging is useful for preoperative planning.

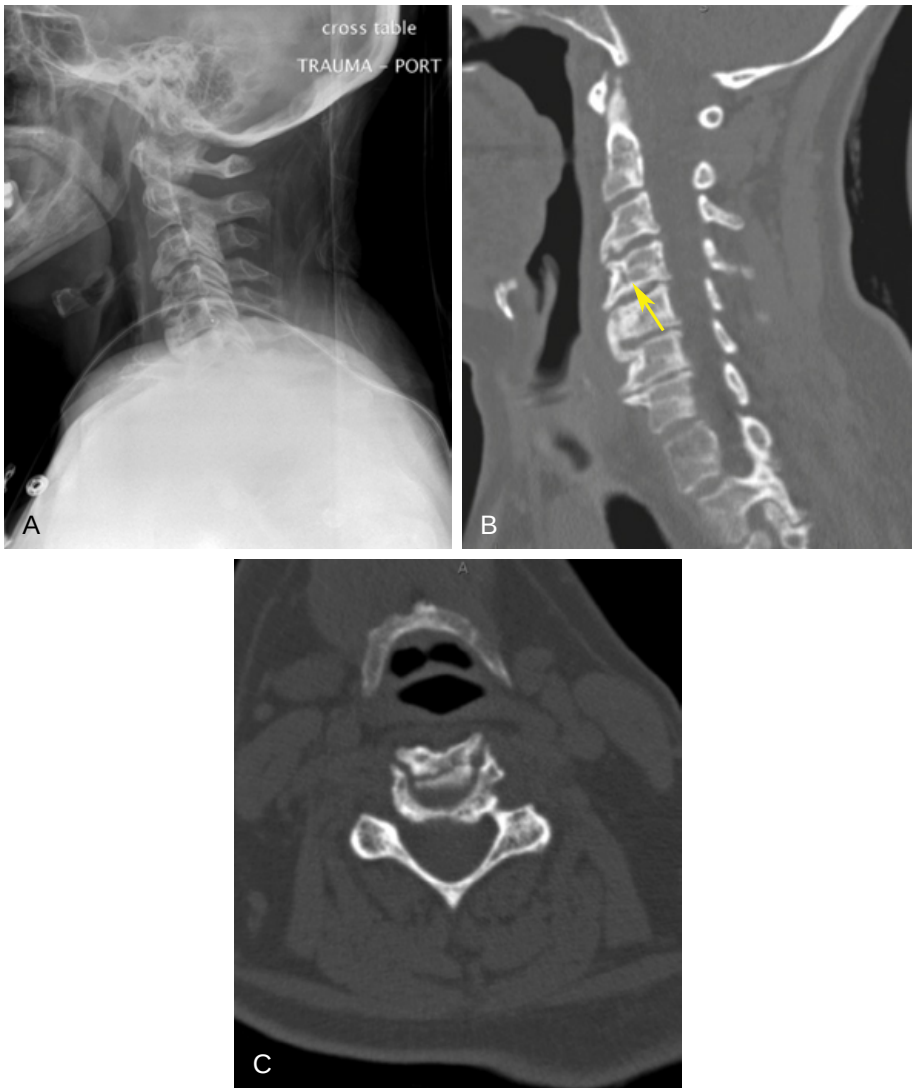

FIGURE 19-2 ■ Cervical spine fracture in a patient with diffuse idiopathic skeletal hyperostosis (DISH). *A,* Conventional x-ray of the lateral cervical spine in a patient with DISH after a motor vehicle crash. High suspicion of injury should be considered when fusion is present (osseous or hardware). Computed tomography (CT) examination is recommended in this clinical setting. *B,* Sagittal reformatted CT demonstrates an oblique fracture through the C4 vertebral body (*arrow*). *C,* An axial CT image through the C4 vertebral body demonstrates the fracture.

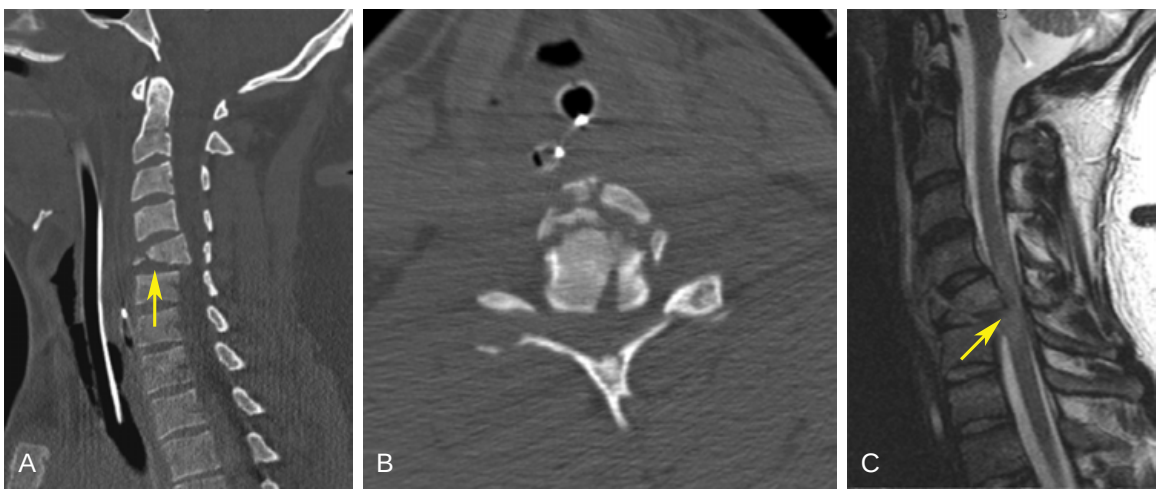

FIGURE 19-3 ■ Burst fracture of the C5 vertebra. *A,* Sagittal reformatted computed tomography (CT) demonstrates a burst fracture of the C5 vertebra (*arrow*). *B,* An axial CT image demonstrates a burst C5 fracture. An endotracheal tube and nasogastric tubes are present. *C,* Sagittal T2-weighted magnetic resonance imaging demonstrates mass effect on the cord with hematoma (*arrow*).

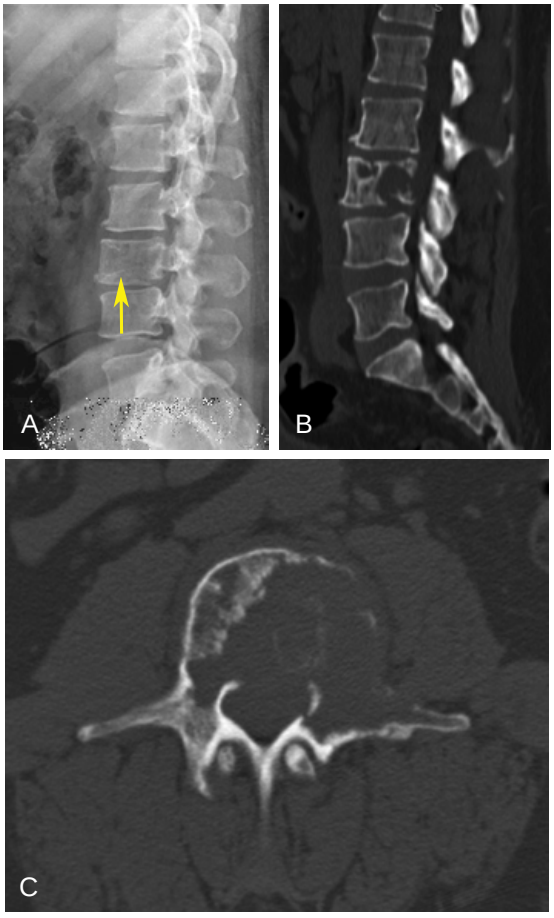

FIGURE 19-4 ■ Lytic lesion with a pathologic fracture. *A,* Lateral x-ray through the lumbar spine demonstrates a lytic lesion through the L3 vertebral body (*arrow*). *B,* Sagittal reformatted computed tomography (CT) demonstrates a lytic lesion through the L3 vertebral body with a pathologic fracture. *C,* Axial CT through the L3 vertebral body demonstrates a large lytic lesion.

repeat scan for specific evaluation of thoracic or lumbar injury may be necessary.

CT examination provides accurate depiction of the extension of fractures into posterior elements and of fracture fragments into the spinal canal. Volume rendering can provide additional assessment and compromise on soft tissues. MRI can be used as a complementary examination if the patient exhibits neurologic deficits.

In the lumbar spine, spondylolysis (pars interarticularis defect) is a common post-traumatic entity that is clearly shown by CT. Pars defects can be readily identified in an axial slice at the mid-vertebral body. Structures present at this level include the basivertebral plexus, which is always in the posterior aspect at the level of the mid-vertebral body, and the pedicles. The lamina should be a continuous bony ring on a mid-body slice, and a defect in the bony ring is a pars interarticularis break (Fig. 19-5). A pars interarticularis defect can be overlooked, particularly if the defect is smooth along its margins and resembles facet joints. For this reason, any defect in the bony ring that occurs on a slice that includes the basivertebral plexus is a spondylolysis until proven otherwise. Another way to identify a pars interarticularis defect is to recognize that facet joints should not be present on every axial image obtained through the vertebral body. If facet joints are noted on each image, a pars interarticularis defect is likely.

Pelvis and Hip

Fractures of the pelvis and hip are often complex and difficult to define on conventional radiographs. MDCT has greater sensitivity for detection of pelvic fractures when compared with conventional radiographs, particularly for sacral and acetabular fractures. The relationship of the fracture to the sacral foramina is well seen on CT and especially on three-dimensional rendering. CT is also useful for detecting intra-articular fragments, fragment interposition, impaction, and occult pelvic-ring fractures. For patients who have suffered a hip dislocation, CT of the hip after reduction should be performed to search for fracture fragments or loose bodies within the joint space. If such fragments or bodies go undetected, they can lead to accelerated wear of the articular cartilage as a result of irregular joint articulation (Fig. 19-6).

Spiral CT data sets and volume rendering allow visualization of the pelvis in any plane or view without having to move or rotate the patient and reduce the need for additional x-ray views and radiation exposure. Treatment decisions can be altered in up to 30% of cases as a result of MDCT and volume rendering. Manipulation of reconstructed images can inform preoperative planning by orthopedic surgeons.

A sacral insufficiency fracture has a unique appearance in the sacrum. This type of fracture can be mistaken for metastatic disease and is found primarily in patients with osteoporosis and those who have undergone pelvic radiation. CT demonstrates a fracture line most often parallel to the sacroiliac joint. The fracture can be unilateral or bilateral (Fig. 19-7). Stress fractures of the sacrum can occur as a result of athletics and are observed most often in long-distance runners. These individuals typically have normal bone density and are often clinically misdiagnosed as having lumbar spine disc disease. CT images demonstrate a fracture line or increased sclerosis representing callus formation.

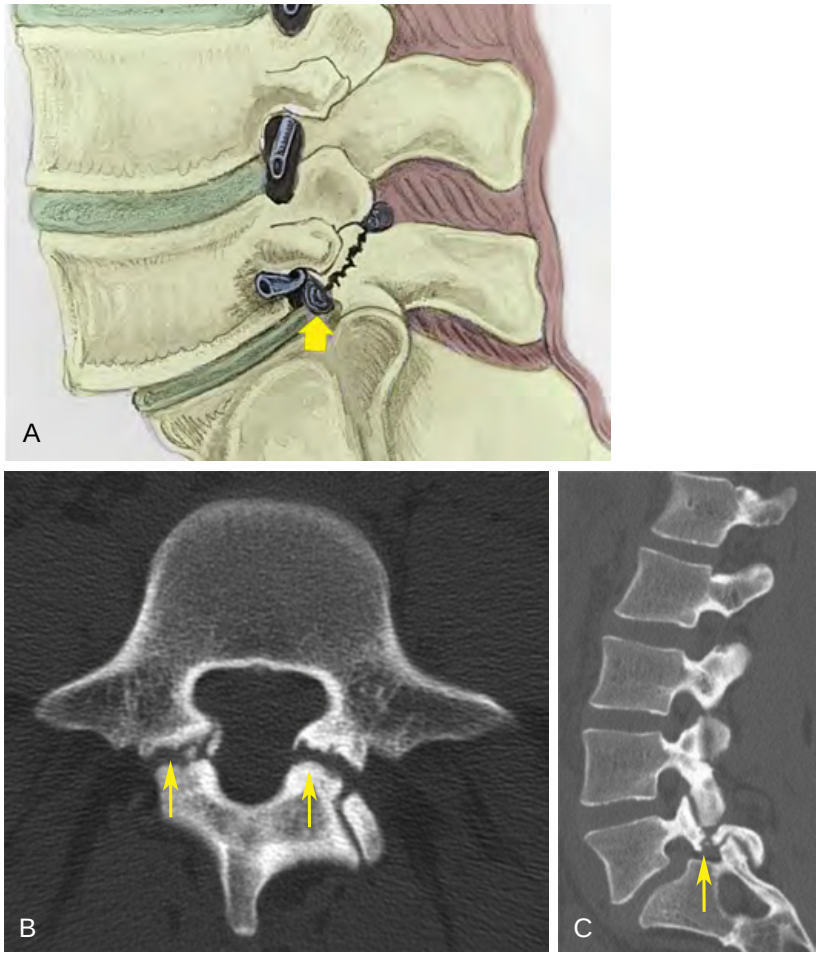

FIGURE 19-5 ■ Spondylolysis. *A,* Drawing showing a pars interarticularis break (*arrow*). *B,* Axial computed tomography (CT) demonstrates a bilateral pars interarticularis defect (*arrows*). *C,* Reformatted sagittal CT demonstrates a pars interarticularis defect (*arrow*). There is no evidence of spondylolisthesis.

Extremities

Scapula

Fractures of the scapula can be difficult to identify on conventional radiography. CT assessment with volume rendering can accurately depict and characterize such fractures and inform surgical planning. Fractures of the scapula should be considered in patients who have experienced significant trauma to the shoulder, chest wall, and lung.

MRI is the optimal modality for assessing the soft-tissue sequelae of glenohumeral dislocation. The extent of bone injury to the glenoid can be accurately assessed with CT (Fig. 19-8). In addition, if there is a contraindication to MRI, CT with intra-articular contrast can be performed (Fig. 19-9).

Elbow

CT is indicated when conventional radiographs are equivocal and when x-rays demonstrate a complex injury pattern. In such cases, volume rendering can accurately depict the interrelationship among fracture fragments and articulations.

Wrist

The indications for volume-rendered CT include equivocal conventional radiographs and further evaluation of a complex injury. The wrist is unique in that direct coronal scanning can eliminate the need for multiple imaging planes. In addition, an advantage of CT evaluation is that studies can be performed through cast material without significant image degradation.

The scaphoid deserves special mention. Accurate and timely diagnosis of a fracture is essential for minimizing both the risk of avascular necrosis of the proximal pole and nonunion development. Current recommendations suggest MRI as the most appropriate investigation after conventional radiography for imaging of a suspected occult

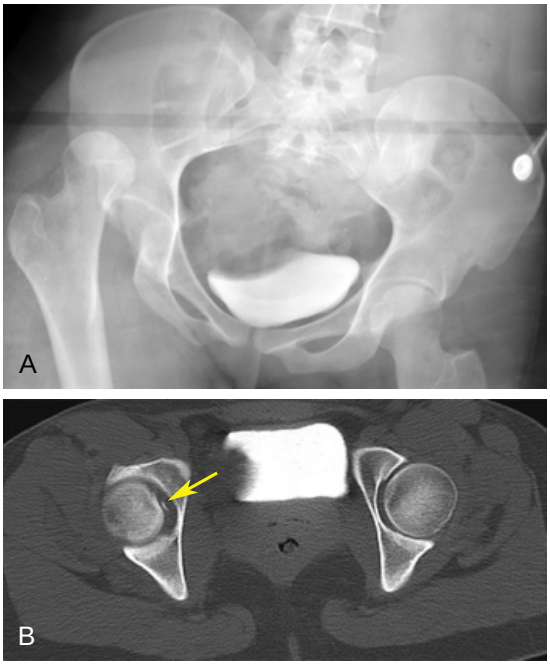

FIGURE 19-6 ■ Hip dislocation. *A,* Conventional x-ray of the pelvis demonstrates a right hip dislocation. *B,* Axial computed tomography after hip relocation demonstrates an intra-articular body in the right hip joint (*arrow*).

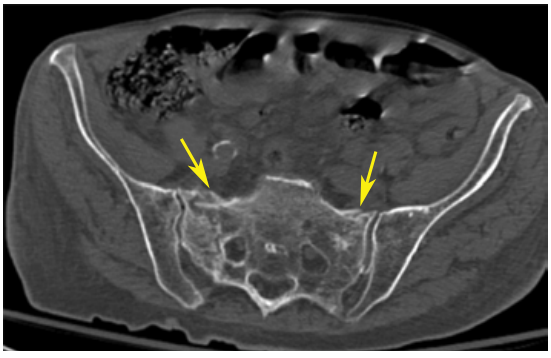

FIGURE 19-7 ■ Sacral insufficiency fracture. Axial computed tomography demonstrates bilateral sacral insufficiency fractures (*arrows*).

acute fracture of the scaphoid. In scaphoid fracture evaluation CT can play a role in assessing the degree of displacement and angulation, which is predictive of nonunion development (Fig. 19-10). Partial union is a common occurrence and can be difficult, if not impossible, to assess with conventional radiographs. Partial unions usually progress to complete union over time without prolonged immobilization or internal fixation. The "humpback" deformity of a malunion can be readily assessed with MDCT and volume rendering.

The density of the proximal pole of the scaphoid should also be assessed in chronic scaphoid fractures for the development of avascular necrosis. A fracture of the hook of hamate bone can be extremely difficult to identify on conventional radiographs. CT examination readily identifies the fracture (Fig. 19-11). MRI can be useful in this clinical setting in assessing the proximity of the fracture fragment to the adjacent neurovascular bundle.

Knee

The role of MDCT in evaluation of the knee is largely the detection of intra-articular fractures, usually of the tibial plateau. These fractures are often complex but may be subtle, and the ability to reformat allows accurate depiction of joint line injuries and fracture fragments for preoperative planning (Fig. 19-12). MRI has been utilized in assessing injuries to soft tissues such as ligaments and menisci. MDCT is neither sensitive nor specific when evaluating the meniscus, but three-dimensional CT has been used to guide surgical replacement of cruciate ligaments.

Ankle

Triplane distal tibial fractures involve the closing distal tibial epiphysis in skeletally immature patients. These complex fractures occur in all three planes and are a result of external rotation when the foot is in plantar flexion. MDCT with reformation is more reliable than conventional radiography in preoperative assessment and planning.

As for the wrist, CT scans can be performed through cast material without image degradation. In addition, direct coronal acquisition is also possible.

Foot

MDCT evaluation in suspected Lisfranc ligament injury is recommended for patients who have suffered an acute hyperflexion injury. Conventional radiography, including weight-bearing views, does not satisfactorily indicate the severity of the injury. An acute hyperflexion injury requires immediate attention, so the rapidity of CT examination is helpful in treatment planning.

MDCT can accurately depict fractures of the calcaneus. The MDCT technique allows examination of the foot in nonanatomical positions adopted as a result of fracture or for patient comfort. Associated subtalar joint, intra-articular, and other osseous injuries can also be easily identified with MDCT. Accurate depiction of fractures, including fragmentation, joint incongruity, and displacement, is important for surgical planning.

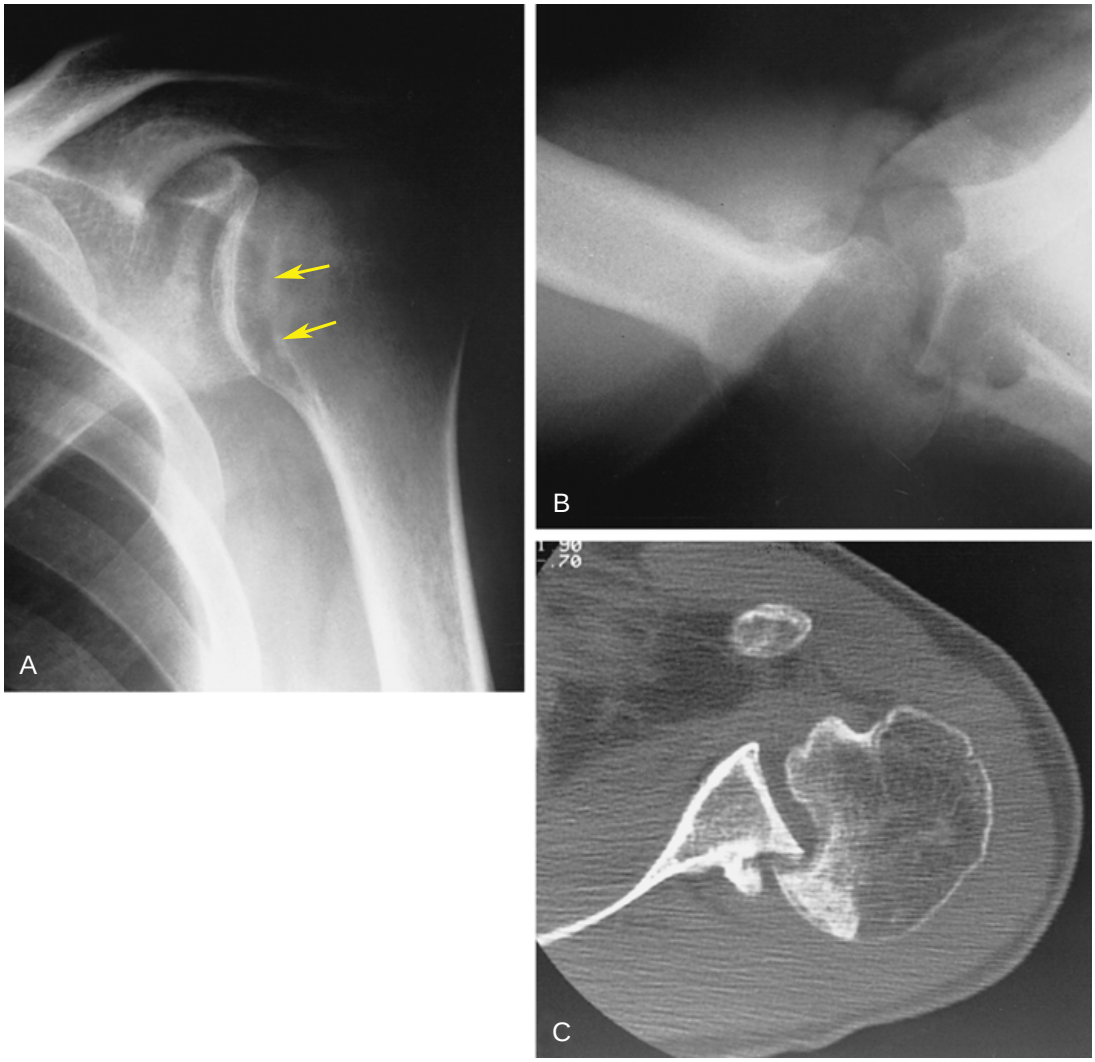

FIGURE 19-8 ■ Posterior shoulder dislocation. *A*, A conventional anteroposterior x-ray of the shoulder shows a vertical lucency (*arrows*), termed a trough sign, indicating impaction from a posterior dislocation. *B*, An axillary view shows that the humeral head is posteriorly dislocated and impacted on the glenoid. *C*, Axial computed tomography demonstrates an impacted humeral head and avulsion of the posterior glenoid.

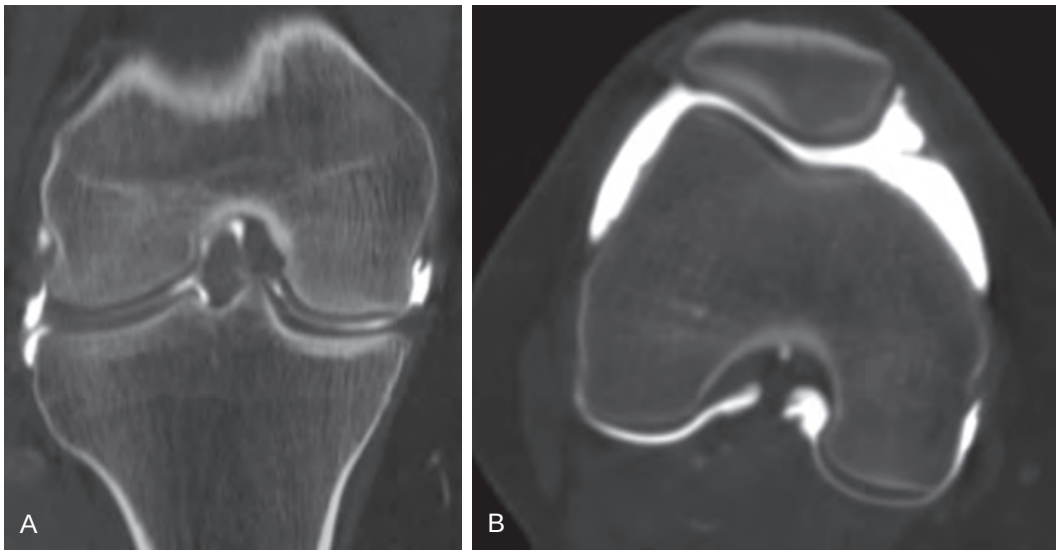

FIGURE 19-9 ■ Computed tomography (CT) arthrogram of the knee. *A*, Coronal reformatted CT of the knee demonstrates contrast material within the joint and outlining the articular cartilage. No articular cartilage defects are noted. *B*, Axial CT through the knee joint demonstrates contrast outlining the normal patellofemoral articular cartilage.

FIGURE 19-10 ■ Scaphoid fracture. Coronal computed tomography performed through plaster-cast material demonstrates fracture lucency through the waist of the scaphoid (*arrow*).

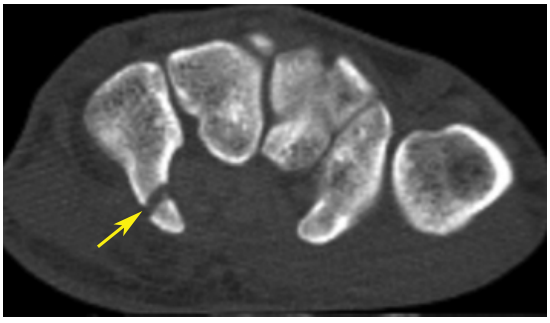

FIGURE 19-11 ■ Fracture of the hook of hamate bone. Axial computed tomography demonstrates a fracture through the hook of hamate bone (*arrow*).

Muscle

Myositis ossificans (MO) is the formation of peripheral calcification in muscle that has been injured. CT is useful in determining the pattern of calcification in suspected MO (Fig. 19-13). Conventional radiography may not always clearly differentiate peripheral calcification, a benign entity, from the central calcification observed for parosteal osteosarcoma, a more sinister lesion. CT is recommended for discrimination of MO from other lesions because MRI evaluation can result in a misleading appearance of a more aggressive soft-tissue lesion.

CONCLUSION

Imaging of the trauma patient should be fast, efficient, and accurate for timely diagnosis and

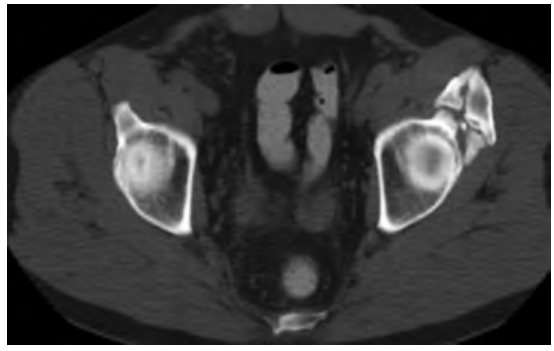

FIGURE 19-13 ■ Myositis ossificans. Ossification at the attachment of the left rectus femoris is noted. The peripheral circumferential ossification is characteristic. Recognition of this pattern is important to avoid biopsy.

FIGURE 19-12 ■ Subtle fracture of the tibial plateau. *A*, A lateral x-ray demonstrates joint effusion after trauma. *B*, Coronal reformatted computed tomography on follow-up demonstrates a subtle fracture of the lateral tibial plateau (*arrow*) that is minimally displaced and mildly impacted.

management. MDCT with volume rendering achieves these goals and allows depiction of complex and difficult anatomical areas such as the spine, pelvis, shoulder girdle, and foot.

SUGGESTED READING

Inaba K, Munera F, McKenney M, et al.: Visceral torso computed tomography for clearance of the thoracolumbar spine in trauma: A review of the literature. *J Trauma* 60:915–920, 2006.

Munera F, Rivas LA, Nunez DB, Quencer RM: Imaging evaluation of adult spinal injuries: Emphasis on multidetector CT in cervical spine trauma. *Radiology* 263:645–660, 2012.

Watura R, Cobby M, Taylor J: Multislice CT in imaging of trauma of the spine, pelvis and complex foot injuries. *Br J Radiol* 77:S46–S63, 2004.

West AT, Marshall TJ, Bearcroft PW: CT of the musculoskeletal system: What is left is the days of MRI? *Eur J Radiol* 19:152–164, 2009.

CHAPTER 20

CT IN MUSCULOSKELETAL NONTRAUMA

Nancy M. Major

DISK DISEASE

Computed tomography (CT) provides the capability of examining in detail not only disks but also bone and soft-tissue structures in and around the spine, including the facets, neuroforamen, thecal sac and nerve roots as they exit the thecal sac, ligamentum flavum, and vascular structures. This chapter discusses how CT can be used to diagnose disk disease and spinal stenosis in the lumbar spine. Magnetic resonance imaging (MRI) has largely replaced CT for routine evaluation of disk disease and back pain. However, CT can be useful, particularly for the postoperative spine, for which imaging artifacts from metal can be problematic in MRI. CT in this setting can evaluate bone fusion mass, as well as residual stenosis. In addition, CT can be performed in a patient who may not be suitable for MRI Myelography is usually not necessary because pathology is clearly depicted without a myelogram.

Technical Considerations

A proper imaging protocol for a diagnostic lumbar spine study is critical to reduce the chance of overlooking an abnormality. Patients should be scanned in a supine position with the knees slightly flexed over a pillow or other similar object. Anteroposterior (AP) and lateral scout films are obtained. An AP scout film allows the radiologist to determine if transitional vertebrae are present. Recognition of transitional vertebrae and correct identification of vertebral body levels can prevent surgery at the wrong level. The lateral scout view is used to place cursors over the intended scan area. Contiguous slices, no thicker than 5 mm, should be scanned from the midbody of L1 through the top of S1. The radiologist should avoid performing angled gantry slices through the disk space alone. This approach leaves spaces or gaps in evaluation of the central canal that are not imaged, allowing for migrated free fragments of disk material and pars defects (spondylolysis) at the mid–vertebral-body level to be missed if imaging is performed only through the disk spaces (Fig. 20-1). It is believed that angled images through the disk space more accurately characterize disk protrusions than stacked, contiguous axial images. Changing the angle of the gantry will not identify or eliminate disk protrusions that have a mass effect on the thecal sac. Thus, contiguous imaging will identify disk disease, pars defects, and free fragments.

Images should be obtained with bone and soft-tissue windows. Images obtained with soft-tissue windows are not suitable for accurate diagnosis of facet disease or other bony abnormalities. Soft-tissue windows can mimic hypertrophy of the normal anatomy. Sagittal and coronal reformatting is performed to assist in the diagnosis of foraminal narrowing, as well as bony fusion in the postoperative setting.

Pathology

Terminology is important when evaluating disk disease in the lumbar spine. The situation in which a disk bulges or protrudes beyond the endplate has been given several names, some of which have more sinister connotations than others. The terms *herniated nucleus pulposus* and *bulging annulus fibrosus* have been utilized, as well as *contained*, *extruded*, and *sequestered* disks. Terminology is probably not as important as recognizing the pathology and distinguishing a bulge from a sequestered or free fragment (Fig. 20-2). It is best to use the terminology preferred by the referring clinician. Disk bulges can be diffuse, broad-based, or focal. When disk material migrates from the parent disk, it is termed *sequestered*, a *free fragment*, or *extruded*. Clinicians want to know if disk material of any kind is causing a mass effect against neural tissue.

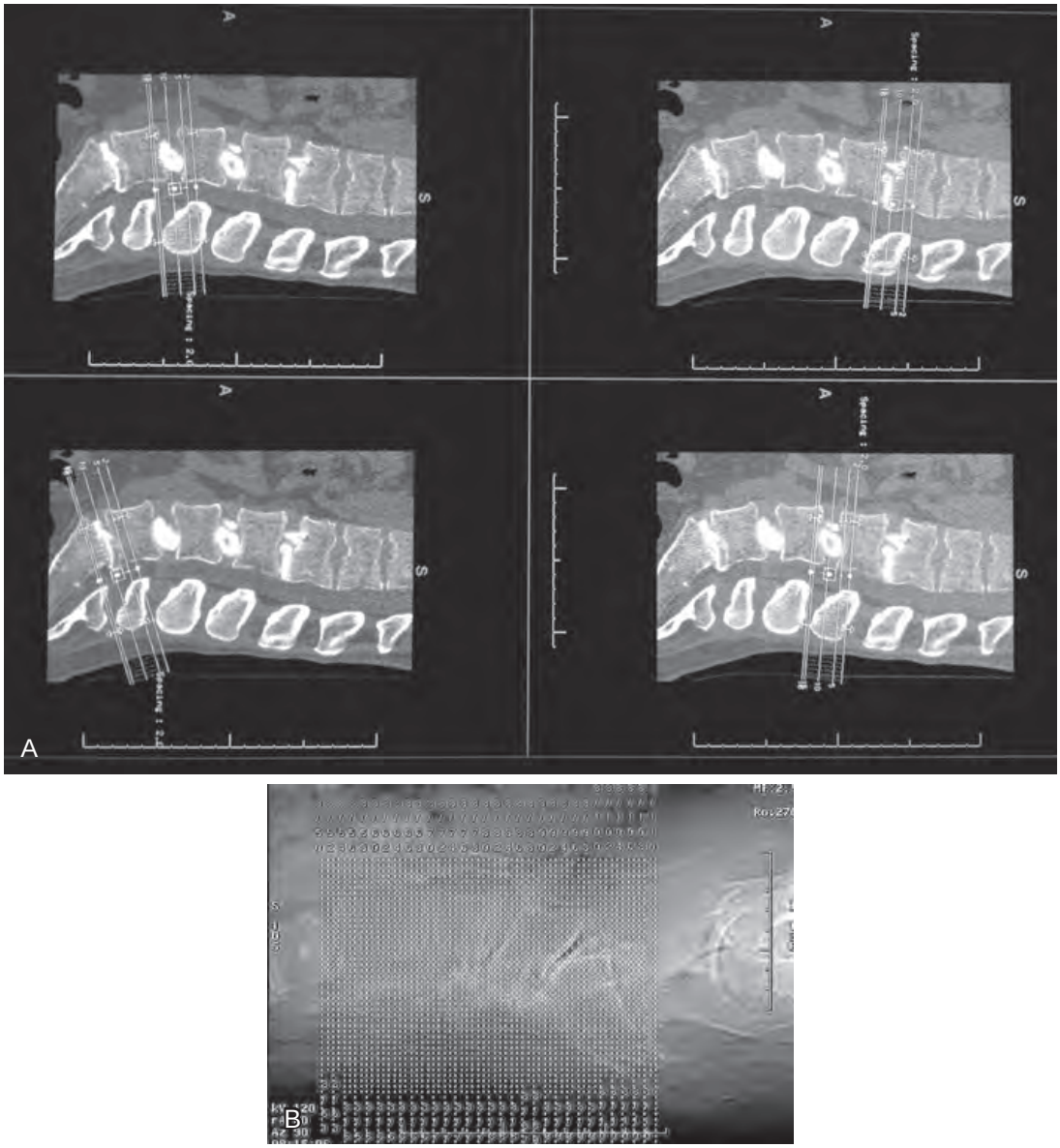

FIGURE 20-1 ■ Lateral scout film of the lumbar spine after a diskogram. *A*, A lateral scout view demonstrates a gantry angled parallel to the end plates through the disk spaces. A gap is present between the lumbar levels, where a free fragment, pars interarticularis defect, or spinal stenosis could be missed. Note the contrast in the disk spaces. *B*, A proper scanning technique demonstrates a lateral scout view with contiguous axial slices from L3 to S1 without intervening gaps. This is an adequate protocol for evaluation of disk disease, spinal stenosis, and pars interarticularis defects.

Disk material may impress the thecal sac or exhibit a mass effect on a nerve root yet may not be clinically symptomatic. The CT findings must be correlated with a clinical examination. A large disk protrusion is much more likely to be symptomatic if it has a mass effect on the thecal sac (Fig. 20-3).

A careful search for sequestration or free fragments is recommended on identification of a large disk protrusion. Failure to recognize sequestration can lead to failed surgical diskectomy. A free fragment should be suggested when disk material is identified caudal or cephalad to the level of the disk space (Fig. 20-4). If a soft-tissue density is identified caudal or cephalad to the disk space, the radiologist should determine if it is of similar density to the thecal sac or is of higher density. Higher density would suggest disk material and a free fragment. If the soft-tissue density cephalad or caudal to the disk space is isodense to the thecal sac, it is not a free fragment and is most likely a perineural cyst or Tarlov cyst, or a conjoined

nerve root. A Tarlov cyst (perineural cyst) is an enlarged nerve-root sheath. It is a normal variant and not a cause of symptoms (Fig. 20-5). Tarlov cysts can become quite large and result in bone erosion secondary to persistent pulsations from cerebrospinal fluid.

A conjoined nerve root is a congenital anomaly of two nerve roots exiting the thecal sac together instead of individually. The two nerve roots traverse the lateral recess together and appear as a soft-tissue density on CT. A free fragment can have a similar appearance but will have higher attenuation compared to the thecal sac and conjoined nerve roots. The conjoined roots will invariably exit through their appropriate foramen (Fig. 20-6). An "empty" foramen is not encountered. Conjoined nerve roots are associated with a slightly wider lateral recess than on the contralateral side. Conjoined roots occur in 1% to 3% of all patients and are incidental findings with no reported symptomatology. The importance of their recognition is to avoid erroneous diagnosis of these normal variants as disk extrusions, which can result in explorations for free fragments and potential unfortunate neural damage at surgery. By noting density differences between conjoined roots and free fragments, the radiologist can avoid errors.

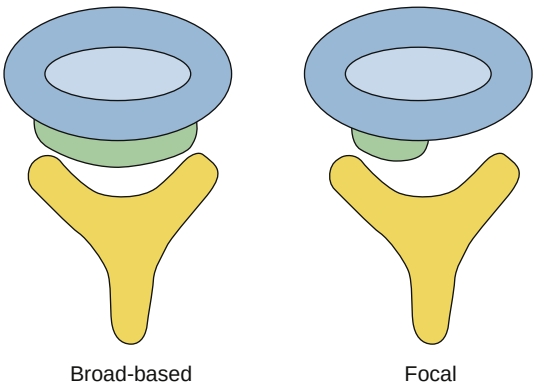

FIGURE 20-2 ■ Drawings of a broad-based disk bulge and focal protrusion. A broad-based disk protrusion has a uniform bulge that extends across the entire central canal. A focal protrusion extends only into a portion of the central canal.

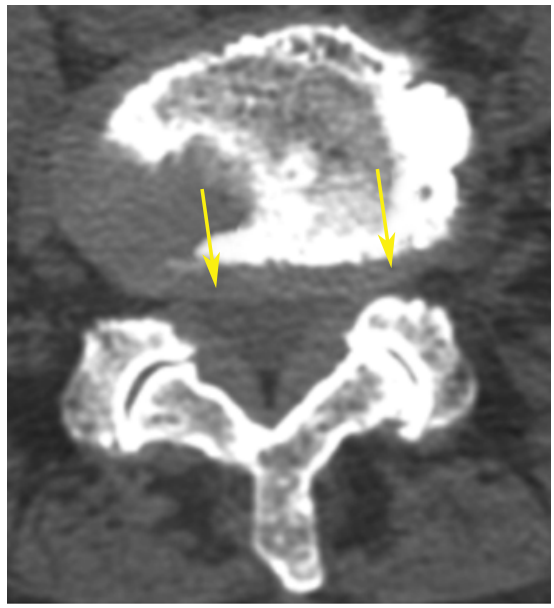

FIGURE 20-3 ■ Broad-based disk bulge. An axial computed tomography image reveals a broad-based disk bulge (*arrows*) demonstrating flattening of the anterior thecal sac.

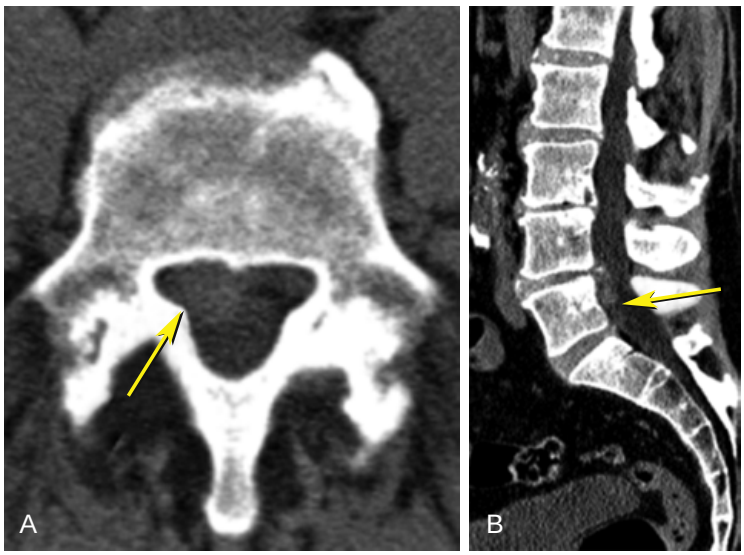

FIGURE 20-4 ■ Free fragment. *A,* An axial computed tomography (CT) image demonstrates a free fragment in the right lateral recess (*arrow*). The free fragment is higher in density than the thecal sac. *B,* Sagittal reformatted CT demonstrates a free fragment emanating from the disk space between L4 and L5 *(arrow*).

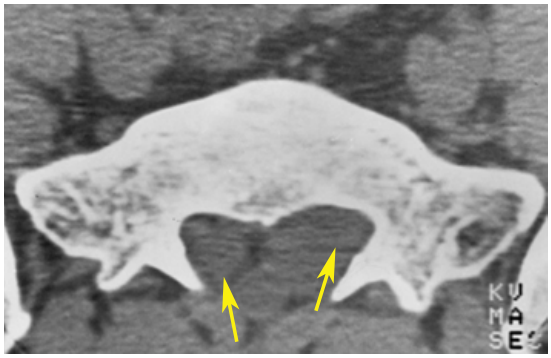

FIGURE 20-5 ■ Tarlov cyst. An axial image through the sacrum demonstrates large dilatation of the nerve root sheaths, causing some erosion into the vertebral body. The cysts are filled with cerebrospinal fluid and are of the same density as that of the thecal sac. This finding helps to distinguish between a free fragment (higher density) and a Tarlov cyst.

A lateral disk is a disk protrusion that occurs lateral to the neuroforamen and is one of the more commonly missed disk protrusions simply because it is overlooked. The search pattern should always include the region lateral to the foramen. A lateral disk has huge implications for the surgeon. First, a lateral disk will irritate a nerve root that has already exited the neural foramen and will therefore mimic a disk protrusion at a more cephalad level. For example, if a disk protrusion is present posteriorly at the level of L4-L5, it will usually have a mass effect on L5. However, the L5 root can also be irritated from a lateral disk protrusion at the level of L5-S1. Therefore, if overlooked, such a disk protrusion can result in surgery at the level of the wrong disk space (Fig. 20-7). This situation is particularly problematic in patients with multilevel disk abnormalities when attempting to determine the proper surgical level. Another important

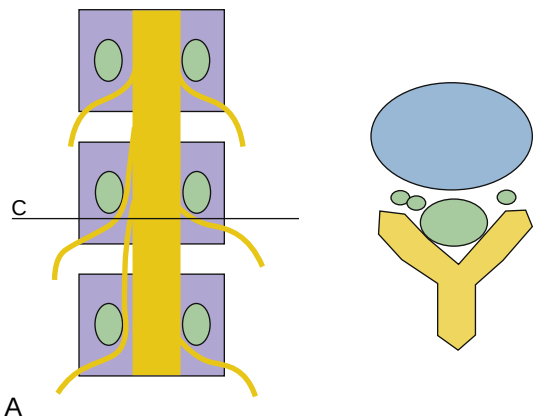

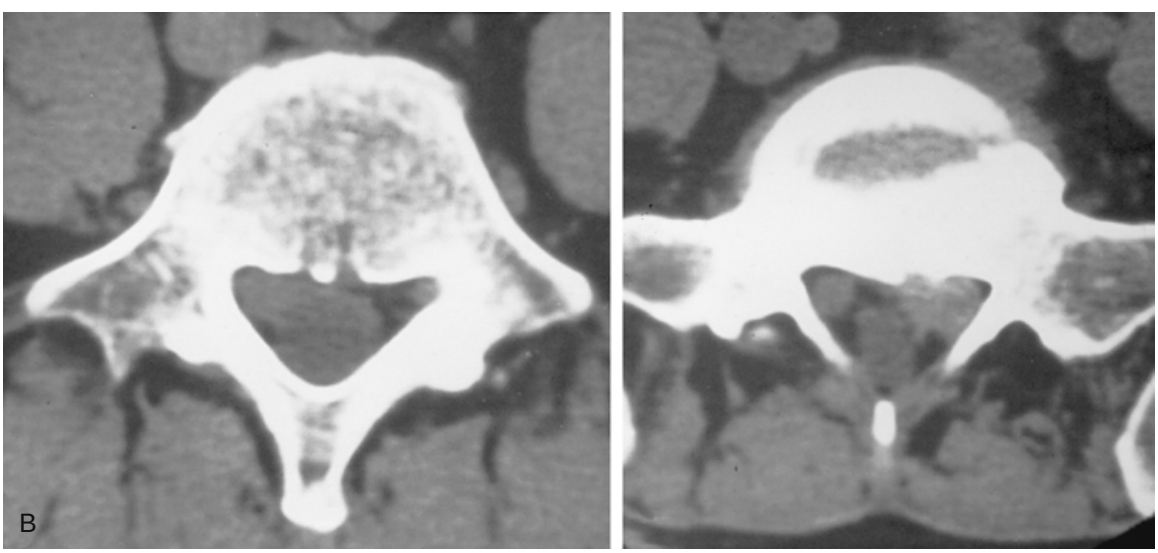

FIGURE 20-6 ■ Conjoined nerve root. *A*, Drawing showing two nerve roots arising from the thecal sac on the right in an asymmetrical manner, in contrast to the left. C, cursor level. *B*, Computed tomography images at the level of the cursor in *A*. Two roots are visualized in an axial slice on the right, one of which could be confused with a free fragment. The nerve root will be of lower density compared to disk material as seen in left lateral recess.

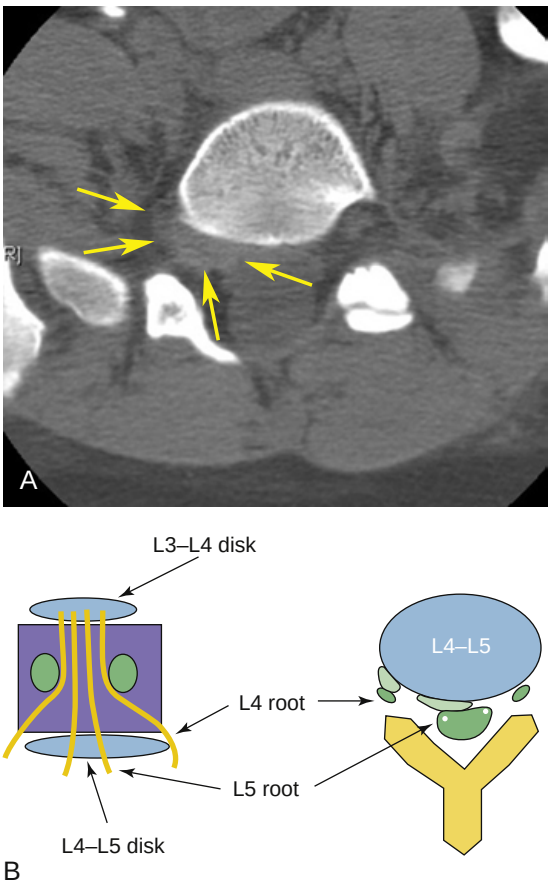

FIGURE 20-7 ■ Lateral disk. A, Axial CT image through the level of L5–S1 shows a soft-tissue mass on the right side just lateral to the neural foramen (*arrows*). *B,* Drawing of a lateral disk demonstrating how a posterior disk protrusion at L4–L5 typically affects the L5 nerve root, yet a lateral disk at the same level affects the L4 nerve root. Typically, an L4 nerve root is affected by a posterior disk protrusion at L3–L4. A lateral disk at L4–L5 could result in inappropriate surgery in the disk space between L3 and L4.

surgical implication for lateral disks is that a lateral disk does not require a laminectomy because it can be approached from outside the bony central canal. The location of a lateral disk is not an area that a surgeon would normally explore. Lateral disks occur in less than 5% of patients but should be part of the search pattern in every patient at each disk level.

SPINAL STENOSIS

Spinal stenosis has been classically divided into two types, congenital and acquired. Patients who experience congenital stenosis include achondroplastic dwarfs, patients with Morquio disease, and individuals born with a congenitally small thecal sac who have idiopathic spinal stenosis. Acquired stenosis includes degenerative joint disease with or without degenerative disk disease, post-traumatic stenosis, postsurgical stenosis, Paget disease, and calcification of the posterior longitudinal ligament.

A preferred classification for spinal stenosis is based on anatomic location. Stenosis can be described as central canal stenosis, neuroforaminal stenosis, or lateral recess stenosis. In each of these areas the most common cause of stenosis is degenerative joint or degenerative disk disease.

Central Canal Stenosis

For decades, radiologists have been asked to measure the central canal to diagnose spinal stenosis. Discordance in the size of the bony canal and the thecal sac must be present for stenosis to be clinically manifest. Simple measurement of the central canal does not address the "fit" of the thecal sac within the canal, so such measurements are virtually meaningless. An exception to this situation may be the cervical spine, for which a narrow central canal has been correlated with increased risk of spinal cord injury in football players.

The most useful CT criteria for diagnosing central canal stenosis are obliteration of the epidural fat and flattening of the thecal sac. Both of these findings can be present without symptoms of spinal stenosis, and therefore stenosis can only be suggested by the radiologist and clinical correlation is required.

The most common cause of central canal stenosis is secondary to facet degenerative disease, which results in hypertrophy of the facet joints and encroachment of the central canal and lateral recess (Fig. 20-8). Another common cause of central canal stenosis is "hypertrophy" of the ligamentum flavum. The ligamentum flavum does not actually hypertrophy, but rather buckles inward because of facet slippage and associated narrowing of the disk space (Fig. 20-9). Because this condition represents soft-tissue encroachment, measurements of the size of the bony canal would not reflect this process, which is another reason why measurements are not reliable indicators of spinal stenosis.

Paget disease affecting a vertebral body, which occurs less often now than in the past, involves enlargement of the vertebral body and can occasionally result in central canal stenosis, as can ossification of the posterior longitudinal ligament. It has been reported that up to 25% of patients with diffuse idiopathic skeletal hyperostosis (DISH), a common entity in individuals older than 50 years, have ossification of the posterior longitudinal ligament. Other causes of central canal stenosis include trauma and postoperative changes.

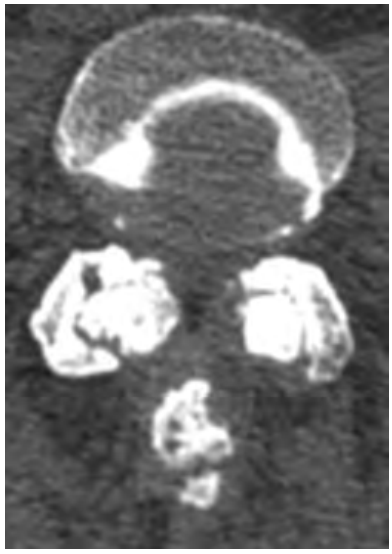

FIGURE 20-8 ■ Central canal stenosis. An axial image demonstrates a combination of a broad-based disk bulge, facet arthropathy, and ligamentum flavum thickening resulting in central canal stenosis. The thecal sac is difficult to visualize because the epidural fat has been obliterated. When the epidural fat is not visualized, spinal stenosis should be suspected.

Neuroforaminal Stenosis

The causes of neuroforaminal stenosis, as in central canal stenosis, can be diverse but are usually caused by degenerative joint disease. Osteophytes emanating from the vertebral body or from the superior articular facet are most often the cause, but disk protrusions and postoperative scarring can also occur in the foramen.

The nerve root exits the central canal in the superior aspect of the neural foramen. Encroachment in the inferior aspect of the foramen, near the disk space, is an infrequent cause of clinical problems. The nerve root is immobile in the neuroforamen rather than free to move about. Therefore even a small amount of stenosis in the superior aspect of the foramen can cause severe clinical symptomatology, whereas severe stenosis of the inferior aspect of the foramen may result in no symptoms at all. For these reasons, the amount of narrowing of the neural foramina often does not correlate with clinical findings.

Although many believe that sagittal reformatted images through the neuroforamen are adequate for identification of stenosis, axial images are by far more reliable in fully demonstrating the degree of neuroforaminal stenosis and its cause. The neuroforamen and the nerve root can be seen in their entirety with axial images, whereas a single reformatted sagittal image will show volume rendering of the axial slice (Fig. 20-10).

FIGURE 20-9 ■ Ligamentum flavum thickening. The ligamentum flavum is thickened and bowed inward (*arrows*), and is encroaching on the central canal and contributing to spinal stenosis.

A cause of unsuccessful back surgery is failure to preoperatively note neuroforaminal stenosis in a patient undergoing disk treatment, which can result in performance of an inadequate procedure. Disk disease and stenosis in any of its forms most often occur together and should be identified by the radiologist.

Lateral Recess Stenosis

The lateral recess is the bony portion of the central canal that is just caudad and cephalad to the neural foramen. When the neuroforamen ends as one proceeds caudad, the lateral recess begins. This area has also been referred to as the "nerve root canal" because the nerve roots, after they exit the thecal sac and before they exit the central canal through the neuroforamen, run in this bony triangular space. In the bony lateral recess, the nerve roots are vulnerable to being impinged by osteophytes, disk fragments, and scar tissue from previous surgery (Fig. 20-11). As with the neuroforamen, the amount of stenosis often does not correlate with the clinical presentation. Therefore, it is best to note whether the lateral recess is or is not normal in appearance. Narrowing must be correlated clinically.

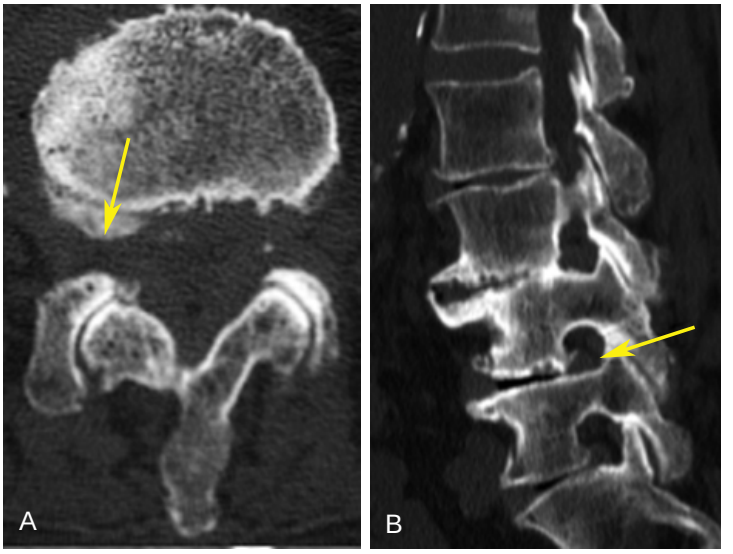

FIGURE 20-10 ■ Neuroforaminal narrowing. *A,* An osteophyte arising from the posterior right aspect of the vertebral body is extending into the right neuroforamen, resulting in neuroforaminal stenosis (*arrow*). *B,* Sagittal reformatted computed tomography demonstrates neuroforaminal narrowing (*arrow*). The soft-tissue density identified within the neuroforamen narrows the foramen and obliterates the fat.

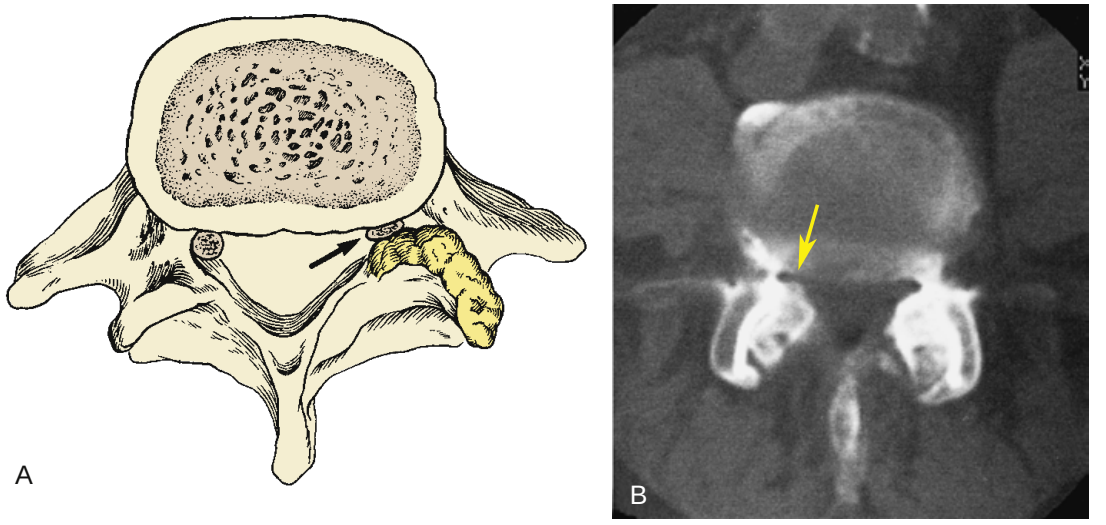

FIGURE 20-11 ■ Lateral recess stenosis. *A,* Drawing illustrating a nerve root (*arrow*) impinged in the lateral recess by bony overgrowth. *B,* The right lateral recess (*arrow*) is narrowed due to bony overgrowth. The nerve root lies in the lateral recess and may or may not be impinged enough by this process to cause symptoms.

SPONDYLOLYSIS AND SPONDYLOLISTHESIS

Spondylolysis (pars interarticularis defect, discussed in Chapter 19) can cause low back pain and sciatica but only occasionally causes spinal stenosis. A fibrocartilaginous mass can develop around a pars break that can extend into the central canal and cause a mass effect on the thecal sac or nerve roots. Although this condition is uncommon, the radiologist should search for it in patients with a pars defect to avoid the unfortunate situation of spinal fusion being performed without removal of the offending soft-tissue mass within the central canal.

Spondylolisthesis is defined as anterior displacement of a cephalad vertebral body with respect to the caudad vertebral body and is graded in severity of slip relative to the lower vertebral body. Grade 1 is defined as <25%, grade 2 as 25% to 50%, grade 3 as 50% to 75%, and grade 4 as 75% to 100% slip relative to the caudal vertebral body. Spondylolisthesis can cause central canal stenosis, and a more advanced grade can cause neuroforaminal stenosis. Occasionally, the pars defect will extend into the neural foramen and impinge on the nerve root. Spondylolisthesis may be a result of spondylolysis or spondylosis (degenerative facet joint disease).

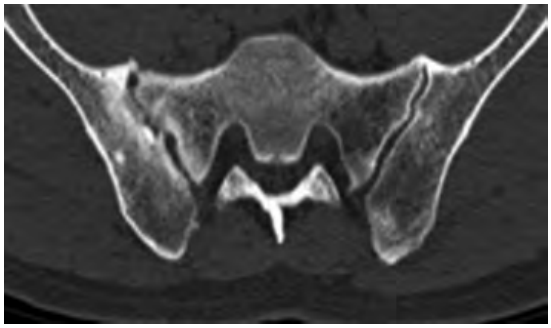

FIGURE 20-12 ■ Sacroiliitis. Axial computed tomography image through the sacroiliac joints demonstrates right-sided sclerosis and erosions. The left sacroiliac joint is fused anteriorly.

SACROILIAC JOINTS

Conventional radiography of the sacroiliac (SI) joints can be extremely difficult to interpret secondary to anatomic obliquity of the joints themselves and the overlying soft tissues. CT is a more reliable examination than conventional radiography and is also more reproducible, more sensitive, and more accurate than conventional radiography and results in less radiation exposure. CT evaluation can be performed rapidly and at relatively low cost, so SI joint evaluation by CT is more cost-effective than conventional radiography. This can be accomplished by decreasing the number of slices necessary to evaluate the SI joints. The gantry is reversed so that it is at a steep angle parallel to the SI joints. Eight to ten 3-mm-thick slices are sufficient to cover the SI joints.

SI joint symptoms can occasionally be the cause of back pain. SI joint abnormalities are part of the symptom complex of many arthritides, particularly the spondyloarthropathies (Fig. 20-12).

SI joint sclerosis and erosions can be identified with much more clarity on CT than on conventional radiographs. Osteoarthrosis of the SI joints can also cause erosion and can mimic a spondyloarthropathy or infection. It has been shown that erosions and sclerosis in the SI joints increase with age, so patients older than 40 years often have SI joint abnormalities.

Osteitis condensans ilii is diagnosed when triangular foci of sclerosis are noted in the ilium abutting the SI joint. This is an incidental finding and is not associated with any symptoms.

OSTEITIS PUBIS

Osteitis pubis was historically defined as infection in the pubic symphysis, most often identified after bladder surgery. The name implies an inflammatory change in the joint space. However, any changes identified are not usually caused by an inflammatory process. Rather, stress changes, most often identified in athletes, lead to erosions and sclerosis within the pubic symphysis. Coexisting erosions and sclerosis are often seen in the SI joints in these individuals. Osteoarthrosis can also result in erosions and sclerosis at the pubic symphysis (Fig. 20-13).

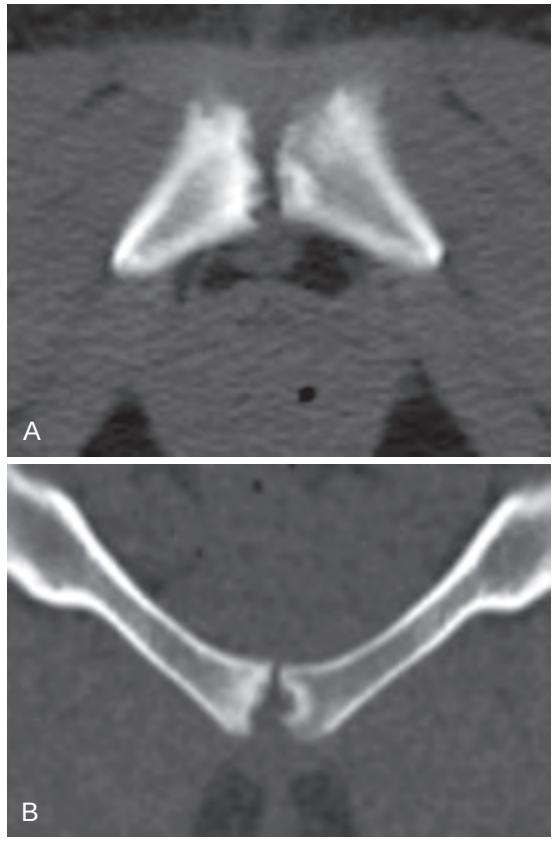

FIGURE 20-13 ■ Stress changes in the pubic symphysis. *A,* Axial and *B,* coronal reformatted computed tomography demonstrates erosions of the pubic symphysis resulting from stress changes.

COALITION

Tarsal coalition is fusion of two or more bones and can result in foot and ankle pain. Multidetector CT (MDCT) can delineate the coalition and aid in surgical planning to determine resection versus arthrodesis. Calcaneonavicular coalition is depicted on long-axis images of the foot and is the most common coalition. Broadening of the medial aspect of the anterior and dorsal calcaneus is consistently recognized in this entity. Changes in nonosseous

FIGURE 20-14 ■ Subtalar coalition. *A,* Axial computed tomography through the hindfoot demonstrate an osseous talocalcaneal coalition (*arrow*). *B,* Coronal and *C,* sagittal reformatted images demonstrate a fibrous subtalar coalition (*arrows*).

coalition are subtle, with narrowing of the joint space and minimal reactive changes noted on CT.

Talonavicular coalition is the second most common coalition and is best depicted on long-axis and sagittal imaging of the foot or ankle.

Talocalcaneal coalition typically involves the middle facet and can be depicted in short-axis and sagittal reformatted images (Fig. 20-14). Fusion in osseous coalition, as well as reactive sclerosis and subchondral cyst formation in non-osseous coalition, can be identified. Involvement in the anterior and posterior subtalar joints is variable (Fig. 20-15). Coexisting conditions such as tendon and ligament abnormalities and stress changes within the bone marrow can be present. For these reasons and for further evaluation of foot and ankle pain, MRI has replaced CT at many institutions.

TUMORS AND INFECTION

The role of CT in evaluating tumors and infection has been replaced by MRI given its soft-tissue contrast and multiplanar capabilities. CT is important in the assessment of bone lesions, for which it can provide more information than MRI and conventional radiography in evaluating the presence of calcification and ossification and cortical involvement. If myositis ossificans is suspected, CT examination is preferred over MRI to demonstrate the peripheral calcification (Fig. 20-16). If the pattern of ossification in myositis ossificans is not appreciated and a biopsy is performed, multiple mitotic cells in the biopsy specimen can suggest an aggressive process, resulting in erroneous diagnosis and radical surgery. Myositis ossificans on MRI, as discussed previously,

FIGURE 20-15 ■ Calcaneonavicular coalition. Sagittal reformatted computed tomography demonstrates a fibrous calcaneonavicular coalition (*arrow*).

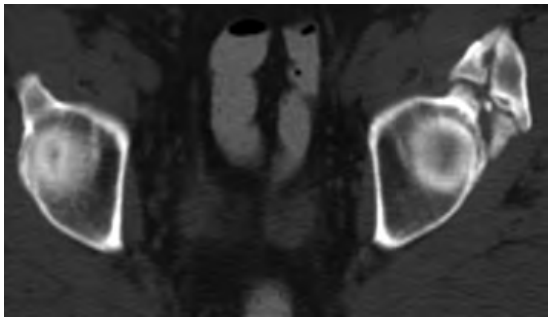

FIGURE 20-16 ■ Myositis ossificans. Ossification is noted in the region of the left rectus femoris origin as a result of a previous injury.

can mimic a sinister lesion, but it has a characteristic appearance on CT imaging.

CT can be helpful in diagnosing bone involvement in multiple myeloma before such involvement becomes apparent on conventional x-rays. In particular, CT of the spine can show diffuse lytic lesions resembling *Swiss cheese* in appearance. When myeloma has been more long-standing, the few remaining normal trabeculae within the vertebral body undergo compensatory hypertrophy and the resulting appearance comprises thick, sclerotic bony struts with lytic areas between them (Fig. 20-17). A similar appearance of trabecular thickening within the vertebral body can be seen in plasmacytoma. This pattern for multiple myeloma and plasmacytoma can occasionally be confused with a spinal hemangioma. However, the latter reveals trabecular struts that are more ordered and symmetrical (Fig. 20-18).

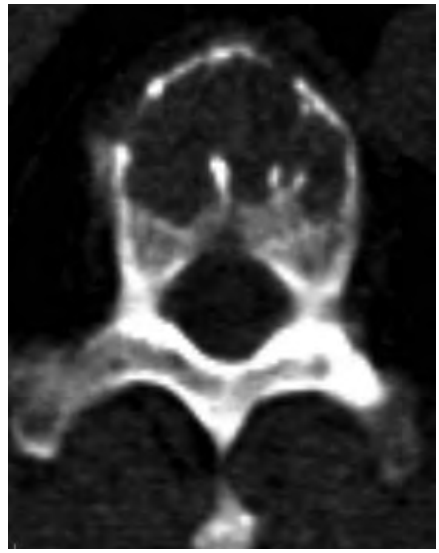

FIGURE 20-17 ■ Multiple myeloma. Axial computed tomography through the L3 vertebral body demonstrates a lytic lesion at the anterior aspect of the vertebral body. Note the thickened trabecular struts. This finding can be seen in multiple myeloma and plasmacytoma.

FIGURE 20-18 ■ Hemangioma. Dense, hypertrophied trabeculae are arranged in a columnar fashion. Hypertrophic trabeculae are symmetrical in appearance, unlike the appearance in chronic myeloma and plasmacytoma.

CT is useful for evaluating osteoid osteoma. Clinically and radiographically this lesion can be confused with infection. CT can reveal the location of the nidus (lytic focus within dense sclerosis) and facilitate its removal (Fig. 20-19). This is especially useful in joints such as the hip and spine. Identification of lucency surrounded by sclerosis is not pathognomonic for the nidus of osteoid osteoma. This pattern of imaging can also be seen

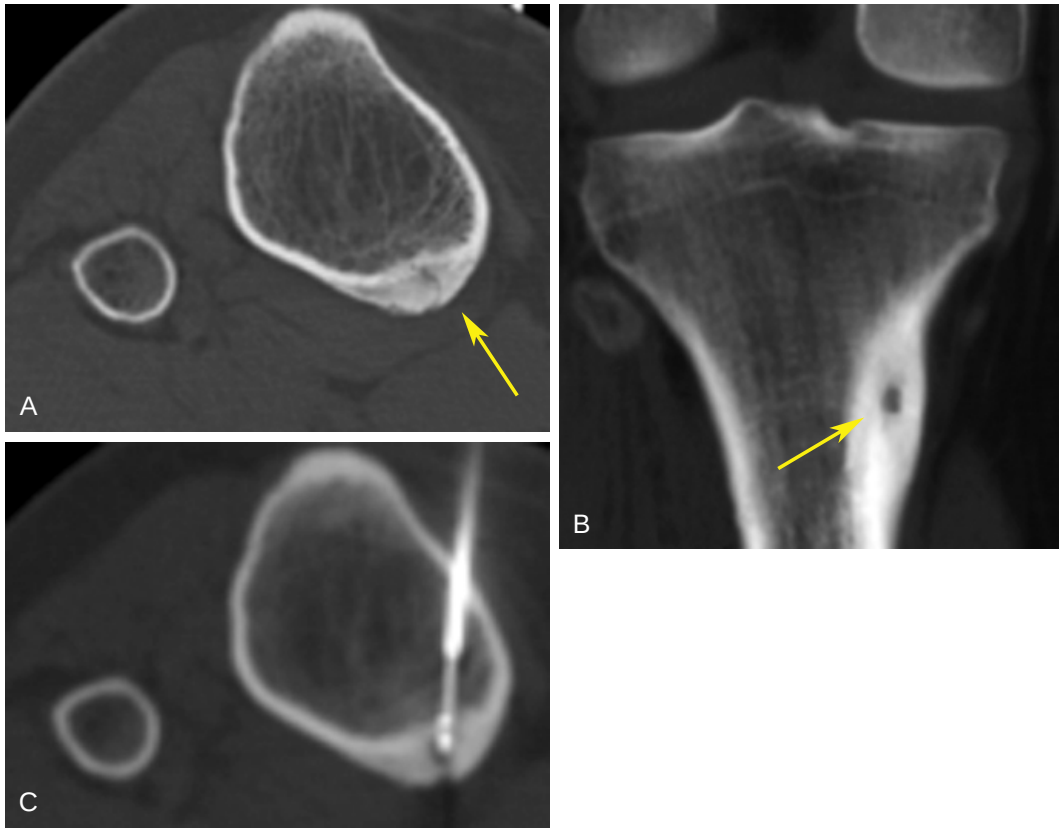

FIGURE 20-19 ■ Osteoid osteoma. *A,* Axial and *B,* coronal reformatted computed tomography (CT) demonstrates a lytic nidus with a dense periosteal reaction in the posterior tibia (*arrows*). *C,* Axial CT-guided placement of a radiofrequency probe for ablation of osteoid osteoma.

with osteomyelitis, because a small abscess can have an identical appearance. The nidus of osteoid osteoma often partially calcifies and then resembles a sequestrum of osteomyelitis. Radionuclide bone scans can usually differentiate between osteoid osteoma and osteomyelitis by revealing focal increased uptake against a background of increased radiotracer uptake by osteoid osteoma. This uptake is caused by the increased radionuclide affinity of the hypervascular nidus. In comparison in osteomyelitis, the reactive new bone surrounding the nidus takes up the radionuclide to a lesser degree. In osteomyelitis a small abscess will be photopenic on radionuclide examination.

CT can also play a role in osteoid osteoma treatment. Percutaneous radiofrequency ablation (RFA) is a safe, minimally invasive method for treating osteoid osteoma. This approach has proven to be as effective as operative treatment but is associated with shorter hospital stays and fewer complications in comparison to surgical removal. MDCT is used to guide the RFA needle into the center of the nidus and to reposition the needle in lesions >1 cm. In the case of "beaded" osteoid osteomas, MDCT can ensure successful nidus ablation.

An increasing number of CT examinations are being performed in evaluating known or suspected musculoskeletal infections. This increase is likely due to the prevalence of intravenous drug use and the growing population of immunocompromised patients, including those with human immunodeficiency virus, acquired immunodeficiency syndrome, an organ transplant, or a known malignancy, and renal dialysis patients. Spiral CT with volume rendering is valuable in detecting infection and determining compartment involvement and the extent of the process. This information is important for patient management (surgical versus medical) and for monitoring responses to treatment. Spiral CT with volume rendering can be used to evaluate cortical bone and associated soft-tissue masses in suspected osteomyelitis. Multiplanar and three-dimensional images are useful in surgical planning, especially when the area of involvement is extensive. Iodinated contrast is helpful in identifying rim enhancement of an abscess (Fig. 20-20).

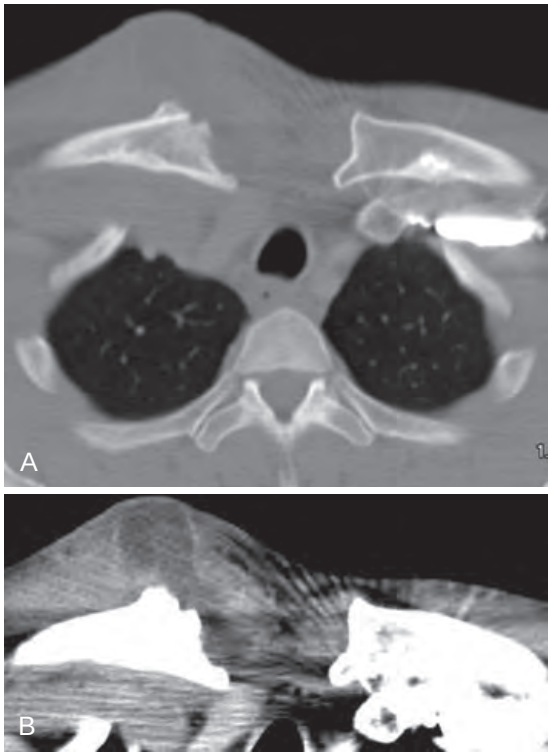

FIGURE 20-20 ■ Sternoclavicular joint infection. *A,* Axial computed tomography with a bone algorithm demonstrates soft-tissue fullness superficial to the right sternoclavicular joint. The medial clavicle demonstrates erosion. *B,* A soft-tissue window demonstrates circumferential contrast enhancement around a low-density center representing abscess emanating from the joint space seen as soft-tissue fullness with the bone algorithm.

CT can also play a role in identifying sequestrations in osteomyelitis. Identification of a sequestration has both diagnostic and therapeutic significance. The diagnostic significance is that only a few entities have been described as commonly having a sequestration. These include osteomyelitis, eosinophilic granuloma, desmoid tumors, and pleomorphic undifferentiated sarcoma (malignant fibrocystic histiocytoma). As mentioned in the previous discussion, a partially calcified nidus of an osteoid osteoma can have an identical appearance to osteomyelitis with a sequestrum. The therapeutic significance is that a sequestrum usually requires surgical removal. Antibiotic therapy alone generally does not suffice, because a sequestrum does not have a blood supply and therefore cannot be reached by antibiotics.

Necrotizing fasciitis may have a nonspecific presentation, and a timely diagnosis is needed. The rapidity of the spread and the subsequent deterioration in the patient's condition require rapid diagnosis. Imaging studies should not delay surgical intervention. The characteristic finding

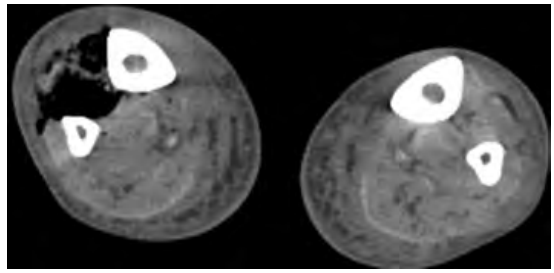

FIGURE 20-21 ■ Necrotizing fasciitis. Axial computed tomography through the lower extremities demonstrates gas in the anterior soft tissues. Necrotizing fasciitis is a clinical diagnosis. Imaging may lead to a delay in treatment.

is gas in the soft tissues (Fig. 20-21). The CT characteristic of necrotizing fasciitis is soft-tissue air associated with fluid collections within the deep fascia. Potential advantages of CT imaging include the ability to detect underlying infectious sources (diverticulitis, osteomyelitis) and vascular rupture.

METAL IMPLANTS

Imaging of postoperative patients with metallic implants may present a challenge. There is often a need to evaluate osseous fusion following fracture fixation, joint fusion, or complications of joint replacement surgery (loosening or periprosthetic fracture). MDCT can also be used in preoperative assessment of prostheses before revision to evaluate the bone stock quality and the potential for bone grafting and mesh reconstruction (Fig. 20-22). Metal causes artifacts such as beam hardening. These artifacts depend on the composition of the hardware, and are lowest for titanium and highest for cobalt chrome alloys. Artifacts also depend on the thickness and orientation of the implant and are most severe in the direction of the thickest portion of the implant. When possible, the body part should be positioned with the minimal cross-sectional area of the prosthesis presented to the x-ray beam. Metal artifacts also depend on the peak voltage, current, reconstruction algorithm, slice thickness, and orientation. A high peak voltage decreases artifacts by increasing the likelihood of x-ray penetration. An increase in current increases the photon flux striking the CT detectors and reduces artifacts, but this must be balanced against the increase in radiation dose. The use of bone or edge enhancement should be avoided because this increases hardware artifacts. It is recommended that standard bone or soft-tissue reconstruction algorithms are used when imaging patients with dense metal implants. Use of a

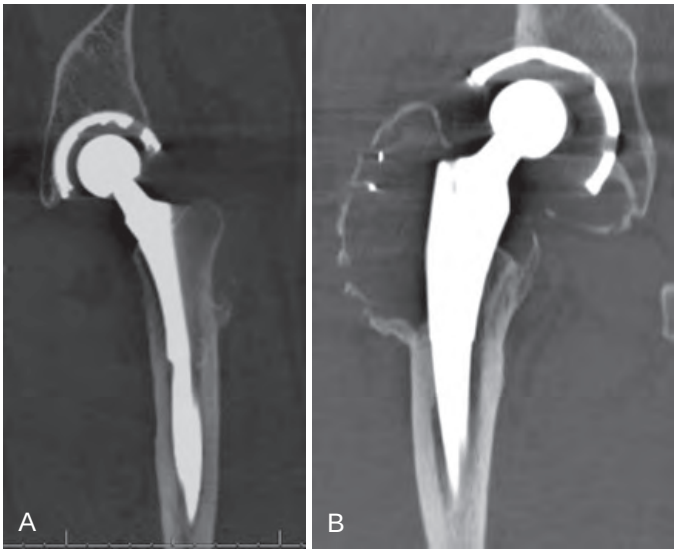

FIGURE 20-22 ■ Total hip arthroplasty. *A*, Coronal reformatted image of a normal total hip arthroplasty. The reformatted image reduces the metallic artifact effect. *B*, Total hip arthroplasty with demonstration of bony expansion and tiny metallic foci representative of particle disease.

thicker slice width also reduces metal artifacts by averaging the pixels.

INTERVENTION

MDCT allows extremely accurate placement of needles for biopsy and diagnostic and therapeutic injection because of its rapid imaging acquisition, high spatial resolution, and ability to accurately define bone. Particularly in the setting of distorted anatomy (congenital, post-traumatic, or postsurgical), MDCT-guided injection may be the technique of choice. Due to its ability to provide excellent anatomic detail, MDCT is also frequently used for guidance of diagnostic or therapeutic nerve root injections.

MEASUREMENTS

Almost any measurement performed with plain films, such as a scanogram for leg length discrepancy, can be done more accurately and with considerably less radiation by using CT. The measurements can be made and accurately obtained with CT by taking an AP scout film of the extremities and placing cursor points under bony landmarks for measurement. The computer gives distance measurements between the chosen points (Fig. 20-23). This technique is reproducible and accurate but suffers in that it is not possible for the patient to bear weight during the procedure. Most of the time a weight-bearing examination is not necessary; however, if such an examination is required, then a CT scanogram cannot replace a conventional scanogram. It has been estimated that the radiation dose is 50- to 100-fold less for a CT scanogram than for a conventional scanogram. The cost is also lower for a CT scanogram than for a conventional scanogram

FIGURE 20-23 ■ Scanogram. Scout views of the lower extremities can assist in determining leg length. Computed tomography (CT) scanograms are accurate and reliable. The diaphysis of bones is included in CT scanograms, unlike conventional scanograms. To determine the actual leg length, a native hip is measured from the top of the femoral head to the lower edge of the intercondylar notch. In a prosthetic hip, the measurement is from the upper edge of the acetabular cup to the lower edge of the intercondylar notch. The tibial length is measured from the center of the intercondylar eminence to the center of the tibial plafond. This measurement must be distinguished from measurement of leg length discrepancy. There are several ways to obtain the latter measurement that are beyond the scope of this book.

because of the low cost of scout views, which comprise the imaging portion of the examination.

CONCLUSION

CT has utility in evaluating pathology in the lumbar spine and can demonstrate disk protrusions that are central, lateral, and sequestered. The ability to fully evaluate bone and soft-tissue structures is one of the greatest assets of CT and has helped to diminish the incidence of unsuccessful back surgery. The use of CT in evaluating sacroiliitis and osteitis pubis is being replaced by MRI in large part because of intramedullary bone marrow edema. However, erosions are more readily appreciated by CT. MRI is much more efficacious in the evaluation of soft-tissue tumors. However, CT with contrast can easily distinguish an abscess and is often used for evaluating infection of the appendicular skeleton. Although MRI is replacing CT in evaluation of tarsal coalition and associated soft-tissue changes, CT can accurately characterize the extent of bone involvement. MDCT with volume rendering can compensate for streak artifacts, and studies are usually diagnostic in the presence of hardware or prostheses. Scanograms can be performed quickly and effectively in patients for whom absolute measurements of leg length are required. The advantage of CT scanograms is visualization of the diaphysis of the long bones that is not otherwise obtained with conventional x-ray scanograms.

SUGGESTED READING

Bibbo C, Lin S, Abidi N, et al.: Missed and associated injuries after subtalar dislocation: The role of CT. *Foot Ankle Int* 22:324–328, 2001.

Buckwalter KA, Rydberg J, Kopecky KK, et al.: Musculoskeletal imaging with multislice CT. *AJR Am J Roentgenol* 176:979–986, 2001.

Preidler KW, Peicha G, Lajtai G, et al.: Conventional radiography, CT and MR imaging in patients with hyperflexion injuries of the foot: Diagnostic accuracy in the detection of bony and ligamentous changes. *AJR Am J Roentgenol* 173:1673–1677, 1999.

Rosenthal DI, Hornicek FJ, Wolfe MW, et al.: Percutaneous radiofrequency coagulation of osteoid osteoma compared with operative treatment. *J Bone Jt Surg Am* 80:815–821, 1998.

Watura R, Cobby M, Taylor J: Multislice CT in imaging of trauma of the spine, pelvis and complex foot injuries. *Br J Radiol* 77:S46–S63, 2004.

West AT, Marshall TJ, Bearcroft PW: CT of the musculoskeletal system: What is left is the days of MRI?. *Eur J Radiol* 19:152–164, 2009.

White LM, Buckwalter KA: Technical considerations: CT and MR imaging in the postoperative orthopedic patient. *Semin Musculoskelet Radiol* 6:5–17, 2002.

CHAPTER 21

INCIDENTAL FINDINGS

Nancy M. Major

Bone structures are included in computed tomography (CT) evaluations of the chest, abdomen, and pelvis. Bone pathology can occasionally be encountered during these examinations. This chapter provides examples of bone pathology that can be seen incidentally. It is not meant to be an atlas of all possible bone lesions, but instead discusses and shows examples of lesions that are commonly encountered or might be potentially confusing during CT examination.

METASTATIC DISEASE AND MULTIPLE MYELOMA

A common indication for CT of the chest, abdomen, or pelvis is evaluation of possible metastatic disease in a patient who has a known primary cancer. The bones are carefully evaluated for evidence of involvement. Bone windows are necessary to more accurately characterize bone lesions. Not every bone lesion in a patient with a known primary cancer will be metastatic disease. A helpful sign of an aggressive lesion is a permeative appearance within the bone. This finding can be seen with metastatic disease and multiple myeloma. However, metastatic disease can have many appearances, including sclerotic, lytic, and mixed lytic–sclerotic lesions (Figs. 21-1 and 21-2). Metastatic lesions can be found in any portion of the body, and thus the location of a lesion is not as important as its character in making a diagnosis of metastatic disease. Infection, a benign process, can also have a permeative appearance on CT examination. The clinical history should distinguish between metastatic disease and infection.

Endosteal scalloping or the appearance of a scalloped cortex along the medullary canal is not a specific diagnosis for metastatic disease or myeloma (Fig. 21-3). This finding can also be seen in many benign entities such as enchondroma, fibrous dysplasia, and nonossifying fibroma.

Not all blastic lesions should be considered worrisome for metastatic disease. A bone island, for instance, is a blastic process that is benign (Fig. 21-4) and is essentially a hamartoma of bone. Stellate margins and a lack of distortion of bone are useful signs in trying to discriminate a bone island from metastatic disease.

The presence of a soft-tissue mass around a lytic lesion is also not helpful in distinguishing metastatic disease or multiple myeloma from a benign process. There are benign entities that can have an associated soft-tissue mass such as infection, eosinophilic granuloma, and giant cell tumor, among others (Fig. 21-5).

In the spine, multiple myeloma can have a characteristic appearance. The trabeculae can hypertrophy and become thickened as the bone around these areas is destroyed due to the disease process. This is a unique appearance for multiple myeloma and plasmacytoma. This characteristic appearance can alleviate the need for biopsy because it is unique to this lesion (Fig. 21-6).

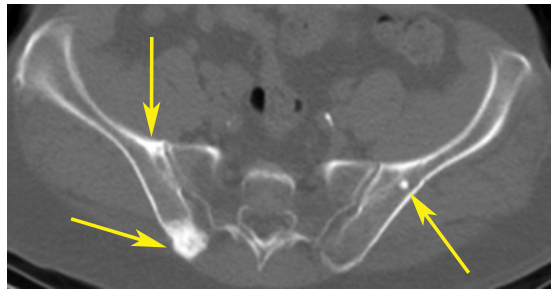

FIGURE 21-1 ■ Sclerotic metastases. Axial computed tomography through the pelvis demonstrates sclerotic foci (*arrows*) in a patient with confirmed lung cancer.

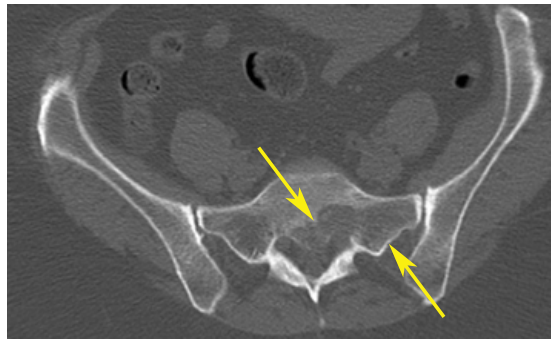

FIGURE 21-2 ■ Lytic metastatic lesion. Axial computed tomography through the pelvis in a patient with melanoma demonstrates a large lytic lesion within the left hemisacrum (*arrows*).

In summary, concern regarding metastatic lesions or multiple myeloma is raised when a permeative process is identified in bone in the correct clinical setting.

HEMANGIOMA

Hemangiomas of bone can have a variety of appearances. However, when a hemangioma is located in the spine, the trabeculae hypertrophy in a uniform and organized pattern. Such trabecular thickening has been likened to the appearance of vertical striations, yielding a "corduroy" or "jail cell" appearance. In general, hemangiomas contain some fat within the lesion. This can be seen as low density on CT adjacent to the trabecular struts (Fig. 21-7). The organized appearance of the striations is unique to hemangioma, whereas the trabecular thickening that occurs in plasmacytoma is disorganized. Hemangiomas can be located anywhere within the vertebral body and are worth reporting even though they occur so commonly. Review of the CT examination by a clinician may raise a concern that the hemangioma is something more sinister.

Hemangiomas can also involve the cortex of bone. When this condition occurs, it is generally a result of a vascular malformation and not necessarily a hemangioma. The cortex of the involved bone will exhibit "holes" that are well defined. On cross-sectional imaging, involvement of the cortex versus involvement of the medullary space is easily determined. A vascular malformation involving the bone cortex can be readily distinguished from a permeative process that involves the medullary space indicating an aggressive lesion. The cortical holes are a result of vessels tunneling through the cortex. Sometimes phleboliths can be seen in association with hemangiomas, and these calcifications can be helpful in making the diagnosis.

FIGURE 21-3 ■ Endosteal scalloping. The inner margin of the cortex is scalloped secondary to a noncalcified cartilage lesion that proved to be benign on biopsy.

SCHMORL NODES

Schmorl nodes are commonly encountered in routine CT imaging. These entities are not truly nodes but are rather herniation of disk material through the end plate of a vertebral body (Fig. 21-8). On CT axial imaging, a Schmorl node can occasionally be difficult to characterize and may mimic a lytic lesion. A helpful observation in determining if a lesion is a Schmorl node is to recognize that the end plate must be involved. A Schmorl node can occur in any portion of the vertebral body as long as it involves the end plate but is most often seen in the center of the vertebral body. A lateral scout film or conventional x-ray may be helpful in determining the presence of a Schmorl node. The intervertebral disk is avascular. Therefore after administration of contrast, there is no enhancement of a Schmorl node.

TARLOV CYSTS

Tarlov cysts are nerve sheath dilatations. As mentioned in Chapter 20, the density usually allows adequate distinction of a Tarlov cyst from a disk fragment. If a Tarlov cyst becomes large enough, and particularly when located in the sacrum, it can lead to bone erosion due to the pressure effect of pulsation of cerebrospinal fluid (CSF) and the presence of the cyst (Fig. 21-9). Recognition of this process is important to avoid a biopsy. The margins are well defined, and the density of the lesion immediately adjacent to the excavated bone is that of CSF. A soft-tissue mass causing bone erosion has a higher density than that of CSF. In general, the findings are straightforward. However, if CT imaging is not diagnostic, magnetic resonance imaging (MRI) is strongly indicated before an attempt to perform a biopsy. MRI will show the fluid nature of the lesion. There is no bone marrow edema associated with Tarlov cysts

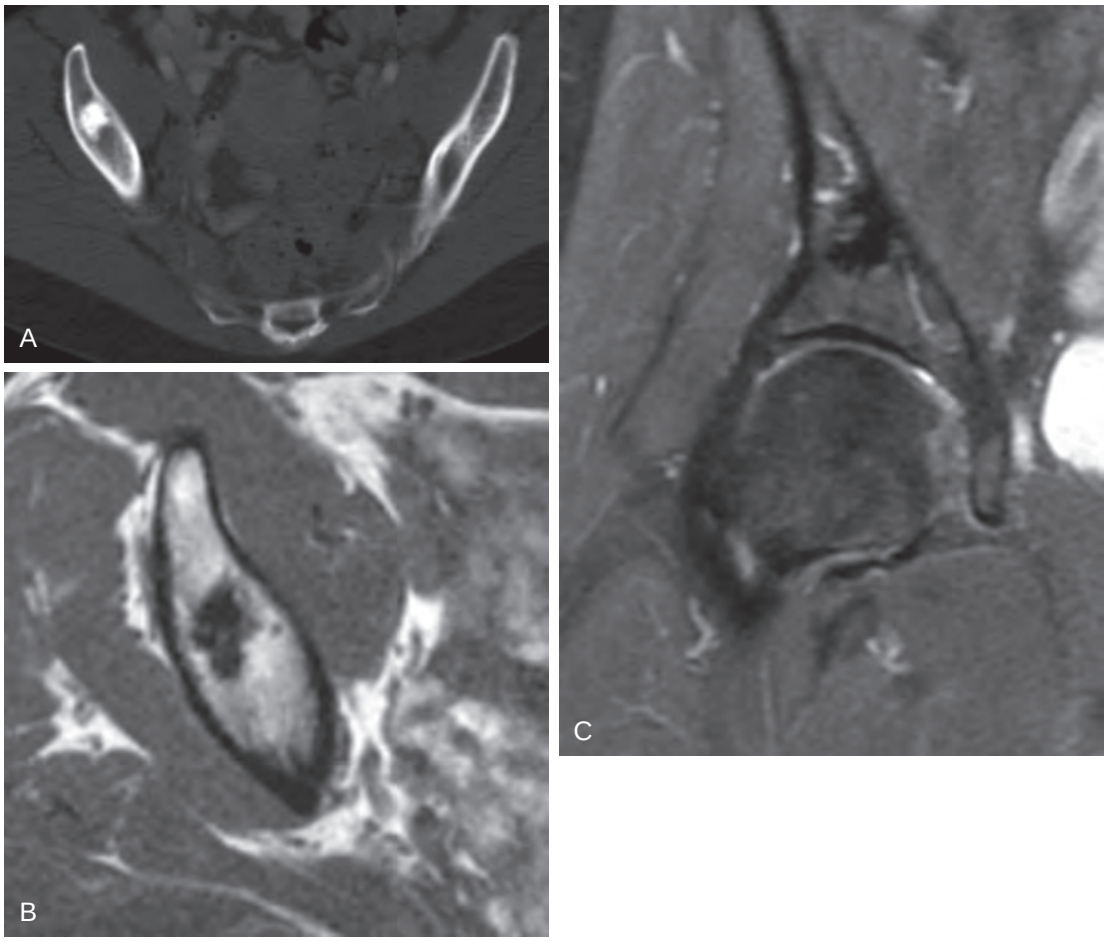

FIGURE 21-4 ■ Bone island. *A*, Axial computed tomography (CT) through the pelvis demonstrates a sclerotic lesion with stellate margins extending into the marrow of the right supra-acetabulum. *B*, axial and, *C*, Coronal T1- and fat-suppressed T2-weighted magnetic resonance imaging demonstrates a low-signal lesion corresponding to the sclerotic focus on CT. A bone island (enostoma) is a hamartoma of bone.

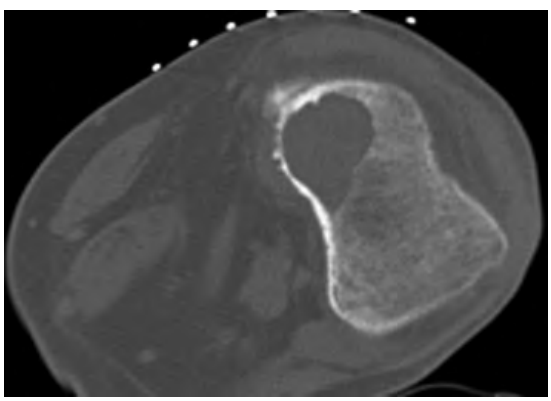

FIGURE 21-5 ■ Giant cell tumor. Axial computed tomography of the proximal tibia demonstrates a lytic lesion with an associated soft-tissue component adjacent to the lesion. This proved to be a giant cell tumor. Benign lesions can have associated soft-tissue masses. This finding is not helpful in distinguishing a benign from a malignant lesion. The metallic markers on the skin surface are in preparation for biopsy.

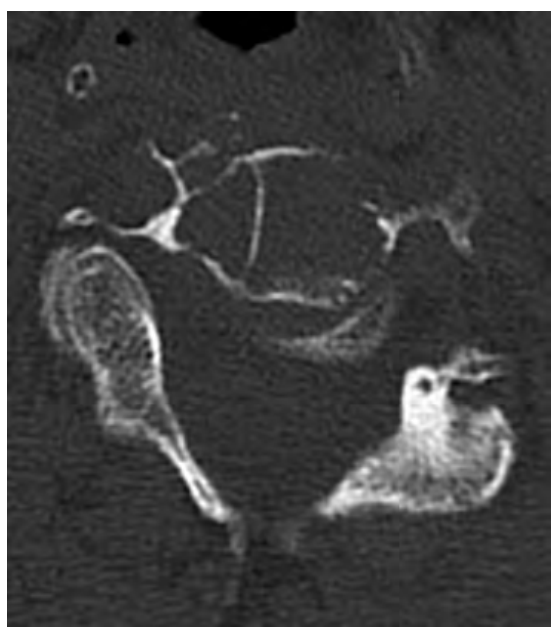

FIGURE 21-6 ■ Plasmacytoma. An axial image through a vertebral body in the cervical spine demonstrates a lytic lesion. There is sparing of a few bony trabeculae in a linear fashion.

FIGURE 21-7 ■ Hemangioma. Axial computed tomography through a thoracic vertebral body demonstrates a well-defined lesion with fat attenuation and punctate foci representing a linear pattern of trabeculae that is characteristic of hemangioma.

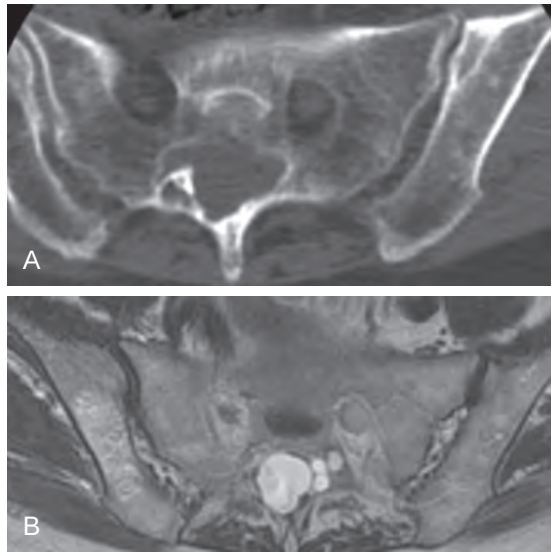

FIGURE 21-9 ■ Tarlov cyst. *A*, Axial computed tomography through the pelvis demonstrates a mass contiguous with the thecal sac with the same density as that of cerebrospinal fluid (CSF). There is bone erosion, a finding that can be seen with pressure effects and long-standing (per Webster's) processes. *B*, The corresponding axial T2-weighted image demonstrates a signal of CSF intensity, verifying that the lesion is a Tarlov cyst.

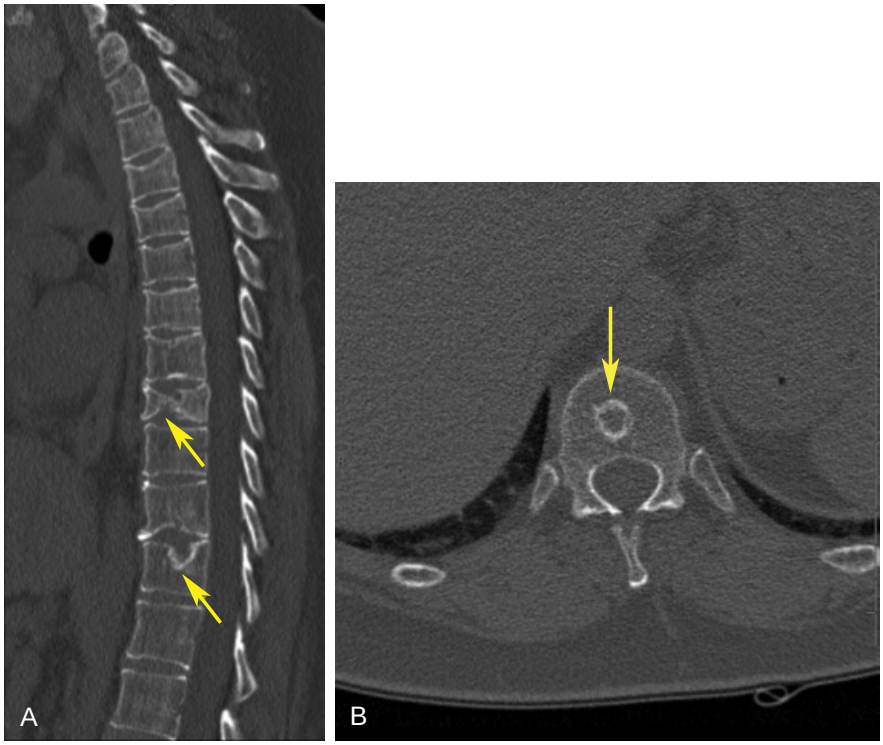

FIGURE 21-8 ■ Schmorl node. *A*, Sagittal reformatted computed tomography demonstrates a scalloped appearance of the end plate (*arrows*) and disk herniation into the end plate. *B*, An axial image through the vertebral body demonstrates the appearance of the "node" with smooth sclerotic borders. In this example the finding is in the central vertebral body (*arrow*).

on MRI. A pelvic mass or sacral tumor eroding into the bone may have an associated finding on MRI of bone marrow edema or a soft-tissue mass.

PAGET DISEASE

Paget disease is an abnormality not infrequently encountered, although it seems to be declining in prevalence. Paget disease can affect any bone in the body and has different appearances. The condition may be purely lytic, in which case it has a well-defined leading edge. The disease can also be purely sclerotic, or mixed lytic and sclerotic. Paget disease has associated findings of bone overgrowth, cortical thickening, and trabecular thickening. The trabecular thickening is not organized as in a hemangioma, making it relatively easy to distinguish from a hemangioma. In addition, accompanying cortical thickening is present, which is not seen with hemangiomas. Paget disease can be distinguished from multiple myeloma by the cortical thickening and bone overgrowth, findings not seen in multiple myeloma (Fig. 21-10). In long bones, Paget disease generally begins at one end of the bone at the articular surface and migrates to the other end. In the pelvis, a more common location of Paget disease, there may be thickening of the iliopectineal and or ilioischial lines, but this is not always the case. It seems that the greatest confusion arises when imaging a patient for prostate carcinoma and a blastic process is encountered in the pelvis. Assessment for additional findings such as cortical thickening, trabecular thickening, and bone enlargement may help to distinguish Paget disease from other blastic processes including metastatic disease from prostate carcinoma.

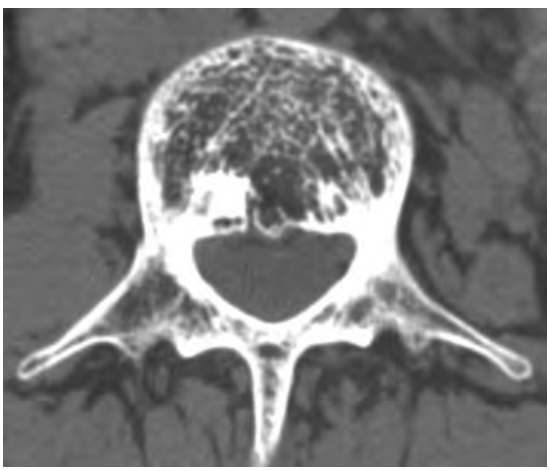

FIGURE 21-10 ■ Paget disease. Axial computed tomography through the lumbar spine demonstrates trabecular thickening and mild bone overgrowth.

FIBROUS DYSPLASIA

Fibrous dysplasia (FD) is a congenital disorder of bone leading to the presence of fibrous and chondral tissues and even cysts within the lesion located within the bone marrow. Because of these different tissue types, FD can have a wide variety of appearances on CT. In general, FD is asymptomatic and is therefore an incidental finding. FD is a well-defined lesion that is occasionally associated with thickened cortices but does not exhibit the trabecular thickening or bone enlargement of Paget disease (Fig. 21-11). Calcifications may be seen within the lesion,

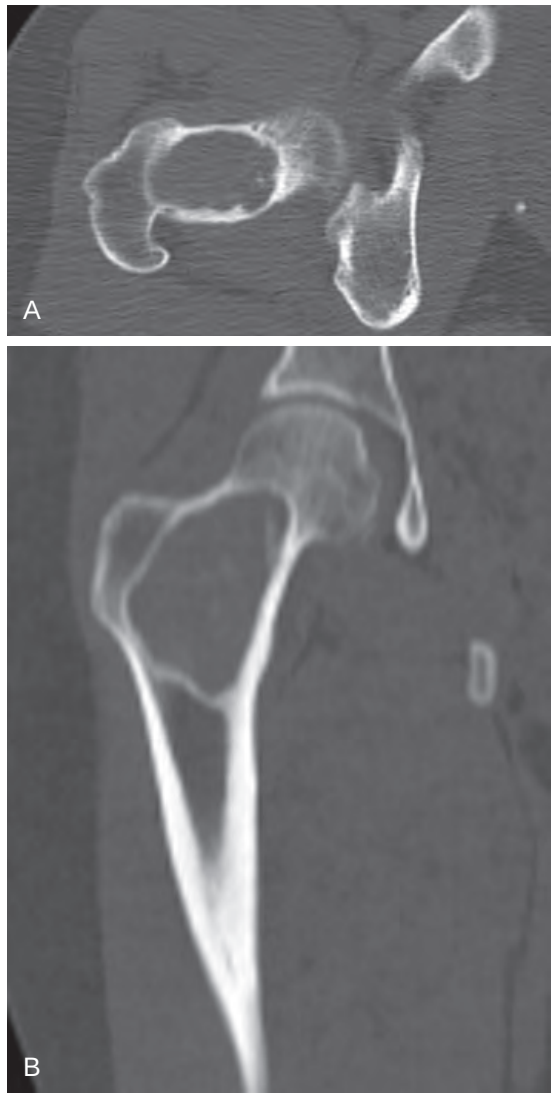

FIGURE 21-11 ■ Fibrous dysplasia. *A,* An axial image through the right intertrochanter region demonstrates a well-defined lesion with a sclerotic margin, indicating a benign entity. *B,* A coronal reformatted image shows the well-defined nature and extent of the lesion. The appearance in this location is characteristic of fibrous dysplasia.

caused by the chondral elements reported in 10% to 30% of FD lesions. There may be associated endosteal scalloping, because FD is a medullary-based process, or a sclerotic border, particularly if FD occurs in the intertrochanter region. In summary, FD appears similar to many conditions on CT, but the lesion will not look aggressive. There will be no associated soft-tissue mass, permeative appearance, or periosteal reaction (unless a pathologic fracture is present). If a soft-tissue mass is encountered or periosteal reaction is present (without identification of a fracture) in association with the bone lesion, FD is not the diagnosis.

In general, for bony lesions encountered during CT that cannot be diagnosed clearly, conventional radiography can be useful for further evaluation. As a rule, when evaluating primary lesions of bone, conventional radiography is the ideal way to distinguish a benign from an aggressive process. CT should be used only to evaluate the matrix of the lesion. Thus, when CT is performed and lesions are encountered, conventional radiography is extremely helpful for characterization of lesions.

ENCHONDROMA

An enchondroma is typically centrally located within bone and in long bones is associated with a chondroid matrix. The typical appearance of a chondroid matrix comprises calcified arcs and circles resembling the letters C and O (Fig. 21-12). An enchondroma can be associated with endosteal scalloping. Enchondromas are painless lesions and are identified incidentally. Enchondromas can occur in any bone.

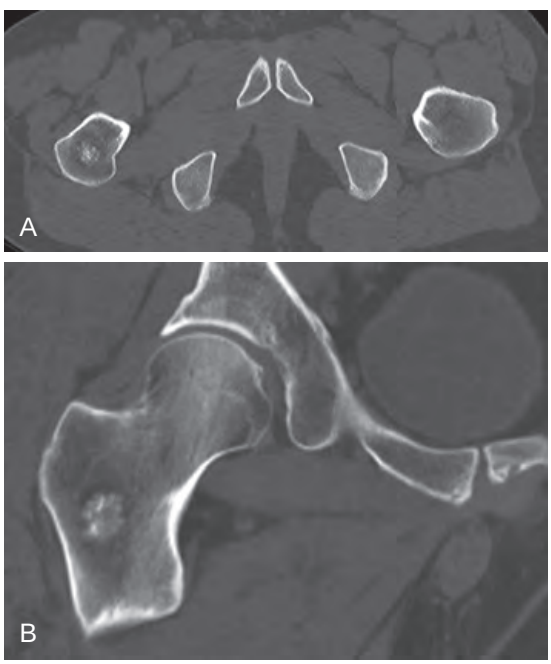

FIGURE 21-12 ■ Enchondroma. *A*, Axial and *B*, coronal reformatted computed tomography demonstrates a lobular, calcified lesion in the central medullary canal of the proximal right femur. The calcified matrix has the appearance of arcs and circles typical of a chondroid matrix. These are painless lesions.

AVASCULAR NECROSIS

Avascular necrosis (AVN) is a progressive process leading to bone death. MRI and conventional x-rays are utilized for staging and diagnosis. CT plays little role in AVN diagnosis. When AVN is identified on CT, curvilinear sclerosis in a subarticular location is pathognomonic. Subchondral lucency is a late finding in AVN. MRI is sensitive and specific for this diagnosis and is recommended for evaluation and grading. MRI may reveal AVN not detected by normal CT and conventional x-rays (Fig. 21-13).

CONCLUSION

In summary, although all possible lesions cannot be reviewed in this chapter, some helpful tips have been provided for commonly encountered lesions. Primary lesions of bone are best characterized on conventional radiographs. If an

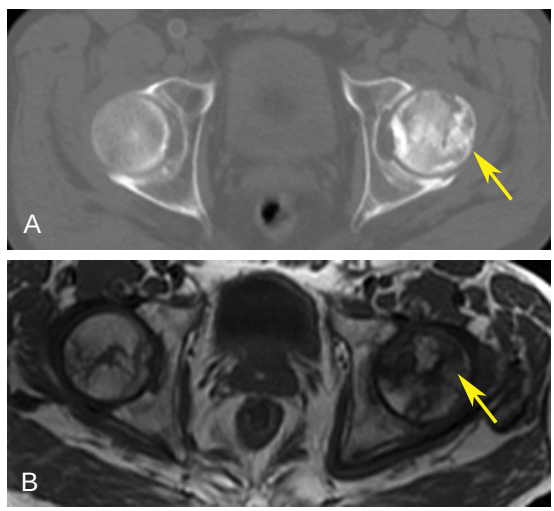

FIGURE 21-13 ■ Avascular necrosis (AVN). *A*, Axial computed tomography (CT) through the femoral heads demonstrates sclerosis and subchondral lucency in the left femoral head diagnostic of AVN (*arrow*). *B*, Axial T1-weighted magnetic resonance imaging demonstrates a curvilinear, low-signal lesion corresponding to the sclerosis and subchondral lucency observed on CT. Note the low signal within the right femoral head corresponding to AVN of the right femoral head that is not appreciated on the CT (*arrow*).

incidental lesion is encountered on CT, the radiologist should assess the margins and potential matrix and, if necessary, correlate the findings with conventional x-ray observations to avoid unnecessary biopsies.

SUGGESTED READING

Matamedi K, Ilaslan H, Seeger LL: Imaging of the lumbar spine neoplasms. *Semin Ultrasound CT MRI* 25:474–489, 2004.

Resnick D: *Diagnosis of bone and joint disorders*, ed 4, vol. 3. Philadelphia, PA, 2002, Elsevier, pp 2203–2205. (2718–2721.

Rodallec MH, Feydy A, Larousserie F, et al.: Diagnostic imaging of solitary tumors of the spine: What to do and say. *Radiographics* 28: 1019–1041, 2008.

Whitehouse RW: Paget's disease of bone. *Semin Musculoskelet Radiol* 6:313–322, 2002.